YOVZA

Construction *Simplified*

Advances in Building Technologies and Construction Materials 2018

Lead Guest Editor: João M. P. Q. Delgado
Guest Editors: Robert Cerný, Antonio Gilson Barbosa de Lima, and Ana S. Guimarães
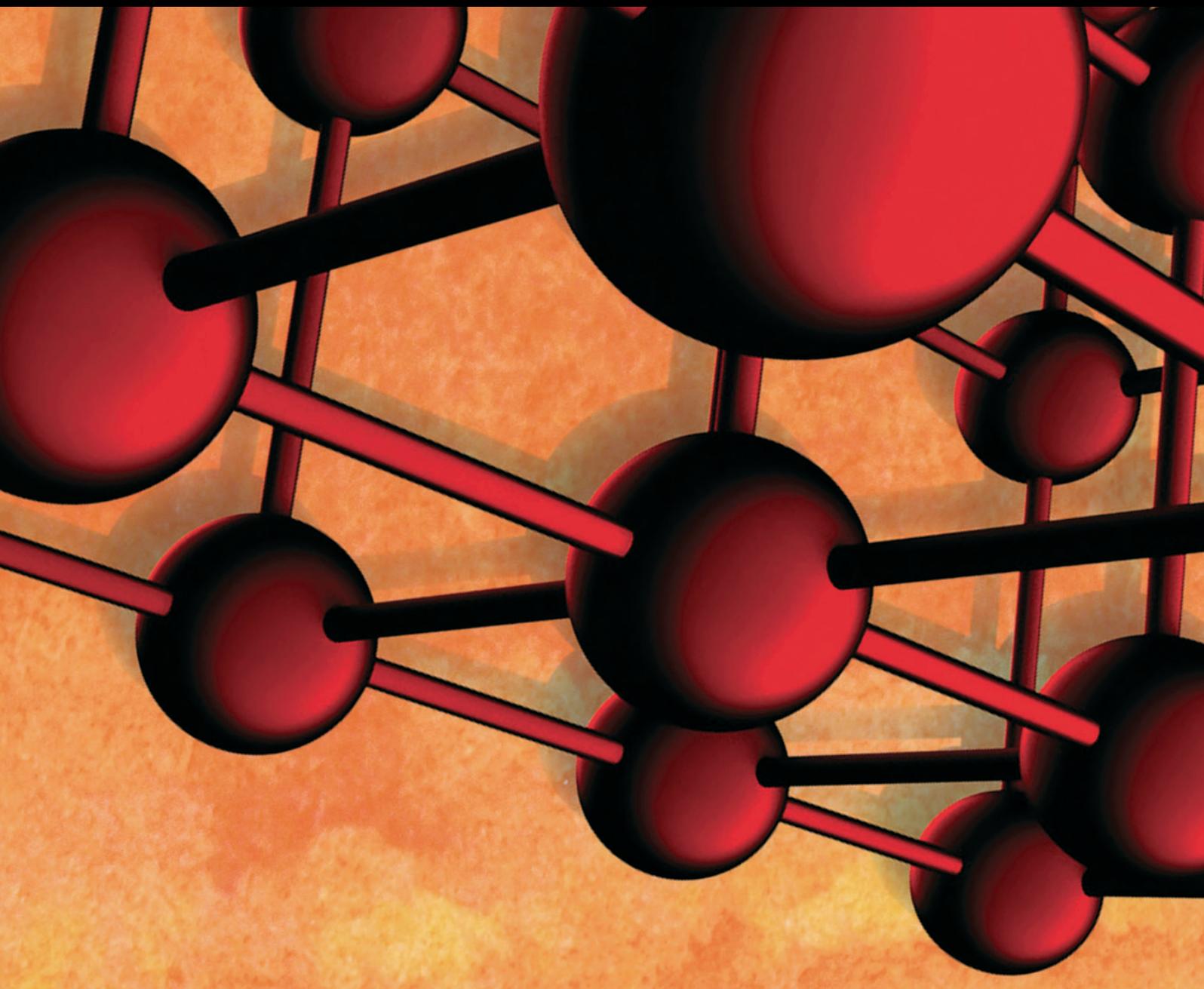
Advances in Building Technologies and Construction Materials 2018

Advances in Building Technologies and Construction Materials 2018

Lead Guest Editor: João M. P. Q. Delgado
Guest Editors: Robert Cerný, Antonio Gilson Barbosa de Lima, and Ana S. Guimarães

Contents

Editorial

Advances in Building Technologies and Construction Materials 2018

J. M. P. Q. Delgado [iD],[1] **Robert Černý,**[2] **A.G. Barbosa de Lima** [iD],[3] **and A. S. Guimarães** [iD][1]

[1]*CONSTRUCT-LFC, Faculty of Engineering, University of Porto, Rua Dr. Roberto Frias, s/n, 4200-465 Porto, Portugal*
[2]*Department of Materials Engineering and Chemistry, Faculty of Civil Engineering, Czech Technical University in Prague, Thákurova 7/2077, 166 29 Prague 6, Czech Republic*
[3]*Department of Mechanical Engineering, Federal University of Campina Grande, Av. Aprígio Veloso, 882, 58429-900 Campina Grande, PB, Brazil*

Correspondence should be addressed to J. M. P. Q. Delgado; jdelgado@fe.up.pt

The development of civil engineering in the course of centuries meant a constant struggle with available materials, spans, or height, active loads, and the forces of nature: water, fire, wind, and earthquakes.

While construction activities improve the quality of human lives, they also have significant impact on the environment. The production of construction materials requires energy and generates greenhouse gases. Low-cost or affordable construction technologies and building materials are often pushed as a magic potion in meeting the ever-growing demand for rapid housing delivery in developing economies. New advanced materials offer opportunities to change the way in which we construct and retrofit buildings. They give added value in terms of increased performance and functionality. The reduction of carbon footprint for construction materials can start at the production phase, where energy-efficient processes can be developed and waste or recycled materials can be employed. New materials can also help address the new challenges of durability in a changing climate.

This special issue is the result of the huge success presented by previous special issues of the same topic, and as the previous special issues had a great acceptation by the scientific community with 61 papers submitted and 26 papers accepted for publication.

A considerable number of experimental and numerical papers address new research advances and applications in the concrete material. J. Yue presents a numerical model to analyse the multilevel nonlinear mechanism of the reinforced concrete framed structures in five structural levels. Based on the presented deformation equivalent principle, a generalized stiffness damage model was developed for each structural level. An impact factor was proposed to reflect the damage correlations between different structural levels. In order to verify this method, the proposed method was used to study the damage evolutions at various structural levels of a 12-storey frame structure. Zhao et al. present an extension of Balshin's model to develop a prediction model of compressive strength for three types of high-porosity cast-in-situ foamed concrete (cement mix, cement-fly ash mix, and cement-sand mix) with dry densities of less than $700 \, \text{kg/m}^3$. Zhao et al. present the development of steel fiber-reinforced expanded-shale lightweight concrete (SFRELC) with high freeze-thaw resistance. Based on the test results, suggestions are given out for the optimal mix proportion of SFRELC to satisfy the durability requirement of freeze-thaw resistance. M. J. Kim and K. Y. Ann evaluate the corrosion risk of internal chloride and external chloride from three different exposure conditions. They concluded that an increase of the drying ratio in the exposure condition resulted in an increase of the corrosion rate after initiation. Also, the authors predicted the chloride penetration with different exposure conditions to determine the service life of the reinforced concrete structure. Lee et al. investigate experimentally the dowel behaviour of rebars in small concrete blocks for the sliding slab track on railway bridges. This work can be useful

for developing a more rational model to represent the actual dowel behaviour of the rebars embedded in small concrete blocks. Gu et al. investigate the macroperformance and microstructure of ultrahigh-performance concrete (UHPC) before and after the freezing-thawing action. They show that UHPC possessed very excellent freezing-thawing resistance due to its dense microstructure. After the freezing-thawing action, cracks occurred, and the authors considered that the mismatch of the thermal expansion coefficients of the aggregate and the paste is the reason for the cracking at the sand-paste interface. Yan et al. investigate the mechanical properties, the mesodamage properties, and the micro-properties of cement-emulsified asphalt in plastic concrete by computed tomography, scanning electron microscopy, X-ray diffraction, and thermogravimetric analysis. X. Yang and H. Wang analyse, experimentally, the seismic behaviour of rammed earth walls with precast concrete tie columns. Luo et al. present the development of a new structural material named "steel fiber polymer structural concrete (SFPSC)" with features of both high strength and high toughness and its application to bridge superstructures, in hot-wet environments.

The chemical attack of concrete structures and other building materials is analysed in detail by some authors. S. I. Hong and K. Y. Ann present a study to assess the service life of concrete structures exposed to the tidal zone with the proposed numerical model for predicting the moisture and chloride transport in concrete. Wang et al. study numerically and experimentally the behaviour of the calcium silicate board metallic-framework drywall assembly with a junction box. This is innovative research that put forward, in first time, the quantitative research on influence of the embedded junction box on fire resistance of metal frame walls and analyzes the weakness.

Besides those, there are several interesting topics in the issue of cement materials. Rubia et al. present the preparation of cement pastes with simultaneous functional additions (micro- and nanosilica and nanozinc oxide) by a novel low shear rate dispersion method, in order to avoid health risks. They concluded that the common manual mixing method and the novel method presented a similar hydration behaviour of the different cement pastes prepared, but the novel method avoided the exposure to the nanoparticles, therefore minimizing health risks. H. Yang and Y. Che analyse the effects of nano-$CaCO_3$/limestone composite particles on the hydration products and pore structure of cementitious materials. Kim et al. investigate the rheological properties of blended cement pastes using a rotational viscometer and a dynamic shear rheometer. The results showed that the rotational viscometer can be used to study the flow characteristics of cement pastes with or without mineral admixtures. Tongyuan et al. present a series of experiments on restriction-induced cracking behaviours as well as free shrinkage, water loss, and mechanical properties of dry-mixed plastering mortar (DMPM), in order to evaluate the cracking resistance of DMPM and analyse the influence of environmental conditions on the cracking tendency of DMPM.

Another important issue is the ecology of building materials. Gómez-Balbuena et al. present the technological application of the solid waste resulted from the activities of carved Quarry extraction in a new polymeric material with properties similar to those of a traditional mortar. They concluded that the polymeric material uses low amounts of cement with respect to the traditional mortar, and it is elaborated with the recycled quarry as they are presented in its granulometry. Al-Khateeb et al. evaluate the use of a waste stone sawdust filler with asphalt binders and compare the mechanical properties of the waste filler-asphalt mastic with those of the asphalt mastic produced using the typical limestone filler. Estévez-Cimadevila et al. study the bending behaviour of T-section beams composed of a glulam web and an upper cross-laminated timber flange. The variation in the stiffness depended on the relation between the compressive and tensile moduli of elasticity parallel to the grain, and its influence on the deflection was analysed using a finite element method. Li et al. study the deterioration mechanism of recycled plaster (R-P). The large specific surface area (SSA), improper preparation temperature, increased water requirement of R-P, and microstructure of its hardened body were analysed. Zhou et al. propose a new connector for the bamboo (timber) frame joint based on a comprehensive analysis of the mechanical performance of several wood connections. The authors, also, proposed a simplified moment-rotation hysteresis model for the joint.

Studies on soils are presented by J. Zhai and X. Cai, who analyse the physical and mechanical characteristics of expansive soils from Pingdingshan (China), which provide a reliable basis for engineering design and can be used in the calculation of slope stability. The finite element method was used to calculate the different positions of the soil slope layers and select the corresponding strength parameters. Lu et al. analyse the influence of cumulative plastic strain, dry-wet cycles, and amplitudes on the soil resistivity. A new damage factor based on resistivity is proposed to evaluate the long-term performance of the compacted clay material. The results show that the dry-wet cycles and amplitudes have a significant effect on the damage of the compacted soil, which indicates that the dry-wet cycling of compacted soil materials should not be ignored in road engineering, especially in rainy and humid areas. Hua et al. present the use of four derived acceleration indexes to characterize the soil compaction degree, including the acceleration peak value, acceleration root mean square value (arms), crest factor value, and compaction meter value. A two-part field compaction test was performed to analyse and judge the test effects of the four indexes on the rockfill and other dam materials. Gao et al. propose a comprehensive chemical grouting construction technology, which comprises initiative closing, concentrated bypass flow, water plugging priority, and twice sand curing for the inclined shaft passing over the drift-sand layer. This engineering application effect is very prominent in controlling water burst and leakage at the drift-sand layer, in mine constructions.

Finally, Wang et al. present a finite element analysis and lightweight optimization design of the main frame structure of a large electrostatic precipitator, and Çıra et al. analyse the effects of material properties of marble on surface roughness and glossiness (surface quality).

We hope that readers of this special issue will find not only accurate data and updated reviews on the building technologies and construction materials field area but also important questions to be resolved. This special issue includes both theoretical and experimental developments, providing a self-contained major reference that is appealing to both the scientists and the engineers. At the same time, these topics will encounter a variety of scientific and engineering disciplines, such as chemical, civil, agricultural, and mechanical engineering.

J. M. P. Q. Delgado
Robert Černý
A. G. Barbosa de Lima
A. S. Guimarães

Research Article

New Chemical Grouting Materials and Rapid Construction Technology for Inclined Shaft Penetrating Drift-Sand Layer in Coal Mine

Xicai Gao [iD],[1] **Xinyu Wang,**[2] **and Xiangdong Liu**[3]

[1]*Key Laboratory of Western Mine Exploitation and Hazard Prevention, Ministry of Education, Xi'an University of Science and Technology, Xi'an, Shaanxi 710054, China*
[2]*College of Civil Engineering, Henan Polytechnic University, Jiaozuo, Henan 454000, China*
[3]*Shanghai Miwei Mining Technology Co., Ltd., Shanghai 201100, China*

Correspondence should be addressed to Xicai Gao; gxcai07@163.com

Drift-sand layer is a common weak stratum in mine construction. The construction of the shaft passing over the drift-sand layer is very difficult. Traditional construction method faces many problems such as long construction period, high construction cost, poor working environment, and uncontrollability of the support effect. In view of the loose and fragile rock mass with great deformation of sinking and driving engineering penetrating drift-sand layers in coal mine, the reaction mechanism and shortcomings of conventional chemical grouting materials were analyzed. New-type polymer grouting materials were prepared with catalysts and vinyl epoxy resin, which was made from epoxy resin. A comprehensive chemical grouting construction technology was proposed, which comprises initiative closing, concentrated bypass flow, water plugging priority, and secondary sand curing for the inclined shaft passing over the drift-sand layer. Results show that new-type polymer sand-cured materials have lower viscosity, better grout ability, and fire resistance, and the solidified material has stronger bonding strength and better deformation resistance compared with traditional chemical grouting materials. The engineering application effect is very prominent in controlling water burst and leakage at the drift-sand layer; thus the on-site comprehensive construction progress and safety are guaranteed.

1. Introduction

With the increasing depth of underground coal mine and the deterioration of engineering geologic environment, weak or harmful strata (i.e., water burst, drift sand, and sludge) are frequently encountered and easily result in roof collapse, caving and deformation of permanent supports, thus presenting great difficulty for mine construction [1, 2]. Joints, mining-induced fractures, and poor geologic structure in surrounding rock mass provide good groundwater courses for groundwater, which often results in the abrupt increase of mine and water disasters and brings tremendous challenges for construction progress and safety [3]. Grouting consolidation technology has become the main method of controlling water burst disaster in the underground coal-mining projects [4, 5].

Traditional particle-type grouting materials (e.g., cement-water and glass-type grouting materials) easily become diluted and dispersed under water-flowing conditions because of their poor grout ability and cannot meet the engineering requirements [6]. So, the chemical grouting materials with lower viscosity, better liquidity and grout ability into microfissures, and adjustable range of curing time have been widely applied to the management of underground coal mine water bursts. The chemical grouting materials such as polyurethanes, urea resin, and epoxy resin are used commonly in grouting reinforcement projects. The polyurethane grouting materials have been widely applied because of their volume expansion and plastic deformation when curing. However, these materials have obvious defects, such as higher viscosity, weaker fire resistance, and

strength reduction, caused by foaming and reacting with water. Especially during the reaction with water, they release hazardous gas and bring serious harm to human health [7–11]. Urea resin is a water-dilatable resin produced by the reaction of urea with formaldehyde. It has the advantages of lower cost and viscosity, but its adhesive property and induration strength are weak. Moreover, urea resin decomposes with water, and a large quantity of free formaldehyde separates out, polluting the environment [12]. Conventional chemical grouting reinforcement materials have defects such as toxicity, high viscosity, weak grout ability, lower strength, and poor anticorrosion and fire resistance, and these defects restrict the large-scale engineering application. Because of the high TDS (total dissolved solid) and corrosive components in mine groundwater, the conventional chemical grouting reinforcement cannot meet permanent supporting requirements penetrating drift sands in the shaft, which will affect construction progress and safety in production.

Aiming at the special geologic conditions of sinking and driving engineering passing through the drift-sand layer, the polymer two-component chemical grouting materials and pregrouting construction technology, which have the functions of both water plugging and consolidation were put forward. Thus, the water burst passing over the drift-sand layer under complicated conditions was effectively controlled, and the shaft construction progress and safety were ensured.

2. Materials and Experimental Methods

A new type of the vinyl epoxy resin material is the compound organic grouting material, which consists of components A and B. Component A consists of epoxylite and an accelerant according to a certain proportion, and component B consists of epoxylite and a curing agent according to a certain proportion. The control of reaction progress and curing time is realized by adjusting the amount of component B. The basic components of epoxylite include A-type E-51 epoxy resin, unsaturated carboxylic acid, reaction-type fire retardant, catalyst, polymerization inhibitor, and chemical cross-link agent. These components were sufficiently stirred in a flask with a mixer, thermometer, and rectifying tower. The pale yellow epoxy resin grouting materials were obtained after gradual warming, cooling, and filtering. The epoxy resin components are listed in Table 1.

2.1. Viscosity.
The grouting material was prepared by mixing components A and B with a standard matching ratio, and the viscosity under different temperature conditions was measured by a viscometer (NDJ-9S digital viscometer). The results show that the viscosity under ambient temperature (25°C) is 80~100 MPa·s, and the value slightly increases with the decrease of temperature. The chemical grouting viscosity is 150~300 MPa·s under 5°C. The viscosity can be regulated by changing the standard matching ratio of components A and B.

2.2. Curing Time.
A two-component grouting material was selected. Components A and B were mixed based on

Table 1: Formula design of epoxy resins.

Raw material	Mass percentage
Epoxy resin	30~45%
Unsaturated monocarboxylic acid	5~20%
Fire retardant	10~20%
Catalyst	0.15~0.35%
Polymerization inhibitor	0.01~0.09%
Chemical cross-link agent	30~45%

Table 2: Main characteristics of the chemical grouting material.

Category	Material characteristics
Density	1.3 g/cm^3
Viscosity (25°C)	80~100 MPa·s
Point of flammability	>185°C
Flame-retardant property	MT113-1995 standard
Response time	2 min~200 min
Setting time	10 min~250 min

a certain proportion. The initial viscosity measured under ambient temperature condition (25°C) was 100 MPa·s. The curing speed can be accelerated with the addition of a curing agent and an accelerant. The ratio of the curing agent and accelerant can be adjusted within 0.25%~4%. The polymerization reaction time of the mixture can be adjusted between 2 min and 200 min, and the curing time can be adjusted between 10 min and 250 min. The main characteristics of the chemical grouting material are shown in Table 2.

A two-component (resin component A and catalyst component B) epoxy resin grout and a chemical additive were prepared with a ratio of 1.5 : 1. A certain amount of sand with moisture content being 1.85% and particle size being 0.2~0.5 mm was selected and put into a plastic pot. The prepared chemical grout was poured into the pot and sufficiently mixed with the sand before standing for four hours. And then, a cured mass of the resin grout was formed. An autocore drilling machine and a cutting machine were used to process the resin grout mass to the standard cylindrical specimen (i.e., the specimen diameter is 50 mm and the length is 100 mm). The universal compression testing was conducted by using the rock mechanic system (MTS Corporation, USA), and the physical and mechanical properties and the stress-strain curve of the cured material were obtained according to the international rock mechanic test standard. The stress-strain curve is shown in Figure 1; the main rock mechanical properties of the cured material are determined and listed in Table 3.

The test results show that the resin grout and sand are cemented into a compact structure after being cured. The macroscopic structure is featured by a stronger bearing capacity, and the compressive strength reaches 10.3~13.1 MPa. The product generated by the resin grout and sand has a stronger plastic deformation capacity and an evident Poisson's ratio effect.
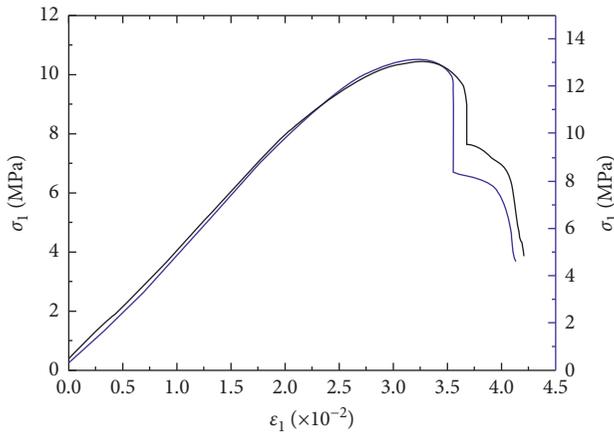
Figure 1: Stress-strain curves of the solidification material.

Table 3: Main properties of the cured material.

Category	Mechanical characteristics
Density	1.6938 g/cm^3
Compressive strength	10.38~13.09 MPa
Strength of extension	0.32~0.53 MPa
Elasticity modulus	401.37~490.64 MPa
Poisson's ratio	0.447~0.846
Cohesion	0.866 MPa
Internal friction angle	49.38°

3. Engineering Application of Chemical Pregrouting

3.1. Project Overview. Songxinzhuang mine is a newly constructed mine, with a production capacity of 1.2 million t/a and a designed service life of 59 years. The geologic data and geologic report indicate that the vice inclined shaft is 630 m long and passes through the quaternary stratum and tertiary stratum. The quaternary stratum mainly has wind-borne sand and floury soil with a thickness of about 1.6~3.75 m. Half-agglutinating clay and argillaceous substance contain a large quantity of silt and fine sand. The engineering geological conditions are poor. Moreover, hydrogeological conditions in this mining area are complicated. The shaft construction process is frequently under water burst influence from the confined aquifers of the Jurassic Zhiluo rock mass group and Yan'an rock mass group.

The section of the vice inclined shaft passage is a vertical-wall semicircular arch with a net width of 4400 mm, a net height of 3800 mm, and a net section area of 14.6 m^2. The preliminary support pattern at the drift-sand segment adopts reinforced concrete support, lay rubble mortar, and reinforced concrete-hardened baseboard. The vertical-wall semicircular arch was adopted reinforced support with the concrete thickness being 400 mm and the strength grade of the concrete being C30. Flagstone mortar metal net concrete pouring of the roadway baseboard is conducted with a bedding thickness of 600 mm and a flagstone strength not less than MU30. The upper concrete thickness is 200 mm, and the total bedding is

800 mm. The strength grade of the bedding concrete is C20. A reinforcing steel bar adopts a Φ 20 mm deformed steel bar. Two adjacent reinforcing steel bars are lapped by welding. The preliminary support section is shown in Figure 2.

The drift-sand layer of the vice inclined shaft project first appeared on September 15, 2010, at the location 58.3 m. The sandstone layer is quite soft and loose and will easily drop down when meeting water. This sand layer contains loess, which forms liquid yellow mud. The delaminating and wall caving phenomena are seen after layer tunneling, which is accompanied by a water inflow of 25 m^3/h. This results in wall caving, roof caving, and the sinking and deformation of permanent support. And the average excavation footage per day is 0.82 m because of the construction conditions of sinking and driving engineering.

Figure 2: Preliminary supporting section.

3.2. Multistep Grouting Construction Technology. Considering the above specific engineering geological conditions, the multistep pregrouting and rapid construction technology is used for construction of the shaft according to the experience of water prevention and control in nearby mines.

The shaft construction reveals that the seepage channels of surrounding rocks are mainly holes with weak permeability. The alkaline water has a negative influence on the reaction of the grout and the durability of curing materials.

The compound chemical grouting materials (i.e., sand curing material MGS and water plugging material Midwest213) with lower viscosity and controllable curing time are selected. The sand curing material MGS also has other advantages such as higher safety without aldehyde, acid and alkali resistance, and fire resistance; thus, MGS is applicable in an aquifer of sandstone, which is rich in soluble salts, drift-sand layer curing, and water inflow plugging. The relevant technical parameters of chemical grouting materials were shown in Tables 4 and 5.

3.3. Multistep Pregrouting Design Scheme

3.3.1. Distributed Grouting and Plugging at Water Bursting Positions of the Shaft. A concrete wall was first constructed

TABLE 4: Main technical parameters of construction chemical grouting.

Category	Two-component ratio	Width of the smallest crack (mm)	Setting time (min)	Resin viscosity (MPa·s)	Catalyst viscosity (MPa·s)
MGS	1 : 1~1 : 2	0.01	10~250	150	50~80

TABLE 5: Main technical parameters of water plugging chemical grouting.

Category	Two-component ratio	Solid content (%)	Dilatation coefficient	Setting time (min)	Resin viscosity (MPa·s)	Catalyst viscosity (MPa·s)
Midwest213	1.5 : 1	100	8~10	2~900	350	150~180

at the driving face in the shaft passing over the drift-sand layer with a thickness of 600 mm. A relief hole was set in the middle bottom of the wall with a hole diameter of 80~100 mm.

In order to leave the grout enough time for reaction and curing before flowing to the relief hole, the grouting holes were drilled using the common electric coal drill from the bottom to the top. A specific method was used for water plugging and drilling at the location where the sealing wall was far away from the water exit along the roadway border, and the chemical grouting material Midwest213 was used for water plugging. And then, the water flow in the drift-sand layer inside the sealing wall was relatively stable.

According to the situation, the grouting drilling depth was preliminarily set as 850 mm. A six-decimeter galvanized pipe was adopted to seal the end. Some 5 mm diameter holes were drilled every other 150~200 mm along the galvanized pipe. The length of the grouting pipe was 950 mm. About 100 mm from the pipe orifice was left outside the concrete wall. Cotton yarn and grout or accelerated cement was used to seal the seam between the grouting pipe and the concrete wall. The layout of the water plugging well location is shown in Figure 3.

Feed pipes of components A and B were plugged into a bucket. When the normal construction was being conducted, it was mixed according to the matching ratio of the grout. During the process of grouting into grouting holes, the best practice was to use low-pressure grouting because the underground water pressure is 0.5 MPa. The grouting pressure was then set within 1~2 MPa, which was same or twice as water pressure, and should be gradually increased. The pressure gauge of the pump and situation of the working face must be given attention. Grouting should be stopped when the value indicated on the pressure gauge of the pump reaches above 2 MPa or grout spillover occurs.

3.3.2. Rapid Curing of Rock Mass Grouting at the Drift-Sand Layer.
The sealing wall was used as a grouting pad at the jointing part between the vertical wall and the concrete shaft at the middle lower part of the sealing wall. The drills were constructed by the common hand drill, and the chemical material MGS was grouted. The location of the one-way valve was confirmed based on the on-site fracture development. The exposure part should not be more than 50 mm. Grouting can be started after confirming that preparation
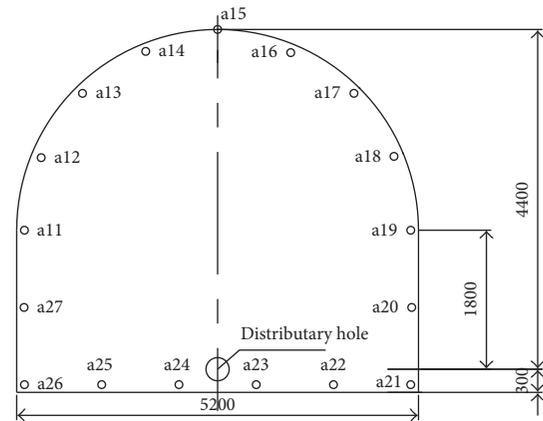
FIGURE 3: Layout of the water plugging well location.

has been made. The layout of the construction well location is shown in Figure 4.

3.3.3. Grout Sealing of Major Jointing Parts of Shaft Secondary Support Concrete.
After the multistep chemical grouting, curing, and water plugging of the shaft were completed, "short excavation and short supporting" construction technology was adopted for shaft excavation. Pipe shed, plank, and meshes were used as the temporary support, and the single reinforced concrete was used as the permanent support.

The supporting template or footage of the monolayer-reinforced concrete of the shaft is generally 0.9 m. Jointing parts between the concrete templates are the weakest parts of the shaft, which usually are the flow channel of groundwater. The grouting technology with shallow holes and high pressure is adopted to seal the jointing parts of the shaft permanent support.

4. Result Evaluation and Discussion

The slant angle of the vice inclined shaft is 6°, and the drift-sand layer thickness is 1.4 m. And the slant length is 13.9 m in the project of the Songxinzhuang coal mine at first. The comprehensive construction method of self-closing, highest-priority water plugging, and secondary sand curing at the drift-sand layer is confirmed. Two liquid compound chemical
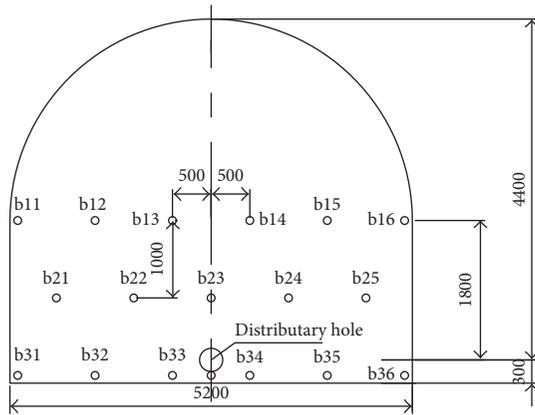
Figure 4: Layout of the construction well location.

grouting materials with lower viscosity and controllable curing time are applied on the sand curing, water plugging, and grouting for shaft passing through the drift-sand layer.

Twelve water plugging and grouting drill holes were set on the sealing wall. The amount of the chemical grout Midwest213 used was 1900 kg. The grouting material quantity for each hole was 158.3 kg. The water inflow of roadway became 1.5 m³/h upon completion. Water flow at the drift-sand layer inside the sealing wall of the shaft was relatively stable. The sealing wall was used as a grouting pad. About 28 holes with a depth of 350 mm were drilled for sand curing construction. The amount of the chemical grouting material MGS used was 3000 kg. The grouting material quantity for each hole was 107.1 kg. A rock sample was drilled after grouting construction was finished to evaluate the grouting effect. No water burst and sand drifting phenomenon and the solidified bodied strength were stronger after the sealing wall was broken. Sand curing and water plugging effects are prominent. Thus, the water burst passing over the drift-sand layer under complicated conditions is effectively controlled, and the normal excavation speed of the shaft is guaranteed.

5. Conclusion

(1) The new vinyl epoxy resin materials are two-component polymer chemical grouting materials with lower viscosity, polymerization reaction, accurate and controllable curing time, and better grout ability. Lower viscosity guarantees the sufficient permeation and diffusion of the grout in rock mass. After curing and expansion, the resin grout is cemented with sand particles into a compact structure. This compact structure is featured by a stronger bearing capacity. Thus, the new chemical grouting materials have a broad application prospect in coal mining.

(2) According to the characteristics of the vice shaft surrounding rock mass in the Songxinzhuang coal mine, the new vinyl epoxy resin of sand consolidation and the water plugging material are specially developed. The comprehensive grouting scheme of initiative self-closing, highest-priority water plugging, and secondary sand curing and rapid construction method are put forward to achieve effective control of water burst at the drift-sand layer under complicated conditions.

Conflicts of Interest

The authors declare that they have no conflicts of interest.

Acknowledgments

References

[1] H. Kang, J. Wand, and J. Lin, "Case studies of rock bolting in coal mine roadways," *Chinese Journal of Rock Mechanics and Engineering*, vol. 29, no. 4, pp. 650–652, 2010.

[2] X. Gao and Y. Wu, "Deformation mechanism and floor heave control technology of roadway in deep-buried full seam chamber," *Coal Science and Technology*, vol. 41, no. 4, pp. 1–4, 2013.

[3] X. Gao and Y. Wu, "Study on water-inrush risk evaluation and control technology in extra thick seam of overburden strata with water-rich," *Safety in the Coal Mine*, vol. 45pp. 54–56, 1, 2014.

[4] Q. Meng, L. Han, and R. Shi, "Study and application of construction technology for inclined shafts penetrating drift sand strata in coal mine," *Chinese Journal of Geotechnical Engineering*, vol. 37, no. 5, pp. 901–909, 2015.

[5] H. Zhang, "Advanced pipe-shed grouting reinforcement technique and application in inclined shaft through drift sand strata," *Mine Construction Technology*, vol. 34, no. 3, pp. 20–22, 2013.

[6] H. Xu, Y. Gao, and Y. Xu, "Application of transformed chemical slurry in water prevention and leakage blocking of the auxiliary shaft in Qianyingzi coal mine," *Coal Geology & Exploration*, vol. 40, no. 3, pp. 55–57, 2012.

[7] Z. Yang, Y. Sun, X. Guan, and C. Zhang, "Preparation and properties of novel silicate-based inorganic/organic composite grouting material to reinforce coal," *Materials Review*, vol. 27, no. 4, pp. 120–123, 2013.

[8] Z. Feng and H. Kang, "Development and application of new waterproof grouting material of polyurethane," *Chinese Journal of Geotechnical Engineering*, vol. 32, no. 3, pp. 375-376, 2010.

[9] H. Wu, H. Wei, F. Tian, H. Li, W. Li, and J. Xiang, "Performances features and research orientation of mine high molecular grouting reinforced material," *Coal Science and Technology*, vol. 40, no. 5, pp. 26–28, 2012.

[10] X. Wang, L. Wang, T. Qiang, and L. Ren, "Research progress in flame-retardant polyurethane," *Materials Review*, vol. 27, no. 2, pp. 90–95, 2013.

[11] M. Xu, X. He, J. Li, D. Lv, H. Huang, and X. Cao, "Research on application of polyurethane grouting material for mining," *Materials Review*, vol. 28, no. 9, pp. 96–100, 2014.

[12] X. Hong, D. Yang, and X. Zhou, "Study on preparation and performance of modified urea-formaldehyde resin grouting materials," *Materials Review*, vol. 27, no. 4, pp. 116-117, 2013.

Research Article

Mechanical Behavior of Asphalt Mastics Produced Using Waste Stone Sawdust

Ghazi G. Al-Khateeb [1] **, Taisir S. Khedaywi,[1] and Motaz F. Irfaeya[2]**

[1]Department of Civil Engineering, Jordan University of Science and Technology, P.O. Box 3030, Irbid 22110, Jordan
[2]Skills Co. for Engineering Services, Al-Khaleel, West Bank, State of Palestine

Correspondence should be addressed to Ghazi G. Al-Khateeb; ggalkhateeb@just.edu.jo

This study intended to evaluate the use of waste stone sawdust filler with asphalt binders and compare the mechanical properties of the waste filler-asphalt mastic with those of the asphalt mastic produced using the typical limestone filler. The mastics were prepared at four filler-to-asphalt ratios by volume of asphalt binder: 0.05, 0.10, 0.20, and 0.30. A dynamic shear rheometer (DSR) strain-controlled frequency sweep test was used to evaluate the properties of the control asphalt binder and the mastics. The test used a constant strain of 10% and loading frequencies of 10, 5.6, 3.1, 1.78, 1.0, 0.56, 0.31, 0.178, and 0.1 Hz and was conducted at wide range of temperatures: 10, 20, 30, 40, 50, 60, and 70°C. The test measured the complex shear modulus (G^*) value and the phase angle for the binder and the mastics. The findings of this study showed that the stone sawdust filler demonstrated higher resistance to fatigue and rutting behavior than the limestone filler. However, the elastic behavior of the two asphalt mastics was nearly similar and increased with the increase in volume ratio. It was also found that the best-fit model described the relationship between the volume ratio and each of $|G^*|/\sin \delta$ and $|G^*|\cos \delta$, and the mastic-to-binder modulus ratio was the exponential model with high coefficient of determination (r^2). The differences in the G^* value between the limestone filler and the stone sawdust filler were relatively insignificant particularly at low loading frequencies and high temperatures. Finally, the mastic-to-binder modulus ratio decreased with the increase in loading frequency.

1. Background

Although asphalt mixture is approximately composed of only 5% asphalt binder and the remaining is aggregate, the mechanical properties and behavior of asphalt binder affect significantly the properties of asphalt mixture and hence play a big role in the performance of asphalt pavements.

The complexity of asphalt binder comes from the viscoelastic nature of this material. Its properties and behavior are time and temperature dependent. In addition, the mode of loading impacts this behavior. High stiffness and elastic behaviors are desired properties for asphalt binders used in hot-mix asphalt design and production. High stiffness is required to resist rutting under heavy loads in pavements. On the other hand, elastic behavior is also needed to recover and heal part of the deformations in pavements under loading to minimize

fatigue cracking. Researchers in the asphalt technology field have been always attempting to enhance and optimize properties of asphalt used in the pavement construction.

Modification of asphalt binders is done by utilizing several modifiers that are available on a wide spectrum in the industry. Some of these modifiers are manufactured so that they are used in the asphalt technology at a feasible cost. However, other modifiers are waste or recycled materials that can be used in asphalt to serve twofold purpose: (1) enhancing the properties of asphalt and (2) helping to clean environment.

Many research studies have used waste materials and available filler materials to enhance the properties of asphalt binders and mixtures. Waste materials such as rubber of waste tires, oil shale ash, medical ash, and toner waste [1–4] have been used to enhance the properties of asphalt binders

used in the hot-mix asphalt technology. In addition, some researchers took advantage of agricultural tree and plant waste such as the empty fruit bunch of date and oil palm trees [5] to produce cellulose fiber to be used as additives in the asphalt binder.

Other research studies have been conducted to investigate the effect of mineral fillers on the mechanical properties of asphalt binders. The complex characteristics of fatigue behavior were evaluated in a study of asphalt binders and mastics produced using limestone and hydrated lime fillers [6]. The effect of filler-to-asphalt ratio on low- and high-temperature properties of asphalt mastics using mineral fillers was studied [7]; it was found that the optimum range of the filler-to-asphalt ratio is 0.9–1.4 to balance the low- and high-temperature properties according to the study. The effect of basalt and hydrated lime fillers on the behavior of rutting, fracture, and thermal cracking resistance of asphalt mastics was investigated [8]; the addition of hydrated lime improved the low-temperature and rutting performance as well as fracture resistance.

The Portland cement filler was used to modify the asphalt binder [9]. It was shown that the increase in the cement-to-asphalt ratio improved the Superpave high performance grade and the rutting resistance of asphalt binders by increasing the stiffness and the $G^*/\sin\delta$ parameter. In a study that used waste materials in asphalt concrete mixtures [10], it was found that marble powder and fly ash could be used as filler materials instead of stone powder in the asphalt concrete, and rubber particles of the size between no. 4 and no. 200 showed the best results in terms of the indirect tensile test.

Rutting and fatigue are considered two major distresses that occur in asphalt pavements. The asphalt binder plays a big role in the performance of asphalt mixture and hence in controlling the two distresses. Different modifiers and fillers were tried in the literature as seen in the above paragraphs to enhance the mechanical properties of asphalt binders. In this study, a waste material (the stone sawdust) is used to achieve two objectives: to enhance and improve the mechanical properties of asphalt binders that are related to rutting and fatigue resistance, and at the same time to get rid off the waste material and keep the environment clean.

There are no available statistical data about the amount of stone sawdust waste in Jordan since this waste is not among the waste types being managed by municipal authorities or private sector. However, burnt stone slurry (a solid waste powder) has been reported in [11] to be about 53000 tons per year collected from 1000 quarries and tiles factories in Jordan. The cost of transporting and dumping this big amount of waste is about 1 million dollars.

In this study, the waste stone sawdust collected from stone-manufacturing sites for building purposes was used as a filler material in the asphalt binder to investigate the mechanical properties of the produced asphalt mastics. The waste stone sawdust is retained from stone fabrication. Hence, this waste material is the material generated from the same rock quarries as for the limestone filler typically used in the production of hot-mix asphalt in the area. For this purpose, a comparison between the two fillers in this study was made.

2. Objectives

The main objectives of this study are as follows:

(1) To investigate the effect of stone sawdust as a filler material in the filler-asphalt mastic

(2) To assess the effect of stone sawdust on the mechanical properties of asphalt binders

(3) To check whether the stone sawdust fillers can be a replacement for the limestone filler in asphalt mastics by comparing the behavior of these two fillers when mixed with asphalt.

3. Asphalt Materials and Fillers Used in the Study

The 60/70-penetration grade asphalt binder was used in this study. This asphalt binder is the most common asphalt binder widely used in producing asphalt mixtures for highway asphalt pavements in Jordan. The properties of the asphalt binder were determined and are summarized in Table 1.

Two filler materials were utilized in the study: limestone and stone sawdust. These materials are considered waste materials from construction sites in Jordan. The limestone was obtained from a local quarry, and the stone sawdust was obtained from the manufacturing process of building stones. Both materials were sieved using wet sieving process. The material portion passing sieve no. 200 (75 μm) was obtained and dried in an oven for approximately 24 hours at an intermediate temperature.

The specific gravity, plasticity index, and angularity were measured for the two filler materials. The results of these properties are shown in Table 2.

4. Methodology

4.1. Preparation of Filler-Asphalt Mastics. The preparation of the filler-asphalt mastic (limestone-asphalt mastic and stone sawdust-asphalt mastic) samples was done according to the following procedure. The filler material was heated for one hour in an oven at 150°C in order to simulate the conditions during the mixing process. The asphalt binder was also heated at the same temperature (150°C) for about 20 minutes in small containers. Mixing was done manually for about 15 minutes by gradually adding the filler to the asphalt binder and mixing using a glass rod to ensure homogeneity and to prevent excessive balling. The filler-asphalt mastic was produced at four volume ratios (VRs): 0.05, 0.10, 0.20, and 0.30 by volume of the asphalt binder.

To prepare the dynamic shear rheometer (DSR) test samples of the asphalt binder and the filler-asphalt mastic, the asphalt material (binder or mastic) was heated in an oven at a temperature of about 150°C until it became sufficiently fluid to be poured. The standard silicone mold having a diameter of 25 mm was used to produce the asphalt samples for DSR testing (Figure 1). The sample was allowed to cool for a proper period of time until it became solid enough to be removed from the mold.

Table 1: Original asphalt binder properties.

Asphalt binder 60/70	
Test	Result
Penetration (dmm)	65
Ductility (cm)	106
Specific gravity	1.00
Flash point (°C)	316
Softening point (°C)	54

Table 2: Properties of fillers used in the study.

Property	Filler material	
	Limestone	Stone sawdust
Specific gravity	2.610	2.460
Plasticity index	Nonplastic	Nonplastic
Angularity	67%	61%
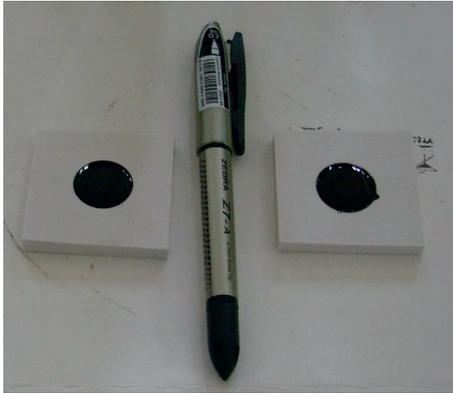
Figure 1: Samples for DSR testing.

4.2. Frequency Sweep Tests of Asphalt Binders and Mastics.

The DSR (Figure 2) was used to measure the mechanical properties of the control asphalt binder and the filler-asphalt mastics at a variety of temperatures. The asphalt sample (binder or mastic) was placed into the device between two plates, and the gap (the thickness of the sample) was set to 1 mm (Figure 3). The sample was tested by applying a sinusoidal dynamic strain using the oscillating upper plate. A strain-controlled frequency sweep test was used. The constant strain was 10%, and the loading frequency varied from 0.1 to 10 Hz and covered the values: 0.1, 0.178, 0.31, 0.56, 1.0, 1.78, 3.1, 5.6, and 10 Hz. The test temperatures covered a wide range of temperatures (10, 20, 30, 40, 50, 60, and 70°C). The frequency sweep testing matrix used in this study is shown in Table 3.

The complex shear modulus ($|G^*|$) value and the phase angle (δ) were recorded during the frequency sweep test. The shear modulus represents the stiffness of the asphalt material that is responsible for the resistance to deformation (rutting) under continuous shearing of the binder at the desired temperature and loading frequency. On the other hand, the phase angle represents the time lag between the elastic and viscous response of the asphalt material that is behaving as a viscoelastic material.

Figure 2: Dynamic shear rheometer (DSR).
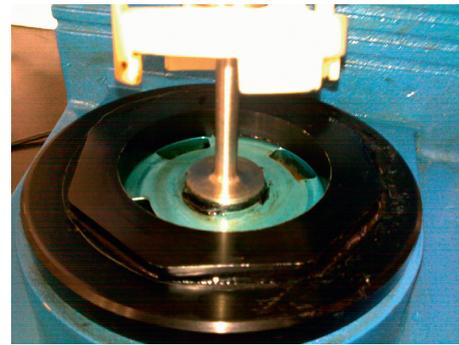
Figure 3: Sample sandwiched between the two plates.

Table 3: Testing matrix.

Test variable	Number	Values
Volume ratio	5	0.00, 0.05, 0.10, 0.20, and 0.30
Asphalt binder	1	60/70-penetration grade
Filler type	2	Limestone and stone sawdust
Loading frequency	9	0.1, 0.178, 0.31, 0.56, 1.0, 1.78, 3.1, 5.6, and 10 Hz
Temperature	7	10, 20, 30, 40, 50, 60, and 70°C
Replicates	2	Two replicates
Total number of tests		$5 \times 1 \times 2 \times 9 \times 7 \times 2 = 1260$ tests

4.3. Fatigue, Rutting, and Elastic Parameters Used in the Analysis.

In the Superpave system [12], the fatigue and rutting parameters used in the asphalt binder performance criteria are $|G^*|\sin\delta$ and $|G^*|/\sin\delta$, respectively. $|G^*|$ refers to the complex shear modulus value of the asphalt binder, and δ is the phase angle value of the binder. The $|G^*|\sin\delta$ parameter value is obtained for the asphalt binder at intermediate temperatures to verify the fatigue performance of the binder; the maximum value specified by the Superpave is 5000 kPa based on specified protocols and procedures that have to be done on the asphalt binder. On the other hand, the $|G^*|/\sin\delta$ is obtained for the asphalt binder at high temperatures to investigate the rutting behavior of the binder; the minimum value specified by the Superpave is 1.00 kPa for original asphalt binder and 2.20 kPa for short-term aged binder according to the protocols described in the Superpave system.

Additionally, the $|G^*|\cos\delta$ is also used in the analysis of data in this study that refers to the elastic part of the asphalt material. It is well known that the phase angle of the asphalt binder (a viscoelastic material) indicates the lag between the applied stress/strain and the resulting strain/stress; as the asphalt binder becomes more elastic, the phase angle decreases, and as the asphalt binder behaves more viscous, the phase angle increases. The horizontal component of the complex shear modulus value of the asphalt binder is $|G^*|\cos\delta$ that represents the elastic part of the binder; it improves as the phase angle decreases.

5. Analysis of Data and Results

This part presents the results and analysis of the frequency sweep test data obtained for the control asphalt binder, the limestone-asphalt mastic, and the stone sawdust-asphalt mastic [13]. The analysis includes four different aspects: the fatigue resistance, the rutting resistance, the elastic behavior, and frequency sweep test results and master curves of the control asphalt binder and the filler-asphalt mastics in addition to a comparison between limestone-asphalt mastics and stone sawdust-asphalt mastics.

5.1. Fatigue and Rutting Behaviors of Asphalt Mastics. The value of $|G^*|\sin\delta$ was recommended by the Superpave as a fatigue parameter of asphalt binders. As fatigue occurs at intermediate temperatures, this parameter was determined for the control asphalt binder and the two mastics at intermediate temperatures. Figures 4 and 5 illustrate the fatigue behavior of the binder and the two mastics at two low temperatures (20 and 30°C) and one loading frequency (1.78 Hz). These figures clearly show that the two fillers increased the $|G^*|\sin\delta$ value and hence improved the fatigue resistance of asphalt binder with the increase in volume ratio. In general, the stone sawdust filler showed higher resistance to fatigue than the limestone.

The rutting parameter in the Superpave system is the value of $|G^*|/\sin\delta$. This value is measured at high temperatures (typically more than 45°C) to characterize asphalt binders for rutting behavior. In this study, seven temperatures were used: three (50, 60, and 70°C) are considered high temperatures for rutting and four (10, 20, 30, and 40°C) are considered intermediate temperatures for fatigue cracking. As the $|G^*|$ value gets higher, the asphalt material (asphalt binder or mastic) becomes stiffer and hence more resistant to rutting. On the other hand, as the δ value gets smaller, the asphalt material becomes more elastic and therefore more resistant to rutting due to the recovery of part of the deformation.

Figures 6 and 7 show the rutting behavior of the control asphalt binder and the two mastics at the two extreme temperatures (50 and 70°C). These two figures represent only two examples at one loading frequency (1.78 Hz). Both figures clearly show that the fillers improved the rutting parameter with the increase in volume ratio. The stone sawdust-asphalt mastic showed higher resistance to rutting than the limestone-asphalt mastic. The relationship between $|G^*|/\sin\delta$ and volume ratio was found to be exponential. The exponential models with the coefficients of determination
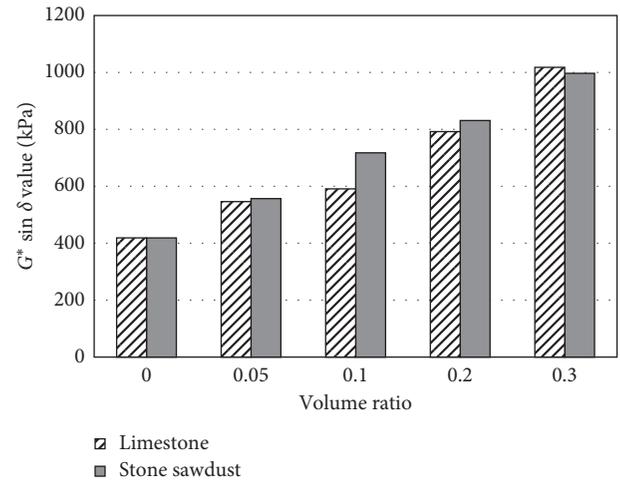
Figure 4: Fatigue behavior at 20°C.
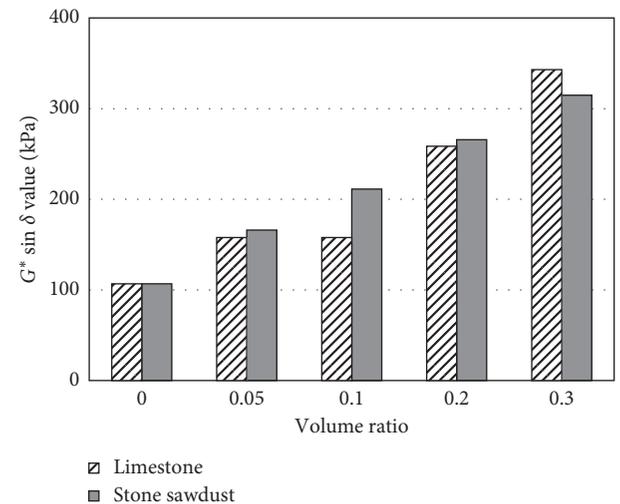
Figure 5: Fatigue behavior at 30°C.

(r^2) for the two mastics at all high temperatures are summarized in Tables 4 and 5.

5.2. Elastic Behavior of Asphalt Mastics. The value of $|G^*|\cos\delta$ represents the elastic portion of the complex shear modulus of the asphalt material. This elastic part helps the asphalt material to resist deformation under shear loading particularly at low and intermediate temperatures. Consequently, this parameter plays a role in the healing process of deformations for rutting and fatigue cracking of asphalt.

Figures 8 and 9 demonstrate the elastic behavior ($|G^*|\cos\delta$) of the original binder and the two mastics at two extreme temperatures (10 and 70°C), different volume concentrations (0.0, 0.05, 0.10, 0.20, and 0.30), and one single frequency (1.78 Hz).

The elastic behavior of the two asphalt mastics increased with the increase in volume ratio as shown in these two figures. The $|G^*|\cos\delta$ values for the stone sawdust and
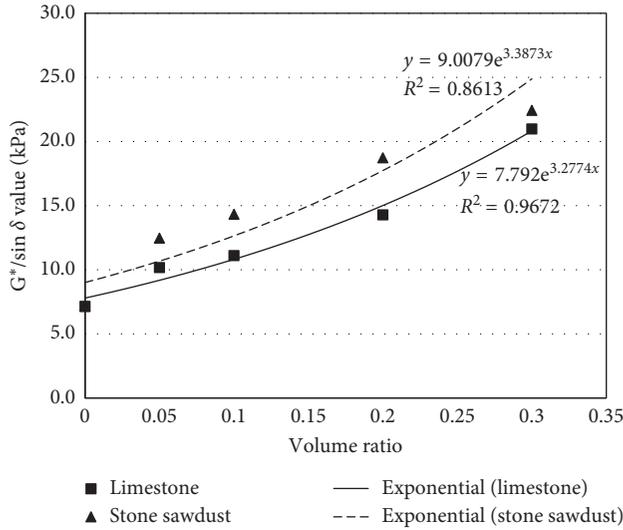
FIGURE 6: Rutting behavior of asphalt mastics at 50°C.
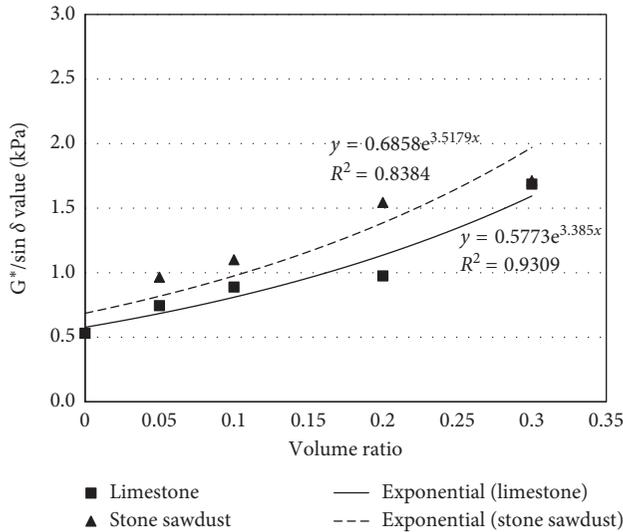
FIGURE 7: Rutting behavior of asphalt mastics at 70°C.

TABLE 4: Relationship between $|G^*|/\sin\delta$ and VR for the limestone-asphalt mastic.

Temperature (°C)	Model	r^2 value
50	$|G^*|/\sin\delta = 7.792e^{3.277VR}$	0.97
60	$|G^*|/\sin\delta = 2.000e^{3.423VR}$	0.94
70	$|G^*|/\sin\delta = 0.577e^{3.385VR}$	0.93

TABLE 5: Relationship between $|G^*|/\sin\delta$ and VR for the stone sawdust-asphalt mastic.

Temperature (°C)	Model	r^2 value
50	$|G^*|/\sin\delta = 9.008e^{3.387VR}$	0.86
60	$|G^*|/\sin\delta = 2.358e^{3.485VR}$	0.85
70	$|G^*|/\sin\delta = 0.686e^{3.518VR}$	0.84
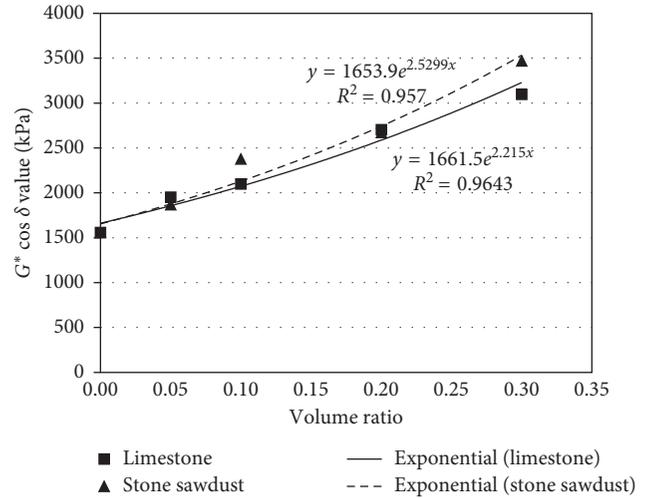
FIGURE 8: Elastic behavior of asphalt mastics at 10°C and 1.78 Hz versus VR.
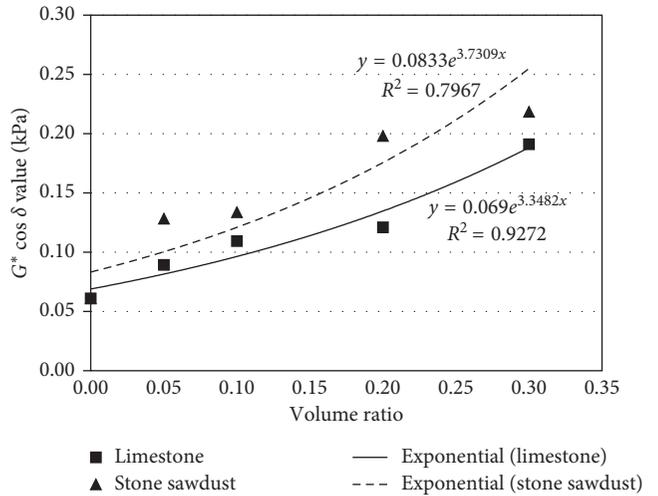
FIGURE 9: Elastic behavior of asphalt mastics at 70°C and 1.78 Hz versus VR.

limestone mastics were approximately similar at all frequencies and temperatures. The best-fit model that described the relationship between the volume ratio (VR) and the $|G^*|\cos\delta$ value is the exponential model. The coefficient of determination (r^2) for the model was high in all cases as shown in Tables 6 and 7.

With the increase in temperature, the $|G^*|\cos\delta$ value decreased for the two mastics and this is typical.

Nevertheless, the rate of reduction in this value at lower temperatures was very sharp and significant compared to high temperatures as shown in Figures 10 and 11. The stone sawdust filler was compared with the limestone filler in terms of the mastic $|G^*|\cos\delta$. Figure 12 demonstrates this comparison for the smallest volume ratio (0.05) and the highest volume ratio (0.30) at a loading frequency of 1.78 Hz. The figure shows that the elastic behavior of both filler-asphalt mastics is similar. This finding is important and

Table 6: Relationship between $|G^*|\cos\delta$ and VR for the limestone mastic (1.78 Hz).

Temperature (°C)	Model	r^2 value
10	$|G^*|\cos\delta = 1661.5e^{2.215\text{VR}}$	0.96
20	$|G^*|\cos\delta = 376.1e^{3.950\text{VR}}$	0.94
30	$|G^*|\cos\delta = 66.56e^{4.274\text{VR}}$	0.92
40	$|G^*|\cos\delta = 11.92e^{3.567\text{VR}}$	0.95
50	$|G^*|\cos\delta = 2.055e^{3.381\text{VR}}$	0.94
60	$|G^*|\cos\delta = 0.3536e^{3.570\text{VR}}$	0.94
70	$|G^*|\cos\delta = 0.0690e^{3.348\text{VR}}$	0.93

Table 7: Relationship between $|G^*|\cos\delta$ and VR for the stone sawdust mastic (1.78 Hz).

Temperature (°C)	Model	r^2 value
10	$|G^*|\cos\delta = 1653.9e^{2.530\text{VR}}$	0.96
20	$|G^*|\cos\delta = 414.3e^{3.562\text{VR}}$	0.91
30	$|G^*|\cos\delta = 74.51e^{3.718\text{VR}}$	0.87
40	$|G^*|\cos\delta = 13.46e^{3.392\text{VR}}$	0.85
50	$|G^*|\cos\delta = 2.423e^{3.555\text{VR}}$	0.81
60	$|G^*|\cos\delta = 0.4301e^{3.702\text{VR}}$	0.80
70	$|G^*|\cos\delta = 0.0833e^{3.731\text{VR}}$	0.80

Figure 11: $|G^*|\cos\delta$ versus temperature for the stone sawdust mastic (1.78 Hz).

Figure 10: $|G^*|\cos\delta$ versus temperature for the limestone mastic (1.78 Hz).
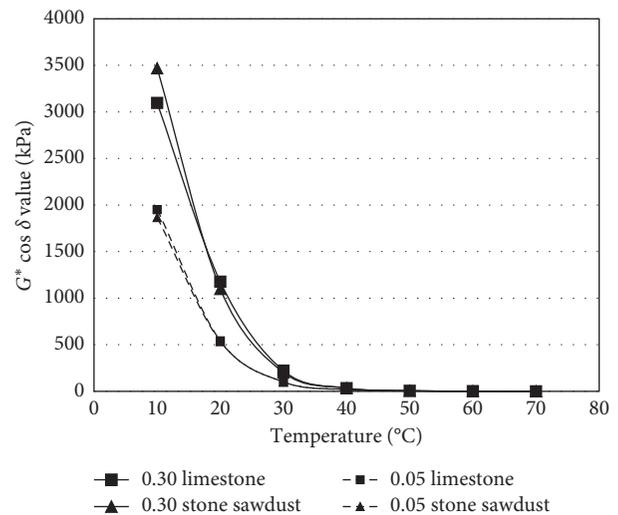
Figure 12: $|G^*|\cos\delta$ comparison between stone sawdust and limestone (1.78 Hz).

indicates that the waste stone sawdust can replace the limestone filler in asphalt mix particularly that the source of the two materials is the same, which is the stone used for building and construction in the area. In other words, the other physical properties of the two materials are also the same.

6. Frequency Sweep Test Results and Master Curves

As the frequency sweep test was conducted at nine loading frequencies and seven temperatures, the master curves

for the control binder and each of the eight filler-asphalt mastics could be obtained. Figures 13–17 show the flow curves (G^* value versus frequency) for the control asphalt binder, the limestone mastic, and the stone sawdust mastic (examples at 0.05 and 0.30 volume ratios).

The above flow curves show how the stiffening behavior of asphalt binder and mastic changed due to the increase in loading frequency and test temperature. In addition, the G^* value increased due to three factors: (1) a decrease in temperature, (2) an increase in loading frequency, and (3) an increase in volume ratio.

Master curves are used to represent huge data at multi-temperatures and loading frequencies such as the case in this study. One master curve for each volume ratio at a reference temperature is obtained to describe the behavior of the asphalt
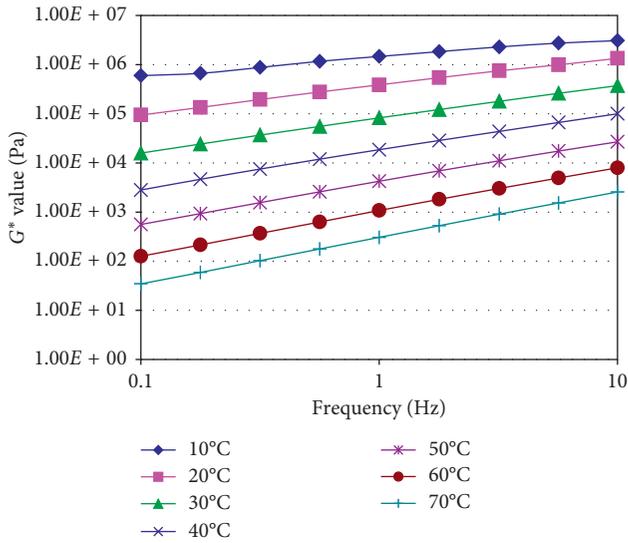
FIGURE 13: G^* value versus loading frequency for the control asphalt binder.
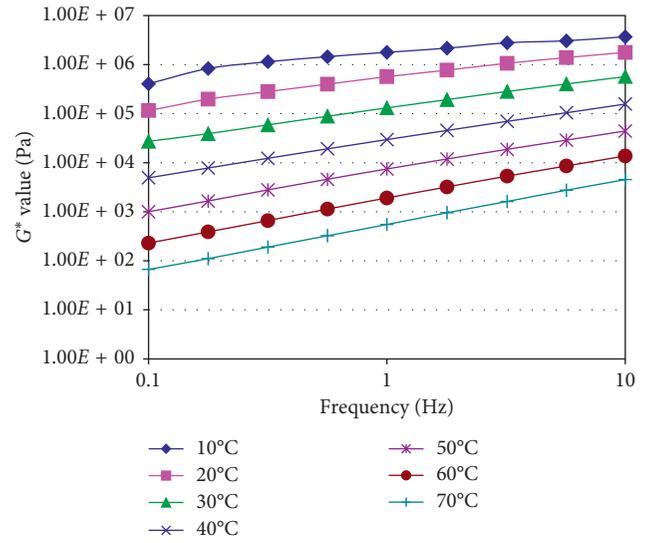
FIGURE 15: G^* value versus loading frequency for the stone sawdust mastic (VR = 0.05).
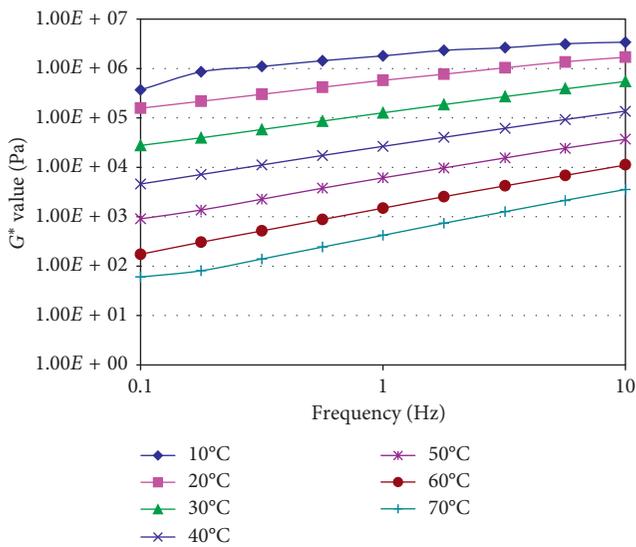
FIGURE 14: G^* value versus loading frequency for the limestone mastic (VR = 0.05).
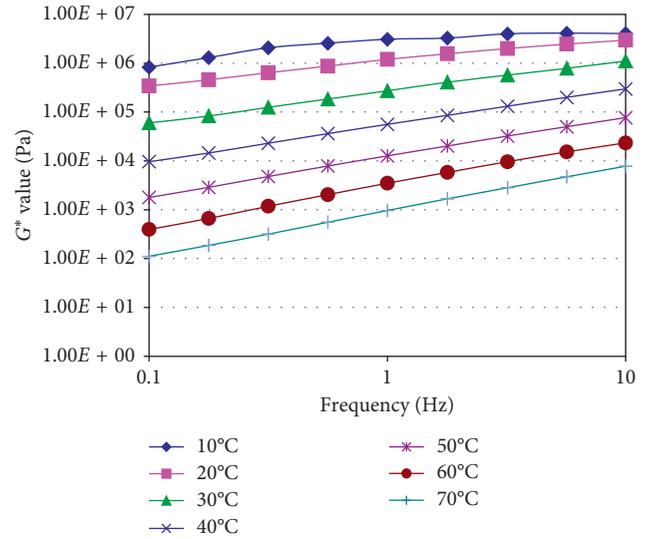
FIGURE 16: G^* value versus loading frequency for the limestone mastic (VR = 0.30).

material (asphalt binder or mastic) at a variety of temperatures and loading frequencies.

The $|G^*|$ master curves for the control asphalt binder and the eight filler-asphalt mastics were obtained. Using a reference temperature of 40°C for the master curves, the shift factors for the other temperatures were calculated for each master curve. Table 8 illustrates an example of the shift factors for the 0.05 stone sawdust mastic.

Figures 18–22 show the master curves for the two mastics at the following volume ratios: 0.00, 0.05, 0.10, 0.20, and 0.30, respectively. These curves can be used easily to determine the behavior of the asphalt material at a specific frequency and temperature.

The master curves of the two mastics at the four volume ratios reveal several important findings. The differences in the complex shear modulus (G^*) value between the limestone filler and the stone sawdust filler are relatively small particularly at low reduced frequencies (i.e., at low loading frequencies and high temperatures). These differences become larger at high loading frequencies and low temperatures; yet, they are still insignificant between the two fillers. These findings again suggest that the stone sawdust may be used as alternative filler for the limestone in asphalt mixtures.

The ratio of the mastic modulus to the control asphalt binder modulus was found to decrease as the loading
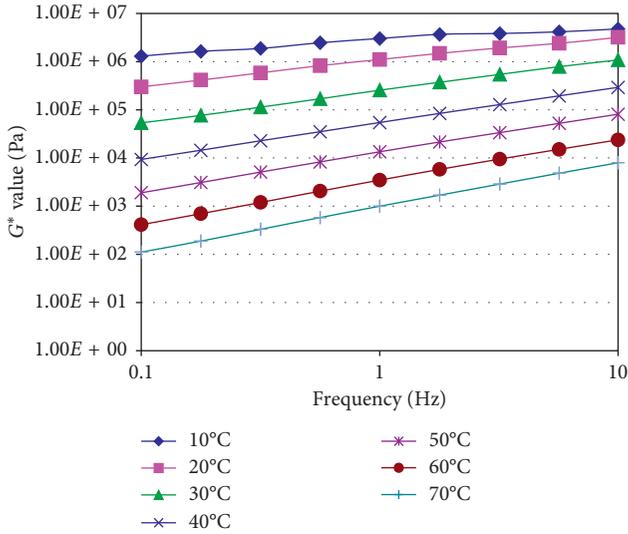
FIGURE 17: G^* value versus loading frequency for the stone sawdust mastic (VR = 0.30).

TABLE 8: Shift factors for the 0.05 stone sawdust-asphalt mastic.

Temperature (°C)	10	20	30	40	50	60	70
log (a_T)	2.871	1.895	0.898	0	−0.762	−1.441	−2.024
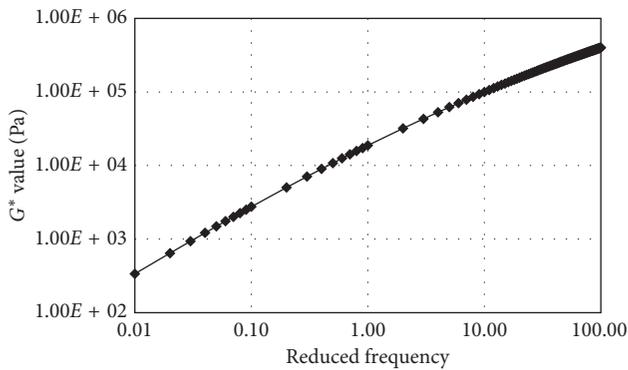
FIGURE 18: G^* value master curve for the control asphalt binder (VR = 0.00).

frequency increased; this is demonstrated in Figure 23. The figure shows the comparison between the two mastics at a temperature of 40°C and volume ratio of 0.30. Similar trends were also obtained at the other temperatures and volume ratios.

The complex shear modulus ratio (mastic to binder) was also plotted against the volume ratio for both mastics (limestone and stone sawdust). Figure 24 illustrates this relationship for the two mastics at a temperature of 40°C and loading frequency of 1 Hz. The modulus ratio increased with the increase in the volume ratio as seen in this figure. A similar trend was obtained at the other temperatures and loading frequencies. The best-fit model that described this relationship was found to be the exponential model as displayed in the figure with high coefficient of
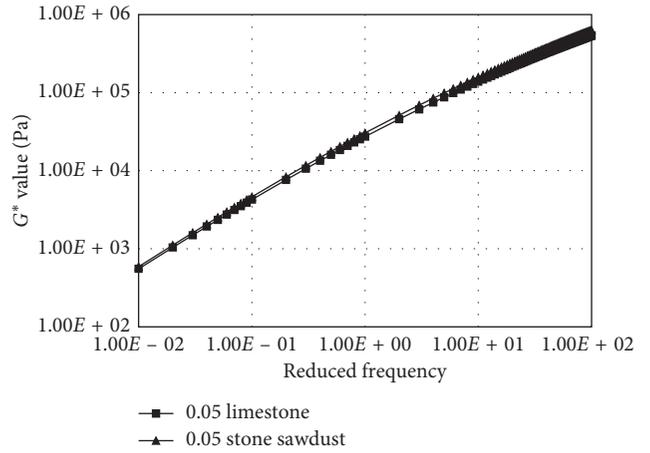
FIGURE 19: G^* value master curve for the two mastics (VR = 0.05).
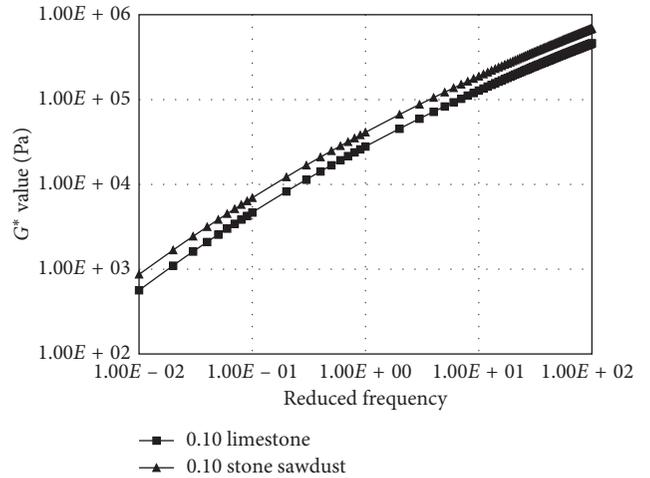
FIGURE 20: G^* value master curve for the two mastics (VR = 0.10).
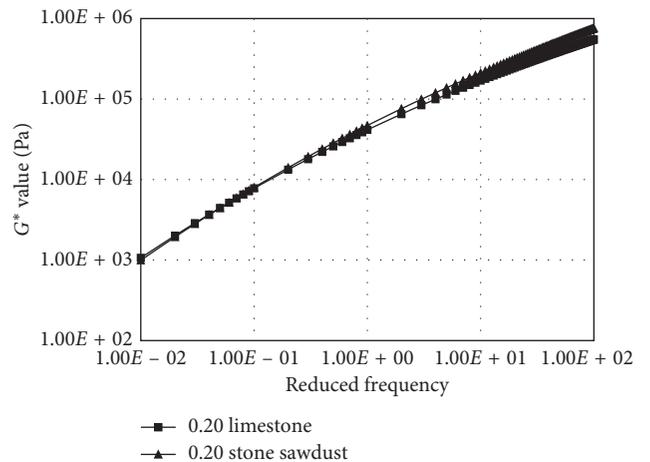
FIGURE 21: G^* value master curve for the two mastics (VR = 0.20).

determination (r^2) for both mastics. This applied to all combinations of the seven temperatures and nine loading frequencies.

FIGURE 22: G^* value master curve for the two mastics (VR = 0.30).
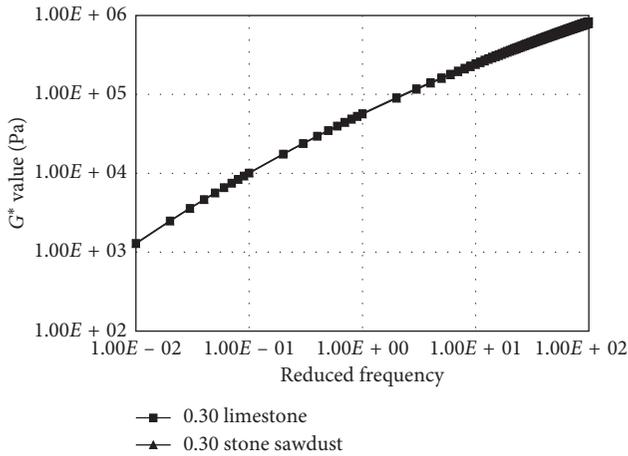
FIGURE 23: Mastic-to-binder modulus ratio versus frequency ($T = 40°C$ and VR = 0.30).
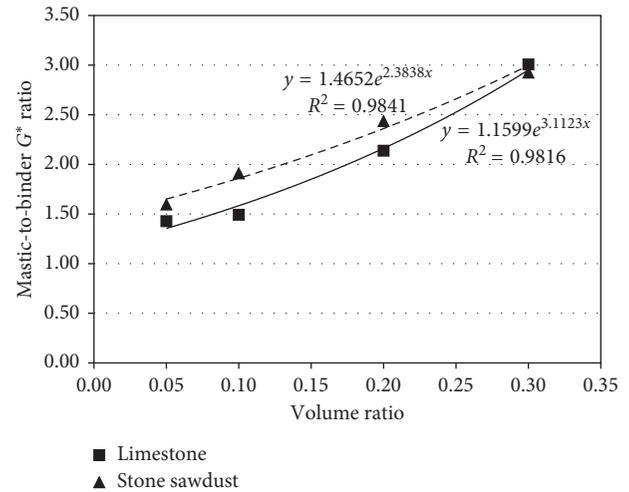
FIGURE 24: Mastic-to-binder modulus ratio versus volume ratio ($T = 40°C$ and $f = 1$ Hz).

(4) The two fillers showed a typical reduction in the $|G^*|\cos\delta$ value with temperature. Yet, the rate of reduction at lower temperatures was very sharp and significant compared to high temperatures.

(5) The differences in the complex shear modulus (G^*) value between the limestone filler and the stone sawdust filler were found relatively small and insignificant particularly at low loading frequencies and high temperatures.

(6) The mastic-to-binder modulus ratio was found to decrease with the increase in loading frequency at all temperatures and volume ratios. In addition, the modulus ratio increased nonlinearly with the increase in the volume ratio; the best model that described this relationship is the exponential model with a high coefficient of determination (r^2).

Data Availability

The data used to support the findings of this study are included within the article. Any additional data related to the paper may be requested from the corresponding author.

Additional Points

Practical Application. The above findings suggest that the waste stone sawdust could replace the limestone filler in asphalt mix production as both materials demonstrated similar mechanical behaviors and trends in this study. Moreover, it is important to mention that the source of the two materials is the same. The limestone filler is part of the limestone crushed in local quarries from limestone rocks, and the stone sawdust is a waste material collected from stone-manufacturing sites for building purposes. For this reason, the other physical properties of the two materials are expected to be the same. In conclusion, this study provides an alternative (the waste stone sawdust filler) for the limestone filler material that is used in the production of hot-mix asphalt.

7. Conclusions

The analysis and the results of this study revealed the following major conclusions:

(1) The stone sawdust filler showed higher resistance to fatigue than the limestone filler.

(2) The stone sawdust-asphalt mastic also showed higher resistance to rutting than the limestone-asphalt mastic. The relationship between $|G^*|/\sin\delta$ and volume ratio was found to be exponential. The exponential models with the coefficients of determination (r^2) for the two mastics were summarized.

(3) The elastic behavior of the two asphalt mastics increased with the increase in volume ratio. However, the $|G^*|\cos\delta$ values for the stone sawdust and limestone mastics were nearly similar at all frequencies and temperatures. The best-fit model that described the relationship between the volume ratio (VR) and the $|G^*|\cos\delta$ value is the exponential model. The coefficient of determination (r^2) for the model was high in all cases.

Disclosure

Ghazi G. Al-Khateeb is on leave at University of Sharjah, P.O. Box 27272, Sharjah, UAE.

Conflicts of Interest

The authors declare that there are no conflicts of interest regarding the publication of this paper.

References

[1] G. G. Al-Khateeb and K. Z. Ramadan, "Investigation of the effect of rubber on rheological properties of asphalt binders using superpave DSR," *Korean Society of Civil Engineers (KSCE) Journal of Civil Engineering*, vol. 19, no. 1, pp. 127–135, 2015.

[2] K. Ghuzlan, G. Al-Khateeb, and A. Abu Damrah, "Using oil shale ash waste as a modifier for asphalt binders," *Journal of Material Cycles and Waste Management*, vol. 15, no. 4, pp. 522–529, 2013.

[3] T. Khedaywi, G. Al-Khateeb, and M. Irfaeya, "Effect of medical ash on shear properties of asphalt binder using superpave dynamic shear rheometer (DSR)," *Journal of Solid Waste Technology and Management (JSWTM)*, vol. 38, no. 1, pp. 19–27, 2012.

[4] T. S. Khedaywi, "Study on utilising waste toner in asphalt cement," *Journal of Road Materials and Pavement Design*, vol. 15, no. 2, pp. 446–454, 2014.

[5] R. Muniandy, H. Jafariahan, R. Yunus, and S. Hassim, "Determination of rheological properties of bio mastic asphalt," *American Journal of Engineering and Applied Sciences*, vol. 1, no. 3, pp. 204–209, 2008.

[6] Y. Kim, D. Little, and I. Song, "Effect of mineral fillers on fatigue resistance and fundamental material characteristics: mechanistic evaluation," *Transportation Research Record: Journal of the Transportation Research Board*, vol. 1832, pp. 34–54, 2003.

[7] T. Yi-qiu, Z.-H. Li, X.-Y. Zhang, and Z.-J. Dong, "Research on high- and low-temperature properties of asphalt-mineral filler mastic," *Journal of Materials in Civil Engineering*, vol. 22, no. 8, pp. 811–819, 2010.

[8] A. K. Das and D. Singh, "Investigation of rutting, fracture and thermal cracking behavior of asphalt mastic containing basalt and hydrated lime fillers," *Construction and Building Materials*, vol. 141, no. 15, pp. 442–452, 2017.

[9] G. G. Al-Khateeb and N. M. Al-Akhras, "Properties of Portland cement-modified asphalt binder using superpave tests," *Construction and Building Materials*, vol. 25, no. 2, pp. 926–932, 2011.

[10] M. Tuncan, A. Tuncan, and A. Cetin, "The use of waste materials in asphalt concrete mixtures," *Waste Management and Research*, vol. 21, no. 2, pp. 83–92, 2003.

[11] N. Al-Akhras, A. Ababneh, and W. A. Alaraji, "Using burnt stone slurry in mortar mixes," *Construction and Building Materials Journal*, vol. 24, no. 12, pp. 2658–2663, 2010.

[12] Asphalt Institute (AI) Superpave Series No. 1 (SP1), *Superpave Performance Graded Asphalt Binder Specifications and Testing*, 2003.

[13] M Irfaeya, *Utilizing Superpave Dynamic Shear Rheometer (DSR) to Investigate Asphalt Mastics Behavior Through Micromechanics in Jordan*, Master Dissertation, Department of Civil Engineering, Jordan University of Science and Technology, Irbid, Jordan, 2009.

Research Article

The Standard Fire Testing and Numerical Modelling of the Behavior of Calcium Silicate Board Metallic-Framework Drywall Assembly with Junction Box

Yinuo Wang [iD],[1] Ying-Ji Chuang,[2] Ching-Yuan Lin,[2] and Hao Zhang[1,3]

[1]*China Academy of Building Research, Beijing 100013, China*
[2]*Department of Architecture, National Taiwan University of Science and Technology, Taipei, Taiwan*
[3]*University of Science and Technology, Beijing, China*

Correspondence should be addressed to Yinuo Wang; wyn_up@foxmail.com

The metallic-framework drywall is used as the specimens in this research. The standard fire test and finite element simulation were performed once on 300 cm × 300 cm area specimen and twice on 100 cm × 100 cm area specimens, to quantify and evaluate the effect of the junction boxes on the fireproof property after being embedded into the metallic-framework drywall. The results of the experiment show that the temperature of unexposed surface rises faster due to the higher thermal conductivity of the internal metal junction box. The general junction box whose material is PVC can be softened off when heated, affecting the integrity of the firewall and also leading to rapid transfer to the unexposed surface. The prediction of finite element simulation temperature is highly correlated with the results of the real experiment. It is effective to strengthen the original weaknesses by adding a calcium silicate board behind the junction box and using metal panels instead of PVC. The temperature of the temperature junction box surface which is the highest temperature point of unexposed surface decreased most significantly at 72.9°C after the reinforcement. In addition, after reinforcement, the fire resistance time can reach to 1 hour by inserting the junction box into the metallic-framework drywall.

1. Introduction

With the development of architectural technology and fire engineering during the last decade, the construction project tends to develop high-rise and giant buildings. To adapt the tendency, a method of reducing the weight of the building, avoiding the construction risks and shortening the constructional duration, becomes an important issue for architectural engineering. In addition, the usage of thick and heavy building materials such as traditional brick wall or concrete wall must be reduced. For example, different dry metallic-framework wall systems which are expected to replace the traditional thick and heavy building materials appear constantly. These systems have features of optimization of construction methods, short constructional duration, and various constructional methods and light materials whose quality is more stable

than concrete. With the gradual popularity of new materials and new constructional methods, such as dry metallic-framework wall system, whether they can achieve a certain time of fire resistance and can be applied in the fire division become more and more important. Whether the building components have the appropriate fire safety should be detected by the standard fire test [1–6]. In addition, they should be applied to the buildings after they are equipped with the capacity of thermal resistance or fire integrity [7]. Based on the test time, these products can be classified by the fire resistance. For example, the firewalls can be classified into 1-hour, 2-hour, or 3-hour fire resistance.

There are many investigated studies on the performance issues of the dry metallic-framework wall partitioning system. Lin et al. [8] investigated the combination of metallic framework and calcium silicate board. Ho and Tsai [9]

proposed that the quality of boards had a great effect on the fire resistance of the wall. Nithyadharan and Kalyanaraman [10] researched on the strength of the connection of screw and calcium silicate board. Chuang et al. [11] came up with the conclusion that the room temperature had a direct influence on the surface temperature when the specimen was tested for fire resistance. Maruyama et al. [12] researched the aging of calcium silicate board and found that its strength weakened as time goes by.

The above research studies on the fire resistance of dry metallic-framework wall are based on the standard fire test experiments. With CAE (computer-aided engineering) increasingly being applied in various engineering fields, as an important part of CAE, CFD (computational fluid dynamics) has been developed rapidly during the last two decades. The principle of CFD is to solve the differential equations of nonlinear simultaneous quality, energy, component, momentum, and scalar with numerical methods. The results of solutions are able to predict the details of movement, heat transmission, mass transmission, and burning, becoming an efficient tool to optimize process equipment and enlarge quantitative design. The basic features of CFD are numerical modelling and computer experiment. Beginning from the fundamental physical theorems, to a large extent, they replaced the expensive equipment for fluid dynamic experiments, greatly influencing the scientific researches and engineering technology.

CFD is mainly applied in cutting-edge designs, such as aerospace design, automobile design, and turbine design. In addition, more and more numerical simultaneous aided researches in building field are processed by making use of CFD. For example, Collier and Buchanan [13] presented the prediction model for fire resistance of drywall by the finite element method; Do et al. [14] came up with that the thermal conductivity of porous material is mainly related to the thermal conductivity of its components and spatial arrangement of its complex structure by formula, microstructure observation, and experiments; Nassif et al. [15] presented the comparison of thermal conductivity of a dry gypsum board wall by the standard fire experiment and by numerical modelling.

According to regulations in different countries or the above researches which focus on the standard fire test experiment or computer simulation, they are only studying and discussing focusing on the wall. Wang et al. [16] once proposed that installing devices, such as the embedded junction box in the wall, could influence the fire resistance of the wall. However, this research focused on the quality control of the board with standard fire test experiment. It does not consider numerical modelling and corresponding quantitative research.

Based on the above foundation, this research takes the dry metallic-framework wall with embedded junction box as the experimental specimens. The quantitative analysis of its fire resistance through a physical experiment and CFD numerical modelling gives improvement measures for its destruction behavior. Aiming at disruptive behaviors, filling the existing gaps, and supplementing the fields are not involved in regulations of various countries at present.

The research conducts a total of 3 standard fire resistance tests and numerical modelling simulations. Test 1 uses the standard of ISO 834-1 [2] to perform the test on a test specimen with a of size 300 cm (width) ∗ 300 cm (height), proposes the numerical model to simulate the process of transient heat transmission, compares the results of computer simulation and the test results, and properly optimizes the digital model parameters. In Test 2, the fire area of the specimen is 100 cm (width) ∗ 100 cm (height), and an embedded junction box in the testing specimen was used to compare the numerical modelling of CFD models. By quantitative analysis, the weakness of the embedded junction box in the wall can be analyzed, which influences the fire resistance, and the reinforcement scheme was proposed. Test 3 simulates the feasibility of the reinforcement scheme by CFD numerical modelling, tests on the specimen of which fire area is 100 cm (width) ∗ 100 cm (height), and verifies the feasibility of numerical modelling and reinforcement scheme by the use of the standard fire test.

2. Experimental Details

2.1. Fire Test Furnaces. In this research, two sets of test equipment are applied, and both can conduct material testing horizontally or vertically. The large test furnace of the first equipment is 300 cm (width) ∗ 300 cm (height) ∗ 240 cm (depth) (Figure 1). The small test furnace of the second equipment is 120 cm (width) ∗ 120 cm (height) ∗ 120 cm (depth) (Figure 2). They both adopt the electronic ignition, and the control system used is the computer PID temperature controller. There are 8 burners in the large test furnace among which only 4 are switched on for the wall test. In the furnace, there are two thermocouples to, respectively, control the operation of 2 high-speed burners on two sides and other 7 thermocouples are to measure the temperature in the furnace. All thermocouples are inserted from the top of the test furnace. There are 4 burners in the small test furnace. When the wall is tested, only 2 burners which are close to the wall are opened. In the furnace, there are two thermocouples to, respectively, control the operation of 1 high-speed burner on two sides and other 2 thermocouples are to measure the temperature in the furnace. All thermocouples are inserted from the left side to right side of the test furnace. The ceramic wool is paved around and the top of the furnace wall of which maximum temperature is 1400°C and density is 240 kg/m^3. The furnace bottom is made by the adiabatic board of which thermal resistance is 1400°C and density is 1140 kg/m^3. The refractory mortar is applied in the gap and connection of adiabatic boards. The exterior body of the test furnace is made by steel plate and steel frame. At the back of the test furnace, there is an air outlet for exhaust air, and it is connected to the outdoor chimney. All the thermocouples are 10 cm away from the fire testing area of the specimen. The temperature in the furnace is measured by a K-type thermocouple of which specification conforms to the regulation of CNS 5534 [17] that the thermocouple shall possess property above 0.75 Grade. The thermocouple wire is covered by the heat-resistant stainless steel pipe of which the diameter is 6.35 mm

(a)

(b)
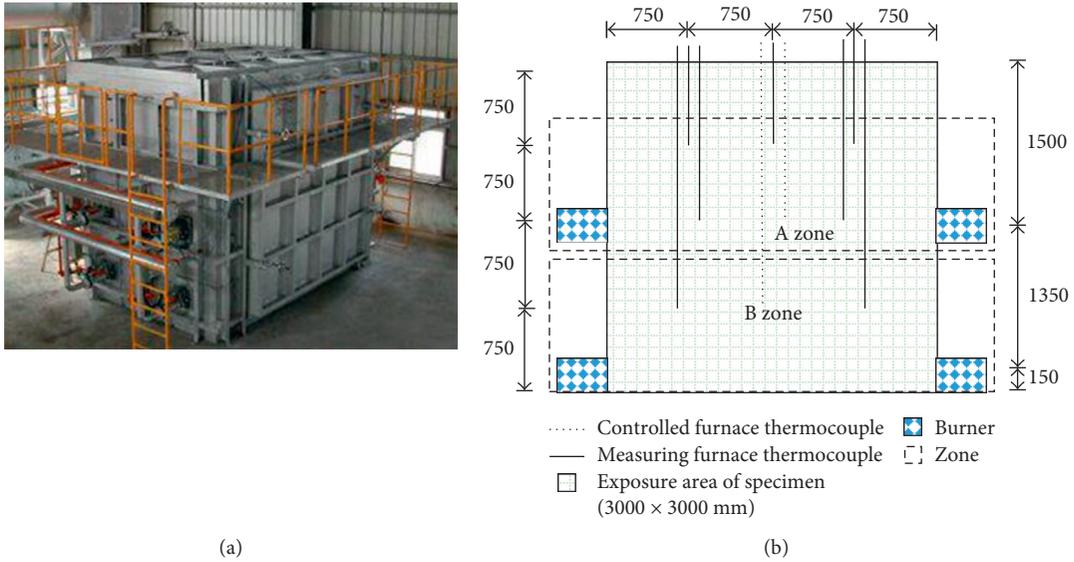
FIGURE 1: Full-size high-temperature furnace (inner size: 300 cm in width, 300 cm in height, and 240 cm in depth).

(a)

(b)
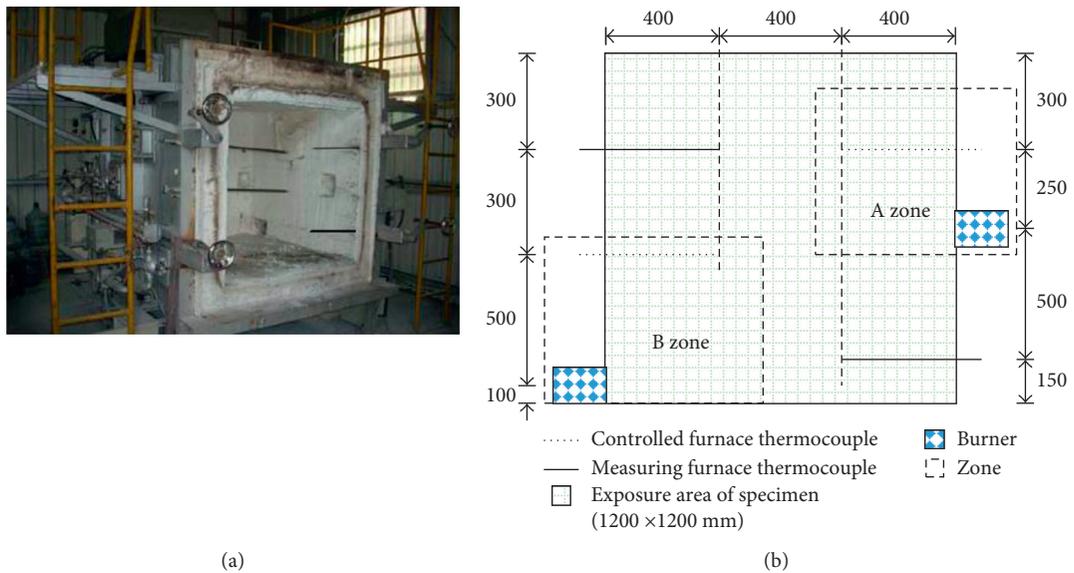
FIGURE 2: Small-size high-temperature furnace (inner size: 120 cm in width, 120 cm in height, and 120 cm in depth).

(16 gauge). In addition, the heat-resistant stainless steel pipe is placed in the insulated stainless steel pipe with an inner diameter of 14 mm and the front end is open and the hot junction of front end extrudes 25 mm. All the thermocouples in the furnace have been placed in the environment at a temperature of 1000°C for 1 hour [2] before the first use to increase the sensitivity of measuring the temperature, and the accuracy requirement is ±3%. All instrument signals are connected to the DS600 data recorder first, and DS600 processes and converses the signal to DC 100. At last, the data capture recorder converses the signal and outputs to the ThinkPad W540 laptop by a network cable. The data capture recorder is set to record once in every 6 seconds.

2.2. Test Specimens. The material used in the research is 9 mm calcium silicate board which is an erect blanking plate and fixed by a self-tapping screw. The self-tapping screw's diameter, length, and distance are 3.5 mm, 25.4 mm, and 250 mm, respectively. Its column is $65 \times 35 \times 0.6$ mm C-shaped steel, and the upper and down channels are $67 \times 25 \times 0.6$ mm C-shaped steel. The distance of the intermediate column is 406 mm, and the distance of the column away from two sides is 297 mm. The thickness of mineral wool is 50 mm, and a density of 60 kg/m^3 is applied to the material. For the size of the embedded socket, the external switch panel is 120 mm × 70 mm, and the internal junction box is $101 \times 55 \times 36$ mm. There are two kinds of external switches. In Test 2, the material of the switch panel

Fireside
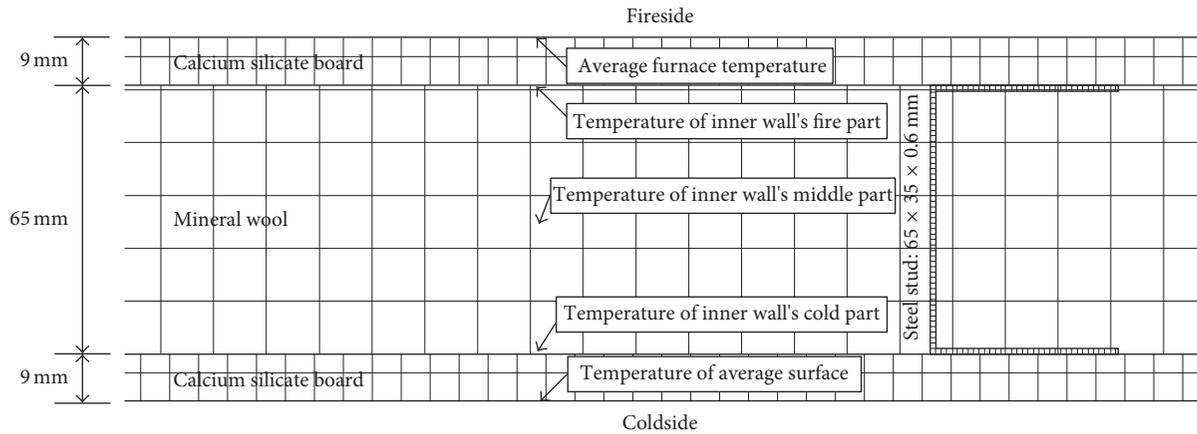
FIGURE 3: Cross section of the wall with indication of numerical modelling and the thermocouple position in Test 1.
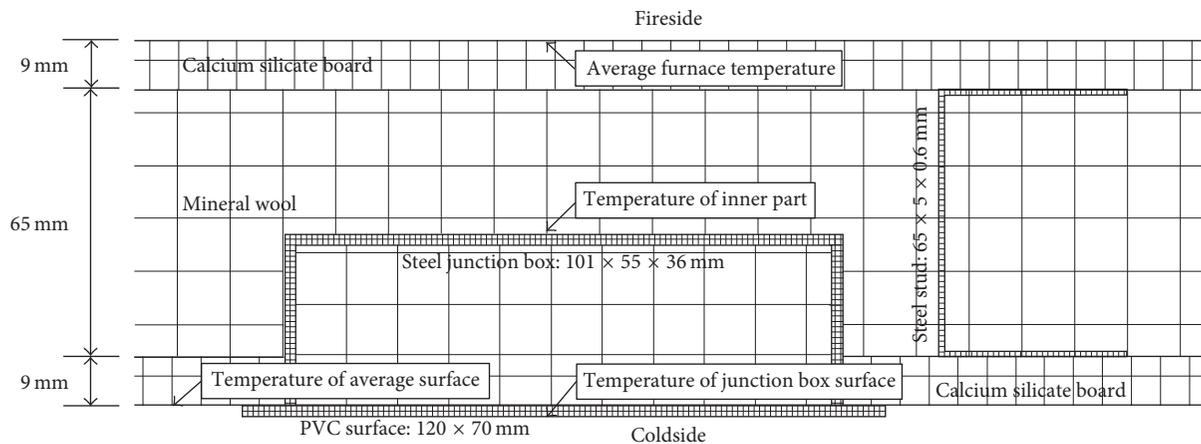
FIGURE 4: Cross section of the wall with indication of numerical modelling and the thermocouple position in Test 2.

is PVC (polyvinyl chloride), and the internal material is galvanizing steel box. In Test 3, the material of the external switch panel is steel, and the internal material is the galvanizing steel box. The junction box in Test 2 is not equipped with any reinforcement measures. Besides that the steel is selected in Test 3 as the material of the external panel, 9 mm calcium silicate board is added behind the junction box which is close to the fire source.

Three 60-minute standard heating tests were performed in the research. Test 1 is a standard test in which the specimen size is 3 m (height) × 3 m (width) and the density of fireproof cotton is 60 kg/m³ as shown in Figure 3. Test 2 is a standard test with small high-temperature furnace in which the specimen size is 1 m (height) × 1 m (width) and the density of fireproof cotton is 60 kg/m³. The socket junction box is embedded in the unexposed surface of the specimen. In addition, the material of the switch panel is PVC (polyvinyl chloride), and the internal material is the galvanizing steel box as shown in Figure 4. Test 3 is a test with small high-temperature furnace in which the specimen size is 1 m (height) × 1 m (width) and the density of fireproof cotton is 60 kg/m³. The socket junction box is embedded in the unexposed surface of the specimen. In addition, the material of the switch panel is steel, and the internal material

is the galvanizing steel box. A 9 mm calcium silicate board is added at the back of the box, as shown in Figure 5. Because there is no limit for the height that the socket junction box should be placed in the wall, this research expects to observe and simulate the most typical model in reality. In addition, according to the regulations of ISO 834-1 [2] that the weakness of the specimen shall be located in the center, the specimen of this research is 1 m (height) × 1 m (width) and the socket junction box is placed in the position 55 cm away from the ground. The furnace pressure is lower when it is more close to the bottom of the furnace. In short, the furnace pressure increases linearly as the height of the specimen increases. However, the furnace pressure is the negative pressure when it is 50 cm below the ground. As a result, the socket junction box is placed in the positive pressure position. As the test expects to verify the similarity of results of numerical modelling and test by Test 1, it takes the full-scale standard test of 3 m (height) × 3 m (width). The research expects to discuss the devastation that the embedded electronic junction box affects the components of wall, propose the reinforcement measures combining with the result of numerical modelling, and verify these measures through Test 2 and Test 3. As a result, it selects the test with small high-temperature furnace, and the size of the specimen is 1 m (height) × 1 m (width).
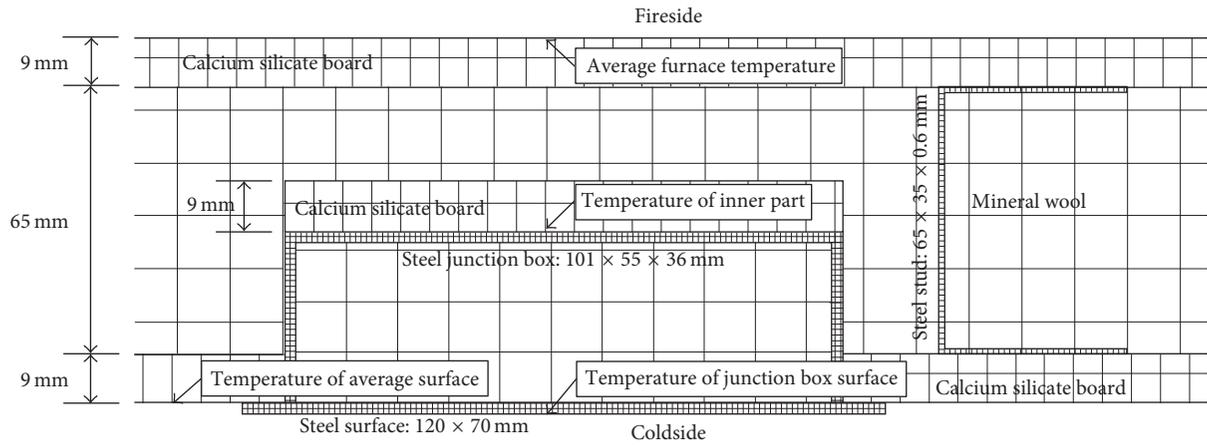
FIGURE 5: Cross section of the wall with indication of numerical modelling and the thermocouple position in Test 3.

2.3. Test Conditions. Test 1 follows the ISO 834-1 [2] standard. The size of the fire testing specimen is 3 m (height) × 3 m (width), and the zero pressure of the test furnace is at the height of 50 cm from the furnace bottom. As a result, according to the regulation of ISO 834-1 [2], 8 Pa should increase as the height increases every 1 m and the furnace pressure on the top of the specimen should not exceed 20 Pa; the standard heating curve of the test furnace is calculated using the following equation, and the furnace pressure measurement is recorded by a computer every 6 seconds:

$$T = 20 + 345 \times \log_{10}(8t + 1), \tag{1}$$

where T: average standard furnace temperature (°C) and t: time (min).

The heating temperature of Test 2 and Test 3 is adopted from the ISO 834-1 [2] standard heating curve, and the furnace pressure of the specimen is also set that the zero pressure is at the height of 50 cm from the furnace bottom. As a result, according to the regulation of ISO 834-1 [2], 8 Pa should increase as the height increases every 1 m and the furnace pressure on the top of the specimen is 4 Pa, and the pressure of the junction box is about 0.8 Pa.

2.4. Measurement and Recording of the Temperature of Standard Fire Test of Specimens. Test 1 sets 8 thermocouples on the unexposed surface of the specimen, as shown in Figure 6. According to the requirements of ISO 834-1 [2], temperature distribution is observed. Because it is required to compare the similarity of results of numerical modelling and tests and optimize the computer model, three measuring points are set in the middle layer of the wall and the measuring points are, respectively, in the position of 9 mm, 41 mm, and 74 mm, as shown in Figure 3. In Test 2 and Test 3, they, respectively, install the thermocouples on the unexposed surface of the specimens, as shown in Figure 7; four thermocouples are, respectively, located in the center of unexposed surface of the specimen, one in the center of wall, one on the panel of junction box, and another one in the center of mineral wool. The temperature measurement is recorded once in
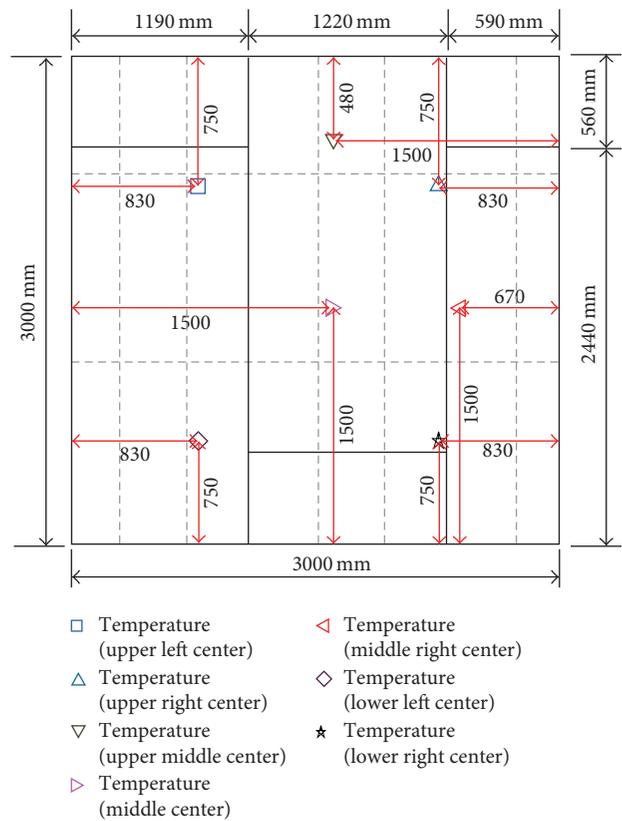
FIGURE 6: Test 1: the unexposed surface of the specimen and geometry of the thermocouple.

every 6 seconds by a computer, and it is recorded by photographs during the test.

3. Numerical Modelling

3.1. General Modelling. In this study, numerical modelling is based on CFD technology for a series of computer simulation analysis, the use of software fluent to solve [18]. It can be roughly divided into three parts: preprocessing, solve, and postprocessing. Preprocessing mainly focuses on how to build the geometric model and mesh. This research needs to
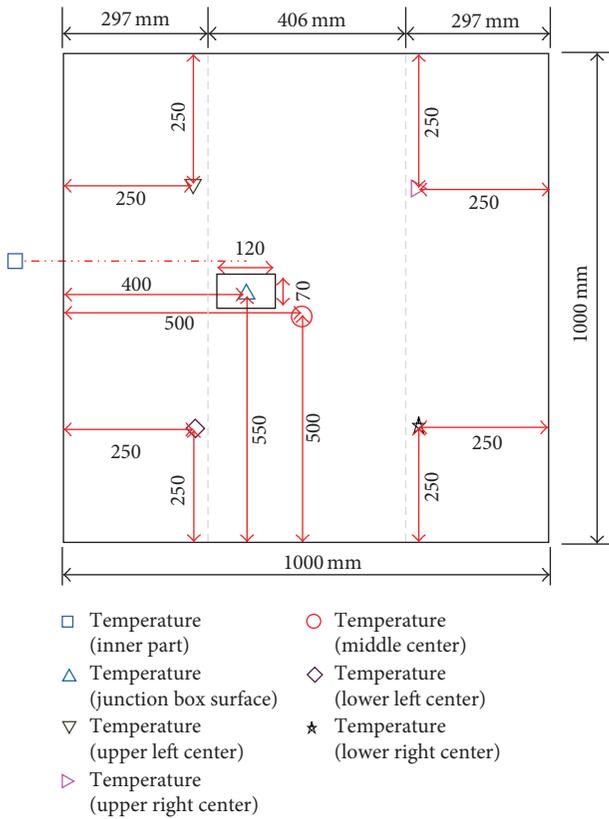
FIGURE 7: Test 2 and Test 3: the unexposed surface of the specimen and geometry of the thermocouple.

FIGURE 8: Numerical model of meshing.
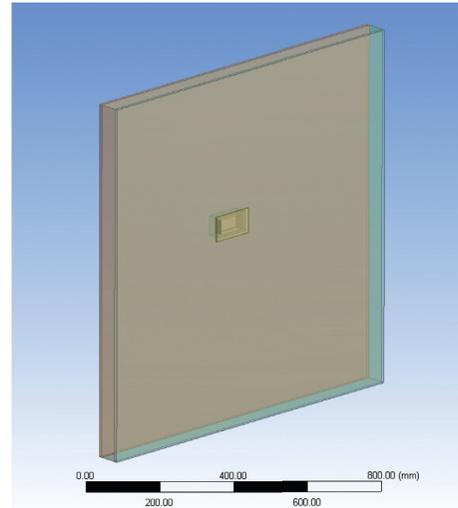
FIGURE 9: Numerical geometric model of wall embedded with the junction box.
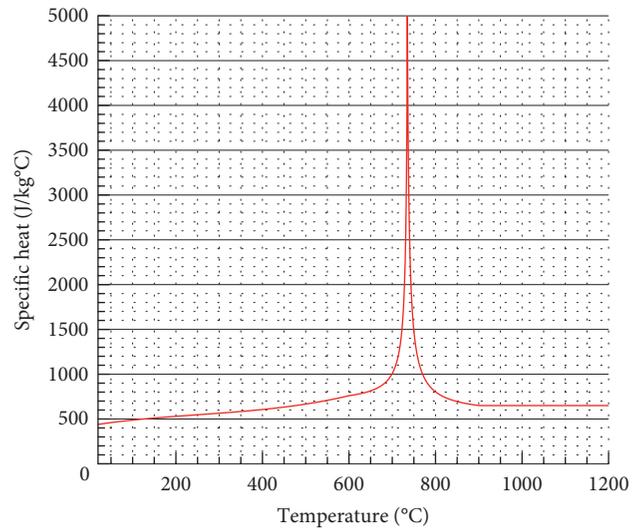
FIGURE 10: Specific heat for steel at elevated temperatures (BS EN 1993).

get the computer model which matches the standard fire test result, so the geometric model is designed corresponding to the standard fire test of the specimen. The numerical modelling takes the finite element numerical analysis in which the principle is to divide the solution domains into several interrelated subdomain units, assume a proper approximate solution to every unit, deduce the general satisfied conditions of the domain, and work out the solution of the question. Therefore, it is necessary to build the geometric model and mesh it into several units. Based on the shape and size of building components, Test 1 meshes it by hexahedron, as shown in Figure 8. The meshing sizes of the calcium silicate board, steel stud, and fireproof cotton are $9 \times 9 \times 9$ mm, $0.6 \times 0.6 \times 5$ mm, and $25 \times 25 \times 25$ mm, respectively. The geometric model in Test 2 and Test 3 is added with the embedded junction box, as shown in Figure 9. In addition, this part is added to the meshing. The meshing size is $0.5 \times 0.5 \times 0.5$ mm, and the other part is the same as Test 1. Solve mainly includes how to set up the related material parameters, set boundary conditions, and select the mathematics model and calculation methods. Postprocessing aims to analyze the data solved by modelling.

3.2. Parameter Setting. The materials used in the test include steel, calcium silicate board, PVC, and mineral wool. The parameters involved in the modelling material are specific heat (J/kg°C), thermal conductivity (W/m°C), and density

(kg/m^3). The parameters used in steel refer to the regulations of BS EN 1993 [19]. In addition, the specific heat of steel linearly increases as the temperature rises, as shown in Figure 10. The thermal conductivity of steel is 53.3 W/m°C when the temperature is 20°C, and it rises to 27.4 W/m°C

when the temperature is 800°C. However, the thermal conductivity is stable when the temperature is more than 800°C. The density of steel is 7850 kg/m³. Walker and Pavía [20] performed research on the thermal performance of a series of insulation materials. According to their related data, the specific heat of the calcium silicate board is 819.4 J/kg°C. The

$$
\lambda = \begin{cases} 0.0564 + 7.786 \times 10^{-5} \times t + 7.8571 \times 10^{-8} \times t^2 & (t \leq 500°C) \\ 0.0937 + 1.67397 \times 10^{-10} \times t^3 & (500 < t \leq 800°C), \\ 0.179 & (t > 800°C) \end{cases} \tag{2}
$$

where λ: thermal conductivity (W/m°C) and t: temperature (°C).

In this research, the PVC (polyvinyl chloride) panel of the junction box used in Test 2 conforms to the regulations of CNS 3142 [22]. According to the related researches made by Mansour et al. [23], the values of the specific heat, thermal conductivity, and density of PVC are 900 J/kg°C, 0.16 W/m°C, and 1380 kg/m³, respectively. In this research made by Nassif et al. [15], it presents some material property parameters related to mineral wool. Combining the specifications of mineral wool used in this research, the specific heat, respectively, is 840 J/kg°C and thermal conductivity increases as the temperature rises [24], as shown in Table 1. The density of mineral wool is, respectively, 60 kg/m³. The specific setting is shown as Table 2.

4. Results and Discussion

4.1. Test Results. The test time for Test 1 lasted 60 minutes. After 9 minutes of the test, trace smokes with abnormal smell burst out above the unexposed surface of the specimen and the seams of framework. At this time, all temperatures of measuring points obviously tend to rise (Figure 12). Until the 14th minute, the temperature of the measuring point on unexposed surface tends to decline until the 35th minute. From the 35th minute to the end, the temperatures rise all the time. The temperature of the inner wall's fire part rises rapidly after 9 minutes, and it slowly rises to the end after 22 minutes. At the end of test time, the temperature of the measuring point is 738.1°C. The temperature of the inner wall's middle part rises rapidly after the test begins till 9 minutes, and the rise begins to slow down towards the end after 38 minutes. At the end of test time, the temperature of the measuring point is 487.8°C. The situation of temperature of the inner wall's cold part is generally the same to that of the temperature of the side wall within the first 18 minutes. After that, the temperature gradually goes up to the end, and the final temperature is 316.5°C. At the 21st minute, a transverse crack appears on the upward side of the left board of the unexposed surface, and the crack extends to the center at 38th minute. When the test time is over, the temperature in the upper left center is the highest one (104.7°C) among temperatures on the unexposed surfaces, and the highest average temperature was 97.5°C (Figure 13), which does not exceed the stipulated fire

regulation of GB/T 10699-1998 [21] stipulates the thermal conductivities of the calcium silicate board at various temperatures and other parameters. Its thermal conductivity is shown in the following equation, and the thermal conductivity of the calcium silicate board linearly increases as the temperature rises, as shown in Figure 11:

resistance given in regulations of ISO 834-1 [2]. After the test, the integrity of the unexposed surface of the specimen is still good (Figure 14). Therefore, the specimen meets the demand of 60-minute fire resistance.

The test time of Test 2 lasted 60 minutes. After 6 minutes of the test, some smokes burst out and all temperatures of measuring points obviously tend to rise. Until the 37th minute, the temperatures of the thermocouple steadily increase, and the temperature junction box surface rises most sharply. It can be found that the embedded junction box has a great effect on the fire resistance of the metallic wall system. After that, the temperature significantly decreases and maintains around 40°C until the end of test. This is because the external panel of the junction box is PVC. According to the regulation of CNS 3142 [22], the softening temperature of PVC is not less than 73°C. The temperature of the thermocouple is higher than 100°C at the 28th minute, and the external panel of the junction box softens comprehensively (Figure 15) and falls out. This thermocouple is placed on the panel of the junction box, so the recorded temperature tends to plunge. Other temperatures of measuring points increase steadily. Among them, the temperature of the upper left center rises most significantly. This is because the furnace pressure is in a rising trend, and the temperature of the upper specimen is higher than that of the below specimen. The junction box is placed left-to-center, so the hot gas is released to the unexposed side from the weak surface after the weak surface is destroyed. After that, the hot gas rises rapidly making the temperature of the thermocouple higher than other temperatures. Until the 57.6th minute, the temperature of the upper left center is 207.8°C (Figure 16) and its initial temperature is 25°C, increasing by 182.8°C. According to ISO 834-1 [2], when the highest temperature of the unexposed surface is higher than the initial temperature by 180°C, it can be judged that the fire resistance is destroyed. After the test, the junction box panel on the unexposed surface of the specimen falls out, so the integrity is destroyed (Figure 17). Therefore, this specimen does not meet the demand of original 60 min fire resistance.

The test time of Test 3 lasted 60 minutes. After 6 minutes of the test, some smokes burst out and all temperatures of measuring points obviously tend to rise. After 15 minutes, the temperature of the inner part increases more obviously and the temperature is 463.4°C at the end of the test. All
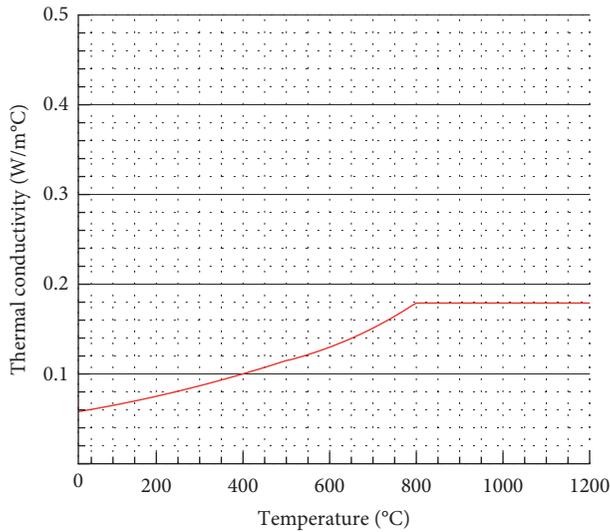
FIGURE 11: Thermal conductivity for the calcium silicate board at elevated temperatures.

TABLE 1: Thermal conductivity of the mineral wool.

Mineral wool					
Temperature (°C)	23.9	93	149	260	371
Thermal conductivity (W/m°C)	0.038	0.045	0.057	0.069	0.082

TABLE 2: Thermal properties.

Material	Specific heat (J/kg°C)	Thermal conductivity (W/m°C)	Density (kg/m³)
Steel	According to Figure 10	20°C, 53.3 $T \geq 800°C$, 27.4	7850
Calcium silicate	819.4	According to (2)	1350
PVC	900	0.16	1380
Mineral wool	840	According to Table 1	60

temperatures steadily rise. From 20th to 30th minute, the temperatures rise more sharply. After that, they tend to be stable until the 48th minute. From the 48th minute, the rising range of the temperature becomes greater towards the end. Among the temperatures, the temperature of the junction box surface rises most obviously, followed by the temperature of the upper left center. It is because the junction box fire resistance performance is still weaker than the surrounding integrated wall although it has been strengthened. Therefore, the junction box temperature is higher than other places. At the end of test, the temperature of the junction box surface is highest on the unexposed surface which is 198.2°C (Figure 18). The initial temperature is 25°C, increasing by 173.2°C. The highest average temperature of all the measuring points is 136.5°C, increasing by 111.5°C. According to ISO 834-1 [2], the highest temperature rise of unexposed surfaces should not be higher than 180°C from the initial temperature and the
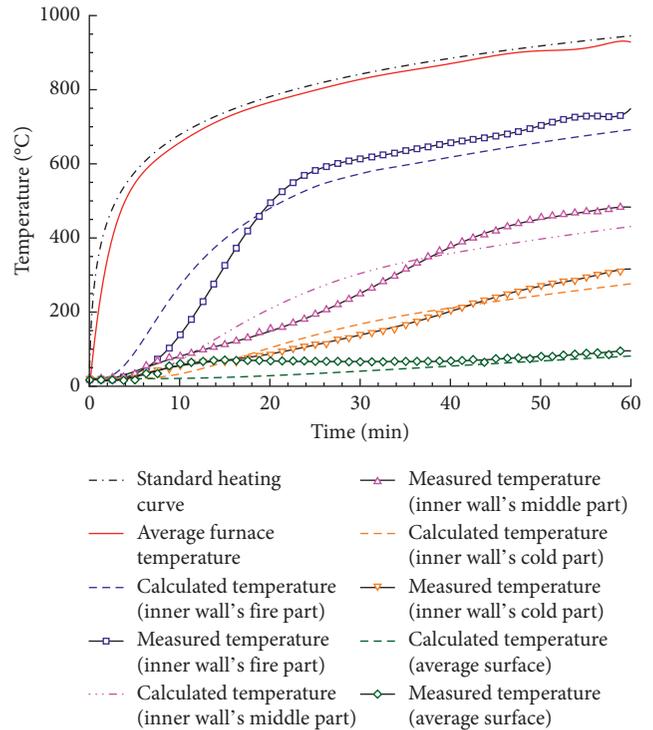
FIGURE 12: Measured temperatures compared to the calculated values in Test 1.
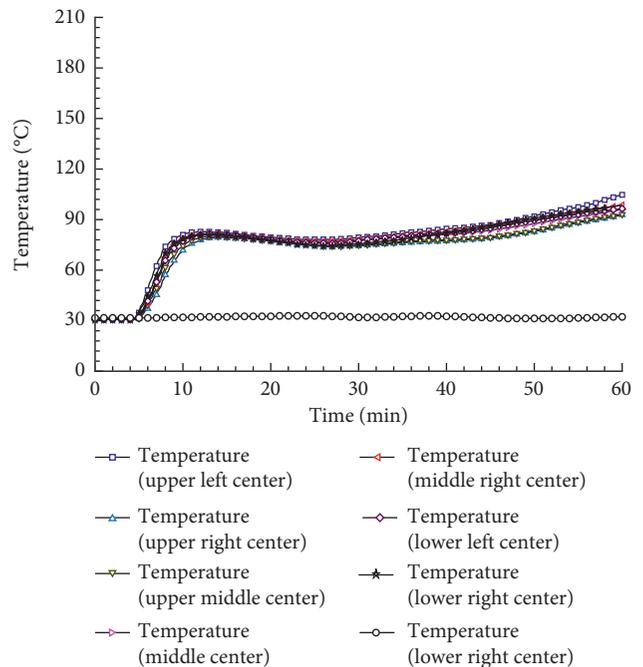
FIGURE 13: Time-temperature chart for the specimen in Test 1.

average temperature rise should not be higher than 140°C. During the test, these temperatures did not exceed the value given in the regulation of ISO 834-1 [2]. After the test, the integrity of unexposed surface of the specimen is still good (Figure 19). Therefore, the specimen meets the demand of 60-minute fire resistance.

(a)
(b)
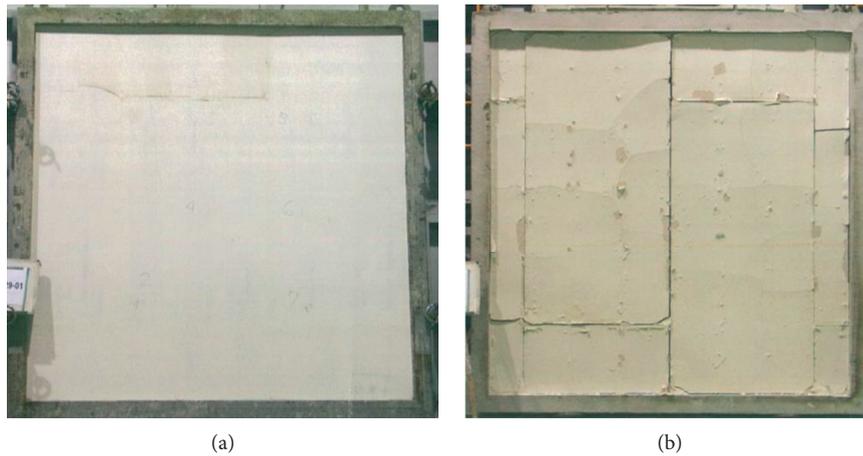
FIGURE 14: The result of the specimen after 60 min standard fire test in Test 1. (a) Unexposed surface. (b) Exposed surface.

4.2. General Discussion. Test 1 is the full-scale standard test with 3 m (height) × 3 m (width), and its standard fire test specimen and measuring temperatures of CFD finite element numerical modelling are in accordance with the test. The results obtained by comparing numerical modelling and standard fire test are shown in Figure 12. The heating curve of the test furnace is in accordance with the modelling standard heating curve which shows that the standard fire test temperature confirms with the regulation of ISO 834-1 [2]. In the standard fire test, the temperature of the inner wall's fire part rises faster in the first 22 minutes of the test and rises slower from 22nd minute to 60th minute. Similarly, the heating curve of numerical modelling on this measuring point is relatively ideal, which is basically coincident with the escalating trend of this measuring point in the standard fire test. In the first 20 minutes, the temperature of the inner wall's middle part rises slower, and after that, it rises faster. It is because at the 21st minute, a transverse crack appears on the upward side of the left board of unexposed surface and causes the temperature to rise faster. Because the numerical modelling is in an ideal condition, the numerical modelling temperature on this point rises slowly and continuously, so there will be a curve alternating situation of temperature slope and solid test temperature slope. However, the overall escalating trends are highly coincident. The temperature of the inner wall's cold part is away from the fire source, so its temperature heating curve is gentler than previous two temperatures, and it is highly correlated to the numerical modelling temperature. In the standard fire test, trace smokes with abnormal smell burst out above the unexposed surface of the specimen and the seams of framework at the 9th minute, so the average temperature on the unexposed surface greatly rises but tends to rise slower, corresponding with the numerical modelling temperature. Through the comparison, it can be found that the temperature ascending curves of different measuring points of numerically predicted values are highly correlated with the data of all temperature measuring points in the standard fire test in 60 minutes.

From Test 1, it can be found that the specimen without the junction box can meet the demand of 1-hour fire

FIGURE 15: The external panel of the junction box softens at 28th minute in Test 2.

resistance and the CFD numerical modelling result is highly correlated with the standard fire test. Test 2 expects to focus on exploring the effect of the specimen with the embedded junction box on the fire resistance and whether its related numerical modelling has correlation with the standard fire test result. Therefore, in Test 2, the specimen size is designed to be 1.0 m (height) × 1.0 m (width) and the junction box is embedded into the unexposed surface. The external panel of the junction box is PVC (polyvinyl chloride). In addition, the numerical model is added to the junction box, including the construction of the internal box and the external panel. The comparison of the standard fire test result and the numerical modelling result is shown in Figure 20. In the figure, it can be seen that the temperature heating curve of the test high-temperature furnace is very close to the standard heating curve in 60 minutes. It shows that the temperature of the burning furnace in the standard fire test meets the demand of ISO 834-1 [2]. The temperature value of the inner part in the standard fire test has limited difference from the numerical modelling temperature value on
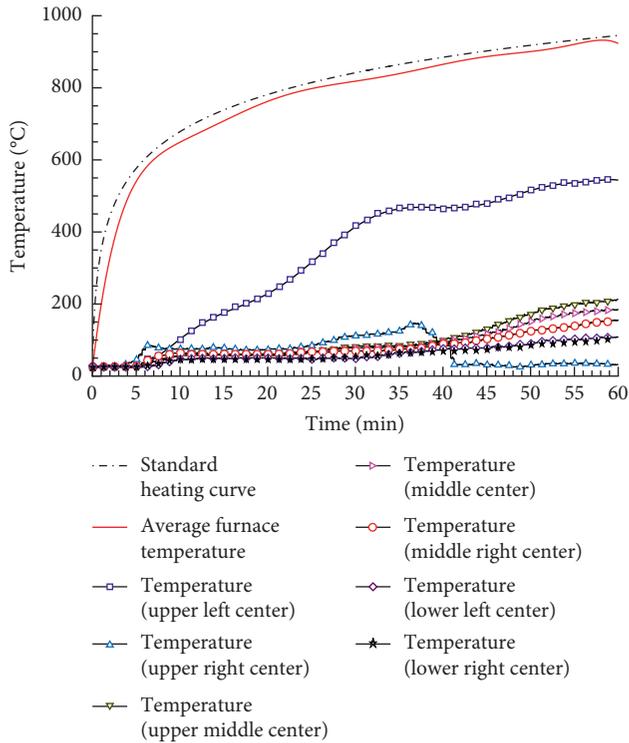
Figure 16: Time-temperature chart for the specimen in Test 2.
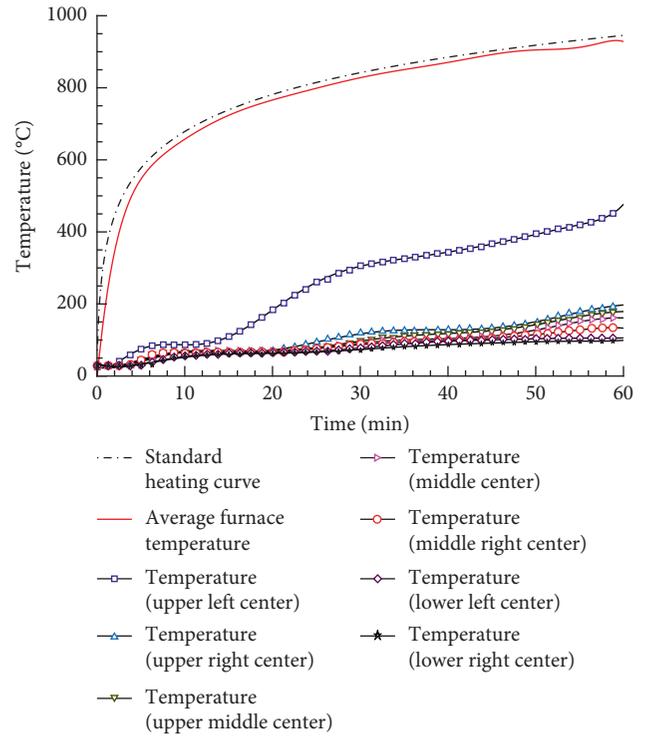
Figure 18: Time-temperature chart for the specimen in Test 3.

Figure 17: The result of the specimen after the 60 min standard fire test in Test 2.

Figure 19: The result of the specimen after the 60 min standard fire test in Test 3.

this point, and their escalating trends are basically corresponding and highly correlated. The actual temperature of the junction box surface is highly correlated with the temperature of the calculated junction box surface from test beginning to 37th minutes. After that, the test recorded temperatures dramatically reduce until the end of the test. This is because the external panel of the junction box is PVC. According to the regulation of CNS 3142 [22] that the softening temperature of PVC is not less than 73°C, the temperature of the thermocouple is more than 100°C at 28th minutes and the external panel of the junction box softens

comprehensively and falls out at 37th minute. As a result, the test temperature dramatically reduces after that, which is obviously different from the calculated temperature after 37 minutes. The average surface temperature and calculated average surface temperature's escalating trends are highly correlated. By comparison, it can be found that the standard fire test result is in accordance with the numerical modelling result in Test 2. Through the observation of the standard fire test and prediction of numerical modelling, it can be seen that after the junction box is embedded in the wall member, it will cause damage in two aspects, resulting in the
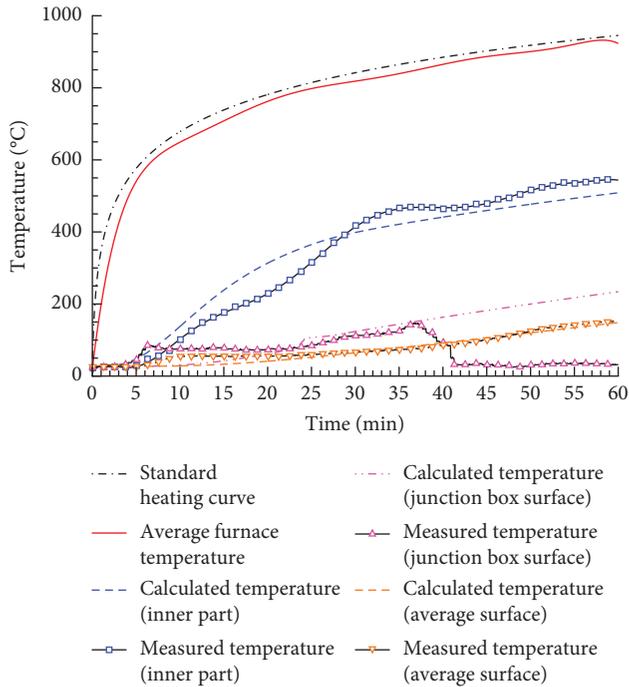
Figure 20: Measured temperatures compared to the calculated values in Test 2.
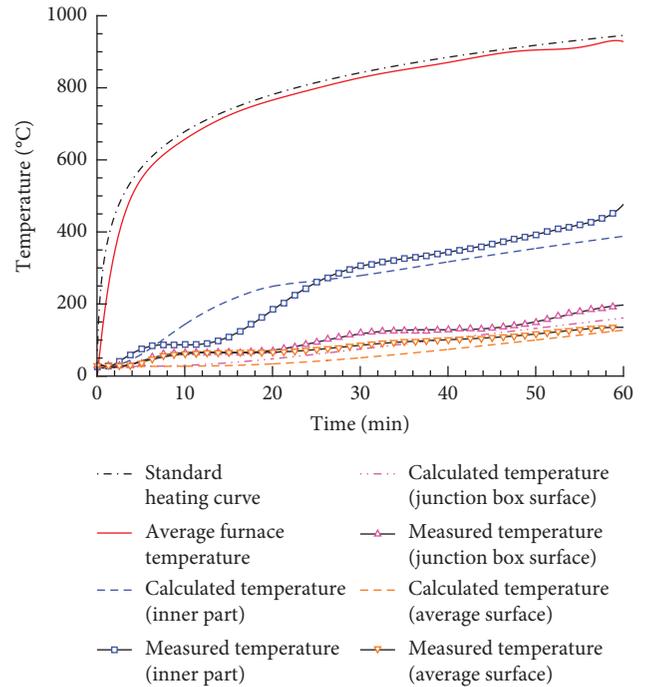
Figure 21: Measured temperatures compared to the calculated values in Test 3.

component failing to reach the original 1-hour fire resistance limitation. First, the material of the junction box is metal and its thermal conductivity is much higher than that of mineral wool and calcium silicate board, so the heat transmits to the unexposed surface faster. Second, the external panel material of the junction box is PVC and it begins to soften when the temperature is at 80~100°C. When the temperature rises, the panel falls out and the external junction box exposes. The material of the junction box is metal and it has high thermal conductivity, so it destroys the fire resistance of component.

The result of Test 2 shows that the position of the embedded junction box has a higher temperature than other parts and that the PVC junction box panel softens and falls out in heat which destroys the integrity of wall. According to above weaknesses, Test 3 proposes related reinforcement measures. Considering the density of the calcium silicate board as 1350 kg/m³ and the mineral wool as 60 kg/m³, the fire resistance performance of the calcium silicate board is much better than that of the mineral wool under the same thickness, although its thermal conductivity is slightly higher than the mineral wool. Therefore, a reasonable reinforcement measure is adding the calcium silicate board to the back of junction box and changing the PVC material to metal material. After these adjustments, modify the numerical models and parameters. When the modelling result meets the demand of 1-hour fire resistance, the standard fire test can be processed to verify. The final comparison of the standard fire test result and numerical modelling result is shown in Figure 21. According to the regulation of GB/T 10699-1998 [21], the water content of the calcium silicate board is not more than

10%. Therefore, the board contains certain water. The specific heat of water is higher and the heating temperature variation is not obvious, so the temperature of the inner part of the standard fire test at the beginning of heating is lower than the numerical modelling temperature. However, after the water evaporates completely, the temperature rapidly rises, which is highly correlated with the numerical modelling temperature. As shown in Figure 21, it can be seen that the temperature of the junction box surface is still higher than the temperature of the average surface. Although two aspects on the weakness are reinforced, it is still limited by the material and it cannot be completely identical with the original wall. The temperature of the junction box surface is the highest temperature on unexposed surface, but it can meet the demand of 1-hour fire resistance. The final result of the standard fire test in Test 2 shows that the temperature of the average surface is 153.0°C. When the standard fire test of Test 3 is over, this temperature is 138.2°C, reducing by 14.8°C. Because the panel falls out at after 37 minutes, the measurement of the temperature of the junction box surface in Test 2 distorts. The final temperature of the junction box surface of the standard fire test in Test 3 is 186.2°C, conforming to the standard of ISO 834-1 [2]. When the numerical modelling of Test 2 is over, the temperature of the average surface is 148.6°C and temperature of the junction box surface is 234.2°C. When the numerical modelling of Test 3 is over, the temperatures are, respectively, 127.5°C and 161.3°C, reducing by 21.1°C and 72.9°C, respectively. It can be seen that compared with Test 2, the temperatures on unexposed surface obviously reduce after reinforcement in Test 3 and the temperature of the junction box surface reduces most

significantly. However, in numerical modelling and standard fire test, the metallic-framework walls with embedded junction boxes after reinforcement in Test 3 can meet the demand of 1-hour fire resistance.

This is an innovative research. It is the first time to put forward the quantitative research on influence of embedded junction box on fire resistance of metal frame walls and analyze the weakness. In addition, it proposes effective reinforcement aiming at the weakness. After the reinforcement, the wall meets the demand of 1-hour fire resistance when the metallic-framework wall is embedded with the junction box. During the process, it successfully builds the CFD numerical models which is corresponding with the specimens, successfully predicts the effect of reinforcement by modified model parameters, and verifies it in the following standard fire test. This research not only systematically analyzes the metallic-framework wall with the embedded junction box and proposes effective reinforcement measures but also predicts them by CFD numerical modelling and verifies them successfully in the test. It is proved that the pattern of numerical modelling before the standard fire test is effective. Similar patterns can be applied to other researches on the wall systems and that can greatly save the cost of the test. Before the test, the numerical modelling can be processed to work out the predicted results. When the predicted result is satisfying, the standard fire test can be processed to verify.

5. Conclusions

(1) When the junction box is embedded into the metallic wall, the fire resistance of wall may be damaged because the metal junction box has a larger thermal conductivity and transfers the heat faster, while the PVC panel of the junction box softens in heat.

(2) The result of numerical modelling predicting the temperature by finite element is highly correlated to the result of standard fire test.

(3) After reinforcement, the temperature of the junction box surface decreases most significantly, and in Test 3, it reduces by 72.9°C when compared to Test 2.

(4) Adding the calcium silicate board to the back of the junction box and using the metal panel instead of the PVC panel can reinforce the original weakness effectively and help the metallic wall with the embedded junction box to meet the demand of 1-hour fire resistance.

(5) Making use of the finite element numerical modelling method to predict the test result is an effective way. It can be applied to other related fire prevention research and product development.

Conflicts of Interest

The authors declare that there are no conflicts of interest regarding the publication of this paper.

References

[1] NFPA 251, *Standard Methods of Tests of Fire Resistance of Building Construction and Material*, National Fire Protection Association, Quincy, MA, USA, 2006.

[2] ISO 834-1, *Fire-Resistance Tests-Elements of Building Construction: Part 1: General Requirements*, International Organization for Standardization, Geneva, Switzerland, 1999.

[3] JIS A 1304, *Method of Fire Resistance Test for Structural Parts of Buildings*, Japan Standards Association, Tokyo, Japan, 1994.

[4] CNS 12514, *Method of Fire Resistance Test for Structural Parts of Building*, Taiwan Standard, 2005.

[5] UL 263, *Fire Tests of Building Construction and Materials*, UL, Northbrook, IL, USA, 1997.

[6] BS 476-22, *Fire Tests on Building Materials and Structures. Methods for Determination of the Fire Resistance of Non-Loadbearing Elements of Construction*, BSI Group, London, UK, 1987.

[7] CNS 14652, *Glossary of Terms Used for Fire Protection in Building-Fire Test*, Taiwan Standard, 2008.

[8] S.-H. Lin, C.-L. Pan, and W.-T. Hsu, "Monotonic and cyclic loading tests for cold-formed steel wall frames sheathed with calcium silicate board," *Thin-Walled Structures*, vol. 74, pp. 49–58, 2014.

[9] M.-C. Ho and M.-J. Tsai, "Relative importance of fire resistance performance of partition walls," *Journal of Marine Science and Technology*, vol. 18, no. 3, pp. 430–434, 2010.

[10] M. Nithyadharan and V. Kalyanaraman, "Experimental study of screw connections in CFS-calcium silicate board wall panels," *Thin-Walled Structures*, vol. 49, no. 6, pp. 724–731, 2011.

[11] Y.-J. Chuang, W.-T. Wu, H.-Y. Chen, C.-H. Tang, and C.-Y. Lin, "Experimental investigation of fire wall insulation during a standard furnace fire test with different initial ambient air temperatures," *Journal of Applied Fire Science*, vol. 15, no. 1, pp. 41–55, 2006.

[12] I. Maruyama, G. Igarashi, Y. Nishioka, and Y. Tanigawa, "Carbonation and fastening strength deterioration of calcium silicate board: analysis of materials collected from a ceiling collapse accident," *Journal of Structural and Construction Engineering*, vol. 78, no. 689, pp. 1203–1208, 2013.

[13] P. C. R. Collier and A. H. Buchanan, "Fire resistance of lightweight timber framed walls," *Fire Technology*, vol. 38, no. 2, pp. 125–145, 2002.

[14] C. T. Do, D. P. Bentz, and P. E. Stutzman, "Microstructure and thermal conductivity of hydrated calcium silicate board materials," *Journal of Building Physics*, vol. 31, no. 1, pp. 55–67, 2007.

[15] A. Y. Nassif, I. Yoshitake, and A. Allam, "Full-scale fire testing and numerical modelling of the transient thermo-mechanical behaviour of steel-stud gypsum board partitionwalls," *Construction and Building Materials*, vol. 59, pp. 51–61, 2014.

[16] Y. Wang, Y.-J. Chuang, and C.-Y. Lin, "The performance of calcium silicate board partition fireproof drywall assembly with junction box under fire," *Advances in Materials Science and Engineering*, vol. 2015, Article ID 642061, 12 pages, 2015.

[17] CNS 5534, "Thermocuples," *Part 4: General Structural Matters*, Taiwan Standard, 1982.

[18] W. Yinuo, *The Standard Fire Testing and Numerical Modelling of the Behavior of Calcium Silicate Board Light Partition Wall Assembly with Junction Box*, Ph.D. thesis, National Taiwan University of Science and Technology, Taipei, Taiwan, 2018.

[19] BS EN 1993-1-2, *Eurocode 3: Design of Steel Structures—Part 1–2: General Rules Structural Fire Design*, BSI Group, London, UK, 2005.

[20] R. Walker and S. Pavía, "Thermal performance of a selection of insulation materials suitable for historic buildings," *Building and Environment*, vol. 94, pp. 155–165, 2015.

[21] GB/T 10699-1998, *Calcium Silicate Insulation, Part 5: Technical Requirements for Physical Performance*, China Standard, 1998.

[22] CNS 3142, *Polyvinyl Chloride Board, Part 3: General Quality*, Taiwan Standard, 2013.

[23] S. A. Mansour, M. E. Al-Ghoury, E. Shalaan, M. H. I. El Eraki, and E. M. Abdel-Bary, "Thermal properties of graphite-loaded nitrile rubber/poly(vinyl chloride) blends," *Journal of Applied Polymer Science*, vol. 116, no. 6, pp. 3171–3177, 2010.

[24] H. Kim, D. Park, E. S. Park, and H. M. Kim, "Numerical modeling and optimization of an insulation system for underground thermal energy storage," *Applied Thermal Engineering*, vol. 91, pp. 687–693, 2015.

Research Article

Multilevel Seismic Damage Behavior Correlation Analysis for RC Framed Structures

Jianguang Yue ⓘ

College of Civil Engineering, Nanjing Tech University, Nanjing 211800, China

Correspondence should be addressed to Jianguang Yue; jgyue@njtech.edu.cn

Five structural levels, that is, material level, section level, member level, storey level, and structure level, were proposed to analyze the multilevel nonlinear mechanism of the reinforced concrete (RC) framed structures. Based on the presented deformation equivalent principle, a generalized stiffness damage model was developed for each structural level. At each structural level, the stiffness damage value can be calculated by the integration of the material stiffness damage. Furthermore, an impact factor was proposed to reflect the damage correlations between different structural levels. In order to verify this method, the proposed method was used to study the damage evolutions at various structural levels of a 12-storey frame structure. The numerical model utilizing the proposed analysis method produces results in good agreement with the test results of the 12-storey frame structure. It shows that the proposed method is useful to assess the structure multilevel damage performance and to design a new structure.

1. Introduction

In damage mechanics of concrete structures, a damage model can directly calculate the inherent damage states of structures, members, or sections. For this reason, in the performance-based design method (PBDM), the damage degree is often evaluated in an explicit way by introducing the damage performance levels, which corresponds to the seismic intensity levels. The performance levels describe damage with the aid of damage models. However, in actual design works by now, the damage model is usually used to assess the nonlinear behavior for structure level or member level and very limitedly used in designing. The most important reason is that there is no any perfect damage model to describe the damage states for every structural level, and the damage correlations between the different levels are unknown. That is to say, it is not like the force-based design method which can clearly calculate the force relations between the structure level, storey level, member level, section level, and material level. Therefore, it is necessary to propose a new damage model which can calculate damage for every structural level and find

a way to reflect the damage correlations between different structural levels.

For different analytical purposes, the damage model can be defined by different mechanical indicators, such as stiffness, deformation, energy, and vibration characteristics. For example, the hysteretic energy-based damage model is often used to evaluate the damage for structure level or member level [1, 2]. In some researches, the deformation has been verified as a good damage indicator not only for the bending-failure-type members (RC columns, beams, and walls) but also for the shear-failure-type members [3]. The deformation-characterized interstorey drift ratio or plastic rotation was used to define the damage model by the study of Banon and Veneziano [4] and Wang et al. [5]. The widely-known Park and Ang damage model [6] was defined by both maximum displacement and plastic energy of dissipation. The strains of concrete and rebar were used to establish a procedure of damage determination for member level by Sharifi et al. [7]. Moreover, the bearing capacity of the M-N relationship can be used to evaluate the damage of section level [8], and the variations of the stiffness or intrinsic
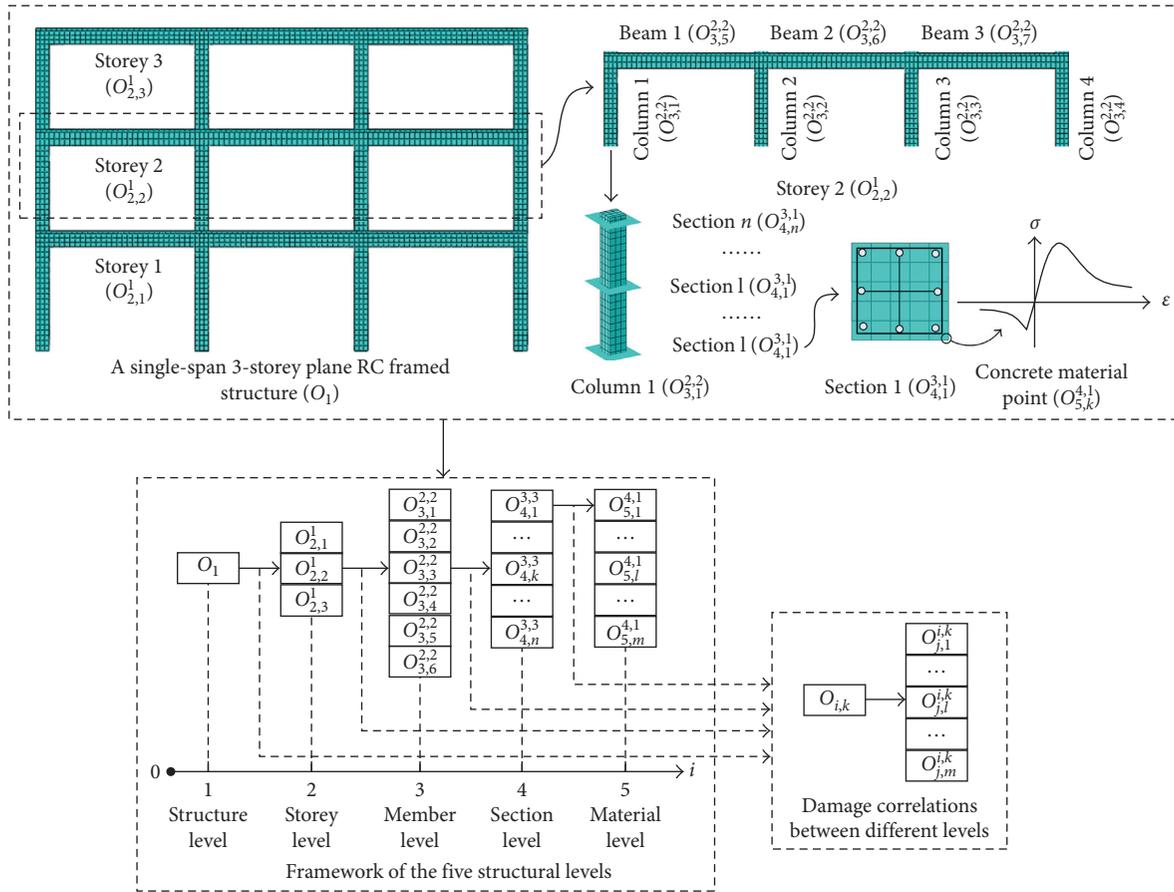
FIGURE 1: Illustration of multilevel damage definition.

period can be used to evaluate the damage of structure level [9].

In the theory of engineering mechanics, the stiffness means the deformation-resistant capacity, that is, the ratio of force to deformation, for any structural level. Thus, the stiffness could be an ideal damage indicator for the multilevel damage assessment. In fact, the stiffness-based damage index in a well-known concrete plastic-damage model [10] has been widely used for the nonlinear numerical analysis [11, 12]. It was proposed from the strain equivalent principle [13] that the strain of damage material caused by nominal stress is equal to the strain of undamaged material caused by the effective stress. Furthermore, this stiffness-based damage index using the integrating method with the weight coefficient (such as the lengths or important factors of the damage zones) can be used to predict the damage performance of the structure level [14–16].

In this paper, a deformation equivalent principle was firstly proposed based on the strain equivalent principle. Secondly, a generalized stiffness-based damage model was presented for every structural level. Its arithmetic expression in an integrating form and the correlation impact factor were used to analyze the multilevel damage mechanism. As an example, a shaking table seismic test of a single-span 12-storey RC framed structure was analyzed by the proposed method.

2. Multilevels for RC Framed Structure

Under earthquake seismic motion, the mechanical behavior-like deformation capacity, bearing capacity of material, member, or structure can be characterized at material level, section level, member level, storey level, and structure level. As shown in Figure 1, each structural level can be expressed as the analysis object O_i, in which the letter i means the structural level. The values of i are 1, 2, 3, 4, and 5 for the structure level, storey level, member level, section level, and material level, respectively. An example for the multilevel definition is shown in Figure 1. In Figure 1, the subscript i of $O_{i,k}$ denotes the structural level i and the subscript k is the object number; that is, $O_{i,k}$ means the object k at level i, and O_1 means the object at structure level (the global structure). The superscript "i, k" of $O_{j,l}^{i,k}$ means it is a part of $O_{i,k}$; that is, $O_{j,l}^{i,k}$ means the object l at level j as a part of $O_{i,k}$. As shown in Figure 1, the global structure is denoted as O_1 and storey 2 is denoted as $O_{2,2}^1$. In storey 2 ($O_{2,2}^1$), the columns 1, 2, 3, and 4 are denoted as $O_{3,1}^{2,2}$, $O_{3,2}^{2,2}$, $O_{3,3}^{2,2}$, and $O_{3,4}^{2,2}$, respectively, and the beams 1, 2, and 3 are denoted as $O_{3,5}^{2,2}$, $O_{3,6}^{2,2}$, and $O_{3,7}^{2,2}$, respectively. In column 1 ($O_{3,1}^{2,2}$), section 1 can be written as $O_{4,1}^{3,1}$. The material point k of section 1 is denoted as $O_{5,k}^{4,1}$.

According to the definition, the affiliation framework of the five structural levels is expressed in Figure 1. This
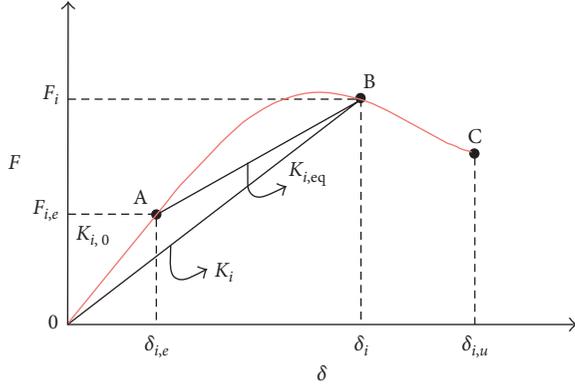
FIGURE 2: Generalized force-deformation relationship [17].

affiliation framework shows the analysis object for each structural level. It can be used to find which object is important for the structural mechanism. Moreover, the correlations between different levels can be abstractly expressed (Figure 1). It can represent the correlation between any two different structural levels.

3. Deformation Equivalent Principle

In general, local damage in RC structures subjected to a severe seismic motion is usually caused by the microcracking and crushing of concrete, yielding of the steel reinforcement, and bond deterioration of the steel-concrete interfaces. The local damage on a cross section can be adequately evaluated by the degradations of the sectional bending stiffness and moment bearing capacity. The overall combination of all local damages leads to the global stiffness and strength deterioration of the structure. Damage models are used to characterize the damage state of the structure after an earthquake seismic motion and can be used to assess the design aims or the postearthquake bearing capacity. According to the principle of strain equivalence, the damage at material level is defined by the concept of effective stress. The effective stress σ' is the stress applied on an element of undamaged material with the same deformation of a damaged element subjected to the current stress σ.

Essentially, the strain equivalence assumption describes the material stress-strain relation by introducing the damage variable d. Considering this principle can be popularized to any structural level, the definition is reasonably deduced as follows: the effective force F' (Figure 2) applied to an element of undamaged object (material, cross section, member, storey, or structure level) will have same deformation like a damaged element subjected to the current force F (Figure 2).

4. Seismic Stiffness Damage Model

Therefore, a generalized force-deformation relation [17], as shown in Figure 2, can be used to describe the behavior at any structural levels. In Figure 2, point A represents the

initial damage state and curve 0AB represents the nonlinear behavior caused by material damage.

In Figure 2, δ is the generalized deformation for every structural level, and δ_i, $\delta_{i,e}$, and $\delta_{i,u}$ represent the deformation, elastic limit deformation, and ultimate deformation of level i, respectively; F is the generalized force which corresponds to the generalized deformation δ, F_i represents the force for damaged configuration, $F_{i,e}$ is the elastic limit bearing capacity; $K_{i,0}$, K_i, and $K_{i,eq}$ are the initial stiffness, secant stiffness, and equivalent stiffness, respectively. The equivalent stiffness $K_{i,eq}$ represents the damage effect on stiffness of the undamaged configuration and is expressed as

$$K_{i,\text{eq}} = \frac{\delta_i K_i - \delta_{i,e} K_{i,0}}{\delta_i - \delta_{i,e}}. \tag{1}$$

Here, the point A in Figure 2 is assumed to represent the initial damage state. Therefore, based on the deformation equivalent principle, the generalized damage variable d_i is

$$d_i = 1 - \frac{K_{i,\text{eq}}}{K_{i,0}}. \tag{2}$$

Equation (2) is the generalized stiffness damage variable which can reflect the stiffness degradation for every structural level. This model can also be formulated in the material configuration for thermodynamically stable problems with no temperature time variation. Thus, the mathematical form for the free energy is assumed as [18, 19]

$$\psi_5(\varepsilon, d_5) = (1 - d_5)\psi_5^0(\varepsilon) = (1 - d_5)\left[\frac{1}{2\rho_0}\varepsilon^T \sigma_0\right]$$

$$= (1 - d_5)\left[\frac{1}{2\rho_0}\varepsilon^T E_0 \varepsilon\right], \tag{3}$$

$$d_5 = 1 - \frac{E_{\text{eq}}}{E_0}; \quad E_{\text{eq}} = \frac{\varepsilon E - \varepsilon_0 E_0}{\varepsilon - \varepsilon_0},$$

where ψ_5 and ψ_5^0 ($i = 5$ for material level) are the free energy of damaged material and undamaged material, respectively; d_5 is the material stiffness damage variable; ε and ε_0 are the strain tensor and elastic limit strain tensor of material, respectively; σ_0 is the stress tensor of undamaged material; ρ_0 is the material density; and E_0 is the initial elastic modulus, E_{eq} is the equivalent modulus, E is the secant stiffness. Specially, if $d_5 = 0$, then $\psi_5(\varepsilon, d_5 = 0)$ means the strain energy of undamaged material.

The potential energy $W_{i,k}^p$ of object $O_{i,k}$ can be obtained by integrating ψ_5 with mass through the volume of $O_{i,k}$ and expressed as

$$W_{i,k}^p = \int_{V_{i,k}} \psi_5 \, dm = \int_{V_{i,k}} (1 - d_5)\psi_5^0 \rho_0 \, dV = (1 - d_5)W_{i,k}^{p,0}, \tag{4}$$

where $W_{i,k}^{p,0}$ is the potential energy of undamaged object $O_{i,k}$ and $W_{i,k}^{p,0} = \int_{V_{i,k}} \psi_0 \rho_0 \, dV$. Thus, the stiffness damage $d_{i,k}$ of $O_{i,k}$ can be calculated from (4) and expressed as

$$d_{i,k} = 1 - \frac{W_{i,k}^p}{W_{i,k}^{p,0}} = \frac{\int_{V_{i,k}} \psi_5^0 \, dV - \int_{V_{i,k}} (1 - d_5)\rho_0 \psi_5^0 \, dV}{\int_{V_{i,k}} \rho_0 \psi_5^0 dV}$$

$$= \frac{\int_{V_{i,k}} d_5 \rho_0 \psi_5^0 \, dV}{\int_{V_{i,k}} \rho_0 \psi_5^0 \, dV} \approx \frac{\sum_e^{i,k} d_5 \psi_5^0}{\sum_e^{i,k} \psi_5^0}, \tag{5}$$

where $\sum_e^{i,k}$ means the summation for all elements of object $O_{i,k}$. Equation (5) shows that the stiffness damage $d_{i,k}$ for any structural level i can be calculated by the material damage d_5.

If the damage $d_{j,l}$ and the free energy $\psi_{j,l}^0$ of object $O_{j,l}^{i,k}$ are known, it has the relationships of $\sum_e^{j,l} \psi_5^0 = \psi_{j,l}^0$ and $\sum_m \psi_{j,l}^0 = \sum_e^{i,k} \psi_5^0$. The damage $d_{i,k}$ of object $O_{i,k}$ ($j > i$) can be obtained by substituting these two above relationships into (5), and the resulting expression is as follows:

$$d_{i,k} = \frac{\sum_m d_{j,l} \psi_{j,l}^0}{\sum_m \psi_{j,l}^0}, \tag{6}$$

where $\sum_m$ means the summation for total parts of $O_{i,k}$ and m is the part number of $O_{i,k}$. Equation (6) shows that the damage $d_{i,k}$ can also be obtained by the summation of $d_{j,l}$ with the weighted coefficient $\psi_{j,l}^0$.

Therefore, an impact factor $\gamma_{i,k}^{j,l}$ is proposed here to calculate the damage effect from $O_{j,l}^{i,k}$ to $O_{i,k}$. Based on (6), its expression is

$$\gamma_{i,k}^{j,l} = \frac{d_{j,l} \psi_{j,l}^0}{\sum_m d_{j,l} \psi_{j,l}^0}, \tag{7}$$

where $0 \leq \gamma_{i,k}^{j,l} \leq 1$, and the higher value of $\gamma_{i,k}^{j,l}$ means higher damage effect from $O_{j,l}^{i,k}$ to $O_{i,k}$.

5. Test Model and Numerical Simulation

A shaking table test of a 12-storey RC frame model (Figure 3) of the State Key Laboratory of Disaster Reduction in Civil Engineering in Tongji University [20] was used to verify the proposed analysis method of the damage correlations of different structural levels. The ABAQUS computer program [21] was used to perform numerical simulation of the test model which was subjected by the earthquake seismic motions. In the finite element model, the material behavior of concrete was described by the concrete plastic-damage model presented by Lubliner et al. [10], which can calculate the compression and tensile damage of concrete. The concrete was modeled by C3D8R elements which are 8-node linear brick elements with reduced integration and hourglass control. The material behavior of the steel reinforcement was described by an elastoplastic model with 1% strain hardening. The steel reinforcements were modeled by the T3D2 elements which are 2-node linear displacement truss elements and embedded in the concrete elements.

The 12-storey model frame structure has one single bay in the X- or Y-direction, a total height of 3.6 m and a storey height of 0.3 m. The plan and elevation views of the structure are shown in Figure 3. The compressive strength of concrete is from 5.74 MPa to 8.20 MPa. The cross-sectional size of all columns and beams are 50×60 mm and 30×60 mm, respectively. Reinforcement layouts are identical in all beams and columns. The yield strength and ultimate strength of rebar number 1 (nominal diameter is 2.11 mm) are 390 MPa and 560 MPa, respectively. The yield strength and ultimate strength of rebar number 2 (nominal diameter is 0.9 mm) are 327 MPa and 397 MPa, respectively. The average elastic modulus of concrete is 7.75×10^3 MPa.

Four earthquake seismic motions were used as the test loading input: (1) El-Centro waves, (2) Kobe waves, (3) Shanghai artificial waves, and (4) Shanghai bedrock waves. The range of the input peak acceleration was 0.090–0.904 g. The standard storey and top storey were subjected by additional masses of 19.4 kg and 19.7 kg, respectively. Totally 54 loading cases were calculated and compared with the test results.

In loading case number 53, the values of input peak ground acceleration in X-, Y-, and Z-direction were 0.904 g, 0.769 g, and 0.452 g of EI-Centro waves, respectively. In loading case number 53, vertical cracks occurred at the ends of beams from storey 2 to 8. The damages from storey 3 to 8 were most serious, where the maximum width of cracks was about 4 mm and plastic hinges appeared at the ends of beams. There was almost no damage from storey 11 to 12.

As shown in Figure 4, the calculated acceleration responses of A2, AY2, A7, and AY7 of loading case number 53 were compared with the test results. The acceleration responses of A2 and A7 were along the X-direction, and the responses of AY2 and AY7 were along the Y-direction. The calculated results agreed well with the test results. It shows that the numerical model can depict the nonlinear seismic responses of the test model with well accuracy. The multilevel damage evolutions of the test model can be analyzed based on the numerical responses. In the following, the loading case number 53 was used to be analyzed with the proposed method.

6. Multilevel Damage Analysis

6.1. Structure Level and Storey Level. The structural final damage state of loading cases number 53 is shown in Figure 5(a). The abbreviation PEEQT stands for the equivalent plastic tensile strain which reflects the onset of cracks. According to (6), the stiffness damage evolutions can be calculated for each structural level. Thus, the calculated stiffness damage evolutions of the global structure and each storey (from storeys F2 to F12 in Figure 3) are shown in Figure 5(b). The letter F followed by the number 1 to 12, denotes the floor or storey. The damage of storey F1 was close to zero, so it was not shown in Figure 5(b).

In Figure 5, the calculated damages from storeys F3 to F8 were the most serious with the maximum damage value of 0.8. The damage evolution curves show that damages at
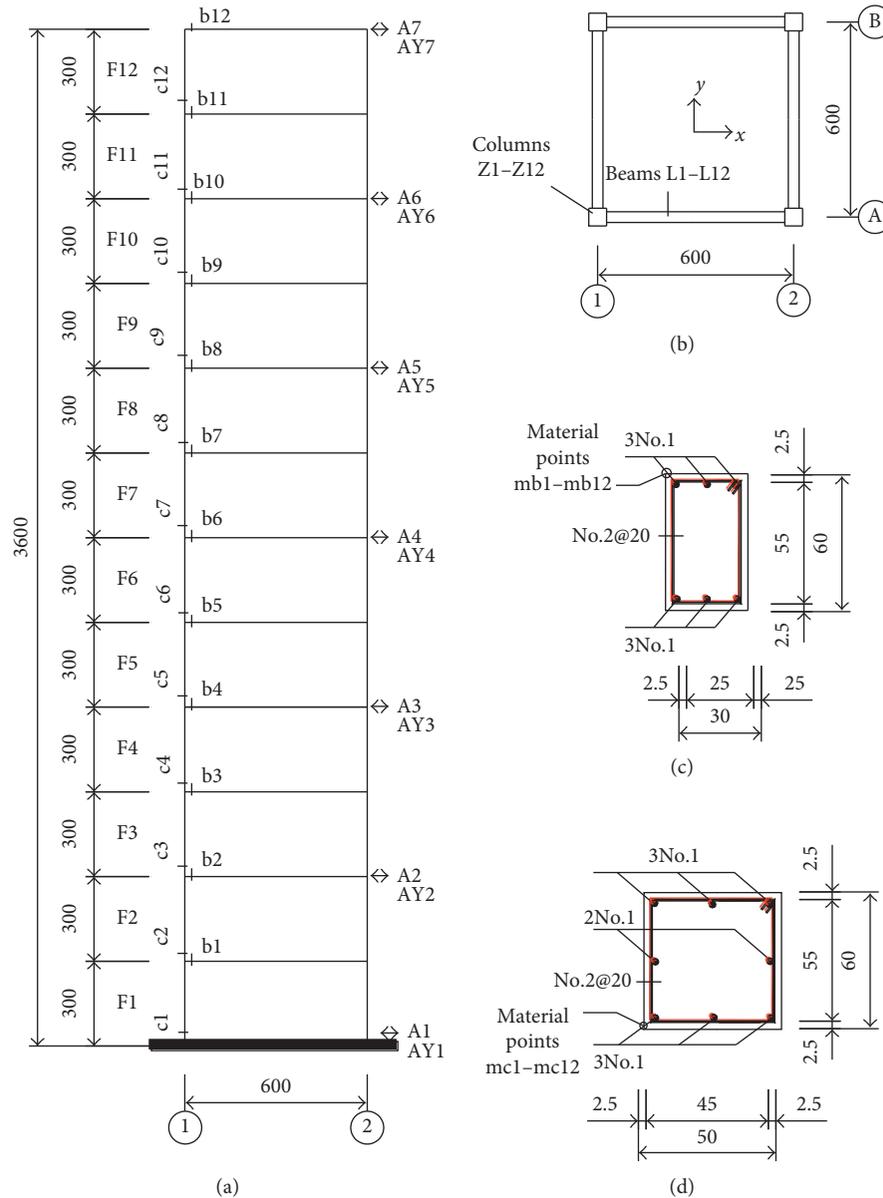
FIGURE 3: Geometrical details of the 12-storey RC frame test model [20]. (a) Elevation and acceleration sensor placement. (b) Structure plan. (c) Beam cross section. (d) Column cross section.

storeys F2 to F8 occurred almost at the same time. The calculated maximum damage of storey F2 was 0.5. The maximum damage value of the global structure was 0.7. Compared with the test damage states (Figure 5(a)), it shows that the calculated results were in good agreement with the test responses. Moreover, Figure 5(b) reflects the damage mechanism at storey level and structure level. The analysis results indicate that the structure level damage was mainly due to the damages of storeys F5 to F7.

6.2. Member Level, Section Level, and Material Level. The columns Z1 to Z12 (Z means column) and beams B1 to B12 (B means beam) were analyzed for the member level. In Figure 6, if the damage value was close to zero, it will not be shown.

As shown in Figure 6(a), the onset of damage of columns Z2 and Z8 and beams from L2 to L8 started at the same time, that is, about 0.25 s. The damage evolutions of beams from L3 to L7 developed faster than other members. At storey F2, the damage evolution of column Z2 developed faster than beam L2. At storey F8, the damage evolution of column Z8 developed faster than beam L8.

The maximum damage values of columns Z2 and Z8 were 0.6 and 0.8, respectively. The maximum damage values of column Z2 and beams L3 to L7 were about 0.8. The maximum damage value of beam L8 was about 0.65. The maximum damage values of column Z2 and beam L2 were about 0.5.

According to Figure 6(a), the damages of storeys from F3 to F7 were mainly due to the beams, the damage of storey F8
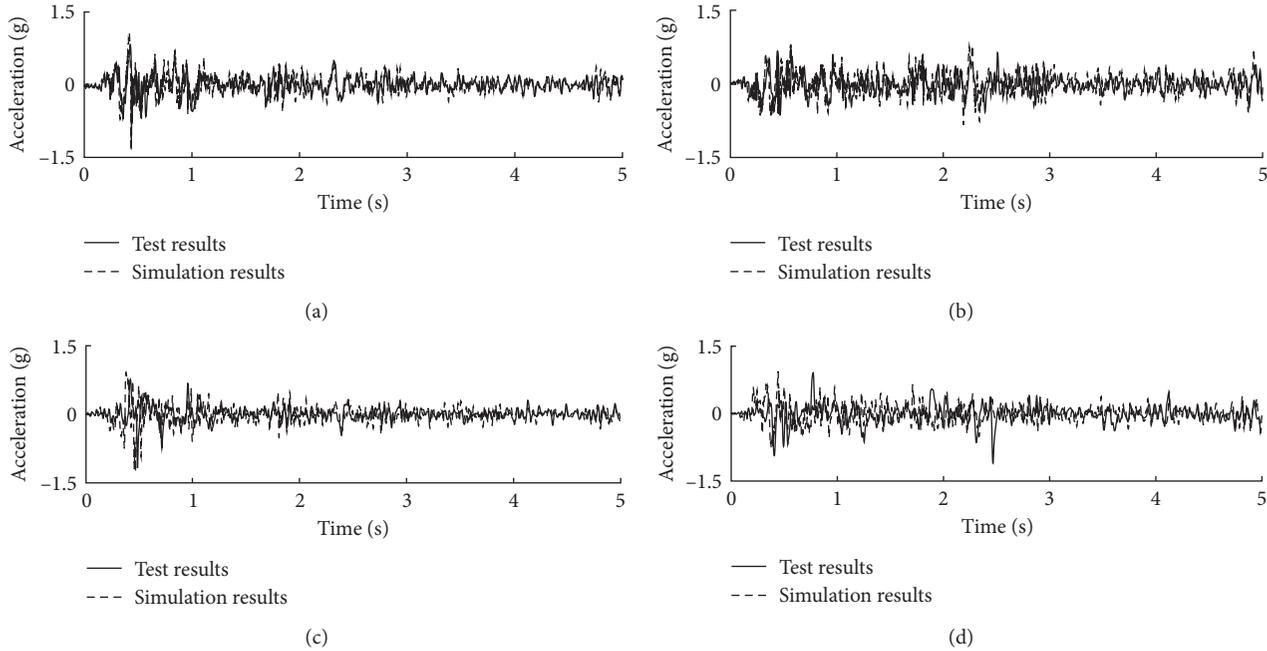
FIGURE 4: Comparisons of calculated and tests responses [20]. (a) Case 53: A2 acceleration comparison. (b) Case 53: AY2 acceleration comparison. (c) Case 53: A7 acceleration comparison. (d) Case 53: AY7 acceleration comparison.

was mainly due to the columns, and the damage of storey F2 was due to both columns and beams. Based on this analysis, only the sections of columns Z5 to Z7 and beams L5 to L7 were necessary to be analyzed for the section level (Figure 6(b)). In Figure 6(b), the letters c and b mean the sections of column and beam, respectively.

Based on the comparison of Figures 5 and 6, it can be found that the damage of section level, member level, storey level, and structure level almost began at the same time (about 0.25 s). The maximum damage values of sections c5, c6, and c7 were small (about 0.3) which corresponded to the damage values of columns Z5, Z6, and Z7. The maximum damage values of sections b5, b6, and b7 were large (about 0.9) which corresponded to the damage values of beams L5, L6, and L7. Therefore, it means that the damages from storey F5 to F7 were mainly caused by the bending-type failures of beams.

Thus, only the material points mb5 to mb7 of beam sections L5 to L7 were necessary to be analyzed for material level (Figure 6(c)). It can be found that the damage of material level began at the same time with the other structural levels. However, the damages of mb5 and mb6 reached to their peak values earlier than mb7. The damage evolutions of material agreed with the responses of beams L5 and L6.

7. Damage Correlation Analysis

Although the multilevel damage analysis can respect the structural damage mechanism for different structural levels, it still cannot provide quantitative values to describe the correlations between different structural levels.

In this section, the damage correlations were analyzed to explore the inherent nonlinear behavior of the structure and to help designing a new structure. As mentioned above in Section 4, the presented impact factor $\gamma_{i,k}^{j,l}$ of (7) was used here to reflect the damage correlations quantitatively.

Firstly, the damage effect from storey level to structure level was analyzed (Figure 7(a)). It shows that the impact factor curves of sotreys F4, F5, and F6 started to increase at about 0.25 s and quickly reached to the peak values of 0.39, 0.28, and 0.18, respectively, at about 0.5 s. Then, the impact factor curves of F4, F5, and F6 began to decrease and finally reached to the minimum value of 0.11, and meanwhile the structure reached to its maximum value. The impact factor curves of storeys F2, F3, F7, and F8 also started to increase at 0.25 s and reached to the maximum values of 0.19, 0.15, 0.12, and 0.19, respectively, while then began to decrease, and meanwhile the structure reached to the maximum value. It can be seen from the above results that the structure damage was caused by the storeys F4, F5, and F6 in the beginning and then caused by the storeys F2, F3, F7, and F8. Comparatively, the damage effect from storeys F5 and F6 was the most serious for the global structure. Thus, the damage effect from beam L5 and column Z5 to the storey F5 (Figure 8) was analyzed in the following (Figure 7(b)).

In Figure 7(b), the impact factor values of column Z5 were very close to zero. It indicates that column Z5 did not affect storey F5. While the impact factor curve of beam L5 started to increase at 0.25 s and reached to the maximum value of 0.25, and meanwhile, the storey F5 reached to about half of its maximum value. It indicates that the damage of storey F5 was mainly caused by the beams.
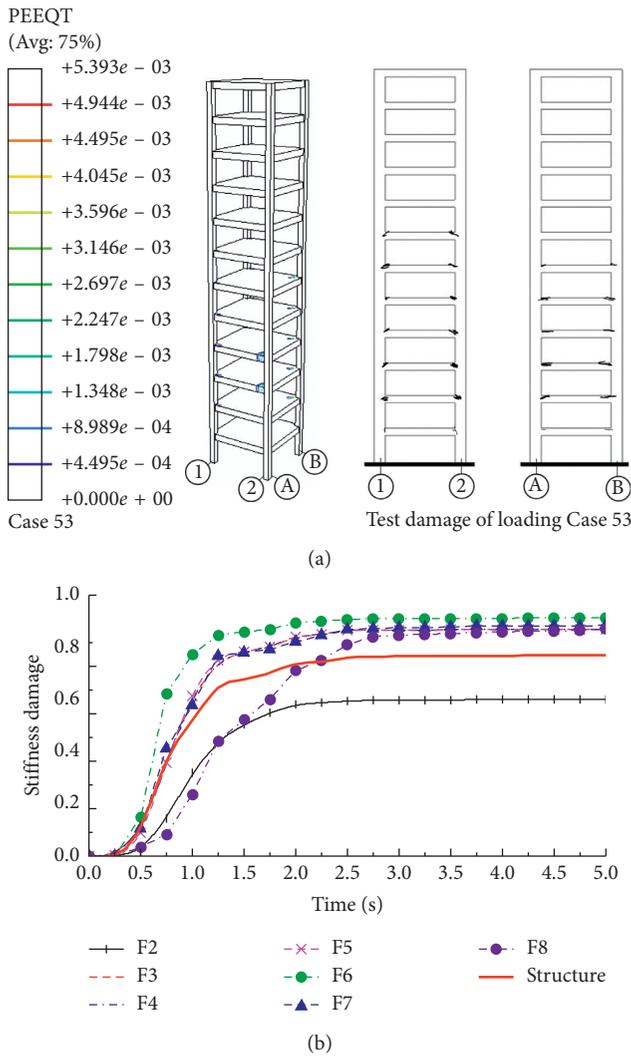
Figure 5: Damage results for structure level and storey level. (a) Final damage comparisons of calculation and test [20]. (b) Damage evolutions for storey level and structure level.

Furthermore, the damage effect from two cross sections (one is at the beam end and another is at the middle span in Figure 8) and one diagonal section (near the beam end in Figure 8) to beam L5 was analyzed as follows (Figure 7(c)).

It can be found that the impact factor values of sections b5-2 and b5-3 were close to zero while the maximum value of section b5-1 was 0.66. That means the damage of beam L5 was mainly caused by the cross-sectional damage at its end which was the bending-type failure. Thus, three material fibers (Figure 8) were analyzed to reflect the damage effect from material points to the cross section b5-1. Here, each fiber, including three element nodes, was used as the representative for the material level. The impact factor curves of fiber 2 and fiber 3 were very close, and their values were larger than the value of fiber 1. The impact factor maximum values of fiber 2 and fiber 3 were about three times of fiber 1. It indicates that the damage effect of the bottom fibers was more serious than the fibers at the top of the section.
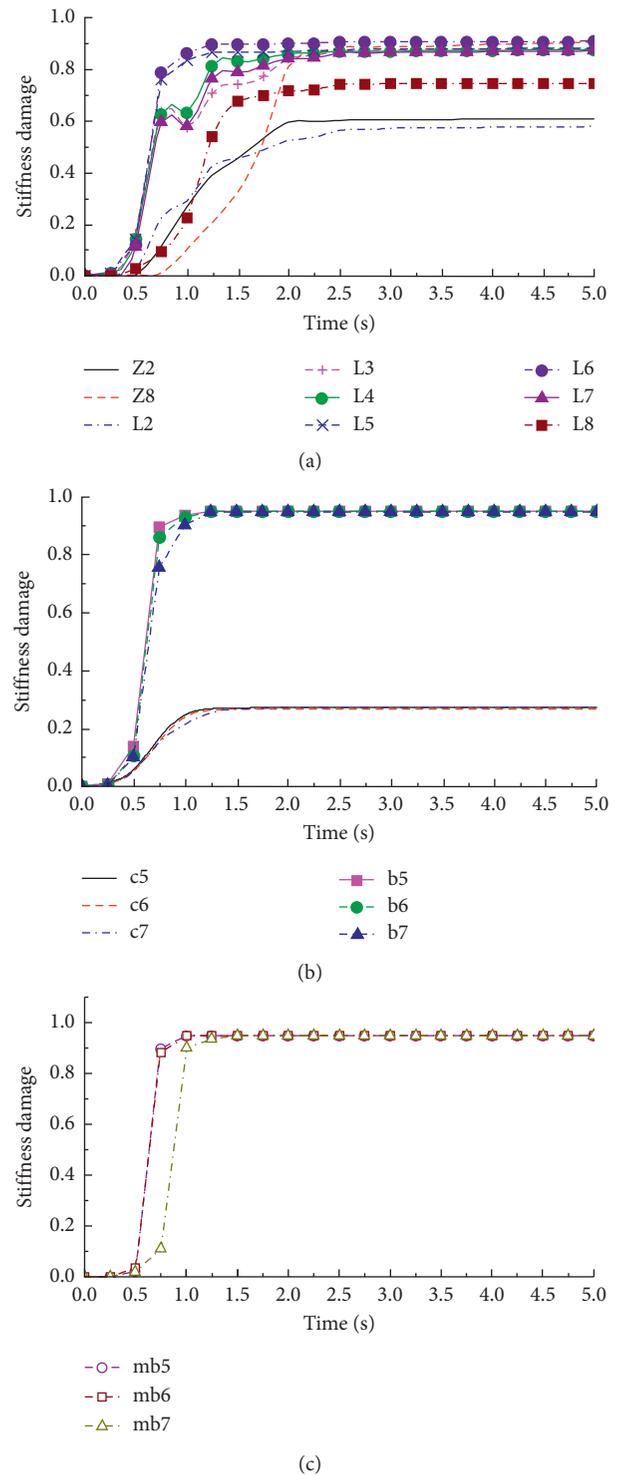
Figure 6: Damage evolutions for (a) member level, (b) section level, and (c) material level.

Based on the above analysis, the failure of this 12-storey-framed structure model (noted as object O^1) was the plastic hinge failure mode of beams. The seriously damaged storeys were F5, F6, and F7 in which the damage effect from F5 (noted as $O^1_{2,5}$) was the most serious. The damage of F5 was mainly due to the damage of beams which was mainly

(a)

(b)

(c)

(d)
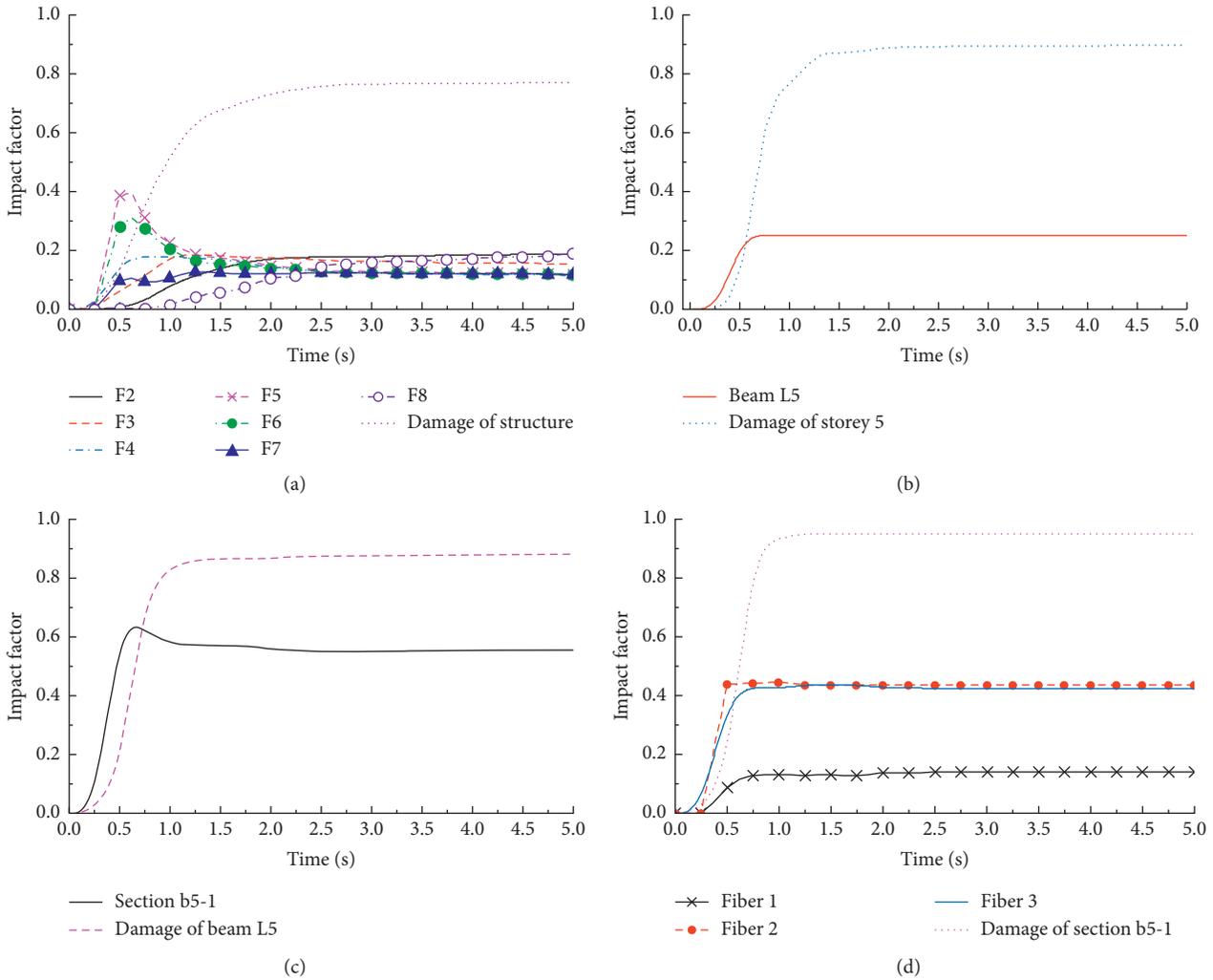
FIGURE 7: Damage correlations between different levels. (a) Storey level to structure level. (b) Member level to storey level. (c) Section level to member level. (d) Material level to section level.
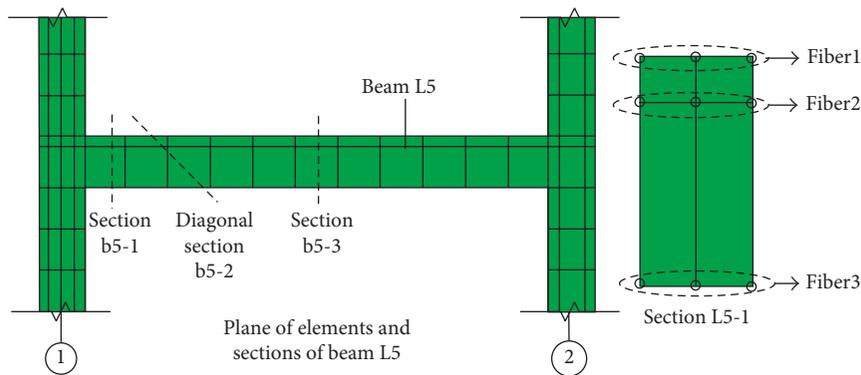
FIGURE 8: The analysis objects of member level, section level, and material level.

caused by the cross-sectional damage at the ends of the beam.

The impact factor values are listed in Table 1. It represents qualitatively the damage effect between different structural levels. It shows the damage effect degree of the level i comes from another level j. For example, about 12%

damage of the global structure was caused by the storey F5, and about 25% damage of storey F5 was caused by beam L5. Only 3% damage of the global structure was caused by beam L5, and only 1.7% damage of the global structure was caused by the section L5-1. It can be seen that the damage mechanism of the structure can be described very clearly in

TABLE 1: Damage correlations between different structural levels at limit state.

Structural level	Structure	Story F5	Beam L5	Section L5-1	Fiber 3
Stiffness damage	0.769	0.896	0.882	0.951	0.951
γ_{i+1}^i	—	0.120	0.249	0.554	0.425
γ_i^1	—	0.120	0.030	0.017	0.007

a quantitative way. Obviously, this analysis method is very helpful to design a new structure.

8. Conclusions

In order to explore the multilevel damage mechanism of the RC framed structure, five structural levels (structure level, storey level, member level, section level, and material level) were proposed as the multilevel analysis objects. Based on the generalized deformation equivalent principle, a generalized stiffness damage model is proposed for every structural level. The stiffness damage for each structural level can be calculated by integrating material stiffness damage. Furthermore, an impact factor was proposed to reflect quantitatively the damage correlations between different levels. As an example, a single-span 12-storey RC framed model was analyzed using this method. The results show that the multilevel damage analysis method can evaluate accurately the damage correlations between different levels. It should be very useful for the damage assessment and design of structures.

Data Availability

The data used to support the findings of this study are available from the corresponding author upon request.

Conflicts of Interest

The author declares that there are no conflicts of interest.

Acknowledgments

References

[1] W. B. Kratzig, I. F. Meyer, and K. Meskouris, "Damage evolution in reinforced concrete members under cyclic loading," in *Proceedings of 5th International Conference on Structural Safety and Reliability*, vol. 2, pp. 795–802, San Francisco, CA, USA, August 1989.

[2] H. Sucuoglu and A. Erberik, "Energy-based hysteresis and damage models for deteriorating systems," *Earthquake Engineering and Structural Dynamics*, vol. 33, pp. 69–88, 2004.

[3] E. Erduran and A. Yakut, "Component damage functions of reinforced concrete frame structures," *Engineering Structures*, vol. 29, no. 9, pp. 2242–2253, 2007.

[4] H. Banon and D. Veneziano, "Seismic safety of reinforced concrete members and structures," *Earthquake Engineering and Structural Dynamics*, vol. 10, no. 2, pp. 179–193, 1982.

[5] J. F. Wang, C. C. Lin, G. L. Lin, and C. H. Yang, "Storey damage identification of irregular buildings based on earthquake records," *Earthquake Spectra*, vol. 29, no. 3, pp. 963–985, 2013.

[6] Y. J. Park and A. H. S. Ang, "Mechanistic seismic damage model for reinforced concrete. Journal of Structural Engineering," *ASCE*, vol. 111, no. 4, pp. 722–739, 1985.

[7] A. Sharifi, M.-R. Banan, and M.-R. Banan, "A strain-consistent approach for determination of bounds of ductility damage index for different performance levels for seismic design of RC frame members," *Engineering Structures*, vol. 37, pp. 143–151, 2012.

[8] G. S. Kamaris, G. D. Hatzigeorgiou, and D. E. Beskos, "A new damage index for plane steel frames exhibiting strength and stiffness degradation under seismic motion," *Engineering Structures*, vol. 46, pp. 727–736, 2013.

[9] E. DiPasquale and A. S. Cakmak, "Detection and assessment of seismic structural damage," Technical Report NCEER-87–0015, National Center for Earthquake Engineering Research, State University of New-York, Buffalo, NY, USA, 1987.

[10] J. Lubliner, J. Oliver, S. Oller, and E. Oate, "A plastic-damage model for concrete," *International Journal of Solids and Structures*, vol. 25, no. 3, pp. 299–329, 1989.

[11] L. Jie and Y. Weizhong, "Elastoplastic stochastic damage constitutive law for concrete," *China Civil Engineering Journal*, vol. 42, no. 2, pp. 31–38, 2009.

[12] GB 50010-2010, *Code for Design of Concrete Structures*, China Architecture and Building Press, Beijing, China, 2010, in Chinese.

[13] J. Lemaitre, "Evolution of dissipation and damage in metals, submitted to dynamic loading," in *Proceedings of the I.C.M.1*, Kyoto, Japan, 1971.

[14] A. D. Hanganu, E. Onate, and A. H. Barbat, "A finite element methodology for local/global damage evaluation in civil engineering structures," *Computers and Structures*, vol. 80, no. 20-21, pp. 1667–1687, 2002.

[15] C. J. Shao, Y. H. Wu, and Y. H. Qian, "Evolution of nonlinear seismic damage of concrete bridge structure," *China Journal of Highway and Transport*, vol. 19, no. 5, pp. 41–45, 2006, in Chinese.

[16] H. Z. Shen, C. H. Zhang, and L. H. Kou, "Performance-based seismic damage assessment model for concrete gravity dams," *Journal of Tsinghua University*, vol. 47, no. 12, pp. 2114–2118, 2007, in Chinese.

[17] J. Yue, J. Qian, and D. E. Beskos, "A generalized multi-level seismic damage model for RC framed structures," *Soil Dynamics and Earthquake Engineering*, vol. 80, pp. 25–39, 2016.

[18] J. Oliver, M. Cervera, S. Oller, and J. Lubliner, "Isotropic damage models and smeared crack analysis of concrete," *Proceedings of the 2nd ICCAADCS*, vol. 2, pp. 945–958, Pineridge Press, Zell Am See, Austria, 1990.

[19] J. C. Simó and J. W. Ju, "Strain and stress based continuum damage models—part I formulation," *International Journal of Solids and Structures*, vol. 23, no. 7, pp. 281–301, 1987.

[20] State Key Laboratory of Disaster Reduction in Civil Engineering of Tongji University, *Benchmark Test of a 12-Story Reinforced Concrete Frame Model on shaking table*, Tongji University, Shanghai, China, 2004, in Chinese.

[21] ABAQUS, *Abaqus Analysis User's Manual, Version 6.4*, Hibbitt, Karlsson & Sorensen, Inc., Pawtucket, RI, USA, 2003.

Research Article

Viability Study of a Safe Method for Health to Prepare Cement Pastes with Simultaneous Nanometric Functional Additions

M. A. de la Rubia [ID],[1] **E. de Lucas-Gil** [ID],[2] **E. Reyes**,[1] **F. Rubio-Marcos** [ID],[2] **M. Torres-Carrasco**,[2] **J. F. Fernández**,[2] **and A. Moragues**[1]

[1]*Department of Civil Engineering-Construction, School of Civil Engineering, Polytechnic University of Madrid, C/Professor Aranguren s/n, 28040 Madrid, Spain*
[2]*Electroceramic Department, Instituto de Cerámica y Vidrio (CSIC), C/Kelsen 5, 28049 Madrid, Spain*

Correspondence should be addressed to M. A. de la Rubia; ma.rubia@caminos.upm.es

The use of a mixing method based on a novel dry dispersion procedure that enables a proper mixing of simultaneous nanometric functional additions while avoiding the health risks derived from the exposure to nanoparticles is reported and compared with a common manual mixing in this work. Such a dry dispersion method allows a greater workability by avoiding problems associated with the dispersion of the particles. The two mixing methods have been used to prepare Portland cement CEM I 52.5R pastes with additions of nano-ZnO with bactericide properties and micro- or nanopozzolanic SiO$_2$. The hydration process performed by both mixing methods is compared in order to determine the efficiency of using the method. The hydration analysis of these cement pastes is carried out at different ages (from one to twenty-eight days) by means of differential thermal analysis and thermogravimetry (DTA-TG), X-ray diffraction (XRD), scanning electron microscopy (SEM), and Fourier transform infrared spectroscopy (FTIR) analyses. Regardless of composition, all the mixtures of cement pastes obtained by the novel dispersion method showed a higher retardation of cement hydration at intermediate ages which did not occur at higher ages. In agreement with the resulting hydration behaviour, the use of this new dispersion method makes it possible to prepare homogeneous cement pastes with simultaneous functional nanoparticles which are physically supported on the larger particles of cement, avoiding exposure to the nanoparticles and therefore minimizing health risks. Manual mixing of cement-based materials with simultaneous nanometric functional nanoparticles on a large scale would make it difficult to obtain a homogenous material together with the health risks derived from the handling of nanoparticles.

1. Introduction

Cement is the most used binder material in construction and building, with it mainly being a fundamental component of mortar and concrete. The microstructure and functional behaviour of cement-based materials strongly depend on the chemical composition and additions, water-cement ratio, and rate of hydration. The incorporation of additions to modify and improve its fresh properties and its physical, mechanical, and durability properties, as well as to obtain new functional properties such as photocatalysis [1, 2], antibacterial effects (Sikora et al. [3, 4]), hydrophobicity (Tittarelli [5] and Nunes and Slizkova [6]), and fungicide effects (De Muynck et al. [7]) among others is currently an important research topic. In recent years, nanotechnology applied to cement-based materials has been growing since the use of additions of nanometric size significantly increases the effects on their mechanical and functional properties, and the combination of several additions might be very promising (Sikora et al. [4], León et al. [8], and Mohseni et al. [9]). However, the simultaneous addition of several functional nanoparticles simultaneously is an even greater challenge due to their tendency to agglomeration and by the risk to health during its manipulation (Vishwakarma et al. [10], Albrecht et al. [11], and Mueller and Nowack [12]).

In the case of the addition of silica, the pozzolanic activity and filling capacity are the two main characteristics that significantly influence the cement-based material properties (Haruehansapong et al. [13], Senff et al. [14], and Lu and Poon [15]). Pozzolanic materials provide an increase

in the amount of calcium-silicate-hydrate (CSH) gels, as well as a denser and more discontinuous and tortuous microstructure via pozzolanic reactions. As a result, an improvement of the mechanical and durable properties of the cement-based materials occurs (Massana et al. [16] and Ramezanianpour and Moeini [17]). A significant factor is the distribution particle size of silica, related with the specific surface. Silica fume is a by-product and generally shows a wide particle size range from submicronic particles to a few tens of microns. In contrast, in the case of nanosilica, the particle size is lesser. Smaller sized particles provide nucleating sites to hydration products since the high surface area, particularly in the case of nanosilica, allows the formation of calcium-silicate-hydrate (CSH) gel seeds on its surface formed by an early pozzolanic reaction that accelerate silicate hydration (Cheng-yi and Feldman [18], Larbi et al. [19], Thomas et al. [20], and Land and Stephan [21]). The surface area of silica becomes higher so does the acceleration of hydration (Land and Stephan [21]).

Zinc oxide, ZnO, can present three crystalline structures, with the most stable being the hexagonal structure, wurtzite. ZnO is an n-type semiconductor with a band gap of 3.2 eV at room temperature RT. ZnO is produced directly by oxidizing zinc metal, a reduction of an ore to zinc metal followed by re-oxidation and to a lesser extent, by precipitation of oxide or carbonate from aqueous solution and a final thermal treatment (Moezzi et al. [22]). This oxide has a large number of applications, with a vulcanization activator in the rubber industry being the main function. ZnO is a highly important raw material in ceramics (glazes and enamels in tiles and sanitary ware), in electroceramics such as overvoltage protection devices (varistors) (Sendi [23] and Xu [24]), and in optoelectronics (Kahouli et al. [25], Hussein et al. [26], and Torchynska et al. [27]). It is currently being researched as a photocatalyst and novel antifungal precursor. The morphology of the ZnO particles mainly depends on the synthesis techniques, precursors, process conditions, and pH (Moezzi et al. [22]).

According to Klingshirn, the use of ZnO particles in concrete increases the setting time and, therefore, the workability for early ages, and provides an improvement in its resistance against water (Klingshirn [28]). The main effects of zinc oxide additions to the Portland cement have been known for some time: retardation of setting and hardening (reducing the rate of heat evolution) leads to an improvement in whiteness and final strength (Ramachandran [29]). Recently, authors such as Nivethitha et al. have suggested that the addition of nano-ZnO particles may also improve the mechanical properties of ordinary Portland cement mortar (Nivethitha and Dharmar [30]).

Several authors have studied the influence of ZnO on the hydration of the Portland cement. Arliguie showed that the delay in hydration is due to the precipitation of an amorphous $Zn(OH)_2$ layer around the anhydrous C_3S grains which inhibits cement dissolution (Arliguie and Grandet [31]). The hydration of C_3A in the presence of ZnO occurs too, when there is a significant presence of SO_3. When the pore concentration of Ca^{2+} and OH^- is enough, the hydration reaction starts again and the amorphous $Zn(OH)_2$ layer transforms into crystalline calcium zinc hydroxide $CaZn_2(OH)_6 \cdot 2H_2O$ (CZ) (Arliguie and Grandet [31]). Yousuf et al. identified a calcium zinc hydroxide crystalline phase by means of Fourier transform infrared spectroscopy (FTIR) in paste samples with ZnO cured for 28 days (Yousuf et al. [32]). Some authors corroborate the formation of this calcium hydroxyzincate dihydrate $CaZn_2(OH)_6 \cdot 2H_2O$ (CZ), suggesting that the formation of this phase controls Zn solubility in cementitious materials (Cocke et al. [33]). Johnson and Kersten showed that solid solution is a possible binding mechanism for Zn(II) in the CSH gel, indicating that at least 10% of Zn may be incorporated in the CSH structure (Johnson and Kersten [34]). In such a way, Lieber and Gebauer confirmed the formation of crystalline calcium hydroxyzincate during the retardation period as an intermediate product (though after some days of reaction, it is no longer detectable) (Lieber and Gebauer [35]). In a recent study, Ataie et al. [36] in contrast with Arliguie, indicated that the mechanism by which ZnO retards hydration reaction could be nucleation and/or growth poisoning of CSH and suggested that ZnO does not inhibit cement dissolution. Ataie showed that ZnO strongly delays the cement hydration and the retardation increases as the ZnO quantity in the cement rises, so the amount of ZnO added is directly correlated with such an increase in the retardation period. Zn ions hinder nucleation and growth of hydrated products poisoning the hydration product nuclei. When there are not enough dissolved Zn ions, retardation ends and a greater acceleration of hydration occurs. In the same sense, various authors suggest that the CSH gel is the most probable site for metal fixation in cement and Zn^{2+} is incorporated in the interlayer CSH (Stumm et al. [37], Ouki and Hills [38], Ziegler et al. [39], and Ziegler and Johnson [40]).

Therefore, calcium hydroxyzincate dihydrate $CaZn_2(OH)_6 \cdot 2H_2O$ (CZ) has an important influence in the retardation of the Portland cement hydration (Arliguie and Grandet [31]) and in the prevention from corrosion of the galvanized steel in concrete when this hydroxyzincate phase forms a coating on the rebars (Tittarelli and Bellezze [41]). Protection against corrosion is due to the formation of a compact and protective layer of this phase at high pH values between 12.2 and 13.3.

ZnO and compounds such as $CaZn_2(OH)_6 \cdot 2H_2O$ are being researched as antifungal, bactericide, and photocatalyst materials (Xie et al. [42], Sirelkhatim et al. [43], Madhusudhana et al. [44], Gomez-Ortiz et al. [45], and Hernandez Sierra et al. [46]). Gomez-Ortiz et al. used CZ as the antifungal precursor of protective coatings for marble and limestone (Gomez-Ortiz et al. [45]). A drawback when using both ZnO and SiO_2 nanoparticles as an addition in the Portland cement may involve the requirement of a greater amount of mixing water due to a greater amount of fines, which increases the water-cement ratio. The use of superplasticizers is common in order to improve the workability.

Nanoparticles, due to their high specific surface area, have a high tendency to form agglomerates. Such agglomeration drastically reduces the effectiveness and modifies the properties regarding the dispersed state of nanoparticles avoiding obtaining homogeneous mixtures. Therefore, agglomeration

should be avoided in order to achieve homogeneous admixtures using a low amount of nanoparticles and minimizing the health risks derived from its management. The difficulty in avoiding the agglomeration of functional nanoparticles and the difficulty in obtaining a material with high homogeneity increase in manual mixing when trying to introduce several additions simultaneously in cement pastes. Manual mixing to achieve homogeneous admixtures implies an increase in exposure time to nanoparticles and therefore an increase in health risks.

Nanotechnology is increasingly used in production processes. Currently, it is difficult to determine the risks to health and the environment during handling in the preparation of composites. Because of this, it is infeasible to prepare cement-based materials with functional nano-additions (silica, zinc oxide, and titania, among others) at an industrial level by a manual mixing method to achieve a homogeneous dispersion of functional nanoparticles, given that they have a high health risk due to a small particle size. Therefore, in order to minimize health risks derived from the use of nanoparticles, it is necessary to minimize exposure time and handling. The patented low-energy dry dispersion method (Fernandez Lozano et al. [47]) allows the nanoparticles to be incorporated in an effective way, by simplifying the steps, avoiding exposure, and handling nanoparticles, as the dispersion of the nanoparticles takes place on dry larger particles (cement particles). These nanoparticles are supported on the cement particles by cohesive forces, thus avoiding or decreasing spreading. A consistent powder with a particle distribution consisting of nanoparticles dispersed and anchored by short-range forces on particles of different morphologies is obtained. Such short-range forces avoid the presence of free nanoparticles when the composite powder is handled or used, decreasing the health risk. This process is in the absence of solvents (dry process) and does not require high shear rates. Implementation of such a process would be viable at an industrial level in a cement production plant.

The object of this study, therefore, is to assess the feasibility of preparing homogeneous functional cement-based powders with simultaneous functional nanoadditions (SiO_2 and ZnO) by means of an easy-to-use dry dispersion method minimizing health risks and avoiding exposure to nanoparticles during the preparation of cement pastes.

2. Materials and Methods

2.1. Materials. The cement paste is a 52.5R Type I commercial Portland cement with a particle size d_{50} of 6.3 μm and specific surface of 1.45 m^2/g. The nanometric ZnO was obtained as a product of hydrozincite ($Zn_5(CO_3)_2(OH)_6$) calcination at 500°C for five minutes in air. The XRD characterization indicates that the phase matches the hexagonal wurtzite structure ZnO (JCPDS card number 36-1451), without peaks, of other phases. The nanometric ZnO shows a specific surface area of 18.59 m^2/g determined by the Brunauer–Emmett–Teller (BET) method and a monomodal distribution with an average particle size of 53 nm from field emission scanning electron microscopy FE-SEM micrographs. The micrometric

SiO_2 (MS) used is silica fume produced in the manufacturing of ferro-silicon alloy. It is noncrystalline silica with wide distribution particle sizes with a d_{50} of 45.2 μm and a specific surface area of 28.52 m^2/g. Microsilica contains 91 wt.% of SiO_2 and 5.3 wt.% of Fe_2O_3.

The nanometric SiO_2 (NS) Sipernat® 22S from Evonik Industries [48] is manufactured hydrophilic silica in a liquid-phase precipitation process that obtains aggregates with a micrometer size of 14 μm composed of tiny primary particles (5–100 nm). The advantages of using Sipernat 22S involve an amorphous structure and a high surface area of 180 m^2/g. Sipernat 22S increases the early strength and consistency of concrete, reduces bleeding and segregation in self-compacting concrete, and has a hydrophobic effect that improves the water resistance of concrete (Aerosil, Aeroxide, and Sipernat products, Evonik Industries, Technical Information). Due to the difference between the specific surface area of microsilica (MS) and nanosilica (NS), the pozzolanic reactivity of nanosilica Sipernat is much higher. Both have an acidic character.

2.2. Sample Preparation. Three cement paste mixtures were studied, including 52.5R Type I Portland cement and different combinations of additions of nano-ZnO (NZ), nanosilica, and microsilica as a substitute of anhydrous cement: one with 2 wt.% of nano-ZnO (NZ), another with 2 wt.% of nano-ZnO (NZ) and 10 wt.% of nanosilica (NS), and the last one with 2 wt.% nano-ZnO (NZ) and 10 wt.% of microsilica (MS). The mixtures were prepared by two mixing methods. A first mixing method involved a common manual mixing. The other mixing method used was the dispersion of the different functional particles (nano-ZnO, microsilica, and nanosilica) over the 52.5R Type I Portland cement particles, using the aforementioned low-energy dry dispersion (low shear rate) novel method (Fernandez Lozano et al. [47]). In this method of dry dispersion, the cement particles as the different additions were dried and then mixed in a Turbula-type shaker with 15 mm diameter alumina balls (Lorite et al. [49] and Alonso-Domínguez et al. [50]). The water-cement ratio was fixed at 0.35 for the admixtures except for that which had 2 wt.% nano-ZnO (NZ) + 10 wt.% nanosilica with a ratio fixed at 0.6 since nanosilica has a high specific surface and demands more water to obtain complete hydration of the mixture.

In order to obtain good rheological properties such as flowability but without segregation, a policarboxilate-based superplasticizer (Sika ViscoCrete® 5720) was used. The superplasticizer quantities depend on the wt.% of cement replaced, as well as the morphological characteristic of the functional particles. Ghafari et al. pointed out that cement paste composites containing 0.4 wt.% ZnO nanoparticles (specific surface area of 54 ± 20 m^2/g) or lower showed excellent workability retention compared to the reference mix and a poor workability retention was observed at higher dosage (Ghafari et al. [51]). Once the dosages have been prepared by both mixing methods, they are placed in a rotary mixer that contains the required water and the superplasticizer (following with a low-speed knead for 90 seconds).
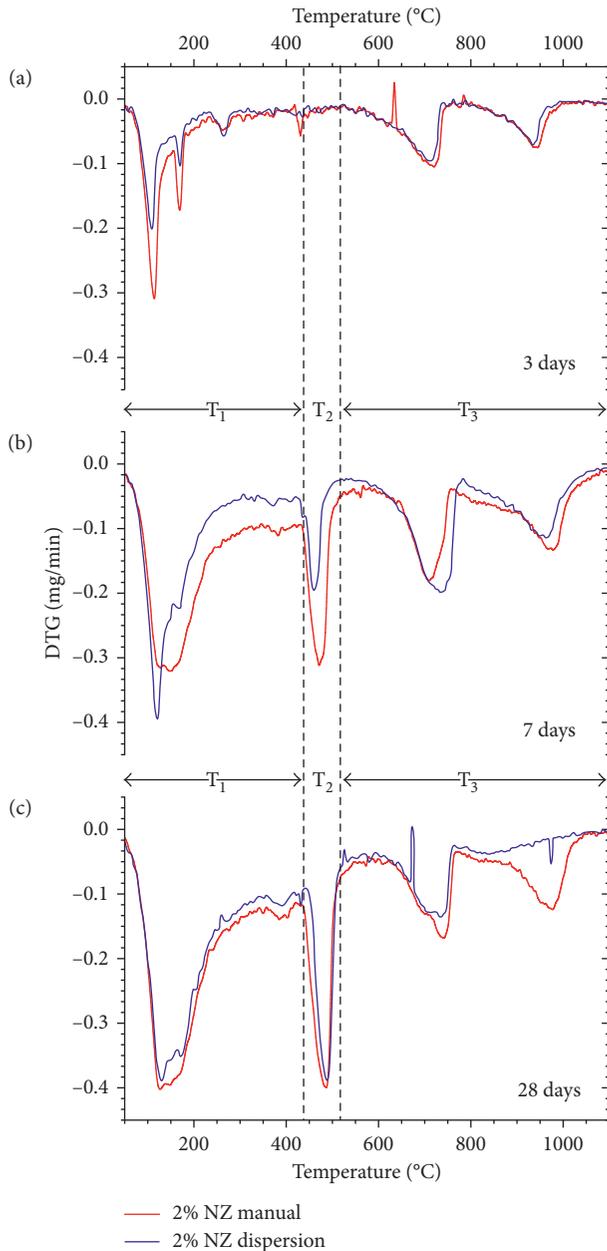
FIGURE 1: DTG-T^a analysis for cement paste with 2 wt.% of nanozinc (NZ) for (a) 3, (b) 7, and (c) 28 days.

After 30 seconds of rest, the mixture was mixed again for 90 seconds at a low speed. After mixing, the cement pastes were shaped as a prismatic bar in molds and covered with a plastic bag and placed in a curing chamber with the temperature and humidity controlled ($20 \pm 2°C$ and >95%, resp.). As zinc oxide is a cement hydration retarder, samples were demolded after 72 hours and cured in water inside the chamber. In order to stop the hydration of the samples at the ages analyzed, the cement paste was placed in vacuum for 30 minutes and then in acetone for two hours, following 24 hours in a stove at $60°C$. The sample was stored in a stove at $40°C$ until its structural and microstructural characterization had been obtained. Cement pastes were cured for one, two, three, seven, and

twenty-eight days in water and characterized by means of DTA-TG, SEM, FTIR, and XRD.

2.3. Characterization of Cement Pastes with Additions. The differential thermal analysis and thermogravimetry (DTA-TG) of the cement pastes were performed by using LABSYS evo equipment provided by SETARAM Instrumentation, in the range of $25°C$ to $1100°C$ with a heating rate of $10°$/min in N_2 atmosphere in alumina crucibles. The cement pastes were microstructurally characterized by scanning electron microscopy (SEM) with a JEOL JSM 6335F microscope, and the energy dispersive spectroscopy (EDS) analysis was carried out with a detector provided by Oxford Instruments, the X-Max^N of $80 \, mm^2$ with a resolution between $127 \, eV$ and $5.9 \, KeV$. In addition, X-ray diffraction (XRD) was carried out by means of a powder diffractometer Bruker D8 AD-VANCE with Cu $K\alpha$ radiation, with a high-speed detector (Lynxeye). The identification of the crystalline phases was done by comparison with the Joint Committee on Powder Diffraction Standards (JCPDS) guidelines. FTIR analysis of the cement pastes shaped in the KBr pellet method was performed by a PerkinElmer Spectrum 100 spectrophotometer from 400 to $4000 \, cm^{-1}$.

3. Results and Discussion

The thermogravimetric derivative (DTG) versus temperature plot represents the mass change rate with temperature (T^e) and allows a better resolution of the complex thermogravimetric curves. By quantifying the water related with the CSH gel and the portlandite phase (CH), it is possible to analyze the hydration grade. The DTG versus T^e plot of cement pastes shows the following characteristic bands: first, the free water loss occurs approximately at $100°C$, then the interlayer water loss occurs at around $120°C$, and finally, from $140°C$ until $430°C$, the water of gel (water combined in the CSH gel, T1) loss occurs. The portlandite content is related with the water weight loss that takes place in the temperature range between $430°C$ and $515°C$ (labeled as T2). Due to the possible portlandite carbonation, it is necessary to adjust the portlandite quantity and include it in the temperature range where the carbonate loss takes place ($515°C$–$1100°C$). Villain et al. [52] indicated that the calcium carbonate ($CaCO_3$) ensuing of the CSH carbonation dissociates in a lower temperature range than the $CaCO_3$ ensuing of the portlandite carbonation allowing it to differentiate both carbonations thermally. The authors consider that the water contained in the carbonates is 40 wt.% of the total weight loss in this temperature range. The 40 wt.% weight loss in this temperature range ($515°C$–$1100°C$) will be termed T3.

Figures 1(a)–1(c) and Table 1 show the plot of DTG versus temperature, such as mass losses in the temperature ranges previously examined (T1, T2, and T3, resp.) for cement pastes with a substitution of 2 wt.% of nano-ZnO (NZ), obtained by both mixing methods at cured ages of three, seven, and twenty-eight days, in comparison with a cement paste without addition as reference. In the DTG plot of three-day samples (Figure 1(a)), there appear peaks corresponding to weight loss of water consequence of

TABLE 1: Water losses associated with different phases in cement pastes with 2 wt.% of nanozinc (NZ).

	2% NZ manual mixing			2% NZ low shear rate dispersion			52.5R		
	3 d	7 d	28 d	3 d	7 d	28 d	3 d	7 d	28 d
T1 (140°C–430°C) wt.%	2.0	7.3	9.2	1.5	4.6	8.6	6.6	7.0	7.8
T2 (430°C–515°C) wt.%	0.3	2.7	3.5	0.2	1.4	3.2	3.4	3.5	3.5
T3 (515°C–1100°C) wt.%	1.3	3.0	2.7	1.2	2.9	1.8	2.6	2.8	2.6
Total combined water (T1 +T2 + T3) wt.%	3.6	13.0	15.4	2.9	8.9	13.6	12.6	13.3	13.9
Equivalent calcium (T2 + T3) wt.%	1.6	5.7	6.2	1.4	4.3	5.0	6.0	6.3	6.1
CSH gel (T1) wt.%/total portlandite (T2 + T3) wt.%	1.25	1.28	1.48	1.07	1.07	1.72	1.10	1.11	1.28

hydration of tricalcium aluminates C_3A (170°C and 265°C) corresponding to the initial formation of hexagonal phases. Subsequently, these will be converted to a C_3AH_6 cubic phase according to the literature and weight loss of carbonates as consequence carbonation of the samples (Ramachandran et al. [53]). The DTG of hydrated calcium hydroxyzincate ($CaZn_2(OH)_6 \cdot 2H_2O$) synthesized (Mellado et al. [54]) shows three peaks, the first two overlapped in a temperature range between 140°C and 220°C corresponding to the two first stages' decomposition of $CaZn_2(OH)_6 \cdot 2H_2O$. At the lowest temperature, the dehydration of $CaZn_2(OH)_6 \cdot 2H_2O$ takes place, and between 160°C and 220°C in the DTG, a wide peak appears corresponding to the decomposition of $CaZn_2(OH)_6$ in ZnO and $Ca(OH)_2$. Finally, at temperature around 500°C, the $Ca(OH)_2$ decomposition takes place. In Portland cement samples with 0.1% of Zn(II), Mellado et al. indicated the presence of two peaks in DTG at 180 and between 270°C and 290°C corresponding to the decomposition of hydrated calcium hydroxyzincate $CaZn_2(OH)_6 \cdot 2H_2O$ and hydrozincite $Zn_5(CO_3)_2(OH)_6$, respectively.

In Figures 1(a)–1(c), two peaks appear before 200°C and 300°C, respectively, that could correspond to the decomposition of hydrated calcium hydroxyzincate ($CaZn_2(OH)_6 \cdot 2H_2O$) and hydrozincite according to Mellado et al. [54]. In Figure 1(a), these peaks can appear overlapping with the hydration of tricalcium aluminates and therefore have a greater intensity.

Figure 1(a) and Table 1 data indicate that the hydration of calcium silicates has not taken place at this age, confirming the hydration retarder behaviour of ZnO on cement pastes in agreement with Mellado et al. that confirmed the absence of portlandite decomposition in cement pastes containing 1% of Zn(II) at 3 days due to the delay in the setting of the cement. Pastes at seven days show that hydration is taking place according to Figure 1(b) and Table 1 to a greater extent for cement paste prepared by a manual mixing method since the water of the CSH gel combined with portlandite for manual mixing cement pastes is higher than that obtained by the low shear dispersion method. For 28 days (Figure 1(c)), the hydration process for cement pastes obtained by both mixing methods is very similar. Only small differences can be observed in regard to the total combined water, in particular, due to the water contained in carbonates (Table 1, T3). According to Villain et al. [52], calcium carbonate $CaCO_3$ ensuing form the degradation of the CSH gel gives place to vaterite and/or aragonite whose dissociation takes place between 650°C and 800°C and $CaCO_3$ calcite ensuing from portlandite $Ca(OH)_2$ carbonation dissociated between 850°C

and 1000°C according to Figures 1(a)–1(c). For 28 days, the water loss combined with portlandite indicates that about 24% of total loss is due to the portlandite, with the portlandite content for samples obtained by both mixing methods being about 14 wt.%. The CSH gel-portlandite ratio is higher for samples with nanozinc oxide than for the reference cement paste at 28 days for both experimental methods of obtaining the cement pastes. This result is a consequence of a higher content of water (higher combined water) in the gel (T1), though this does not mean that there is more CSH gel since the portlandite content (equivalent calcium) for all the samples with and without nano-ZnO is similar. This higher water content for samples with nano-ZnO could be due to the water bound to zinc in the calcium hydroxyzincate, given that, in these samples, there is no silica and the pozzolanic reaction cannot take place to form a secondary CSH gel. The hydration process in the first ages is different for each cement paste with nanozinc oxide depending on its mixing method, although in both cases hydration is later, with it being higher for cement pastes obtained at low shear rate dispersion. ZnO is not involved in the hydration process in cement pastes prepared by this method in the first ages, and the water bonded is lower than that in pastes prepared by manual mixing. For 28 days, hydration is similar for cement pastes obtained by both mixing methods. Cement pastes obtained by the novel dispersion method show a higher CSH gel-to-portlandite ratio than the manual mixing ones, indicating a higher Ca/Si ratio and denser CSH gels.

The Ca/Si ratio in a CSH gel of cement pastes obtained by both mixing methods was determined by SEM-EDX analysis at a different point of the surface of each sample at the age of 28 days. The Ca/Si ratio for both mixing methods was similar, with the values of 2.44 and 2.52 for manual and dispersing methods, respectively. These Ca/Si ratios are slightly higher than those for 52.5R cement pastes with a Ca/Si ratio of 2.28. Accordingly, the ZnO addition increases the Ca/Si ratio in the CSH gel.

FTIR analysis for cement pastes with nano-ZnO additions (Figure 2) is in agreement with the DTA-TG characterization. At three days, the hydration of calcium silicates has not started, and only the hydration of the calcium aluminates can be observed in the cement pastes and the mixing methods studied. FTIR analysis identified alite (A) as unhydrated cement particles and an ettringite (E) phase, as a consequence of calcium aluminate hydration. The carbonate peaks as a consequence of paste carbonation and peaks corresponding to bending water or in capillaries are
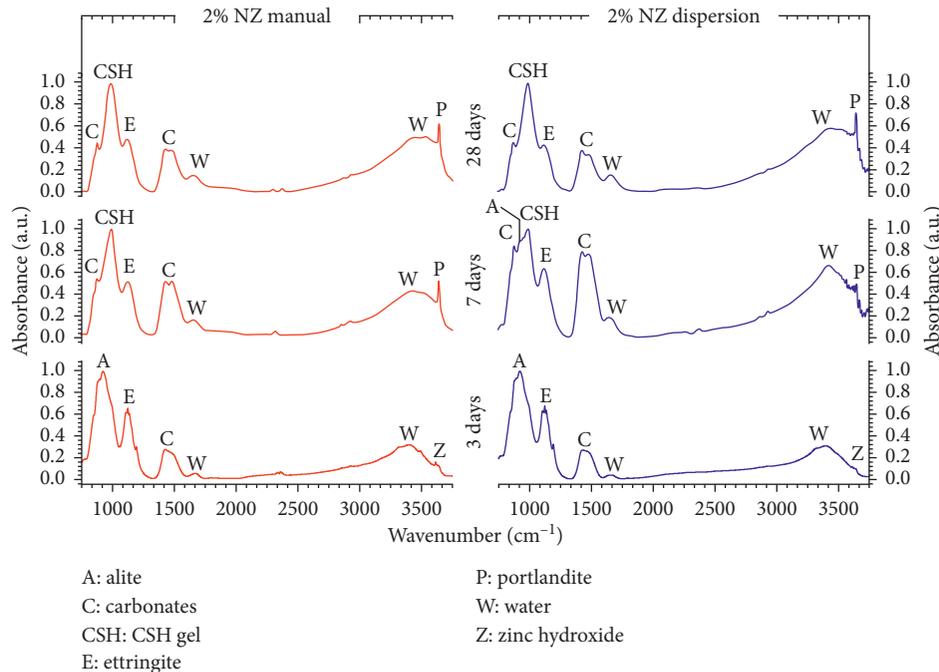
FIGURE 2: FTIR analysis for cement paste with 2 wt.% of nanozinc (NZ).

identified too. The point to the presence at three days of the cement paste by mixing oxide of a weak peak at $3615\,cm^{-1}$ that could be attributed to OH groups joined to Zn ions (zinc hydroxide) (Mollah et al. [55] and Trezza [56]). These results are in agreement with Arliguie, who pointed out that the formation of an amorphous layer of zinc hydroxide on the surface of anhydrous cement particles inhibits cement hydration (Arliguie and Grandet [31]). For cured cement pastes at seven days, there is agreement with the DTA-TG analysis, with the hydration of manual mixing cement pastes being almost complete since the displacement of the peak corresponding to the unhydrated alite phase from 920 to $985\,cm^{-1}$ and corresponding to the C_3S hydration product (formation of the CSH gel) is clearly identified. In this sample, a sharp peak at $3645\,cm^{-1}$ corresponding to the O-H stretching of portlandite $Ca(OH)_2$ formed together with the CSH gel in the hydration of calcium silicates is identified. For dispersed samples at seven days, portlandite identification is not possible, although the formation of the CSH gel takes place according to the incipient peak at $985\,cm^{-1}$ such as a decrease in the alite phase, confirming the progress of hydration. In agreement with the literature (Vázquez Moreno [57]), the intensity of the band corresponding to ettringite decreases with its transformation in monosulfoaluminates. In this case, for pastes with NZ, this change takes place when the age increases from three to seven days. For 28 days, FTIR analysis would indicate a slightly greater advance of hydration of cement pastes obtained by a manual mixing method as the greater intensity of the portlandite and CSH gel peaks, together with alite, is not identified.

X-ray diffraction characterization (Figure 3) is in agreement with DTA-TG and FTIR analyses for cement pastes with nanozinc oxide additions for both mixing methods. For samples at three days, calcium silicate hydration has not started (alite and belite identification), with there even being aluminates identified. For pastes at seven days, hydration is at a greater point of advance in cement pastes obtained by manual mixing than for low shear rate dispersion for seven days. At this age, manual mixing sample characterization shows that the peaks corresponding to the alite phase (A) have a lower intensity than those corresponding to low shear rate dispersion ones. For 28 days, according to XRD analysis, there are no hydration differences between cement pastes obtained by both mixing methods. At this age, by means of this characterization technique, it is possible to identify traces of unhydrated alite. It should be noted that it is possible to identify the crystalline calcium hydroxyzincate dihydrate $CaZn_2(OH)_6 \cdot 2H_2O$ (CZ) phase at any cured age. The identification by the FTIR of the amorphous zinc hydroxide $Zn(OH)_2$ phase at the earliest age (three days) and crystalline calcium hydroxyzincate dihydrate $CaZn_2(OH)_6 \cdot 2H_2O$ (CZ) for all ages in XRD analysis would agree with the Arliguie and Grandet proposal [31] where these authors indicated that the delay in hydration is due to the precipitation of an amorphous $Zn(OH)_2$ layer around the anhydrous C_3S grains which inhibits cement dissolution. When the hydration reaction starts again, the amorphous $Zn(OH)_2$ layer transforms into a crystalline calcium hydroxyzincate $CaZn_2(OH)_6 \cdot 2H_2O$ (CZ). In a recent published study, Andrade et al. studied cement pastes with zinc oxide addition for electric arc furnace dust (EAFD) recycling (Andrade Brehm et al. [58]). They proposed a model to explain hydration reactions of cement admixed with ZnO. In this work, the authors identified the $CaZn_2(OH)_6 \cdot 2H_2O$ (CZ) phase at two days and suggested the starting of the hydration reactions in these cement pastes with ZnO in agreement with Arliguie and stated that $Zn(OH)_2$ is not the responsible phase of retardation of setting time since, according to the pH diagram at the pH of the cement pastes
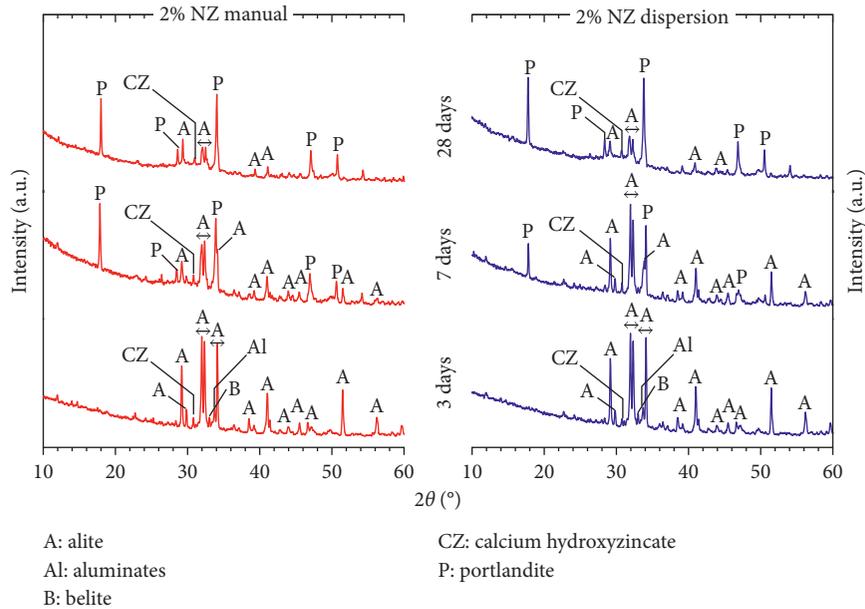
FIGURE 3: XRD characterization for cement paste with 2 wt.% of nanozinc (NZ).

A: alite
Al: aluminates
B: belite

CZ: calcium hydroxyzincate
P: portlandite

($\approx$12), there would be a small amount of this phase. The most important result, regardless of the characterization technique, is that there are no significant differences in hydration of cement pastes at 28 days with a substitution of 2 wt.% of nano-ZnO obtained by both mixing methods.

Figures 4(a)–4(c) and Table 2 show the DTG (mass change speed) versus temperature as mass loss from the TG data for the interest temperature ranges defined previously (T1, T2, and T3) and associated with water loss of a different nature for cement pastes with a cement substitution of 2 wt.% nano-ZnO and 10 wt.% microsilica (MS) obtained for both mixing methods at ages of three, seven, and twenty-eight days, respectively.

DTG analysis and water losses associated with different phases (Table 2) of three-day samples with ZnO and microsilica (Figure 4(a)) are close to the three-day pastes only with nanoparticles for both mixing methods. The hydration of calcium silicates has not taken place at this age. Pastes at seven days (Figure 4(b)) show that calcium silicate hydration has taken place for manual mixing samples but not so for low shear rate dispersion pastes. The total water combined with cement pastes prepared by low shear rate dispersion at seven days is similar to that at three days. Water loss that takes part in the CSH gel (T1) and water combined with portlandite (T2) are low compared with manual mixing pastes according to Table 2. The absence of the peaks corresponding to the water loss that takes part in the CSH gel (T1) and water combined with portlandite (T2) in DTG analysis confirms that the hydration of calcium silicates either has not started or is at an only slightly advanced at seven days for pastes prepared by the dispersion method. There are meaningful differences related to the quantities of water that are part of the CSH gel, as well as water combined with portlandite, that indicate a higher hydration of calcium silicate of manual mixing cement pastes. Pastes only with ZnO hydration at seven days have started in both mixing methods, although higher advanced points for

pastes are obtained by manual mixing. In Figures 4(a)–4(c), two peaks appear before 200°C and 300°C, respectively, that could correspond to the decomposition of hydrated calcium hydroxyzincate $(CaZn_2(OH)_6 \cdot 2H_2O)$ and hydrozincite according to Mellado et al. [54]. In Figure 4(a), these peaks can appear overlapping with the hydration of tricalcium aluminates and therefore have a greater intensity.

At 28 days, the hydration process for cement pastes with NZ and MS obtained for both mixing methods is identical according to DTG analysis and associated water losses (Figure 4(c) and Table 2). At 28 days, the water loss combined with portlandite indicates that about 16 wt.%. of total loss is due to portlandite and the portlandite content for samples obtained by both mixing methods being about 9% of total weight. This minor content, compared with pastes, is only with nanozinc and is a consequence of the pozzolanic reaction between portlandite and the microsilica.

Similar to Figures 1(a)–1(c), calcium carbonate $CaCO_3$ dissociation ensuing form the degradation of the CSH gel takes place between 650°C and 800°C and $CaCO_3$ calcite ensuing from portlandite $Ca(OH)_2$ carbonation dissociated between 850°C and 1000°C according to Figures 4(a)–4(c).

The CSH gel-portlandite ratio is higher for samples with nanozinc oxide and microsilica than for the reference cement paste at 28 days for both experimental methods of obtaining the cement pastes, as occurred in the case of the cement pastes only with nanozinc oxide. Unlike cement pastes only with zinc oxide, this result is a consequence not only of the higher content of water (higher combined water) in the gel (T1) due to the water bound to zinc in calcium hydroxyzincate but also of the formation of the CSH gel because of the pozzolanic reaction due to microsilica addition. As a result of the pozzolanic reaction, the portlandite content (equivalent calcium) for the cement pastes with nano-ZnO regardless of the mixing method is similar and lower than that for reference pastes without ZnO. As for cement pastes with only ZnO, the
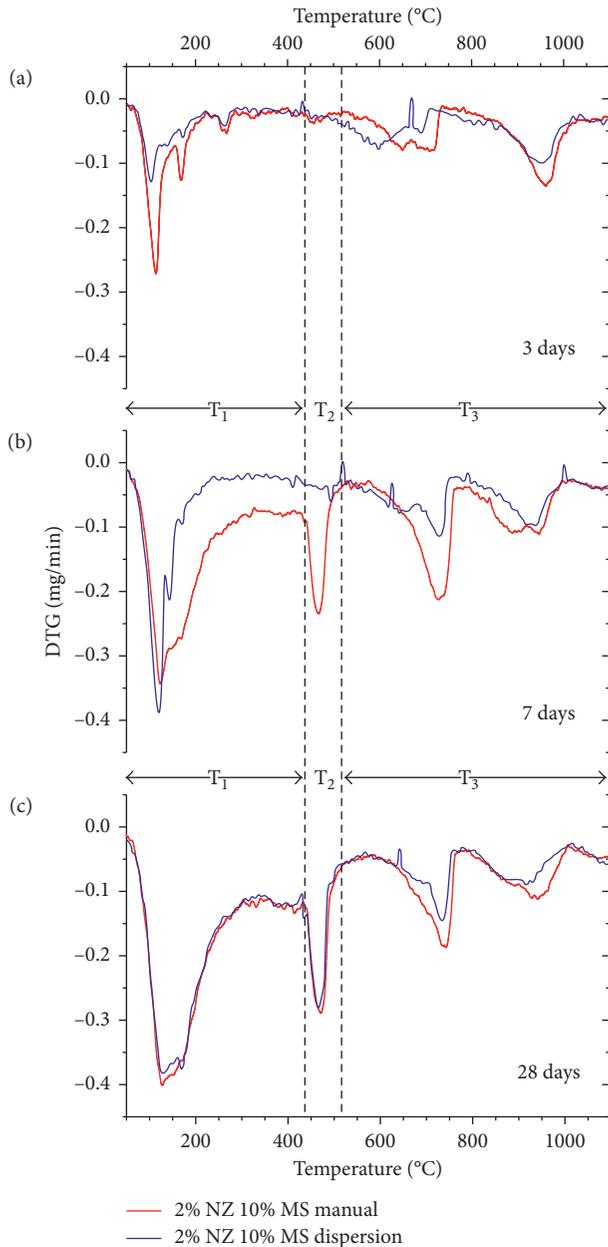
Figure 4: DTG-T^a analysis for cement paste with 2 wt.% of nanozinc (NZ) + 10 wt.% microsilica (MS) for (a) 3, (b) 7, and (c) 28 days.

hydration process in the first ages is different for each cement paste with nanozinc oxide and microsilica depending on its mixing method, although in both cases hydration is later, with this being higher for cement pastes obtained at low shear rate dispersion. ZnO does not occur in the hydration in cement pastes prepared by this method in the first ages, and the water bonded is lower than that in pastes prepared by manual mixing. At 28 days, hydration is similar for cement pastes obtained by both mixing methods. Cement pastes obtained by the novel dispersion method show a higher CSH gel-portlandite ratio than the manual mixing ones, indicating a higher Ca/Si ratio and therefore denser CSH gels.

The CSH gel-portlandite ratio is higher for samples with nanozinc oxide and microsilica than for the reference

cement paste at 28 days for both experimental methods of obtaining the cement pastes, due in part to the water content in calcium hydroxyzincate and because it is not related to the CSH gel (there is also a formation of secondary CSH gel consequence of the pozzolanic reaction). This result would provide better mechanical properties for samples with nanozinc oxide and microsilica substitutions for both mixing methods compared with the reference pastes. The CSH gel-portlandite ratio for samples with zinc oxide and microsilica is higher than that for samples only with zinc oxide due to the pozzolanic reaction forming a secondary CSH gel.

The Ca/Si ratio in the CSH gel of cement pastes with NZ and MS obtained by SEM-EDX analysis at 28 days shows such a ratio for both mixing methods as similar, although slightly higher for manual mixing, with the values of 2.20 and 2.25, respectively. The Ca/Si ratio decreases with the addition of SiO_2.

As the plot of DTG versus T^a of cement pastes that contain NZ and nanosilica NS is close to that of cement pastes that contain NZ and MS, it is not shown in this article. Table 3 shows the mass loss from the TG data for the interest temperature ranges defined previously (T1, T2, and T3) and associated with the water loss of different nature for cement pastes with NZ and NS for three, seven, and twenty-eight days, respectively.

At three days of hydration, cement pastes with NZ and NS obtained by both mixing methods, as for cement pastes with NZ and MS, the hydration of calcium silicates has either not taken place or at a little advanced point according to the gel water losses. Pastes at seven days show that calcium silicate hydration has taken place for manual mixing samples but not so for low shear rate dispersion pastes. The total water combined with the cement paste prepared by low shear rate dispersion at seven days is similar to that at three days, as shown in Table 3. According to this DTG analysis and the values shown in Table 3, the result would indicate that at seven days for manual mixing pastes, hydration is already advanced and for dispersing samples, it would be starting. According to findings in another study, nanosilica accelerated C_3S hydration [21]; however, in this study, the hydration retarder effect of ZnO prevailed. Water losses that took part in the CSH gel (T1) and combined with portlandite (T2) in the first ages (three and seven days) are similar for samples that do not contain silica or contain micro- or nanosilica. For 28 days, the hydration process for cement pastes obtained for both mixing methods is similar. Water loss that takes part in the CSH gel (T1) at 28 days for cement pastes with NS is higher than that for the MS ones, with this indicating that nanosilica produces a higher quantity of hydrated phase and showing agreement with the literature (Tobón et al. [59]).

It is important to note, in agreement with the literature, that nanosilica has a pozzolanic reactivity higher than microsilica and, that is, produces additional CSH gel (Land and Stephan [21]). According to Table 3, cement pastes with nanosilica for both mixing methods at 28 days show a higher water loss that takes part in the CSH gel (T1) than the water loss for samples with microsilica (Table 3) which correspond

TABLE 2: Water losses associated with different phases in cement pastes with 2 wt.% of nanozinc (NZ) + 10 wt.% microsilica (MS).

	2% NZ + 10% MS manual mixing (wt.%)			2% NZ + 10% MS low shear rate dispersion (wt.%)			52.5R		
	3 d	7 d	28 d	3 d	7 d	28 d	3 d	7 d	28 d
T1	1.8	6.1	8.8	1.3	2.0	9.0	6.6	7.0	7.8
T2	0.4	1.8	2.5	0.4	0.5	2.5	3.4	3.5	3.5
T3	2.1	3.0	3.0	2.0	2.2	2.6	2.6	2.8	2.6
Total combined water (T1 + T2 + T3) wt.%	4.3	10.9	14.3	3.7	4.7	14.1	12.6	13.3	13.9
Equivalent calcium (T2 + T3) wt.%	2.5	4.8	5.5	2.4	2.7	5.1	6.0	6.3	6.1
CSH gel (T1) wt.%/total portlandite (T2 + T3) wt.%	0.72	1.27	1.60	0.54	0.74	1.76	1.10	1.11	1.28

TABLE 3: Water losses associated with different phases in cement pastes with 2 wt.% of nanozinc (NZ) + 10 wt.% nanosilica (NS).

	2% NZ + 10% NS manual mixing (wt.%)			2% NZ + 10% NS low shear rate dispersion (wt.%)			52.5R		
	3 d	7 d	28 d	7 d	28 d	28 d	3 d	7 d	28 d
T1	3.0	8.0	11.2	2.7	3.8	10.5	6.6	7.0	7.8
T2	0.8	1.7	2.0	0.7	1.0	2.1	3.4	3.5	3.5
T3	1.3	3.0	2.8	0.9	1.9	3.0	2.6	2.8	2.6
Total combined water	5.1	12.7	16.0	4.3	6.7	15.6	12.6	13.3	13.9
Equivalent calcium (T2 + T3) wt.%	2.1	4.7	4.8	1.6	2.9	5.1	6.0	6.3	6.1
CSH gel (T1) wt.%/total portlandite (T2 + T3) wt.%	1.43	1.70	2.33	1.68	1.31	2.06	1.10	1.11	1.28

with a higher CSH gel formation. A higher CSH gel formation is important since this phase is responsible for the mechanical properties, adherence, and contribution to the durability of cement-based materials. For 28 days, water loss combined with portlandite indicates that about 9 wt.% of total loss is due to the portlandite (the portlandite content for samples obtained by both mixing methods is about a 6% total weight). This minor portlandite content, compared with pastes only with nanozinc, is a consequence of the pozzolanic reaction. According to the literature, nanosilica promotes the pozzolanic reaction since the pozzolanic reaction is proportional to the specific surface available for the reaction. Micro- and nanosilica, in this work, have a surface area of 28 and $150 \, m^2/g$, respectively (Jo et al. [60]). For samples with nanozinc oxide and with or without microsilica, the CSH gel-portlandite ratio is higher for samples with nanozinc oxide and nanosilica than for the reference cement paste at 28 days regardless of the mixing method. The explanation is the same as that for samples with microsilica. Cement pastes with nanosilica for both mixing methods show the highest CSH gel-portlandite ratios as a consequence of a higher extent of the pozzolanic reaction since such a reaction is proportional to the surface area of silica and is one order of magnitude higher for nanosilica than for microsilica. In all cement paste mixtures, the hydration process at early ages is different for each mixing method; although in both types, the hydration process is retarded (such an effect is greater for cement pastes obtained by low shear rate dispersion). ZnO is not involved in the hydration in cement pastes prepared by this method in the first ages, and the water bonded is lower than that in pastes prepared by manual mixing. At 28 days, hydration is similar for cement pastes obtained by both mixing methods.

The Ca/Si ratio in a CSH gel of cement pastes obtained by SEM-EDX analysis at the age of 28 days shows such a ratio for both mixing methods as similar with values of 1.95 and 1.78 for manual and dispersion mixing methods, respectively. The addition of silica decreases the Ca/Si ratio in the CSH gel, with this decrease being more meaningful when nanosilica (NS) is added.

FTIR analysis (Figure 5) for cement pastes with NZ and MS obtained by both mixing methods shows at three days that the cement paste by mixing oxide could be forecast as the peak corresponding to OH^- groups joined to Zn ions (zinc hydroxide), although in this case it is even weaker. The hydration behaviour is similar to that identified in cement pastes only with NZ: calcium silicate hydration has not started and the hydration of the calcium aluminates has only happened, according to the identification of alite (A) and ettringite (E). Pastes at seven days show that calcium silicate hydration has taken place for manual mixing samples but not so in the case of low shear rate dispersion pastes, in agreement with DTA-TG analysis. As can be observed in Figure 5, in manual mixing samples, the peak corresponding to the unhydrated alite phase has moved from 920 to $995 \, cm^{-1}$, corresponding to the C_3S hydration product (formation of the CSH gel) in addition to the portlandite phase. The hydration advance is higher for cement pastes prepared by a manual mixing method than for low-shear one. This is illustrated by the displacement of the peak corresponding to the CSH gel formation and also by a weak peak identified at $3645 \, cm^{-1}$ corresponding to the O-H stretching of portlandite, formed together with the CSH gel in the hydration of calcium silicates. For cured cement pastes at 28 days, FTIR analysis shows an identical hydration of cement pastes obtained by both mixing methods. When the hydration age is 28 days, there is a meaningful decrease in the peak corresponding to the ettringite phase regardless of the mixing method used in agreement with the literature

A: alite
C: carbonates
CSH: CSH gel
E: ettringite

P: portlandite
W: water
Z: zinc hydroxide
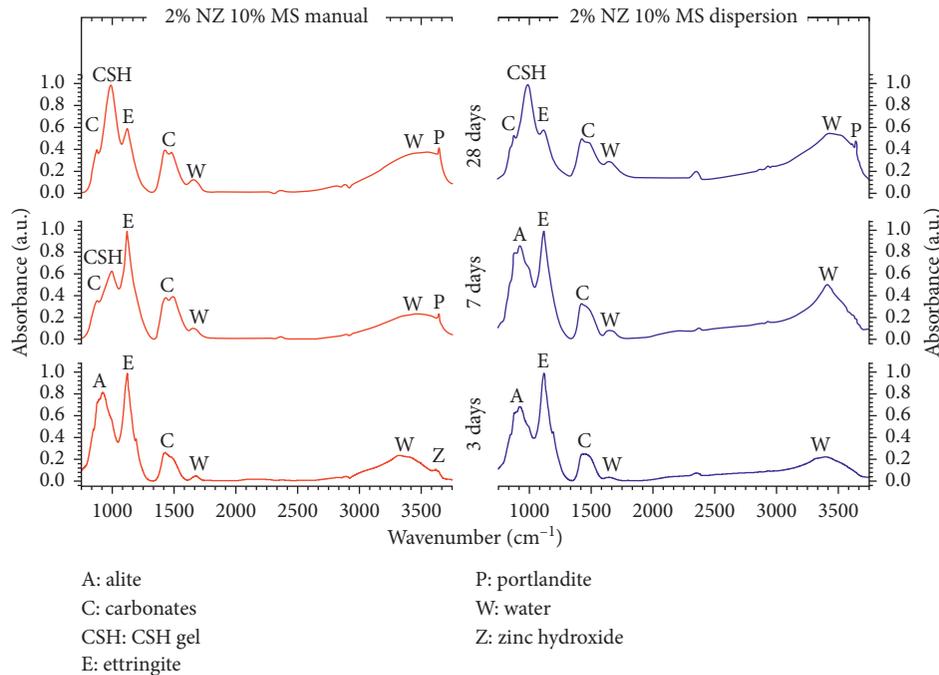
FIGURE 5: FTIR analysis for cement paste with 2 wt.% of nanozinc (NZ) + 10 wt.% microsilica (MS).

[57]. The intensity of the band corresponding to ettringite decreases as its transformation in monosulfoaluminates occurs. The only exceptions are cement pastes with only NZ as an addition, in which this change takes place when the age increases from three to seven days. It is important to note that the peak corresponding to portlandite ($3645\,\text{cm}^{-1}$) in samples with microsilica (seven and 28 days) shows a significantly lower intensity than for samples without silica due to portlandite reacting with silica in the presence of water to form a secondary CSH gel according to the following equation given by Neville and Brooks [61]:

$$\text{Ca(OH)}_2 + \text{SiO}_2 + \text{H}_2\text{O} \rightarrow \text{CSH gel.} \tag{1}$$
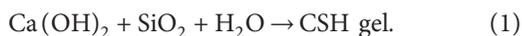
Although the pozzolanic reaction does not lead to a higher water loss T1, if the values provided in Tables 1 and 2 are compared, where in samples only with ZnO, the pozzolanic reaction cannot take place. Secondary CSH gels show lower Ca/Si ratios, in accordance with the literature (Al-Dulaijan et al. [62]).

FTIR analysis for cement pastes with NZ and NS obtained by both mixing methods is similar to cement pastes that contain NZ and MS. For this reason, this is not shown in the article.

At three days, in all cement pastes obtained by both mixing methods, it is possible to observe calcium silicates (alite) and ettringite but not CSH gels. Therefore, the hydration process has been delayed by ZnO. Pastes at seven days show that calcium silicate hydration takes place for manual mixing samples but not so for low shear rate dispersion pastes in agreement with DTG-T[a] analysis since for manual mixing samples the displacement of the peak corresponding to the unhydrated alite phase from 920 to $995\,\text{cm}^{-1}$ corresponding to the C_3S hydration product (formation of CSH gel) has

taken place. For cured cement pastes at 28 days, FTIR analysis shows an identical hydration of cement pastes obtained by both mixing methods. When the hydration age is at 28 days, there is a meaningful decrease in the peak corresponding to ettringite phase regardless of the mixing method used to obtain the cement pastes. It is important to note that the peak corresponding to portlandite ($3645\,\text{cm}^{-1}$) is not identified for any of the samples, as a consequence of a further extension of the pozzolanic reaction according to its higher surface area.

X-ray diffraction characterization (Figure 6) for cement pastes with NZ and MS shows agreement with DTA-TG analysis and FTIR in that hydration at three days is delayed for both mixing methods since only unhydrated phases are identified (calcium silicates and aluminates) in addition to calcium hydrozincite. At seven days, hydration is at a more advanced point in cement pastes obtained by manual mixing than for low shear rate dispersion. At this cured age, manual mixing sample characterization shows peaks corresponding to the portlandite phase (P), unlike dispersing samples in which such a phase is not identified. For pastes obtained by dispersion, as the XRD pattern for ages three and seven days is identical, hydration is delayed. At 28 days, according to XRD analysis, there are no hydration differences between cement pastes obtained by both mixing methods. It should be noted that it is possible to identify the crystalline calcium hydroxyzincate dihydrate $\text{CaZn}_2(\text{OH})_6\cdot 2\text{H}_2\text{O}$ (CZ) phase to any cured age for both pastes as in the pastes only with ZnO. As in the case of the pastes only with ZnO, given that an alite phase in cement pastes at ages of 28 days is identified, there are unhydrated cement particles.

X-ray diffraction characterization for cement pastes with NZ and NS is identical to cement pastes with NZ and MS (Figure 6). At three days, hydration is delayed for both mixing methods, with unhydrated phases (calcium silicates

A: alite
Al: aluminates
B: belite

CZ: calcium hydroxyzincate
P: portlandite
Q: quartz
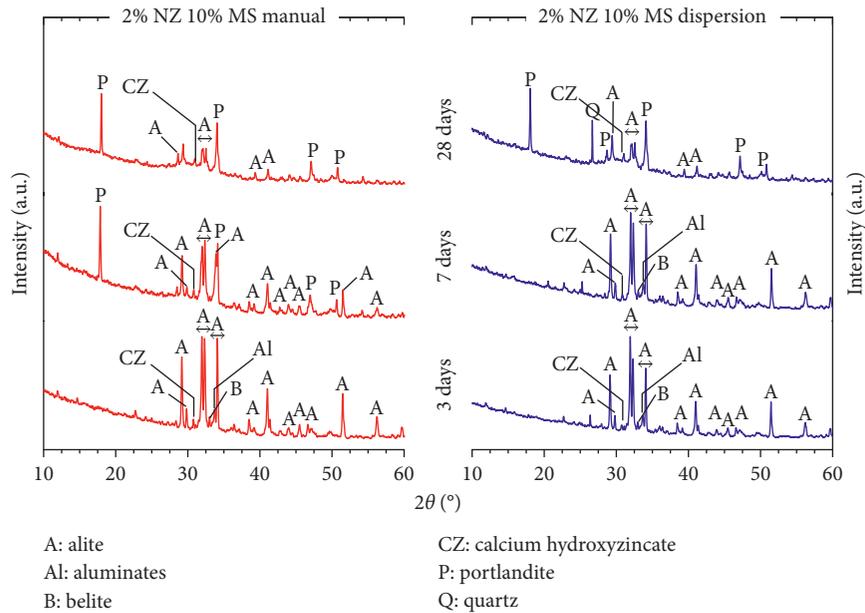
FIGURE 6: XRD characterization for cement paste with 2 wt.% of nanozinc (NZ) + 10 wt.% microsilica (MS).

and aluminates) being identified. At seven days, hydration is at a more advanced point in cement pastes obtained by manual mixing than for low shear rate dispersion. The portlandite phase only can be observed in pastes obtained by manual mixing. At 28 days, hydration for cement pastes obtained by both mixing methods is identical. It should be noted that it is possible to identify the crystalline calcium hydroxyzincate dihydrate $CaZn_2(OH)_6 \cdot 2H_2O$ (CZ) phase to any cured age for both pastes, as in the pastes only with ZnO or with ZnO and microsilica. As in the case of other pastes, a small quantity of alite in cement pastes for both mixing methods at ages of 28 days is identified, indicating that there are unhydrated cement particles as a consequence of the hydration relay by the ZnO addition. By means of XRD diffraction, it is not possible to confirm the greatest extent of the pozzolanic reaction for pastes with NS than for MS (T2 values in Tables 2 and 3 and Figure 5) according to the intensity of the peak associated to the portlandite phase.

4. Conclusions

In this work, cement pastes with simultaneous functional additions (micro- and nanosilica and nanozinc oxide) have been prepared by means of two different mixing methods: a common manual mixing method and a novel low shear rate dispersion method. It highlights the viability of using a new dispersion method based on a low shear mixing to prepare cement pastes with nanometric simultaneous functional additions and limit exposure to the nanoparticles in order to avoid health risks.

At earliest age, hydration for both mixing methods has not started and it is identified by the amorphous zinc hydroxide phase, responsible for the hydration inhibition. When hydration is restarted, it is identified by the crystalline calcium hydroxyzincate phase in cement pastes prepared by both methods. The delay in hydration is higher for cement

pastes obtained by low shear rate dispersion than with manual mixing. Nevertheless, at 28 days, hydration is similar for cement pastes obtained by both mixing methods.

In all the cement pastes with additions, the CSH gel-portlandite ratio is higher than that for the reference cement paste without additions at 28 days regardless of the mixing method, with cement pastes with nanozinc oxide and nanosilica reaching the highest ratio value. This result is a consequence of the higher content of water (higher combined water) in the gel (T1) due to the water bound to zinc in calcium hydroxyzincate for cement pastes with nano-ZnO. In addition, the formation of a secondary CSH gel due to the pozzolanic reaction is greater for cement pastes with nanosilica because of its higher surface area.

The most important result obtained in agreement with the similar hydration behaviour of the different cement pastes prepared by both mixing methods is associated with the feasibility of using the novel low energy dry dispersion method to prepare cement pastes with simultaneous nanometric functional additions avoiding the exposure to the nanoparticles and therefore minimizing health risks.

Conflicts of Interest

The authors declare that there are no conflicts of interest regarding the publication of this paper.

Acknowledgments

References

[1] L. Yang, A. Hakki, F. Wang, and D. E. Macphee, "Photocatalyst efficiencies in concrete technology: the effect of photocatalyst placement," *Applied Catalysis B: Environmental*, vol. 222, pp. 200–208, 2018.

[2] J. Chen, S.-c. Kou, and C.-s. Poon, "Photocatalytic cement-based materials: comparison of nitrogen oxides and toluene removal potentials and evaluation of self cleaning performance," *Building and Environment*, vol. 46, no. 9, pp. 1827–1833, 2011.

[3] P. Sikora, A. Augustyniak, K. Cendrowski et al., "Characterization of mechanical and bactericidal properties of cement mortars containing waste glass aggregate and nanomaterials," *Materials*, vol. 9, no. 8, p. 701, 2016.

[4] P. Sikora, K. Cendrowski, A. Markowska-Szczupak, E. Horszczaruk, and E. Mijowska, "The effects of silica/titania nanocomposite on the mechanical and bactericidal properties of cement mortars," *Construction and Building Materials*, vol. 150, no. 309, pp. 738–746, 2017.

[5] F. Tittarelli, "Oxygen diffusion through hydrophobic cement-based materials," *Cement and Concrete Research*, vol. 39, no. 10, pp. 924–928, 2009.

[6] C. Nunes and Z. Slizkova, "Hydrophobic lime based mortars with linseed oil: characterization and durability assessment," *Cement and Concrete Research*, vol. 61-62, pp. 28–39, 2014.

[7] W. De Muynck, N. De Belie, and W. Verstraete, "Antimicrobial mortar surfaces for the improvement of hygienic conditions," *Journal of Applied Microbiology*, vol. 108, no. 1, pp. 62–72, 2009.

[8] N. León, J. Massana, F. Alonso, A. Moragues, and E. Sanchez-Espinosa, "Effect of nano-SiO_2 and nano-Al_2O_3 on cement mortars for use in agriculture and livestock production," *Biosystems Engineering*, vol. 123, no. 1, pp. 1–11, 2014.

[9] E. Mohseni, B. Mehdizaded, J. Yang, and M. Ali Yazdi, "Singel and combined effects of nano-SiO_2, nano-Al_2O_3 and nano-TiO_2 on the mechanical, rheological and durability properties of self-compacting mortars containing fly ash," *Construction and Building Materials*, vol. 84, pp. 331–340, 2015.

[10] V. Vishwakarma, S. Sekhar Samal, and N. Manoharan, "Safety and risk associated with nanoparticles. A review," *Journal of Minerals and Materials Characterization and Engineering*, vol. 9, no. 5, pp. 455–459, 2010.

[11] M. A. Albrecht, C. W Evans, and C. L Raston, "Green chemistry and the health implications of nanoparticles," *Green Chemistry*, vol. 8, no. 5, pp. 417–432, 2006.

[12] N. C. Mueller and B. Nowack, "Exposure modeling of engineered nanoparticles in the environment," *Environmental Science and Technology*, vol. 42, no. 12, pp. 4447–4453, 2008.

[13] S. Haruehansapong, T. Pulngern, and S. Chucheepsakul, "Effect of the particle size of nanosilica on the compressive strength and the optimum replacement content of cement mortar containing nano-SiO_2," *Construction and Building Materials*, vol. 50, pp. 471–477, 2014.

[14] L. Senff, J. A. Labrincha, V. M. Ferreira, D. Hotza, and W. Repette, "Effect of nano-silica on rheology and fresh properties of cement pastes and mortars," *Construction and Building Materials*, vol. 23, no. 7, pp. 2487–2491, 2009.

[15] J.-X. Lu and C.-S. Poon, "Improvement of early-age properties for glass-cement mortar by adding nanosilica," *Cement and Concrete Composites*, vol. 89, pp. 18–30, 2018.

[16] J. Massana, E. Reyes, J. Bernal, N. León, and E. Sanchez-Espinosa, "Influence of nano and micro-silica additions on the durability of a high performance self-compacting concrete," *Construction and Building Materials*, vol. 165, pp. 93–103, 2018.

[17] A. A. Ramezanianpour and M. A. Moeini, "Mechanical and durability properties of alkali activated slag coating mortars containing nanosilica and silica fume," *Construction and Building Materials*, vol. 163, no. 28, pp. 611–621, 2018.

[18] H. Cheng-yi and R. F. Feldman, "Hydration reactions in Portland cement-silica fume blends," *Cement and Concrete Research*, vol. 15, no. 4, pp. 585–592, 1985.

[19] J. A. Larbi, A. L. A. Fraay, and J. M. Bijen, "The chemistry of the pore fluid of silica fume-blended cement systems," *Cement and Concrete Research*, vol. 20, no. 4, pp. 506–516, 1990.

[20] J. J. Thomas, H. M. Jennings, and J. J. Chen, "Influence of nucleation seeding on the hydration mechanism of tricalcium silicate and cement," *Journal of Physical Chemistry C*, vol. 113, no. 11, p. 4237, 2009.

[21] G. Land and D. Stephan, "The influence of nano-silica on the hydration of ordinary Portland cement," *Journal of Materials Science*, vol. 47, no. 2, pp. 1011–1017, 2012.

[22] A. Moezzi, A. M. McDonagh, and M. B. Cortie, "Zinc oxide particles: synthesis, properties and applications," *Chemical Engineering Journal*, vol. 185-186, pp. 1–22, 2012.

[23] R. K. Sendi, "Effects of different compositions from magnetic and nonmagnetic dopands on structural and electrical properties of ZnO nanoparticles-based varistor ceramics," *Solid State Sciences*, vol. 77, pp. 54–61, 2018.

[24] D. Xu, K. Song, Y. Li, L. Jiao, and J. Song, "Sc_2O_3 doped Bi_2O_3-ZnO thin film varistors prepared by sol-gel method," *Journal of Alloys and Compounds*, vol. 746, pp. 314–319, 2018.

[25] M. Kahouli, N. Toursi, H. Guermazi, and S. Guermazi, "Enhanced structural and optical properties of ZnO nanopowder with tailored visible luminescence as a function of sodium hydroxide to zinc sulfate mass ratio," *Advanced Powder Technology*, vol. 29, no. 2, pp. 325–332, 2018.

[26] A. M. Hussein, A. V. Lefanova, R. T. Koodali, B. A. Logue, and R. V. Shende, "Interconnected ZrO_2 doped ZnO/TiO_2 network photoanode for dye-sensitized solar cells," *Energy Reports*, vol. 4, pp. 56–64, 2018.

[27] T. V. Torchynska, B. El Filali, G. Polupan, A. L Diaz Cano, and I. Ballardo, "Luminescence, structure and aging c-axis-oriented silver doped ZnO nanocrystalline films," *Materials Science in Semiconductor Processing*, vol. 79, no. 1, pp. 99–106, 2018.

[28] C. Klingshirn, "ZnO: from basics towards applications," *Physica Status Solidi B*, vol. 244, no. 9, pp. 3027–3073, 2007.

[29] V. S. Ramachandran, *Handbook of Thermal Analysis of Construction Materials*, Noyes Publications, New York, NY, USA, 2002.

[30] D. Nivethitha and S. Dharmar, "Effect if zinc oxide nanoparticle on strength of cement mortar," *International Journal of Scientific Engineering and Technology*, vol. 3, no. 5, pp. 123–127, 2016.

[31] G. Arliguie and J. Grandet, "Influence de la composition d'un ciment Portland sur son hydratation en presence de zinc," *Cement and Concrete Research*, vol. 20, no. 4, pp. 517–524, 1990.

[32] M. Yousuf, A. Mollah, T. R. Hess, Y. N. Tsai, and D. L. Cocke, "An FTIR and XPS investigations of the effects of carbonation on the solidification/stabilization of cement based systems-Portland Type V with zinc," *Cement and Concrete Research*, vol. 29, pp. 55–61, 1999.

[33] D. L. Cocke, M. Y. A. Mollah, T. R. Hess, and T. C. Lin, "In aqueous chemistry and geochemistry of oxides, oxyhydroxides and related materials," *Materials Research Society*, vol. 432, pp. 63–68, 1997.

[34] C. A. Johnson and M. Kersten, "Solubility of Zn(II) in association with calcium silicate hydrates in alkaline solutions," *Environmental Science and Technology*, vol. 33, no. 13, pp. 2296–2298, 1999.

[35] W. Lieber and J. Gebauer, "Einbau von zink in calciumsilikathydrate," *Zem.-Kalk-Gips*, vol. 22, pp. 295–303, 1969.

[36] F. F. Ataie, M. C. G. Juenger, S. C. Taylor-Lange, and K. A. Riding, "Comparison of the retarding mechanisms of zinc oxide and sucrose on cement hydration and interactions with supplementary cementitious materials," *Cement and Concrete Research*, vol. 72, pp. 128–136, 2015.

[37] A. Stumm, K. Garbev, G. Beuchle et al., "Incorporation of zinc into calcium silicates hydrates, part I," *Cement and Concrete Research*, vol. 35, no. 9, pp. 1665–1675, 2005.

[38] S. K. Ouki and C. D. Hills, "Microstructure of Portland cement pastes containing metal nitrate salts," *Waste Management*, vol. 22, no. 2, pp. 147–151, 2002.

[39] F. Ziegler, A. M. Scheidegger, C. A. Johnson, R. Dahn, and E. Wieland, "Sorption mechanism of zinc to calcium silicate hydrate: x-ray absorption fine structure (XAFS) investigation," *Environmental Science and Technology*, vol. 35, no. 7, pp. 1550–1555, 2001.

[40] F. Ziegler and C. A. Johnson, "The solubility of calcium zincate ($CaZn_2(OH)_6·2H_2O$)," *Cement and Concrete Research*, vol. 31, no. 9, pp. 1327–1332, 2001.

[41] F. Tittarelli and T. Bellezze, "Investigation of the major reduction reaction occurring during the passivation of galvanized steels rebars," *Corrosion Science*, vol. 52, no. 3, pp. 978–983, 2010.

[42] Y. Xie, Y. He, P. L. Irwin, T. Jin, and X. Shi, "Antibacterial activity and mechanism of action of zinc oxide nanoparticles against *Campylobacter jejuni*," *Applied and Environmental Microbiology*, vol. 77, no. 7, pp. 2325–2331, 2011.

[43] A. Sirelkhatim, S. Mahmud, A. Seeni et al., "Review on zinc oxide nanoparticles. Antibacterial activity and toxicity mechanism," *Nano-Micro Letters*, vol. 7, no. 3, pp. 219–242, 2015.

[44] N. Madhusudhana, K. Yogendra, K. Mahadevan, and S. Naik, "Photocatalytic degradation of coralene dark red 2B azo dye using calcium zincate nanoparticles in presence of natural sunlight: an aid to environmental remediation," *International Journal of Chemical Engineering and Applications*, vol. 2, no. 4, pp. 294–298, 2011.

[45] N. M. Gomez-Ortiz, W. S. Gonzalez Gomez, S. C. de la Rosa-Garcia et al., "Antifungal activity of $Ca[Zn(OH)_3]_2\ 2H_2O$ coatings for the presentation of limestone monuments: an in vitro study," *International Biodeterioration and Biodegradation*, vol. 91, pp. 1–8, 2014.

[46] J. F. Hernandez-Sierra, F. Ruiz, D. C. Cruz Pena et al., "The antimicrobial sensitivity of Streptococcus mutans to nanoparticles of silver, zinc oxide and gold," *Nanomedicine, Nanotechnology, Biology, and Medicine*, vol. 4, no. 3, pp. 237–240, 2008.

[47] J. F. Fernández Lozano, I. Lorite Villalba, F. Rubio Marcos et al., "Method for dry dispersion of nanoparticles and production of hierarchical structures and coatings," US Patent WO2010/010220 A1, 2014.

[48] *Aerosil®, Aeroxide® and Sipernat® Products for the Construction Materials Industry, Technical Information 1398*, Evonik Industries, Essen, Germany.

[49] I. Lorite, L. Pérez, J. J. Romero, and J. F. Fernández, "Effect of the dry nanodispersion procedure in the magnetic order of the Co_3O_4 surface," *Ceramics International*, vol. 39, no. 4, pp. 4377–4381, 2013.

[50] D. Alonso-Domínguez, I. Álvarez-Serrano, E. Reyes, and A. Moragues, "New mortars fabricated by electrostatic dry deposition of nano and microsilica additions: enhanced properties," *Construction and Building Materials*, vol. 135, pp. 186–193, 2017.

[51] E. Ghafari, S. A. Ghafari, Y. Feng, F. Severgnini, and N. Lu, "Effect of zinc oxide and Al-zinc oxide nanoparticles on the rheological properties of cement paste," *Composites Part B: Engineering*, vol. 105, pp. 160–166, 2016.

[52] G. Villain, M. Thiery, and G. Platret, "Measurement method of carbonation profiles in concrete: thermogravimetry, chemical analysis and gammadensimetry," *Construction and Building Materials*, vol. 37, no. 8, pp. 1182–1192, 2007.

[53] V. S. Ramachandran, R. M. Paroli, J. J. Beaudoin, and A. H. Delgado, *Handbook of Thermal Analysis of Construction Materials*, Noyes Publications/William Andrew Publishing, New York, NY, USA, 2003.

[54] A. Mellado, M. V. Borrachero, L. Soriano, J. Payá, and J. Monzó, "Immobilization of Zn(II) in Portland cement pastes," *Journal of Thermal Analysis and Calorimetry*, vol. 112, no. 3, pp. 1377–1389, 2013.

[55] M. Y. A. Mollah, J. P. Pargat, and D. L. Cocke, "An infrared spectroscopic examination of cement-based solidification/stabilization systems-Portland Types V and IP with zinc," *Journal of Environmental Science and Health*, vol. 27, no. 6, pp. 1503–1519, 1992.

[56] M. A. Trezza, "Hydration study of ordinary Portland cement in the presence of zinc ions," *Materials Research*, vol. 10, no. 4, pp. 331–334, 2007.

[57] T. Vázquez Moreno, "Contribución al estudio de las reacciones de hidratación del cemento portland por espectroscopia infrarroja," *Materiales de Construcción-CSIC*, vol. 16, no. 163, pp. 51–63, 1976.

[58] F. Andrade Brehm, C. A. Mendes Moraes, R. C. Espinosa Modolo, A. C. Faria Vilela, and D. C. Coitinho Dal Molin, "Oxide zinc addition in cement paste aiming electric arc furnace," *Construction and Building Materials*, vol. 139, pp. 172–182, 2016.

[59] J. I. Tobón, J. J. Payá, M. V. Borrachero, and O. J. Restrepo, "Mineralogical evolution of Portland cement blended with silica nanoparticles and its effect on mechanical strength," *Construction and Building Materials*, vol. 21, pp. 1351–1355, 2007.

[60] B.-W. Jo, C.-H. Kim, G. Tae, and J.-B. Park, "Characteristics of cement mortar with nano-SiO_2 particles," *Construction and Building Materials*, vol. 21, no. 6, pp. 1351–1355, 2007.

[61] A. M. Neville and J. J. Brooks, *Concrete Technology*, Longman Group, London, UK, 2nd edition, 2010.

[62] S. U. Al-Dulaijan, A.-H. Al-Tayyib, M. M. Al-Zahrani, G. Parry Jones, and A. I. Al-Mana, "Si MAS-NMR study of hydrated cement paste and mortar made with and without silica fume," *Journal of the American Ceramic Society*, vol. 78, no. 2, pp. 342–346, 1995.

Research Article

Models for Strength Prediction of High-Porosity Cast-In-Situ Foamed Concrete

Wenhui Zhao [ID],[1,2] **Junjie Huang** [ID],[1,2] **Qian Su,**[1,2] **and Ting Liu**[1,2]

[1]*School of Civil Engineering, Southwest Jiaotong University, Chengdu, China*
[2]*MOE Key Laboratory of High-Speed Railway Engineering, Southwest Jiaotong University, Chengdu, China*

Correspondence should be addressed to Junjie Huang; jjhuang_swjtu@126.com

A study was undertaken to develop a prediction model of compressive strength for three types of high-porosity cast-in-situ foamed concrete (cement mix, cement-fly ash mix, and cement-sand mix) with dry densities of less than $700 \, \text{kg/m}^3$. The model is an extension of Balshin's model and takes into account the hydration ratio of the raw materials, in which the water/cement ratio was a constant for the entire construction period for a certain casting density. The results show that the measured porosity is slightly lower than the theoretical porosity due to few inaccessible pores. The compressive strength increases exponentially with the increase in the ratio of the dry density to the solid density and increases with the curing time following the composite function $A_2 (\ln t)^{B_2}$ for all three types of foamed concrete. Based on the results that the compressive strength changes with the porosity and the curing time, a prediction model taking into account the mix constitution, curing time, and porosity is developed. A simple prediction model is put forward when no experimental data are available.

1. Introduction

Foamed concrete is an important type of geotechnical material [1]. It is a light solidification material mainly composed of cement, a filler, and a percentage of stable tiny bubbles and possesses the advantages of being light weight, vertically stable, and convenient for construction [2–5]. The statistical results compiled by the China Concrete and Cement Products Association (CCPA) indicate that the annual production volume of foamed concrete was over 40 million·m³ in China in 2016, of which more than 80% was cast-in-situ foamed concrete. Due to the increase in large-scale construction and civil engineering projects, the applications of foamed concrete will increase in the future. Therefore, it is important to control the quality of foamed concrete. In the application of foamed concrete for engineering projects, the quality indicators are the casting density during the casting process and the compressive strength during the design stage. However, it is important to know the compressive strength of the foamed concrete at different times after the casting process and during the initial construction period. Therefore, it is

necessary to develop a compressive strength prediction model by considering the important parameters and the mix compositions. The strength of foamed concrete is influenced by a number of parameters that have been determined in previous studies [6–8]. The uniaxial compressive strength is given by

$$\sigma = f\left(\sigma_0, p, m, \frac{m_w}{m_c}, \dots\right), \tag{1}$$

where σ_0 is the uniaxial compressive strength of concrete at a porosity of 0; p is the porosity; m is the degree of hydration, $0 \le m \le 1$, $m = 0$ means the start of the hydration and $m = 1$ means the completion of the hydration; and m_w/m_c is the water/cement ratio.

Based on (1), for the same curing conditions and mix composition, the strength of the foamed concrete is mainly influenced by the porosity, the degree of hydration, and the water/cement ratio. Several models have been proposed to express this ratio, and they are listed in Table 1. It is evident that several compressive strength prediction models for foamed concrete are based on the Powers model and the

TABLE 1: Review of compressive strength prediction models for foamed concrete.

Author	Material composition	Models
Balshin [8]	Cement	$\sigma = \sigma_0 (1 - p)^n$
Neville [9]	Cement, sand, fly ash	$\sigma = kg^n$
Tam et al. [10]	Cement	$\sigma = k(1/(1 + m_w/m_c + m_a/m_c))^n$
Durack and Weiqing [11] Nambiar and Ramamurthy [12]	Cement, sand, fly ash	$\sigma = k((2.06\alpha V_c)/(1 - V_{fl} - V_c(1 - \alpha)))^n$
Hoff [13]	Cement	$\sigma = \sigma_0 ((d_c(1 + 0.2\rho_c))/((1 + k_s)\rho_c\gamma_w))^b$
Kearsley and Wainwright [14]	Cement, sand, fly ash	$\sigma = \sigma_0 ((d_c(1 + 0.2\rho_c + s_v))/((1 + k_s)(1 + s_w)\rho_c\gamma_w))^b$

σ = the uniaxial compressive strength of foamed concrete; p = porosity; g = gel-space ratio; m_a/m_c = the air/cement ratio; d_c = casting density; ρ_c = the specific gravity of cement; γ_w = unit weight of water; k_s = water-solid ratio by weight; σ_0 = uniaxial compressive strength of concrete at a porosity of 0; s_w = filler-cement ratio by weight; s_v = admixture-cement ratio by volume; k = gel strength; α = hydration water-cement ratio by weight; V_c = volume of cement; V_{fl} = filler volume of unit volume; d_c = fresh density; b, n = empirical constant.

(a)   (b)
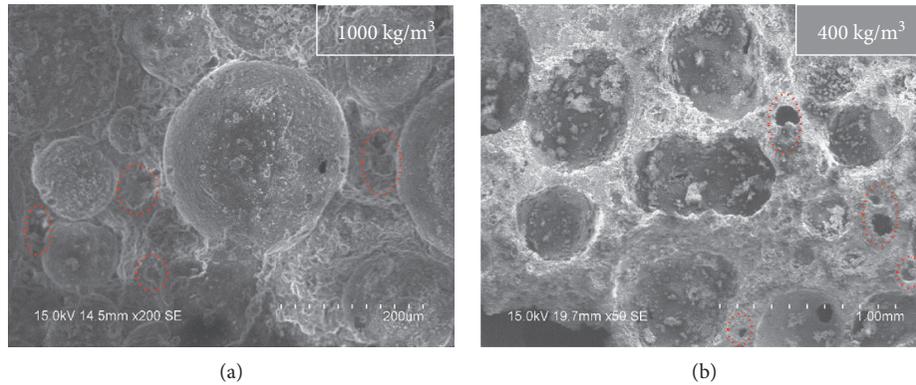
FIGURE 1: Comparison of voids in (a) high-density and (b) low-density casting of foamed concrete. Red dotted circles: small voids in the pore walls.

Balshin model; most prediction models have limitations in terms of the influencing factors of porosity, the degree of hydration, and the water/cement ratio.

As can be seen in Figure 1, foamed concrete is a typical noncompacting type of concrete; therefore, the porosity of foamed concrete is controlled by the volume of the voids in the concrete. The voids include gel pores, microcapillaries, macrocapillaries, and artificial air pores [15, 16]. Based on (1), its compressive strength is related to the proportion occupied by voids. Odler and Rößler [7] established a relationship between porosity and strength for a series of cement pastes with different water/cement ratios after periods of hydration. The research showed that the relationship between the compressive strength and the porosity is linear for porosity values between 5% and 28%. Fagerlund [17] stated that it is necessary to determine a limit for the porosity. When the porosity is below the limit, an equation fits the experimental data. For higher porosities, a different equation is required. As the foamed concrete density increases, the pore spaces become smaller and the pore walls become thicker. When the dry density of foamed concrete is more than 700 kg/m³ (the relative density is about 0.3), there is a transitional change and the material changes from a porous structure to a solid structure containing isolated pores [18]. The dry density of foamed concrete used as roof insulation material ranges from 160 to 300 kg/m³. For heat insulation material, the dry density ranges from 300 to 500 kg/m³. When used as geotechnical fill material, its dry density ranges from 400 to 600 kg/m³ [19, 20]. As we can see, all values all smaller than 700 kg/m³.

For a given casting density of foamed concrete, when the water/cement ratio is low, the added bubbles will burst while the mixture is being stirred and the flow requirement of the foamed concrete cannot be reached. When the water/cement ratio is high, instability will occur for the fresh foamed concrete and the bubbles float on top of the foamed concrete slurry. This separation phenomenon between the foam and the cement slurry influences the casting results [21, 22]. These two phenomena related to bubble instability are shown in Figure 2. For the cast-in-situ foamed concrete during construction, the flow value is regulated between 160 and 180 mm. As for the cast-in-situ foamed concrete, a superplasticizer was not added during the production process due to limitations in the construction conditions and the construction equipment; therefore, the water/cement ratio was a constant value for a given casting density.

The degree of hydration of the foamed concrete is a function of time, curing temperature, and other parameters. As the curing time increases, the cement hydration in the foamed concrete may produce solid products that fill the pores of the sample. At the same time, the self-weight consolidation and evaporation of water may significantly increase the stiffness and density of the samples [23]. A study on the effect of the relationship between water permeability and pore connectivity under different curing times indicated that the sample had a coarse structure during the early stage,

(a) (b)
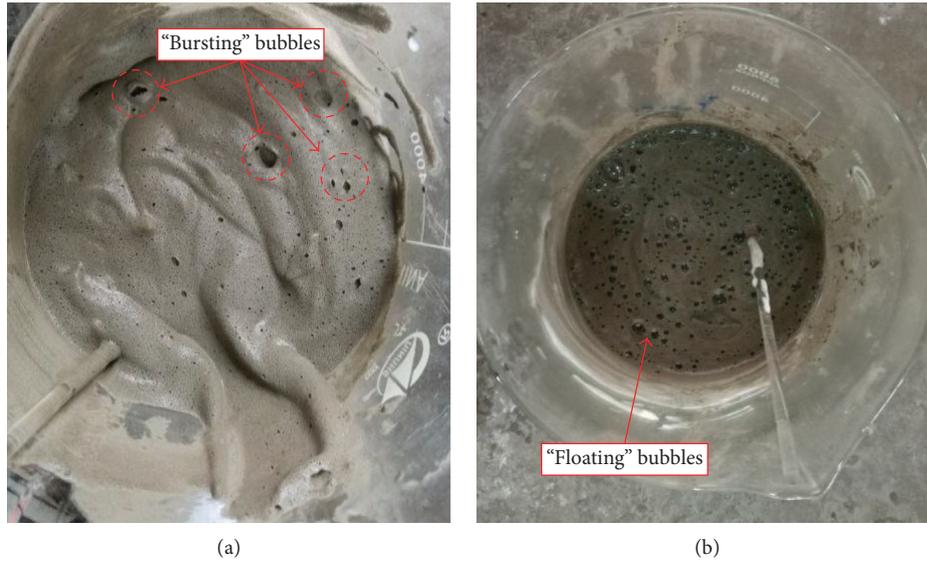
Figure 2: Bubble instability phenomena: (a) bubble bursting; (b) bubble floating.

Table 2: The constituent materials of the foamed concrete.

Materials	Remarks
Cement	Type I Portland cement conforming to GB 175-2007
Sand	Finer than 300 microns, specific gravity = 2.5
Fly ash	Class F Type I conforming to GB/T 1596-2005
Foaming agent	Synthetic type, specific gravity = 1.06
Water	Tap water

whereas the pore structure in the hardened cement paste became denser as the curing time increased [24, 25]. For the same casting density and curing conditions, the compressive strength of foamed concrete varies with the curing time; therefore, it is necessary to know the compressive strength for different curing times.

In view of these observations, it is necessary to develop a model for compressive strength prediction of high-porosity cast-in-situ foamed concrete that should consider the porosity and the degree of hydration. The model can help determine the mix composition of the foamed concrete, the casting density, and the compressive strength. At the same time, it will provide a reference for the initial construction time of the engineering project.

2. Materials and Methods

2.1. Materials. The foamed concrete used in this study was made from ordinary Portland cement, fine sand, fly ash, and bubbles. The constituent materials used in the experiments are shown in Table 2. In this research, a synthetic type of foaming agent was used because it was highly eco-friendly and its air bubbles were strong. The bubbles were entrained or entrapped within the slurry to promote lightness [26, 27].
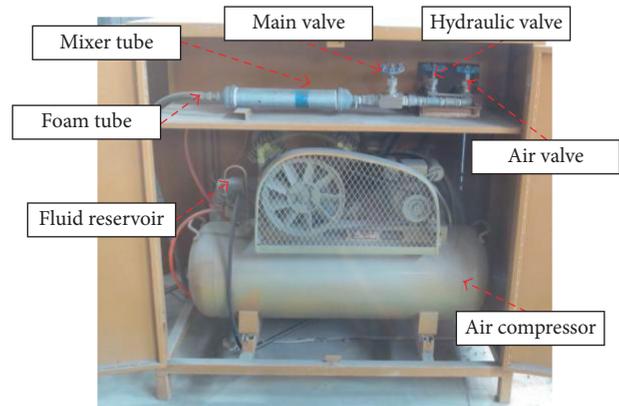
Figure 3: Air bubble generator.

2.2. Mix Design Procedure. To produce the bubbles for the production of the samples, the foaming agent was diluted with water at a ratio of 1 : 60 (namely, the multiple of dilution equals 60). A prefoaming method was used to produce the foamed concrete. In this method, the air bubbles were first foamed by a bubble generator, which is shown in Figure 3. The density of air bubbles was set at $35 \pm 5 \, \text{kg/m}^3$.

A flowchart of the foamed concrete mix method is shown in Figure 4. The cement, fly ash, and sand were mixed with water at a certain ratio to produce a cement slurry as shown in Table 3. After that, the air bubbles were mixed well with the cement slurry by stirring with an electric blender to produce the foamed concrete.

2.3. Samples and Maintenance Procedure. Twenty-one densities of foamed concrete were cast; the corresponding mix proportions and major parameters are listed in Table 3. For each density, the number of groups was decided by the testing time. Six identical samples (100 mm long × 100 mm wide × 100 mm high) were prepared for each group and
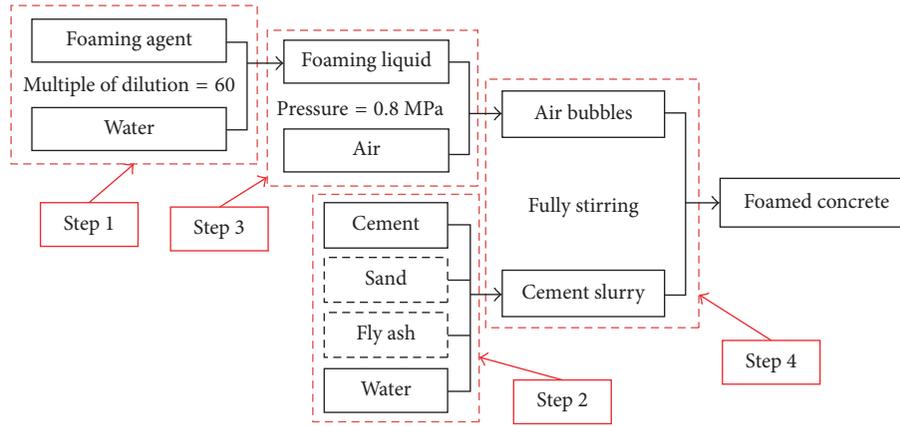
FIGURE 4: Flowchart of the foamed concrete mix method [28].

testing time. Three samples were used to test the compressive strength, and the others were used to measure the dry densities. The samples were demoulded after 24 h to ensure that they were sufficiently hard for further handling. Then, all the test samples were subjected to standard curing.

2.4. Testing Method

2.4.1. Compressive Strength. The cubes were tested by using a compressive machine at the pace rates of 2.00 kN/s according to the "Test method of autoclaved aerated concrete" (GBT 11969-2008). The stress data were recorded to determine the unconfined compressive strength. The data used for the analysis consisted of the average of three sample test results.

2.4.2. Porosity. The measured porosity of the foamed concrete was determined using a vacuum saturation apparatus. The samples were placed in an electric, constant-temperature drying oven at 60°C for 24 h. After that, the temperature was increased to 80°C and maintained for 24 h. The samples were dried at 100°C until the weight of the samples was constant. After the samples were placed into the vacuum saturation apparatus (Figure 5), the pressure was maintained at −1 MPa for 2 h. After turning on the air valve, water flowed into the device slowly until the samples were immersed in the liquid. Prior to the weighing tests, the samples were saturated for another 22 h. The measured porosity was calculated using the following formula [29]:

$$P = \frac{\left(W_{sat} - W_{dry}\right)}{\left(W_{sat} - W_{wat}\right)} \times 100, \tag{2}$$

where P is the vacuum saturation porosity (%), W_{sat} is the weight in air of the saturated sample, W_{wat} is the weight in water of the saturated sample, and W_{dry} is the weight of oven-dried sample.

3. Results and Discussion

Nambiar and Ramamurthy [12, 30] expressed the theoretical porosity of foamed concrete using the variables of casting density, water-solid ratio, filler-cement ratio of the freshly foamed concrete mixture, specific gravity of the cement, and unit weight of water, which can be seen in (3) and (4). According to previously determined data, the porosity values vary from 0.18 to 0.23 for different kinds of raw materials and different proportions of ingredients [10, 31, 32]. The ratio of hydration water to cement by weight is assumed to be 0.2.

$$n = 1 - \frac{d_c\left(1 + 0.2\rho_c\right)}{\left(1 + k_s\right)\rho_c\gamma_w}, \tag{3}$$

$$n = 1 - \frac{d_c\left(1 + 0.2\rho_c + s_v\right)}{\left(1 + k_s\right)\left(1 + s_w\right)\rho_c\gamma_w}. \tag{4}$$

These equations are inconvenient and flawed. First of all, there are many variables that need to be calculated. Secondly, it is assumed that the hydration of the cement is complete, which ignores the degree of cement hydration. Lastly, these equations do not consider the difference in the hydration water between the cement and the admixtures. In order to avoid these problems, the following equation can be used to determine the theoretical porosity [18]:

$$n = 1 - \frac{\rho^*}{\rho_s}, \tag{5}$$

where ρ^* is the dry density of foamed concrete and ρ_s is the dry density of the solid material.

In (5), the dry density can be considered a certain value for the same mix constitution for the same brand of material when it is completely hydrated. When the constitution proportions of the materials change, ρ_s can be obtained based on the proportions of the constitutions. The hydrations of the cement and admixtures are functions of the curing time, and the degree of hydration will affect the dry density. When the hydration is complete and the testing time is long enough, (3) and (4) are applicable. However, (5) applies in all cases. In addition, this equation is simple and intuitive.

The relationship between the measured and theoretical porosities (after 1 year) of foamed concrete is shown in Figure 6. It is evident that deviations exist between the measured and theoretical porosities. For all mixes, the

TABLE 3: Mix proportions and major parameters of foamed concrete.

Mix number	$m_c + m_m + m_s$	f/c	s/c	w/binder	Water (kg)	Cement (kg)	Fly ash (kg)	Sand (kg)	Air bubbles (l)	Dry density (kg/m³)	Casting density (kg/m³)	Flow value (cm)	Testing time (d)
1		0	0	0.75	173.0	230.7	0.0	0.0	752.6	291.3	430.1	16.1	7, 28, 90, 180, 270, 365
2	A	0	1:1	0.63	144.2	115.4	0.0	115.4	772.5	255.8	401.9	17.7	7, 28, 90, 180, 270, 365
3		1:1	0	0.75	173.0	115.4	115.4	0.0	745.4	274.5	429.8	16.8	7, 28, 90, 180, 270, 365
4		0	0	0.70	204.5	292.2	0.0	0.0	701.2	367.3	521.3	16.2	28, 365
5	B	0	1:1	0.59	172.4	146.1	0.0	146.1	722.0	324.8	489.9	16.5	28, 365
6		1:1	0	0.70	204.5	146.1	146.1	0.0	692.1	345.4	521.0	16.9	28, 365
7		0	0	0.65	229.9	353.7	0.0	0.0	656.0	427.6	606.6	16.5	28, 365
8	C	0	1:1	0.56	196.4	176.9	0.0	176.9	675.8	391.8	573.8	16.6	28, 365
9		1:1	0	0.65	229.9	176.9	176.9	0.0	645.0	421.3	606.2	17.2	28, 365
10		0	0	0.60	249.1	415.2	0.0	0.0	616.9	514.9	685.9	16.8	7, 28, 90, 180, 270, 365
11	D	0	1:1	0.52	215.9	207.6	0.0	207.6	634.1	461.5	653.3	17.5	7, 28, 90, 180, 270, 365
12		1:1	0	0.60	249.1	207.6	207.6	0.0	604.1	496.2	685.5	17.4	7, 28, 90, 180, 270, 365
13		0	0	0.55	262.2	476.7	0.0	0.0	584.0	585.4	759.3	16.8	28, 365
14	E	0	1:1	0.49	233.6	238.4	0.0	238.4	594.1	526.4	731.2	17.1	28, 365
15		1:1	0	0.55	262.2	238.4	238.4	0.0	569.3	561.2	758.8	17.7	28, 365
16		0	0	0.54	290.6	538.2	0.0	0.0	535.8	645.6	847.6	17.1	28, 365
17	F	0	1:1	0.48	258.3	269.1	0.0	269.1	547.2	597.2	815.7	16.8	28, 365
18		1:1	0	0.54	290.6	269.1	269.1	0.0	519.1	638.1	847.0	17.6	28, 365
19		0	0	0.53	317.8	599.7	0.0	0.0	488.7	705.4	934.6	16.7	7, 28, 90, 180, 270, 365
20	G	0	1:1	0.47	281.9	299.9	0.0	299.9	501.5	663.8	899.1	17.5	7, 28, 90, 180, 270, 365
21		1:1	0	0.53	317.8	299.9	299.9	0.0	470.1	687	934.0	17.4	7, 28, 90, 180, 270, 365
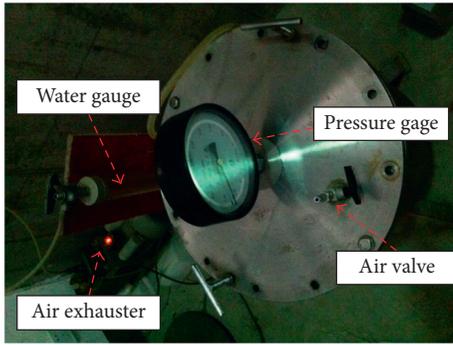
Figure 5: Vacuum saturation device.
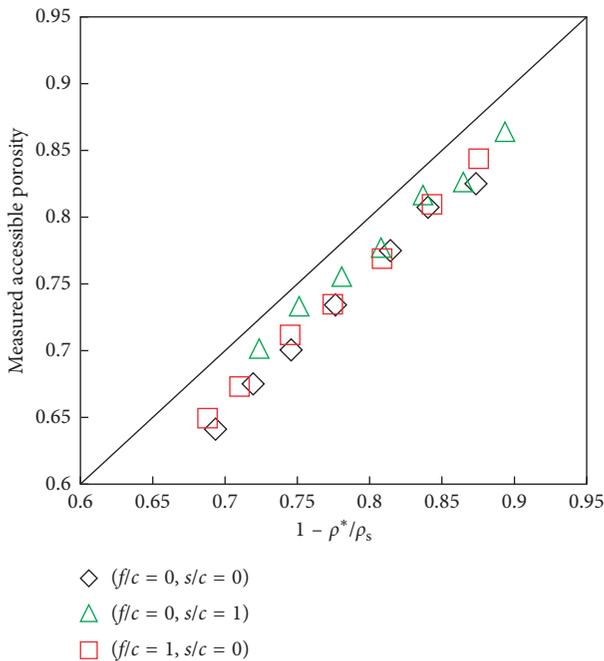
Figure 6: Relationship between measured porosity and $1 - \rho^*/\rho_s$.

measured values are lower than the theoretical values. The reason is that foamed concrete has closed pores, which are difficult to fill entirely with water. The closed pores differ for different casting densities. In high-density casting, the closed pores occur in the pore structures and pore walls, while in low-density casting, the closed pores mainly occur in the pore walls. A comparison of the differences between the measured and theoretical porosities for the three types of foamed concrete of the same casting density indicates that the difference is largest for the cement mix, followed by the cement-fly ash mix and the cement-sand. After the addition of fly ash, the initial setting time of the foamed concrete increases resulting in instability of the foamed concrete slurry and an increase in the number of connected holes [14]. For the foamed concrete containing sand, the pore walls become thinner and the number of the connected holes increases due to the reduction in the cement proportion and the increase in the density of the solid material [33, 34]. When the number of connected holes increases, there is

a higher likelihood that the voids are filled with water, which decreases the deviations between the measured and the theoretical porosities.

3.1. Effect of Porosity on Compressive Strength. The relationship between the theoretical porosity and the compressive strength (28 days and 1 year) of the foamed concrete is shown in Figure 7. The data show that the compressive strength increases exponentially with the increase in ρ^*/ρ_s as described in (6); this occurs for all types of foamed concrete for the 1 yr duration and the 28 d duration.

$$\sigma = A_1 \left(\frac{\rho^*}{\rho_s} \right)^{B_1}. \tag{6}$$

A comparison between Figures 7(a) and 7(b) shows that the dry density is slightly higher for 1 yr than for 28 d for the same density of foamed concrete because the hydration reaction is not fully complete at 28 d, which is consistent with previously reported results [2]. For the three conditions ($f/c = 0$, $s/c = 0$; $f/c = 0$, $s/c = 1$; $f/c = 1$, $s/c = 0$), the A_1 value is higher for 1 yr than for 28 d. The B_1 value is lowest for the cement-sand mix, followed by the cement mix and the cement-fly ash mix.

Table 4 lists the constants of the strength-porosity models of the foamed concrete with various mix constituents. It shows that the values of the constants obtained in this study are close to the values obtained by Hoff [13] using cement paste. However, the constants obtained in this study are lower than those obtained by Nambiar and Ramamurthy [12] for cement-sand. Nambiar and Ramamurthy [21] stated that foamed concrete with a fly ash additive was less dependent on the pore parameters than foamed concrete with sand; these results differ from our results. Figure 8 shows the microscopic photographs of the pore wall structures of the foamed concrete with different casting densities. The pore wall structure is dense for the high-density casting and less dense for the low-density casting. In the low-porosity foamed concrete ($f/c = 0$, $s/c = 1$), the sand has an interlocking effect under pressure. In the high-porosity foamed concrete ($f/c = 0$, $s/c = 1$), the hole walls are thinner and less dense, which reduces the interlocking effect. Therefore, in this study, the σ_0 parameter of high-porosity foamed concrete only reflects the uniaxial compressive strength of the mix constitution.

3.2. Effect of Curing Time on Compressive Strength. Most of the existing compressive strength prediction models have been used to predict the strength of the foamed concrete after casting at particular times, while the compressive strength of foamed concrete increases with the curing time. Because the use of the foamed concrete begins at 28 d after casting or earlier, it is important to predict the strength of foamed concrete immediately after casting and thereafter.

The effects of the curing time on the compressive strengths of three casting densities are shown in Figure 9. It can be seen that the compressive strength increases with the

(a)

(b)
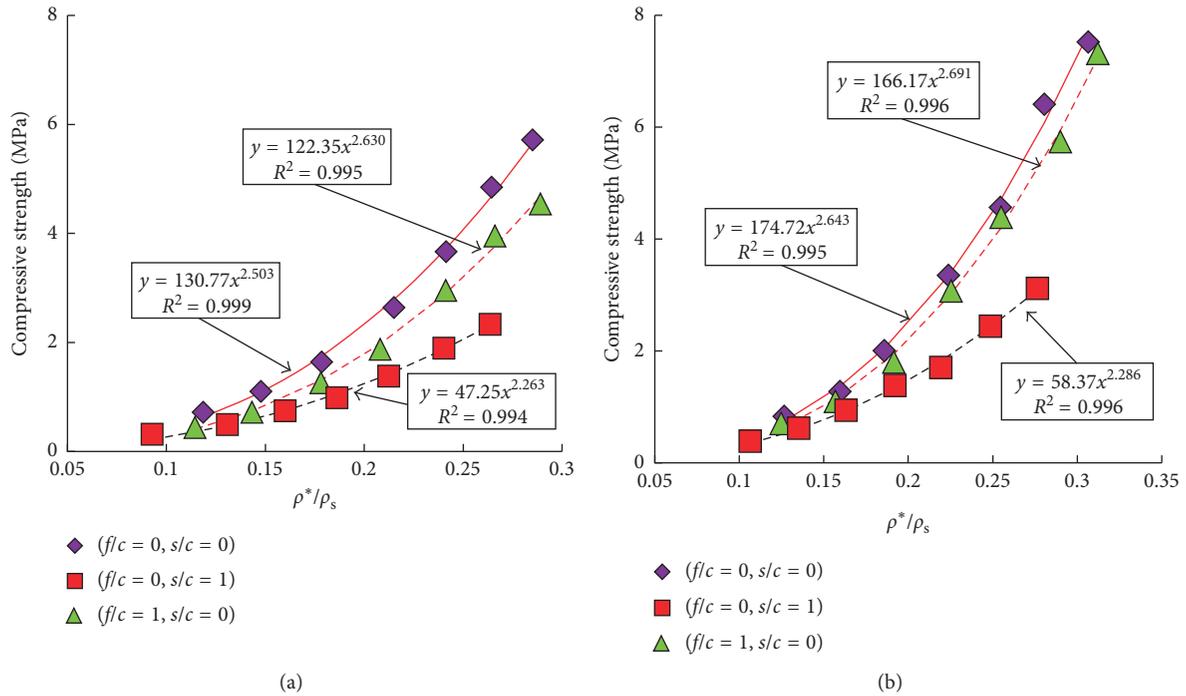
FIGURE 7: Effect of porosity on compressive strength at (a) 28 days and (b) 1 year.

TABLE 4: Comparison of the constants of various strength-porosity models.

Model by	Mix constituents	Constants	
		σ_0	b
Hoff [13]	Cement	115–290	2.7–3
Kearsley and Wainwright [14]	Cement with and without fly ash	188	3.1
Nambiar and Ramamurthy [12]	Cement-sand	155.66	4.3
	Cement-sand-fly ash	105.14	2.58
Present study	Cement	174.72	2.643
	Cement-sand	58.37	2.286
	Cement-fly ash	166.17	2.691

(a)

(b)
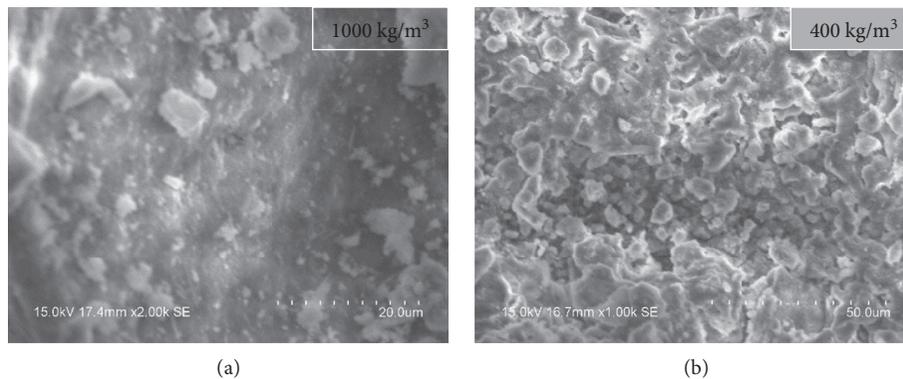
FIGURE 8: Microscopic photographs of the pore wall structures of (a) high-density and (b) low-density casting foamed concrete.

curing time; initially, the rate of increase in the compressive strength is large and it slows as the curing time increases. The relationship between the compressive strength and the curing time can be expressed by the following equation for a given density and mix constitution:

$$\sigma = A_2 (\ln t)^{B_2}. \qquad (7)$$

A comparison of the results shown in Figures 9(a)–9(c) indicates that for the same casting density and curing time, the compressive strength is highest for the cement mix, followed by

(a)

(b)

(c)
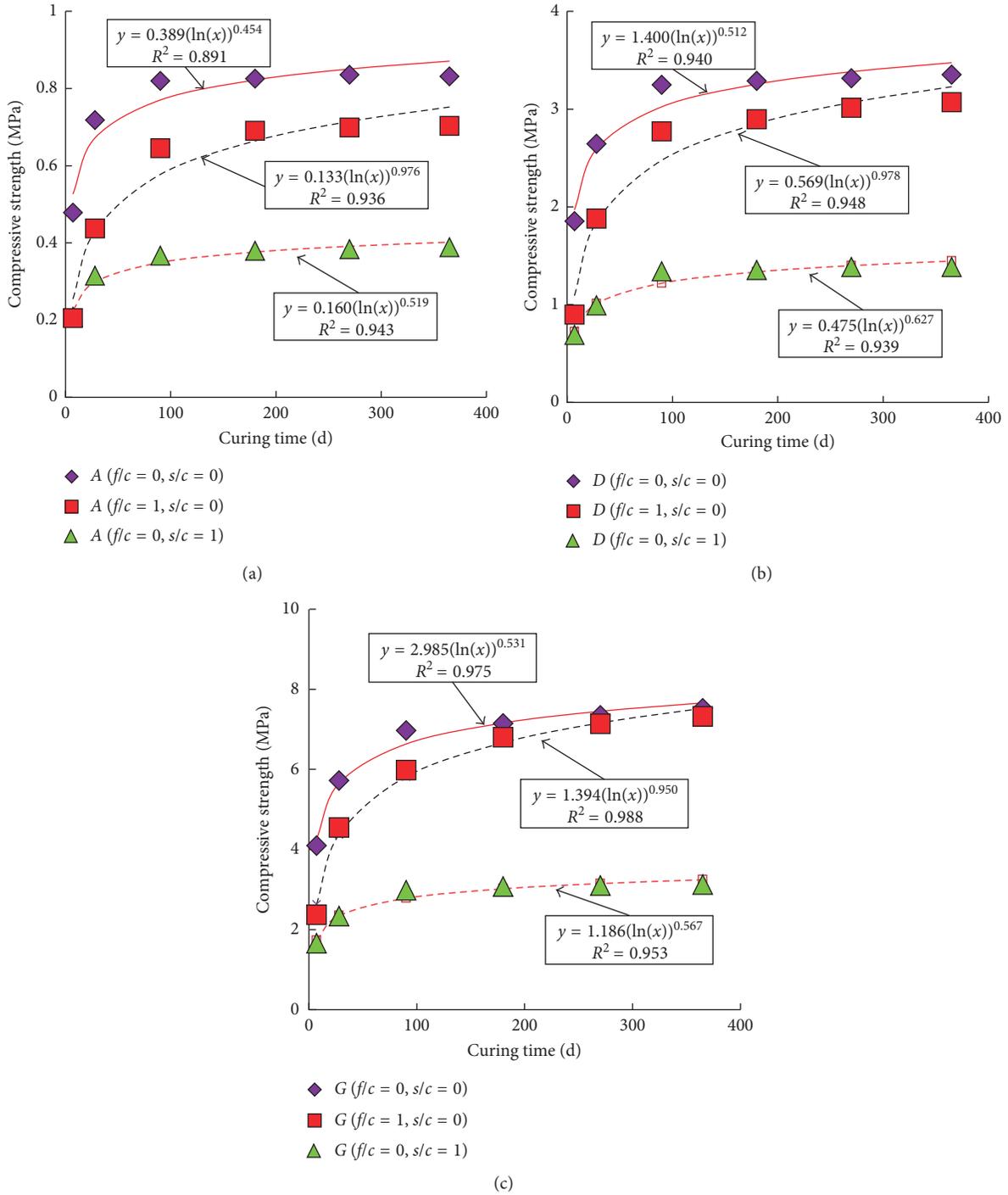
FIGURE 9: Effect of curing time on compressive strength for the three casting densities: (a) A, (b) D, and (c) G.

the cement-fly ash mix and the cement-sand mix. The compressive strength is almost stable at 90 d for the cement mix and the cement-sand mix; the compressive strength does not increase after 180 d for the cement-fly ash mix. It is evident that the values provided by the prediction model are lower during the early stage and higher during the late stage compared with the test values. The compressive strength decreases when fly ash is added, but the attenuation ratio decreases with an increase in the casting density. The B_2 values are similar for the cement

mix and the cement-sand mix, but the B_2 value is lower for the cement-fly ash mix. Because the hydration reaction material in the cement mix and the cement-sand mix is cement, the hydration rates are very similar under the same curing conditions [35], while the hydration rate of the fly ash is lower. The B_2 value represents the hydration rate of the raw material.

3.3. Proposed Model. Based on the above results, the compressive strength of foamed concrete is a function of the mix

TABLE 5: Comparison of the constants of various mix constituents.

Mix constituents	A	B	C	$A(\ln 365)^B$	R^2
Cement	110.255	0.204	2.568	158.362	0.997
Cement-sand	34.989	0.305	2.292	60.123	0.995
Cement-fly ash	59.551	0.531	2.603	152.830	0.993

TABLE 6: Comparison of the constants of various mix constituents ($\rho^* = \rho^*_{365}$).

Mix constituents	A	B	C	$A(\ln 365)^B$	R^2
Cement	60.640	0.470	2.459	139.655	0.988
Cement-sand	22.771	0.518	2.244	57.106	0.991
Cement-fly ash	33.315	0.821	2.548	143.055	0.982

constitution, curing time, and porosity. The following equation is derived from (6) and (7):

$$\sigma = A(\ln t)^B \left(\frac{\rho^*}{\rho_s}\right)^C, \tag{8}$$

where t is the curing time, $1 < t \le 365$; A is the parameter associated with the compressive strength of concrete; B is the parameter reflecting the hydration rate of the mix constituents; and C is the parameter reflecting the porosity and pore structure, which is associated with the pore quality including pore size, pore shape, and so on.

When (8) is used to fit the test data, ρ^* is measured when the compressive strength is tested. Table 5 shows the constants of various mix constituents. It can be inferred that there is no obvious difference in the B value for cement and cement-sand, whereas the B value of the cement-fly ash is high, which is in agreement with the foregoing conclusions. Compared with the B values shown in Figure 9, the values are lower in Table 5 because the hydration rate of the mix constituent is reflected by the parameters B and C. When parameter C is added to the equation, the value of B decreases.

The parameter ρ^* is rarely measured outside the laboratory when a strength prediction model is used. It is important to reduce the number of measurements. The dry densities are similar for different curing times for the same casting densities. When the differences are ignored, the dry densities are only measured after 1 yr. The results are shown in Table 6.

A comparison of the data shown in Tables 5 and 6 shows that the A and C values are lower in Table 6 for the same mix constitutions, while the B values are higher. The degree of fit decreases for all mix constitution, although a high degree of fit is still ensured. Therefore, the assumption of $\rho^* = \rho^*_{365}$ is reasonable in order to simplify the model. At the same time, ρ^* can be simply calculated using (9) according to the "Technical specification for application of foamed concrete" (JGJT341-2014):

$$\rho^* = S_a(m_c + m_m) + m_s, \tag{9}$$

where S_a is an empirical constant for certain cement and admixture factories, m_c is the cement dosage of foamed concrete per cubic meter, m_m is the admixture dosage of foamed concrete per cubic meter, and m_s is the fine aggregate dosage of foamed concrete per cubic meter.

In this study, S_a equals to 1.211, 1.216, and 1.175 for the cement mix, cement-sand mix, and cement-fly ash mix, respectively. The values are very similar for the cement mix and the cement-sand mix. The value is slightly lower for the cement-fly ash mix because cement is a hydraulic binding material and fly ash is the active mineral admixture; the addition of fly ash reduces the value of S_a. Cement is the hydration reaction material in the cement-sand mix, and sand is the nonactive admixture; therefore, the S_a values are similar for the cement mix and the cement-sand mix. Combined with the other results, (9) can be used to calculate the dry density, in which S_a is an empirical constant for a given mix constitution and a given cement factory. When there are no measurements of dry density, the following equation can be used to predict the compressive strength of foamed concrete:

$$\sigma = A(\ln t)^B \left(\frac{S_a(m_c + m_m) + m_s}{\rho_s}\right)^C. \tag{10}$$

4. Conclusion

The following conclusions can be drawn based on the experimental and comparative results:

(1) The measured porosity is slightly lower than the theoretical porosity due to few inaccessible pores.

(2) The compressive strength increases with the increase in the ratio of dry density to solid density following the equation $A_1(\rho^*/\rho_s)^{B_1}$ for all three types of foamed concrete. The B_1 value is similar for the cement mix and the cement-fly ash mix. The value of B_1 is lowest for the cement-sand mix, followed by the cement mix and the cement-fly ash mix.

(3) The compressive strength increases with the curing time following the composite function $A_2(\ln t)^{B_2}$ for all three types of foamed concrete. The B_2 values are similar for the cement mix and cement-sand mix, but the B_2 value is lower for the cement-fly ash mix.

(4) Based on the results that the compressive strength changes with the porosity and the curing time, a prediction model taking into account the mix constitution, curing time, and porosity is proposed. A simple prediction model is put forward when no experimental data are available.

Conflicts of Interest

The authors declare that there are no conflicts of interest regarding the publication of this paper.

Acknowledgments

References

[1] C. Hu, H. Li, Z. Liu, and Q. Wang, "Research on properties of foamed concrete reinforced with small sized glazed hollow beads," *Advances in Materials Science and Engineering*, vol. 2016, Article ID 5820870, 8 pages, 2016.

[2] K. Ramamurthy, E. K. K. Nambiar, and G. I. S. Ranjani, "A classification of studies on properties of foam concrete," *Cement and Concrete Composites*, vol. 31, no. 6, pp. 388–396, 2009.

[3] Z. Liu, K. Zhao, C. Hu, and Y.-F. Tang, "Effect of water-cement ratio on pore structure and strength of foam concrete," *Advances in Materials Science and Engineering*, vol. 2016, Article ID 9520294, 9 pages, 2016.

[4] P. Onprom, K. Chaimoon, and R. Cheerarot, "Influence of bottom ash replacements as fine aggregate on the property of cellular concrete with various foam contents," *Advances in Materials Science and Engineering*, vol. 2015, Article ID 381704, 11 pages, 2015.

[5] Y. S. Jeong and H. K. Jung, "Thermal performance analysis of reinforced concrete floor structure with radiant floor heating system in apartment housing," *Advances in Materials Science and Engineering*, vol. 2015, Article ID 367632, 7 pages, 2015.

[6] M. Rößler and I. Odler, "Investigations on the relationship between porosity, structure and strength of hydrated Portland cement pastes I. Effect of porosity," *Cement and Concrete Research*, vol. 15, no. 2, pp. 320–330, 1985.

[7] I. Odler and M. Rößler, "Investigations on the relationship between porosity, structure and strength of hydrated Portland cement pastes. II. Effect of pore structure and of degree of hydration," *Cement and Concrete Research*, vol. 15, no. 3, pp. 401–410, 1985.

[8] M. Y. Balshin, "Relation of mechanical properties of powder metals and their porosity and the ultimate properties of porous metal-ceramic materials," *Doklady Akademii Nauk SSSR*, vol. 67, no. 5, pp. 831–834, 1949.

[9] A. Neville, *Properties of Concrete*, Wiley, New York, NY, USA, 1996.

[10] C. T. Tam, T. Y. Lim, R. Sri Ravindrarajah, and S. L. Lee, "Relationship between strength and volumetric composition of moist-cured cellular concrete," *Magazine of Concrete Research*, vol. 39, no. 138, pp. 12–18, 1987.

[11] J. M. Durack and L. Weiqing, "The properties of foamed air cured fly ash based concrete for masonry production," in *Proceedings of the Fifth Australasian Masonry Conference*, Gladstone, QLD, Australia, July 1998.

[12] E. K. K Nambiar and K. Ramamurthy, "Models for strength prediction of foam concrete," *Materials and Structures*, vol. 41, no. 2, pp. 247–254, 2008.

[13] G. C. Hoff, "Porosity-strength considerations for cellular concrete," *Cement and Concrete Research*, vol. 2, no. 1, pp. 91–100, 1972.

[14] E. P. Kearsley and P. J. Wainwright, "The effect of high fly ash content on the compressive strength of foamed concrete," *Cement and Concrete Research*, vol. 31, no. 1, pp. 105–112, 2001.

[15] A. A. Hilal, N. H. Thom, and A. R. Dawson, "On entrained pore size distribution of foamed concrete," *Construction and Building Materials*, vol. 75, pp. 227–233, 2015.

[16] Z. Pan, H. Li, and W. Liu, "Preparation and characterization of super low density foamed concrete from Portland cement and admixtures," *Construction and Building Materials*, vol. 72, pp. 256–261, 2014.

[17] G. Fagerlund, "Strength and porosity of concrete," in *Proceedings of the International Symposium on Pore Structure and Properties of Materials (RILEM/IUPAC)*, pp. 51–141, Prague, Czech Republic, September 1973.

[18] L. J. Gibson and M. F. Ashby, *Cellular Solids: Structure and Properties*, Cambridge University Press, Cambridge, UK, 1999.

[19] X. Tan, W. Chen, Y. Hao, and X. Wang, "Experimental study of ultralight (<300 kg/m^3) foamed concrete," *Advances in Materials Science and Engineering*, vol. 2014, Article ID 514759, 7 pages, 2014.

[20] B. Dolton and C. Hannah, "Cellular concrete: Engineering and technological advancement for construction in cold climates," in *Proceedings of the 2006 Annual General Conference of the Canadian Society for Civil Engineering*, Calgary, AB, Canada, May 2006.

[21] E. K. K. Nambiar and K. Ramamurthy, "Fresh state characteristics of foam concrete," *Journal of Materials in Civil Engineering*, vol. 20, no. 2, pp. 111–117, 2008.

[22] M. R. Jones, K. Ozlutas, and L. Zheng, "Stability and instability of foamed concrete," *Magazine of Concrete Research*, vol. 68, no. 11, pp. 542–549, 2016.

[23] E. K. K. Nambiar and K. Ramamurthy, "Sorption characteristics of foam concrete," *Cement and Concrete Research*, vol. 37, no. 9, pp. 1341–1347, 2007.

[24] K. Kurumisawa and K. Tanaka, "Three-dimensional visualization of pore structure in hardened cement paste by the gallium intrusion technique," *Cement and Concrete Research*, vol. 36, no. 2, pp. 330–336, 2006.

[25] T. H. Wee, S. B. Daneti, and T. Tamilselvan, "Effect of w/c ratio on air-void system of foamed concrete and their influence on mechanical properties," *Magazine of Concrete Research*, vol. 63, no. 8, pp. 583–595, 2011.

[26] E. Kuzielová, L. Pach, and M. Palou, "Effect of activated foaming agent on the foam concrete properties," *Construction and Building Materials*, vol. 125, pp. 998–1004, 2016.

[27] D. K. Panesar, "Cellular concrete properties and the effect of synthetic and protein foaming agents," *Construction and Building Materials*, vol. 44, pp. 575–584, 2013.

[28] W. H. Zhao, Q. Su, T. Liu, and J. J. Huang, "Experimental study on the frost resistance of cast-in-situ foamed concrete," *Electronic Journal of Geotechnical Engineering*, vol. 22, pp. 5509–5523, 2017.

[29] J. G. Cabrera and C. J. Lynsdale, "A new gas permeameter for measuring the permeability of mortar and concrete," *Magazine of Concrete Research*, vol. 40, no. 144, pp. 177–182, 1988.

[30] E. P. Kearsley and P. J. Wainwright, "The effect of porosity on the strength of foamed concrete," *Cement and Concrete Composites*, vol. 32, no. 2, pp. 233–239, 2002.

[31] H. F. W. Taylor, *Cement Chemistry*, Thomas Telford Ltd., London, UK, 1997.

[32] P. Hewlett, *Lea's Chemistry of Cement and Concrete*, Butterworth-Heinemann, Oxford, UK, 2003.

[33] E. K. K. Nambiar and K. Ramamurthy, "Models relating mixture composition to the density and strength of foam concrete using response surface methodology," *Cement and Concrete Composites*, vol. 28, no. 9, pp. 752–760, 2006.

[34] F. Batool and V. Bindiganavile, "Air-void size distribution of cement based foam and its effect on thermal conductivity," *Construction and Building Materials*, vol. 149, pp. 17–28, 2017.

[35] E. K. K. Nambiar and K. Ramamurthy, "Influence of filler type on the properties of foam concrete," *Cement and Concrete Composites*, vol. 28, no. 5, pp. 475–480, 2006.

Research Article

Numerical Prediction of Chloride Penetration in Concrete Exposed to a Marine Environment at Tide

Sung In Hong [ID] **and Ki Yong Ann** [ID]

Department of Civil and Environmental Engineering, Hanyang University, Ansan 15588, Republic of Korea

Correspondence should be addressed to Ki Yong Ann; kann@hanyang.ac.kr

Reinforced concrete structures under cyclic exposure to the corrosive environment such as the tidal zone as a part of marine structure entail the higher risk of steel corrosion. In this paper, chloride penetration in concrete exposed to the tidal zone was predicted using a combined moisture and chloride transport model. For the analysis of moisture transport, pore size distribution in concrete was determined from the experimental observation and used to determine the moisture permeability and degree of saturation. Then, the chloride profile through nonsaturated concrete cover was calculated by applying the moisture distribution along the penetration depth to the chloride convection and diffusion model. To assess sensitivity of the service life to the environment and concrete mix conditions, this study used three types of tide levels and water to cement ratios in the simulation. Under 10 years of tidal exposure condition, the minimum required cover depth at which the threshold chloride concentration reaches on the steel embedment increases only about 1.13 times as the tide level increases from the minimum to the highest while that for the w/c ratio increases about 1.69 times.

1. Introduction

The chloride-induced corrosion in RC structures especially exposed to marine environment has been regarded as a major problem in the aspect of structural safety. When a sufficient amount of chloride reaches on the steel surface in concrete, the passive film, maintained by high alkalinity of concrete pore solution, starts to dissolve and steel corrosion easily occurs [1]. After that, serial expansions of the corrosion products can cause concrete cracking from the location of steel embedment, thereby resulting in delineation of the concrete cover [2]. Thus, to assess the risk of chloride-induced corrosion and prevent the deterioration process during the life cycle of RC structures, a proper prediction model able to reflect the effects of material and environment actions on chloride ingress would be required.

Under the marine environment, the rate of chloride penetration in concrete largely depends on the exposure condition that changes with daily variation of the tide level [3]. Nevertheless, a number of studies for assessing the chloride ingress at the tidal zone with a single diffusion model have been carried out based on the assumption that the concrete pore network is fully saturated [3–6]. However, most of the concrete structures exposed to the tidal environment are in nonsaturated state, and the chloride transport is driven by both diffusion via concentration gradient through continuous pore water channel and convection via moisture movement through nonsaturated pores. In fact, as the exposure area becomes higher from the lowest tide level, chloride distribution in concrete becomes hard to be described with a single diffusion analysis since the moisture gradient in concrete simultaneously occurs during the repeated wet/dry cycles [7].

In the consideration of the transport mechanism in nonsaturated concrete, several prediction models have been developed [8–11]. Saetta et al. first suggested the S-shaped curve equation relating the chloride diffusivity with the moisture level to predict the chloride penetration under nonsaturated environment [8]. Based on this semiempirical expression of chloride diffusivity, the two-dimensional

numerical model for predicting temperature, relative humidity, and chloride transport in concrete was developed by Martin-Pérez et al. [9]. Nielsen and Geiker proposed the moisture dependent chloride diffusivity with a composite theory of the cement matrix to assess the chloride diffusion in nonsaturated state [10]. Recently, Sleiman et al. used the S-shaped curve relation of chloride diffusivity and moisture level to assess the effect of types of moisture adsorption isotherms on the ionic penetration in concrete [11]. However, moisture level at given humidity level largely changes with the concrete pore size distribution which also determines the moisture diffusivity as functions of humidity level and mix condition [12] and thus could affect the rate of chloride penetration in nonsaturated concrete.

The main topic in this study is to evaluate the dependences of tide level and the water to cement ratio on the chloride penetration using the combined moisture and chloride transport model. To implement the numerical calculation of the nonlinear transport behavior in the tidal zone, the finite element method (FEM) was adopted in solving the partial derivative equations with time-dependent boundary conditions. Moisture transport under the wet/dry cycles was modelled based on the statistical permeability theory to relate the pore size distribution in concrete to the moisture permeability. Then, chloride penetration in nonsaturated concrete can be predicted by applying the calculated spatial values of moisture transport to the chloride transport model.

2. Methodology

2.1. Moisture Transport. To predict the chloride transport in nonsaturated concrete, moisture distribution through the concrete depth was determined, considering the liquid and vapour transport which can be expressed as

$$\frac{\partial w}{\partial t} = \nabla \left(-K_l \nabla P_c + K_v \nabla P_v \right), \tag{1}$$

where w is the moisture content (kg/m^3), t is the time, K_l is the permeability of the liquid water (kg/m·s·Pa), P_c is the capillary pressure (Pa), K_v is the permeability of water vapour (kg/m·s·Pa), and P_v is the water vapour pressure (Pa). Assuming the thermodynamic equilibrium condition in concrete, it is possible to relate the pressure terms in (1) to the relative humidity (h) such that

$$\ln h = \ln \frac{P_v}{P_0} = -\frac{P_c M_w}{\rho_w RT}, \tag{2}$$

where P_0 is the saturation vapour pressure (Pa), ρ_w is the density of water (kg/m^3), R is the gas constant (J/kg·K), T is the temperature (K), and M_w is the water molecular weight (kg/mol). Thus, combining (1) and (2), moisture distribution in concrete in terms of relative humidity can be expressed as

$$\frac{\partial w}{\partial h} \cdot \frac{\partial h}{\partial t} = \nabla \left(K_l \frac{\rho_w RT}{M_w h} \nabla h + K_v P_0 \nabla h \right), \tag{3}$$

where $\partial w / \partial h$ is the moisture storage capacity (kg/m^3), denoting the slope of water vapour isotherms for adsorption and desorption.

As the humidity level increases, the liquid permeability (K_l) increases due to the increase in the water content in concrete, while the vapour permeability (K_v) decreases due to the decrease in the nonsaturated porosity. K_l was determined based on the statistical permeability model [13], considering the probabilistic effect of the variation of pore sizes on the moisture flow in the porous cement matrix such that

$$K_l = \frac{\rho_w \varnothing^2}{8\tau^2 \eta} \left(\int_0^{r_c} r f(r) dr \right)^2, \tag{4}$$

$$\tau = -1.5 \cdot \tanh \left[8.0 \left(\varnothing - 0.25 \right) \right] + 2.5, \tag{5}$$

$$f(r) = B \cdot \exp(-B \cdot r), \tag{6}$$

where $\varnothing$ is the porosity, τ is the tortuosity determined using a semiempirical model suggested by Nakarai et al. [14], η is the viscosity of liquid water (Pa·s), $f(r)$ is the normalized pore size distribution, B is the parameter of the Rayleigh–Ritz (R-R) density function, and r_c is the critical radius below which the pores are fully saturated (m), which can be expressed as

$$r_c = t_a + r_k, \tag{7}$$

where t_a is the thickness of water molecules on the pore wall (m) and r_k is the capillary condensation radius (m). t_a can be determined according to the BET model [15] such that

$$t_a = \frac{3 \times 10^{-10} \exp(855/T)}{(1-h)[1 + (\exp(855/T) - 1)h]}. \tag{8}$$

In the assumption of the cylindrical pore shape, r_k can be determined by using Kelvin's law such that

$$r_k = -\frac{\delta \gamma M_w}{\rho_w RT} \cdot \frac{1}{\ln h}, \tag{9}$$

where δ is the constant dependent on the curvature of liquid-vapour interface [12, 15] and γ is the surface tension of water (N/m). For the simplicity of the analysis, change in δ during the moisture adsorption and desorption was not considered and assumed to be unity.

Before capillary condensation, adsorption of water molecules occurs through the nonsaturated pores, and the rate depends on the vapour permeability that can be described with the Knudsen diffusion model such that

$$K_v = \frac{D_v(1-S)}{\tau [1 + l_m/2(r_m - t_a)]} \left(\frac{M_w}{RT} \right), \tag{10}$$

where S is the degree of saturation, l_m is the mean free path of the water molecule (m), r_m is the mean of pore radii over unsaturated pores (m) which was assume to be 2.5 μm equal to one-half of the maximum pore size, and D_v is the diffusion coefficient of water vapour in air (m^2/s), which was determined by taking into account the water vapour pressure and temperature differences [16] such that

$$D_{\mathrm{v}} = D_{\mathrm{ref}}\frac{P_{\mathrm{ref}}}{P_{\mathrm{v}}}\left(\frac{T}{T_{\mathrm{ref}}}\right)^{1.88}, \tag{11}$$

where D_{ref} is the water vapour diffusivity at reference values of pressure (P_{ref}) and temperature (T_{ref}) ($D_{\mathrm{ref}} = 21.6E - 6\,\mathrm{m}^2/\mathrm{s}$, $P_{\mathrm{ref}} = 11,325\,\mathrm{Pa}$, and $T_{\mathrm{ref}} = 273.16\,\mathrm{K}$). In this study, the moisture content resulting from the vapour adsorption in nonsaturated pores was excluded due to its marginal influence on the chloride transport. Thus, the degree of saturation at wetting (S_{w}) was determined based on the pore size distribution such that

$$S_{\mathrm{w}} = \int_0^{r_{\mathrm{c}}} f(r)dr. \tag{12}$$

When vapour desorption proceeds, partial water contents remain through ink-bottle pores. By taking into account a probability of interconnection between larger pores and smaller at the given humidity level [13], the degree of saturation at drying (S_{d}) can be determined as

$$S_{\mathrm{d}} = S_{\mathrm{w}}\left(1 - \ln\left(S_{\mathrm{w}}\right)\right). \tag{13}$$

When sea water contacts with the concrete surface, it was assumed that water vapour adsorption proceeds into the concrete cover, and the degree of saturation (S) was calculated with (12). When water vapour desorption proceeds from the inner concrete depth to the environment, the degree of saturation was calculated with (13).

2.2. Chloride Transport.

Under the nonsaturated condition, chloride transport in concrete is driven by both diffusion via concentration gradient and convection via moisture flux. Considering the chloride binding during the combined ionic penetration, the mass balance equation for the chloride transport can be expressed as

$$\left(\frac{\partial C_{\mathrm{b}}}{\partial C_{\mathrm{f}}} + S\varnothing\right)\frac{\partial C_{\mathrm{f}}}{\partial t} = \nabla\left(S\varnothing D_{\mathrm{e}}\nabla C_{\mathrm{f}}\right) + \nabla\left(S\varnothing C_{\mathrm{f}}D_{\mathrm{h}}\nabla h\right), \tag{14}$$

where C_{b} is the bound chloride concentration in concrete (kg/m^3), C_{f} is the free chloride concentration in pore solution (kg/m^3), D_{e} is the effective chloride diffusion coefficient (m^2/s), and D_{h} is the moisture diffusion coefficient (m^2/s) which accounts for the rate of combined liquid and vapour transport and can be obtained from (3) such that

$$D_{\mathrm{h}} = \left(K_{\mathrm{l}}\frac{\rho_{\mathrm{w}}RT}{M_{\mathrm{w}}h} + K_{\mathrm{v}}P_0\right)\frac{\partial h}{\partial w}. \tag{15}$$

The Langmuir isotherm was used to describe a nonlinear relationship between free and bound chlorides. The derivative formula of the relation indicates the chloride binding capacity [9], which can be expressed as

$$\frac{\partial C_{\mathrm{b}}}{\partial C_{\mathrm{f}}} = \frac{\alpha}{\left(1 + \beta C_{\mathrm{f}}\right)^2}, \tag{16}$$

where α and β are the binding parameters for the Langmuir isotherm.

TABLE 1: Boundary conditions for the moisture and chloride transport simulations.

Condition	Notation	Unit	Value
Wetting	h_{en}	—	0.995
	C_{en}	kg/m^3	17.75
Drying	h_{en}	—	0.7
	C_{en}	kg/m^3	0
Initial	H	—	0.995
	C_{f}	kg/m^3	0

2.3. Boundary Conditions.

To mimic a typical tidal environment, three types of exposure conditions to the concrete surface were considered as low, medium, and high tide levels, corresponding to 0.3, 0.5, and 0.7 days of daily drying time, respectively. Accordingly, daily wetting time for the chloride ingress decreases from 0.7 to 0.3 days with increasing the tide levels. To do this, moisture and chloride fluxes into or out of the concrete surface were simulated using the following boundary conditions [8]:

$$\begin{aligned}\vec{n}\cdot\left(D_{\mathrm{h}}\nabla h\right) &= B_{\mathrm{h}}\left(h_{\mathrm{s}} - h_{\mathrm{en}}\right),\\ \vec{n}\cdot\left(D_{\mathrm{e}}\nabla C_{\mathrm{f}}\right) &= nB_{\mathrm{c}}\left(C_{\mathrm{s}} - C_{\mathrm{en}}\right) + C_{\mathrm{en}}B_{\mathrm{h}}\left(h_{\mathrm{s}} - h_{\mathrm{en}}\right),\end{aligned} \tag{17}$$

where $\vec{n}$ is the outward unit normal at the boundary, B_{h} and B_{c} are the mass transfer coefficients, respectively, for the relative humidity and chloride (m/s), h_{s} and C_{s} are the relative humidity and free chloride concentration at concrete surface, h_{en} and C_{en} are the relative humidity and free chloride concentration at environment, and n is the environment factor, accounting for 1 during wetting and 0 during drying. Other values for the boundary condition are given in Table 1.

2.4. Input Parameters.

To investigate the effects of the mix condition on the chloride penetration in nonsaturated concrete, 0.4, 0.5, and 0.6 of the water to cement ratio (w/c) were considered by using each porosity and pore size distribution, which were determined based on the mercury intrusion porosimetry (MIP). For the MIP test, mortar specimens with 0.4, 0.5, and 0.6 of w/c and 2.15 of the sand to cement ratio were fabricated using ordinary Portland cement (OPC). After water curing at $20 \pm 1°$C for 56 days, the samples were dried in an oven for 3 days to remove the inside pore solution. Then, mercury intrusion was implemented on the treated samples under a constant contact angle ($130°$). Mercury pressure was gradually increased up to 228 MPa, which then converted into the pore size distribution by using Washburn's equation. With the cumulative porosity data obtained from the MIP, B in (6) was determined with a nonlinear curve fitting method to the data. As for the effective chloride diffusivity, the values for 0.4, 0.5, and 0.6 of w/c were assumed to be 3.9, 7.8, and $12.6E - 12\,\mathrm{m}^2/\mathrm{s}$ [17] which were then used in the chloride transport simulation. Other input parameters were assumed to be irrespective of w/c and are given in Table 2.

TABLE 2: Input parameters for the moisture and chloride transport simulations.

Property	Notation	Unit	Value
Moisture equilibria at 20°C	P_0	Pa	2333.4
	ρ_w	kg/m^3	994.6
	η	Pa·s	0.001
	l_m	m	$1E-7$
	γ	N/m	0.0728
	M_w	kg/mol	0.018
Chloride binding	α	—	1.15
	β	—	0.28
Surface transfer	B_h	m/s	$4.05E-7$
	B_c	m/s	$1.0E-6$
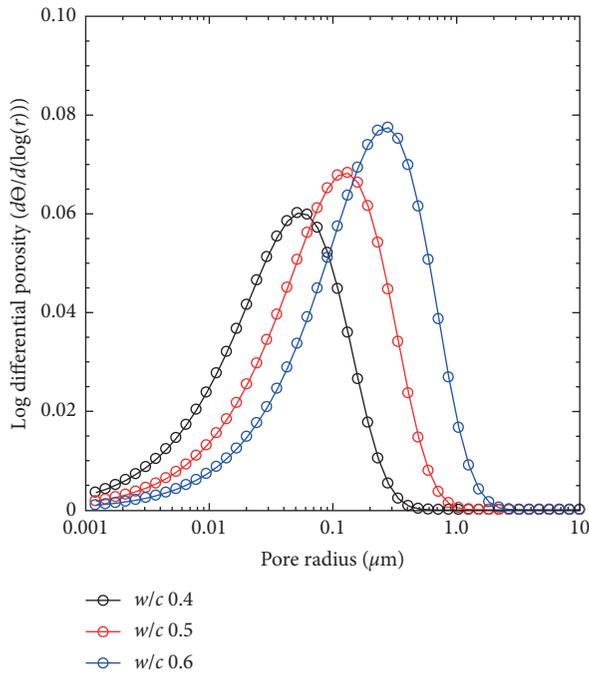
FIGURE 1: Pore size distributions with variation of water to cement ratios.

3. Result and Discussion

3.1. Pore Size Distribution.

For the analysis of the combined moisture and chloride transport in concrete, pore size distribution depending on w/c was determined by regression analysis to the MIP data with R-R density function given in (6). As shown in Figure 1, the pore radius at maximum porosity increment increases with w/c, accounting for 0.051, 0.115, and 0.244 μm, respectively, for 0.4, 0.5, and 0.6 of w/c. In addition, porosity also increases with w/c, accounting for 0.16, 0.18, and 0.21. These observations indicate that the higher surplus of mixing water increases the portion of large capillary pores and water-filled porosity when concrete is saturated.

Based on the calculated pore size distribution, moisture adsorption and desorption isotherms can be determined using (12) and (13). As shown in Figure 2, the degree of saturation increases nonlinearly with the relative humidity,
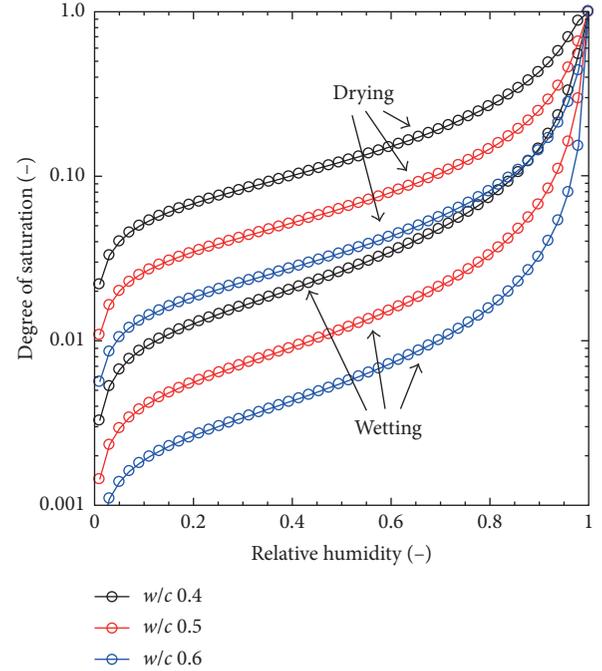
FIGURE 2: Moisture adsorption and desorption isotherms with variation of water to cement ratios.

and the difference in moisture level between wetting and drying always occurs due to the moisture entrapment through the ink-bottle pores. However, at given humidity level, degree of saturation decreases with w/c since the lower w/c leads to the higher portion of small capillary pores. This can imply that the higher the w/c is, the higher the amount of water content can be adsorbed during wetting or desorbed during drying.

3.2. Transport under Tidal Environment.

To solve the nonlinear partial differential equations for the moisture and chloride transport, MATLAB PDE toolbox was used for the FEM analysis. Numerical calculation with convergence criteria (i.e., below 10^{-4}) was carried out on a two-dimensional rectangle domain with 4820 of the triangle mesh and 0.1 days of time step. Then, one-dimensional spatial values were obtained by interpolating the two-dimensional simulation results through a straight line from the concrete surface contacted with the ambient condition to the interior of material.

Due to the fluctuation of sea level in the tidal zone, moisture and chloride are transported into or out of the concrete surface to distort the concentration distributions with time. When the exposure condition changes from wetting to drying in the medium tide level, corresponding distributions of the moisture and chloride in concrete with 0.5 of w/c were calculated and depicted in Figure 3. As shown in Figure 3, the chloride profile at the end of wetting shows a steep increment in the concentration observed from the concrete surface to about 4 mm of depth below which the cover is nearly saturated. However, the chloride profile at the end of drying shows lower concentration increment up to
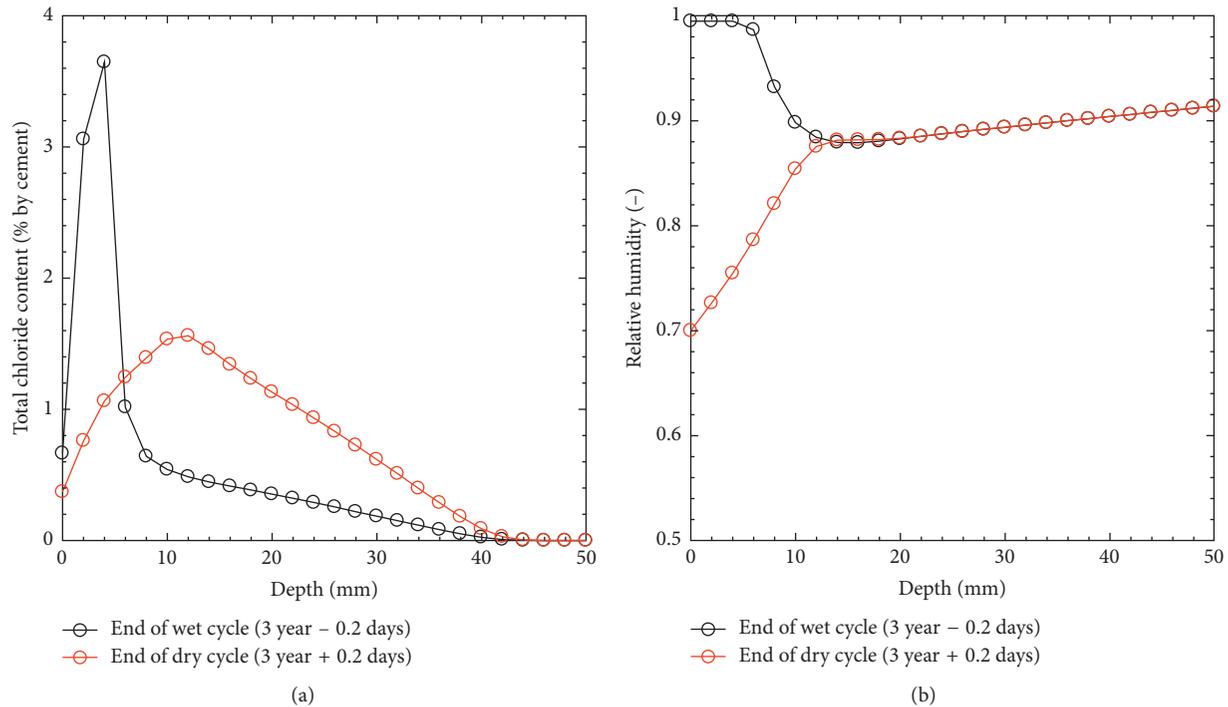
FIGURE 3: Change in concentration distributions of (a) chloride and (b) relative humidity during one cycle of drying process.

about 12 mm of depth below which moisture evaporation toward the concrete surface locally reduces the moisture content. Hence, the maximum chloride concentration accumulated near the concrete surface due to the wet/dry cycles is generated in the convection zone where the moisture intake during wetting and loss during drying repeatedly occur [18]. As shown in Figure 3(b), the convection zone ranges from the concrete surface to about 12 mm. However, over the convection zone, the chloride concentration generally decreases with the penetration depth and the variation of moisture level is relatively low. Thus, the convection zone occurs through the concrete depth up to the position at the peak value of the concentration generated after one cycle of drying. Simultaneously, the diffusion zone occurs from the end of the convection zone to inner concrete depth where the chloride transport is mostly governed by diffusion rather than convection [19]. Moreover, as shown in Figure 3(a), the chloride profile redistributed during drying always maintains higher concentration through the inner concrete depth since the higher concentration gradient in the convection zone generated during wetting could accelerate the ionic penetration into the diffusion zone during drying.

To investigate the influences of the tide level and mix condition on the chloride penetration in concrete, three types of daily drying time and w/c were reflected in the moisture and chloride profiles, respectively, as given in Figures 4 and 5. In these cases, 0.5 of w/c was used as a mix condition for the simulation in Figure 4, and the medium tide level was used as a boundary condition for the simulation in Figure 5.

As shown in Figure 4(a), the chloride profiles at the tidal zone show lower concentrations at the surface, accounting

for 0.27–0.44% by cement which is about two times less than that for the submerged zone due to the diffusion into the sea water with lower concentration. However, the maximum concentrations accumulated at the interface between convection and diffusion zones exceed the surface concentration obtained in the submerged condition by about 1.3–2.5 times through 1–10 years, increasing with the tide level and exposure time. Specially, as the tide level increases, the concentration at 50 mm for 10 years increases from 0.45 to 0.74% by cement, which could lead to the higher risk of chloride-induced corrosion [20] as compared to that for the submerged condition. As shown in Figure 4(b), the maximum chloride concentration at the interface is shown to increase with the moisture evaporation rate from the inner concrete depth to the surface which is higher as the tide level increases. As the moisture evaporation rate increases at the same exposure time, more chloride sources can be accumulated at the interface due to the increase in nonsaturated porosity during drying [21] which can enhance the convective flow in concrete to draw out the chloride concentration in the diffusion zone to the convection zone at a higher rate. Consequently, chloride penetration in concrete is accelerated as tide level increases to elevate the concentration gradient toward the inner depth, despite little variation of water content through the diffusion zone.

As shown in Figure 5(a), chloride transport is highly dependent on w/c, revealing that as w/c increases, chloride concentration at the interface and the overall rate of ionic penetration increase at the same exposure time. For example, the maximum penetration depth for 0.4 of w/c increases from about 16 to 30 mm from 1 to 3 years while that for 0.6 of w/c increases from about 34 to over 50 mm for the
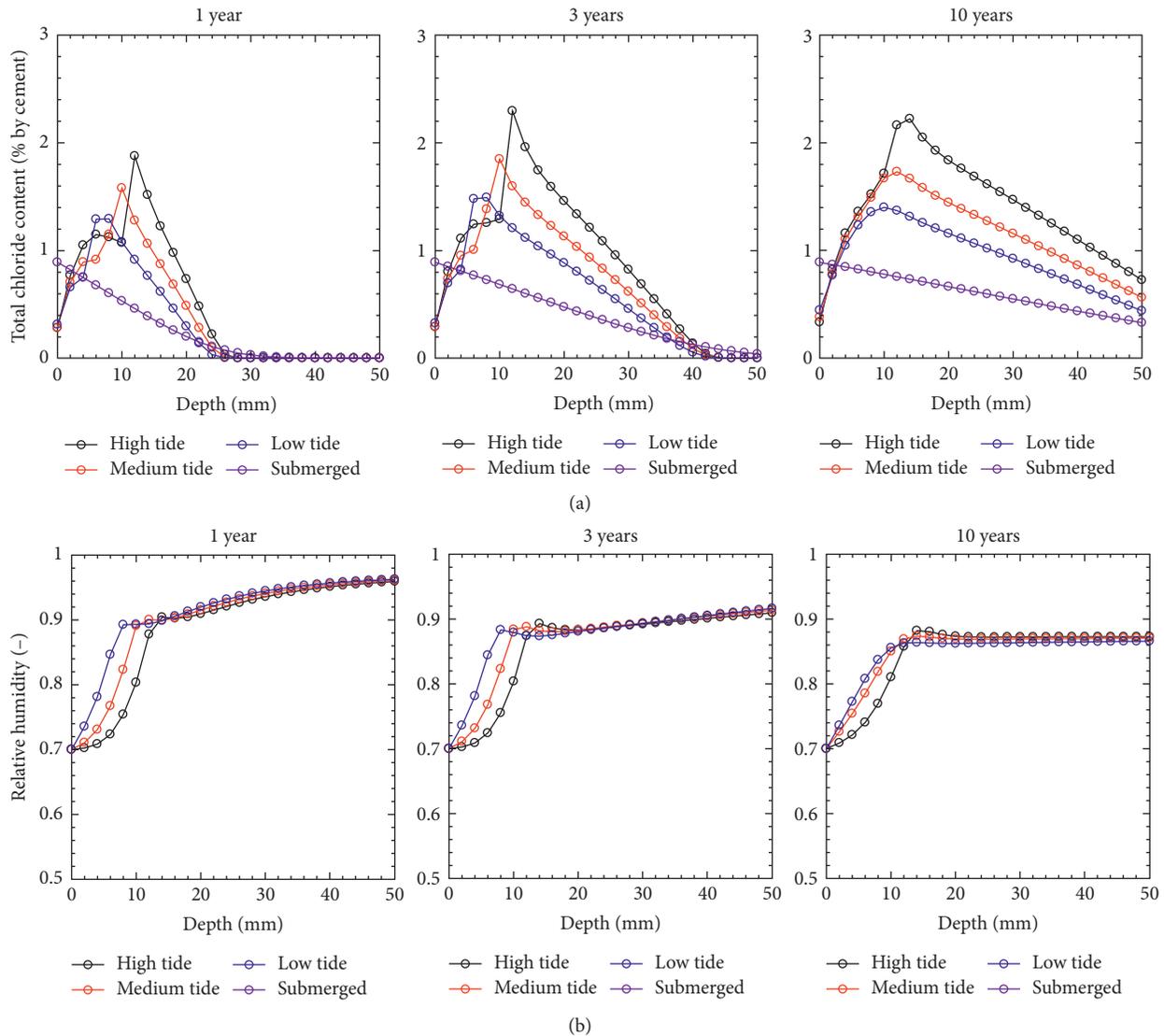
FIGURE 4: Concentration distributions of (a) chloride and (b) relative humidity depending on tide level at 0.5 of the water to cement ratio.

same period. In general, the higher w/c leads to the higher pore connectivity to decrease the tortuosity for the pathway of mass transfer in concrete [22]. According to (5), the tortuosity for 0.4, 0.5, and 0.6 of w/c was calculated to be 3.9, 3.2, and 2.9, respectively. Therefore, the increased moisture permeability arose from the decreased tortuosity could promote both the moisture permeation during wetting to allow more chloride source into the concrete and moisture evaporation during drying to enhance the concentration buildup at the interface. Simultaneously, the fraction of large capillary pores generally increases with w/c, as indicated in Figure 1, which can also elevate the ionic diffusion rate [23] due to the large increase in the water-filled porosity through inner concrete depth. As shown in Figure 5(b), moisture level over the diffusion zone for 0.6 of w/c is always higher than that for 0.4 of w/c, implying that the higher rate of chloride diffusion due to the increased water filled porosity as well as the effective chloride diffusivity could enhance the overall ionic penetration in nonsaturated concrete.

3.3. Service Life Assessment. To relate the influential factors (i.e., tide level and w/c) to the service life of RC structures built in tidal environment, the maximum chloride concentration at the interface, which largely depends on those factors, was calculated and is depicted in Figure 6. Then, by relating the maximum concentration to the onset of chloride-induced corrosion, sensitivity analysis for designing the minimum required cover depth was carried out on those factors, which are depicted in Figure 7. In this case, the steel corrosion in concrete was assumed to initiate at which the chloride threshold level (CTL) reaches the steel embedded depth (i.e., cover depth). For the CTL, 0.4% by cement as a total chloride content [24] was used to all the simulations since a large variation in the value, depending on the detection method and chloride exposure condition, has been reported [20].

As shown in Figure 6, all the maximum chloride concentrations were determined at drying with 10 days of increments since more chloride sources penetrate into the
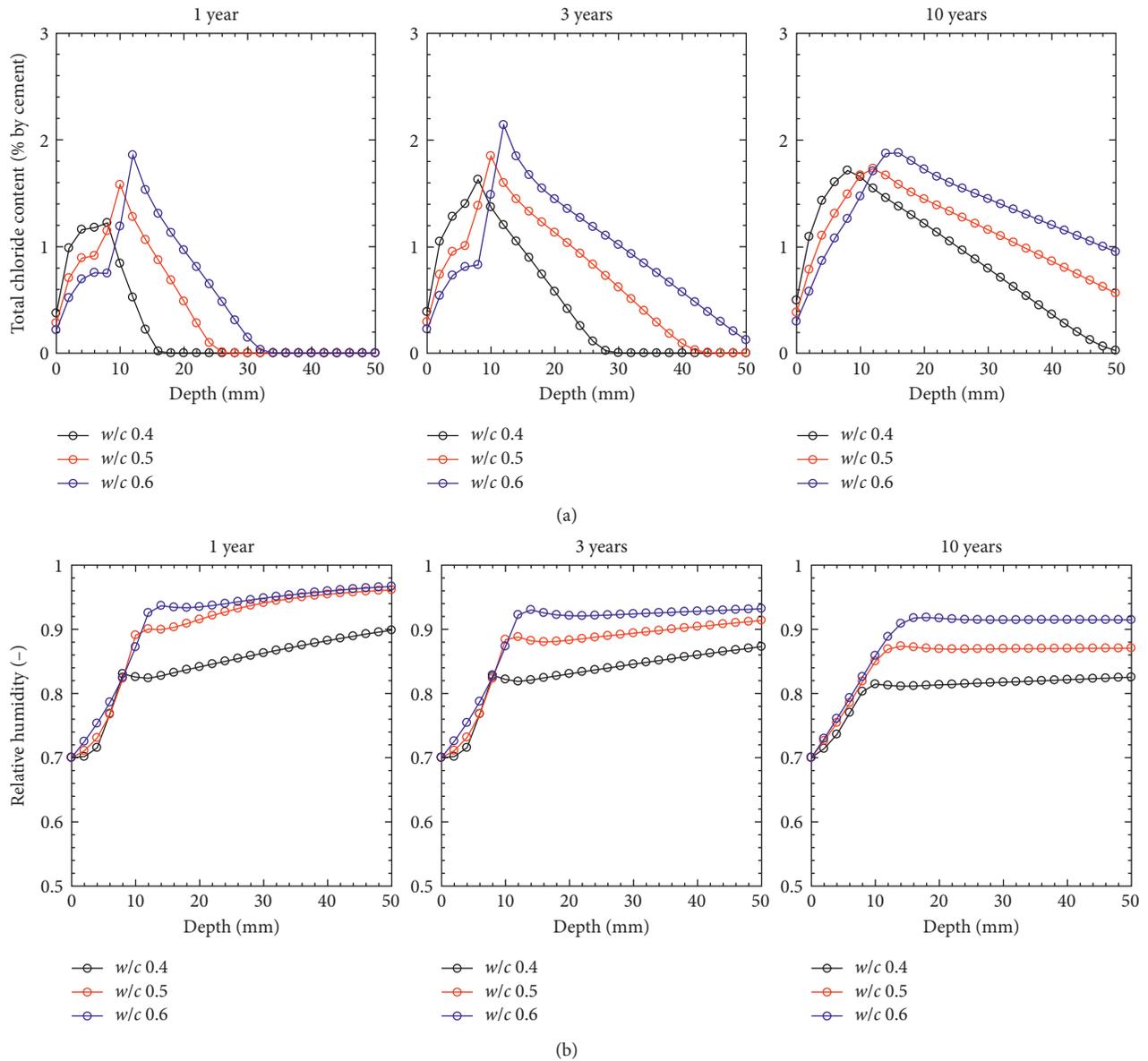
Figure 5: Concentration distributions of (a) chloride and (b) relative humidity depending on mix condition at medium tide level.

inner concrete depth after one cycle of wetting, as indicated in Figure 3(a). As shown in Figure 6(a), chloride concentrations at the interface are distinctively increased with tide level at the same exposure time while in Figure 6(b), the concentration evolution depending on w/c is less significant. For example, at 10 years of exposure time, the concentration from the low to high tide increases from 1.6 to 2.3% by cement, while that from the 0.4 to 0.6 of w/c only increases from 1.8 to 2.1% by cement. Hence, the convective chloride transport is more significant as the tide level increases than the variation of w/c.

As shown in Figure 7, the minimum required cover depth, defined as the depth with the CTL (i.e., 0.4% by cement), generally increases with the maximum chloride concentration through all the factors. However, the increasing rate of cover depth highly depends on the maximum concentration at the interface. Before reaching about 1.2–1.8% by cement, the cover depth in Figure 7(a) increases proportionally with the concentration and then increases notably while the transient increase in the cover depth in Figure 7(b) starts to occur at about 1.4–1.6% by cement. The chloride concentration at the transient increase of the cover depth would be the one at which the chloride buildup at the interface becomes marginal with time, generally observed over 1–2 years in Figure 6. Thus, it can be inferred that after a certain amount of chloride accumulate at the interface, chloride diffusion would control the overall transport rate due to the large concentration gradient, which are more sensitive to w/c than tide level. In fact, as shown in Figure 7(b), the required cover depth for 10 years exposure to the medium tide level increases from 41.3 to 71.8 mm as w/c increases from 0.4 to 0.6, while at the same time and mix condition (i.e., 0.5 w/c), the increment in the

(a)

(b)
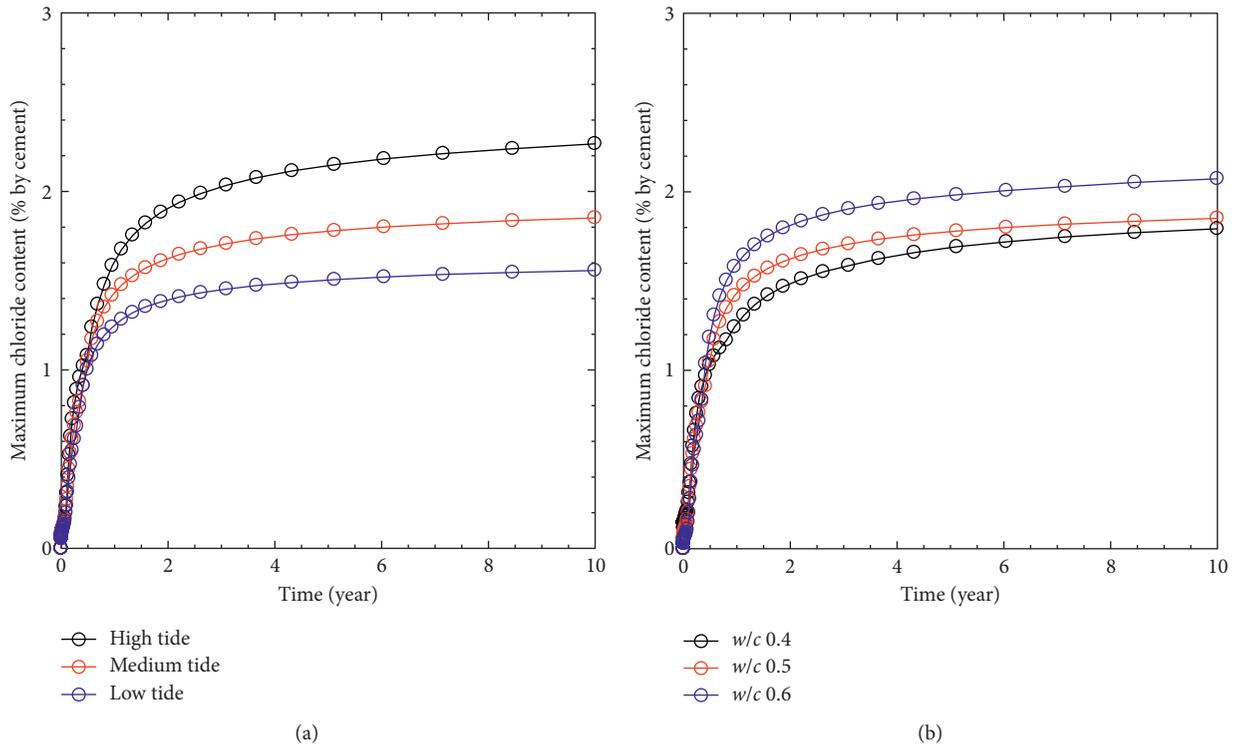
Figure 6: Concentration buildup at the interface between convection and diffusion zones depending on (a) tide level and (b) water to cement ratio.

(a)

(b)
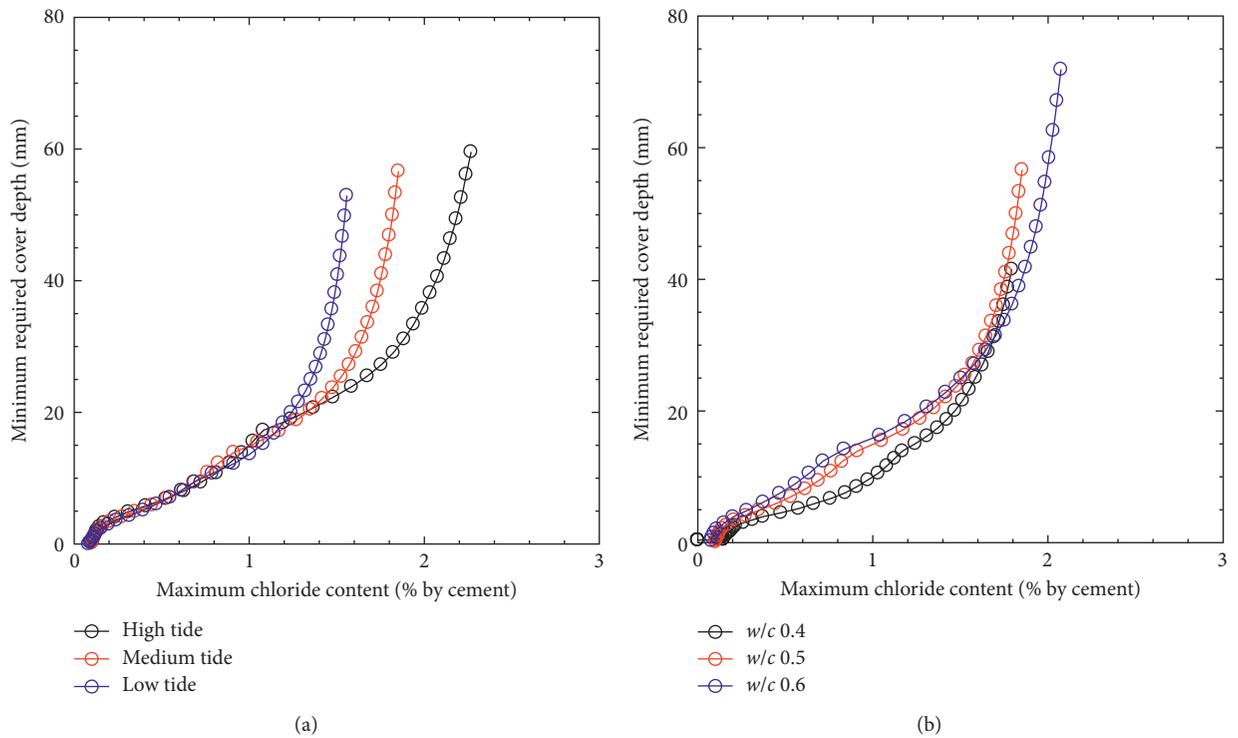
Figure 7: Minimum required cover depth against chloride-induced corrosion depending on (a) tide level and (b) water to cement ratio.

cover depth in Figure 7(a) shows a little variation from 52.9 to 59.6 mm with the tide level. Hence, to enhance the durability of RC structures built in the tidal environment, lowering w/c is primarily recommended otherwise regular maintenance, for example, using the technique of electrochemical chloride removal [25], to reduce the chloride content accumulated at the interface may be essential.

4. Conclusion

The present study aims to assess the service life of concrete structures exposed to the tidal zone with the proposed numerical model for predicting the moisture and chloride transport in concrete. As the influential factors of the service life, three types of daily wet/dry durations in the tidal zone and water to cement ratios in concrete mix were considered in the simulation. From the result, the following conclusion was drawn:

(1) Pore size distribution, obtained by fitting the R-R density function to the cumulative porosity data in the MIP, was used to determine the moisture permeability and degree of saturation in nonsaturated concrete. Based on the pore size distribution, it was found that the higher w/c in concrete mix leads to the higher portion of large capillary pores and the lower degree of saturation at given humidity level.

(2) Moisture and chloride distribution in concrete with variations of the tide level and w/c was calculated over 10 years of exposure period. As the tide level increases, the moisture evaporation rate toward the concrete surface increases to promote the chloride buildup at the interface between convection and diffusion zones and increases the rate of chloride penetration into the concrete cover at the same exposure time. Similarly, as w/c increases, the maximum chloride concentration at the interface increases and simultaneously the rate of diffusion increases due to the higher effective chloride diffusivity and water-filled porosity, thereby increasing the ionic penetration depth at the same exposure time.

(3) Sensitivity analysis of the service life to the tide level and w/c was carried out on the calculated chloride profiles over 10 years of exposure time. As a result, the required cover depth at which the CTL reaches on the steel embedment generally increases with the maximum concentration at the interface while the rate of increase in the cover depth with concentration is much higher when the w/c increases from the lowest to the highest, as compared with those for the tide level.

Conflicts of Interest

The authors declare that they have no conflicts of interest.

Acknowledgments

References

[1] C. L. Page, "Mechanism of corrosion protection in reinforced concrete marine structures," *Nature*, vol. 258, no. 5535, pp. 514-515, 1975.

[2] A. M. Neville, *Properties of Concrete*, Longman Group, London, UK, 4th edition, 1995.

[3] H.-W. Song, C.-H. Lee, and K. Y. Ann, "Factors influencing chloride transport in concrete structures exposed to marine environments," *Cement and Concrete Composites*, vol. 30, no. 2, pp. 113–121, 2008.

[4] M. D. A. Thomas and P. B. Bamforth, "Modelling chloride diffusion in concrete: effect of fly ash and slag," *Cement and Concrete Research*, vol. 29, no. 4, pp. 487–495, 1999.

[5] S.-W. Pack, M.-S. Jung, H.-W. Song, S.-H. Kim, and K. Y. Ann, "Prediction of time dependent chloride transport in concrete structures exposed to a marine environment," *Cement and Concrete Research*, vol. 40, no. 2, pp. 302–312, 2010.

[6] M. K. Moradllo, M. Shekarchi, and M. Hoseini, "Time-dependent performance of concrete surface coatings in tidal zone of marine environment," *Construction and Building Materials*, vol. 30, pp. 198–205, 2012.

[7] A. Da Costa, M. Fenaux, J. Fernández, E. Sánchez, and A. Moragues, "Modelling of chloride penetration into non-saturated concrete: case study application for real marine offshore structures," *Construction and Building Materials*, vol. 43, pp. 217–224, 2013.

[8] A. V. Saetta, R. V. Scotta, and R. V. Vitaliani, "Analysis of chloride diffusion into partially saturated concrete," *Materials Journal*, vol. 90, no. 5, pp. 441–451, 1993.

[9] B. Martin-Pérez, S. Pantazopoulou, and M. Thomas, "Numerical solution of mass transport equations in concrete structures," *Computers and Structures*, vol. 79, no. 13, pp. 1251–1264, 2001.

[10] E. P. Nielsen and M. R. Geiker, "Chloride diffusion in partially saturated cementitious material," *Cement and Concrete Research*, vol. 33, no. 1, pp. 133–138, 2003.

[11] H. Sleiman, O. Amiri, A. Ait-Mokhtar, and J.-M. Loche, "Chloride transport through unsaturated concrete: chloride profile simulations and experimental validation," *Magazine of Concrete Research*, vol. 64, no. 4, pp. 351–359, 2012.

[12] Q. Huang, Z. Jiang, X. Gu, W. Zhang, and B. Guo, "Numerical simulation of moisture transport in concrete based on a pore size distribution model," *Cement and Concrete Research*, vol. 67, pp. 31–43, 2015.

[13] R. Chaube, T. Kishi, and K. Maekawa, *Modelling of Concrete Performance: Hydration, Microstructure and Mass Transport*, CRC Press, New York, NY, USA, 2005.

[14] K. Nakarai, T. Ishida, and K. Maekawa, "Multi-scale physicochemical modeling of soil-cementitious material interaction," *Soils and Foundations*, vol. 46, no. 5, pp. 653–663, 2006.

[15] H. Ranaivomanana, J. Verdier, A. Sellier, and X. Bourbon, "Toward a better comprehension and modeling of hysteresis cycles in the water sorption–desorption process for cement based materials," *Cement and Concrete Research*, vol. 41, no. 8, pp. 817–827, 2011.

[16] D. Quenard and H. Sallee, "Water vapour adsorption and transfer in cement-based materials: a network simulation," *Materials and Structures*, vol. 25, no. 9, pp. 515–522, 1992.

[17] V. Ngala, C. Page, L. J. Parrott, and S. Yu, "Diffusion in cementitious materials: II, further investigations of chloride and oxygen diffusion in well-cured OPC and OPC/30% PFA pastes," *Cement and Concrete Research*, vol. 25, no. 4, pp. 819–826, 1995.

[18] K. Li, C. Li, and Z. Chen, "Influential depth of moisture transport in concrete subject to drying–wetting cycles," *Cement and Concrete Composites*, vol. 31, no. 10, pp. 693–698, 2009.

[19] C. Andrade, M. Climent, and G. de Vera, "Procedure for calculating the chloride diffusion coefficient and surface concentration from a profile having a maximum beyond the concrete surface," *Materials and Structures*, vol. 48, no. 4, pp. 863–869, 2015.

[20] K. Y. Ann and H.-W. Song, "Chloride threshold level for corrosion of steel in concrete," *Corrosion Science*, vol. 49, no. 11, pp. 4113–4133, 2007.

[21] H. Chang, S. Mu, D. Xie, and P. Wang, "Influence of pore structure and moisture distribution on chloride "maximum phenomenon" in surface layer of specimens exposed to cyclic drying-wetting condition," *Construction and Building Materials*, vol. 131, pp. 16–30, 2017.

[22] L. Liu, W. Sun, G. Ye, H. Chen, and Z. Qian, "Estimation of the ionic diffusivity of virtual cement paste by random walk algorithm," *Construction and Building Materials*, vol. 28, no. 1, pp. 405–413, 2012.

[23] N. Olsson, V. Baroghel-Bouny, L.-O. Nilsson, and M. Thiery, "Non-saturated ion diffusion in concrete–a new approach to evaluate conductivity measurements," *Cement and Concrete Composites*, vol. 40, pp. 40–47, 2013.

[24] British Standard, *Structural Use of Concrete: Code of Practice for design and Construction, BS 8110*, British Standard Institute, London, UK, 1985.

[25] Y. Wang, L. Li, and C. Page, "A two-dimensional model of electrochemical chloride removal from concrete," *Computational Materials Science*, vol. 20, no. 2, pp. 196–212, 2001.

Research Article

Electric Resistance Tests on Compacted Clay Material under Dynamic Load Coupled with Dry-Wet Cycling

Zheng Lu [ID],[1] Xiaowen Wu,[1,2] Zhi Hu,[2] Shaohua Xian,[1] and Ran Fang[1]

[1]*State Key Laboratory of Geomechanics and Geotechnical Engineering, Institute of Rock and Soil Mechanics,*
Chinese Academy of Sciences, Wuhan 430071, China
[2]*School of Civil Engineering, Architecture and Environment, Hubei University of Technology, Wuhan 430068, China*

Correspondence should be addressed to Zheng Lu; lzwhrsm@163.com

The study of compacted clay material under dynamic load coupled with dry-wet cycling is one of the most important areas in the field of transportation. In this paper, experiments in terms of compacted clay under dynamic load coupled with dry-wet cycling are performed, and synchronous resistivity tests are also conducted. According to the test results, the influences of cumulative plastic strain, dry-wet cycles, and amplitudes on the soil resistivity are analyzed. Then a new damage factor based on resistivity is proposed to evaluate the long-term performance of compacted clay material. The result of research shows that the evolution of the soil resistivity can be divided into two stages, which has a contrary tendency with that of cumulative plastic strain. The dry-wet cycles and amplitudes have a significant effect on the damage of the compacted soil, which indicates that the dry-wet cycling of compacted soil materials should not be ignored in road engineering, especially in rainy and humid areas.

1. Introduction

Roadways and railways commonly consist of upper pavement or ballast layers (track slab) over one or more silty clay layers which are together compacted over a suitable soil subgrade. As it is well known, compacted clay material provides the most important structural element in the road system because, in most cases, the cumulative deformation phenomenon takes place mainly in the subgrade layer causing progressive fatigue cracking of upper road layers [1–3]. So, it is essential to control the long-term performance of the subgrade so as to carry traffic safely, conveniently, and economically during its entire lifespan. However, the subgrade suffers from the humidity change and variation of temperature for a long term; besides, the cyclic traffic loads and other climate also bring adverse effects on it. Therefore, it is of great significance to study the long-term performance and damage laws of compacted clay material under the comprehensive effect of dynamic load and dry-wet cycling.

The damage of compacted soil is usually accompanied by the change of soil structure, and the electric resistance can reflect the feature of the composition of soil particles and pore structure well. Thus, resistivity can be used in the study of soil structure change and structural damage [4]. Archie [5] first studied the relationship between soil resistivity and its structure and proposed the soil structural factor-resistivity structure factor F (formation resistivity factor). Then, he established the exponential function relation between resistivity structure factor and sandy soil porosity. Miao et al. [6, 7] investigated the resistivity characteristic of cement-stabilized soil; the relationship between soil resistivity and unconfined compressive strength, cement mixing ratio, and age were obtained. Fukue and Liu et al. [8–10] developed a geotechnical resistivity test system and established the resistivity model of expansive soil and soft soil structure, and they put forward an average apparent structure factor concept for this type of soil. Subsequently, Lin et al. [11] conducted indoor experiments on the resistivity of loess, on the basis of which the influence of contact pressure, temperature, and measurement frequency on resistivity was studied and the variation rule of the resistivity of loess was analyzed. However, the literature on

TABLE 1: Material properties of the compacted clay.

Natural water content (%)	Natural density (g/cm^3)	Saturated water content (%)	Plastic limit (%)	Liquid limit (%)	Specific gravity	Maximum dry density (g/cm^3)	Optimum water content (%)	Permeability (cm/s)
23.7	1.68	23.8	21.1	34.8	2.72	1.90	14.1	6.5e-7

TABLE 2: Testing program of dynamic load coupled with dry-wet cycling.

Parameters	Values
Initial water content (%)	14.1
Number of drying-wetting cycles	0, 2, 4, 9
Amplitude of drying-wetting cycles (±%)	0, 2, 4, 6
Initial static deviatoric stress (kPa)	20
Confining pressure (kPa)	40
Amplitude of dynamic stress (kPa)	40
Loading frequency (Hz)	5
Number of loading cycles	10^5

electric resistance tests on compacted clay material under dynamic load coupled with dry-wet cycling is rarely published. Therefore, experiments of dynamic load coupled with dry-wet cycling are performed in this paper, and the synchronous resistivity tests on compacted clay material are conducted at the same time. According to the experimental results, the evolution of resistivity with cumulative plastic strain, dry-wet cycles, and amplitudes is analyzed, and then, a damage factor based on resistivity is proposed to evaluate the long-term performance of compacted clay material. The study can provide a reference for the damage assessment of the compacted subgrade soil under complex environment and traffic loads.

2. Experimental Procedures

The experimental clay material was taken from Sanmenxia along the Zhengxi Passenger Railway in China. The main material characteristics are listed in Table 1. All the test samples are reshaped in a cylinder-shaped sampler of 76 mm in height and 38 mm in diameter. The samples are compacted to an initial dry density of 1.81 g/cm^3 to meet the compaction requirement's degree of the specification [12].

In order to simulate the actual service condition of the road subgrade under traffic loads and climate changes, dynamic triaxial tests are conducted on the samples subjected to different dry-wet cycles and amplitudes. Aimed at simulating the field stress state of subgrade soil, the bias consolidation of the soil samples is carried out under a certain confining pressure for 15 hours before starting the triaxial tests. The experimental scheme for the dynamic load coupled with dry-wet cycling is designed and shown in Table 2. In fact, the testing program shown in Table 2 is designed according to the practical road subgrades subjected to traffic loads and climate changes. It is reported that the mechanical properties of compacted clay soil could finally tend to stabilize after 8~10 dry-wet cycles. Thus, the maximum number of drying-wetting cycles is fixed at 9 in this research. Moreover, in terms of clay soil material, the maximum water

content of subgrades under climate changes is usually no more than OWC + 6% (here, OWC means the optimum water content of subgrades). The maximum amplitude of drying-wetting cycles is fixed at 6% in the experiment.

For the purpose of describing the damage state of compacted clay material under dynamic load coupled with dry-wet cycling, the soil sample resistivity is tested simultaneously with the dynamic triaxial test in this paper. According to the principle of measurement, the resistivity test method can be divided into the dipole method and the quadrupole method [13], and the two kind of measuring devices are shown in Figure 1. The quadrupole method provides a certain voltage through a type AB electrode, the resistance of soil sample can be obtained by the means of measuring the voltage of MN electrode and the current in the pathway, and then the soil sample resistivity will be obtained through the resistivity calculation formula. The dipole method is a special case that the electrode MN is shared with the electrode AB in the quadrupole method. When using the dipole method, the contact resistance will be greater because of the poor contact with the electrode and the soil sample; therefore, contact resistance size should be determined before the formal test [14]. The quadrupole method has the advantages of not considering the contact resistance compared to the dipole method, but the measuring electrode usually needs to be inserted into the soil sample. Thus, it is not suitable for the measurement of resistivity for which soil sample integrity requirements are high. For this purpose, the dynamic triaxial apparatus is upgraded and modified to satisfy the synchronous test requirements of dynamic characteristics and resistivity of the samples, as shown in Figure 2. In terms of the soil sample integrity, circuit installation, and operability of instrument, the dipole method is adopted to measure the soil sample resistivity in this paper. The resistivity is collected by WDJD-4 multifunctional digital DC exciter, as shown in Figure 3.

It is noted that temperature can affect the soil resistivity significantly; thus, the measured resistivity needs to be corrected. In this paper, the resistivity tests are firstly carried out at different temperatures to derive the temperature correction curve, as shown in Figure 4. In order to eliminate the effect of temperature, the resistivity of the soil sample in the standard state is adopted uniformly in the following analysis. According to the test results, the relationship between the resistivity of the standard state and the measured resistivity can be described by using the following formula:

$$\rho_{25} = \rho_{T}[1 + \alpha(T - 25)], \tag{1}$$

where ρ_{25} and ρ_{T} are the soil sample resistivity of the standard state (25°C) and the measured temperature, T (°C), respectively. T is the experimental temperature, α is the
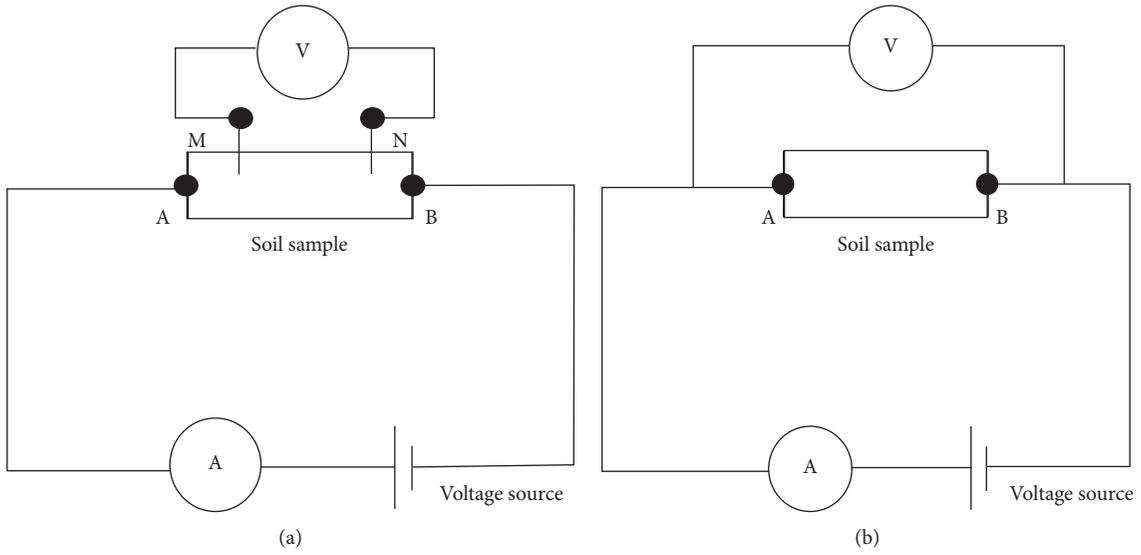
FIGURE 1: Resistivity test method for the soil samples: (a) the quadrupole method and (b) the dipole method.
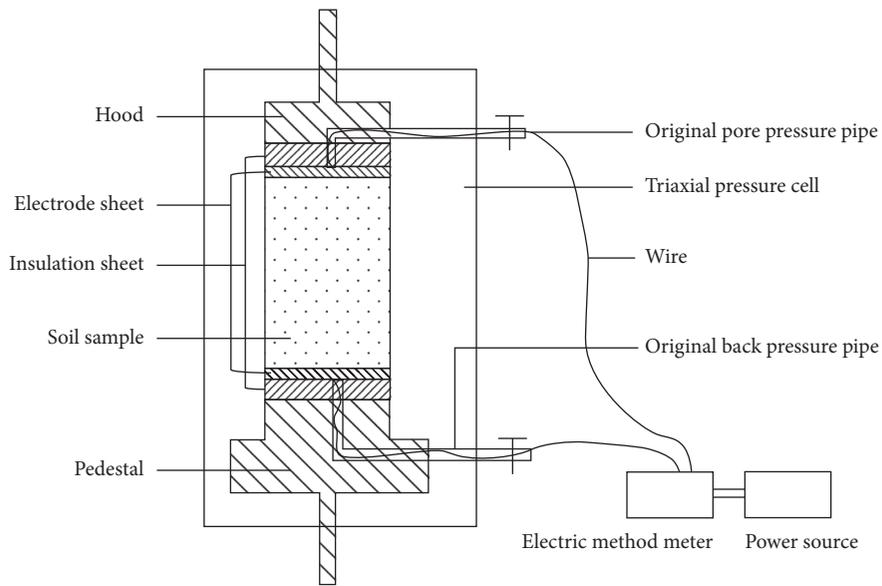
FIGURE 2: Schematic diagram of the soil sample resistivity test on the dynamic triaxial apparatus.

FIGURE 3: Soil resistivity acquisition instrument.
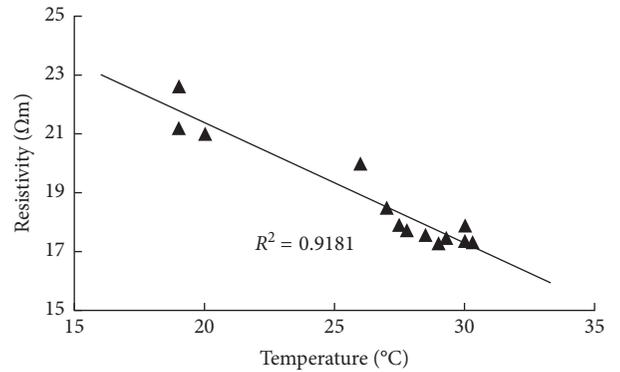
FIGURE 4: Temperature correction curve for soil sample resistivity.
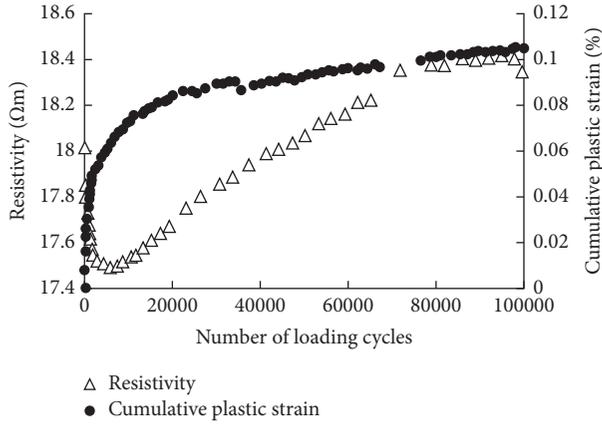
FIGURE 5: Variations of the soil sample resistivity and cumulative plastic strain with the number of loading cycles.
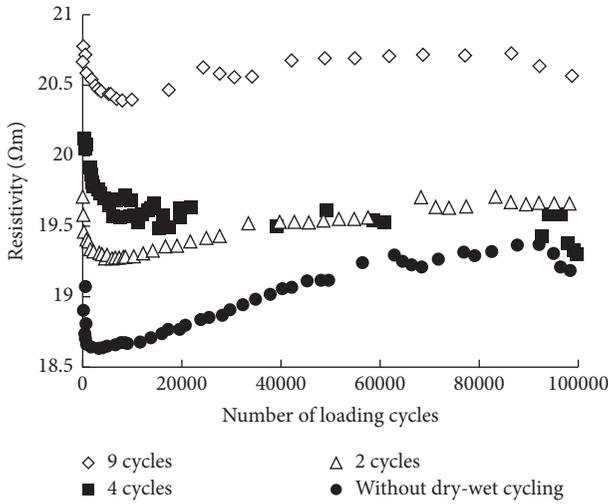
FIGURE 6: Effect of dry-wet cycles on the soil sample resistivity.

temperature correction coefficient, and $\alpha = 0.0207°C^{-1}$ in this paper based on the test results.

The measured resistivity is calculated by the following equation:

$$\rho_T = \frac{\left(\Delta U - \Delta U_{sp}\right)S}{IL}, \tag{2}$$

where ΔU is the voltage between the two electrodes, ΔU_{sp} is the initial potential difference, I is the current value of the soil sample, and S and L are the surface area and height of the soil sample, respectively.

3. Results and Discussion

Figure 5 shows the variations of the soil sample resistivity and cumulative plastic strain with the number of loading cycles. It can be seen from Figure 5 that the evolution of the resistivity can be divided into two stages. The first stage is the early stage of cyclic loading: the cumulative plastic strain of soil sample increases rapidly and the resistivity decreases greatly. With the growth of the accumulative plastic strain,
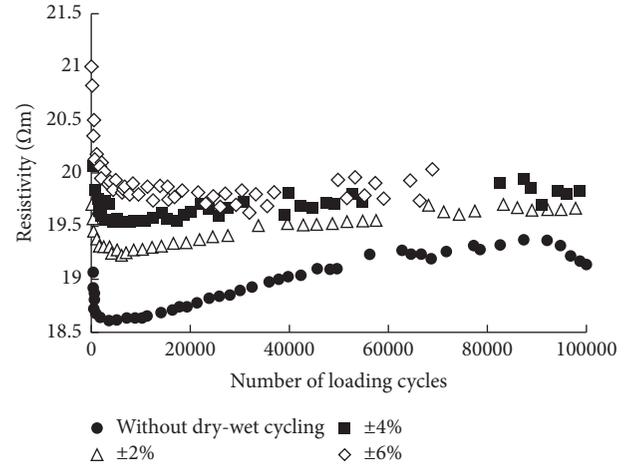
FIGURE 7: Effect of dry-wet cycling amplitudes on the soil sample resistivity.

the soil sample resistivity further reduces and then reaches the minimum value at a certain number of loading cycles. The second stage is the late cyclic loading: the growth rate of the accumulative plastic strain continues to decrease, and the values of accumulative plastic strain gradually stabilize. However, the soil sample resistivity increases inversely with the increasing loading cycles. At the first stage, the native micropores and microfractures of the soil sample gradually close because of the initial loadings, which causes larger soil compactness and better interconnectedness of pore water, thus leading to the increase of conductive passage in the soil sample [6]. When the resistivity reaches the minimum, the repair of the internal defect of the soil sample reaches its limit. At the second stage, the resistivity of the soil sample increases inversely, which indicates that the cyclic load causes new micropores or microcracks. The above results show that the resistivity can reflect the damage state and the process of damage evolution of the soil sample.

Figure 6 presents the variations of the soil sample resistivity with the number of loading cycles for different dry-wet cycles. It can be seen that the soil sample resistivity decreases initially, increases with the increasing number of loading cycles, and finally tends to stabilize, which are consistent with the rule of Figure 5. It also can be observed from Figure 6 that the soil sample resistivity increases gradually with the increasing dry-wet cycles, which indicates that the repeated dry-wet cycling can cause internal damage of the soil sample, thus leading to the density decrease. The effects of the dry-wet cycling amplitude on the soil sample resistivity are investigated in Figure 7. It can be seen from Figure 7 that the soil sample resistivity increases with the increase of the dry-wet cycling amplitude. This indicates that the different dry-wet cycling amplitudes can also cause internal damage and reduce compactness of the clay soil and thus results in a strength decreasing, which is consistent with those results obtained by Liu et al. [15, 16]. Therefore, the resistivity can be used to determine the strength of compacted soil materials indirectly, and then the internal damage of the subgrade under complex environment and
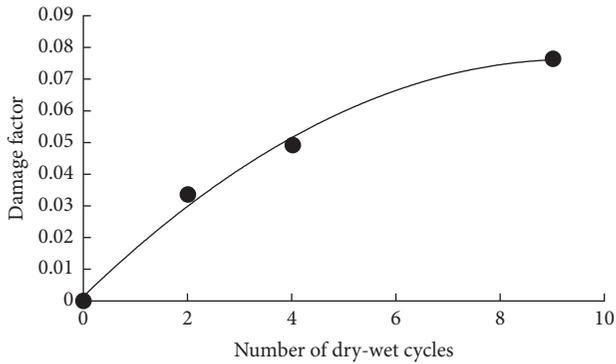
Figure 8: Variation of damage factor with the dry-wet cycles.
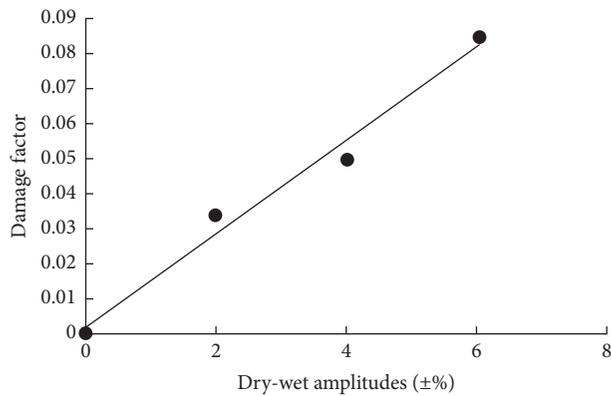
Figure 9: Variation of damage factor with the dry-wet amplitudes.

load can also be evaluated by adopting the resistivity measuring method.

In order to evaluate the damage property of compacted clay soil materials quantitatively using the resistivity measuring method, a damage factor based on resistivity is defined by the following equation:

$$D_\rho = 1 - \frac{\rho_0}{\rho}, \tag{3}$$

where D_ρ is the soil damage factor based on resistivity. Here, D_ρ is defined as a parameter to indicate the soil degradation. The bigger the parameter, the more serious the damage is. ρ_0 is the resistivity of the nondestructive soil sample. Here, the samples not experiencing the dynamic load coupled with dry-wet cycling are considered as nondestructive soil. ρ is the resistivity of the damage soil.

According to the above definition, the resistivity of the nondestructive soil sample can be measured, $\rho_0 = 19.07$ Ωm in this paper. By employing (3), the damage characteristics of compacted soil materials under the dynamic load coupled with dry-wet cycling can be evaluated and analyzed. The measured sample resistivity increases with the increasing number and amplitude of drying-wetting cycles, but no more than 20.95 Ωm in this paper. Therefore, the values of the damage factor defined in (3) vary from 0 to 0.1, as far as Sanmenxia clay material is concerned. The variations in the damage factor of compacted soil with the dry-wet cycles and amplitudes are presented in Figures 8 and 9, respectively. As

can be seen from Figure 8 that when there is a small number of dry-wet cycles, the damage factor increases dramatically with increasing dry-wet cycles. However, when the number of dry-wet cycles exceeds 4, the effect of the dry-wet cycles on the damage factor becomes relatively slight. This indicates that the long-term performance of compacted soil will tend to be stable after a certain number of dry-wet cycles. It can be observed from Figure 9 that the damage factor increases almost linearly with the increase of the dry-wet amplitudes. This result reveals that the dry-wet amplitudes have a significant effect on the damage of the compacted soil. The dry-wet cycling of compacted soil materials should not be ignored in road engineering, especially in rainy and humid areas.

4. Conclusions

In this paper, a series of experiments of dynamic load coupled with dry-wet cycling are performed, and the synchronous resistivity tests on compacted clay material are conducted. The influences of cumulative plastic strain, dry-wet cycles, and amplitudes on the soil resistivity are analyzed. Furthermore, a new damage factor based on resistivity is proposed to evaluate the long-term performance of compacted clay material. The main conclusions of this study can be summarized as follows:

(1) The evolution of the soil resistivity can be divided into two stages. The first stage is the early stage of cyclic loading: the cumulative plastic strain of soil sample increases rapidly and the resistivity decreases greatly. The second stage is the late cyclic loading: the soil sample resistivity increases inversely with the increasing loading cycles. It shows that the resistivity can reflect the damage state and the process of damage evolution of compacted clay material.

(2) The repeated dry-wet cycling can cause internal damage of the soil sample, thus leading to the density decrease. Therefore, the resistivity can be used to determine the strength of compacted soil materials indirectly, and then the internal damage of the subgrade under complex environment and load can also be evaluated by adopting the resistivity measuring method.

(3) The dry-wet cycles and amplitudes have a significant effect on the damage of the compacted soil, which indicates that the dry-wet cycling of compacted soil materials should not be ignored in road engineering, especially in rainy and humid areas.

Conflicts of Interest

The authors declare that they have no conflicts of interest.

Acknowledgments

References

[1] N. D. Beskou and D. D. Theodorakopoulos, "Dynamic effects of moving loads on road pavements: a review," *Soil Dynamics and Earthquake Engineering*, vol. 31, no. 4, pp. 547–567, 2011.

[2] A. Gomes Correia and J. Cunha, "Analysis of nonlinear soil modelling in the subgrade and rail track responses under HST," *Transportation Geotechnics*, vol. 1, no. 4, pp. 147–156, 2014.

[3] Z. Lu, H. Yao, J. Liu, and Z. Hu, "Experimental evaluation and theoretical analysis of multi-layered road cumulative deformation under dynamic loads," *Road Materials and Pavements Design*, vol. 15, no. 1, pp. 35–54, 2014.

[4] H. E. Stewart, "Permanent strains from cyclic variable-amplitude loadings," *Journal of Geotechnical Engineering*, vol. 112, no. 6, pp. 646–660, 1986.

[5] G. E. Archie, "The electrical resistivity log as an aid in determining some reservoir characteristics," *Transactions of the AIME*, vol. 146, no. 1, pp. 54–62, 1942.

[6] L. Miao, S. Liu, M. Yan et al., "Research on resistivity characteristics of water soil," *Engineering Survey*, vol. 5, pp. 32–34, 2000.

[7] S. Jie, L. Shucai, L. Bin, X. Xinji, W. Chuanwu, and N. Lichao, "Quantitative evaluation method of unsaturated soil compaction based on resistivity characteristics," *Journal of Chang'an University: Natural Science Edition*, vol. 35, no. 6, pp. 33–41, 2015.

[8] M. Fukue, T. Minato, H. Horibe, and N. Taya, "The microstructures of clay given by resistivity measurements," *Engineering Geology*, vol. 54, no. 1-2, pp. 43–53, 1999.

[9] S. Liu, S. Zhan, and X. J. Yu, "Research on the resistivity of soil test," *Journal of Engineering Geology*, vol. 14, no. 2, pp. 216–222, 2006.

[10] S. Chunni, F. Xiang, W. Hewen, S. Shuguo, and G. Jianfeng, "The influence of suction, moisture content and dry density on the shear strength of unsaturated soil," *Rock and Soil Mechanics*, vol. 30, no. 5, pp. 1347–1351, 2009.

[11] W. Lin hao, B. Xiaohong, and F. Junqin, "Discussion on the influencing factors of the shear strength index of compacted loess soil," *Journal of Geotechnical Engineering*, vol. 32, no. S2, pp. 132–135, 2010.

[12] Ministry of Communications of the China, *JTG D30–2015, Specifications for Design of Highway Subgrades*, China Communication Press, Beijing, China, 2015.

[13] L. Miao, S. Liu, M. Yan et al., "Resistivity characteristics of water clay and its engineering application," *Journal of Rock Mechanics and Engineering*, vol. 20, no. 1, pp. 126–130, 2001.

[14] X. Yu, *Research on the Application of Soil Mechanics of Resistivity Structure Model*, Southeast University, Nanjing, China, 2004.

[15] S. Liu, L. Han, and Y. Du, "The resistivity characteristics and application of water soil," *Journal of Geotechnical Engineering*, vol. 28, no. 11, pp. 1921–1926, 2006.

[16] Z. Liu, Y. Zhang, W. Fang et al., "Research on the relationship between the resistivity of loess and its compaction characteristics," *Journal of Xi'an University of Science and Technology*, vol. 33, no. 1, pp. 84–90, 2013.

Research Article

Corrosion Risk of Reinforced Concrete Structure Arising from Internal and External Chloride

M. J. Kim and K. Y. Ann [ID]

Department of Civil and Environmental Engineering, Hanyang University, Ansan 426, Republic of Korea

Correspondence should be addressed to K. Y. Ann; kann@hanyang.ac.kr

The corrosion risk of internal chloride and external chloride from three different exposure conditions was evaluated. The initiation of corrosion was detected by monitoring the galvanic current between cathode metal and embedded steel. The chloride threshold was determined by measuring the corrosion rate of steel by the polarization technique for internal chloride and the chloride profiling test for external chloride. As the result, the initiation of corrosion was accelerated with a cyclic wet/dry condition, compared to the totally wet condition. In addition, it was found that an increase of the drying ratio in the exposure condition resulted in an increase of corrosion rate after initiation. The threshold level of external chloride ranged from 0.2 to 0.3% weight by cement and internal chloride shows higher range, equated to 1.59–3.10%. Based on these data, the chloride penetration with exposure condition was predicted to determine the service life of reinforced concrete structure.

1. Introduction

There is a general agreement that embedded steel in concrete forms a passive film on the surface and protects the steel against corrosion. The passive film is preserved by high alkalinity in concrete; however, breakdown of passive film occurs when the concentration of chloride at the vicinity of steel exceeds the chloride threshold level (CTL) [1]. Owing to this problem, various studies have been carried out to predict chloride transport according to exposure conditions because precise prediction of chloride transport leads to an enhancement of the accuracy of life cycle prediction. The determination of the CTL is another crucial factor influencing on the service life prediction [2]. It is known that the CTL changes with various conditions, such as chloride source, exposure condition, and mixing materials; however, the CTL used in service life prediction is conservative, accounting for 0.2–0.4% by weight of cements [3, 4]. The main reason for this may be attributed to the absence of exact test methods for defining the CTL, of which the complexity moreover depends on the test methods. In previous studies, due to the convenience of experiment and time-saving,

several experiments were conducted to determine the CTL with the steel directly immersed in solution [5, 6] or with admixed chloride [7–9]. In the case of the solution test, the results show that the corrosion of steel initiated in a small amount of chloride, which seems to be unrealistic in that it did not consider the corrosion resistance of concrete. For the chloride admixed test, the CTL varied from 0.1 to 1.0% by weight of the binder; however, it could not fully cover the real condition of reinforced concrete structure exposed to chloride environment. Experiments with external chloride were also conducted with long-time immersed specimens, but considering diverse exposure condition is deficient [10–12]. Hence, it is necessary to define the CTL depending on the chloride sources and consequently to evaluate the corrosion risk of reinforced concrete structure.

The present study discussed about the corrosion risk and CTL for both internal chloride and external chloride. The influence of internal chloride was evaluated by measuring the corrosion current density for 100 days by the polarization technique. For external chloride, the initiation of corrosion with three different exposure conditions was detected by monitoring the galvanic current, and then, the chloride

penetration rate was evaluated to determine the CTL. Subsequently, the CTL was applied to the service life prediction to evaluate the corrosion resistance of the structure.

2. Experimental Work

In this paper, corrosion initiation induced by internal chloride and external chloride was evaluated. For the experiments, mortar specimens were made to reduce the size while considering the influence of the aggregate in the corrosion process. The mix proportion was $1.00 : 4.00 : 2.46$ for ordinary Portland cement, deionized water, and sand (maximum size was 15 mm). The experimental details for both internal/external chloride specimens and corrosion measuring method are stated as follows.

2.1. Chloride Admixed Specimens.

Six levels of chloride were admixed in mixing water as NaCl: 0.2, 0.5, 1.0, 1.5, 2.0, and 3.0% by weight of cement. The mortar specimens were cast in a cylinder mould ($\varnothing 40 \times 80$ mm) with a smooth steel rebar ($\varnothing 10 \times 80$ mm) placed in the center of the specimen. In the process of demoulding, the cement paste (0.25 of w/c ratio) was covered on the end of the steel bars to ensure the protection of corrosion at the exposed part. After then, an epoxy resin was coated at the top and bottom so that ions and current can pass only through the sides. To achieve enough hydration degree and high relative humidity in a pore matrix, the specimens were cured for 28 days in a controlled chamber at $25 \pm 1°C$ and $95 \pm 2\%$ relative humidity. This curing condition was equally applied to external chloride specimens. After 28 days of curing, the corrosion current density of embedded steel was monitored by the polarization technique.

2.2. Immersed Specimens.

Profile specimens and corrosion test specimens were prepared separately to detect the corrosion initiation of steel and determine the CTL. The same cylindrical mortar specimens ($\varnothing 40 \times 80$ mm) containing a smooth steel rebar ($\varnothing 10 \times 80$ mm) were fabricated for corrosion measurement, without any admixed chloride. For the chloride profile test, a mortar disc ($\varnothing 100 \times 50$ mm) was cast and coated, immediately after demoulding, by epoxy resin except the top of the specimen to drive one-dimensional chloride transport. All the specimens were cured in a chamber for 28 days and then exposed to the chloride. Considering the tidal environment, it was classified into three types of exposure condition, that is, 2 days of wetting (immersed)/8 days of drying (to which will be referred as 2w/8d), 5 days of wetting/5 days of drying (5w/5d), and totally immersed (10w). At the immersion stage, the specimens were kept in 1 M NaCl solution at $25 \pm 2°C$ of ambient temperature and stored in a chamber under the dry condition ($25 \pm 1°C$ and 30% related humidity). The galvanic current of the embedded steel was measured every 10 days to observe the corrosion initiation.

2.3. Chloride Profile.

The chloride profile was obtained from the dust samples collected by grinding the mortar surface in 5.0 mm depth increments to 30.0 mm. The free chloride in each sample was extracted by stirring for 5 minutes in a 50°C of deionized water and measured by chloride ion-selective electrode manufactured from Orion™. To determine the surface chloride concentration and diffusion coefficient, the measured chloride concentration data were used to solve Fick's second law of diffusion. Fick's second law in a semi-infinite space is represented as follows:

$$\frac{C(x, t)}{C_s} = \text{erf}\left[\frac{x}{2\sqrt{Dt}}\right], \tag{1}$$

where $C(x, t)$ is the chloride concentration at depth x after time t (s), C_s is the surface chloride concentration ($\%/m^3$), D is the apparent diffusion coefficient (m^2/s), x is the depth from the surface (m), and t is the time of exposure (s). To determine the CTL of immersed specimens, the profile data were obtained at the time when the corrosion initiation was detected by the galvanic current test.

2.4. Corrosion Measurement.

The corrosion initiation was detected by measuring the current flow between the embedded steel and cathode metal (titanium mesh). The specimens were placed with a cylindrical titanium mesh in 1 M sodium hydroxide solution (Figure 1(a)). Although galvanic current measurements did not reveal the quantitative corrosion rate, it is possible to deduce the time of corrosion initiation through the time when the current increases sharply. The galvanic current was determined by calculating the measured potential difference across 10 kΩ resistor, using Ohm's law.

Linear polarization resistance (LPR) measurement was conducted to observe the corrosion current of steel. The schematic diagram of the electrical circuit of the polarization technique is shown in Figure 1(b). The mortar specimen was immersed in 1 M sodium hydroxide solution, and two electrodes (counter and reference electrodes) were arranged and connected with the instrument in the solution. The standard saturated calomel electrode (SCE) and carbon electrode were used as the reference electrode and counter electrode, respectively. Reference 600 from Gamry Instrument was used as the potentiostat. The LPR measurements were performed by applying a potential signal ranged from ± 20 mV about E_{corr} at 0.2 mV/s of the scan rate and measuring the current response. Then, the corrosion current was calculated by the equation as follows:

$$R_p = \frac{\Delta E}{\Delta I},$$

$$I_{corr} = \frac{B}{R_p}, \tag{2}$$

where R_p is the polarization resistance (Ω), ΔE is the change in potential (V), ΔI is the change in current (A), I_{corr} is the corrosion current (A), and B is the Stern–Geary constant. The Stern–Geary constant should be determined empirically; however, it was generally assumed to be 26 mV for active and 52 mV for passive state of steel [13]. I_{corr} was converted to the corrosion rate to surface area of the steel rebar.

(a)

(b)
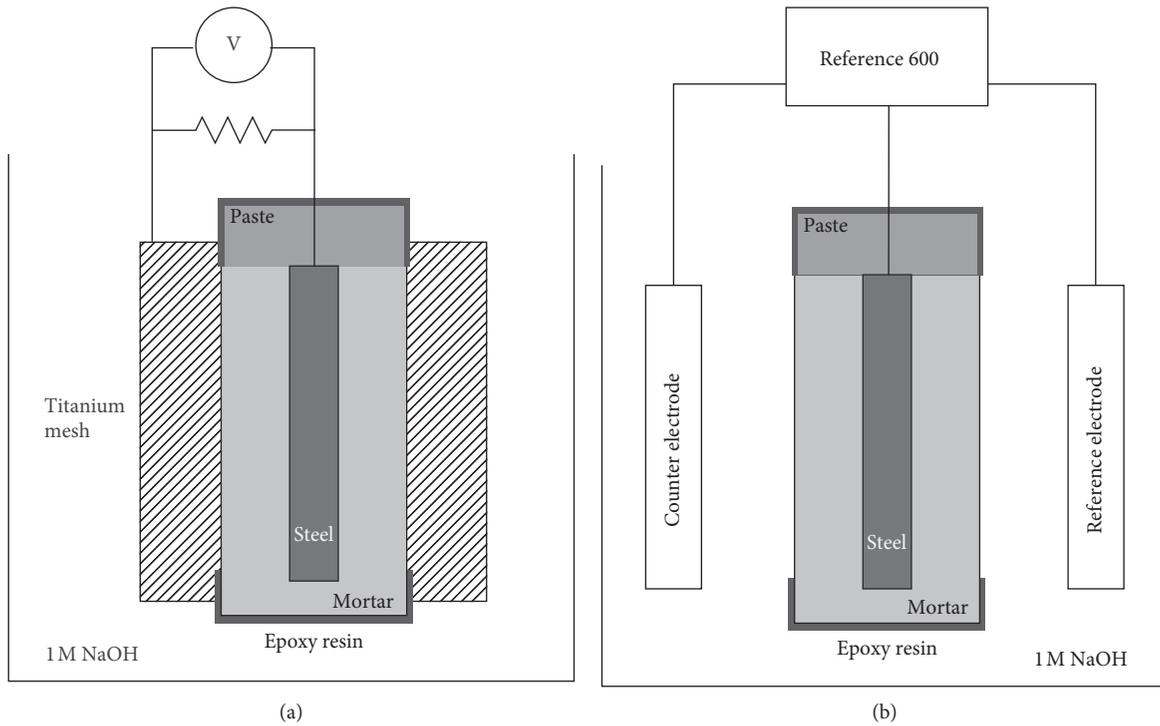
FIGURE 1: Schematic of the experimental setup of (a) galvanic cell monitoring and (b) LPR measurement.
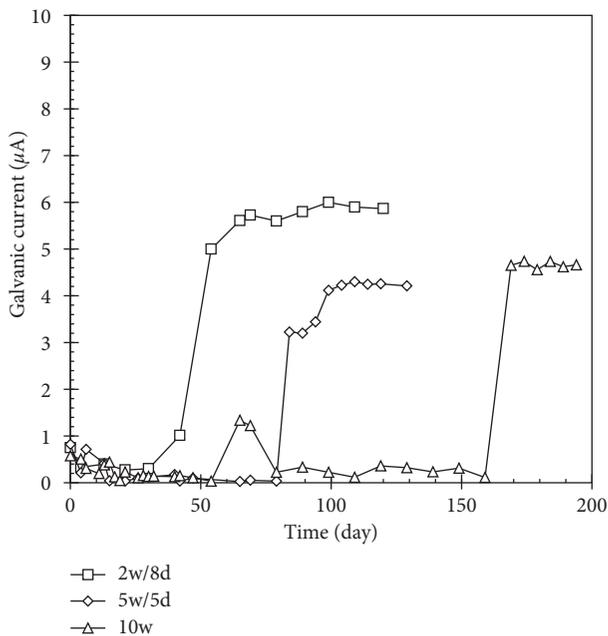
FIGURE 2: Galvanic current monitoring with different wet time proportions.

3. Result and Discussion

3.1. Corrosion Initiation. The corrosion initiation of steel in mortar, exposed to different exposure conditions, was determined by monitoring the galvanic current, as shown in Figure 2. At the beginning of the monitoring, a relatively low galvanic current value appeared, irrespective of the exposure condition. This convinced that the steel in the mortar specimen was free from corrosion (passivated). The corrosion initiation time was varied depending on the exposure condition. The 2w/8d specimen indicated no remarkable change until 40 days and subsequently increased up to about $6\,\mu A$. The increased current remained steadily thereafter. 5w/5d and 10w specimens showed a sharp increase of current at 90 and 160 days, respectively. And the current of the 10w specimen was increased up to $1.3\,\mu A$ at 60 days and then was decreased at 80 days. This result could be supposed as an initiation of localized corrosion and repassivation, though the interpretation of repassivation in galvanic current measurement is still controversial.

Figure 3 shows the changes in the corrosion current density of embedded steel, derived by LPR measurement. According to the previous studies, corrosion current density over $0.1\,\mu A/cm^2$ was identified as the depassivation of steel [14, 15]. Compared with the galvanic current test results, the corrosion of steel in mortar, subjected to different exposure conditions, initiated at similar or later time. For example, the 2w/8d specimen showed a corrosion current density value higher than $0.1\,\mu A/cm^2$ after 60 days and gradually increased after that. The 5w/5d specimen required 90 days to exceed $0.1\,\mu A/cm^2$ and 170 days for the 10w specimen. After 300 days, the current density of each specimen was converged to a constant value, accounting for 30, 8.0, and $0.5\,\mu A/cm^2$ for 2w/8d, 5w/d, and 10w specimens, respectively. It is presumed that the higher corrosion current density of steel, resulting from cyclic wetting and drying exposure conditions, is due to the higher penetration rate of both chloride and oxygen [16]. Thus, it is evident that high drying ratio accelerates the corrosion initiation time and increases the
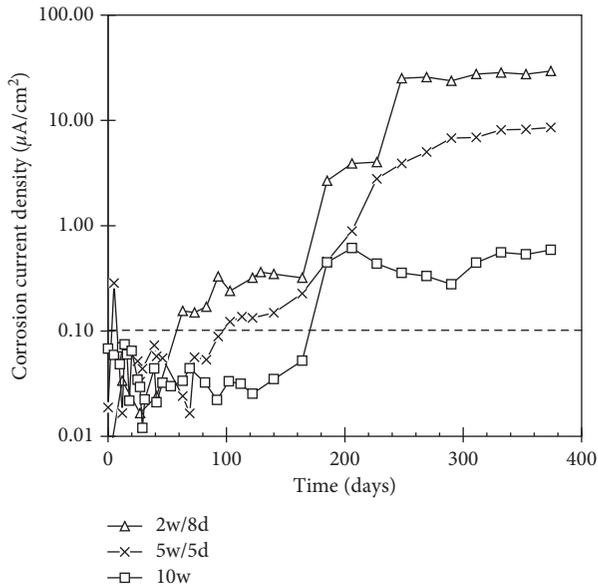
Figure 3: Changes in corrosion current density of the specimen exposed to the external chloride.

Figure 4: Changes in corrosion current density of the specimen with chloride in cast.

corrosion current density in the corrosion propagation phase. This acceleration of corrosion, consequently, may cause a hazardous defect on the marine-reinforced structure, especially exposed to high tide level. Thus, a totally immersed condition imposes a higher CTL of concrete than that exposed to a cyclic wet/dry condition.

3.2. Chloride Threshold Level. To evaluate the influence of internal chloride on the corrosion rate, the corrosion current density was monitored for 100 days. The average corrosion current density was obtained by integrating the measured current density and dividing it by the total number of days to measure. The average corrosion current density of the steel bar in the mortar specimen as a function of the concentration of admixed chloride (total chloride) is depicted in Figure 4. The average corrosion current density showed exponential increase in total chloride. The CTL ranged from 1.74–2.46% of the total chloride content for 0.1–0.2 μA/cm^2. From the prior research, Alonso et al. [14] show a similar CTL ranged from 1.24 to 3.08, and Hope and Ip [8] reported relatively low CTL ranged from 0.92 to 1.35. However, the CTL prescribed by the British Standard or ACI is 0.4 or 0.2% by the weight of cement, and it is significantly lower than this result [17, 18]. This difference may be due to the variation of chloride binding capacity arising from chloride source. In pore solution, free chloride chemically reacted with the hydration products of C_3A or C_4AF into Friedel's salt at the early hydration process. The formation of Friedel's salt could remove the free chloride in the pore solution, which participates in the corrosion process. In fact, the formation of Friedel's salt reduced in the external chloride condition since the chloride penetrates after hydration of the cement proceeds [19, 20]. From a literature review on real structures, the CTL was moreover produced in a wide range, accounting for about 0.2–1.5%, presumably due to environmental influencing factors to corrosiveness of steel,
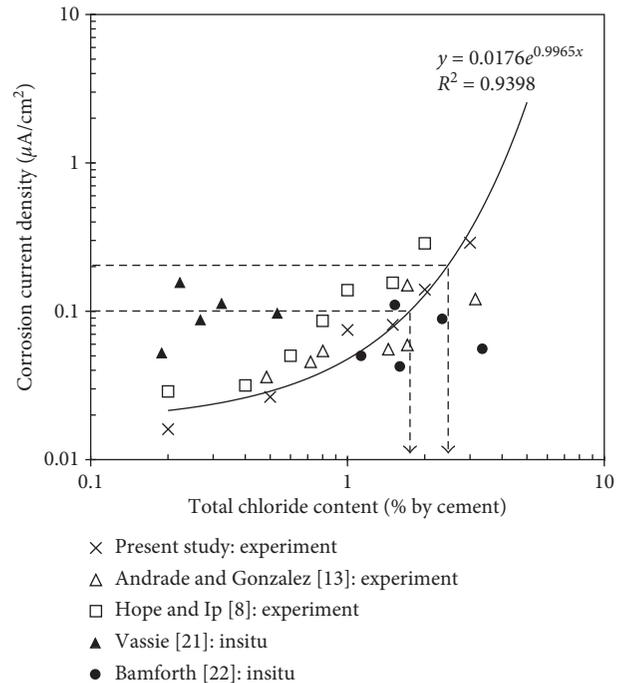
such as relative humidity, moisture level in concrete, and temperature [21, 22]. Thus, it seems very difficult to empirically determine the CTL from real structures, with no adjustment of environmental factors.

The chloride profile with different exposure conditions was conducted at the time when the corrosion initiation was observed (at 40, 90, and 160 days), as shown in Figures 5(a)–5(c). The calculated surface chloride and apparent diffusion coefficient are stated in Table 1. It was found that an increase in the drying ratio resulted in an increase of the total penetrated chloride concentration through all depths from the surface. When the specimen is exposed to dry conditions, the water saturation in the pore decreases and, therefore, the chloride transport is dominated by both diffusion and absorption, particularly at the outer section. Therefore, as the transportation rate of chloride ions induced by absorption is generally higher than diffusion, the 2w/8d specimen shows the highest amount of chloride penetration throughout the depth from the exposed surface. Liam et al. and TWRL [23, 24] reported the rapid penetration of chloride ions as the drying ratio increases; however, they showed relatively high surface chloride concentration, ranged from 1.66 to 4.42% by weight of cement. The long-term exposure to the chloride environment may result in further accumulation of chloride ions at the surface, induced by salt crystallization by drying. Comparing the profile data at the time of corrosion initiation, 2w/8d and 5w/5d specimens show a similar amount of the total chloride content at the steel depth (Figure 5(d)). Since the cover depth of the specimen was 15 mm, the CTL for 2w/8d and 5w/5d specimens is about 0.2% which is similar to the BS and ACI standards, while the CTL of 10w is about 0.3%.
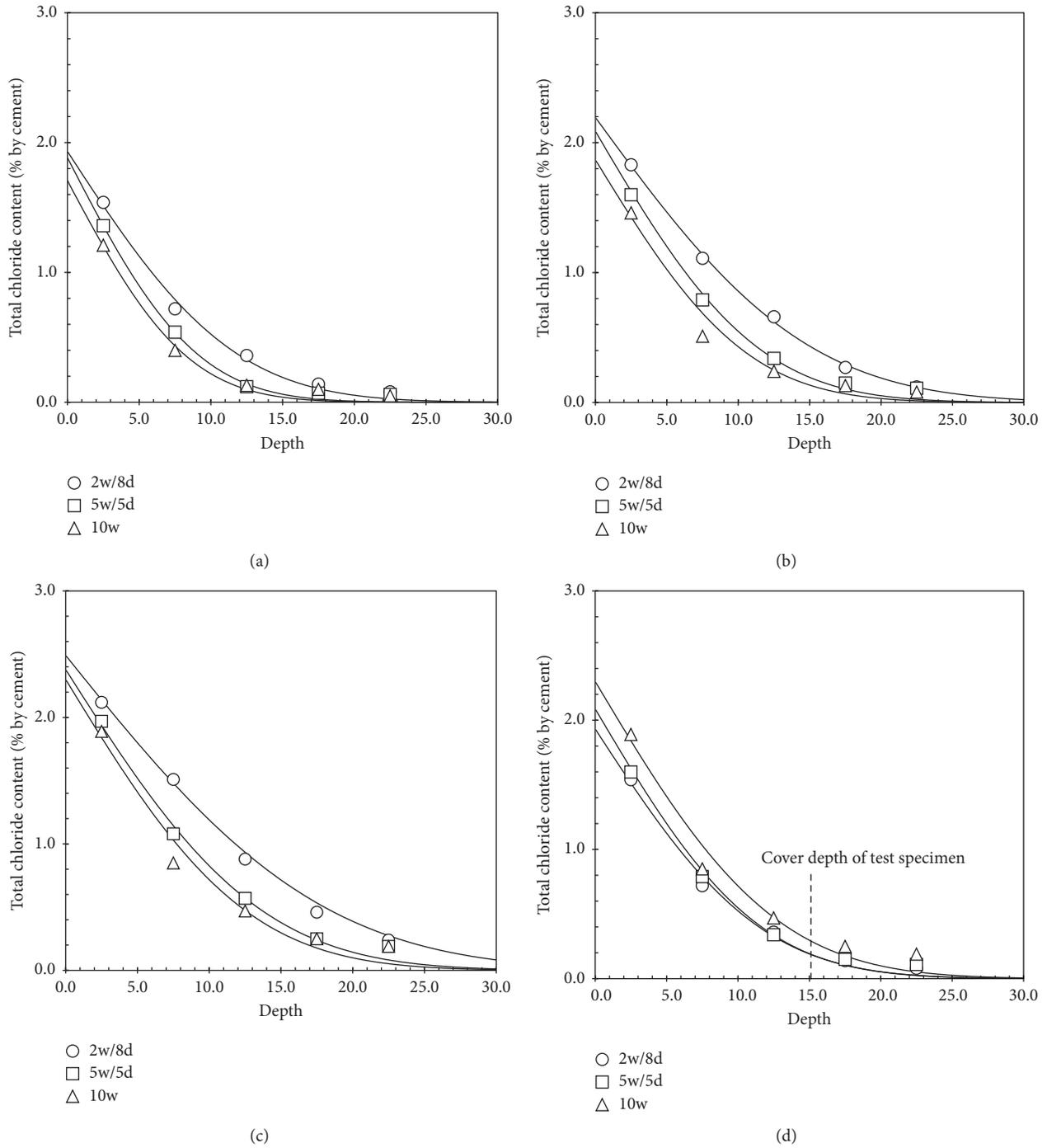
FIGURE 5: Chloride profile results at (a) 40, (b) 90, and (c) 160 days with different exposure condition, and (d) at the time when corrosion initiated.

TABLE 1: Surface chloride and apparent chloride diffusion coefficients at 40, 90, and 160 days.

Exposure condition	40 days		90 days		160 days	
	C_s (%)	D (m^2/s)	C_s (%)	D (m^2/s)	C_s (%)	D (m^2/s)
2w/8d	1.93	11.19*	2.19	8.72*	2.49	7.18*
5w/5d	1.88	7.13*	2.09	5.12*	2.38	4.10*
10w	1.71	6.26*	1.87	4.46*	2.30	3.54*

*$\times 10^{-12}$.

3.3. Life Cycle Prediction. In service life prediction, although the CTL of external chloride is lower than that of internal, it is difficult to determine the corrosion risk according to the chloride source. External chloride takes time to penetrate until steel depth, and increase of cover depth can delay it. On the other hand, internal chloride has a risk of rebar corrosion immediately after casting because it is always present nearby the steel. In addition, quantification of the total chloride content which exists in mixing materials (e.g., water, sand, and gravel) is knotty. Accordingly, in this paper, the chloride penetration and service life prediction were conducted only for external chloride.

To predict the chloride penetration, subsequently to predict the service life, time dependency of chloride transport should be considered [25]. Generally, the chloride transport in concrete was extrapolated based on Fick's law of one-dimensional diffusion with constant diffusivity. It contains some basic assumptions of that (1) the concrete is exposed on the constant chloride concentration and (2) the pore matrix is homogeneous; that is, it shows an identical diffusivity throughout the concrete at the same time. However, from Tang and Nilsson [26], chloride diffusion coefficients at early age decreased with time and they mathematically expressed the reduction, taking into account the time dependency, as follows:

$$D(t) = D_{ref}\left(\frac{t_{ref}}{t}\right)^m,$$

$$m = \frac{\ln(D(t))}{\ln(D_{ref})(t_{ref}/t)}, \tag{3}$$

where m is the age factor and D_{ref} and $D(t)$ are chloride diffusion coefficients at the exposure time of t_{ref} and t, respectively. Based on the experimental results, the apparent diffusion coefficient at 40 days was used as D_{ref}, and m was calculated by (3), corresponding to the values of 0.3208, 0.3473, and 0.3468 for 2w/8d, 5w/5d, and 10w, respectively. In the previous studies [27, 28] and life cycle prediction programs (Life 365, DuraCrete 2000), the recommended value of m varies from 0.2 to 0.55. Therefore, the obtained values of m were considered to be an appropriate value. Using these age factors, the chloride transportation was predicted with time-dependent diffusion coefficient, as shown in Figure 6. For the boundary condition of the prediction model, the chloride concentration at the exposed surface was set to 1.0 M and the cover depth was 50 mm. It was evident that a decrease in drying ratio increases the required time of chloride transport to reach up to CTL at the specified cover depth. The service life was predicted as 2.35, 4.73, and 13.1 years for 2w/8d, 5w/5d, and 10w, respectively. In particular, the predicted service life of 2w/8d and 10w was clearly different because the CTL of 2w/8d is lower than 10w and the chloride transport rate of 2w/8d is basically high. Thus, it is evident that the corrosion initiation is likely to be promoted in the marine structures exposed to the high drying ratio condition, that is, high tide level. Furthermore, reminding that an increase in the drying ratio increases the corrosion rate after corrosion initiation, it is expected that the deterioration of the structure, induced by chloride
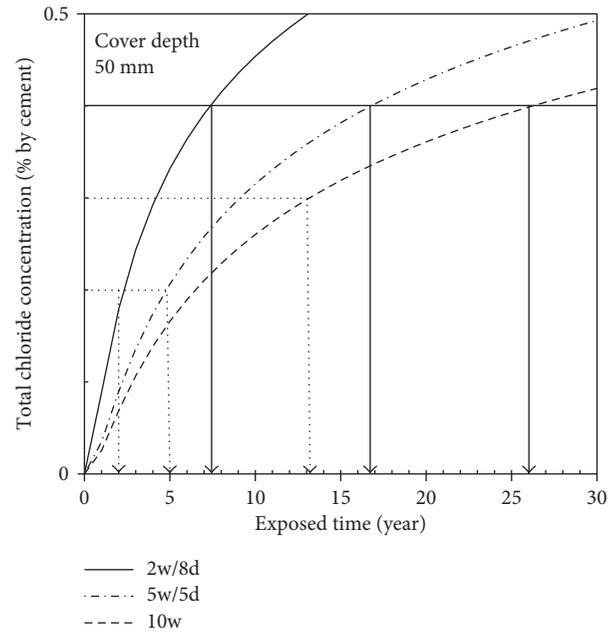
FIGURE 6: Prediction of chloride concentration with time (cover depth: 50 mm).

propagation, will be accelerated. When it comes to a conservative value for the CTL (i.e., 0.4%), the predicted corrosion-free life could be enormously increased up to 13.0, 16.8, and 26.1 years for 2w/8d, 5w/5d, and 10w, respectively. It suggests that the CTL would be a crucial factor to govern the service life of concrete structures exposed to a salt environment. The difference in the CTL in terms of the corrosion resistance from experiment and real structures would arise from the reactivity in the cathodic region on the steel surface. In wet and dry cyclic environments (i.e., in the present study), oxygen and water could percolate the concrete to the depth of the steel, depending on the duration of exposure to the atmospheric condition. Thus, cathodic reaction could accompany the anodic process on the steel surface, leading to accelerate the corrosion process. In turn, the corrosiveness would be rapidly developed, producing the lower CTL. However, in the real structure, the penetrability of cathodic agents may be limited, in particular, to the depth of the steel: the cover depth usually exceeds 50–100 mm in a marine environment, and thus, the access of oxygen and water is restricted to the steel. Substantially, the corrosiveness would be retarded by limited cathodic reaction on the steel surface, thereby producing the increased corrosion resistance in terms of the higher CTL.

4. Conclusion

In the present study, the corrosion risk of reinforced concrete structure arising from internal chloride and external chloride was evaluated. The corrosion rate was monitored, and the chloride transport was analyzed to determine the CTL according to the chloride source. In addition, in the case of external chloride, the service life prediction was conducted with different exposure conditions. The conclusions derived from the experimental works are as follows:

(1) As the results of the monitoring of the galvanic currents, the corrosion initiation was greatly affected by the exposure condition. The wet/dry condition accelerates the onset of corrosion than the totally wet condition, presumably due to the increased penetration of oxygen and chloride.

(2) The measurement of LPR gave an informative data to decide the CTL depending on the chloride source. Internal chloride showed higher CTL than external chloride, which is thought to be caused by the reduction of the amount of free chloride, participating in the corrosion process, by chloride binding in the initial hydration stage.

(3) The dry ratio of the exposure condition increases the corrosion rate after the initiation of corrosion. Accordingly, it is expected that the corrosion propagation will be promoted in marine structure exposed to high tide level.

(4) Consequently, a dramatical decrease of service life was predicted in structures exposed to high tide level. Also, since the corrosion propagation rate is high, accelerated defects of structural behavior are expected.

Conflicts of Interest

The authors declare that they have no conflicts of interest.

Acknowledgments

References

[1] P. Schiessl and M. Raupach, "Influence of concrete composition and microclimate on the critical chloride content in concrete," in *Corrosion of Reinforcement in Concrete*, C. L. Page, K. W. J. Treadaway, and P. B. Bamforth, Eds., pp. 49–58, Elsevier Applied Science, London, UK, 1990.

[2] K. Y. Ann and H. W. Song, "Chloride threshold level for corrosion of steel in concrete," *Corrosion Science*, vol. 49, no. 11, pp. 4113–4133, 2007.

[3] R. D. Hooton, M. R. Geiker, and E. C. Bentz, "Effects of curing on chloride ingress and implications on service life," *ACI Material Journal*, vol. 99, no. 2, pp. 201–206, 2002.

[4] M. Funahashi, "Predicting corrosion free service life of a concrete structure in a chloride environment," *ACI Material Journal*, vol. 87, no. 6, pp. 581–587, 1990.

[5] M. Thomas, "Chloride threshold in marine concrete," *Cement and Concrete Research*, vol. 26, no. 4, pp. 513–519, 1996.

[6] P. Sandberg, *Chloride Initiated Reinforcement Corrosion in Marine Concrete*, Lund Institute of Technology, Dissertation (Report TVBM-1015), Lund, Sweden, 1998.

[7] B. Elsener and H. Böhni, "Corrosion of steel in mortar studied by impedance measurements," *Materials Science Forum*, vol. 8, pp. 363–372, 1986.

[8] B. B. Hope and A. K. C. Ip, "Chloride corrosion threshold in concrete," *Materials Journal*, vol. 84, no. 4, pp. 306–314, 1987.

[9] B. H. Oh, S. Y. Jang, and Y. S. Shin, "Experimental investigation on the threshold chloride concentration for corrosion initiation in reinforced concrete structures," *Magazine of Concrete Research*, vol. 55, no. 2, pp. 117–124, 2003.

[10] K. Pettersson, *Corrosion Threshold Value and Corrosion Rate in Reinforced Concrete, CBI Report 2:92*, Swedish Cement and Concrete Research Institute, Stockholm, Sweden, 1992.

[11] C. Alonso, M. Castellote, and C. Andrade, "Chloride threshold dependence of pitting potential of reinforcements," *Electrochimica Acta*, vol. 47, no. 21, pp. 3469–3481, 2002.

[12] W. Morris, A. Vico, and M. Vazquez, "Chloride induced corrosion of reinforcing steel evaluated by concrete resistivity measurements," *Electrochemica Acta*, vol. 49, no. 25, pp. 4447–4453, 2004.

[13] C. Andrade and J. A. Gonzalez, "Quantitative measurements of corrosion rate of reinforcing steels embedded in concrete using polarization resistance measurements," *Werkstoffe und Korrosion*, vol. 29, no. 8, pp. 515–519, 1978.

[14] C. Alonso, C. Andrade, M. Castellote, and P. Castro, "Chloride threshold values to depassivate reinforcing bars embedded in a standardized OPC mortar," *Cement and Concrete Research*, vol. 30, no. 7, pp. 1047–1055, 2000.

[15] R. B. Polder and W. H. A. Peelen, "Characterisation of chloride transport and reinforcement corrosion in concrete under cyclic wetting and drying electrical resistivity," *Cement and Concrete Composites*, vol. 24, no. 5, pp. 427–435, 2002.

[16] Y. Zhang and W. L. Jin, "Distribution of chloride accumulation in marine tidal zone along altitude," *ACI Materials Journal*, vol. 108, no. 5, pp. 467–475, 2011.

[17] British Standards Institution, *Part 1: Structural Use of Concrete-Code of Practice for Design and Construction*, BS 8110, BSI, London, UK, 1985.

[18] American Concrete Institute, *Corrosion of Metals in Concrete, Manual of Concrete Practice, Part 3*, ACI Committee 222, ACI, Detroit, MI, USA, 1994.

[19] C. Arya, N. R. Buenfeld, and J. B. Newman, "Factors influencing chloride binding in concrete," *Cement and Concrete Research*, vol. 20, no. 2, pp. 291–300, 1990.

[20] O. Wowra and M. J. Setzer, "Sorption of chlorides on hydrated cements and C3S pastes," in *Frost Resistance of Concrete*, M. J. Setzer and R. Auberg, Eds., pp. 147–153, E & FN Spon, London, UK, 1997.

[21] P. Vassie, "Reinforcement corrosion and the durability of concrete bridges," *Proceedings of the Institution of Civil Engineers*, vol. 76, no. 3, pp. 713–723, 1984.

[22] P. B. Bamforth, "The derivation of input data for modelling chloride ingress from eight-year UK coastal exposure trials," *Magazine of Concrete Research*, vol. 51, no. 2, pp. 87–96, 1999.

[23] K. C. Liam, S. K. Roy, and D. O. Northwood, "Chloride ingress measurements and corrosion potential mapping study of a 24-year-old reinforced concrete jetty structure in a tropical marine environment," *Magazine of Concrete Research*, vol. 44, no. 160, pp. 205–215, 1992.

[24] TWRL, *Marine Durability Survey of the Tongue Sand Tower. Concrete in the Oceans*, Tech. Rep. 5, Cement and Concrete Association, London, UK, 1980.

[25] S. W. Pack, M. S. Jung, H. W. Song, S. H. Kim, and K. Y. Ann, "Prediction of time dependent chloride transport in concrete structures exposed to a marine environment," *Cement and Concrete Research*, vol. 40, no. 2, pp. 302–312, 2010.

[26] L. Tang and L. O. Nilsson, "Chloride diffusivity in high strength concrete at different ages," *Nordic Concrete Research Publication*, vol. 11, pp. 162–171, 1992.

[27] L. Wu, W. Li, and X. Yu, "Time-dependent chloride penetration in concrete in marine environments," *Construction and Building Materials*, vol. 152, pp. 406–413, 2017.

[28] O. E. Gjorv, "Durability of concrete structures," *Arabian Journal of Science and Engineering*, vol. 36, no. 2, pp. 151–172, 2011.

Research Article

Dowel Behavior of Rebars in Small Concrete Block for Sliding Slab Track on Railway Bridges

Seong-Cheol Lee,[1] Sangmin Park,[2] Jaeha Lee,[2] and Kyoung-Chan Lee [ID][3]

[1]*Department of Civil Engineering, Kyungpook National University, 80 Daehakro, Bukgu, Daegu 41566, Republic of Korea*
[2]*Department of Civil Engineering, Korea Maritime and Ocean University, 727 Taejong-ro, Yeongdo-Gu, Busan 49112,*
 Republic of Korea
[3]*Advanced Railroad Civil Engineering Divison, Korea Railroad Research Institute (KRRI), 176 Cheoldobangmulgwan-ro,*
 Uiwang-si, Gyeonggi-do 16105, Republic of Korea

Correspondence should be addressed to Kyoung-Chan Lee; eclip77@gmail.com

In recent years, several studies have investigated the sliding slab track for railway bridges. In the design of sliding slab tracks, one of the most important considerations is to evaluate the shear capacity of the lateral supporting concrete blocks in which dowel rebars are embedded. The predictions of the dowel behavior of rebars by existing models are considerably different. Therefore, in this study, the actual dowel behavior of the rebars embedded in a small concrete block was extensively investigated through experiments. Test variables were concrete compressive strength, dowel rebar diameter and yield strength, specimen thickness, and dowel rebar spacing. Existing model predictions were considerably different from test results. The maximum dowel force increased as concrete compressive strength and dowel rebar diameter increased, while it did not increase considerably with other test variables. Unlike in existing models, the shear slip at the maximum dowel force decreased as the dowel rebar diameter increased. Existing models significantly underestimated the maximum dowel force of the dowel rebars with small diameters and overestimated it for the dowel rebars with large diameters. This work can be useful for developing a more rational model to represent the actual dowel behavior of the rebars embedded in small concrete blocks.

1. Introduction

Modern railway bridges are equipped with continuously welded rails (CWRs) without any seams to improve riding comfort and the high-speed driving of a train. In such railway bridges, additional axial stresses can be caused on rails owing to the expansion and contraction of the bridge structure because of temperature change. This behavior is referred to as the track-bridge interaction. Simply supported railway bridges with short spans have been commonly adopted to suppress this effect. The interaction effect should be carefully controlled through special types of fasteners or rail expansion joints in the case of long span bridges. However, the effectiveness of these methods is limited, and

they may cause additional problems such as maintenance issues.

Recently, Lee et al. [1] conducted preliminary research on the design of a sliding slab track, in which a low friction sliding layer is placed between the bottom of a slab track and the top of a bridge deck as an alternative method of reducing track-bridge interaction. The sliding slab track system separates the longitudinal behavior of the concrete slab track and bridge deck to prevent the longitudinal displacement due to the temperature expansion and contraction of the bridge from being transmitted to the CWR through the slab track. Lee et al. [2, 3] reported that the additional axial stress along the rail due to the track-bridge interaction effect was reduced by 80–90% when the sliding
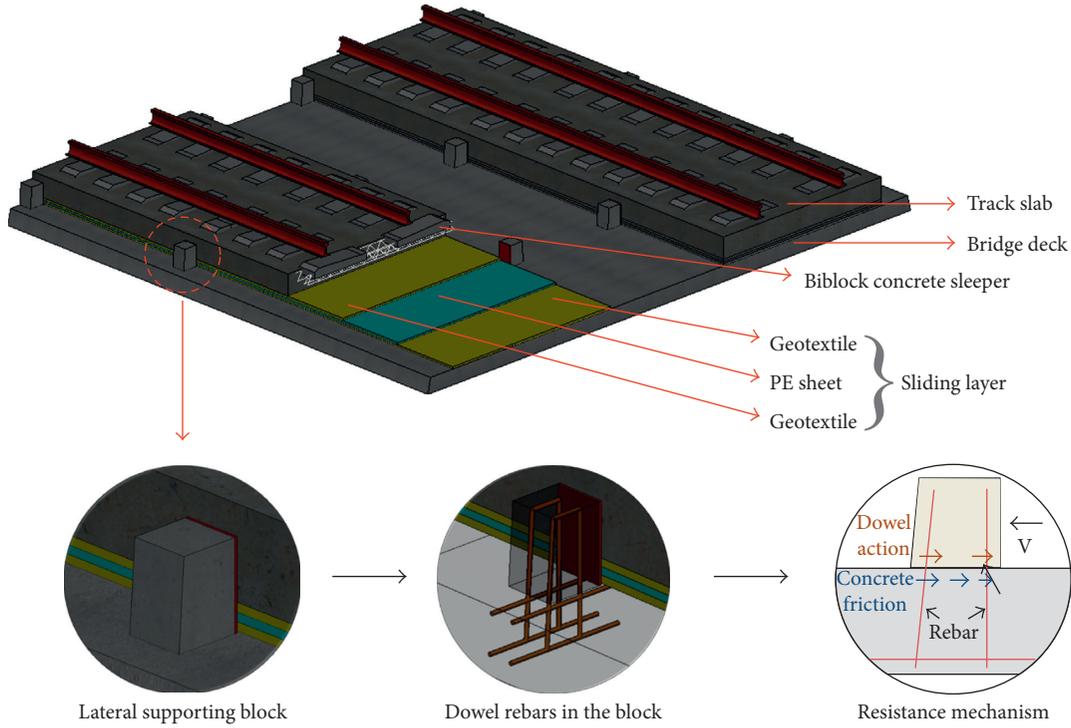
Figure 1: Perspective view of sliding slab track including lateral supporting blocks.

Table 1: Summary of design specifications and previous models for dowel behavior of rebar.

Model	Equations
Soroushian et al. [5]	$D(s) = D_{max}(s/s_{max})^{0.5}$ $D_{max} = 0.5 f_b(0.37\gamma d_b - c)^2 +$ $0.45 f_y d_b^2 (1 - T^2/T_y^2)/\gamma$ $s_{max} = 2.43 \times 10^{-5} D_{max} + 0.24$ mm, where $f_b = 37.6\sqrt{f_c'}/\sqrt[3]{d_b}$, $\gamma = \sqrt[4]{E_s/K_f d_b}$, $K_f = 271.7$ MPa/mm, and $c = 0.05 f_y d_b/f_c'$
Randl [11]	(i) Detailed model $D_{max} = p_{max} d_b^2 [(0.46 L/d_b) + (0.187 f_y d_b/p_{max} L)$ $- 0.005 (d_b/L)^3 (f_y/p_{max})^2]$, where $p_{max} = 3 \sim 4$ times of $f_{cwm} L = \sqrt[4]{(4E_s I/500 d_b)}$ (ii) Simple model $D_{max} = 1.5 A_s \sqrt{f_y} \sqrt{f_{cwm}}$, where f_{cwm} is compressive strength of concrete cube
MC10 [12]	$D(s) = D_{max}(s/s_{max})^{0.5}$ $D_{max} = \kappa_{2,max} A_s \sqrt{f_{co} f_y} \leq (A_s f_y/\sqrt{3})$, where $\kappa_{2,max} \leq 1.6$ for C20~C50 concrete s_{max} is 1~2 times the dowel rebar diameter

track system was adopted, as compared to the conventional slab track system.

As bridges and concrete slab tracks are separated from each other by sliding layers, it is necessary to implement supporting structures for resisting lateral load, which is caused by a train nosing force, lateral wind, centrifugal loads along curved railways, and temperature change in curved rails. Figure 1 is a conceptual drawing of a sliding slab track including a bridge deck, a sliding layer, and lateral supporting concrete blocks. As shown in the figure, several

rebars are installed in the lateral supporting concrete blocks so that they can resist lateral load through the dowel behavior of the rebars.

For the design of lateral supporting concrete blocks, Lee et al. [4] employed an existing model [5, 6] to consider the lateral load that can be resisted by the dowel behavior of rebars. Even though the structural behavior of dowel rebars is the primary issue in the design, experimental verification is relatively limited for the dowel behavior of rebars in a small concrete member such as a lateral supporting
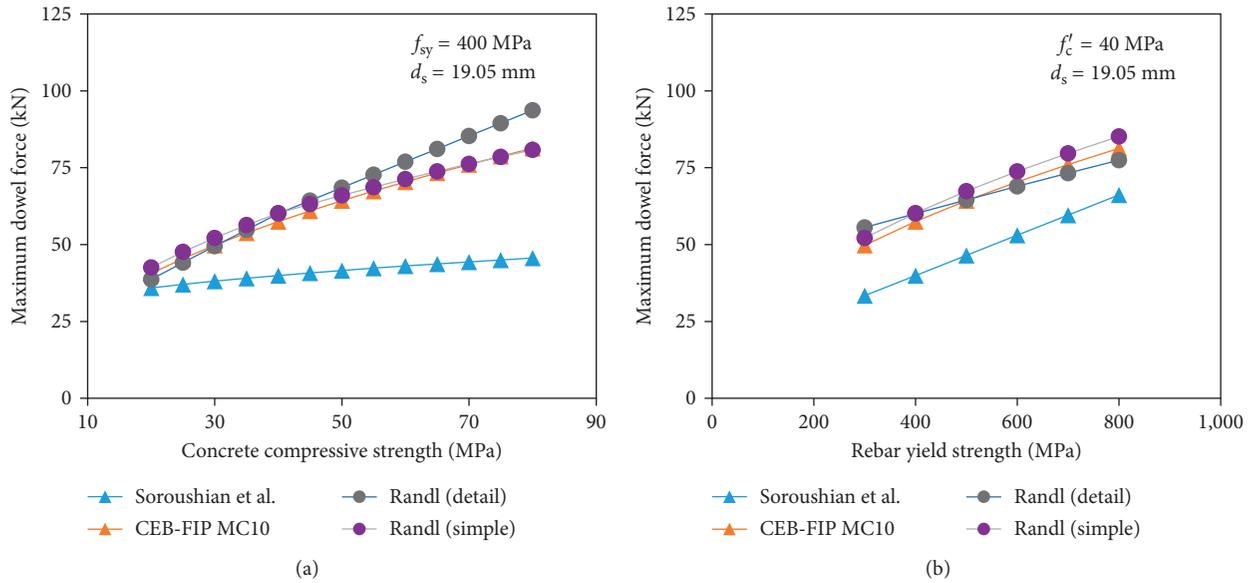
FIGURE 2: Comparison of existing models for the maximum dowel force: (a) effect of concrete compressive strength; (b) effect of rebar yield strength.

TABLE 2: Summary of test specimens for dowel behavior of rebar.

Specimen	Concrete compressive strength (MPa)	Dowel rebar yield strength (MPa)	Dowel rebar diameter (mm)	Dowel rebar spacing (mm)	Specimen thickness (mm)
NC-N13-200	30	400	12.7	200	150
NC-N19-150	30	400	19.05	150	150
NC-N19-200	30	400	19.05	200	150
NC-N19-250	30	400	19.05	250	150
NC-N25-200	30	400	25.4	200	150
NC-H13-200	30	600	12.7	200	150
NC-H19-200	30	600	19.05	200	150
NC-H25-200	30	600	25.4	200	150
HC-N13-200	60	400	12.7	200	150
HC-N19-200	60	400	19.05	200	150
HC-N25-200	60	400	25.4	200	150
HC-H13-200	60	600	12.7	200	150
HC-H19-150	60	600	19.05	150	150
HC-H19-200	60	600	19.05	200	150
HC-H19-250	60	600	19.05	250	150
HC-H25-200	60	600	25.4	200	150
NC-N19-200-2	30	400	19.05	200	200
NC-N19-200-2.5	30	400	19.05	200	250

concrete block. Several studies experimentally investigated the dowel behavior of rebars; however, only one side of the rebars was embedded in concrete [7, 8] or dowel behavior was not perfectly extracted because of shear friction along the concrete interface [9, 10]. In addition, several models have been presented in the literature [5, 11, 12]; however, the predictions of the dowel behavior of rebars by these models are considerably different.

Therefore, in this study, the actual dowel behavior of the rebars in a small concrete member is investigated through an extensive experimental program, focusing on the dowel behavior against concrete core [5], which is dominated by
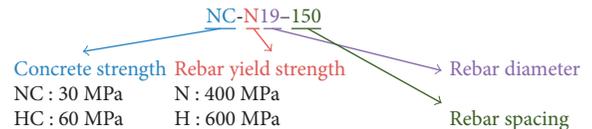
FIGURE 3: Test variables for dowel behavior of rebar in concrete.

concrete bearing strength, and not against concrete cover, which includes splitting cracks [6]. The effects of test variables on dowel behavior are examined based on experimental results. In addition, the applicability of existing
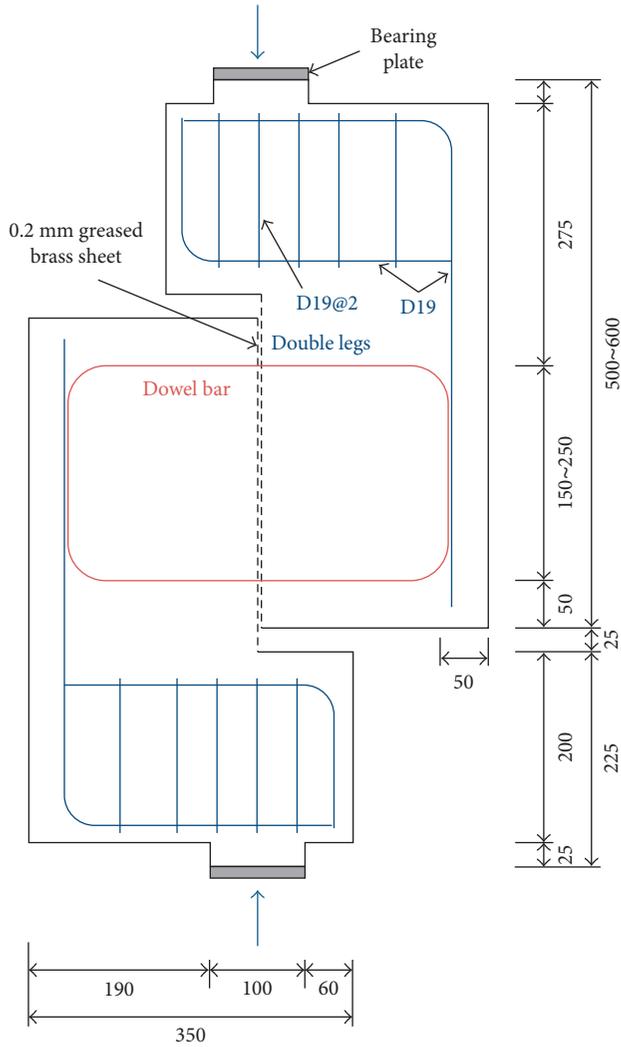
FIGURE 4: Details of test specimens.

FIGURE 5: Instrumentations to measure dowel behavior of rebar.

models is investigated by comparing the experimental results with model predictions.

2. Existing Models for Dowel Behavior of Rebars

The existing models [5, 11, 12] used to theoretically investigate the dowel behavior of the rebars embedded in concrete are summarized in Table 1. It is noted that only models that describe the dowel behavior of rebars against concrete core have been considered. As given in the table, MC10 [12] and Soroushian et al. [5] described the dowel force-shear slip response while Randl [11] analyzed only the maximum dowel force. The primary parameters considered in the models were concrete compressive strength, dowel rebar yield strength, and dowel rebar diameter. The model presented in MC10 is extremely similar to Randl's simple model, while the model proposed by Soroushian et al. is different because it is based on the bearing strength of the concrete under dowel rebars [13]. Randl's detailed model also considers the bearing strength of concrete; however, it is

TABLE 3: Properties of dowel rebar.

Notation	Nominal diameter (mm)	Nominal yield strength (MPa)	Measured	
			Yield strength (MPa)	Tensile strength (MPa)
N13	12.7	400.0	510.9	624.8
N19	19.1	400.0	549.5	617.0
N25	25.4	400.0	539.0	689.6
H13	12.7	600.0	715.8	740.3
H19	19.1	600.0	686.9	778.2
H25	25.4	600.0	668.6	822.6

fundamentally based on the deformed shape of the dowel rebar embedded in concrete.

Figure 2 shows the maximum dowel force evaluated using existing models to investigate the effect of two primary parameters (concrete and rebar strengths) on the dowel behavior of rebars. It is noted that a value of 1.6 was used for $\kappa_{2,\max}$ to consider the upper limit reported by
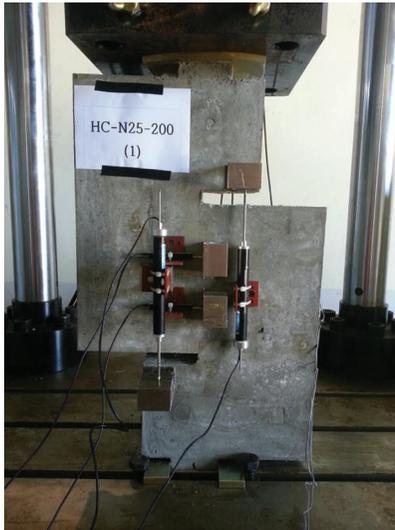
FIGURE 6: Test setup.

MC10 [12]. As seen in the figures, the models proposed by MC10 [12] and Randl [11] provide similar predictions of the maximum dowel force and its variation with concrete compressive strength or dowel rebar yield strength. On the contrary, the maximum dowel force predicted by Soroushian et al.'s model is lower than that predicted by other models. This trend is more evident when concrete compressive strength is increased. As verifications conducted in literature have typically focused on normal strength materials [5, 11], additional experiments should be conducted to investigate the dowel behavior of the rebars embedded in concrete, particularly when concrete with high compressive strength (larger than 50 MPa) or dowel rebars with high yield strength (larger than 400 MPa) are used.

3. Test Program for Dowel Behavior of Rebars in Concrete

In this study, an extensive experimental program was conducted to investigate the dowel behavior of the rebars in a small concrete member. The test variables considered in the program were concrete compressive strength, rebar yield strength, rebar diameter, concrete specimen thickness, and rebar spacing. This section provides an overview of the program.

3.1. Summary of Test Specimens

3.1.1. Test Variables. Concrete compressive strength, rebar yield strength, and rebar diameter were considered as the primary test variables because they have been typically considered in literature [5, 11, 12]. Two target compressive strengths for concrete were considered, that is, 30 and 60 MPa, because a concrete compressive strength of 30 MPa has been adopted for slabs in sliding slab tracks where a concrete anchor block with dowel bars would be

(a)

(b)

(c)

FIGURE 7: Typical failure mode of the test specimens. (a) Front view. (b) Left side. (c) Right side.

(a)

(b)

(c)
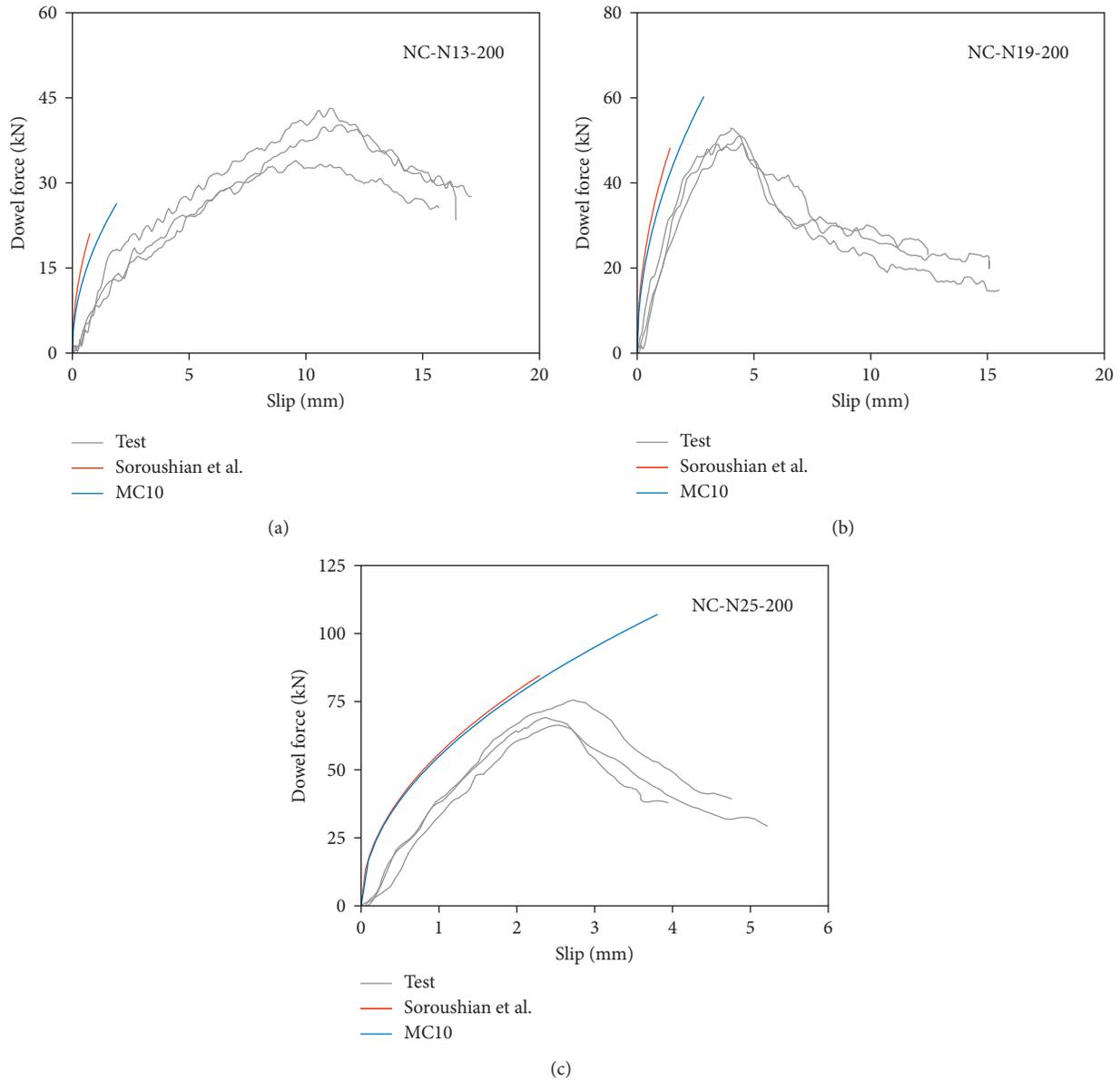
FIGURE 8: Shear slip-dowel force response, NC-200 series. (a) NC-N13-200. (b) NC-N19-200. (c) NC-N25-200.

embedded. In addition, 60 MPa was considered because high strength concrete would be adopted in future. Yield strengths of 400 MPa and 600 MPa were considered for the dowel rebar. Three kinds of nominal rebar diameters were considered, that is, 12.7, 19.1, and 25.4 mm. In addition to the primary test variables, the effects of concrete specimen thickness and dowel rebar spacing were considered.

The test specimens were designed based on the specimens used in previous studies [5]. In the test specimens, several cases were considered for the spacing of the dowel bars, according to the rebar arrangement in the concrete decks of railway bridges. Hence, considering that the longitudinal and lateral rebar spacings in the concrete deck are generally 150 mm, the thickness of the specimen and the

spacing of the dowel rebar in the specimens were set as 150, 200, or 250 mm.

The details of the test variables are provided in Table 2 and Figure 3.

3.1.2. Details of Test Specimens. Considering the test variables, the shape of the specimen including the dowel rebar arrangement is presented in Figure 4. As shown in the figure, to eliminate the contribution of concrete friction along the concrete interface, a smooth thin plate with a thickness of 0.2 mm is installed in the specimens, along the direction of applied load. Two dowel rebars are arranged through the thin plate so that only the rebars can contribute against the applied load.

TABLE 4: Comparison on the maximum dowel force.

Specimen	Test	Soroushian et al.	Randle (detailed)	Randle (simple)	MC10
NC-N13-200	39.3	21.1	26.4	25.8	27.7
NC-N19-150	47.4	48.3	60.3	58.2	63.2
NC-N19-200	51.2	48.3	60.3	58.2	63.2
NC-N19-250	56.0	48.3	60.3	58.2	63.2
NC-N25-200	70.6	84.7	107.1	101.4	112.2
NC-H13-200	46.4	26.5	31.3	29.3	32.8
NC-H19-200	55.6	57.3	67.4	64.0	70.7
NC-H25-200	73.5	100.9	119.2	111.6	125.0
HC-N13-200	65.8	24.6	38.0	44.2	40.2
HC-N19-200	66.1	53.9	87.6	95.9	91.8
HC-N25-200	99.8	92.4	155.4	164.1	162.9
HC-H13-200	60.8	30.0	45.4	47.9	46.2
HC-H19-150	81.6	62.9	97.9	102.1	102.6
HC-H19-200	85.2	62.9	97.9	102.1	102.6
HC-H19-250	77.5	62.9	97.9	102.1	102.6
HC-H25-200	99.1	108.7	173.1	175.1	181.5
NC-N19-200-2	54.5	48.3	60.3	58.2	63.2
NC-N19-200-2.5	62.7	48.3	60.3	58.2	63.2

Unit: kN.

The spacing of the two dowel bars was set as 150, 200, or 250 mm to simulate the spacing of the dowel rebars along the direction of applied shear force. To consider the effect of the effective concrete width surrounding the dowel rebars in the lateral direction, the thickness of the specimens was set as 150 mm in most cases as rebar spacing is generally 150 mm in bridge decks. In addition, two more thicknesses of 200 and 250 mm were considered.

Relatively large amounts of D19 reinforcing bars were embedded close to the loading area to prevent undesirable local failure due to unintentional concrete collapse.

3.1.3. Instrumentation.

Figure 5 shows the details of the instrumentation used to measure the dowel behavior of rebars during the test. As shown in the figure, four LVDTs are attached to the specimen surface; two LVDTs are attached along the direction of the applied load to measure shear slip along the interface between concrete blocks, and two more LVDTs are attached along the dowel rebars to measure interface opening during the test. As two LVDTs are used as one set, the average shear slip and interface opening can be evaluated from measured data. In addition to the LVDTs, two electric strain gauges are attached on the dowel rebar before concrete casting. When the specimen is fabricated, the electric gauges are placed at the interface such that the strain of the dowel rebars can be measured during the test.

3.2. Material Properties.

To measure the actual compressive strength of concrete, $\phi 100 \times 200$ cylinders were fabricated when concrete was casted into the specimens. The actual concrete compressive strength was measured during the test for the dowel behavior of rebars. It is noted that the tests for concrete compressive strength and dowel behavior were conducted at least 28 days after concrete casting. In the compression test with the cylinders, the average compressive strength of concrete for the NC and HC series was measured as 32.1 MPa and 67.6 MPa, respectively.

To measure the yield strength of the dowel rebars, direct tension tests were conducted with the rebars used as dowel rebars in the specimens. The tests were conducted according to the procedure presented in ISO 6892-1: 2009 [14]. The yield strengths of the rebars were evaluated through the 0.2% offset method using the stress-strain response of the rebars, and they are summarized in Table 3. As shown in the table, the dowel rebars used in the test specimens exhibit yield strengths exceeding the nominal yield strength of 400 MPa or 600 MPa.

3.3. Test Procedure.

To investigate the dowel behavior of rebars, load was applied in the direction along the interface on the bearing plates placed on the test specimens. A 1000 kN machine was used to apply the load. Practically, it is hard to attain shear friction along the interface because of the repeated loading due to trains. Therefore, prior to conducting the test, the load corresponding to 5–20% of the design capacity for the maximum dowel force was repeatedly applied 25 times to remove the shear friction due to adhesion between the thin plate and concrete matrix. The cyclic preloading process was referred to the standard test procedure of stud shear connectors provided in Eurocode 4, B.2 [15]. Then, a static loading test was conducted at a displacement control rate of 1 mm per minute. Figure 6 shows the test setup before the load is applied.

(a)

(b)

(c)
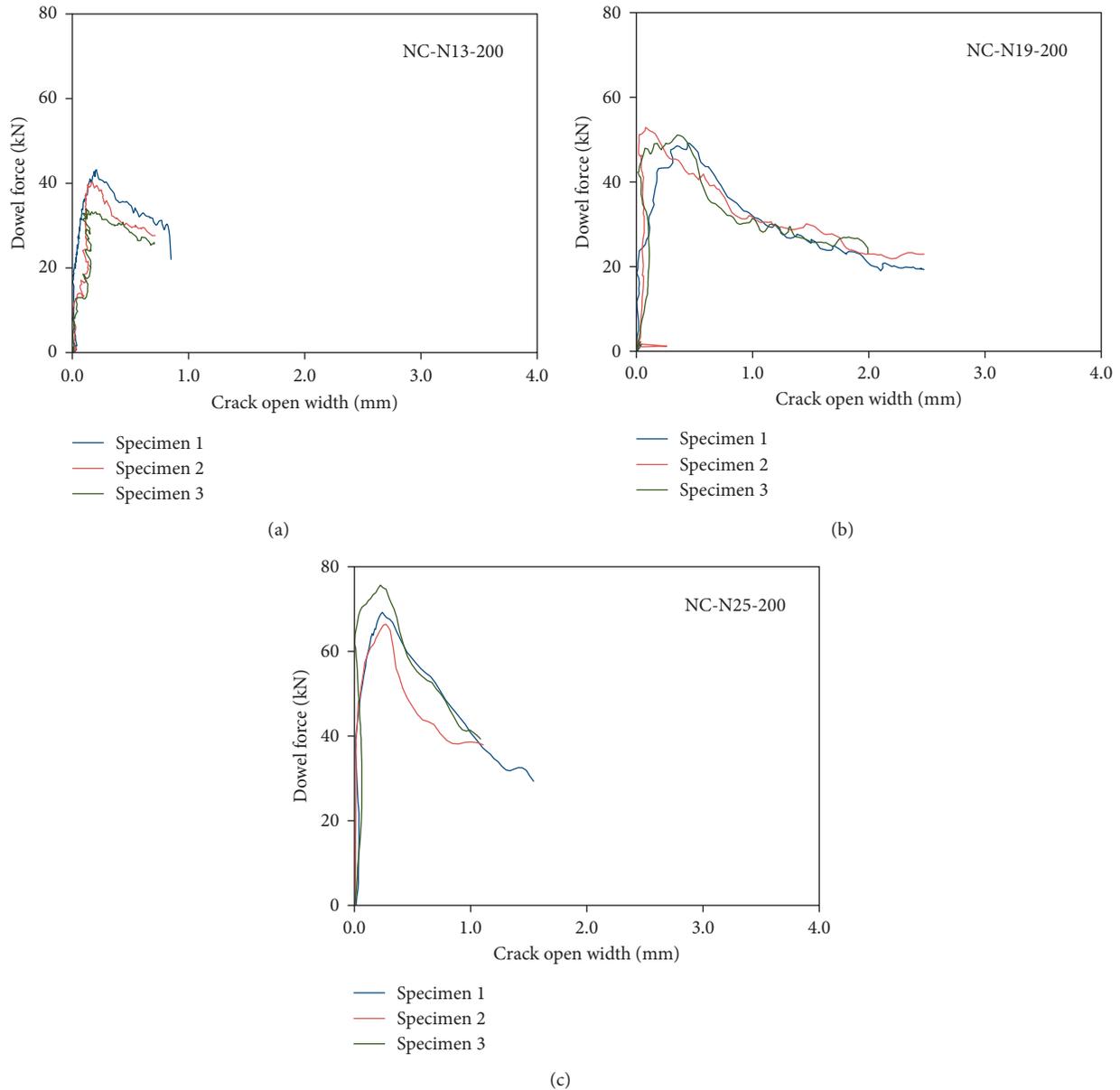
FIGURE 9: Interface opening-dowel force response, NC-200 series. (a) NC-N13-200. (b) NC-N19-200. (c) NC-N25-200.

4. Test Results and Investigation

4.1. Failure Mode and Dowel Behavior of Rebars

4.1.1. Failure Mode. Crack patterns were observed during the test to investigate the typical failure mode for the dowel behavior of rebars. No specimen exhibited splitting cracks before experiencing the maximum dowel force. After the maximum dowel force was reached, the applied force decreased considerably as concrete splitting cracks occurred under the dowel rebars. The typical crack patterns observed after the test are shown in Figure 7.

It can be inferred from these patterns that the shear resistance capacity due to the dowel behavior of the rebars is significantly influenced by the compressive strength of the concrete that supports the rebars, rather than by the yield strength of the rebars. According to the failure mode observed through the test, the maximum dowel force of the rebars can be increased by controlling concrete splitting cracks through the confinement effect, which can be attained by enclosing the concrete close to the dowel rebars with reinforcing bars.

4.1.2. Shear Slip-Dowel Force Responses. The representative shear slip-dowel force responses are presented in Figure 8. These responses were obtained from the tests for specimens NC-N13-200, NC-N19-200, and NC-N25-200. For detailed

(a)

(b)

(c)
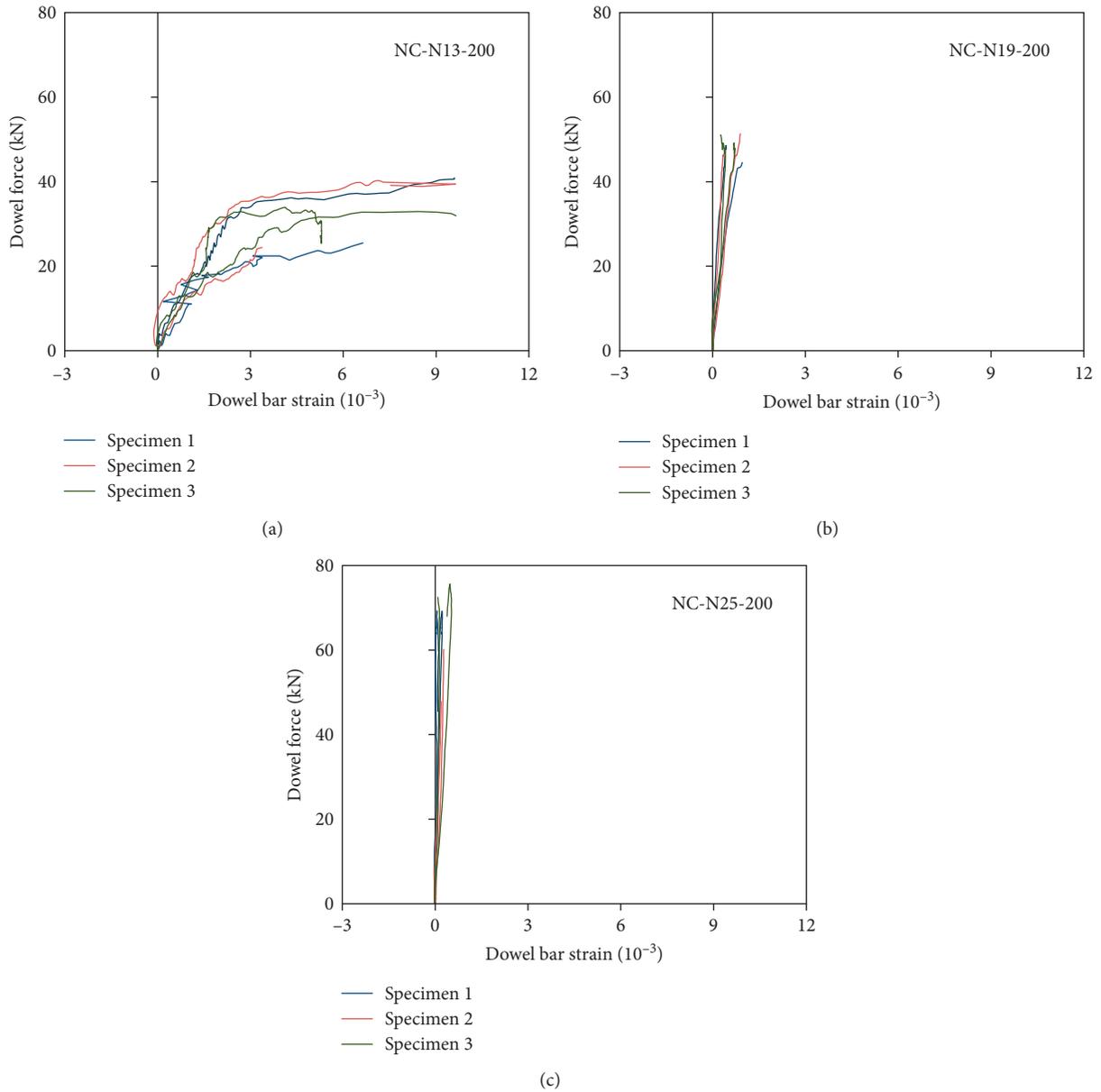
FIGURE 10: Dowel rebar strain-dowel force response, NC-200 series. (a) NC-N13-200. (b) NC-N19-200. (c) NC-N25-200.

analysis, the test results were compared with the dowel behaviors predicted by Soroushian et al. [5] and MC10 [12], who evaluated the maximum dowel force in addition to the shear slip-dowel force response. It is noted that MC10 predicted the shear slip corresponding to the maximum dowel force between 0.1 and 0.2 times the dowel rebar diameter. Hence, in this study, 0.15 times the dowel rebar diameter was selected to predict the shear slip-dowel force response.

As shown in Figure 8(a), in specimen NC-N13-200, the maximum dowel force measured through the test is 39.3 kN, which is significantly higher than the maximum dowel forces of 21.1 kN and 26.4 kN predicted by Soroushian et al. [5] and MC10 [12], respectively. This was primarily due to the small diameter of the dowel rebars.

Because of the small diameter, the kinking effect after the yielding of the dowel rebars contributed considerably to the dowel force before the test specimen exhibited splitting cracks under the dowel rebars. This phenomenon can also be inferred from the shear slip-dowel force response. The stiffness at a shear slip larger than 0.15 times the nominal diameter of the dowel rebars was significantly smaller than that at the earlier stage. In general, existing models [5, 12] do not consider the kinking effect of dowel rebars in the evaluation of the maximum dowel force. Therefore, when the dowel behavior at relatively low stiffness is excluded, the shear resistance capacity due to the dowel behavior of rebars measured through the test is only slightly different from the predictions of existing models. However, the predicted stiffness is higher than the test results when shear
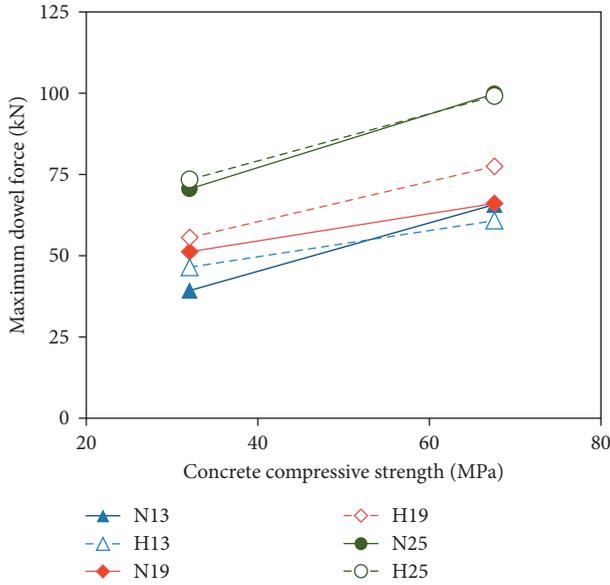
FIGURE 11: Effect of concrete compressive strength on the maximum dowel force.

slip is not larger than 0.15 times the nominal diameter of the dowel rebars.

Figure 8(b) shows the dowel force-shear slip responses for specimen NC-N19-200, which were measured using dowel rebars with a nominal yield strength of 400 MPa in concrete with a nominal compressive strength of 30 MPa. As shown in the figure, the two-phase response before the maximum dowel force that is observed in the test results for N13 dowel rebars is not observed in the test results for N19 dowel rebars. This indicates that the specimen that used the N19 dowel rebars exhibited the maximum dowel force before the kinking effect became apparent. As the kinking effect is not observed in the test with N25 dowel rebars, as seen in Figure 8(c), only the dowel rebars with small diameters exhibit considerable kinking before splitting cracks are observed in the concrete specimen.

In addition, the shear slip corresponding to the maximum dowel force decreases as dowel rebar diameter increases (Figure 8). As summarized in Table 4, this result is considerably different from the results of existing models such as MC10 [12] and Soroushian et al. [5], which predict increase in the shear slip at the maximum dowel force with dowel rebar diameter. The overall stiffness of the dowel rebar before reaching the maximum dowel force is overestimated by existing models. Therefore, further theoretical investigation is required for the dowel behavior of the rebars in a small concrete member.

4.1.3. Interface Opening and Dowel Rebar Strain. Dowel force-interface opening responses are presented in Figure 9. Interface opening is calculated as the average of the values obtained through the LVDTs attached
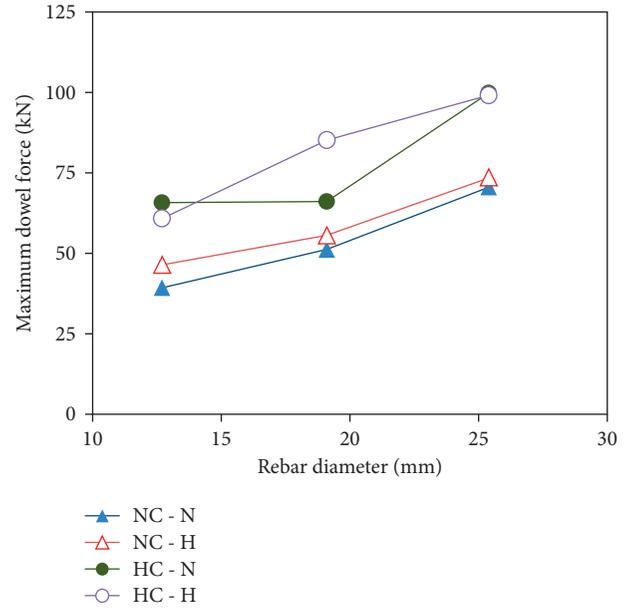
(a)
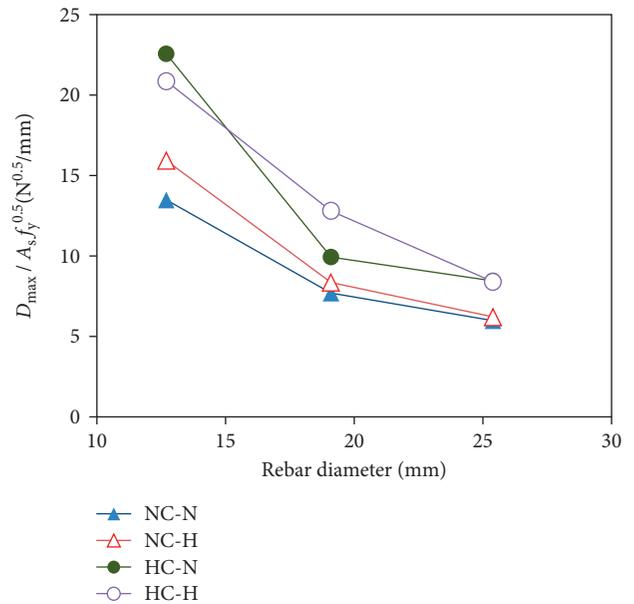
(b)

FIGURE 12: Effect of dowel rebar diameter on the maximum dowel force: (a) maximum dowel force; (b) normalized maximum dowel force.

perpendicular to the interface between the concrete blocks. As shown in the figure, the interface opening for all specimens is extremely small until the maximum dowel force is reached, after which interface opening increases rapidly. MC90 reported that the maximum dowel force can be reduced by a large interface opening [16]; thus, it is important to keep the interface opening small during the test to measure the actual maximum dowel force. Consequently, the test results obtained in this study are reliable for measuring the maximum dowel force under a small interface opening.

Figure 10 shows the dowel force-dowel rebar strain responses for the specimens with normal strength concrete (NC series) and dowel rebars (N series). Three dowel rebar diameters are considered to investigate the effect of the diameter on the response. It is noted that the strains of the dowel rebars were measured through two electronic strain gauges attached on the rebars at the interface. As seen in the figures, the strains of the specimens with N19 or N25 dowel rebars do not increase considerably until the maximum dowel force is reached. On the contrary, the strains of the specimens with N13 dowel rebars increase significantly before the maximum dowel force is reached. In addition, the dowel force in these specimens increases considerably even after the yielding of the dowel rebars, primarily owing to the kinking effect.

4.2. Effect of Test Variables on Dowel Behavior

4.2.1. Effect of Concrete Compressive Strength and Dowel Rebar Strength. The effect of concrete compressive strength and dowel rebar strength on the maximum dowel force is shown in Figure 11. Each point in the figure represents the average of three test results under the same test variables. The maximum dowel force increases with concrete compressive strength; the average increase in the maximum dowel force is 40.5% for an average increase of 110.9% in concrete compressive strength. This result is in agreement with previous models [5, 11, 12], which showed that the maximum dowel force is proportional to the square root of concrete compressive strength. In contrast, the effect of the yield strength of the dowel rebars is not as significant as that of concrete compressive strength; the average increase in the maximum dowel force is only 6.7% for an average increase of 29.7% in dowel rebar yield strength. This result indicates that existing models [11, 12] tend to overestimate the contribution of dowel rebar yield strength to the maximum dowel force. It can be seen from the figure that concrete compressive strength has a stronger effect on the maximum dowel force, as compared to the yield strength of dowel rebars. In other words, the bearing strength of the concrete under dowel rebars strongly affects the maximum dowel force.

4.2.2. Effect of Dowel Rebar Diameter. Figure 12 shows the effect of dowel rebar diameter on the maximum dowel force. As shown in Figure 12(a), the maximum dowel force increases with dowel rebar diameter. This trend is in agreement with existing models [5, 11, 12]; however, there is considerable difference in how strong the effect of the increase in dowel rebar diameter is on the maximum dowel force. For a more detailed investigation, the maximum dowel force is normalized using the nominal area and the square root of the yield strength of the dowel rebar, as shown in Figure 12(b). Existing models generally overestimate the contribution of dowel rebar diameter to the maximum dowel force. As the strain of the dowel rebar at the maximum dowel force is significantly affected by dowel
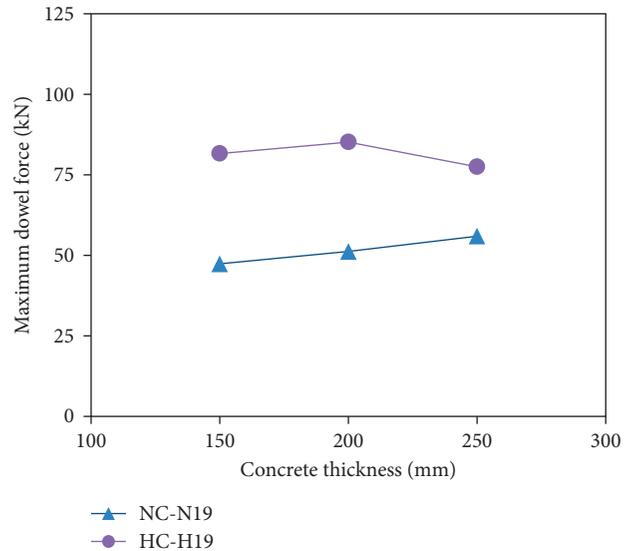
FIGURE 13: Effect of concrete specimen thickness on the maximum dowel force.
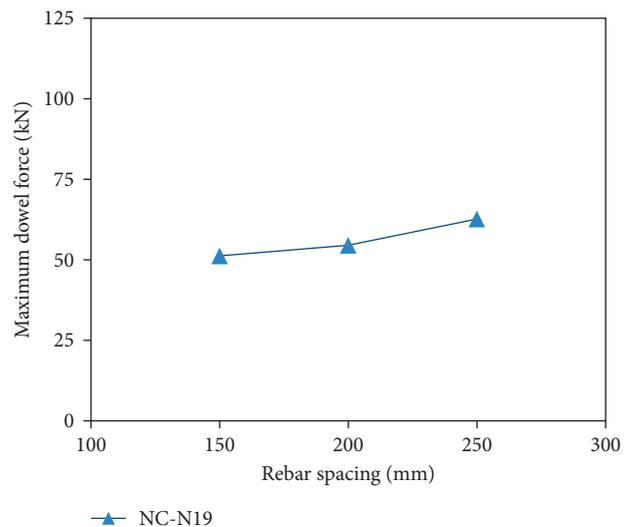
FIGURE 14: Effect of dowel rebar spacing on the maximum dowel force.

rebar diameter, as observed through the comparison of the results shown in Figure 8, a more rational prediction model is required.

4.2.3. Effect of Concrete Specimen Thickness and Dowel Rebar Spacing. The effect of concrete specimen thickness and dowel rebar spacing is investigated using Figures 13 and 14. As shown in Figure 13, the maximum dowel force is not considerably affected by a concrete specimen thickness of more than 150 mm. As shown in Figure 14, the maximum dowel force increases by 6.4 and 22.4% as dowel rebar spacing increases by 33.3 and 66.7%, respectively. Therefore,
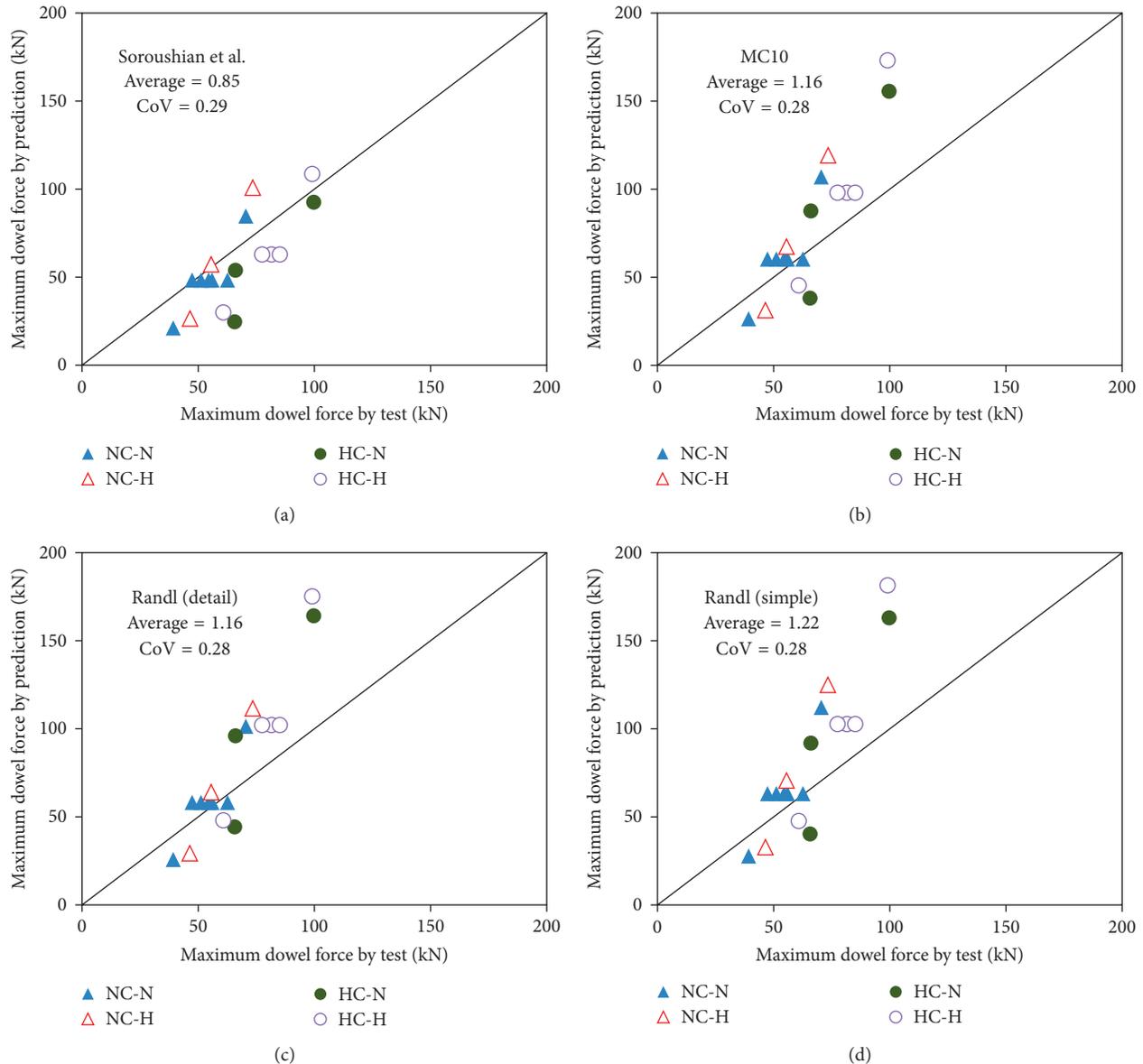
FIGURE 15: Comparison of the test results and several models on the maximum dowel force. (a) Soroushian et al. (b) MC10. (c) Randl (detail). (d) Randl (simple).

the maximum dowel force is not strongly affected by a dowel rebar spacing of more than 150 mm. Consequently, it can be concluded that the maximum dowel force is only weakly affected by concrete specimen thickness and dowel rebar spacing in the ranges considered in this study.

5. Comparison with Design Specification and Previous Models

The maximum dowel force measured through the tests is provided in Table 4. Each value is the average of three test results for a given test variable. In addition, the maximum dowel forces predicted by several existing models [5, 11, 12] are presented in the table. In existing models, the actual

concrete compressive strength and dowel rebar yield strength are considered in the calculation of the maximum dowel force. Figure 15 shows the maximum dowel forces for a more detailed comparison between the test results and predictions, and the ratios of the test results to the predictions are presented in Table 5 and Figure 16, as provided in JCSS [17] and Holický et al. [18].

The test results exhibit slightly better agreement with the prediction results of MC10 [12] and Randl [11] than with the results of Soroushian et al. [5]. In the prediction results of Soroushian et al., the maximum dowel force is generally overestimated for the specimens with large dowel rebar diameters (see specimens NC-N25-200, NC-H25-200, and HC-H25-200). This indicates that the contribution of the nominal area of dowel rebars is overestimated.

TABLE 5: Test/prediction ratio on the maximum dowel force.

Specimen	Soroushian et al.	Randl (detailed)	Randl (simple)	MC10
NC-N13-200	1.86	1.52	1.42	1.49
NC-N19-150	0.98	0.81	0.75	0.79
NC-N19-200	1.06	0.88	0.81	0.85
NC-N19-250	1.16	0.96	0.89	0.93
NC-N25-200	0.83	0.70	0.63	0.66
NC-H13-200	1.75	1.58	1.42	1.49
NC-H19-200	0.97	0.87	0.79	0.82
NC-H25-200	0.73	0.66	0.59	0.62
HC-N13-200	2.68	1.49	1.64	1.73
HC-N19-200	1.23	0.69	0.72	0.75
HC-N25-200	1.08	0.61	0.61	0.64
HC-H13-200	2.03	1.27	1.28	1.34
HC-H19-150	1.30	0.80	0.80	0.83
HC-H19-200	1.35	0.83	0.83	0.87
HC-H19-250	1.23	0.76	0.76	0.79
HC-H25-200	0.91	0.57	0.55	0.57
NC-N19-200-2	1.13	0.94	0.86	0.90
NC-N19-200-2.5	1.30	1.08	0.99	1.04
Average	1.31	0.95	0.91	0.95
CoV	0.36	0.33	0.34	0.34

On the contrary, the maximum dowel force is considerably underestimated for the specimens with small dowel rebar diameters (see specimens NC-N13-200, NC-H13-200, HC-N13-200, and HC-H13-200). This is primarily because Soroushian et al. [5] considered only the bearing failure of the concrete under dowel rebars [13] and did not include the kinking effect observed in the specimens with small dowel rebar diameters.

Unlike Soroushian et al., the maximum dowel force is overestimated in several cases in the prediction results of MC10 [12] and Randl [11]. This tendency is more evident for the specimens with large rebar diameters, such as NC-N25-200, NC-H25-200, HC-N25-200, and HC-H25-200. For these specimens, the ratio of the predictions to the test results of the maximum dowel force is larger than 1.50. The maximum dowel force is considerably underestimated only for the specimens with small rebar diameters, such as NC-N13-200, NC-H13-200, HC-N13-200, and HC-H13-200, because the kinking effect is not considered.

Consequently, for all test variables, the test results of the maximum dowel force for normal strength concrete and a dowel rebar diameter of 19 mm are in good agreement with all existing models considered in this study. The predictions of the existing models become more scattered as either dowel rebar diameter or the material strength of concrete or dowel rebars is changed. Therefore, further study is required to develop a more rational model to accurately represent the actual dowel behavior in a small concrete member.

6. Conclusions

In this study, an extensive experimental program was conducted to investigate the dowel behavior of the rebars embedded in a small concrete member. In the experimental program, 54 specimens were fabricated and tested. Test variables were concrete compressive strength, dowel rebar yield strength and diameter, concrete specimen thickness, and dowel rebar spacing. The test results were compared with the predictions of three existing models to investigate the applicability of the models. The results obtained in this study can be summarized as follows:

(i) Even though the three existing models considered concrete compressive strength, dowel rebar yield strength, and dowel rebar diameter simultaneously, the predicted maximum dowel forces were considerably different, particularly when a high strength material was used.

(ii) In all specimens, splitting cracks at failure occurred in the concrete under the dowel rebars regardless of the test variables. It can be inferred from the failure mode observed through the tests that splitting cracks have a strong effect on the dowel behavior of the rebars embedded in a small concrete member.

(iii) In the specimens with dowel rebars of small diameters (N13 and H13 series), the kinking effect was strong and the yielding of the dowel rebars occurred before the maximum dowel force was reached. In contrast, the specimens with dowel rebars of large diameters exhibited neither the yielding of the dowel rebars nor a strong kinking effect.

(iv) The test results showed that the maximum dowel force increased with concrete compressive strength and dowel rebar diameter, while the effect of the yield strength of dowel rebars was not evident.

(v) There were no considerable effects of specimen thickness and dowel rebar spacing on the maximum dowel force.
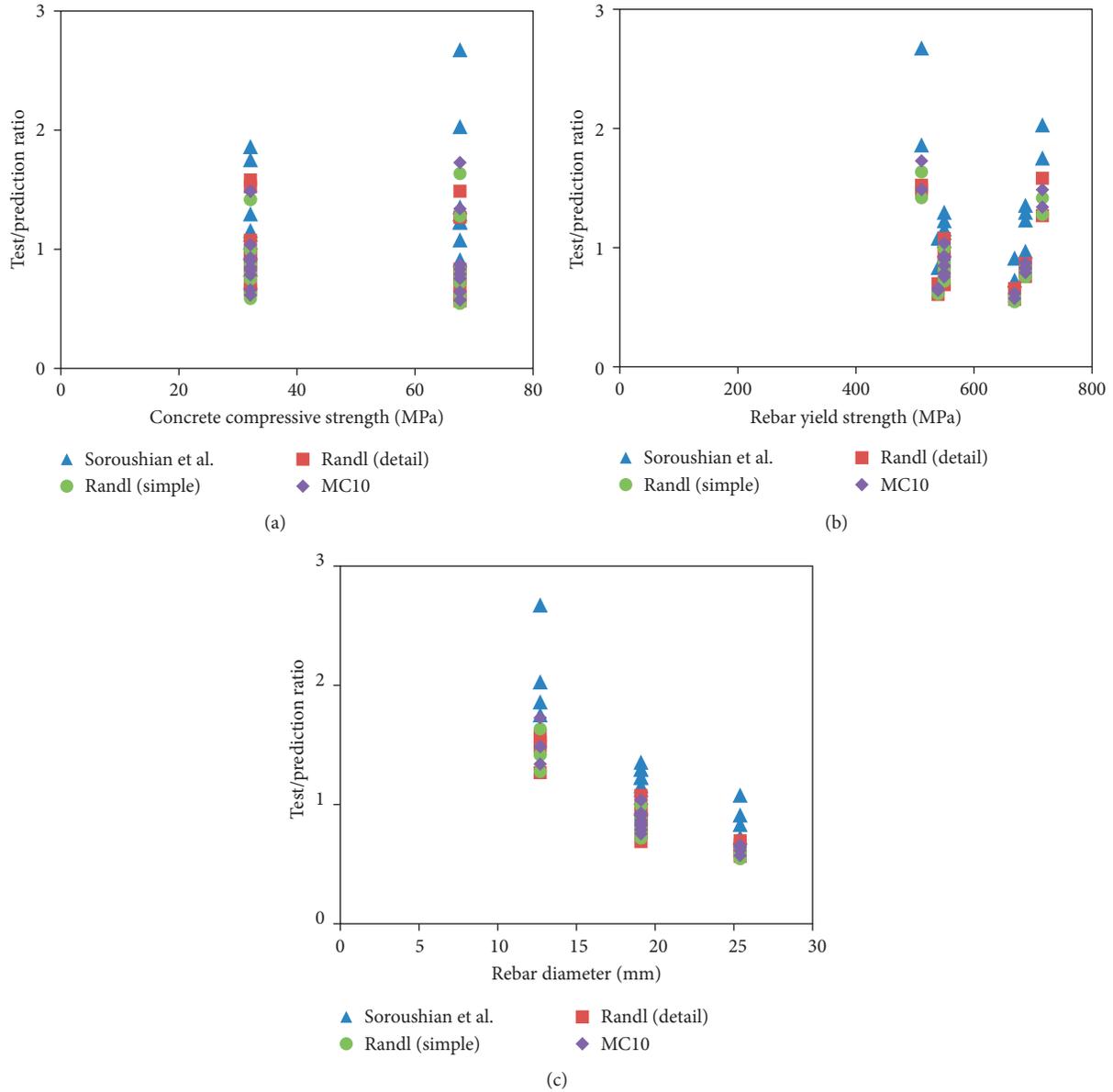
FIGURE 16: Effect of the test variables on the comparison for the maximum dowel force.

(vi) Unlike MC10 and Soroushian et al., who predicted that the shear slip corresponding to the maximum dowel force increases with dowel rebar diameter, the test results showed that shear slip at the maximum dowel force decreased as dowel rebar diameter increased.

(vii) The predictions of the existing models were significantly different from the maximum dowel forces measured in the tests. The existing models considerably underestimated the maximum dowel forces of the rebars with small diameters (N13 and H13 series) because the kinking effect was not considered. On the contrary, MC10 and Randl considerably overestimated the maximum dowel force of the dowel rebars with large diameters (N25 and H25 series).

(viii) The results presented in this paper will be useful for evaluating the actual shear capacity of the lateral supporting blocks in which dowel rebars are embedded. For a more reasonable design of lateral supporting blocks, a more rational model is required to represent the dowel behavior of the rebars embedded in a small concrete member.

Notations

A_s: Cross-sectional area of dowel rebar (mm^2)
c: Length of crushed concrete zone underneath dowel bar (mm)
$D(s)$:   Dowel force (N) for a given slip s (mm)
d_b: Diameter of dowel rebar (mm)
D_{max}:   Maximum dowel force (N)

E_s: Dowel bar modulus of elasticity (MPa)
f_b: Concrete bearing strength (MPa)
f_c': Concrete compressive strength (MPa)
f_{cwm}: Cube strength of concrete (MPa)
f_y: Yield strength of dowel rebar (MPa)
I: Second moment of inertia of dowel bar (mm4)
K_f: Concrete foundation modulus (MPa/mm)
L: Characteristic length of dowel bar (mm)
p_{max}: Maximum possible concrete pressure under dowel bar (MPa)
s_{max}: Slip at D_{max} (mm)
T: Dowel bar axial force (N)
T_y: Dowel bar yield axial force (N)
$\kappa_{2,max}$: Interaction coefficient for flexural resistance at s_{max}.

Conflicts of Interest

The authors declare that they have no conflicts of interest.

Acknowledgments

References

[1] K.-C. Lee, S. Y. Jang, and J. Lee, "Development of sliding slab track to reduce track-bridge interaction," in *Proceedings of the 2017 First International Conference on Rail Transportation*, Chengdu, China, July 2017.

[2] K.-C. Lee, S. Y. Jang, D.-K. Jung, H.-K. Byun, H.-K. Park, and T.-S. Yang, "Rail-structure interaction analysis of sliding slab track on bridge," in *Proceedings of the 2015 Joint Rail Conference*, San Jose, CA, USA., March 2015.

[3] K.-C. Lee, S. Y. Jang, J. Lee, and H.-S. Choi, "Comparative analysis of track-bridge interaction of sliding slab track and rail expansion joint for long-span railway bridge," *Journal of Computational Structural Engineering Institute of Korea*, vol. 29, no. 2, pp. 169–177, 2016, in Korean.

[4] S.-C. Lee, S. Y. Jang, and K.-C. Lee, "Evaluation of shear load carrying capacity of lateral supporting concrete block for sliding slab track considering construction joint," *Journal of Computational Structural Engineering Institute of Korea*, vol. 30, no. 1, pp. 55–61, 2017, in Korean.

[5] P. Soroushian, K. Obaseki, M. C. Rojas, and J. Sim, "Analysis of dowel bars acting against concrete core," *ACI Journal Proceedings*, vol. 83, no. 4, pp. 642–649, 1986.

[6] P. Soroushian, K. Obaseki, M. Rojas, and H. S. Najm, "Behavior of bars in dowel action against concrete cover," *ACI Structural Journal*, vol. 84, no. 2, pp. 170–176, 1987.

[7] E. E. Kazakoff, *Dowel Action in Reinforced Concrete Construction (Beam-Column Connections)*, Master thesis, p. 95, Department of Engineering, The University of British Columbia, Vancouver, Canada, 1971.

[8] S. Dei Poli, M. Di Prisco, and P. G. Gambarova, "Shear response, deformations, and subgrade stiffness of a dowel bar embedded in concrete," *ACI Structural Journal*, vol. 89, no. 6, pp. 665–675, 1992.

[9] T. Paulay, R. Park, and M. H. Phillips, "Horizontal construction joints in cast-in place reinforced concrete," *ACI Special Publication SP-42 Shear in Reinforced Concrete*, vol. 42, pp. 599–616, 1974.

[10] E. W. Bennett and S. Banerjee, "Strength of beam–column connections with dowel reinforcement," *Structural Engineer*, vol. 51, no. 4, pp. 133–139, 1976.

[11] N. Randl, "Load bearing behaviour of cast-in shear dowels," *Beton- und Stahlbetonbau*, vol. 102, no. 1, pp. 31–37, 2007.

[12] Comité Euro-International du Béton, *Fib Model Code for Concrete Structures 2010*, Ernst & Sohn, Berlin, 2013.

[13] P. Soroushian, K. Obaseki, and M. C. Rojas, "Bearing strength and stiffness of concrete under reinforcing bars," *ACI Materials Journal*, vol. 84, no. 3, pp. 179–184, 1987.

[14] ISO 6892-1:2016, *Metallic Materials—Tensile Testing—Part 1: Method of Test at Room Temperature*, International Organization for Standardization, Geneva, Switzerland, 2016.

[15] Comité Euro-International du Béton, *CEB-FIP Model Code 1990. Design Code*, Thomas Telford, London, 1993.

[16] European Standard EN 1994-1-1:2004, "Eurocode 4: design of composite steel and concrete structures- part 1-1: general rules and rules for buildings, annex B.2," *Tests on Shear Connectors*, pp. 110–113, 2009.

[17] JCSS, *JCSS Probabilistic Model Code: Joint Committee on Structural Safety*, JCSS, Japan, 2001.

[18] M. Holický, J. V. Retief, and M. Sýkora, "Assessment of model uncertainties for structural resistance," *Probabilistic Engineering Mechanics*, vol. 45, pp. 188–197, 2016.

Research Article

Investigation of Microstructural Damage in Ultrahigh-Performance Concrete under Freezing-Thawing Action

Chunping Gu [iD],[1,2] **Wei Sun,**[3] **Liping Guo** [iD],[3] **Qiannan Wang,**[3] **Jintao Liu,**[1,2] **Yang Yang** [iD],[1,2] **and Tao Shi**[1,2]

[1]*College of Civil Engineering and Architecture, Zhejiang University of Technology, Hangzhou 310023, China*
[2]*Key Laboratory of Civil Engineering Structures and Disaster Prevention and Mitigation Technology of Zhejiang Province,*
 Zhejiang University of Technology, Hangzhou 310023, China
[3]*School of Materials Science and Engineering, Southeast University, Nanjing 211189, China*

Correspondence should be addressed to Liping Guo; guoliping691@163.com

This work aims to investigate the damage in ultrahigh-performance concrete (UHPC) caused by freezing-thawing action. Freezing-thawing tests were carried out on UHPCs with and without steel fibers. Mercury intrusion porosimetry (MIP), scanning electron microscopy (SEM), and X-ray computed tomography (X-ray CT) were applied to detect the microstructure of the UHPC matrix before and after the freezing-thawing tests. The results showed that UHPC possessed very excellent freezing-thawing resistance due to its dense microstructure. After the freezing-thawing action, cracks occurred and were prone to initiate at the sand-paste interface in the UHPC matrix. MIP results also indicated that cracks appeared in the UHPC matrix after the freezing-thawing action. The number of defects that can be seen by X-ray CT increased in UHPC after the freezing-thawing action as well. The mismatch of the thermal expansion coefficients of the aggregate and the paste is considered to be the reason for the cracking at the sand-paste interface. The steel fibers in UHPC inhibited the propagation of cracks in the matrix and improved the freezing-thawing performance of UHPC.

1. Introduction

Ultrahigh-performance concrete (UHPC) is a novel type of cementitious material, which shows extremely excellent mechanical properties and durability [1, 2]. Due to its excellent performance, UHPC is considered to be a sustainable and economical material for various structures, such as hydraulic structures, thin-layer structures, marine structures, and military structures [3].

UHPC also can be used in some cold regions because of its great resistance to freezing-thawing damage [4, 5]. In cold regions, the freezing-thawing action is a very common cause for the deterioration of concrete structures. The damage process in normal concrete under freezing-thawing action has been widely studied, from the point of views of both microstructure and macroproperties [6–8]. Two types of damage, that is, surface scaling and internal cracking, would

be induced when the concrete undergoes freezing-thawing cycles. In order to quantify these types of damage caused by freezing-thawing action, several methods have been developed. Normally, the surface scaling is evaluated by the mass loss, and the internal cracking is reflected by the change of relative dynamic modulus of elasticity [9, 10]. The internal cracks and pore structures in mortar or concrete damaged by freezing-thawing action also have been characterized by various techniques, such as mercury intrusion porosimetry (MIP) and scanning electron microscopy (SEM) [11–13]. These efforts were mostly made on concretes with a moderate strength, while the freezing-thawing microstructural damage in UHPC was rarely studied. Since UHPC is a promising material with wide potential applications, it is of significance to investigate the damage process of UHPC exposed to freezing-thawing action, especially from the microstructural point of view.

The aim of this paper is to investigate the freezing-thawing resistance of UHPC and to reveal the microstructure evolution of UHPC under the freezing-thawing action. It was anticipated that microstructural observations could improve the understanding of the deterioration mechanism of UHPC subjected to freezing-thawing action. In this paper, SEM was used to detect the cracks caused by freezing-thawing action in UHPC. MIP and X-ray computed tomography (X-ray CT) were applied to track the pore structure evolution of UHPC during the freezing-thawing action. Furthermore, based on the test results, the role of steel fibers in the freezing-thawing resistance of UHPC was also discussed in the paper.

2. Materials and Methods

2.1. Materials. UHPCs with and without steel fibers were prepared in the study. Type P•II 52.5R Portland cement, Class F fly ash (FA), and silica fume (SF) were used as cementitious materials. The chemical and physical properties of the cement, FA, and SF are shown in Table 1 [14]. The addition of FA could reduce the hydration heat and improve the workability of UHPC. The aggregates were river sand, whose particle size was smaller than 2.36 mm. The superplasticizer was a type of the liquid agent with a solid content of 28%. Copper-coated steel fibers were used to improve the ductility of UHPC, and the length and diameter of the fibers were 13 mm and 0.2 mm, respectively.

The proportions of UHPCs are shown in Table 2. All the UHPCs had the same matrix, while UHPC-1%, UHPC-2%, and UHPC-3% were reinforced with different amounts of steel fibers. In order to make the comparison more clearly, the proportion was given in a percentage form. Abbreviations are used in Table 2, that is, C = cement, B = binder, FA = fly ash, SF = silica fume, RS = river sand, Sup = superplasticizer, W = water, and V_f = volume fraction of steel fibers. The binder means the sum of the cement, FA, and SF. The cement usages of UHPCs were more or less the same, which were about 540 kg/m^3. The specimens were cast into 40 mm × 40 mm × 160 mm molds, and after demolding, they were cured in the standard condition (20°C, RH > 95%) for 90 days.

2.2. Mechanical Tests. Flexural and compressive tests were performed following the standard GB/T17671-1999 [15]. Firstly, the three-point bending test was performed to determine the flexural strength. Afterwards, two portions from each specimen broken in flexure were used for compressive tests. Three specimens of each batch were tested.

2.3. Freezing-Thawing Tests. The freezing-thawing tests were performed based on the standard GB/T50082-2009 [16]. The temperature range of a freezing-thawing cycle was −20°C~20°C, and one cycle lasts about 4 hours. After enduring a certain number of freezing-thawing cycles, the mass and relative dynamic modulus of elasticity of the specimens were measured. In the standard, 300

Table 1: Chemical and physical properties of the cement, FA, and SF.

		Binder		
		Cement	Fly ash	Silica fume
Chemical composition (%)	SiO$_2$	20.40	54.88	94.48
	Al$_2$O$_3$	4.70	26.89	0.27
	Fe$_2$O$_3$	3.38	6.49	0.83
	CaO	64.70	4.77	0.54
	MgO	0.87	1.31	0.97
	SO$_3$	1.88	1.16	0.8
	K$_2$O	0.45	1.05	—
	Na$_2$O	0.38	0.88	—
	Loss	3.24	2.56	2.11
Physical properties	Specific density (kg/m^3)	3130	2240	2500
	Specific surface area (m^2/kg)	362	454	22000

Table 2: Mixture proportion of UHPCs.

	C/B	FA/B	SF/B	RS/B	Sup/B	W/B	V_f
Plain UHPC	0.5	0.4	0.1	1.2	3.5%	0.16	0%
UHPC-1%	0.5	0.4	0.1	1.2	3.5%	0.16	1%
UHPC-2%	0.5	0.4	0.1	1.2	3.5%	0.16	2%
UHPC-3%	0.5	0.4	0.1	1.2	3.5%	0.16	3%

freezing-thawing cycles were recommended for testing the freezing-thawing performance of normal concrete. But UHPC normally does not degrade at 300 cycles. Hence, the number of freezing-thawing cycles was increased to 800 in this study.

2.4. SEM. A Sirion field emission scanning electron microscopy was used for the imaging of the cracks induced by the freezing-thawing action. After enduring 800 freezing-thawing cycles, the UHPC specimens were crashed, and small samples were chosen for the SEM tests. Secondary electron images were taken at the fractured surfaces.

2.5. MIP. The porosities and pore size distributions of UHPC specimens were detected with MIP. Crashed pieces of the matrix of UHPCs were served as samples. The samples were immersed in acetone for 7 days to stop the hydration. Then, they were oven-dried at 50°C for 3 days. The dried samples were used for the MIP tests, which were performed with Micromeritics AutoPore IV 9500. The contact angle was set to be 130°, and the detected pore sizes were between 3 nm and 360 μm.

2.6. X-Ray CT. X-ray CT was employed to detect the distribution of defects in UHPC. The YXLON microfocus X-ray CT system was used to scan the UHPC specimens before and after the freezing-thawing tests. The X-ray peak energy and current were 195 kV and 0.41 mA, respectively. The sample was a 40 mm × 40 mm × 160 mm prism, and the obtained voxel size was 64 μm × 64 μm × 64 μm.
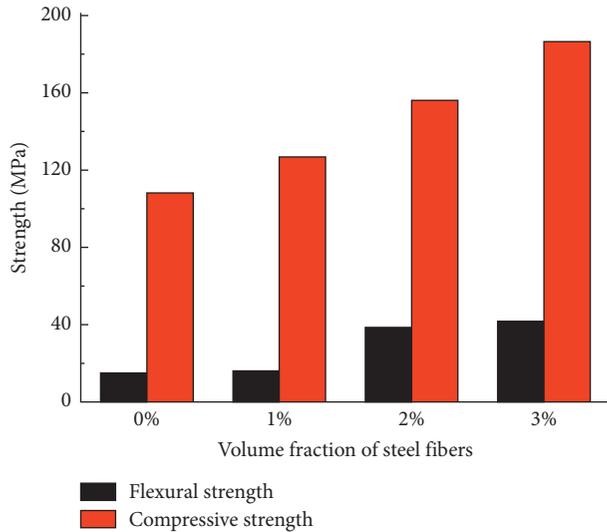
FIGURE 1: Compressive strength and flexural strength of UHPC specimens.
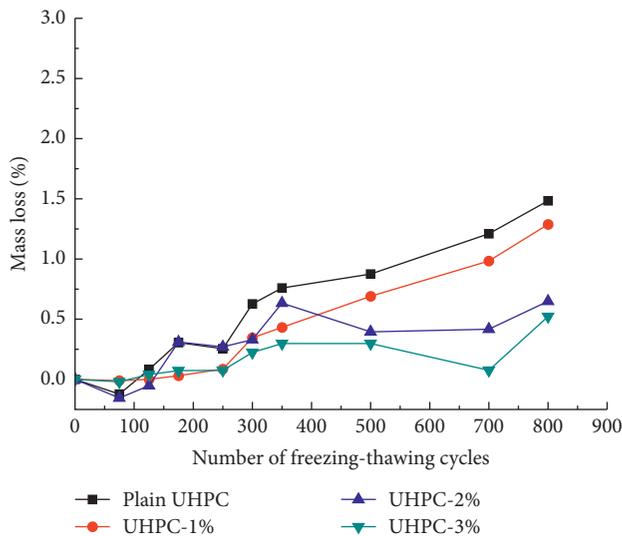
FIGURE 2: Mass loss of UHPCs at different freezing-thawing cycles.

3. Results and Discussion

3.1. Mechanical Properties of UHPC. Figure 1 shows the compressive strength and flexural strength of the UHPC specimens. The addition of steel fibers significantly increased the compressive and flexural strengths of UHPC. Compared to plain UHPC, the compressive and flexural strengths of UHPC-3% were improved by 72.4% and 178.7%, respectively. The strengthening effect of steel fibers in UHPC is much more significant than that in normal concrete [17] because of the strong bond between the fibers and matrix in UHPC.

3.2. Freezing-Thawing Performance of UHPC. The test results showed that UHPC exhibited great freezing-thawing resistance. Figure 2 demonstrates the mass loss of UHPC specimens during the freezing-thawing tests. The mass loss
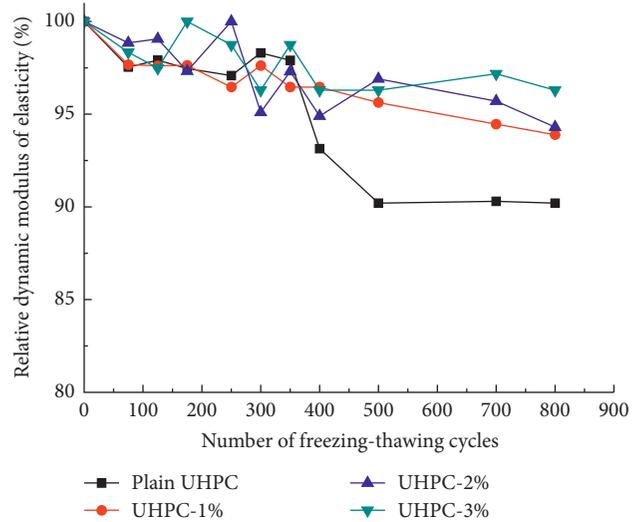
FIGURE 3: Relative dynamic modulus of elasticity of UHPCs at different freezing-thawing cycles.

of UHPC specimens increased slightly with the number of freezing-thawing cycles. After enduring 800 cycles, the mass losses of UHPC specimens were all less than 1.5%. The surface scaling was the main reason for the mass loss. Figure 3 shows the evolution of the relative dynamic modulus of elasticity of UHPC specimens at different freezing-thawing cycles. The relative dynamic modulus of elasticity of UHPC specimens was reduced very slightly with the increase of the cycles until it reached 350 cycles. It suggested that UHPCs did not show significant internal deterioration before that. After the freezing-thawing tests, the relative dynamic modulus of elasticity was approximately more than 90% for all UHPC specimens.

It can also be seen from Figures 2 and 3 that the presence of steel fibers could improve the freezing-thawing performance of UHPC. After going through 800 freezing-thawing cycles, UHPC with higher dosage of steel fibers exhibited lower mass loss and higher relative dynamic modulus of elasticity. The crack-bridging effect of steel fibers plays an importance role for the improvement of freezing-thawing resistance of UHPC.

The findings from other literatures also indicated that UHPC exhibited very excellent freezing-thawing resistance [18–21]. After enduring 300 freezing-thawing cycles, the relative dynamic modulus of elasticity of UHPCs normally did not decrease, and the mass losses were less than 0.5% [18, 19]. In order to clearly reveal the freezing-thawing performance of UHPC, more cycles were adopted in the freezing-thawing tests by several studies. After 600 freezing-thawing cycles, the relative dynamic modulus of elasticity and mass losses of UHPCs with different curing regimes did not obviously change [4, 20], which implied that the degradation in UHPC induced by freezing-thawing cycles was negligible. After 1000 freezing-thawing cycles, the relative dynamic modulus of elasticity of UHPC was 90%, and the compressive strength of UHPC reduced by 6% [21]. Generally, the UHPCs with heat curing have better freezing-thawing performance than standard-cured UHPCs [18, 20].

(a)   (b)
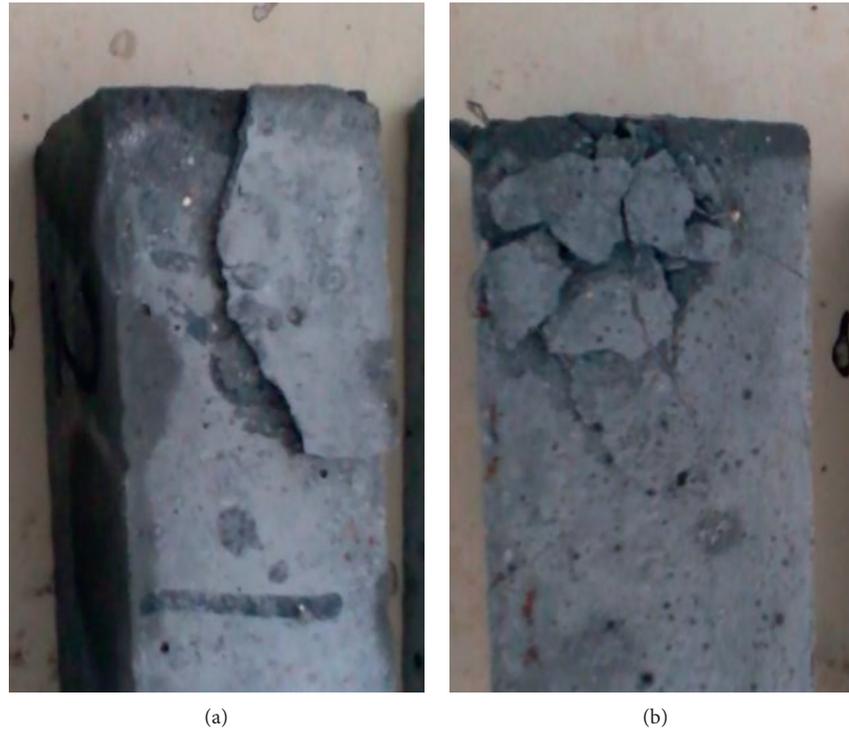
FIGURE 4: Cracked UHPC specimens (40 mm × 40 mm × 160 mm) after enduring 250 freezing-thawing cycles: (a) plain UHPC and (b) UHPC-1%.

The hydration products in UHPC with heat curing were denser than those with standard curing; hence, the freezing-thawing performance of heat-cured UHPC was extremely excellent, and no obvious freezing-thawing damage could be observed. In this study, the standard curing were adopted, so the UHPCs degraded a little after 800 freezing-thawing cycles, and the test results were close to those in the literatures [21].

Besides the test results, an unexpected phenomenon was observed during the freezing-thawing experiments. One plain UHPC specimen and one UHPC-1% specimen were cracked severely after 250 freezing-thawing cycles, as seen in Figure 4. The crack pattern looked like being hit by an impact load. All the other specimens were in good condition, so the data for these two specimens were eliminated when calculating the mass loss and relative dynamic modulus of elasticity.

The reason for this phenomenon is still under investigation. The probable reason lies in the existence of big river sand particles (max. 2.36 mm) or large air pores in UHPC [22]. Both big river sand particles and large air pores could influence the homogeneity of UHPC and arouse stress concentration in UHPC, resulting in sudden severe cracking. The brittleness of the UHPC matrix also contributes to this phenomenon. Based on this finding, at least 2% of steel fibers is recommended to add in UHPC in order to ensure the safety of UHPC structures in cold regions.

3.3. Cracks in UHPC Induced by Freezing-Thawing Action. Before the freezing-thawing action, UHPC had a very dense
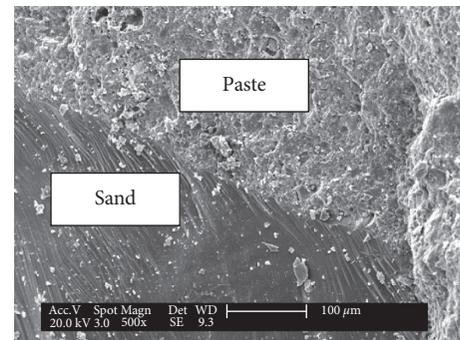
FIGURE 5: The bond between the sand and paste in plain UHPC.

microstructure. Capillary pores and $Ca(OH)_2$ crystals were hardly seen, and the interfacial transition zones (ITZs) almost disappeared in UHPCs. Figure 5 shows the bond between the sand and the paste in plain UHPC, and Figure 6 shows the bond between the fiber and the matrix in UHPC-2%. It was observed that both the sand-paste and fiber-matrix bonds were very intense, and ITZs were difficult to tell. The previous nanoindentation study proved that the micromechanical properties of the ITZ and the bulk paste of the UHPC were similar to each other [23], which indicated that the weak ITZ disappeared in UHPC. This is one of the reasons why UHPC possesses extremely excellent mechanical properties and resistance to aggressive agents.

In addition to the dense microstructure, spherical air voids also can be observed in UHPC as shown in Figure 7. This image was taken from a plain UHPC sample, and air
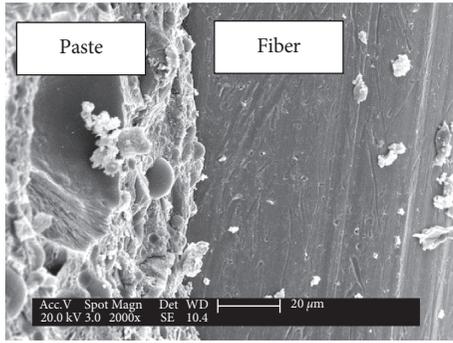
FIGURE 6: The bond between the fiber and the matrix in UHPC-2%.

FIGURE 7: Air void in plain UHPC.

FIGURE 8: Microcracks in plain UHPC after the freezing-thawing tests.

FIGURE 9: Pore size distribution of plain UHPC and UHPC-2% matrix before and after freezing-thawing tests.

voids also existed in UHFC with steel fibers. The fresh UHPC mixture shows higher viscosity than normal concrete, so air bubbles are easily to be trapped in the UHPC mixture during casting. Researches have shown that the incorporation of air voids could improve the freezing-thawing resistance of normal concrete [13, 24].

After enduring 800 freezing-thawing cycles, microcracks can be found in plain UHPC. An example is given in Figure 8. The crack was initiated around the sand particle and went through an air void. Cracks at the ITZ between the fiber and matrix in UHPC with fibers were also detected with SEM. But it was difficult to determine whether the crack was caused by the freezing-thawing action or by sampling. The samples for SEM were prepared by crashing the UHPC specimen. The steel fiber might debond during crashing. For the plain UHPC sample, cracks mostly go through the fine aggregates (as shown in Figure 5) when undergoing mechanical load. Hence, the cracks around aggregates are more probably induced by freezing-thawing action.

3.4. Pore Structure Evolution of UHPC due to the Freezing-Thawing Action. The porosity and pore size distribution of plain UHPC and UHPC-2% matrices before and after the freezing-thawing tests were investigated with MIP. Before the freezing-thawing tests, the total porosities of plain UHPC and UHPC-2% matrix were 1.98% and 1.85%, respectively. After the tests, the total porosities of plain UHPC and UHPC-2% matrix increased to 6.05% and 3.32%, respectively. The increase in porosity due to freezing-thawing action was

reduced by steel fibers. Figure 9 shows the pore size distribution of plain UHPC and UHPC-2% before and after the freezing-thawing tests. It can be seen that, before the tests, most of the pores in plain UHPC and UHPC-2% matrix were gel pores, whose size was smaller than 10 nm. After being subjected to 800 freezing-thawing cycles, several new peaks appeared in the pore size distribution curve for both plain UHPC and UHPC-2% matrix. This implied that cracks were generated during the freezing-thawing tests. Compared with UHPC-2% matrix, more cracks existed in plain UHPC, which confirmed that the presence of steel fibers enhanced the freezing-thawing resistance of UHPC. It also can be seen from Figure 9 that, after the freezing-thawing tests, the peak for gel pores in the size distribution curve disappeared for both plain UHPC and UHPC-2% matrices. This may result from the ongoing hydration during the freezing-thawing tests. Water saturated condition was applied in the freezing-thawing tests, so UHPC could go on hydration and gel pores continued to be refined. Due to the limitation of the MIP test, it cannot detect pores smaller than 3 nm in this study.

It should be noted that the MIP only presents approximate results of the crack information in UHPC samples. As shown in Figure 8, cracks may go across the air voids, which would act as ink-bottle pores in the MIP test and influence the MIP results. In spite of this deviation, the MIP results still indicated that cracks existed in the freezing-thawing damaged UHPC samples.

3.5. Defects Evolution of UHPC due to the Freezing-Thawing Action. The 3D distribution of defects in UHPCs before and after the freezing-thawing tests was detected with X-ray CT. Figure 10 shows the distribution of defects in plain UHPC before the freezing-thawing tests. Because of the resolution limitation, the minimum volume of the defects was $0.002 \, mm^3$. The defects were mostly the air voids in the specimen.

Due to the excellent freezing-thawing resistance of UHPC, the difference between the 3D defects distribution images of UHPC specimens before and after the freezing-thawing action was difficult to distinguish with naked eyes. Nevertheless, the data about the total defects volume and defects size distribution before and after the freezing-thawing action were still comparable. Table 3 shows the volume fraction of defects in UHPC specimens before and after freezing-thawing tests. The defects volume in UHPCs all increased after the freezing-thawing action. The increment for plain UHPC was 43.1%, while the increment for UHPC-3% was only 9.86%. Compared to UHPC-3%, more defects which can be detected with X-ray CT occurred in plain UHPC after the freezing-thawing action.

The defects volume distributions of UHPC specimens before and after freezing-thawing action were shown in Figure 11. The *y*-axis is the number of defects in a $40 \, mm \times 40 \, mm \times 160 \, mm$ UHPC specimen. It was noticed that most of the defects in UHPC were smaller than $0.1 \, mm^3$. Before the freezing-thawing action, UHPC-3% had the largest amount of defects. This may be due to its relatively lower workability, which resulted from the addition of more steel fibers. After the freezing-thawing action, the number of defects all increased for the UHPC specimens. The defects with volume smaller than $0.1 \, mm^3$ had the most significant increase. This was because that some smaller defects, which could not be detected by X-ray CT at first, became larger due to the freezing-thawing action. During the freezing-thawing action, cracks originated at the interface between the paste and aggregates and may go through the air pores, leading to the coalescing of two (or more) separated air voids. If the crack kept propagating, more air voids and cracks would be connected and form 3D crack networks. This phenomenon was observed in normal concrete [12]. Nevertheless, because of the presence of steel fibers and homogeneous microstructure, the crack propagation process in fiber-reinforced UHPC is much slower than that in normal concrete. As shown in Figure 11, the experimental results also proved that the defects in plain UHPC increased more than those in UHPC-3%. The presence of steel fibers improved the resistance of UHPC to freezing-thawing damage.
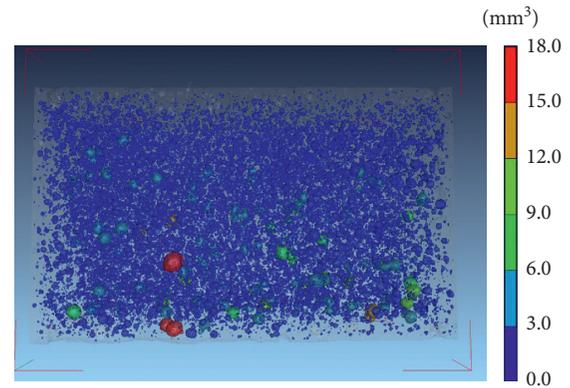
FIGURE 10: 3D defects distribution of a plain UHPC specimen ($40 \, mm \times 40 \, mm \times 160 \, mm$) before the freezing-thawing tests.

4. Discussions

According to the findings in this study, the presence of steel fibers improved the freezing-thawing performance of UHPC. Due to the low water-to-binder ratio and the pozzolanic reactivity of SF, the interfaces between the steel fibers and the matrix were very intense so that the fibers could bridge the cracks very efficiently. Hence, the crack propagation process could be inhibited if the fibers were presented, and more fibers would lead to higher cracking resistance. It is also the case for UHPC under freezing-thawing action. The microcracks induced by freezing-thawing cycles could be effectively bridged by the fibers so that the freezing-thawing performance of UHPC improved. On the other hand, if fibers were not present or not enough, UHPC might be damaged very suddenly (as shown in Figure 4) because of its high brittleness.

The hydraulic pressure and osmotic pressure are considered to be the main reasons for the deterioration of normal concrete subjected to freezing-thawing cycles [25]. When the stress aroused by these two kinds of pressure is higher than the tensile strength of concrete, cracking may occur. But these two pressures are both considered to originate from the icing of the water in the capillary pores of concrete. It is not the case for UHPC. It is well known that the freeze point of water in the porous material is related to the pore size, and it is estimated that water in gel pores does not freeze above $-78°C$ [26]. For UHPC, large capillary pores are hardly seen [3, 27], and most of the pores in UHPC are gel pores. So when UHPC is subjected to freezing conditions, most of the water in gel pores will not turn into ice but continue to exist as liquid water. Therefore, the hydraulic pressure and osmotic pressure are not the main cause for the cracking in UHPC under freezing-thawing action.

According to the structural characteristics of UHPC, it may make more sense that the crack is resulted from the mismatch of the thermal expansion coefficients of the sand and paste. The thermal expansion coefficient of UHPC paste is between 15 and $20 \, \mu m \cdot m^{-1} \cdot K^{-1}$ [28], while the thermal expansion coefficient of natural sand is around $10 \, \mu m \cdot m^{-1} \cdot K^{-1}$ [26], which is much lower than that of

TABLE 3: Total volume fraction of defects in UHPC specimens before and after freezing-thawing tests.

	Plain UHPC	UHPC-1%	UHPC-2%	UHPC-3%
Before freezing-thawing tests	1.67%	2.12%	1.94%	2.84%
After freezing-thawing tests	2.39%	2.73%	2.56%	3.12%
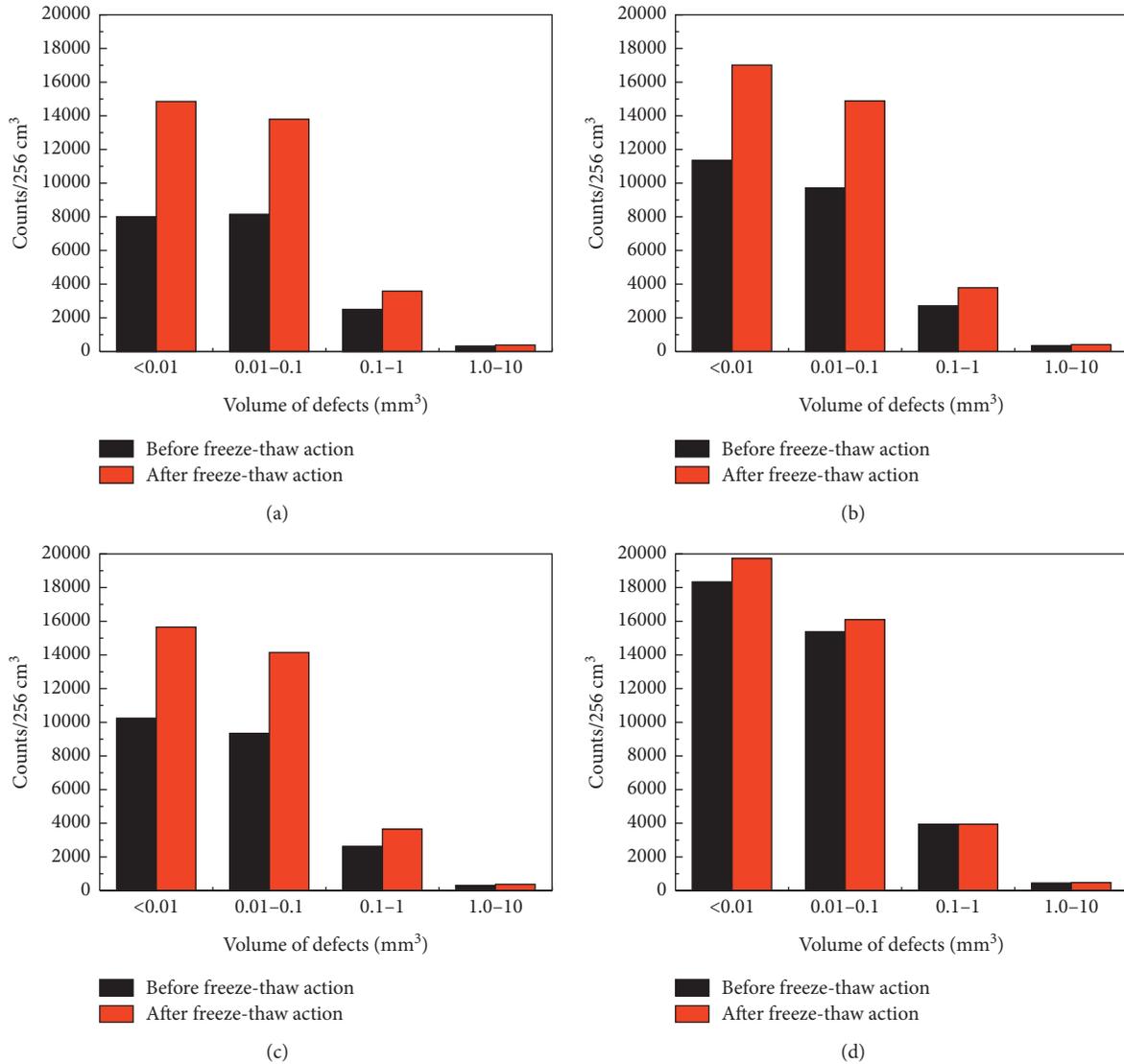
FIGURE 11: Defects volume distributions of UHPC specimens before and after freezing-thawing tests: (a) plain UHPC, (b) UHPC-1%, (c) UHPC-2%, and (d) UHPC-3%.

UHPC paste. The thermal expansion coefficients of the steel fiber and UHPC matrix are around $12\,\mu m \cdot m^{-1} \cdot K^{-1}$ and $11\,\mu m \cdot m^{-1} \cdot K^{-1}$, respectively [3]; hence, the stress aroused at the fiber-matrix interface is much lower than that at the sand-paste interface. Under the freezing-thawing action, the deformations of the sand and paste were different from each other, which aroused stress at the interface. It was more like a fatigue load at the interface of the aggregates and paste, when the temperature went up and down. Cracks initiated at the interface between the paste and aggregates, and may go through the air pores. When

the freezing-thawing action is going on, cracks may connect to each other, and UHPC will fail in the end.

The approximate thermal expansion coefficients of commonly used aggregates were summarized as follows: $5\,\mu m \cdot m^{-1} \cdot K^{-1}$ for limestone; $6\,\mu m \cdot m^{-1} \cdot K^{-1}$ for basalt and gabbro; $7\,\mu m \cdot m^{-1} \cdot K^{-1}$ for granite; $9\,\mu m \cdot m^{-1} \cdot K^{-1}$ for dolerite; $10\,\mu m \cdot m^{-1} \cdot K^{-1}$ for sandstone and natural gravel; and $11\,\mu m \cdot m^{-1} \cdot K^{-1}$ for quartzite [26]. Hence, it is better to use sandstone, natural gravel, and quartzite as aggregates to prepare UHPC from the point of view of freezing-thawing performance. The use of limestone, basalt, and gabbro

should be avoided when preparing UHPCs that serve in cold regions.

5. Conclusions

This paper investigated the macroperformance and microstructure of UHPC before and after the freezing-thawing action. The following conclusions can be drawn:

(1) Compared to normal concrete, UHPC showed excellent freezing-thawing resistance, no matter steel fiber-reinforced or not. But unexpected cracking happened to one plain UHPC specimen and one UHPC-1% specimen. The reason of the cracking is worthy of further studying.

(2) Before the freezing-thawing action, UHPC had a very dense microstructure, but large amounts of air voids were trapped in UHPC. After going through 800 freezing-thawing cycles, cracks were induced in UHPC and prone to initiate at the ITZ between the aggregates and paste.

(3) The cracking in UHPC under freezing-thawing action may arise from the mismatch of the thermal expansion coefficients of the aggregates and paste. Sandstone, natural gravel, and quartzite were recommended to use as aggregates to prepare UHPC in cold regions. The presence of steel fibers could restrain the initiation and propagation of the cracks in UHPC, resulting in a great improvement of freezing-thawing resistance.

Conflicts of Interest

The authors declare that they have no conflicts of interest.

Acknowledgments

References

[1] N. Roux, C. Andrade, and M. A. Sanjuan, "Experimental study of durability of reactive powder concretes," *Journal of Materials in Civil Engineering*, vol. 8, no. 1, pp. 1–6, 1996.

[2] J. Pierard, B. Dooms, and N. Cauberg, "Durability evaluation of different types of UHPC," in *Proceedings of the RILEM-fib-AFGC International Symposium on Ultra-High Performance Fiber-Reinforced Concrete*, pp. 275–284, Marseille, France, October 2013.

[3] C. Gu, G. Ye, and W. Sun, "Ultrahigh performance concrete-properties, applications and perspectives," *Science China Technological Sciences*, vol. 58, no. 4, pp. 587–599, 2015.

[4] B. Graybeal and J. Tanesi, "Durability of an ultrahigh-performance concrete," *Journal of Materials in Civil Engineering*, vol. 19, no. 10, pp. 848–854, 2007.

[5] M. Alkaysi, S. El-Tawil, Z. Liu, and W. Hansen, "Effects of silica powder and cement type on durability of ultra high performance concrete (UHPC)," *Cement and Concrete Composites*, vol. 66, pp. 47–56, 2015.

[6] H. Cai and X. Liu, "Freeze-thaw durability of concrete: ice formation process in pores," *Cement and Concrete Research*, vol. 28, no. 9, pp. 1281–1287, 1998.

[7] X. Ren, X. Wan, and T. Zhao, "Review of mechanism and mathematical model for salt scaling and freezing-thawing damage of concrete," *Concrete*, vol. 20, no. 9, pp. 15–18, 2012, in Chinese.

[8] L. Wang, Y. Cao, Z. Wang, and P. Du, "Evolution and characterization of damage of concrete under freeze-thaw cycles," *Journal of Wuhan University of Technology-Materials Science Edition*, vol. 28, no. 4, pp. 710–714, 2013.

[9] W. Sun, R. Mu, X. Luo, and C. Miao, "Effect of chloride salt, freeze-thaw cycling and externally applied load on the performance of the concrete," *Cement and Concrete Research*, vol. 32, no. 12, pp. 1859–1864, 2002.

[10] W. Sun, Y. Zhang, H. Yan, and R. Mu, "Damage and damage resistance of high strength concrete under the action of load and freeze-thaw cycles," *Cement and Concrete Research*, vol. 29, no. 9, pp. 1519–1523, 1999.

[11] S. Jacobsen, J. Marchand, and H. Hornain, "SEM observations of the microstructure of frost deteriorated and self-healed concretes," *Cement and Concrete Research*, vol. 25, no. 8, pp. 1781–1790, 1995.

[12] I. Vegas, J. Urreta, M. Frías, and R. García, "Freeze-thaw resistance of blended cements containing calcined paper sludge," *Construction and Building Materials*, vol. 23, no. 8, pp. 2862–2868, 2009.

[13] M. A. B. Promentilla and T. Sugiyama, "X-ray microtomography of mortars exposed to freezing-thawing action," *Journal of Advanced Concrete Technology*, vol. 8, no. 2, pp. 97–111, 2010.

[14] C. Gu, W. Sun, L. Guo, and Q. Wang, "Effect of curing conditions on the durability of ultra-high performance concrete under flexural load," *Journal of Wuhan University of Technology-Materials Science Edition*, vol. 31, no. 2, pp. 278–285, 2016.

[15] GB/T17671-1999, *Standard Test Method for Compressive Strength of Cement Mortar*.

[16] GB/T50082-2009, *Standard Test Method for Determining Long-Term Performance and Durability of Ordinary Concrete*.

[17] P. S. Song and S. Hwang, "Mechanical properties of high-strength steel fiber-reinforced concrete," *Construction and Building Materials*, vol. 18, no. 9, pp. 669–673, 2004.

[18] T. M. Ahlborn, D. L. Misson, E. J. Peuse, and C. G. Gilbertson, "Durability and strength characterization of ultra-high performance concrete under variable curing regimes," in *Proceedings of the 2nd International Symposium on Ultra High Performance Concrete*, pp. 197–204, Kassel, Germany, March 2008.

[19] W. Meng, M. Valipour, and K. H. Khayat, "Optimization and performance of cost-effective ultra-high performance concrete," *Materials and Structures*, vol. 50, no. 1, p. 29, 2017.

[20] S. Liu, W. Sun, W. Lin, and J. Lai, "Preparation and durability of a high performance concrete with natural ultra-fine particles," *Journal of the Chinese Ceramic Society*, vol. 11, pp. 1080–1085, 2003.

[21] M. G. Lee, Y. C. Wang, and C. T. Chiu, "A preliminary study of reactive powder concrete as a new repair material," *Construction and Building Materials*, vol. 21, no. 1, pp. 182–189, 2007.

[22] C. Gu, W. Sun, L. Guo, and J. Zong, "X-ray computer tomography studies of meso-defects evolution of UHPCC due to freezing-thawing action," in *Proceedings of the International Conference on Microstructural-Related Durability of Cementitious Composites*, pp. 317–323, Amsterdam, The Netherlands, April 2012.

[23] S. Zhao and W. Sun, "Nano-mechanical behavior of a green ultra-high performance concrete," *Construction and Building Materials*, vol. 63, pp. 150–160, 2014.

[24] N. P. Mayercsik, M. Vandamme, and K. E. Kurtis, "Assessing the efficiency of entrained air voids for freeze-thaw durability through modeling," *Cement and Concrete Research*, vol. 88, pp. 43–59, 2016.

[25] D. Niu, L. Jiang, M. Bai, and Y. Miao, "Study of the performance of steel fiber reinforced concrete to water and salt freezing condition," *Materials and Design*, vol. 44, pp. 267–273, 2012.

[26] P. K. Mehta and P. J. Monteiro, *Concrete: Microstructure, Properties and Materials*, McGraw-Hill, New York, NY, USA, 3rd edition, 2006.

[27] D. Wang, C. Shi, Z. Wu, J. Xiao, Z. Huang, and Z. Fang, "A review on ultra high performance concrete: part II. Hydration, microstructure and properties," *Construction and Building Materials,* vol. 96, pp. 368–377, 2015.

[28] I. Maruyama and A. Teramoto, "Temperature dependence of autogenous shrinkage of silica fume cement pastes with a very low water-binder ratio," *Cement and Concrete Research*, vol. 50, pp. 41–50, 2013.

Research Article

Investigation of Cement-Emulsified Asphalt in Plastic Concrete

Xiaohu Yan,[1,2] **Zaiqin Wang** ⓘ **,**[1,2] **Meijuan Rao** ⓘ **,**[3] **and Mingxia Li**[2]

[1]*College of Water Conservancy and Hydropower Engineering, Hohai University, Nanjing 210098, China*
[2]*Yangtze River Scientific Research Institute, Wuhan 430010, China*
[3]*State Key Laboratory of Silicate Materials for Architecture, Wuhan University of Technology, Wuhan 430070, China*

Correspondence should be addressed to Meijuan Rao; raomeijuanding@163.com

The mechanical, mesodamage, and the microproperties of cement-emulsified asphalt concrete have been investigated by computed tomography (CT), scanning electron microscopy (SEM), X-ray diffraction (XRD), and thermogravimetric analysis (TG) in this work. Emulsified asphalt delayed the hydration of cement, making the early compressive strength of concrete develop slowly. However, the concrete compressive strength increased rapidly with the demulsification of emulsified asphalt. The damage stages of condense, expansion of volume, rapid crack propagation, and damage by real-time scanning have been observed. The CT mean value of the place near the lower end face suffered a larger decline but a smaller decline to the upper part of the sample. The evolution of concrete suffering damage to failure is a gradual development process, and no sharp expansion of brittle failure. The unhydrated cement, incorporation asphalt, fibrous C–S–H gel, CH, needle-shaped ettringite, and other hydration products were interwoven to constitute emulsified asphalt-cement paste, forming a spatial structure.

1. Introduction

With the development of social productive forces, there is a gradual improvement in the quality of material used for constructing buildings. However, there are still some limitations in the building materials, leading to hindrances in the development of strong structural forms. Superior construction methods cannot be implemented completely due to these limitations of the building material. Many technical problems of construction engineering are currently being solved, thanks to the breakthrough achieved in the synthesis of building materials [1]. According to statistics, seepage plays an important role in the destruction of earth-rock dams, indicating that it is very important for improving the quality of earth-rock dams and preventing leakage. At present, there are two problems that should be solved urgently. These problems are caused by the impervious wall in dyke projects; therefore, the traditional building materials must be updated with sophisticated technology. First problem is to develop antiseepage measures to avoid the reinforcement of dangerous reservoirs. Second problem is to effectively suppress the high pressure of earth-rockfill dam,

which is caused by the deep foundation of the covering layer. To solve all these issues, we should judiciously select the impervious materials.

The plastic concrete is a kind of flexible material with moderate properties, so it can be considered as a building material whose quality is somewhere between the soil and the ordinary concrete. This novel material is used to solve the problems faced while using the common concrete cutoff wall [2]. Presently, most of the impervious core wall materials are made of plastic concrete or asphalt concrete in order to improve the impermeability of the impervious wall and to reduce the elastic modulus of the concrete. In general, plastic concrete always contains certain characteristic toughening components, such as bentonite or clay composite bentonite. By incorporating these toughening components, we substantially improve the crack resistance and impermeability of concrete. With this strategy, we also ameliorate the workability and fluidity of concrete. Thus, we make concerted efforts to reduce the cement consumption and concrete cost [3–6]. The characteristics of plastic concrete are as follows: its elastic modulus is relatively low, and the value of this parameter is very close to the elastic modulus of dam

TABLE 1: Properties of emulsified asphalt.

Items	Results	Technical requirements of hydraulic asphalt SG90 by GB 50092-1996	Performance standards
Needle penetration (25°C, 100 g, 5 s) (0.1 mm)	95.5	80~100	
Softening point (ring and ball method) (°C)	43.2	42~52	
Ductility (15°C, 5 cm/min) (cm)	160	≥100	DL/T 5362-2006
Density (25°C) (g/cm^3)	1.01	Measured data	
Solubility (%)	99.6	≥99.5	
Flash point (°C)	290	≥230	

TABLE 2: Chemical composition of cement, fly ash, and clay (%).

Items	SiO$_2$	Fe$_2$O$_3$	Al$_2$O$_3$	CaO	MgO	f·CaO	K$_2$O	Na$_2$O	R$_2$O	SO$_3$	Loss
Cement	21.7	5.0	4.1	62.1	4.8	0.1	—	—	—	0.7	0.2
Fly ash	59.0	8.8	21.6	5.1	1.5	—	0.8	0.2	0.7	0.6	1.4
Clay	55.6	5.9	15.0	5.6	4.6	—	—	—	—	—	—

body and foundation. Furthermore, the ratio of elastic modulus to strength is generally lower than 500; however, the permeability and durability are limited. The permeability coefficient is generally in the range of 10^{-7} cm/s, and the compression strength generally ranges between 2 MPa and 5 MPa in the ageing period of 28 days. In the traditional impervious wall made from plastic concrete, the compressive strength is not that high. To tackle this issue, we conducted sufficient research on how to improve durability of the material. The traditional material is mostly used for constructing impervious cofferdams that sustain for a temporary period. The traditional material is also used for constructing permanent structures having the foundation of low dam and thin overburden. In this paper, we address the deficiency of traditional plastic concrete in order to synthesize a better material that is a good match of different strength grades of concrete. Our aim is to improve the plasticity of the concrete structure; therefore, the new toughening components of emulsified asphalt have been added to plastic concrete [7]. Based on the results of experimental analysis, we propose that plastic concrete should be used for constructing the permanent impervious wall under deep overburden foundation; the same wall may also be built with plastic concrete of high anticracking site, and so on. Thus, we can effectively solve the major technical problems of hydraulic concrete, such as cracking resistance. Our main purpose is to prevent permeability in order to improve the service life of hydraulic structures.

2. Experimental

2.1. Raw Materials.
Cationic emulsified asphalt, Huaxin 42.5 moderate heat Portland cement, clay of a project, Xuanwei grade I fly ash, Jiangsu Bote JM PCA high-efficiency water-reducing agent and GYQ air entraining agent, artificial marble sand, and artificial sandstone rubble were used in this study. The testing result showed that the raw materials meet the relevant technical requirements. Properties of emulsified asphalt and chemical composition of raw materials are shown in Tables 1 and 2.

2.2. Experimental Methods.
Experimental methods and data analysis methods in this study were according to SL 237-99 specification of soil test, and SL 352-2006 test code for hydraulic concrete, DL/T5150-2001 specification of concrete cutoff wall used for hydropower and water conservancy project, and DL/T 5330-2015 code for mix design of hydraulic concrete. Different water-binder ratios (0.3, 0.45, and 0.6), asphalt-cement ratios (0, 0.4, and 0.6), and the clay contents (0%, 20%, and 40%) were considered in the test. The content of fly ash was 15%. For explaining its effects on macroscopic mechanical properties, combined with microtesting methods such as CT, XRD, SEM, TG-DSC, and so on [8], microtopography and chemical composition of hydration products of cement-emulsified asphalt slurry were investigated.

CT scanning technology relies on the principle that the degree of attenuation of radiation passing through the medium is proportional to its density. It combined with computer technology and image processing technology; the physical internal density information will be obtained by digital image reflecting. Shape, internal structure, and composition of the material can be recognized based on the density-related image information. Density information of the CT images shows the gray area of information packets.

CT essentially involves a two-dimensional distribution of a physical quantity in the fault area. The physics is that the linear attenuation coefficients $\mu(x, y)$ and $\mu(x, y)$ are directly related to the density of the object. In the early times, CT technology workers were defined as the standard CT number Hp by the attenuation coefficient of water, which was expressed as

$$\text{Hp} = \frac{\mu_{\text{m}} - \mu_{\text{w}}}{\mu_{\text{w}}} \times 10^3, \tag{1}$$

where μ_{w} and μ_{m} are the attenuation coefficients of water and the medium, respectively.

The CT number of each pixel can be obtained through (1). Each CT number corresponds to a gray value; thus, a tomographic gray scale digital matrix is formed. The CT testing machine will get a set of CT gray scales by continuously scanning objects in the vertical cross-sectional direction.

TABLE 3: Mix proportion parameters of cement-emulsified asphalt concrete.

Samples	Water-binder ratio	Emulsified asphalt-binder ratio	Clay (%)	Fly ash (%)
Xq1	0.30	0.4	20	15
Xq2	0.30	0.6	20	15
Xq3	0.45	0	0	15
Xq4	0.45	0	20	15
Xq5	0.45	0.4	0	15
Xq6	0.45	0.4	20	15
Xq7	0.45	0.4	40	15
Xq10	0.45	0.6	20	15
Xq12	0.60	0.4	20	15
Xq15	0.60	0.6	20	15

TABLE 4: Mix proportion parameters of cement-emulsified asphalt concrete for the microtest.

Samples	Water-binder ratio	Fly ash (%)	Clay (%)	Emulsified asphalt-binder ratio
X0	0.45	15	0	0
X1	0.45	15	0	0.4
X2	0.45	15	20	0
X3	0.45	15	20	0.4

These gray scales will get the whole composition of the interior of the space in the object through three-dimensional reconstruction. Threshold values for each phase medium and CT number of concrete specimens are hardened cement mortar (2000~2200), aggregate (2200~3071), and interfacial transition zone (1000~1600). Mix proportion parameters of cement-emulsified asphalt concrete and mix proportion parameters of cement-emulsified asphalt concrete for the microtest are shown in Tables 3 and 4.

3. Results and Discussion

3.1. The Influence of Water-Binder Ratio on Properties of Cement-Emulsified Asphalt Concrete. Properties of the cement-emulsified asphalt concrete with the water-cement ratios of 0.3, 0.45, and 0.6, respectively, are shown in Table 5.

The results indicate the following effects:

(1) The compressive strength of cement-emulsified asphalt concrete decreased gradually with the steadily increasing water-cement ratio. Compared to the initial phase, the water-binder ratio exerted a slightly greater impact on the compressive strength of concrete at the later stage. This was the result of incorporating emulsified asphalt and clay in order to reduce the dosage of cement in concrete. As a result, there was considerable reduction in the posthydration products. With a large amount of emulsified asphalt, we could significantly alter the strength of concrete. The larger the amount of emulsified asphalt, the lower the compressive strength of concrete would be. The composition and performance of emulsified asphalt was commendable in changing the compressive strength of concrete.

(2) The splitting tensile strength and the tensile strength of emulsified asphalt concrete were reduced by steadily increasing the water-cement ratio. For the concrete, the ratio of compressive strength to the splitting tensile strength was in the range 9.6–11.3. The higher the concrete strength, the greater the ratio would be. In cement-emulsified asphalt concrete, the ratio of compression to tension was slightly lower than the value of ordinary concrete. This indicates that cement-emulsified asphalt concrete had some level of plasticity. The splitting tensile strength was higher than the axial tensile strength. In concrete material, the ratio of splitting tensile strength and axial tensile strength was in the range 1–1.11 on the 28th day; the same ration was in the range 1.08–1.32 on the 90th day. This ratio increased gradually with the increasing age of concrete.

(3) The water-binder ratio had some significant influence on the compressive elastic modulus of cement-emulsified asphalt concrete; the compressive elastic modulus increased when the water-cement ratio decreased steadily; the decline in the water-cement ratio was achieved by increasing the compressive strength of cement-emulsified asphalt concrete.

3.2. Influence of Different Dosages of Emulsified Asphalt on Concrete Properties. The ratio of modulus to strength indicates the internal relationship between the characteristics of tensile strength and elastic modulus of concrete; the modulus is an important index to assess the plasticity of emulsified asphalt concrete [9]. The test results indicate that except for the Xq1 specimen, the elastic moduli of cement-emulsified asphalt concrete specimens were all below 5.2 GPa on the 90th day. The ratio of modulus to strength of concrete was relatively low. In general, this ratio was less than 500. Under some circumstances, it was even below 200. The results indicate that the deformation capacity of emulsified asphalt concrete is greater than the ordinary hydraulic concrete. Therefore, cement-emulsified asphalt concrete has excellent toughness when it is treated with moderate compressive concrete.

Table 6 indicates that the compressive strength, splitting tensile strength, and the tensile strength of cement-emulsified asphalt concrete decreased gradually when we steadily increased the content of emulsified asphalt. In this case, there was sharpest reduction in the compressive strength of concrete; however, the growth rate of long-term strength was higher than that of undoped emulsified asphalt concrete. For emulsified asphalt concrete, the ratio of modulus to strength was significantly lower than the concrete devoid of emulsifying asphalt.

The hydration of cement was delayed by incorporating emulsified asphalt, making concrete own retarding property. This phenomenon can be explained as follows: the emulsified asphalt contained a high amount of water; the water was released after demulsifying the previously emulsified asphalt. The resultant asphalt subsequently participated in the hydration of cement. On the other hand, some bitumen-coated

TABLE 5: Properties of cement-emulsified asphalt concrete under different water-binder ratios.

Samples	Compressive strength (MPa)			Splitting tensile strength (MPa)			Elastic modulus (GPa)			Tensile strength (MPa)	
	14 d	28 d	90 d	14 d	28 d	90 d	14 d	28 d	90 d	28 d	90 d
Xq1	6.7	9.5	15.1	0.64	0.93	1.33	2.96	4.81	10.53	0.88	1.04
Xq6	5.6	8.2	13.3	0.55	0.80	1.19	2.48	3.53	5.14	0.73	0.90
Xq12	4.8	7.2	10.5	0.50	0.70	1.00	1.16	3.04	4.53	0.65	0.85
Xq2	4.1	5.4	7.7	0.38	0.53	0.70	1.98	2.48	3.07	0.50	0.65
Xq10	3.6	5.0	6.9	0.34	0.50	0.68	1.15	2.18	3.16	0.45	0.57
Xq15	3.2	4.0	5.9	0.30	0.38	0.60	0.62	1.01	1.68	0.38	0.50

TABLE 6: Concrete properties under varying dosages of emulsified asphalt (water-cement ratio 0.45).

Samples	Compressive strength (MPa)			Splitting tensile strength (MPa)			Elastic modulus (GPa)			Elastic modulus and compressive strength ratio			Tensile strength (MPa)	
	14 d	28 d	90 d	14 d	28 d	90 d	14 d	28 d	90 d	14 d	28 d	90 d	28 d	90 d
Xq4	13.5	20.8	24.4	0.90	1.60	2.00	12.15	17.79	19.87	900	855	814	1.10	1.78
Xq6	5.6	8.2	13.3	0.55	0.80	1.19	2.48	3.45	5.14	442	430	387	0.75	1.10
Xq10	3.6	5.0	6.9	0.34	0.50	0.68	1.15	2.18	3.16	319	436	485	0.56	0.65

cement particles and hydration products significantly alter the concrete structure, eventually reducing the interfacial bonding strength of the concrete, leading to a decrease in the early strength of the concrete.

3.3. Influence of Varying Dosages of Clay on Concrete Properties.

In plastic concrete, the toughening component is clay as it is able to improve the deformation property of plastic concrete. After mixing emulsified asphalt concrete with clay, we investigated the properties of the mixed material. Thus, we analyzed the influence of varying the dosages of clay on the properties of cement-emulsified asphalt concrete. To obtain the correct mix proportion of emulsified asphalt concrete, we strictly maintained the following parameters: the water-binder ratio of 0.45, the asphalt-cement ratio of 0.4, and the clay content of 0%, 20%, and 40%, respectively. Table 7 presents the test results of this analysis.

The results indicate that clay reduces the elastic modulus of cement-emulsified asphalt concrete. Except for the Xq7 specimen, the ratios of modulus to strength were below 500 for all the specimens. The compressive strength of the Xq6 specimen reached 8.0 MPa, and the ratio of modulus to strength was 430 on the 28th day. When clay is incorporated into plastic concrete, its strength is significantly increased compared to clay-free samples. In both cases, we maintain the same modulus ratio [10].

By increasing the content of clay in cement-emulsified asphalt concrete, it a gradual decrease in the following parameters is observed: the compressive strength, the splitting tensile strength, and the tensile strength. The effect of clay was quite significant on the late compressive strength of concrete. The late growth of splitting tensile strength was faster in cement-emulsified asphalt concrete. In contrast, the late growth of axial tensile strength was slower in cement-emulsified asphalt concrete. Strength was low when cement emulsion asphalt mixed with clay. This is caused by the inert

nature of the clay and the retardation of the emulsified asphalt. By adding clay to the concrete, we have significantly reduced the amount of equivalent cement. As a result, the amount of cement hydration produced is also small. These changes weaken the cementing capacity of gravel aggregates and result in a thinner network structure than normal concrete. All these undesirable reactions led to a significant reduction in the strength of concrete.

3.4. Computed Tomography (CT).

The concrete specimen Xq6 was selected to calculate the CT mean value of each section subjected to continuous loading [11–13]. We successfully obtained the CT mean value of each section. Figure 1 illustrates the following developments in the CT scan of the specimen: seven sections were selected along the concrete column; the cross-sectional area was $66.50 \, \text{cm}^2$, and the spacing for each section was 25 mm. Figure 2 illustrates the gray scale CT scan of each concrete section under different stress. Figures 3(a) and 3(b) illustrate the CT mean values curve of each section subjected to continuous load.

As can be seen in Figures 3(a) and 3(b), the three sections of cement-emulsified asphalt concrete were not damaged, but the other four sections were destroyed seriously. This occurred due to the low strength and plasticity of cement-emulsified asphalt concrete. There was relatively small variation in the CT mean values of the first three sections when they were subjected to different loads. This indicates that the state of concrete altered due to compaction and microdilatancy. In the other four sections of the sample, we observed four different concrete damage evolutions: the compaction of each section increased dramatically as we steadily increased the load. This leads to an increase in the density and CT average of cement-emulsified asphalt concrete. When the load was increased to 5.15 MPa, we observed that the CT value of each section started declining slightly. This indicated the initial stage of concrete damage. When we

TABLE 7: Concrete properties under varying dosages of clay.

Samples	Clay (%)	Compressive strength (MPa)			Splitting tensile strength (MPa)			Elastic modulus (GPa)			Elastic modulus and compressive strength ratio			Tensile strength (MPa)	
		14 d	28 d	90 d	14 d	28 d	90 d	14 d	28 d	90 d	14 d	28 d	90 d	28 d	90 d
Xq5	0	9.2	11.1	16.7	1.00	1.10	1.40	1.97	4.02	7.32	213	362	438	0.95	1.28
Xq6	20	5.6	8.2	13.3	0.55	0.80	1.19	2.48	3.53	5.14	442	430	387	0.75	1.10
Xq7	40	3.1	4.2	6.3	0.20	0.40	0.60	0.83	1.57	3.58	268	374	568	0.40	0.55
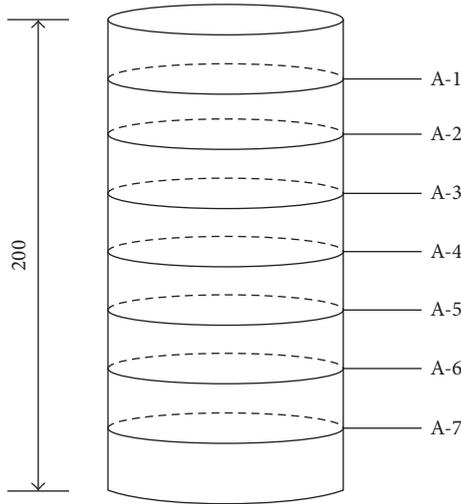
FIGURE 1: Cross sections of cement-emulsified asphalt concrete (size: mm).

increased the limit load to 5.44 MPa, we observed the development of microcrack for the first time. Subsequently, the expansion was substantially enough to accelerate the damage. Then, we observed too many cracks developing in the specimen within a very short period of time. However, there was significant reduction in the volume of specimen expansion, the rapid diminution of the density, and the CT mean value. Finally, we destroyed the lower section of the specimen by increasing the load to 5.30 MPa.

3.5. Analysis of Binary Image. In the mathematical morphology method, we used integral geometry to define geometrical parameters, which were then used to indirectly measure and characterize irregular geometric shapes. Moreover, the random nature of the image was comprehended by random set theory of the method [14–17]. Therefore, it can be used to quantitatively describe CT images of concrete structure. To determine the variation in each pixel gray value and to estimate the crack criterion for each pixel gray value, we used the following equation:

$$H_{i,j} = \max\left(H_{i,j}, H_{i+1,j}, H_{i,j+1}, H_{i+1,j+1}\right), \qquad (2)$$

where $H_{i,j}$ is the CT gray value of the i line and j column pixel, $i, j = 1, 2, 3, \ldots, 1024$. All the image data are represented by 0 and 1; therefore, you can extract the crack by setting a gray threshold as follows: when the intensity is greater than the threshold indicated by 1 or is less than the

threshold indicated by 0. The data matrix of a gray scale image representing 1-pixel size was considered as a unit for statistics; it was substituted into the equation to extract threshold ξ at a certain crack, so it can be realized through binarization of the cracked image, namely, crack extraction. When $H_{i,j} < \xi$, the points are included in the crack area; when $H_{i,j} < \xi$, the points are included in the noncracked area. Figure 4 and Table 8 present the test results of this analysis.

Figure 5 illustrates that there are many cavities in the cement-emulsified asphalt concrete specimens; these cavities have an uneven size in the specimens. In the cement-emulsified asphalt concrete specimens, stress concentration occurs easily and a crack initiation point develops. These undesirable events ultimately lead to widespread cracks that damage the specimen completely.

By examining the CT scan binary image, we can summarize the development trend of the crack in each section of the specimen. In the concrete section A-7, we observed continuous cracks at the microscopic level. However, other sections did not form continuous crack until the loading was increased to 4.9 MPa. In this period, the concrete exhibited alternating stages of compaction and microdilatancy. These observations complied with the results of CT number analysis. When the load was increased continuously, we observed the gradual development of crack in section A-7. First, only two continuity cracks were observed at the edge of the section. The crack width subsequently increased. At the same time, scattered fine cracks were observed in the middle of the cross section, which correlates with the formation at the crack edge. All these cracks substantially destroyed the section of concrete. Based on these observations, we infer that the concrete crack was caused by the hole present in sections A-4 and A-6. When the load was increased to 5.44 MPa in section A-4, we observed intermittent microcracks. Furthermore, we observed continuous cracks when the load was increased to 5.30 MPa. Near the hole, stress concentration appeared when the section A-6 was subjected to stress. Thus, the development of cracks was rapid, extending into the weak zone of the concrete structure. All these developments resulted in the separation of cementitious materials and aggregates at the interface. Such closely connected, adjacent cracks were observed in an interlaced and interconnected fashion, leading to the development of crack propagation. Crack stress unleashed rapidly with the propagation of cracks. When the load was increased in definite increments, we could not observe continuous cracks in the section A-2; the section was minutely examined by the CT image intuitive method.

A-2   A-3   A-4   A-5   A-6

(a)

A-2   A-3   A-4   A-5   A-6

(b)

A-2   A-3   A-4   A-5   A-6

(c)

A-2   A-3   A-4   A-5   A-6

(d)
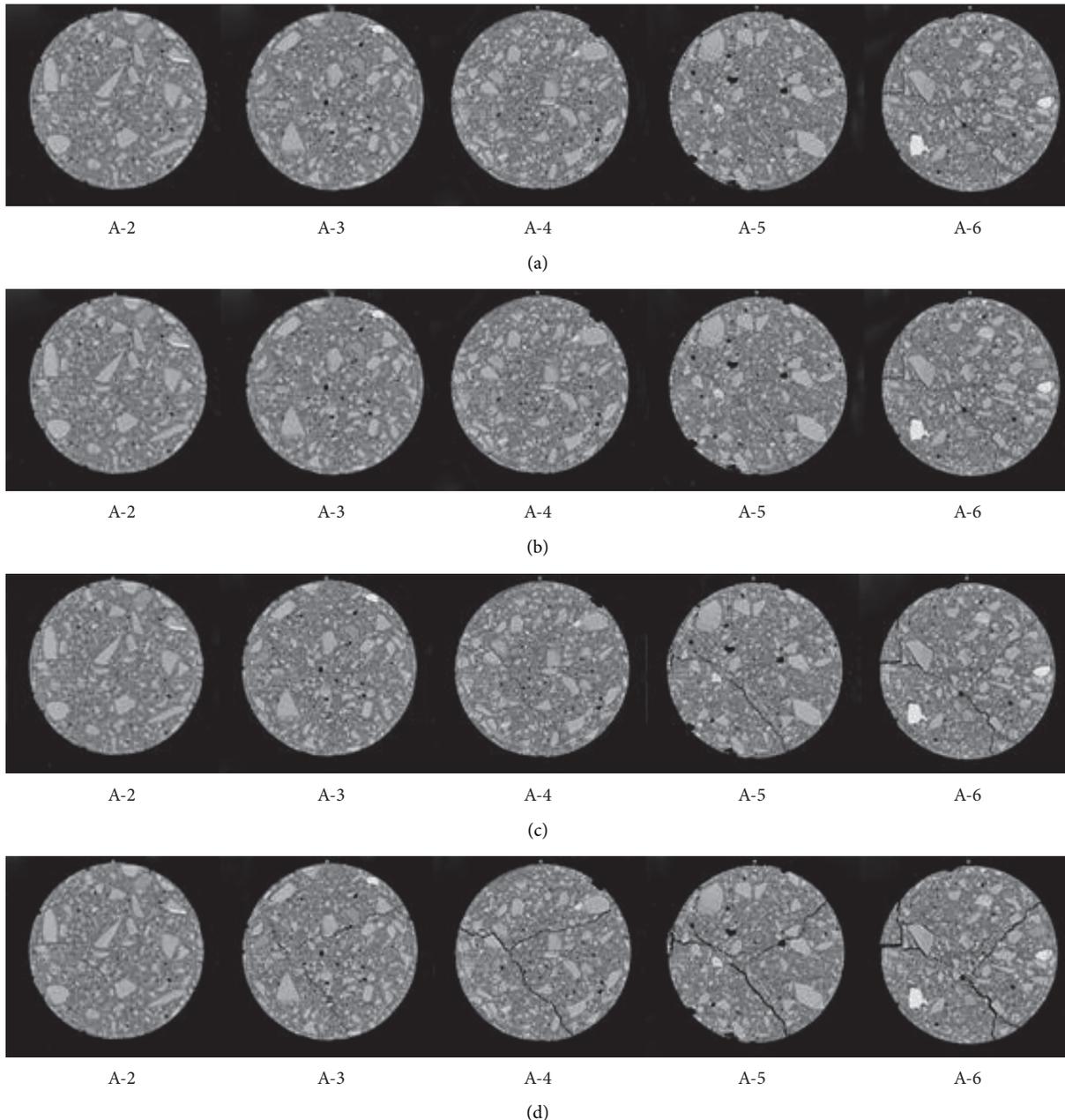
FIGURE 2: Gray CT picture of concrete cross section under various stresses (28d). (a) $\sigma = 3.18$ MPa, (b) $\sigma = 5.15$ MPa, (c) $\sigma = 5.44$ MPa, and (d) $\sigma = 5.30$ MPa.

However, a small piece of continuous crack was detected when we implemented the binary image analysis method on the section exposed to the ultimate load, and the continuous crack developed due to low compressive strength and a certain amount of toughness in cement-emulsified asphalt concrete.

When the cement-emulsified asphalt concrete was subjected to the ultimate load, we observed fine cracks in the upper section; however, these cracks were observed because the upper part was experiencing alternating states of compaction and expansion. Based on these observations, we conclude that a lot of voids had developed in the cement-emulsified asphalt concrete. These cracks were immensely useful in dissipating the external pressure. Furthermore, the toughness of the material increased tremendously when the concrete was mixed with the emulsified asphalt and the clay-toughening component; therefore, the novel hybrid material was experiencing alternating states of compaction, expansion, reconsolidation, and reexpansion when subjected to increasing amounts of load. In the specimen, we mainly observed small cracks and discontinuous cracks. In other words, the specimen does not crack even when subjected to an increased load. In the middle and lower parts, we observed a large connectivity crack under the action of failure load; however, penetrating crack was not observed in the upper and lower layers.

(a)

(b)
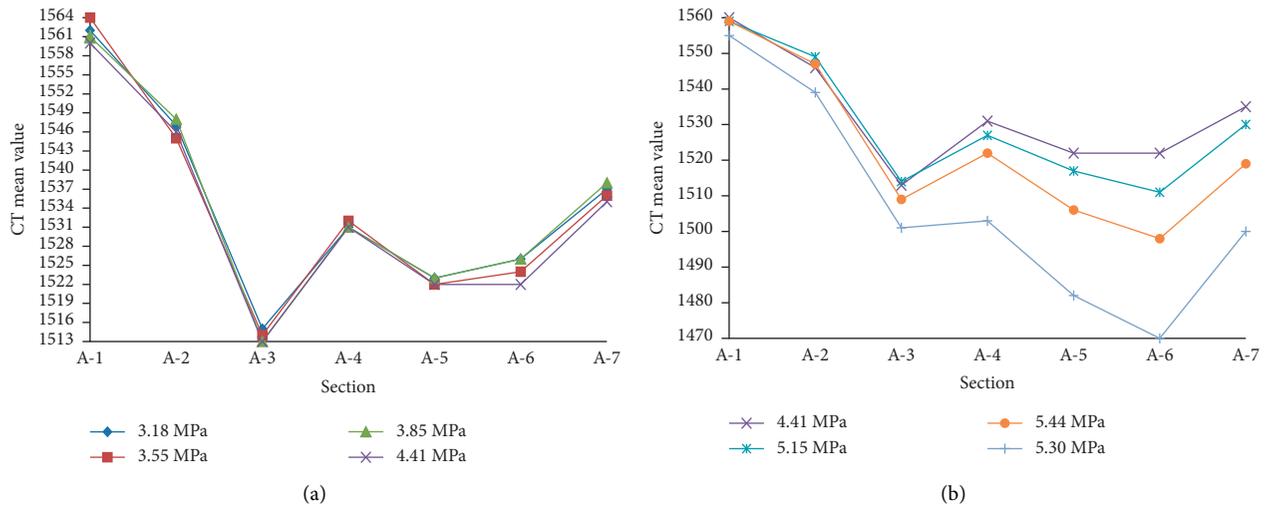
FIGURE 3: (a) CT mean value comparison of each cross section under continuous loading (3.18 MPa, 3.55 MPa, 3.85 MPa, and 4.41 MPa). (b) CT mean value comparison of each cross section under continuous loading (4.41 MPa, 5.15 MPa, 5.44 MPa, and 5.30 MPa).

(a)

(b)
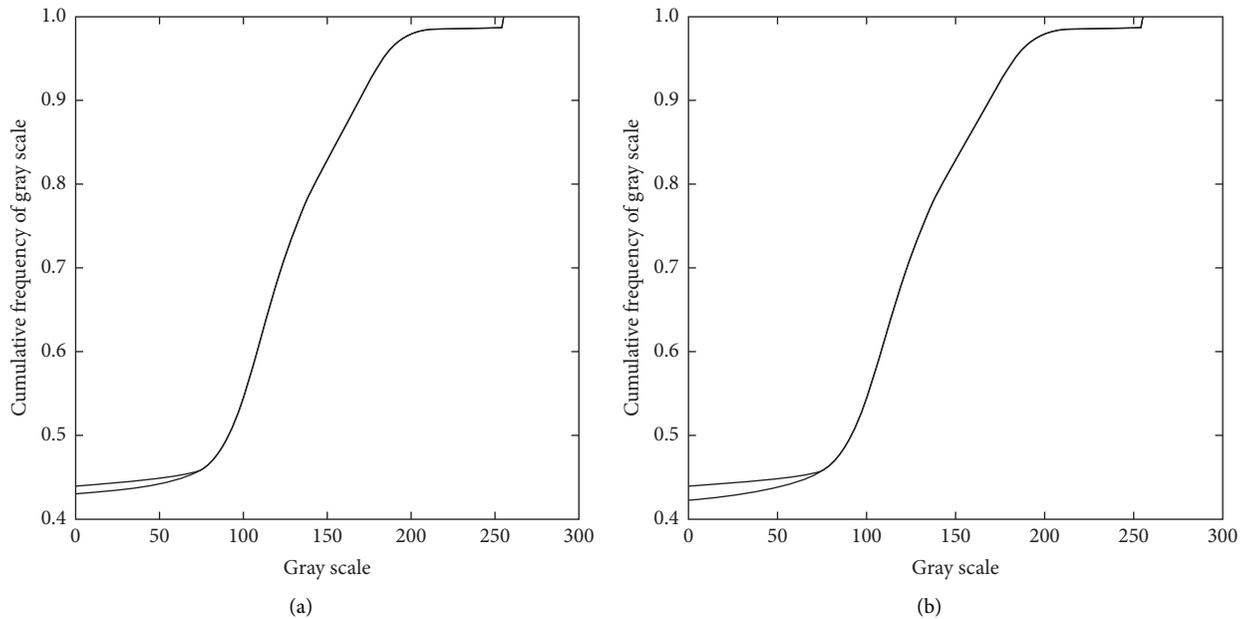
FIGURE 4: (a) Cumulative frequency of gray scale with the load of 5.44 MPa and 3.18 MPa under section A-7 of Xq6. (b) Cumulative frequency of gray scale with the load of 5.30 MPa and 3.18 MPa under section A-7 of Xq6.

TABLE 8: Binary analysis threshold of each section of Xq6.

Sections	5.15 MPa to 3.18 MPa	5.44 MPa to 3.18 MPa	5.30 MPa to 3.18 MPa	Mean
A-2	—	—	75	75
A-4	—	73	69	71
A-6	71	65	62	66
A-7	84	79	81	81

3.6. Scanning Electron Microscope (SEM) Analysis. The SEM images of emulsified asphalt-cement paste specimens' hydration products at 7th and 28th day of different dosage combinations as in Table 4 are shown in Figure 6.

As shown in Figure 6(a), C–S–H gel, Ca(OH)$_2$, AFt, AFm, and other hydration products were observed along with the unhydrated cement clinker particles in the undoped emulsified asphalt and clay cement at the 7th day. Moreover, the slurry was highly porous in nature. In addition, some products had not yet developed into a crystalline form completely at the 7th day: C–S–H gel was mainly type II, but it was difficult to find C–S–H gel particles of type III. There were some needle-shaped ettringite (AFt) in the holes because gypsum and lime stimulated the samples to form ettringite [18, 19] (AFt). When we increased the ageing period in definite increments, we observed that there was a decrease in unhydrated cement particles; however, the

A-2　　　　A-4　　　　A-6　　　　A-7

(a)

(b)

(c)

(d)

(e)

(f)
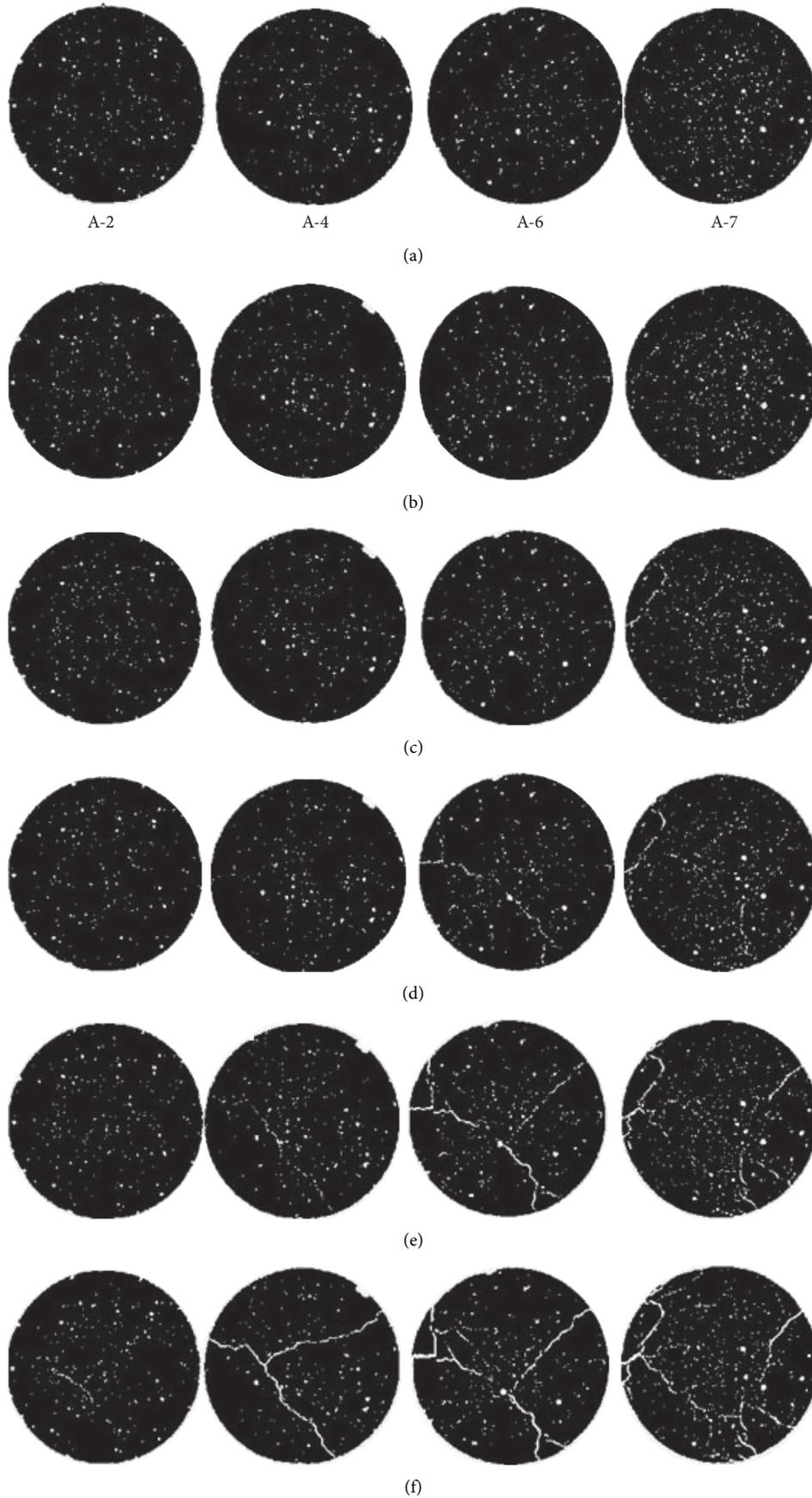
Figure 5: Binary image of the Xq6 specimen under different stress sections (28 d). (a) $\sigma = 3.18$ MPa, (b) $\sigma = 3.55$ MPa, (c) $\sigma = 4.9$ MPa, (d) $\sigma = 5.15$ MPa, (e) $\sigma = 5.44$ MPa, and (f) $\sigma = 5.30$ MPa.

(a)

(b)

(c)

(d)

(e)

(f)

(g)

(h)
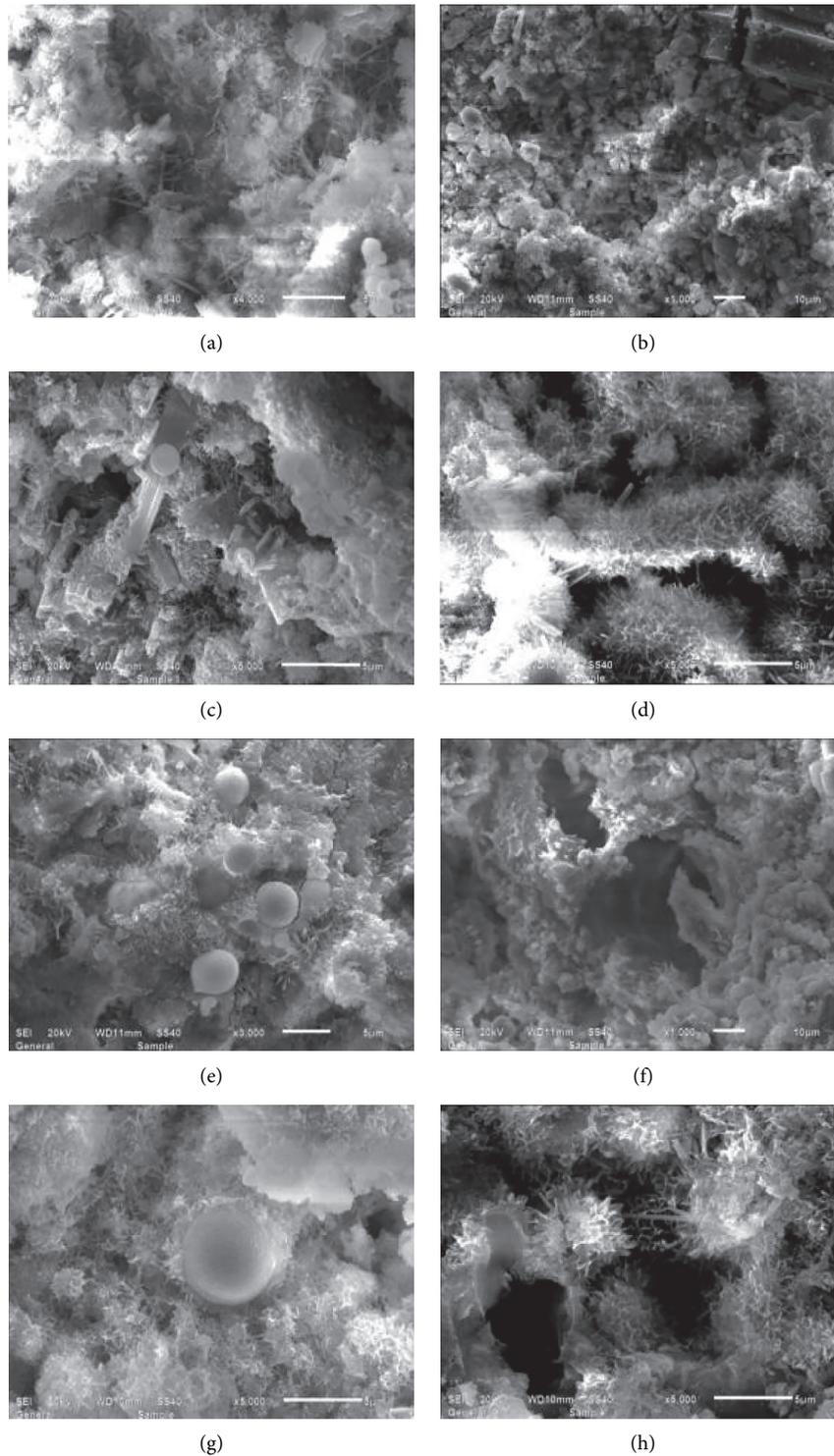
Figure 6: SEM images of cement-emulsified asphalt paste samples: on the 7th day, (a) without emulsified asphalt and clay, (b) with emulsified asphalt, (c) with clay, and (d) with emulsified asphalt and clay; on the 28th day, (e) without emulsified asphalt and clay, (f) with emulsified asphalt, (g) with clay, and (h) with emulsified asphalt and clay.

amount of hydration products increased simultaneously, and the structure gradually became dense. The shape of hydration products C–S–H of cement paste was approximately the same when the cement paste was mixed with single-doped emulsified asphalt [20], single-doped clay, and pure cement; the product was mainly appearing in the form of spherical C–S–H gel. Figure 6(c) illustrates the part where the clay particles fill the void, leading to the formation of a structure that is more compact than the single-doped emulsified asphalt-cement paste. Furthermore, we also

observed a small amount of needle-shaped ettringite (AFT), small pieces of plate-type $Ca(OH)_2$ crystals, and fly ash particles; the hydration products had completely wrapped these minor products. Figures 6(b) and 6(d) illustrate that the emulsified asphalt was not involved in the hydration reaction of cement; however, many pores were observed in the cement-emulsified asphalt paste. These pores were caused by the "vacancy" of bubble burst and water evaporation during the forming process. The surface of the slurry is not smooth; it is very uneven and there is a lot of bump [19, 21–23]. Asphalt particles were round in shape, with a significant portion of particles being encased with cement particles or clay particles. These factors decelerated the cement hydration rate, leading to the slow development of concrete strength.

Figure 6(e) shows the nature of products on the 28th day of ageing: hydration products were fibrous (type I), meshy (type II), and granular (type III) C–S–H gels (some type I of C–S–H gel shape were flowers). Furthermore, we also observed $Ca(OH)_2$ crystal and monosulfate calcium sulfoaluminate hydrates in the form of hexagonal flakes. Figure 6(g) shows that the clay particles were gradually surrounded by fibrous, flocculent, and layered hydration products. In addition, C–S–H gel and hydrated sulfoaluminate had intertwined with each other to form a relatively dense structure, leading to a reduction in the volume of pores. However, crystals of hydration products appeared in a haphazard arrangement. As shown in Figures 6(f) and 6(h), emulsified asphalt contains water that initiates and promotes hydration. As a result, the hydrate content gradually increases. The shape of asphalt particles had changed from a regular sphere to an irregular ball pie. These particles had got attached to the cement hydration products.

3.7. X-Ray Diffraction Analysis (XRD).

The XRD patterns of emulsified asphalt-cement paste specimens' hydration products at 7th day and 28th day of different dosage combinations as in Table 4 are shown in Figures 7 and 8.

As shown in Figures 7 and 8, the hydration products of cement-emulsified asphalt paste were substantially similar even in different proportions; the main hydration products were C_2S, C_3S, $Ca(OH)_2$, and ettringite. The amount of hydration products were increasing gradually with the progress of ageing process, but a different number of hydration products were generated in different cementitious systems. The ettringite diffraction peaks of X2 and X3 specimens are higher than the peaks of X0 and X1 specimens on the 7th and 28th days of ageing.

The patterns clearly illustrate that kaolinite, quartz, and calcite were the main components of clay. By comparing the specimens X0, X2, and X3, we found that this clay was a kind of inert admixture, and it was not involved in the hydration reaction. The reaction played a significant role in generating products, which acted as fillers in the concrete. Thus, the concrete pore structure improved tremendously, and there was a sharp decline in the rate at which the load damaged the concrete. By comparing the X-ray diffraction patterns of both types (doped and undoped) of emulsified asphalt
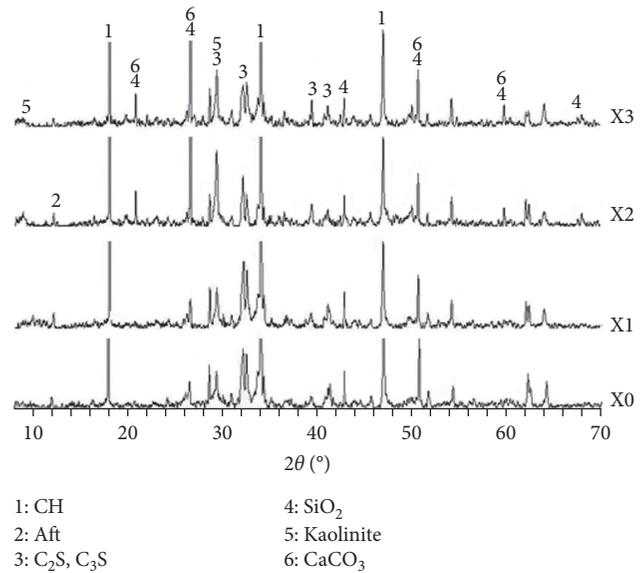
Figure 7: X-ray diffraction pattern of cement-emulsified asphalt paste under different proportions for 7 d.

1: CH 4: SiO_2
2: Aft 5: Kaolinite
3: C_2S, C_3S 6: $CaCO_3$
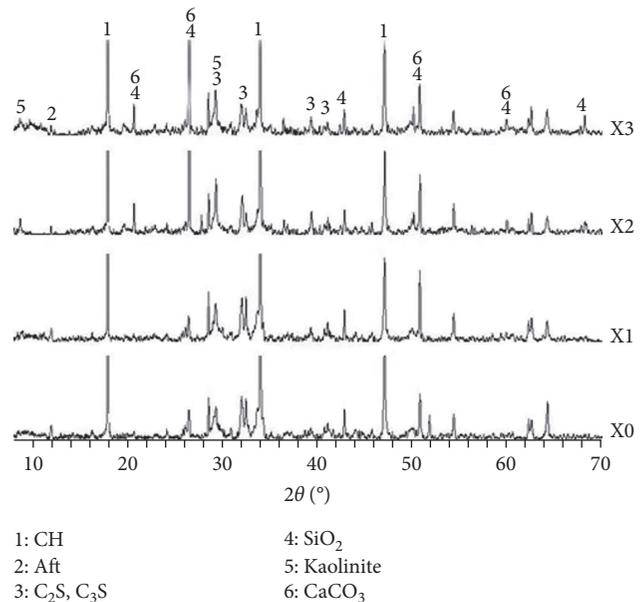
Figure 8: X-ray diffraction pattern of cement-emulsified asphalt paste under different proportions for 28 d.

1: CH 4: SiO_2
2: Aft 5: Kaolinite
3: C_2S, C_3S 6: $CaCO_3$

specimens, we found that there was no chemical reaction between asphalt and cement. Moreover, no new mineral phases were formed in the cement hydration products. Thus, only $Ca(OH)_2$ and other characteristic peaks were observed in the patterns of cement-emulsified asphalt; the patterns included all the characteristic peaks of hydration products obtained from cement. Furthermore, characteristic peaks representing new material were not observed in the patterns. When we used different proportions of specimens, the intensity of diffraction peaks representing the specimens was different at different ages; the diffraction peak of X0
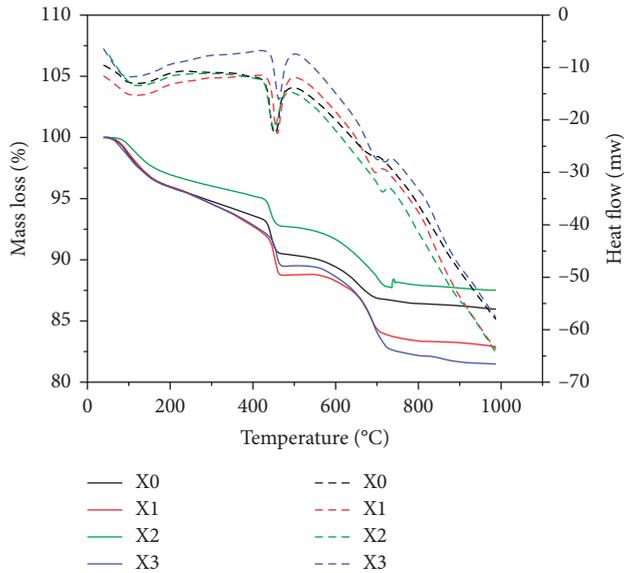
FIGURE 9: TG-DTA curves of paste specimens with different mix ratios for 7 d.
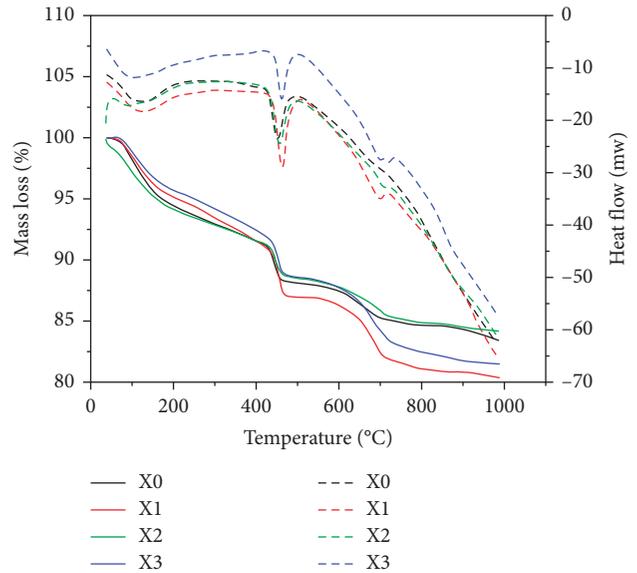
FIGURE 10: TG-DTA curves of paste specimens with different mix ratios for 28 d.

was higher than that of X1 on the 7th day of ageing; however, the diffraction peak of X0 was slightly lower than that of X1 on the 28th day of ageing. Both these effects were related to the retarding property of the dopant in the emulsified asphalt. Furthermore, there were obvious amorphous peaks of components in the diffraction pattern, and these peaks were observed due to the scattering of asphalt.

3.8. Differential Thermal Analysis (TG-DTA). Table 4 shows the results of differential thermal analysis that was performed on mix proportions of cement-emulsified asphalt concrete. Figures 9–11 illustrate the TG-DTA curves of the cement-emulsified asphalt with different mix ratios on the 7th, 28th, and 90th day of ageing.

The TG curves clearly manifest that the changes in the intensity of peak with respect to the three ages; these changes in peak intensity completely agreed with the changes observed with the variation of temperature. A relatively small loss of mass is observed when the X2 specimen is mixed with single clay. In contrast, a massive loss of mass is observed when the X1 specimen is mixed with single-emulsified asphalt. Moreover, the mass loss gradually increased with the increasing ages, indicating that the hydration reaction of paste samples was becoming more adequate when they were allowed to age for a longer period of time. In the graph, a weak peak appeared from 80°C to 100°C; the peak characterized the dehydration of calcium silicate hydrate and ettringite. A sharp peak was observed between 400°C and 500°C, and this peak represented the endothermic valley of Ca(OH)$_2$ dehydration. Finally, a sharp peak was observed between 650°C and 700°C, and it represented the endothermic valley of CaCO$_3$ decomposition. Despite using different proportions, the hydration products of cement paste were
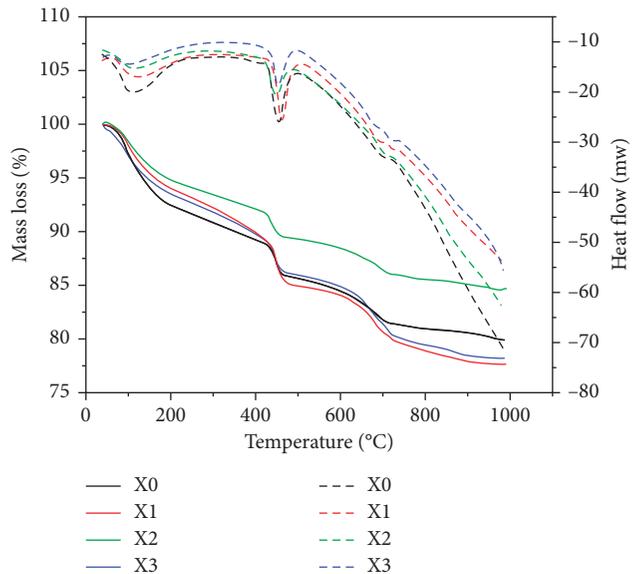
FIGURE 11: TG-DTA curves of paste specimens with different mix ratios for 90 d.

basically the same as that of X0, but the number of products produced was slightly different.

The DTA curve illustrates that there was a steady decrease in the content of Ca(OH)$_2$ crystals in the X0 specimen at the late stages of analysis. This indicates that Ca(OH)$_2$ is involved in the secondary hydration reaction. In the X1 specimen containing single emulsion asphalt and the X3 composite specimen containing the dopant, the content of Ca(OH)$_2$ increased at the late period. The heat flow of X1 was 23 mw, 30 mw, and 25 mw on the 7th, 28th, and 90th day of ageing, respectively. This indicates that the hydration rate of Ca(OH)$_2$ was relatively slow at the early stage; however, it

increased rapidly at the late stage of analysis. This effect has been attributed to the retarding effect of emulsified asphalt, which is in complete agreement with the above analysis results; the results represent the mechanical properties of concrete.

4. Conclusions

(1) Emulsified asphalt incorporation in concrete delayed the hydration of cement, resulting in relatively slow development of early compressive strength of concrete; the late strength of concrete increased rapidly with the demulsification of emulsified asphalt and hydration of cement. The elastic modulus of plastic concrete is small, and the compressive strength is low. Mixed with emulsified asphalt and clay, the concrete whose compressive strength of 28 d could reach 9 MPa was with lower elastic modulus; the ratio of modulus to strength of the concrete was generally less than 500 and even some below 200, and the deformation capacity was greater than that of the ordinary hydraulic concrete.

(2) The CT mean value analysis of cement-emulsified asphalt concrete specimens showed that the failure process of cement-emulsified asphalt concrete could be divided into 4 stages: compaction, dilatancy, crack propagation, and failure. The volume expansion of each section was not consistent, and the variation of the CT mean value of each section was different; the CT mean value of the place near the lower end face suffered a larger decline but a smaller decline to the upper part of the sample. The evolution of concrete suffering damage to failure is a gradual development process, and no sharp expansion of brittle failure, which further showed that the cement-emulsified asphalt concrete had certain toughness.

(3) There were many pores in the cement-emulsified asphalt paste and a lot of uneven bump on slurry surface. A large number of cement hydration products and some asphalt films which cladded on the surface of the hydration product formed the hardened paste skeleton. The unhydrated cement, asphalt, fibrous C–S–H gel, CH, needle-shaped ettringite, and other hydration products were interwoven to constitute emulsified asphalt-cement paste and to form a spatial structure. There was no chemical reaction between cement and asphalt which produced by demulsification of emulsified asphalt, but there was a retarding effect of emulsified asphalt. The cement-emulsified asphalt concrete has certain plasticity, so we can explore it using in the permanent seepage control engineering under deep overburden.

Conflicts of Interest

The authors confirm that the mentioned funding did not lead to any conflicts of interest regarding the publication of this manuscript. Also there are no other possible conflicts of interest in the manuscript.

Acknowledgments

References

[1] Y. Li, *Building Materials*, China Water Power Press, Beijing, China, 2001.

[2] Q. Wang, W. Sun, and H. Xiong, *The Plastic Concrete Cut-Off Wall*, China Water Power Press, Beijing, China, 2008.

[3] J. Ouyang, Y. Tan, Y. Li, and J. Zhao, "Demulsification process of asphalt emulsion in fresh cement-asphalt emulsion paste," *Materials and Structures*, vol. 48, no. 12, pp. 3875–3883, 2015.

[4] A. Mahboubi and A. Ajorloo, "Experimental study of the mechanical behavior of plastic concrete in triaxial compression," *Cement and Concrete Research*, vol. 35, no. 2, pp. 412–419, 2005.

[5] C. Zhang, Y. Chen, and Y. Guo, "Clay concrete for cutoff wall in earth dam," *Journal of Hydraulic Engineering*, vol. 36, no. 12, pp. 1464–1469, 2005.

[6] S. Hinchberger, J. Weck, and T. Newson, "Mechanical and hydraulic characterization of plastic concrete for seepage cut-off walls," *Canadian Geotechnical Journal*, vol. 47, no. 4, pp. 461–471, 2010.

[7] A. M. Sha and Z. J. Wang, "Microstructure of mastics-aggregate interface in cement emulsified asphalt concrete," *Journal of Changan University*, vol. 4, p. 28, 2008.

[8] S. F. Brown and D. Needham, "A study of cement modified bitumen emulsion mixtures," in *Association of Asphalt Paving Technologists Proceedings of the Technical Sessions 2000*, White Bear Lake, MN, USA, 2000.

[9] S. Oruc, F. Celik, and M. V. Akpinar, "Effect of cement on emulsified asphalt mixtures," *Journal of Materials Engineering and Performance*, vol. 16, no. 5, pp. 578–583, 2007.

[10] J. Liu, X. Zheng, S. Li et al., "Effect of the stabilizer on bubble stability and homogeneity of cement emulsified asphalt mortar in slab ballastless track," *Construction and Building Materials*, vol. 96, pp. 135–146, 2015.

[11] J. Zhou, F. Dang, H. Chen et al., "Breakage meso mechanism of concrete based on CT test under uniaxial compression," *Journal of Xi'an University of Technology*, vol. 22, no. 4, pp. 335–360, 2006.

[12] Z. X. Wen and F. W. Liu, *Concrete Quality Inspected by Acoustic Nondestructive CT*, Vol. 9, China Three Gorges Construction, Beijing, China, 2002, in Chinese.

[13] W. Tian and F. Dang, "CT image analysis of meso fracture process of concrete," *Engineering Journal of Wuhan University*, vol. 41, no. 2, pp. 69–74, 2008.

[14] Y. Wu, W. Ding, and G. Cao, "Observation and detection of evolution process of rock crack on CT scale under uniaxial and triaxial compression condition," *Journal of Xi'an University of Technology*, vol. 19, no. 2, pp. 115–119, 2003.

[15] J. Ren, X. Ge, Y. Pu, W. Ma, and Y. Zhu, "Primary study of real-time CT testing of unloading damage evolution law of rock," *Chinese Journal of Rock Mechanics and Engineering*, vol. 19, no. 6, pp. 697–701, 2000.

[16] H. Peng and J. Zhang, "The boundary element method for bond—anchorage length," *International Journal Hydroelectric Energy*, vol. 19, no. 2, pp. 85–88, 2001.

[17] A. M. Nevelle, *Properties of Concrete*, Person Education Press, London, UK, 4th edition, 2008.

[18] F. M. Nejad, M. Habibi, P. Hosseini, and H. Jahanbakhsh, "Investigating the mechanical and fatigue properties of sustainable cement emulsified asphalt mortar," *Journal of Cleaner Production*, vol. 156, pp. 717–728, 2017.

[19] T. Rutherford, Z. Wang, X. Shu, B. Huang, and D. Clarke, "Laboratory investigation into mechanical properties of cement emulsified asphalt mortar," *Construction and Building Materials*, vol. 65, no. 13, pp. 76–83, 2014.

[20] Z. Zhao, "Lime active decay law is studied in the lime soil," *Transportation Science and Technology*, vol. 4, pp. 98–100, 2005.

[21] K. J. Mun, W. K. Hyoung, C. W. Lee, S. Y. So, and Y. S. Soh, "Basic properties of non-sintering cement using phosphogypsum and waste lime as activator," *Construction and Building Materials*, vol. 21, no. 6, pp. 1342–1350, 2007.

[22] Z. Wang, *Structure and Performance of the Interface Zone between Mortar and Aggregate in Cement Emulsified Asphalt Concrete*, Chang'an University, Xi'an, China, 2007.

[23] Z. Wang, Q. Wang, and T. Ai, "Comparative study on effects of binders and curing ages on properties of cement emulsified asphalt mixture using gray correlation entropy analysis," *Construction and Building Materials*, vol. 54, pp. 615–622, 2014.

Research Article

Investigation on the Deterioration Mechanism of Recycled Plaster

Zhixin Li [ID],[1] Kaidong Xu,[1] Jiahui Peng,[2] Jina Wang,[1] Xianwei Ma [ID],[1] and Jishou Niu[1]

[1]School of Material and Chemistry Engineering, Henan University of Urban Construction, Pingdingshan 467036, China
[2]College of Materials Science and Engineering, Chongqing University, Chongqing 400045, China

Correspondence should be addressed to Zhixin Li; li.zhixin1989@163.com

The deterioration mechanism of recycled plaster (R-P) was studied. The large specific surface area (SSA), improper preparation temperature, increased water requirement of R-P, and microstructure of its hardened body were analyzed by particle size distribution (PSD), Blaine method, differential scanning calorimetry (DSC), scanning electron microscopy (SEM), and nitrogen adsorption porosimetry. The results indicated that the properties of R-P were deteriorated, but its strength decreases from 50% at the same manufacturing process to 30%–40% at similar specific surface area. The analysis shows that the large SSA, poor morphology, narrow PSD, and increased internal detects give rise to increase of water requirement. In addition, the deterioration properties are caused by unsuitable temperature of preparation, loose structure, and large average pore diameter in hardened R-P as well.

1. Introduction

The development of economy has brought about the wide use of plaster of Paris (POP) in construction [1–3] and in ceramic factories [4, 5] as the raw materials of slip casting models, thus producing brazen increase of waste gypsum (WG) after their utilization. According to Suárez, the output of gypsum wallboards produced annually is 80 million tons, and the amount of gypsum dumped in landfills is 15 million tons per year [6]. It not only wastes the gypsum resources but also arouses environment problems, endangering human health [7–9]. Hence, recycling WG is necessary for offering cost reduction and environment protection.

Great efforts have been exerted in the utilization of WG and several approaches are also tried, such as using WG as a retarder in making Portland cement [6], soft clay [10–13], ceramic products [14], new drywalls, and non-load-bearing bricks [15]. However, in most of the related application mentioned above, the utilization of WG is limited, and the problems brought by WG can not be effectively solved. Large plate gypsum is also prepared from WG via the wet process [16], which is unfavorable considering the complex process and may not be feasible in

the industrial production on a large scale. β-Hemihydrate of calcined WG (R-P) as a low-energy material can be produced by the reversible reaction between gypsum dihydrate and gypsum hemihydrate in an electric oven at 180°C [16]. Nevertheless, the utilization is still very little owing to the deterioration performances of R-P compared with POP. So, mastering the deterioration mechanism of R-P is of great importance and urgency for its utilization. There have been several investigations on the deterioration mechanism of R-P, and the deterioration is commonly ascribed to its large specific surface area [17]. However, only limited research on other possible factors inducing R-P deterioration except for the large specific surface areas (SSAs) was published in the common sources by the scholars, which seriously hinders the utilization of R-P. Our study found that the unsuitable preparation temperature, increase of water requirement, and microstructure changes of its hardened R-P were also important factors. Thus, deterioration mechanism of R-P studied in our work is systematic.

In this paper, the above mentioned factors have been fully analyzed to investigate the deterioration mechanism of R-P comprehensively. The authors expect the research will lay a ground work for the utilization of R-P.

TABLE 1: Chemical composition of VG used (%).

Virgin gypsum	SO_3	CaO	SiO_2	Al_2O_3	Fe_2O_3	K_2O	SrO
Chemical composition	47.57	38.73	1.15	0.42	0.13	0.07	0.04
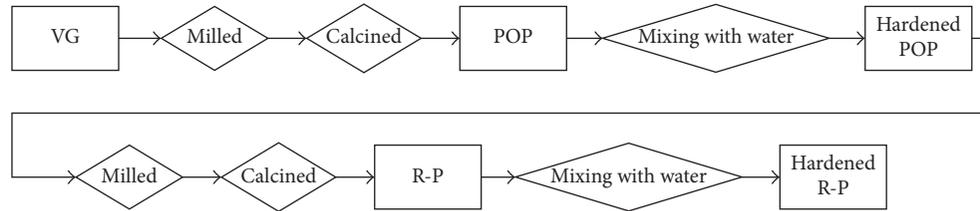
FIGURE 1: The flowchart of preparing R-P and its hardened R-P.

TABLE 2: Properties of POP and R-P under the similar SSA.

Gypsum	SSA ($m^2 \cdot kg^{-1}$)	W/P	Setting time (min)		2 h strength (MPa)		Dry strength (MPa)		Water absorption (%)
			Initial	Final	Flexural strength	Compressive strength	Flexural strength	Compressive strength	
POP	1098	0.68	26	30	2.47	4.59	4.50	6.98	38.89
R-P	1114	0.85	33	46	1.66	2.94	2.70	4.80	40.65

2. Experimental Details

2.1. Materials and Preparation of R-P.
The virgin gypsum (VG) was purchased from Yingcheng in China. The chemical composition of VG determined by X-ray fluorescence (XRF) is shown in Table 1. Preparation of R-P is shown in Figure 1, and their measurement of water-plaster ratio (W/P), setting time, and strength were done according to GB/T 9776-2008 [18]. The experimental details have been introduced in our earlier research [19], and the SSA was tested according to GB/T 8074-2008 [20].

2.2. Experimental Techniques.
To eliminate the effect of SSA of R-P, it is necessary to mill POP into the approximate SSA with R-P (Table 2). Thus, POP with SSA of 1098 m^2/kg and R-P with SSA of 1114 m^2/kg were employed to analyze possible influencing factors that can induce the deterioration of R-P.

In order to study the effect of unsuitable preparation temperature on the deterioration of R-P, the relationship between strength and calcination temperatures was established. Moreover, the calcination temperatures are 130°C, 150°C, 160°C, 165°C, 170°C, 175°C, 180°C, and 200°C (Figure 2), respectively.

To facilitate understanding the going of the work, a diagram for experimental work is presented in Figure 3. Briefly, the properties (water requirement, setting time, strength, and water absorption) were measured first, and then the deterioration mechanism was determined from the large SSA, unsuitable preparation temperature, reasons for increased water requirement, and microstructure changes of its hardened R-P.

2.3. Materials Characterization.
The morphological investigations were observed by the scanning electron microscope (TESCAN VEGA III LMH). The internal detects were measured via simultaneous DSC/TG instrument (SMP/PF7548/MET/400W) [21]. The particle size distribution was analyzed via a laser particle size analyzer (Mastersizer 2000) after dispersing POP and R-P in anhydrous ethanol with an ultrasonic bath. Pore size distribution and porosity of pastes were investigated by an adsorption meter (ASAP 2020) with nitrogen full adsorption.

3. Results and Discussions

3.1. Large Specific Surface Area.
Under the same preparation process as POP, the properties of R-P were deteriorated seriously, which is displayed in Table 3. Clearly, the W/P {ml water/300 g plaster powder (water-plaster ratio)}, setting time, and water absorption were all increased, whereas the strength of R-P was decreased by approximately 50% (Figure 4). At this time, SSA of R-P was increased from 452 m^2/kg to 1114 m^2/kg; thus, the deterioration properties of R-P were caused by its large SSA, which is in harmony with the previous findings [17].

Table 2 gives the properties of R-P and POP under the similar SSA. This table was overwhelmingly proving that the properties of R-P were also deteriorated despite approximate SSA obtained by POP and R-P. To our surprise, the strength decreasing rate was reduced from 50% to 30%–40% (Figure 4). Therefore, it could be concluded that there were, in addition to large SSA brought about, other reasons for property deterioration of R-P.

(a)

(b)
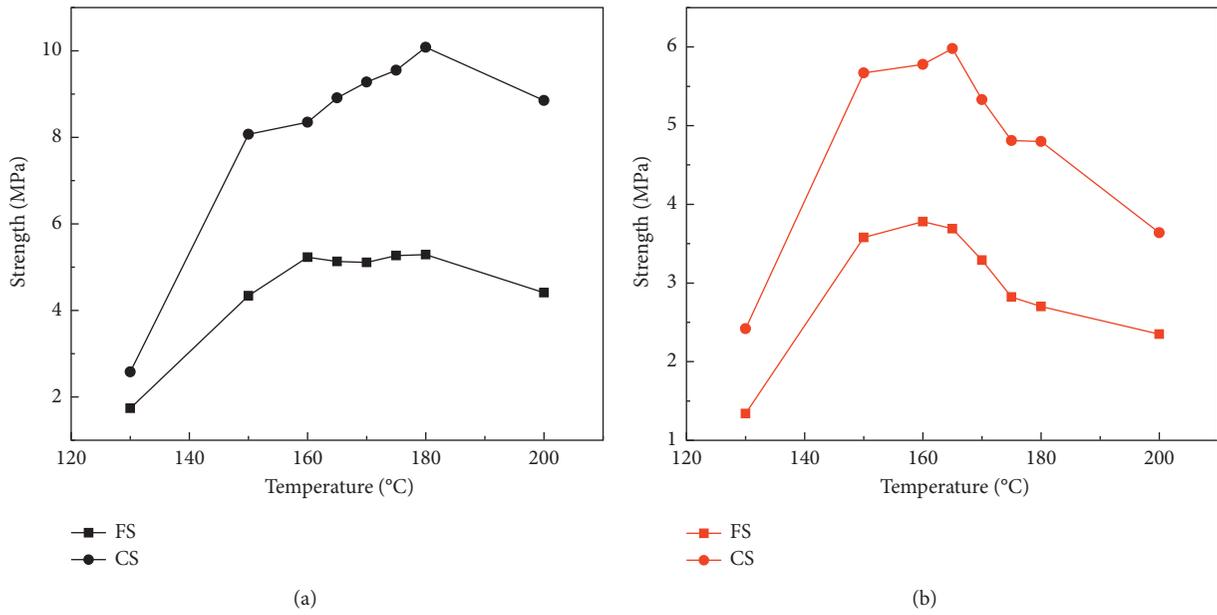
FIGURE 2: Effect of preparation temperatures on the strength of POP and R-P.
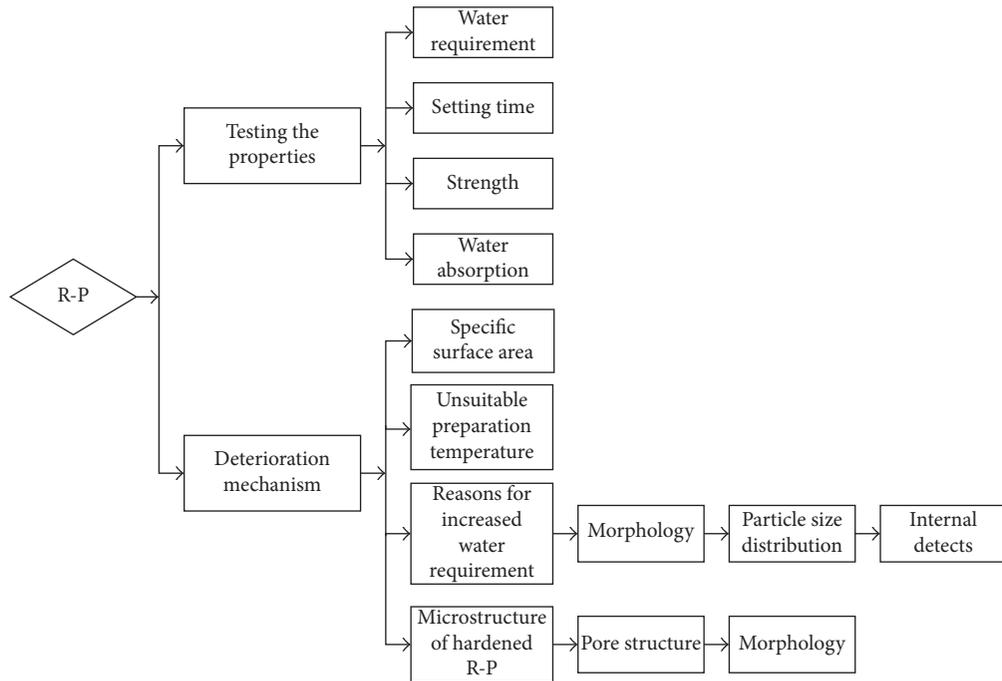
FIGURE 3: The test program.

TABLE 3: Properties of POP and R-P under the same preparation process.

Gypsum	SSA ($m^2 \cdot kg^{-1}$)	W/P	Setting time (min)		2 h strength (MPa)		Dry strength (MPa)		Water absorption (%)
			Initial	Final	Flexural	Compressive	Flexural	Compressive	
POP	452	0.63	8.5	13.5	2.94	5.95	5.29	10.08	29.50
R-P	1114	0.85	33	46	1.66	2.94	2.70	4.80	40.65
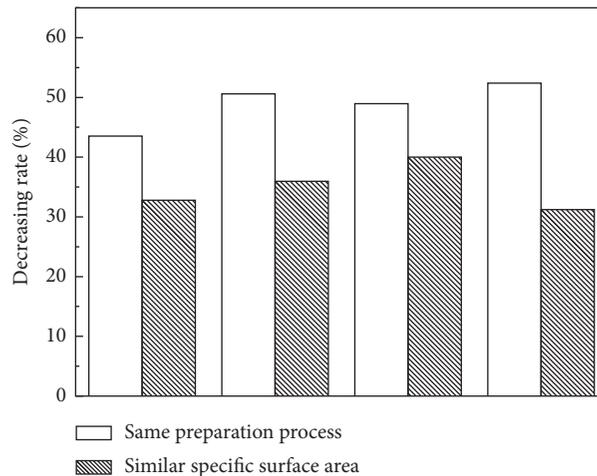
FIGURE 4: The decreasing rate in the strength of R-P.

3.2. Unsuitable Preparation Temperature. It has been reported that under constant experimental conditions, gypsums of different origin have different dehydration characteristics and physical properties [22], and the reactivity of hemihydrate depends largely on the temperature of preparation [23]. So, we conclude that various physical properties of R-P can be observed under different calcination temperatures since it is known that strength is the comprehensive aspect charactering the properties of plaster. Therefore, an attempt has been made to correlate the strength of R-P and POP with different temperatures of preparation so as to find out the effect of preparation temperature on properties of R-P, which is seen in Figure 2.

As the preparation temperature increases, the strength changes of POP and R-P are shown in Figures 2(a) and 2(b), respectively. From the figures, it is clear that the compressive strength (CS) of POP increased rapidly to 10.08 MPa around 180°C and then dropped to 8.85 MPa at 200°C. The flexural strength (FS) of POP rose dramatically to 5.11 MPa around 160°C, and this number remained slightly increased until 180°C but then suffered a sharp drop. Therefore, the suitable preparation temperature of POP is 180°C; at this time, the initial setting time and final setting time are 8.5 min and 13.5 min, respectively, meeting the standard of GB 9776-2008 [18]. While for R-P, the compressive strength and flexural strength were at a peak around 165°C and 160°C, respectively. The setting time can satisfy the standard requirement when the calcination temperature was 165°C. Hence, it could be drawn that the unsuitable preparation temperature led to the deterioration properties of R-P as well.

3.3. Reasons for Increased Water Requirement. The morphology [24], particle size distribution (PSD) [25], and internal detects [21] are of critical factors associated with the water demand property of plaster. Hence, the morphology, PSD, and internal detects of POP and R-P were measured via SEM, laser particle size analyzer, and DSC curves, which are presented in Figure 5.

Figures 5(a) and 5(b) show the crystal morphology of POP and R-P, respectively. It can be seen that the morphology of R-P is totally different from that of POP, depending on their origin of gypsum. The morphology of plaster, made of needle-shaped gypsum crystals, changes with the properties of gypsum. The origin gypsum of POP was relatively dense with almost no pores (Figure 6(a)). However, the origin gypsum of R-P was loose with much pores (Figure 6(b)), which contributed to the morphology changes. Clearly, POP possesses many spheroidal particles and includes some rode-like crystals with an aspect ratio of 1-2. While the aspect ratio of R-P crystals increases, the morphology are changed to acicular-like crystals with an aspect ratio of 5-6, which make R-P crystals occupy acicular-like and rode-like crystals. According to the principle enunciated by Li et al. [19] and Peng et al. [24], the water requirement of plasters are increased with the increase of aspect ratio. The needle-shaped crystal has poor fluidity and can increase the water requirement of plaster greatly, and the ideal crystal has an aspect ratio of 1 : 1 for reducing the water demand. Hence, it can be concluded that the water requirement of R-P is increased by its poor crystals.

Simultaneously, particle size distribution (PSD) results presented in Figure 5(c) further confirm the increase of water demand of R-P. It is noticed that the grading of R-P is, though two peaks are both occupied, obviously different from POP. A broad peak of POP is observed, where the full width at half maximum (FWHM) of the first peak and second peak are 18.75 and 22.50, respectively, if the width of POP is 100. While a narrow peak is seen in R-P, FWHM of the first peak and second peak are 16.25 and 18.75, respectively. Besides, its average particle size of R-P decreases from 54.614 μm to 12.882 μm. The coarse plasters require little water while plasters with narrow PSD reduce the packing density, thus requiring much water for standard consistency [26]. Therefore, much water of R-P is acquired to satisfy the fluidity.

To gain further insight into the reasons for the increase of water requirement, DSC analysis was carried out to evaluate the internal detects of R-P, which is presented in
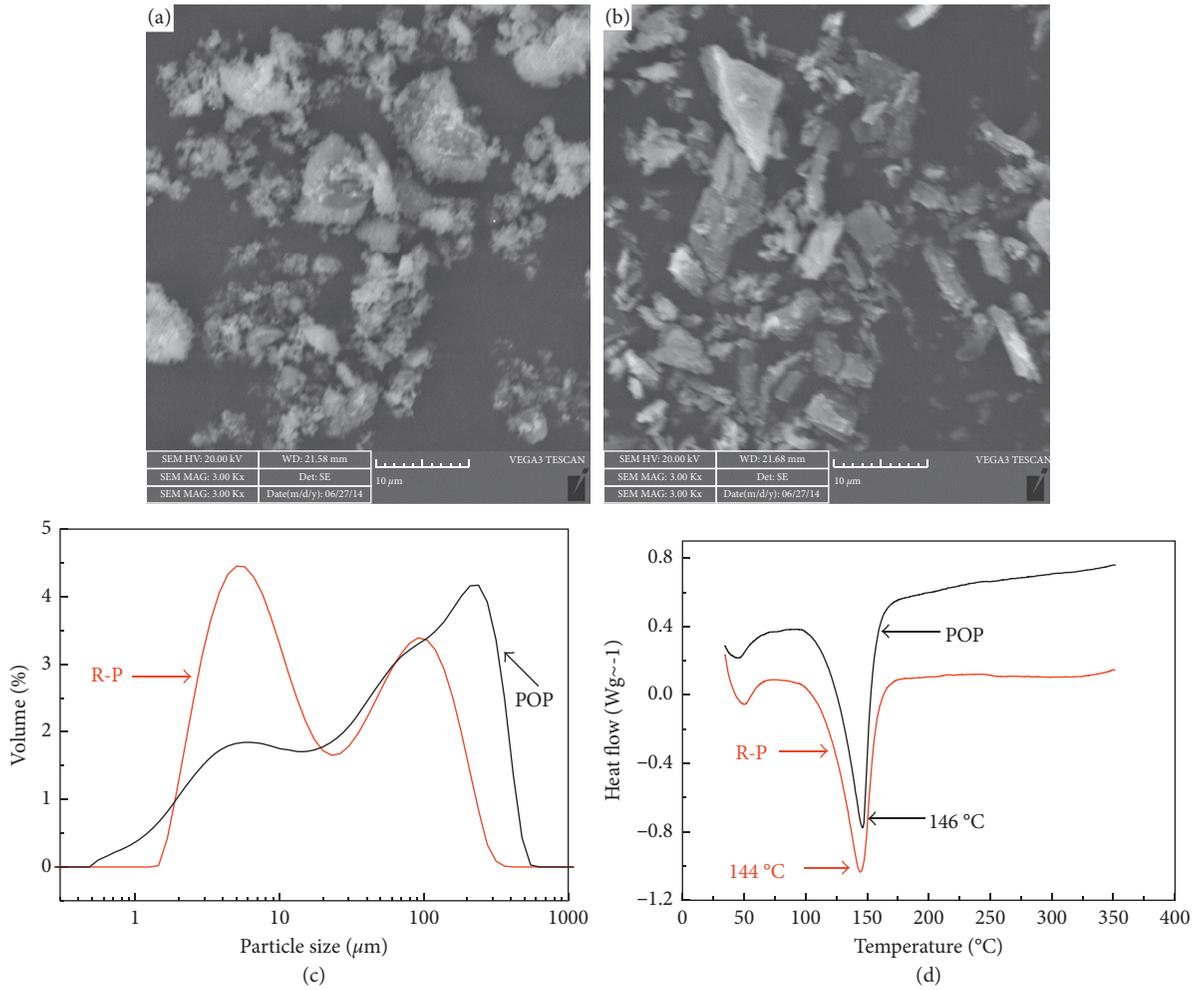
Figure 5: Microstructure, particle size distribution, and DSC curves of POP and R-P.
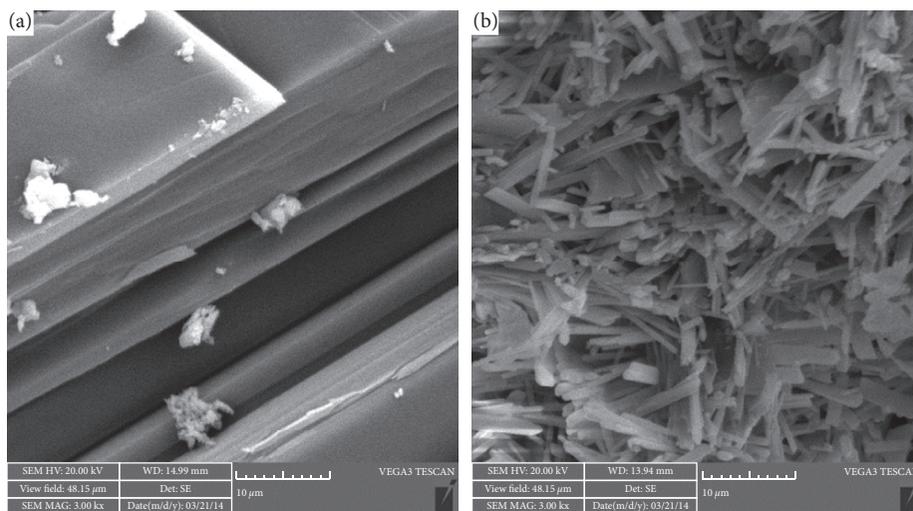
Figure 6: Microstructure of origin gypsum of POP and R-P.

Figure 5(d). Clearly, the decomposition temperature of R-P is 144°C, a little lower than that of POP. Some reported studies have indicated that plasters with little internal detects gain good crystallization while plasters with more internal detects have low decomposition temperature; thus, little internal detects acquire high decomposition temperature [21].
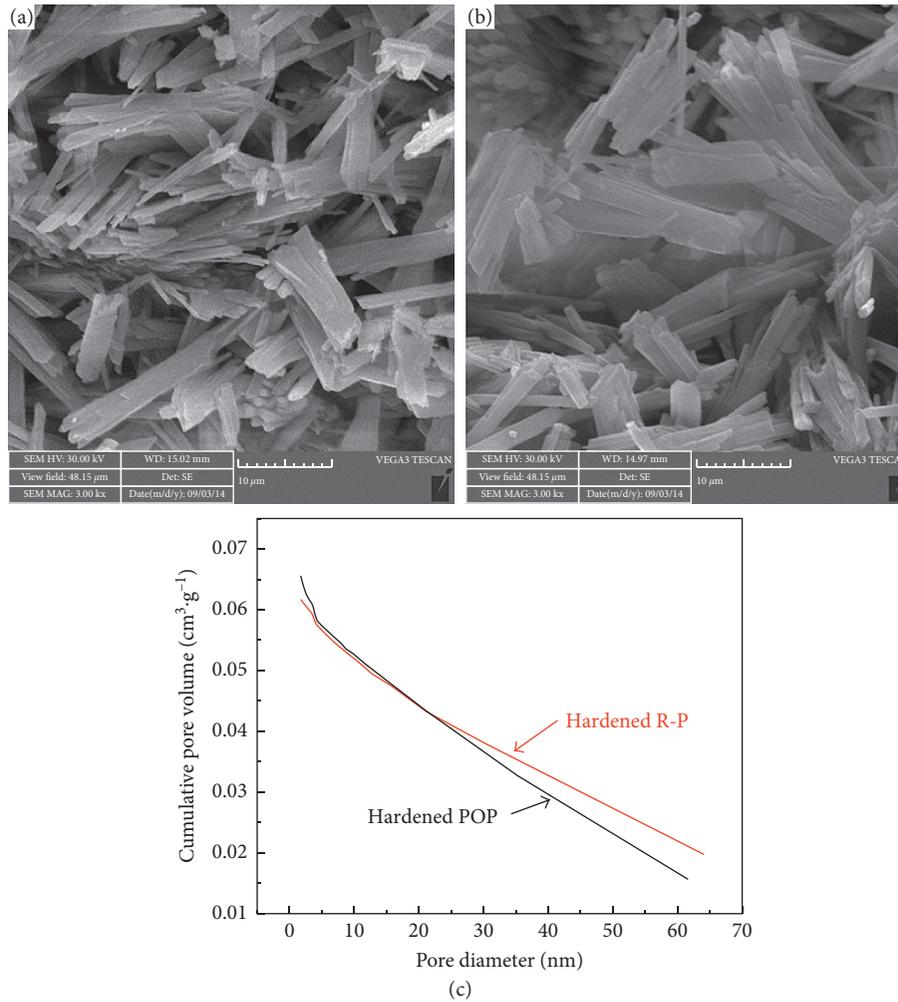
FIGURE 7: The morphology and pore size distribution of hardened POP and hardened R-P.

TABLE 4: Pore characteristics of hardened POP and hardened R-P.

Sample	Average pore diameter (nm)	Cumulative pore volume (cm^3·g^{-1})
Hardened POP	11.5892	0.066
Hardened R-P	14.6917	0.062

So, it could be concluded that more internal detects are obtained by R-P, increasing its water requirement, which is in good agreement with the SEM and PSD results.

Although the increased water requirement of R-P is not conducive for use in construction, it is of great importance for the ground improvement projects. According to Kamei et al., the improvement in strength when R-P was added to the soil was mainly depending on the potential of R-P to absorb water from the tested soil. The presence of R-P in soil mixture had a significant effect on the reduction of natural water content, subsequently the strength was improved.

3.4. Microstructure of Hardened R-P. The strength of R-P paste depends largely on the characteristics of the microstructure, such as crystal morphology and size, and characteristics of matrix joints and pore structure [25].

Therefore, the morphology and pore structure were measured by SEM and nitrogen adsorption porosimetry, respectively, which are shown in Figure 7 and Table 4.

The SEM images of hardened POP and hardened R-P are presented in Figures 7(a) and 7(b), where significant difference can be observed. Owing to the high W/P and low reaction rate, a loose structure with many tufted crystals was shown in hardened R-P. Crystals of short aspect ratio can be clearly observed as well, reducing the overlapping of crystals; consequently, the strength of R-P is weakened. While for hardened POP, the crystals are slightly refined, little rode-like crystals of short aspect ratio can be readily detected. It displays a relatively compacted network with much needle-like crystals of long aspect ratio interweaving together horizontally and vertically, resulting in the preferable development and lapping tightly of crystals attributing high strength of POP.

It is widely known that the characteristics of pore structure are of essential importance for understanding the strength and wettability of hardened R-P [23]. So the porosity and pore size distribution of hardened POP and hardened R-P are measured, which are displayed in Table 4 and Figure 7(c), respectively. Clearly, the average pore diameter of hardened R-P, though the close cumulative pore volumes with hardened POP are obtained, increases drastically. The high quantity of coarse pores existed in hardened R-P is also confirmed by the pore size distribution results in Figure 7(c). Fine pores acquire high strength while pores with big diameter obtain low strength. The pore structure results are good consistent with SEM. The attainment of low strength and high wettability is associated with its coarse pores. It is well known that wettability is an important parameter for construction. R-P presents high water absorption. Therefore, low moisture resistance would be observed under wet environment, and radical decrease of mechanical properties would appear with the increasing moisture as well, which limits its utilization in building construction.

4. Conclusions

The following conclusions can be drawn from this study:

(1) The properties of R-P are deteriorated; nevertheless, the strength decreases from 50% at the same manufacturing process to 30%–40% at similar specific surface area. Therefore, the large specific surface area contributes to the deterioration of R-P.

(2) Except for large specific surface area of R-P, there are other influencing factors increasing the water requirement, such as poor morphology, narrow particle size distribution, and its incremental internal detects.

(3) The suitable preparation temperature of R-P is reduced to 165°C; thus, the properties of R-P are deteriorated severely when unsuitable temperature of preparation is adopted.

(4) Hardened R-P possesses a loose structure and coarse pores, thus decreasing its strength.

(5) In principle, the research on recycled plaster will provide a theoretical basis of efficient utilization of waste gypsum.

Conflicts of Interest

The authors declare that they have no conflicts of interest.

Acknowledgments

References

[1] J. L. Davy, T. J. Phillips, and J. R. Pearse, "The damping of gypsum plaster board wooden stud cavity walls," *Applied Acoustics*, vol. 88, pp. 52–56, 2015.

[2] J. Zhou, Z. Shu, L. Tiantian, Y. Dongxue, Z. Sheng, and Y. Wang, "Novel fabrication route for non-fired ceramic tiles only using gypsum," *Ceramics International*, vol. 41, no. 7, pp. 9193–9198, 2015.

[3] J. Zhou, Z. Sheng, T. Li, Z. Shu, Y. Chen, and Y. Wang, "Preparation of hardened tiles from waste phosphogypsum by a new intermittent pressing hydration," *Ceramics International*, vol. 42, no. 6, pp. 7237–7245, 2016.

[4] H. C. Wu, Y. M. Xia, X. Y. Hu, and X. Liu, "Improvement on mechanical strength and water absorption of gypsum modeling material with synthetic polymers," *Ceramics International*, vol. 40, no. 9, pp. 14899–14906, 2014.

[5] N. B. Singh and B. Middendorf, "Calcium sulphate hemihydrate hydration leading to gypsum crystallization," *Progress in Crystal Growth and Characterization of Materials*, vol. 53, no. 1, pp. 57–77, 2007.

[6] S. Suárez, X. Roca, and S. Gasso, "Product-specific life cycle assessment of recycled gypsum as a replacement for natural gypsum in ordinary Portland cement: application to the Spanish context," *Journal of Cleaner Production*, vol. 117, pp. 150–159, 2016.

[7] O. Bergersen and K. Haarstad, "Treating landfill gas hydrogen sulphide with mineral wool waste (MWW) and rod mill waste (RMW)," *Waste Management*, vol. 34, no. 1, pp. 141–147, 2014.

[8] A. López and A. Lobo, "Emissions of C&D refuse in landfills: a European case," *Waste Management*, vol. 34, no. 8, pp. 1446–1454, 2014.

[9] T. Raghavendra and B. C. Udayashankar, "Engineering properties of controlled low strength materials using fly ash and waste gypsum wall boards," *Construction and Building Materials*, vol. 101, pp. 548–557, 2015.

[10] A. Ahmed, K. Ugai, and T. Kamei, "Investigation of recycled gypsum in conjunction with waste plastic trays for ground improvement," *Construction and Building Materials*, vol. 25, no. 1, pp. 208–217, 2011.

[11] A. Ahmed and K. Ugai, "Environmental effects on durability of soil stabilized with recycled gypsum," *Cold Regions Science and Technology*, vol. 66, no. 2-3, pp. 84–92, 2011.

[12] T. Kamei, A. Ahmed, and T. Shibi, "Effect of freeze–thaw cycles on durability and strength of very soft clay soil stabilised with recycled Bassanite," *Cold Regions Science and Technology*, vol. 82, no. 8, pp. 124–129, 2012.

[13] T. Kamei, A. Ahmed, and T. Shibi, "The use of recycled bassanite and coal ash to enhance the strength of very soft clay in dry and wet environmental conditions," *Construction and Building Materials*, vol. 38, pp. 224–235, 2013.

[14] A. P. Godinho-Castro, R. C. Testolin, L. Janke, A. X. R. Corrêa, and C. M. Radetski, "Incorporation of gypsum waste in ceramic block production: proposal for a minimal battery of tests to evaluate technical and environmental viability of this recycling process," *Waste Management*, vol. 32, no. 1, pp. 153–157, 2012.

[15] K. F. Ragab, *Recycling of Waste Gypsum Board to Produce New Drywalls and Non-Load Bearing Bricks*, American University in Cairo, Cairo, Egypt, 2014.

[16] Y. Kojima and T. Yasue, "Synthesis of large plate-like gypsum dihydrate from waste gypsum board," *Journal of the European Ceramic Society*, vol. 26, no. 4-5, pp. 777–783, 2006.

[17] L. N. Ren, *Reclaimed Gypsum Properties Change Law and Mechanism*, Standardization Administration of China, Beijing, China, 2014.

[18] GB/T 9776-2008, *Calcined Gypsum*, Standardization Administration of China, Beijing, China, 2008.

[19] Z. Li, J. Peng, and X. Qiu, "Effect of different ways of STPP retarder addition on properties of recycled gypsum," *Journal of Wuhan University of Technology*, vol. 32, no. 5, pp. 1125–1131, 2017.

[20] GB/T 8074-2008, *Testing Method for Specific Surface of Cement-Blaine Method*, Standardization Administration of China, Beijing, China, 2008.

[21] M. Guodong, "A study on the phase-transformation of the bassanites during hydration," *Journal of the Chinese Ceramic Society*, vol. 30, no. 4, pp. 532–536, 2002.

[22] R. A. Kuntze, "Differential thermal analysis of calcium sulphate dihydrate," *Nature*, vol. 193, no. 4817, pp. 429–432, 1962.

[23] M. J. Ridge and H. Surkevicius, "Influence of some conditions of calcination on the reactivity of calcium sulphate hemihydrate," *Journal of Chemistry Technology and Biotechnology*, vol. 12, no. 10, pp. 425–432, 1962.

[24] J. Peng, J. Qu, J. Zhang, C. Zou, and M. Chen, "Adsorption characteristics of EDTA on of α-hemihydrate desulfurization gypsum surface and its influence on crystal morphology," *Chinese Journal of Material Research*, vol. 25, no. 6, pp. 566–572, 2011.

[25] B. H. Guan, Q. Ye, Z. Wu, W. Lou, and L. Yang, "Analysis of the relationship between particle size distribution of α-calcium sulfate hemihydrate and compressive strength of set plaster—using grey model," *Powder Technology*, vol. 200, no. 3, pp. 136–143, 2010.

[26] Q. Ye, B. Guan, W. Lou, L. Yang, and B. Kong, "Effect of particle size distribution on the hydration and compressive strength development of α-calcium sulfate hemihydrate paste," *Powder Technology*, vol. 207, no. 1–3, pp. 208–214, 2011.

Research Article

Development of Steel Fiber-Reinforced Expanded-Shale Lightweight Concrete with High Freeze-Thaw Resistance

Mingshuang Zhao,[1,2] Xiaoyan Zhang,[1,3] Wenhui Song,[2,3] Changyong Li ⓘ,[1,3] and Shunbo Zhao ⓘ [1,2]

[1]*International Joint Research Lab for Eco-Building Materials and Engineering of Henan,*
 North China University of Water Resources and Electric Power, Huayuan Campus, No. 36 Beihuan Road,
 Zhengzhou 450045, China
[2]*Henan Province Collaborative Innovation Center for High-Efficient Utilization and Support Engineering of Water Resources,*
 North China University of Water Resources and Electric Power, Longzihu Campus, No. 136 Jinshui East Road,
 Zhengzhou 450046, China
[3]*School of Civil Engineering and Communication, North China University of Water Resources and Electric Power,*
 Huayuan Campus, No. 36 Beihuan Road, Zhengzhou 450045, China

Correspondence should be addressed to Shunbo Zhao; sbzhao@ncwu.edu.cn

For the popularized structural application, steel fiber-reinforced expanded-shale lightweight concrete (SFRELC) with high freeze-thaw resistance was developed. The experimental study of this paper figured out the effects of air-entraining content, volume fraction of steel fibers, and fine aggregate type. Results showed that while the less change of mass loss rate was taken place for SFRELC after 300 freeze-thaw cycles, the relative dynamic modulus of elasticity and the relative flexural strength presented clear trends of freeze-thaw resistance of SFRELC. The compound effect of the air-entraining agent and the steel fibers was found to support the SFRELC with high freeze-thaw resistance, and the mechanisms were explored with the aid of the test results of water penetration of SFRELC. The beneficial effect was appeared from the replacement of lightweight sand with manufactured sand. Based on the test results, suggestions are given out for the optimal mix proportion of SFRELC to satisfy the durability requirement of freeze-thaw resistance.

1. Introduction

On the purpose of utilizing the local raw materials, steel fiber-reinforced expanded-shale lightweight concrete (SFRELC) was developed, which applied the expanded shale as coarse aggregates and the lightweight sand of expanded-shale's byproduct or the manufactured sand as fine aggregates. Based on the systematically experimental studies, SFRELC has reliable basic mechanical properties [1–4], reasonable strength development [5], enhanced carbonization resistance, and reduced shrinkage [5, 6]. To verify the possibility of applying SFRELC in the wet environments at cold and severe cold areas of China [7], the experimental study was carried out on the freeze-thaw resistance of SFRELC in this paper.

After searching the literature, although few investigations were found to research the freeze-thaw resistance of steel fiber-reinforced lightweight aggregate concrete (SFRLAC), the results exhibited a good prospect for the development of SFRELC with high freeze-thaw resistance. Ishida et al. [8] reported that the freeze-thaw resistance of SFRLAC could be improved by the increase in the bond force between slenderer steel fibers with a large bond area and a high-strength matrix. Huo et al. [9, 10] discovered that the freeze-thaw resistance of pumice lightweight concrete could be enhanced by adding hybrid fibers (steel fiber and polypropylene fiber) due to the decrease of strength loss, although the bond between steel fibers and the matrix became weaker with the increase of freeze-thaw cycles. Li et al. [11] concluded that steel fibers can

TABLE 1: Physical properties of lightweight sand and manufactured sand.

Identifier	Fineness modulus	Particle density (kg/m^3)	Bulk density (kg/m^3)	1 h water absorption (%)	Mud content (%)	Stone powder (%)	Methylene blue value (g/kg)
L	3.56	1659	946	9.0	1.5	—	
M	2.50	2730	1930	0.90	—	7.9	0.75
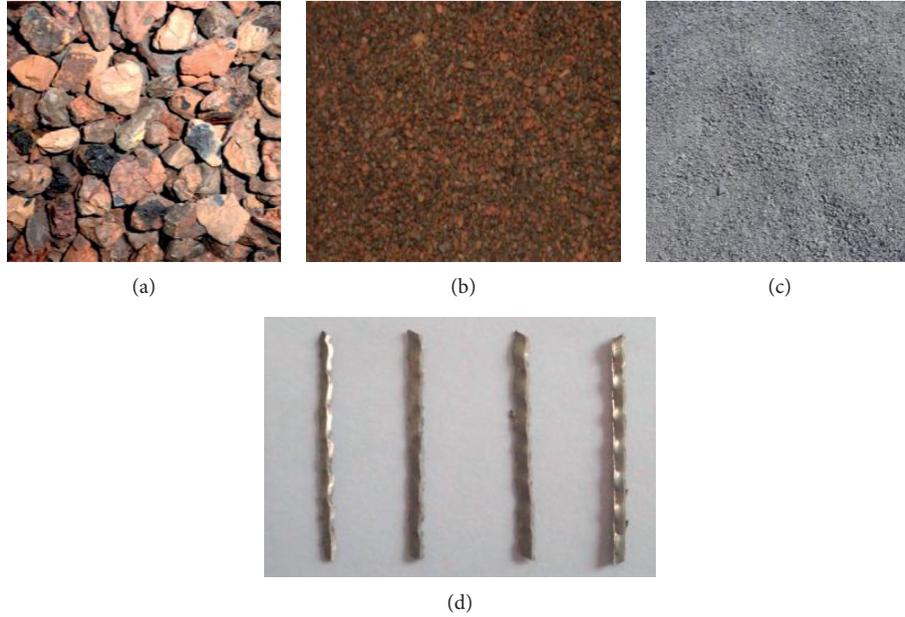
FIGURE 1: Morphology features of aggregates and steel fibers. (a) Expanded shale; (b) lightweight sand; (c) manufactured sand; (d) steel fibers.

improve the freeze-thaw resistance of SFRLAC characterized by the mass loss rate and the relative dynamic modulus of elasticity, as the matrix spalling from frost heaving was restrained by steel fibers.

In view of the benefit of air-entraining to freeze-thaw resistance of concrete [12–16], the content of the air-entraining agent was also considered as a main factor in this paper. The freeze-thaw resistance of SFRELC was experimentally studied and comprehensively evaluated by the indexes of the mass loss rate, relative dynamic modulus of elasticity, and relative flexural strength. The compound effect of the air-entraining agent and steel fibers and the beneficial effect of manufactured sand on freeze-thaw resistance of SFRELC are analyzed. The mechanisms are explored with the aid of test results of water penetration of SFRELC. Suggestions are given out for the optimal mix design of SFRELC with high freeze-thaw resistance.

2. Experiment

2.1. Raw Materials. The ordinary silicate cement was grade 42.5, the water requirement of normal consistency was 26.4%, and the initial and final setting times were 150 min and 248 min. The compressive strength was 22.8 MPa at 3 days and 50.8 MPa at 28 days, and the tensile strength was 4.1 MPa at 3 days and 8.0 MPa at 28 days.

The sintering expanded shale with a maximum size of 20 mm was used as coarse aggregates sieved in continuous gradation based on the maximum density principle [17, 18]. The bulk and particle densities were 800 kg/m^3 and 1274 kg/m^3, the cylinder compressive strength was 5.0 MPa, the 1-hour water absorption was 6.1%, and the mud content was 0.2%.

Two kinds of fine aggregates were used, respectively. One was the lightweight sand made of the byproduct of sintering expanded shale in continuous gradation with a size of 1.6–5 mm [17, 18] and another was the manufactured sand [19, 20]. Table 1 lists their physical properties.

The steel fiber was of milling type with length $l_f = 30$ mm and equivalent diameter $d_f = 0.8$ mm. The aspect ratio $l_f/d_f = 37.5$.

Figure 1 shows the morphology features of coarse expanded shale, lightweight sand, manufactured sand, and steel fibers.

Others were tap water, polycarboxylic acid superplasticizer with 19% water-reducing rate, and polycarboxylic acid air-entraining admixture.

2.2. Mix Proportion of SFRELC. The mix proportion of SFRELC was designed in accordance with the specifications of Chinese standards [17, 21], where the absolute volume method was adopted. The volume fraction of steel fibers (ρ_f),

TABLE 2: Mix proportion of concrete.

Mix no.	m_{ae} (‰)	ρ_f (%)	Cement (kg/m^3)	Water (kg/m^3)	Steel fiber (kg/m^3)	Sand (kg/m^3)	Expanded shale (kg/m^3)
L0.00/0.0	0.00	0.0	460	138	—	490	520
L0.00/0.8	0.04	0.8	550	165	62.4	452	469
L0.04/0.8	0.04	0.8	550	165	62.4	452	469
L0.08/0.8	0.08	0.8	550	165	62.4	452	469
L0.12/0.8	0.12	0.8	550	165	62.4	452	469
L0.08/0.0	0.08	0.0	460	138	—	490	520
L0.08/0.4	0.08	0.4	505	153	31.2	471	494
L0.08/1.2	0.08	1.2	595	179	93.6	432	443
M0.08/0.8	0.08	0.8	550	165	62.4	743	469

the content of the air-entraining agent (m_{ae}), and the type of fine aggregates were considered as the test parameters. Based on previous studies of fundamental properties of SFRELC with good workability [1–6], the water-cement ratio was fixed as $w/c = 0.30$, while the sand ratio was 42% and the dosage of the water reducer was 4.0% cement mass. Table 2 lists their combinations for the test of 9 trials, where the letter in mix no. is the identifier of fine aggregates and the following digits represent m_{ae} and ρ_f.

Based on previous experimental studies, prewetting the lightweight aggregates had beneficial effects on the mechanical properties especially on the shrinkage reduction of SFRELC [1–6]. This may also be beneficial to decrease the water penetration and to increase the freeze-thaw resistance of SFRELC. Zhao et al. [22] reported that the water penetration was reduced for SFRLAC with saturated lightweight aggregates, and Ali et al. [23] reported that the freeze-thaw resistance of lightweight aggregate concrete was improved at early ages by increasing the saturation level of aggregates. Although there were some contract conclusions [24, 25] or no relationship [26, 27] reported, the differences may be resulted from the different pores' structure (open or closed) and water absorption of lightweight aggregates [15, 28, 29]. Therefore, the expanded shale and lightweight sand of this experiment were prewetted as the saturated dry surface by using the additional water counted with the 1-hour water absorption. All mixes of this study had good workability with slump of 120 mm–150 mm.

2.3. Preparation of Specimens. Specimens for the freeze-thaw test were 100 mm × 100 mm × 400 mm prisms; 189 specimens for 9 trials were prepared, and each trial had 21 specimens. Specimens for the water penetration test were circular truncated cones with a bottom diameter of 185 mm, tip diameter of 175 mm, and height of 150 mm; 54 specimens for 9 trials were prepared, and each trial had 6 specimens.

The single horizontal shaft forced mixer was used. The expanded shale and lightweight sand (except for M0.08/0.8) were firstly prewetted in the mixer for 1 hour, and then, the manufactured sand (only for M0.08/0.8), the cement, and half dosage of the mix water were added and mixed for 30 s. During the mixing, the water reducer and air-entraining agent as well as residual mix water were added. After that, the steel fiber was sprinkled into the mixer and mixed for 3 min.

The specimens formed by steel moulds on the vibration platform. After being cast for 24 hours, they moved from moulds and cured in the standard curing room for 28 days before testing.

2.4. Test Methods. Test methods of this experiment were in accordance with the specifications of the Chinese standard GB/T 50082 [30] and ASTM standard C666 [31]. The freeze-thaw resistance was measured by using the test method for rapid freezing and thawing in water, and the main test apparatuses were the rapid freeze-thaw test machine, the tester of the dynamic modulus of elasticity, the hydraulic universal test machine, and the balance. The freeze-thaw resistance was presented by the mass loss rate (Δm_n) and the relative dynamic modulus of elasticity (P_n) calculated as follows:

$$\Delta m_n = \frac{m_0 - m_n}{m_0} \times 100, \tag{1}$$

$$P_n = \frac{f_n^2}{f_0^2} \times 100, \tag{2}$$

where m_0 and m_n are the mass of the specimen at the beginning and after n cycles of the freeze-thaw test, respectively, and f_0 and f_n are the transversal base frequency of the specimen at the beginning and after n cycles of the freeze-thaw test, respectively.

The durability factor (DF) was used to evaluate the freeze-thaw resistance [7]:

$$DF = \frac{f_{300}^2}{f_0^2} \times 100, \tag{3}$$

where f_{300} is the transversal base frequency of the specimen after 300 cycles of the freeze-thaw test.

Before 300 cycles of freezing and thawing, if the relative dynamic modulus of elasticity (P_n) and the mass loss rate (Δm_n) reached 60% and 5%, respectively, at n cycles, then the DF was computed as follows:

$$DF = 0.6 \times \frac{n}{300}. \tag{4}$$

Based on previous studies [9–11], the strength loss of SFRLAC is better to reflect the freeze-thaw resistance. Therefore, the flexural strength of SFRELC was tested in accordance with the specification of the Chinese standard
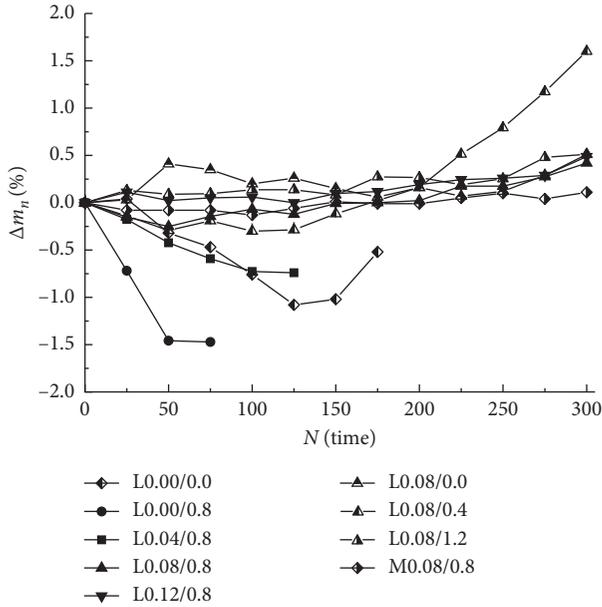
FIGURE 2: Changes of the mass loss rate with freezing-thawing cycles.

FIGURE 3: Test values of the height of water penetration.

GB/T 50081 [32]. The concentrated loads were exerted on the three dividing points, and the relative flexural strength (f_r) was defined as follows:

$$f_r = \frac{f_n}{f_0} \times 100, \qquad (5)$$

where f_0 and f_n are the flexural strength of the specimen at the beginning and after n cycles of the freeze-thaw test, respectively.

To explain the freeze-thaw mechanism in aspect of the water transport property of SFRELC, the depth of water penetration was measured [30]. The main test apparatuses were the testing machine for water penetration of concrete, the hydraulic universal test machine, and the steel ruler. After the specimens in a group were fixed in the testing machine, the hydraulic pressure was exerted within 1.2 ± 0.05 MPa for 24 hours. Then, the specimens were split on the hydraulic universal test machine. The depth of the water stain was measured by the steel ruler at 10 points in equal space divided along the bottom splitting line. The depth of water penetration of each specimen was counted as the mean value of these 10 points and that of one group (h_p) was the mean value of six specimens.

3. Results and Discussion

3.1. Mass Loss Rate. The mass change of the SFRELC matrix comes mainly from two parts: one is the increment due to the water absorbed in the pores and capillaries of concrete during freezing and thawing and another is the decrement due to the surface peeling of set cement and aggregates. When the latter is greater than the former, the mass loss rate computed by formula (1) is positive, which always means the better internal structure the matrix has, and the freeze-thaw

damage takes place from the surface successively. When the latter is lower than the former, the mass loss rate is negative, which always means the poor internal structure the matrix has, and the freeze-thaw damage takes place because of the internal expansion of absorbed water inside the pores and capillaries [12, 33].

Figure 2 presents the changes of mass loss rate of SFRELC with the freeze-thaw cycles. The negative mass loss rate of L0.00/0.0 increased by adding steel fibers in L0.00/0.8. This condition was improved successively by the addition of the air-entraining agent from 0.4‰ to 1.2‰. When the content of the air-entraining agent was not less than 0.8‰, the mass loss rate of SFRELC became positive normally. Under the condition of SFRELC with 0.8‰ air-entraining agent, the mass loss rate changed from negative to positive with $\rho_f = 0.4\%$ and 0.8% before 175 freeze-thaw cycles, and then, it remained positive and increased with the increasing freeze-thaw cycles. When $\rho_f = 1.2\%$, the mass loss rate remained positive all the time. When $N = 300$ and $\Delta m_n = 0.42\%$ and 0.51% for SFRELC with $\rho_f = 0.8\%$ and 1.2%, the mass loss rate was the same for L0.08/0.0 without steel fibers. Compared to L0.08/0.8 with lightweight sand, the mass loss rate of M0.08/0.8 with manufactured sand changed slightly until $N = 300$.

The changes of mass loss rate were identical to the water penetration properties as shown in Figure 3. Compared to L0.00/0.0, L0.08/0.0 had a higher resistance to water penetration with 7.27% reduction of h_p and L0.00/0.8 had a lower resistance to water penetration with 25% increment of h_p. This exhibited the different roles of the air-entraining agent and steel fibers affecting the microstructure of SFRELC. The air-entraining agent imported even dispersed bubbles with minuteness and closed and mutually uncorrelated characteristics [13–15], which led to the higher density of SFRELC matrix with improved uniformity of zigzag capillaries. The steel fibers increased the connectivity of internal pores and capillaries due to the defects of interfaces along steel fibers in the matrix [9, 10, 22]. Therefore, the results of water penetration of SFRELC reflected the compound function of the air-entraining agent and steel fibers.

With the increase of $m_{ae} = 0.04‰–0.12‰$, h_p of SFRELC dropped down obviously. Compared to L0.04/0.8, h_p of
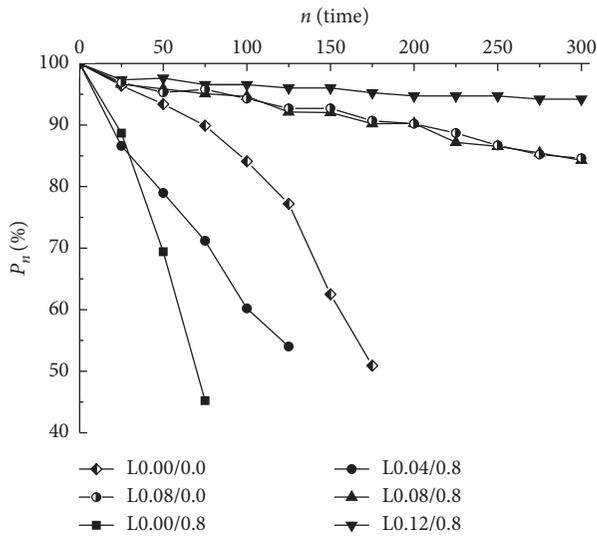
FIGURE 4: Changes of the relative dynamic modulus of elasticity affected by content of the air-entraining agent.

FIGURE 5: Changes of relative dynamic modulus affected by volume fraction of steel fibers and fine aggregates.

L0.08/0.8 and L0.12/0.8 reduced 22.1% and 30.5%, respectively. This reflects the marked benefit of air-entraining to improve the resistance of SFRELC to water penetration. When $m_{ae} = 0.08‰$, h_p of SFRELC with lightweight sand was almost equal except the larger one, 11.2 mm of L0.08/1.2. Combined with h_p of L0.12/0.8, more air-entraining was needed for L0.08/1.2 to get the reduced h_p. In a word, the balance between volume fraction of steel fibers and air-entraining controlled the water permeability of SFRELC.

When replacing lightweight sand by manufactured sand, the resistance of SFRELC to water penetration increased with the reduction of h_p from 10.2 mm to 8.1 mm. This is due to the beneficial effects of stone powder in manufactured sand [19, 20]: the microaggregate filling effect on density, the activity effect and crystal nuclei effect on cement hydration degree, and the enhancement effect on hardness and bond property of the interfaces among the composites. Theoretically, these effects should also comprehensively improve the interfaces among steel fibers and set cement.

Given above, the mass loss rate reflected some information about the freeze-thaw resistance of SFRELC, where the negative and positive values gave the relative degree of water absorption and surface peeling off during the cycles of freezing and thawing. However, because of the integrity maintained and undetected surface scaling of SFRELC specimens, the mass loss rate was less changed with the increasing freeze-thaw cycles, and it was not a sensitive parameter to represent the freeze-thaw resistance of SFRELC.

3.2. Relative Dynamic Modulus of Elasticity. The dynamic modulus of elasticity is closely linked with the constitutes and microstructures of concrete, which is affected sensitively by the interior pores and unsubstantial interface [12, 33]. Figure 4 exhibits the changes of relative dynamic modulus of elasticity with freeze-thaw cycles affected by the content of
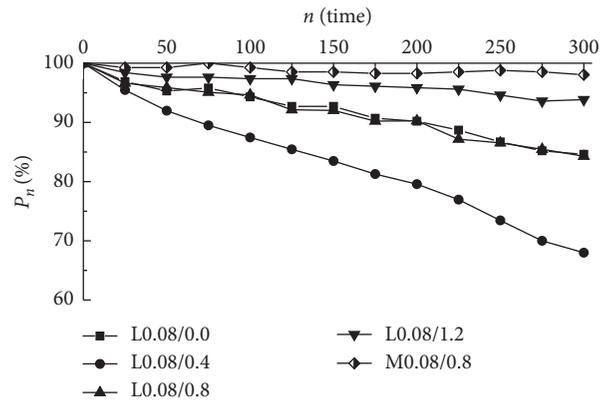
the air-entraining agent. Compared to L0.00/0.0, P_n of L0.08/0.0 decreased slowly with the increasing freeze-thaw cycles. This is identical to the previous studies for the freeze-thaw resistance of lightweight aggregate concrete [9, 13–15], which benefits from the air-entraining effectiveness for the improvement of the microstructure with proper amount of closed and uniformly distributed microbubbles, resulting in the cutting-off of pores and capillaries inside concrete. At the same time, adding steel fibers in L0.00/0.8 without the air-entraining agent led to the drop down of P_n. This is consistent with the increased depth of water penetration as shown in Figure 3. With the increasing content of the air-entraining agent, the reduction of P_n became slow, while the changes of P_n for L0.08/0.8 and L0.08/0.0 were almost the same. When $m_{ae} = 0.12‰$, the P_n of L0.12/0.8 decreased slightly until $N = 300$. Therefore, the P_n of SFRELC was sensitive to the addition of steel fibers and the air-entraining agent. For the design of freeze-thaw resistance of SFRELC, the balance between the beneficial effect of the air-entraining agent and the harmful effect of steel fibers should be comprehensively considered.

Figure 5 exhibits the changes of relative dynamic modulus of SFRELC with freeze-thaw cycles affected by the volume fraction of steel fibers. With $m_{ae} = 0.08‰$, the P_n reduced slowly with the increasing volume fraction of steel fibers. When $\rho_f = 1.2\%$, the P_n reduced slightly. This exhibited that, with proper content of the air-entraining agent, SFRELC reached the higher freeze-thaw resistance with the assistance of a lager amount of steel fibers. Despite the increase of water penetration to some extent as shown in Figure 3, the beneficial effects of steel fibers on the confinement of internal shortages and the bridging on microcracks appeared successively [6, 11], and the integrity of SFRELC was maintained by overcoming the ice expansion in pores with the increasing freeze-thaw cycles. Therefore, the compound effect of the air-entraining agent and steel fibers led to the high freeze-thaw resistance of SFRELC.

Meanwhile, Figure 5 also exhibits the changes of relative dynamic modulus of SFRELC with freeze-thaw cycles affected by the fine aggregate. With $m_{ae} = 0.08‰$ and $\rho_f = 0.8\%$, the SFRELC with manufactured sand had higher

TABLE 3: Test results of the DF of SFRELC.

Specimen no.	L0.00/0.0	L0.00/0.8	L0.04/0.8	L0.08/0.4	L0.08/0.0	L0.08/0.8	L0.12/0.8	L0.08/1.2	M0.08/0.8
DF	0.31	0.12	0.20	0.68	0.84	0.84	0.94	0.94	0.98

TABLE 4: Specified minimum value of the DF.

Design service life	100 years		50 years		30 years	
Environmental condition	Highly saturated	Moderately saturated	Highly saturated	Moderately saturated	Highly saturated	Moderately saturated
Severe cold area	0.80	0.70	0.70	0.60	0.65	0.50
Cold area	0.70	0.60	0.60	0.50	0.60	0.45
Partial freezing area	0.60	0.60	0.50	0.45	0.50	0.40

TABLE 5: Test results of the relative flexural strength of SFRELC.

Specimen no.	Freeze-thaw cycles, N				
	75	150	175	225	300
L0.00/0.0	46.5	18.9	9.8	—	—
L0.00/0.8	62.7	29.7	17.4	3.4	—
L0.04/0.8	71.6	41.6	—	19.6	—
L0.08/0.0	95.3	83.8	—	75.3	63.4
L0.08/0.4	77.5	53.0	—	41.8	26.2
L0.08/0.8	96.6	89.0	—	82.3	74.1
L0.12/0.8	95.2	86.9	—	82.1	74.9
L0.08/1.2	96.1	89.3	—	85.7	80.0
M0.08/0.8	95.3	94.9	—	88.4	81.9

freeze-thaw resistance than that using lightweight sand. This is identical with the experimental results of water penetration shown in Figure 3.

Table 3 lists the test results of the DF of SFRELC. Table 4 presents the minimum value of the DF specified in the Chinese standard for the durability design of concrete structures [7]. It can be seen that air-entraining is quite necessary for the SFRELC with certain freeze-thaw resistance even in the partial freezing area. With proper contents of the air-entraining agent and steel fibers, SFRELC with high freeze-thaw resistance can be applied in every freezing area, even in the highly saturated environmental condition of severe cold areas.

3.3. Relative Flexural Strength of SFRLAC. Table 5 lists the test results of the relative flexural strength of SFRELC with the increase of freeze-thaw cycles. The changes of relative flexural strength were similar to those of relative dynamic modulus of elasticity, which appeared more sensitive to the freeze-thaw cycles. Without adding the air-entraining agent, SFRELC lost the flexural strength rapidly after 75 freeze-thaw cycles. When $\rho_f = 0.8\%$, the relative flexural strength of SFRELC obviously improved with the increase of m_{ae} from 0.04‰ to 0.08‰. When $m_{ae} \geq 0.08‰$, SFRELC with $\rho_f \geq 0.8\%$ had higher relative flexural strength. Replacing lightweight sand with manufactured sand also gave the SFRELC with high relative flexural strength. These demonstrated that the flexural strength of SFRELC decreased with the increase of freeze-thaw cycles due to the weakened bond of steel fibers with the matrix.

4. Conclusion

In this paper, the effects of air-entraining, steel fibers, and fine aggregate type on the freeze-thaw resistance of SFRELC were experimentally studied and explained on the mechanisms in consistent with the test results of water penetration. The conclusions can be drawn as follows:

(1) Due to the water importing and exporting peculiarity of SFRELC, the mass loss rate could not reach the limit of 5%. It was not a good index to evaluate the damage of SFRELC due to freezing and thawing. Comparatively, the relative dynamic modulus of elasticity of SFRELC had a clear trend to reflect the freeze-thaw resistance, and the relative flexural strength of SFRELC was more sensitive to the freeze-thaw cycles.

(2) Air-entraining was quite necessary for the development of SFRELC with high freeze-thaw resistance. Steel fibers were harmful to the freeze-thaw resistance of SFRELC without air-entraining. However, the harmful effect of steel fibers could be overcome with the assistance of air-entraining. With proper air-entraining, the freeze-thaw resistance of SFRELC increased with the increasing volume fraction of steel fibers. This exhibited the compound effect of the air-entraining agent and steel fibers on the freeze-thaw resistance of SFRELC.

(3) The replacement of lightweight sand with manufactured sand in SFRELC could enhance the freeze-thaw resistance. The reduction of relative dynamic modulus of elasticity became slow with the increasing freeze-thaw cycles, while the reduction of relative flexural strength became smaller.

(4) The proper mix proportion design should pay attention to the compound effect of the air-entraining agent and steel fibers, which controlled the degree of freeze-thaw resistance of SFRELC. In this experimental study, several instances of SFRELC with high freeze-thaw resistance were developed to meet the requirement of applying in freezing areas even in severe cold areas under highly saturated environmental condition; however, the quantitative relations for the design should be further studied.

Data Availability

The data used to support the findings of this study are available from the corresponding author upon request.

Conflicts of Interest

The authors declare that they have no conflicts of interest.

Acknowledgments

References

[1] S. B. Zhao, C. Y. Li, and X. J. Qian, "Experimental study on mechanical properties of steel fiber reinforced full lightweight concrete," *Geotechnical Special Publication*, vol. 212, pp. 233–239, 2011.

[2] C. Y. Li, H. Chen, and S. B. Zhao, "Mechanical properties of steel fiber reinforced light-aggregate concrete," *Advanced Materials Research*, vol. 366, pp. 12–15, 2012.

[3] L. Y. Pan, H. Yuan, and S. B. Zhao, "Experimental study on mechanical properties of hybrid fiber reinforced full lightweight aggregate concrete," *Advanced Materials Research*, vol. 197-198, pp. 911–914, 2011.

[4] Z. Shen, M. H. Chen, M. S. Zhao, and X. K. Li, "Experimental study on tensile properties of steel fiber reinforced lightweight-aggregate fly-ash flowable concrete," in *Architectural Engineering and New Materials*, pp. 1–8, Destech Publications Inc., Lancaster, PA, USA, 2015.

[5] X. K. Li, X. Y. Zhang, M. Q. Li, M. S. Zhao, and C. Y. Li, "Experiments on development of strength and carbonization of steel fiber reinforced full-lightweight concrete," *Journal of Civil Engineering and Management*, vol. 34, no. 2, pp. 46–50, 2017.

[6] S. B. Zhao, C. Y. Li, M. S. Zhao, and X. Y. Zhang, "Experimental study on autogenous and drying shrinkage of steel fiber reinforced lightweight-aggregate concrete," *Advances in Material Science and Engineering*, vol. 2016, Article ID 2589383, 10 pages, 2016.

[7] GB/T 50476-2008, *Code for Durability Design of Concrete Structures*, China Building Industry Press, Beijing, China, 2008.

[8] H. Ishida, H. Iwase, K. Rokugou, and W. Koyanagi, "Improvement of freezing and thawing resistance of lightweight concrete by steel fiber addition," *Transactions of the Japan Concrete Institute*, vol. 7, pp. 135–140, 1985.

[9] J. Huo and X. Shen, "Experimental study on frost resistance durability of fiber reinforced lightweight aggregate concrete," *Bulletin of the Chinese Ceramic Society*, vol. 27, no. 5, pp. 952–956, 2008.

[10] J. Huo, D. Liu, X. Shen, J. Chu, and D. Dong, "Freeze-thaw model and service life prediction of hybrid fiber reinforced lightweight aggregate concrete," *Advanced Materials Research*, vol. 250–253, pp. 817–821, 2011.

[11] X. K. Li, W. H. Song, and C. Y. Li, "A review on frost resistance of steel fiber reinforced lightweight aggregate concrete," *Applied Mechanics and Materials*, vol. 438–439, pp. 295–299, 2013.

[12] C. Miu, *High-performance Concrete Admixtures*, Chemical Industry Press, Beijing, China, 2008.

[13] H. Li, X. Shen, and W. Kang, "Experiment on frost resistance durability of air-entrained pumice lightweight aggregate concrete," *Concrete*, vol. 6, pp. 73–76, 2009.

[14] Z. Y. Zhao, B. L. Ji, X. Y. Song, and X. D. Shen, "Frost resistance of lightweight aggregate concrete," *Bulletin of the Chinese Ceramic Society*, vol. 34, no. 9, pp. 2442–2447, 2015.

[15] W. A. Jones and W. W. Jason, "Freezing and thawing behavior of internally cured concrete," *Advances in Civil Engineering Materials*, vol. 4, no. 1, pp. 144–154, 2015.

[16] K.-S. Youm, J. Moon, J.-Y. Cho, and J. J. Kim, "Experimental study on strength and durability of lightweight aggregate concrete containing silica fume," *Construction and Building Materials*, vol. 114, pp. 517–527, 2016.

[17] JGJ 51-2002, *Technical Specification for Lightweight Aggregate Concrete*, China Building Industry Press, Beijing, China, 2002.

[18] GB/T 17431-2010, *Lightweight Aggregate and Its Test Methods*, China Standard Press, Beijing, China, 2010.

[19] X. X. Ding, C. Y. Li, Y. Y. Xu, F. L. Li, and S. B. Zhao, "Experimental study on long-term compressive strength of concrete with manufactured sand," *Construction and Building Materials*, vol. 108, pp. 67–73, 2016.

[20] S. B. Zhao, X. X. Ding, M. S. Zhao, C. Y. Li, and S. W. Pei, "Experimental study on tensile strength development of concrete with manufactured sand," *Construction and Building Materials*, vol. 138, pp. 247–253, 2017.

[21] JG/T 472-2015, *Steel Fiber Reinforced Concrete*, China Standard Press, Beijing, China, 2015.

[22] P. Zhao, Q. Bi, and Z. Yang, "Experimental study on the mechanical properties and durability of hybrid crude fiber reinforced lightweight aggregate concrete," *Bulletin of the Chinese Ceramic Society*, vol. 27, no. 4, pp. 852–856, 2008.

[23] M.-A. Ali, Y. Erhan, and A.-C. Özge, "Water transport of lightweight concrete with different saturation levels," *ACI Materials Journal*, vol. 112, no. 5, pp. 681–691, 2015.

[24] J. Mao, K. Ayuta, H. Qi, and Z. Liu, "Experimental study on freeze-thaw damage mechanism of lightweight aggregate concrete," *Journal of ASTM International*, vol. 7, no. 1, pp. 1–12, 2010.

[25] B. Kucharczyková, Z. Keršner, O. Pospíchal, P. Misák, P. Daněk, and P. Schmid, "The porous aggregate pre-soaking in relation to the freeze-thaw resistance of lightweight aggregate concrete," *Construction and Building Materials*, vol. 30, pp. 761–766, 2012.

[26] L. Emiko, T. H. Wee, and T. Tamilselvan, "Penetrability of lightweight aggregate concrete," *Magazine of Concrete Research*, vol. 62, no. 3, pp. 201–209, 2010.

[27] K. S. Chia and M.-H. Zhang, "Water permeability and chloride penetrability of high-strength lightweight aggregate concrete," *Cement and Concrete Research*, vol. 32, pp. 639–645, 2002.

[28] D. Sun, J. Ding, and Y. Guo, "Comparison of water permeability and chloride penetrability between normal-weight concrete and lightweight concrete made with different lightweight aggregates," *Concrete*, vol. 2, pp. 36–38, 2005.

[29] X. M. Liu, K. S. Chia, and M.-H. Zhang, "Development of lightweight aggregate concrete with high resistance to water

and chloride-ion penetration," *Cement & Concrete Composites*, vol. 32, pp. 757–766, 2010.

[30] GB/T 50082-2009, *Standard for Test Method of Long-Term Performance and Durability of Ordinary Concrete*, China Building Industry Press, Beijing, China, 2009.

[31] ASTM C666-97, *Standard Test Method for Resistance of Concrete to Rapid Freeze and Thawing*, ASTM International, West Conshohocken, PA, USA, 2008.

[32] GB/T 50081-2002, *Standard for Test Method of Mechanical Properties of Ordinary Concrete*, China Building Industry Press, Beijing, China, 2002.

[33] S. B. Zhao, *Design Principle of Concrete Structures*, Tongji University Press, Shanghai, China, 2nd edition, 2013.

Research Article

Influences of Environmental Conditions on the Cracking Tendency of Dry-Mixed Plastering Mortar

Ni Tongyuan,[1,2,3] Yang Yang [ID],[2,3] Wu Dandan,[2] and Jiang Chenhui[4]

[1]*College of Materials Science and Engineering, Zhejiang University of Technology, Hangzhou 310023, China*
[2]*College of Civil Engineering and Architecture, Zhejiang University of Technology, Hangzhou 310023, China*
[3]*Key Laboratory of Civil Engineering Structures and Disaster Prevention and Mitigation Technology of Zhejiang Province, Hangzhou 310023, China*
[4]*Zhejiang College of Construction, Hangzhou 311231, China*

Correspondence should be addressed to Yang Yang; yangyang@zjut.edu.cn

Cracking tendency is one of the important performances of dry-mixed plastering mortar (DMPM). Environmental condition is a key factor to affect the cracking tendency of DMPM. For the purpose of evaluating the cracking resistance of DMPM and revealing the influence of environmental conditions on the cracking tendency of DMPM, a series of experiments were performed on restriction-induced cracking behaviors as well as free shrinkage, water loss, and mechanical properties of DMPM. The restricted shrinkage tests were based on ring tests and plate experiments. The results showed that the initial drying age exhibits significant influence on the cracking tendency of DMPM, and there was a stress balance period when the initial drying age was 2 days. But, the phenomena cannot be observed when the initial age was 3 d, 5 d, and 7 d. In order to eliminate the cracking tendency of DMPM, it should avoid water loss from the plaster layer during construction in practical engineering, especially, before initial drying ages.

1. Introduction

Compared with traditional plaster mortars, dry-mixed plaster mortar (DMPM) is a more environmentally friendly building material by reducing air pollution and waste production on construction sites. It can reduce carbon dioxide emissions, help the construction site keep clean, and allow for more flexibility in storage space for materials while reducing cement redundancy after the cement finishing is completed. Moreover, this new and advanced construction material is convenient to deploy and transport, delivers product with stable quality, helps us to facilitate construction, and saves materials [1–6]. There are many causes resulting in cracking of concrete, and shrinkage is of the upmost importance among them [7–11]. If the concrete is restrained, when the tensile stress induced by drying shrinkage exceeds the tensile strength, cracking would happen [9, 12–15]. By the same token, shrinkage cracking is also an important problem in wall plastering mortar. There

are a variety of wall plastering mortar cracking causes including thermal gradients, moisture gradients, and attacks from external and internal environments [16]. Drying shrinkage, which is one of the major causes of cracking of cement mortar, is related to the water loss from mortar. The early age cracking behavior is very complex because it not only depends on the manifestation rate and magnitude of the shrinkage of the hardened cement paste with ages but also other factors such as strength development, degree of restraint, stress relaxation, and shape of the structure.

Currently, many investigators focus on revealing the mechanisms of cracking by several kinds of experiments and developing prediction models of crack development [12, 16–18]. The ring test is a commonly used method for assessing the potential of shrinkage cracking. Moon and Weiss used the ring test to assess the restrained shrinkage behavior of mortar and concrete under various conditions [5, 8, 9, 12, 17, 19]. They proposed revisions to the estimation equations developed in previous studies to consider the

Grade	Cement	Thickening powder	Fly ash	Water	Sand
DMPM 15	160	7	23	34.2	810

Figure 1: Water loss rate test of the DMPM prism specimen.

Test points: I, II, III, IV
Outside steel ring
Inside steel ring
Plastering mortar specimen
Backplane

$h = 60 \pm 1\,\text{mm}$ $D = 300 \pm 3\,\text{mm}$
$\delta = 20\,\text{mm}$ $d = 260 \pm 3\,\text{mm}$

Figure 2: Schematic diagram of the ring restraint test device.

changes in stress in the cross section because of differential drying shrinkage. These stress changes were caused by different levels of ambient relative humidity, and the position of the cross section of the concrete ring [7, 19].

In this paper, the ring tests were performed to qualitatively assess shrinkage and cracking tendency of DMPM under different environmental conditions, including different wind speed, types of subbase, and initial drying age. In addition, free shrinkage and tensile strength of DMPM specimens were performed with the same cross section in the same environmental condition.

2. Experiment Program

2.1. Raw Materials and Mixture Proportion. Cement type used in this study is P·O 42.5 in accordance with Chinese GB 175-2007, and bentonite was used as a thickening powder agent. Grade I fly ash in accordance with Chinese GB/T 1596-2005 was employed as mineral admixture. The fineness modulus of natural river sand was 2.3, and the rate of water and dry material was 0.18. Table 1 shows the mix proportions of dry-mix plaster mortar.

2.2. Water Loss Rate. In order to study the relationship between drying shrinkage and water loss of mortar specimens, the free shrinkage and the water loss rate of a pyramid specimen were tested, respectively. The size of specimen was 40 mm × 40 mm × 160 mm. The specimens were placed in a 20 ± 2°C, 50 ± 5% RH environment at initial drying age.

It is generally known that the wind can promote water evaporation. In order to investigate the influence of wind environment on DMPM, the water loss rate of the pyramid prism specimen was tested under wind speed at 0 m/s, 4 m/s, and 8 m/s. Figure 1 shows the method for testing the water loss rate of the pyramid prism specimen under different wind speeds.

2.3. Restrained Shrinkage Test A: Ring Test. Due to its practicability, and easy operation to measure strain or stress, the "ring test" was commonly used to assess the potential for
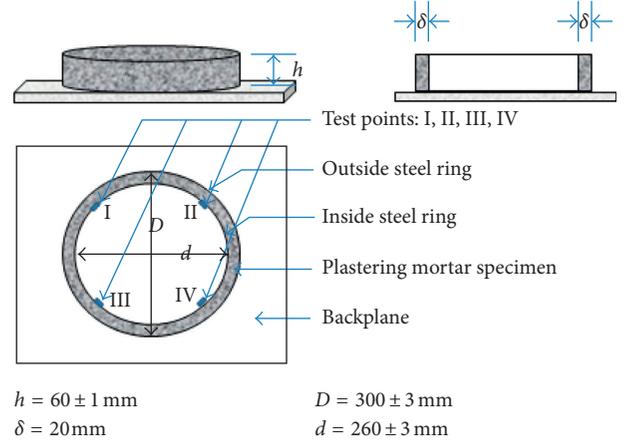
shrinkage cracking. The device consists of a mortar ring specimen that was cast around a steel concentric ring [7, 9, 12, 15, 17, 20, 21]. As the mortar ring dries, the shrinkage was prevented by the steel ring, which results in the development of restrained tensile stress in the mortar specimen. The simple ring specimen geometry allows it to be fabricated easily. In addition, the low cost of the system enables several tests to be conducted concurrently over long periods of time.

This paper utilized the restrained ring test to gather information as internal stress development in the mortar system. Figure 2 shows the ring restraint test device used in this study. The outer steel ring was used as mould during casting the DMPM specimen, and the inner steel ring was used as restraint. The inner ring was fixed on a subbase which was made of hydrophobic surface smooth material.

The internal ring strain induced by the DMPM shrinkage was measured by 4 strain gauges, axisymmetrically fixed at the midheight of the inner surface of the metal rings (Figure 2). On the other hand, in this paper, "a quarter bridge" strain gage was collected to test stress, and data acquisition automatic logging interval was set to 30 min. The constant temperature of test environment is at 20 ± 2°C, and the relative humidity is 50 ± 5 percent.

The ring specimen is shown in Figure 3. The ring was restrained against horizontal movement in the radial direction, and internal pressure, p, develops when the ring shrinks. Based on theory of elasticity, the stress was composited by one component σ_θ (in the circumferential direction) and the other component σ_r (in the radial directions). The stress σ_θ and σ_r can be calculated according by the following equations:

$$\sigma_\theta = \frac{(r_e/r)^2 + 1}{(r_e^2/r_i^2) - 1}\,p, \tag{1}$$

$$\sigma_r = \frac{(r_e/r)^2 - 1}{(r_e^2/r_i^2) - 1}\,p, \tag{2}$$

$$\alpha = \frac{(r_e/r)^2 + 1}{(r_e^2/r_i^2) - 1}, \tag{3}$$
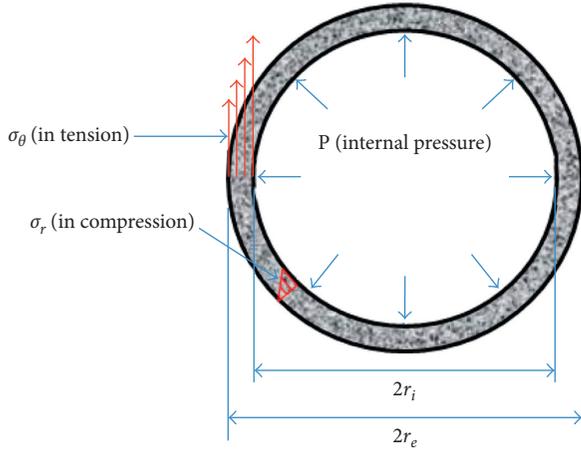
FIGURE 3: Distribution of internal stress and simplification for fracture analysis.

FIGURE 4: Schematic diagram of the plate-restrained test.

where r_e and r_i are the external radius and internal radius, respectively. Distributions of σ_θ and σ_r are indicated in Figure 3. α is a constant associated with the device. p is the internal pressure of the internal ring. The internal pressure, p, can be tested by strain gages at test points I, II, III, and IV. The value of p is average measurements of these four test points. The relationship between circumferential shrinkage and the internal pressure p can be obtained by elastic stress analysis.

$$p = \frac{E\varepsilon_\theta}{(r_e^2 + r_i^2)/(r_e^2 - r_i^2) + \mu},$$

$$\beta = \frac{E}{(r_e^2 + r_i^2)/(r_e^2 - r_i^2) + \mu},$$

(4)

where ε_θ is the shrinkage strain, E is the modulus of elasticity, and μ is Poisson's ratio, and in this paper, $\mu = 0.28$. β is a constant associated with the device.

So, (1) can be rearranged to yield

$$\sigma_\theta = \alpha\beta\varepsilon_\theta.$$ (5)

In this experiment, two identical specimens were conducted. In order to reduce friction between the subbase and the specimens, two layers of plastic film were covered on the upper surface of the subbase. The DMPM mixture was casted into the mould with two layers. And the specimens were placed in standard conditions (the constant temperature of test environment was $20 \pm 2°C$, and the relative humidity was $50 \pm 5\%$) until the initial drying age of 2 d, 3 d, 5 d, and 7 d. Before the dry experiment being started, the specimen surface must be covered with moist layer of linen and stamped with plastic film to prevent moisture to loss. The next step was to remove the outer ring and to seal the outside of the specimen with aluminum foil to ensure that water loses only through the outer surface of the specimen. Then, samples began to dry.

2.4. Restrained Shrinkage Test B: Plate Test. The method of plate test was performed following "cement mortar crack resistance test method" (Chinese technical specification JC/T 951-2005). In order to study the influence of drying conditions on cracking tendency of DMPM, the specimens were exposed to ambient condition at the age of 1 d, 2 d, 3 d, 5 d, and 7 d. During the drying period, the direction of the wind from electric fan was parallel to the surface of the plate specimen. The wind speed in the specimen transverse centerline was 0 m/s, 4 m/s, and 8 m/s. At the same time, two 1000 W power halogen lamps were lighting for 4 h. After 24 h, the width and length of crack were measured and the crack index is calculated. The schematic diagram of the plate-restrained test is shown in Figure 4.

3. Results and Discussion

3.1. Influences of Initial Drying Age and Wind Speed on Flexural Strength and Compressive Strength of DMPM. Strength (compressive strength and flexural strength) characteristics of DMPM played a decisive role in its crack resistance. After an initial moist curing period of 1 d, 2 d, 3 d, 5 d, and 7 d, the development of compressive strength and flexural strength of DMPM was performed with the age increasing.

Figures 5(a)–5(c) show that the initial drying age and wind speed would have adverse effects on the flexural strength of mortar and the same as on compressive strength. On one hand, when DMPM be exposed to drying condition earlier, more water would be evaporated from it. On the other hand, greater wind speed means faster rate of moisture evaporation. The both undermine hydration of DMPM and in turn affect the strength. The influence of DMPM's initial drying age on its strength is more mild than that of different wind speeds.

3.2. Drying Shrinkage (DS) Characteristics of DMPM under Different Conditions. In order to discuss water loss rate (WLR) laws and drying shrinkage characteristics of DMPM, we analyzed the relationship between water loss rules and drying shrinkage of DMPM by experiments.

3.2.1. Influence of Wind Speed on Water Loss Rate (WLR) of DMPM. During the drying process, the free and absorbed
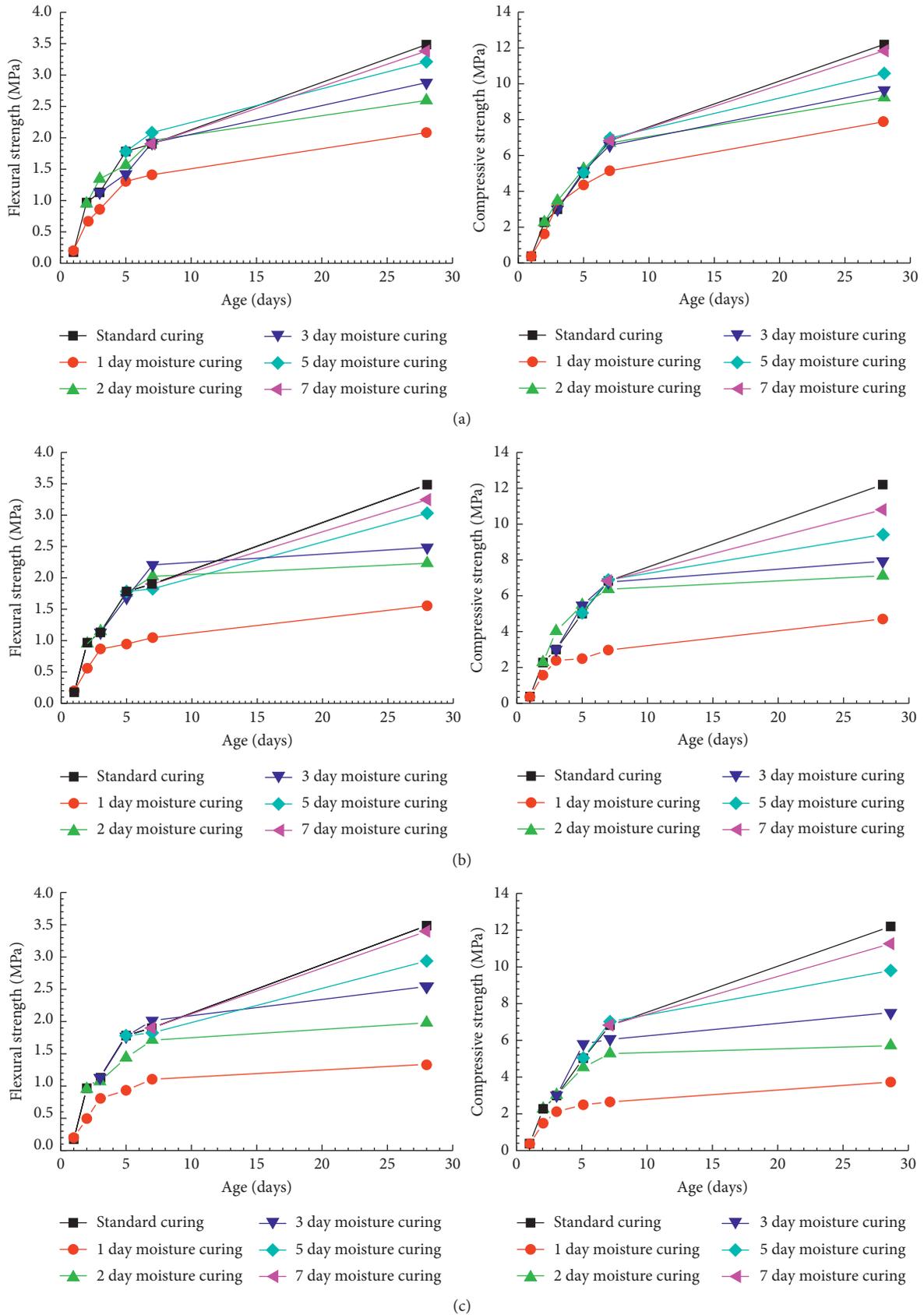
Figure 5: Flexural strength and compressive strength with different wind speeds. (a) 0 m/s. (b) 4 m/s. (c) 8 m/s.
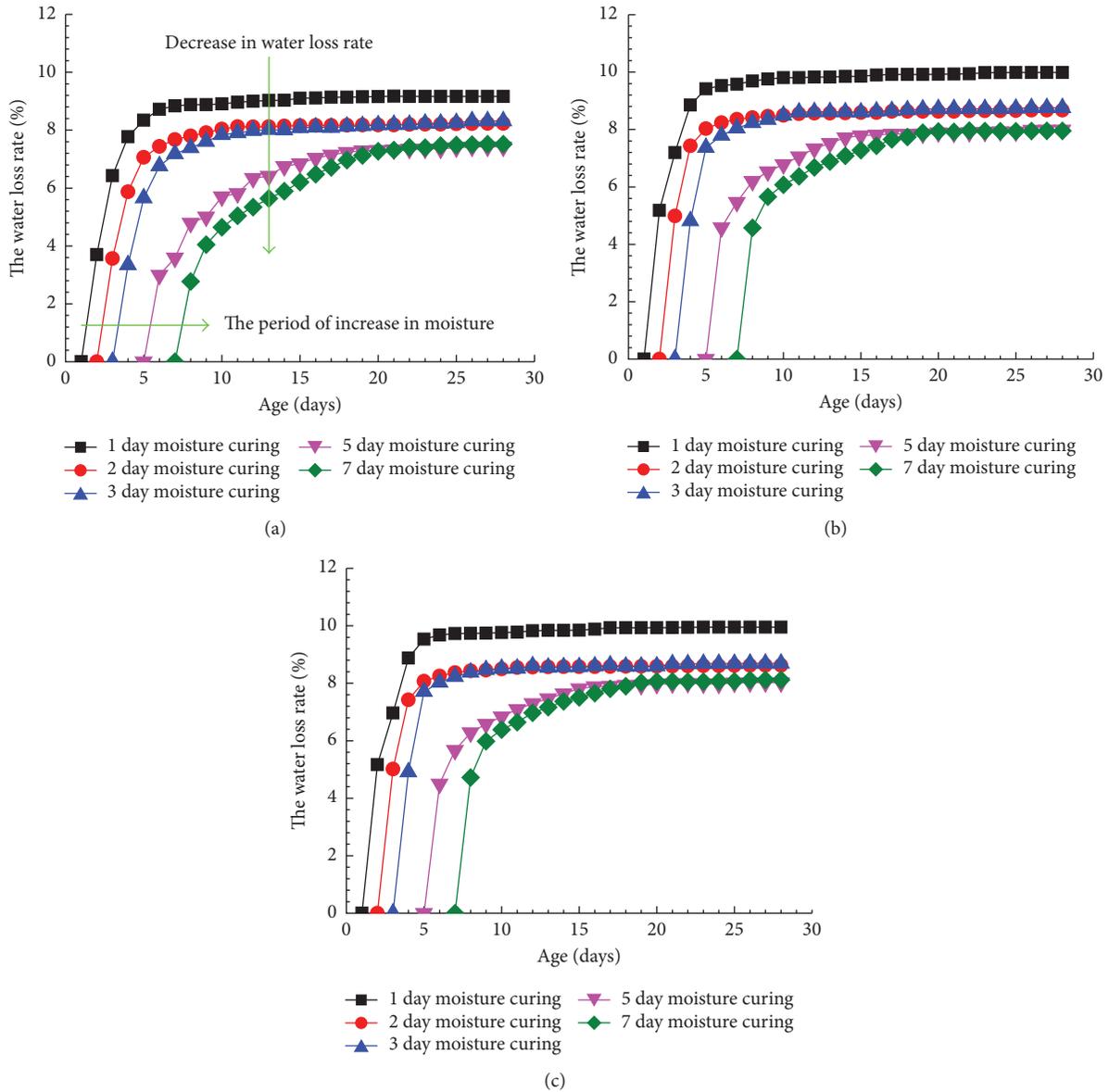
FIGURE 6: The water loss rate with different wind speeds. (a) 0 m/s. (b) 4 m/s. (c) 8 m/s.

water is lost from DMPM. It affects the performance of DMPM. We investigated WLR under different curing conditions, including wind conditions and initial drying age. Figures 6(a)–6(c) show the values of WLR of DMPM in different wind speeds of 0 m/s, 4 m/s, and 8 m/s. The WLR of DMPM was rapid at the early stage, but it decreased with the age, and WRL became slower gradually, until it comes to constant values.

3.2.2. Relationships between Water Loss Rate (WLR), Initial Drying Age, Wind Conditions, and Drying Shrinkage (DS) of DMPM.
Obviously, water loss rate, initial drying age, and wind conditions affect the drying shrinkage of DMPM. The curves of Figures 7(a)–7(e) show the relations between wind speed conditions, initial drying age, and drying shrinkage.

According to the ultimate shrinkage value, we can classify the rate of water loss to three grades: first, maximum WLR, for the initial drying age was 1 day; second, middle WLR, the initial drying age was 2 d and 3 d; and third, minimum WLR, the initial drying age was 5 d and 7 d. We can make different strategies to deal with the water loss of DMPM.

In the early age, drying shrinkage of DMPM increased with age, and then the development of drying shrinkage slowed down. The rate of DMPM drying shrinkage was faster at initial age and then tended to be gentle. On the other hand, in the same wind speed, the later the initial drying age, the larger the drying shrinkage value of DMPM was, which was due to much more water lose, and the volume change was larger. But the effect was remarkable at drying age from 5th day to 20th day. And it was more obvious while the wind speed was 4 m/s and 8 m/s.
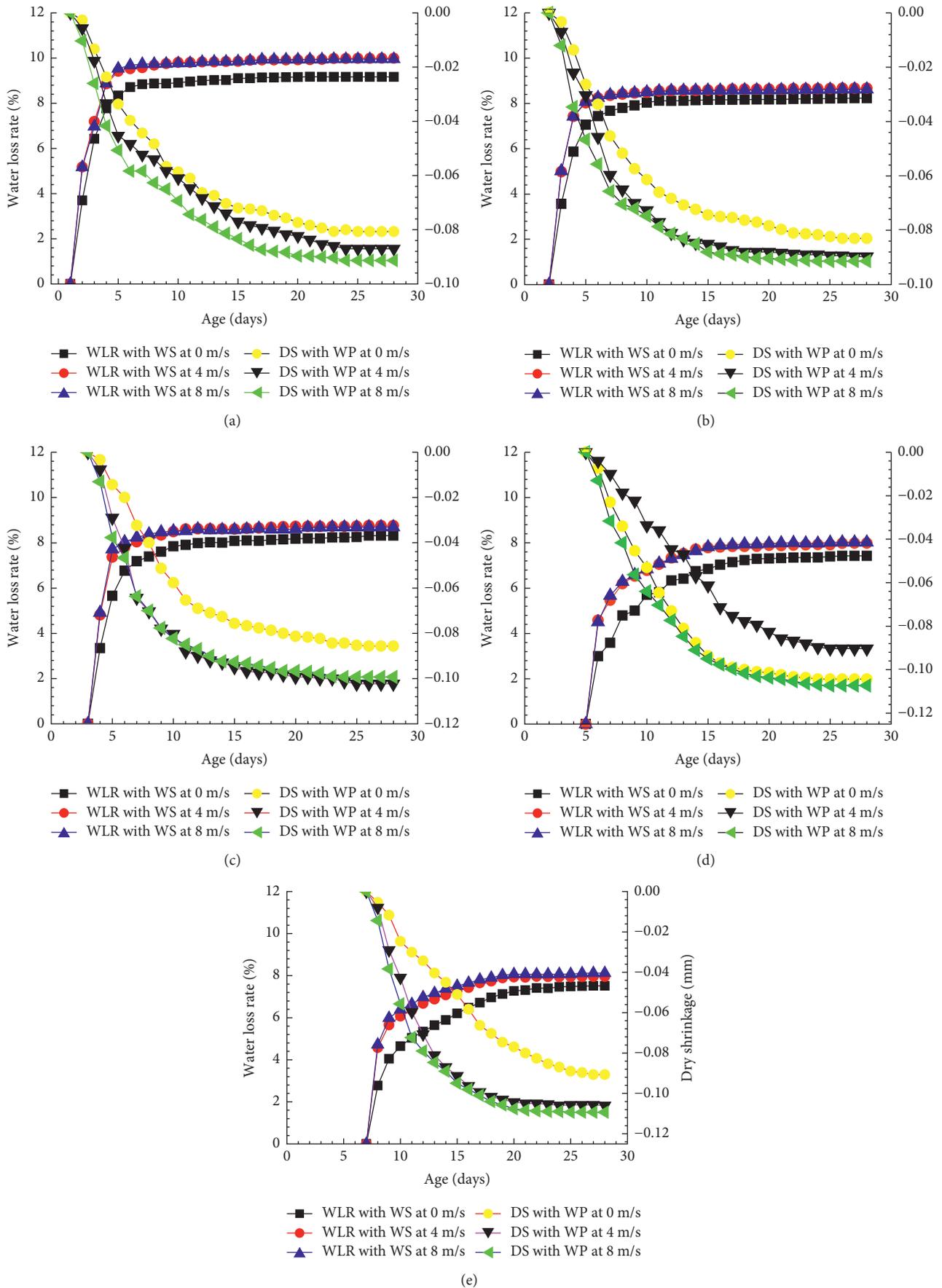
Figure 7: Water loss rate of DMPM with different moisture curing times. (a) 1 day. (b) 2 days. (c) 3 days. (d) 5 days. (e) 7 days.
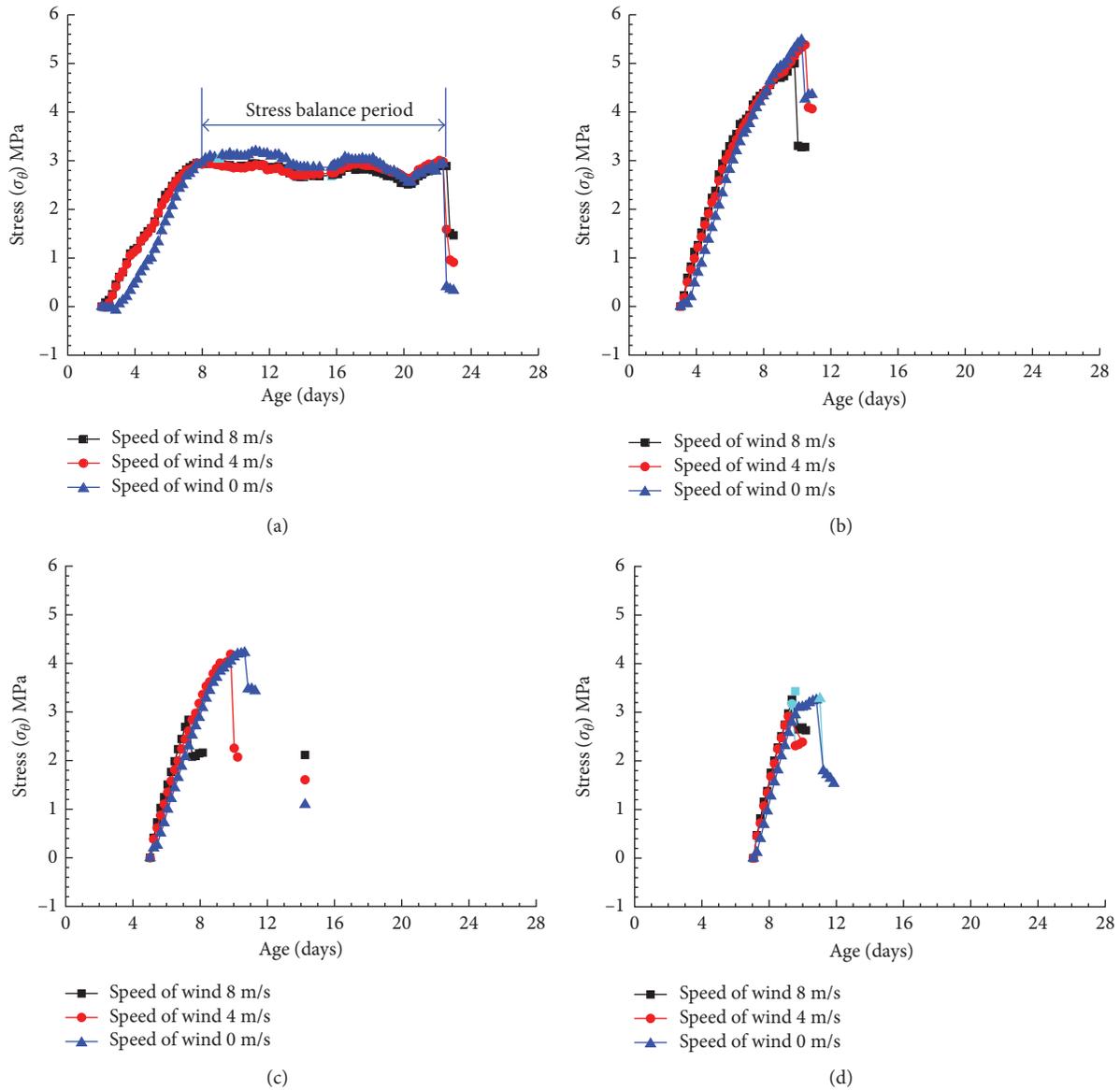
FIGURE 8: Shrinkage stress with different moisture curing ages. (a) 2 days. (b) 3 days. (c) 5 days. (d) 7 days.

3.3. Cracking Tendency of Restrained Shrinkage Test: Ring Test and Plate Test

3.3.1. Ring Test. Obviously, the ring test can provide quantitative information on DMPM early age stress and cracking of DMPM. The tests showed that, firstly, under the same initial drying age, the greater the wind speed, the faster the development of the DMPM ring test strain was and the greater the restraint effect of the steel ring on the DMPM ring, the larger the tensile stress induced by drying shrinkage. The reason was that the water loss occurs earlier while DMPM is exposed in the dry environment, and the elastic modulus of DMPM ring was lower. The test results also showed that the drying shrinkage value that corresponds to the cracking moment was greater as the cracking age of the DMPM ring was delayed. Conversely, if the cracking age of the DMPM ring was earlier, the cracking

stress of the DMPM ring was smaller. It indicated that the DMPM drying shrinkage deformation was smaller. It means that the anticrack performance is weak. Finally, under the same wind speed, the development rate of the tensile stress was smaller while the DMPM sample was exposed to the dry environment sooner.

Figure 8(a) shows that the shrinkage stress development of the DMPM sample, which was exposed to the dry environment after 2 d moisture curing, had a stress balance period and continued for two weeks. But the phenomenon was not observed during the tests of DMPM with other initial drying age. Our interpretation of this is that, first of all, the elastic modulus of the DMPM ring specimen was smaller as the initial drying age was 2 d, and the restrained stress was smaller; secondly, the internal free water of pieces of the DMPM specimen was enough to hydrate and evaporate, and then drying shrinkage of the ring specimen
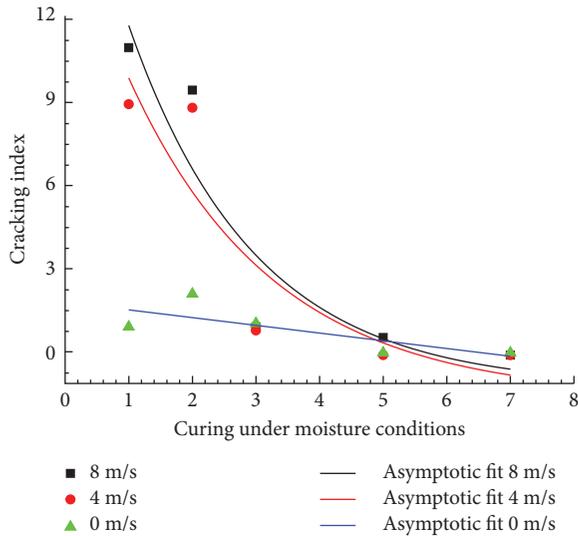
FIGURE 9: The relationship between cracking index and initial drying age.

increases slowly. Due to the abovementioned three reasons, a stress balance period occurs.

3.3.2. Plate Test. The cracking index data of flat test (Figure 9) showed that the cracking occurs more easily while the initial drying age of DMPM was earlier. More cracks would be produced when the plate sample moisture evaporated faster, and the value of cracking index test was larger as the wind speed was larger. But this phenomenon holded only for initial 3 d moisture curing. The plate specimen starts to dry after 3 d curing under moisture conditions, and the value of the crack index had a same appearance in different wind conditions. The results also showed that the cracking index presented an exponential decay with age increasing in wind environment, but appeared linear attenuation in nonwind environment.

4. Conclusions

The aim of this experimental work was to study the influences of environment conditions on cracking tendency of DMPM. Relevant results were obtained during the experimentation:

(1) The steel ring restrained test is an effective experiment method to measure restrained stress and strain of DMPM.

(2) The ring tests showed that under the same initial drying age of DMPM, the greater the wind speed, the faster the development of the ring test strain was, and the greater the restraint effect of the steel ring on the ring test piece, the larger the tensile stress caused by the shrinkage was. If cracking age of circular test pieces was earlier, the DMPM drying shrinkage deformation was smaller. It means that the anticrack performance is weak. Under the same wind speed, the sooner the DMPM sample exposed to the dry environment, the smaller the development rate of the

tensile stress is. The development of internal shrinkage stress of DMPM, which pieces were stored in dry environment after 2 day age curing in moisture condition, possessed a stress balance period and continued for some time

(3) The flat tests showed that the cracks produced more easily while the initial drying age of DMPM was earlier. The cracking index presented an exponential decay with age increasing in wind environment, but appeared linear attenuation in nonwind environment.

In summary, in order to eliminate cracking tendency of DMPM, it should avoid water loss from the plaster layer during construction in practical engineering, especially, before initial drying ages.

Conflicts of Interest

The authors declare that there are no conflicts of interest regarding the publication of this paper.

Acknowledgments

References

[1] C. F. Huang, R. L. Chen, and J. L. Lin, "The current practice and promotion strategy of dry-mix mortars in Taiwan—taking technology acceptance model as an approach," in *Proceedings of the 2011 International Conference on Consumer Electronics, Communications and Networks, CECNet 2011*, Xianning, China, April 2011.

[2] J. N. Eiras, J. S. Popovics, M. V. Borrachero, J. Monzó, and J. Payá, "The effects of moisture and micro-structural modifications in drying mortars on vibration-based NDT methods," *Construction and Building Materials*, vol. 94, pp. 565–571, 2015.

[3] H. Bian and J. Plank, "Effect of heat treatment on the dispersion performance of casein superplasticizer used in dry-mix mortar," *Cement and Concrete Research*, vol. 51, pp. 1–5, 2013.

[4] J. Xianyu, T. Ye, and J. Nanguo, "Early age properties and cracking control of concrete," *Journal of Building Structure*, vol. 30, no. 6, pp. 24–30, 2010.

[5] J. Nanguo, J. Xianyu, and T. Ye, "Analytical prediction and experimental research on shrinkage cracking of restrained early-age concrete," *Journal of Zhejiang University*, vol. 41, no. 9, pp. 1499–1502, 2007.

[6] T. Ohkubo, T. Inohara, and S. Matsumoto, "A study on influence the construction time of year affects the cracks of plastering mortar restrained by concrete," *Journal of Structural and Construction Engineering*, vol. 77, no. 673, pp. 333–340, 2012.

[7] S. A. Al-Saleh, "Comparison of theoretical and experimental shrinkage in concrete," *Construction and Building Materials*, vol. 72, pp. 326–332, 2014.

[8] T. H. Nguyen, A. Toumi, A. Turatsinze, and F. Tazi, "Restrained shrinkage cracking in steel fibre reinforced and rubberised cement-based mortars," *Materials and Structures*, vol. 45, no. 6, pp. 899–904, 2012.

[9] D. P. Bentz, M. R. Geiker, and K. K. Hansen, "Shrinkage-reducing admixtures and early-age desiccation in cement pastes and mortars," *Cement and Concrete Research*, vol. 31, no. 7, pp. 1075–1085, 2001.

[10] C. Zhicheng and Y. Peiyu, "Autogenous shrinkage of shrinkage-compensating concrete," *Journal of the Chinese Ceramic Society*, vol. 38, no. 4, pp. 568–573, 2010.

[11] M. Miao and Y. Peiyu, "Influences of water-binder ratio and dosage of fly ash on autogeneous shrinkage of shrinkage-compensating concrete," *Journal of the Chinese Ceramic Society*, vol. 40, no. 11, pp. 1607–1612, 2012.

[12] C. Z. Hu Hui, W. Xiaoying, C. Ke, W. Xin, and C. Ke, "Cracking tendency prediction model of early-age restrained mortar ring," *Journal of Civil, Architectural and Environmental Engineering*, vol. 3, pp. 19–25, 2015.

[13] I. B. Topcu and T. Bilir, "Experimental investigation of drying shrinkage cracking of composite mortars incorporating crushed tile fine aggregate," *Materials and Design*, vol. 31, no. 9, pp. 4088–4097, 2010.

[14] S. Xu and Y. Zhu, "Experimental determination of fracture parameters for crack propagation in hardening cement paste and mortar," *International Journal of Fracture*, vol. 157, no. 1-2, pp. 33–43, 2009.

[15] S. P. Shah, C. Ouyang, S. Marikunte et al., "A method to predict shrinkage cracking of concrete," *ACI Materials Journal*, vol. 95, no. 4, pp. 339–346, 1998.

[16] C. Jiang, Y. Yang, C. Ma et al., "Evaluation of anti-cracking performance for concrete based on temperature-stress test and analytic hierarchy process," *Journal of the Chinese Ceramic Society*, vol. 43, no. 8, pp. 1017–1023, 2015.

[17] H. Choi, M. Lim, R. Kitagaki, T. Noguchi, and G. Kim, "Restrained shrinkage behavior of expansive mortar at early ages," *Construction and Building Materials*, vol. 84, pp. 468–476, 2015.

[18] G. Rishi and B. Nemkumar, "Plastic shrinkage cracking prediction in cement-based materials using factorial design," *Journal of Materials in Civil Engineering*, vol. 27, no. 9, p. 04014244, 2015.

[19] A. B. Hossain and J. Weiss, "Assessing residual stress development and stress relaxation in restrained concrete ring specimens," *Cement and Concrete Composites*, vol. 26, no. 5, pp. 531–540, 2004.

[20] X. Ma, X. Li, C. Wang, and Z. Han, "Numerical simulation and assessment of self-induced tensile stresses in steel ring restrained concrete," *Journal of Wuhan University of Technology–Materials Science Edition*, vol. 25, no. 3, pp. 530–533, 2010.

[21] C. F. Nilsen and K. N. Subramanian, "The role of strain-rate and phase boundary geometry on the deformation behaviour of two-phase bicrystals of alpha-beta brass," *Journal of Materials Science*, vol. 19, no. 3, pp. 768–776, 1984.

Research Article

Experiment on Behavior of a New Connector Used in Bamboo (Timber) Frame Structure under Cyclic Loading

Junwen Zhou [1,2] **Dongsheng Huang,** [1] **Chun Ni,** [3] **Yurong Shen,** [1] **and Longlong Zhao** [1]

[1]*School of Civil Engineering, Nanjing Forestry University, Nanjing 210037, China*
[2]*School of Civil Engineering and Architecture, Changzhou Institute of Technology, Changzhou 213033, China*
[3]*FPInnovations, Vancouver, BC, Canada V6T 1Z4,*

Correspondence should be addressed to Dongsheng Huang; dshuang@njfu.edu.cn

Connection is an important part of the bamboo and timber structure, and it directly influences the overall structural performance and safety. Based on a comprehensive analysis of the mechanical performance of several wood connections, a new connector for the bamboo (timber) frame joint was proposed in this paper. Three full-scale T-type joint specimens were designed to study the mechanical performance under cyclic loading. The thickness of the hollow steel column was different among three specimens. The specimens were loaded under displacement control with a rate of 10 mm per minute until the specimens reach failure. It was observed that the failures of three specimens were caused by the buckling of flanges in the compression and that the steel of connections does not yield. The load-displacement hysteretic curve for three specimens is relatively plump, and the stiffness of connection degenerates with the increasing of cyclic load. The maximum rotation is 0.049 rad, and the energy dissipation coefficient is 1.77. The thickness of the hollow steel column of the connector has significant impact on the energy dissipation capacity and the strength of the connection. A simplified moment-rotation hysteresis model for the joint was proposed.

1. Introduction

Timber is a natural organic material, and people easily get it from nature and use it without much processing; therefore, timber was employed as a construction material a long time ago. Timber has higher strength in tension and compression parallel to grain, light mass, and good durability, some 1000-year timber buildings still stand well [1]. Because of friendly environment, graceful timber texture, and simple nature, timber building will still be enormously appealing to people. For the timber frame structure, the beam-to-column connection is usually the most unsubstantial part on account of fabricated construction. The mechanical behavior of timber joints directly influences the overall timber structural performance and safety. As a result, the design of timber joints is extremely important. In some Asian countries such as China, South Korea, and Japan, mortise and tenon joints [1–5] are traditionally used in timber buildings from dwelling houses to palaces. In these joints, steel fasteners are not used, therefore keeping the original beauty of the timber. However, due to the

slippage between the mortise and tenon, the energy dissipation capacity of the whole structure is affected under earthquake load. The whole building can even collapse due to the separation between the mortise and tenon. In addition, the mortise-to-tenon connection wakens the column cross section at the connection, which reduces the vertical load-carrying capacity and also negatively affects the energy dissipation capacity of the column. To prevent the mortise-to-tenon connection from separation and improve the strength of connection, Bulleit et al. [6] used wooden pegs to fasten mortise-to-tenon connection. But the study showed that the split failure owes to prying force of the wood peg occurred along with a peg hole when there is a distance between the tenon and the sill of mortise, and either shear failure of the tenon appeared. Moreover, Hong et al. [7] employed a T-type steel plate to strengthen the mortise-to-tenon connection and not to enhance the energy dissipation capacity of the joint.

Steel plate-bolted connection is another joint commonly used to connect the beam and column in a timber structure, which often is applied in the heavy timber structure and has

architecture beauty because the connecting steel plate is covered with wood. However, for these types of joints, the brittle failure mode was obvious [8–10]. Split failure along the bolt hole in the beam is the main failure mode in this kind of joint, and it reduces the load-carrying capacity of the joint. As the beam and column are slotted to accommodate the steel plate, the vertical load-carrying capacity is reduced. Under cyclic loading, the hysteretic curve shows a clear "pinching" effect because of the gap between the bolt and wall of the hole [8–10].

Glued-in-rod connection is also commonly used to connect the beam and column in a timber building. The rod is embedded in timber to connect the beam and column and to transfer the load from the beam to the column. With appropriate materials and good construction quality, the glued-in-rod connection has demonstrated good structural performance [11, 12]. The glued-in-rod connection has been widely studied and used in various projects [13]. The advantage of glued-in-rod connection is that the steel rod is embedded in timber to protect the steel rod from corrosion, and the durability is better. In order to get good construction quality, generally, the steel rod should be glued well with one timber first part in advance and then being connected with another part. Thus, the rod hole position on the beam and column must be precise. As timber and glue are brittle materials, the principle of energy dissipation is not obvious. Vašek [14, 15] used two U-type steel connectors located at upper and bottom edges of the beam to fasten the steel rods embedded in the timber beam and column. This new method could reduce stress concentration to the beam and column and increase the energy dissipation capacity of the joint by the deformation of U-type steel connectors. In addition, the U-type steel connectors are applied to connect the timber beam and column, and the position of the hole on the steel connector can easily be changed, which is convenient for connection construction on site.

Bolted timber-timber connection is a simple and practical connection for the timber beam-to-column joint. Only bolts are used to fasten the timber beam and column and to carry load from the girder to the post [16, 17]. Steel nails sometimes are used to substitute for bolts. The different mechanical performance of connection can be obtained by changing the quantity and arrangement style of bolts. Some special materials, such as steel plate or hard wood, are inserted into the contacted surface of the beam and column to improve the performance of connection as well.

For the timber beam-to-column joint, load-carrying capacity and energy dissipation are the two primary factors to judge the performance of the joint. Huang [18] gave a better energy dissipation connector for the timber frame joint, but the connection between the beam and column is not robust, slippage happens under earthquake, and shear stiffness of the joint is less. Based on the comprehensive analysis of the abovementioned joints, a new beam-to-column connector was developed and presented in this paper. The joint can connect top and bottom columns and also link beam and column parts without weakening the column cross section. As the mechanical behavior of this joint under the earthquake load is unknown, an experimental study was conducted to evaluate the stiffness, strength, energy dissipation, and resilience of the joint with different thicknesses of the hollow steel column.

2. Joint Details and Fabrication

The joint consists of two parts. One part is beam and column members made of parallel strand bamboo (PSB) [19–21]. The beam is 55 mm in width, 200 mm in depth, and 1050 mm in length. Two beams were assembled in parallel. At the end of the beams where a bolt hole was located, carbon fiber-reinforced plastic, 8 mm in width, was used to wrap the beams to prevent it from cracking along the bolt hole. The top and bottom columns are 200 mm in width, 240 mm in depth, and 700 mm in length. The column depth is paralleled to the beam axis. The other part is a steel connector, which is the most important part of the joint. The details of the connector are shown in Figure 1. Four steel plates are welded together to form a hollow column, and then, a horizontal steel plate is welded in the middle of the hollow column to reinforce the hollow column and to transfer load from the top column to the bottom column. The top and bottom plates (flanges) of the I-shaped steel beam were bent into L shape and welded to the hollow steel column. A steel plate web was welded between the top and bottom flanges to form an I-shaped steel beam. Two shear connection plates were welded to the hollow steel column and fastened to the web of the I-shaped steel beam with a 16 mm diameter bolt. This is to ensure the connection between the hollow steel column and the I-shaped steel beam in case the welding between the hollow steel column and I-shaped steel beam flanges is broken.

The PSB columns were placed into the hollow steel column and connected to the hollow steel column with four 14 mm diameter bolts. Two PSB beams were connected to the steel web with four 16 mm diameter bolts.

3. Description of the Experiment

3.1. Specimen Designing. Three joint specimens were fabricated in site. Except for the thickness of the hollow steel column, the specimens are identical. Details of the specimens are shown in Figure 2. Holes in bamboo specimen (beam and column) and steel plate are 1.5 mm greater than those of bolts, which is easy to assemble. A detailed description of thickness of each tested steel connection plate is reported in Table 1.

3.2. Mechanical Properties of Materials. All the steel plates are of grade Q235B in accordance with the Chinese standard (GB/T700-2006) [22]. The material properties of the steel plates are determined according to EN10002-1 [23]. Table 2 lists the mechanical properties of the steel plates. The 14 mm diameter bolts, which were used to fasten the hollow steel column and PSB columns, had the average yield strength of 804 MPa under tension. The 16 mm diameter bolts had the average yield strength of 2241 MPa under bending.

According to the ASTM standard D143-09 [24], the ultimate compressive and tensile strength values of PSB parallel to grain are 65 MPa and 100 MPa, respectively, and the ultimate tensile strength value of PSB perpendicular to grain is 4.4 MPa.
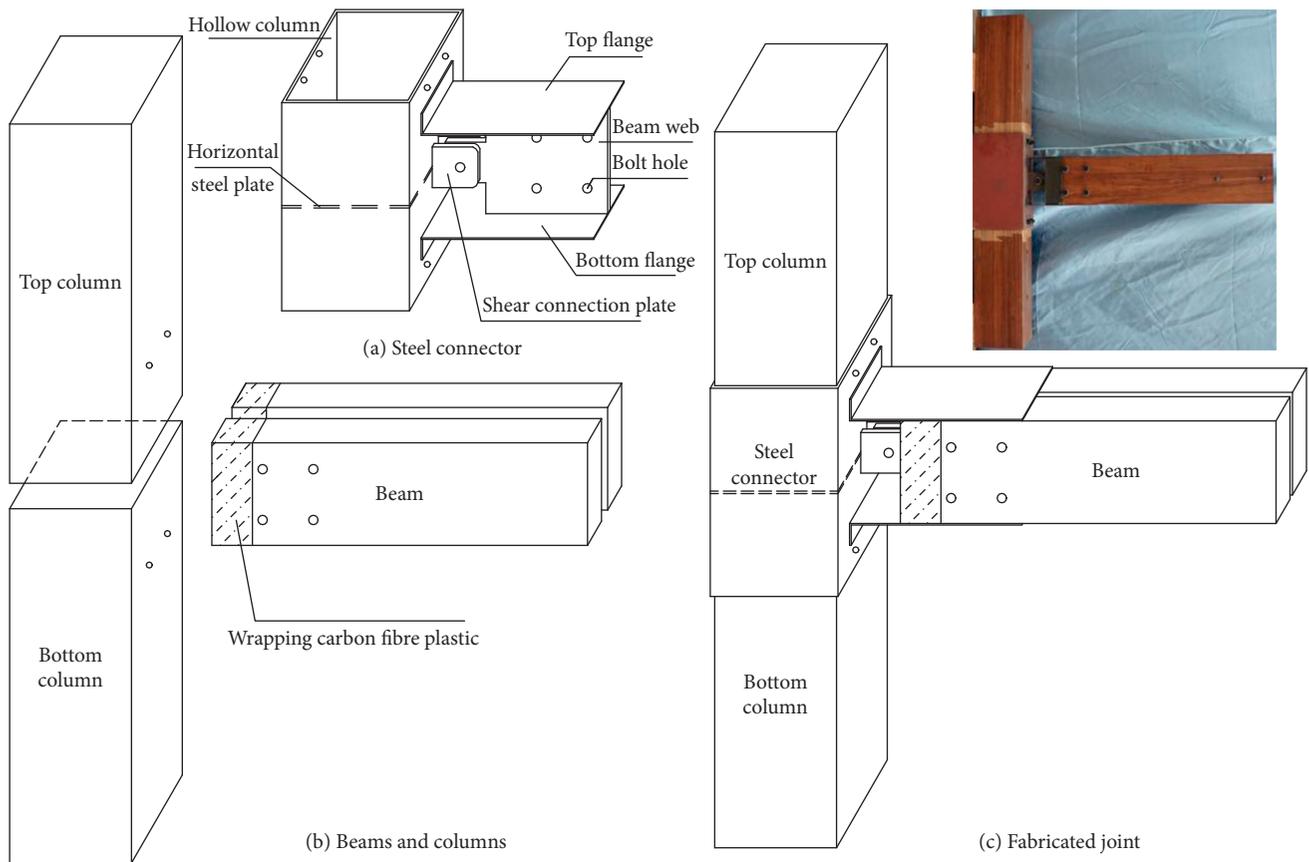
Figure 1: Constructional detail of the joint. (a) Steel connector, (b) beams and columns, and (c) fabricated joint.

3.3. Test Setup.

A schematic illustration of the test setup is shown in Figure 3. The main purpose of this research is to study the mechanical performance of the connection specimens under cyclic loading. In order to load the specimen with the existing loading frame, the column was rotated an angle of 90° and was fixed to the floor channel with four 30 mm diameter bolts. A two-way 250 mm hydraulic actuator (100 kN capacity) was used to apply the cyclic load. The center of the actuator was 1000 mm above the top surface of the PSB column, and the head of the actuator was about 150 mm away from the PSB beam.

The beam displacements were monitored by a laser displacement sensor, and the corresponding load value was measured by a load cell mounted on the actuator rod. Two laser displacement sensors #3 and #4 were located at the beam flange to measure the rotation of the connection. The other two sensors #1 and #2 were located at the hollow steel column to measure the defection of the hollow column.

For the three specimens, the sensors were located at the same locations of the specimen.

3.4. Loading Schedule.

In this study, a controlled cyclic displacement scheme was used. The maximum displacement was 10 mm in the first two cyclic loading, and the loading rate was 10 mm per minute. The maximum displacement was then increased by 10 mm after each step until specimen failure which showed specimen lost bearing loading capacity. The loading scheme is shown in Figure 4.

It was assumed that the actuator force in compression was positive, and the beam displacement moving away from the reaction wall was positive.

4. Test Results and Analysis

The test results of the three specimens are shown in Table 3. For each experiment, the failure mode, the energy dissipation, and the resilience model of each specimen will be discussed in the following sections.

4.1. Failure Mode.

From Figure 3, it can be observed that one lateral beam flange was pulled and the opposite beam flange was compressed under loading. For the three specimens, the failure occurred when the beam flange buckled under compressive force. Figures 5–7 show the failure mode of the three specimens. It was noticed that the beam flange buckling occurred suddenly without yielding of the steel plate, which is a brittle failure and results in the failure of test specimens. Besides the beam flange buckling, for the specimen CJ2 in which the hollow steel column is 4 mm in thickness, the hollow steel column was also deformed around the beam flange because of tensile fore of the beam flange. The bolts and PSB members with larger cross-sectional dimensions were still in good condition after the tests.

(a) Detailed drawing for joint.

Detailed drawing for steel connector

a-a

b-b

Web plate

(b) Detailed diagramtic drawing for steel connector.

Figure 2: Detailed parameters for the specimen (mm).

Table 1: Steel plate thickness of the connector (mm).

Specimen	Hollow steel column	Beam flange	Beam web	Shear connection plate	Hollow column stiffener
CJ1	5	3	10	8	5
CJ2	4	3	10	8	5
CJ3	6	3	10	8	5

Grade Q235B is available for all steel plates.

Table 2: Mechanical property of the steel plate.

Thickness of the steel plate (mm)	σ_y (MPa)	σ_u (MPa)	ε_y (%)	ε_u (%)	E_s (MPa)
3	263	372	1.983	18.32	19523
4	256	381	1.831	20.23	19871
5	260	358	1.920	19.56	20522
6	249	363	1.853	18.92	20246
8	251	368	1.915	19.014	20042
10	238	375	2.052	18.76	19197

σ_y is the yield stress; σ_u is the limit stress; ε_y is the yield strain; ε_u is the limit strain; E_s is the elasticity modulus.

Figure 3: Experiment setup (mm).

According to tested results, it was also observed that the three specimens with the same thickness in the beam flange lost capacity in the same location and for the same reason, but they had obvious difference in ultimate bearing capacity; the main reason was that the boundary conditions of the compressed beam flange were not ideal situation under axial loading.

4.2. Load-Displacement Hysteretic Loop at the End of the Beam. The load-displacement hysteretic curve of the joint reflects the overall performance of connection. The load-displacement hysteretic curves at the end of the beam are shown in Figures 8–10. As can be seen from the figures, all three specimens exhibit good performance. The strength deterioration with the progress of the cyclic load was not observed. The rotational stiffness, however, deteriorated with the increase of cyclic load.

For the specimen CJ2 (4 mm thick hollow steel column), the beam flange in compression buckled suddenly after 9 displacement cycles. For the specimen CJ1 (5 mm thick hollow steel column) and the specimen CJ3 (6 mm thick hollow steel column), the beam flange in compression buckled suddenly after 8 displacement cycles.

FIGURE 4: Loading scheme for the experiment.

TABLE 3: Test results of the three specimens.

Specimen	P_{max} (kN)	U_{max} (mm)	Failure mode
CJ1	−8.56	−39.19	Compressed buckling of the beam flange
CJ2	10.20	−50.00	Compressed buckling of the beam flange
CJ3	11.92	48.57	Compressed buckling of the beam flange

P_{max} is the maximum load value documented in a test. U_{max} is the maximum displacement value documented at summit from sensor #5 in a test.

FIGURE 5: Beam flange buckled under compression for the specimen CJ1.

FIGURE 7: Beam flange buckled under compression for the specimen CJ3.

FIGURE 6: Beam flange buckled under compression for the specimen CJ2.

Figure 9 shows that the load in the specimen CJ2 is asymmetric. This indicates that the stiffness in positive direction is larger than that in negative direction.

Slight pinching of load-deflection hysteretic curves was observed in all three specimens. Such a phenomenon may be contributed to the following reasons: on one hand, because of the gap of the bolt connection between the shear connection plate and the bolt, slippage is inevitable under the cyclic loading; on the other hand, shear deformation is not ignored due to less effective antishear section dimension in the bear-to-column connection; of course, the deformation of the hollow column frame plate also contributes to the slippage.

4.3. Moment-Rotation Relationship Curve. Because of the large cross section of the PSB column, the stiffness of the column is quite large. As a result, it is assumed that there is no rotation in the column. Furthermore, as the PSB columns were fixed to the floor by four 30 mm diameter bolts, it was assumed that the PSB column did not slide under the cyclic loading. Based on the above assumptions, the rotation of
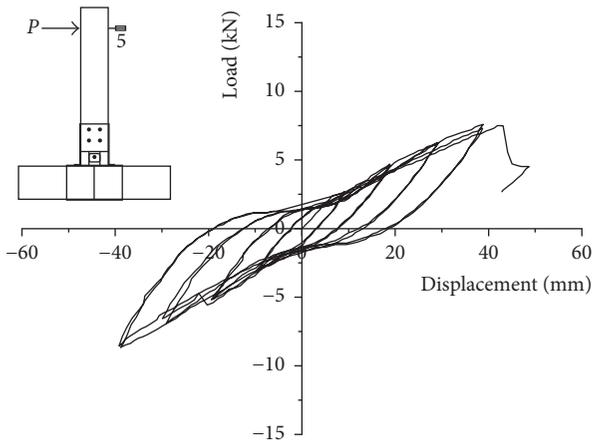
FIGURE 8: Load-displacement hysteretic loop of the specimen CJ1.
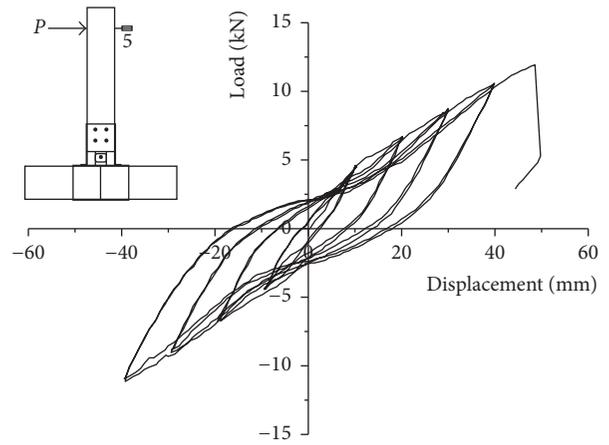
FIGURE 10: Load-displacement hysteretic loop of the specimen CJ3.
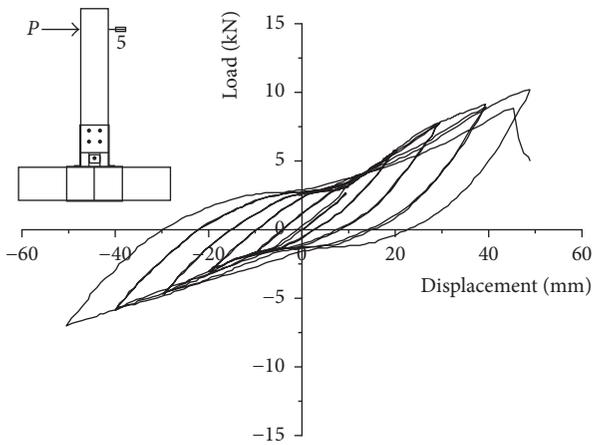
FIGURE 9: Load-displacement hysteretic loop of the specimen CJ2.

connection is the sum of the rotation due to the deflection of the hollow steel column, deflection of the beam flange, and the gap between the bolt and shear connection plate. In this test, the rotation of connection can be calculated as follows:

$$\varphi = \arctan\left(\frac{\Delta_4}{300}\right), \tag{1}$$

where Δ_4 is the displacement of laser sensor #4 under cyclic loading and 300 is the distance from sensor #4 to the surface of the column.

When calculating the rotation of the joint, the displacements from sensors #3, #4, and #5 all can be used. However, the displacement of sensor #5 includes the elastic deformation of the PSB beam, so the result from sensor #5 cannot be used to calculate the joint rotation. As for sensor #3, which was placed at 100 mm away from the beam flange where beam web ends, the velocity of reciprocating deformation of the beam flange which is lagging behind the loading velocity in the beam tip affects the result of sensor #3; therefore, the rotation of the joint based on sensor #3 is not used.

The maximum rotation for each specimen is shown in Table 4. It is noted that the rotation for the specimen CJ2 with a 4 mm thick hollow steel column is the biggest among

the three specimens. The specimen CJ3 with a 6 mm thick hollow steel column has the least rotation.

Because the deformation of the column is not taken into account, the moment of the joint is obtained by multiplying the load and the length from the loading point to the surface of the column. The equation for joint moment is given as follows:

$$M = P \times L_{\text{load}}, \tag{2}$$

where P is the load applied to the beam and L_{load} is the distance from the load point to the upper surface of the column.

Figures 11–13 show the moment-rotation hysteretic behavior of the three specimens. It shows that, for all three specimens, the hysteretic behavior is stable until the buckling of the beam flange.

The initial stiffness K_{ini} of each specimen, which is the ratio of the maximum moment to the corresponding rotation in the first cycle, is shown in Table 4. The initial stiffness increases with the increasing thickness of the hollow steel column. The relative parameters for the moment-rotation curve of the three specimens are showed in Table 4.

4.4. Envelope Curve. Envelope curve is defined as the line which connects the maximum rotation and corresponding moment in the first cycle of the displacement step. Figure 14 shows moment-rotation envelope curves of the three specimens. It is noted that the envelope curve of each specimen is similar.

Yielding phenomenon was not observed in the whole envelope curve, but the load increase appears to slow down with the increase of cyclic displacement. Such a phenomenon is mainly due to substantial losses in stiffness of the beam flange and hollow steel column under cyclic loading. It is evident that the thickness of the hollow steel column has a significant influence on the envelope curve.

From the envelope curves in the third quadrant shown in Figure 14, the specimen CJ3 has the largest load and the specimen CJ1 has the smallest load at the same displacement. This corresponds to the thickness of the hollow steel column of

TABLE 4: Test results.

Specimen	Loading direction	M_{max} (kN·m)	Φ_{max} (rad)	K_{ini} (kN·m/rad)
CJ1	Push	7.58	0.0375	333
	Pull	−8.65	−0.0375	
CJ2	Push	10.2	0.049	221
	Pull	−7.00	−0.0465	
CJ3	Push	11.92	0.044	354
	Pull	−11.14	−0.039	

Note. Φ_{max} corresponds to M_{max}.
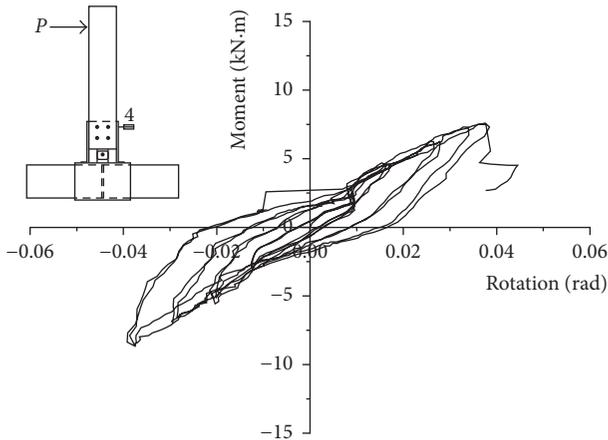
FIGURE 11: Moment-rotation hysteretic curve of the specimen CJ1.
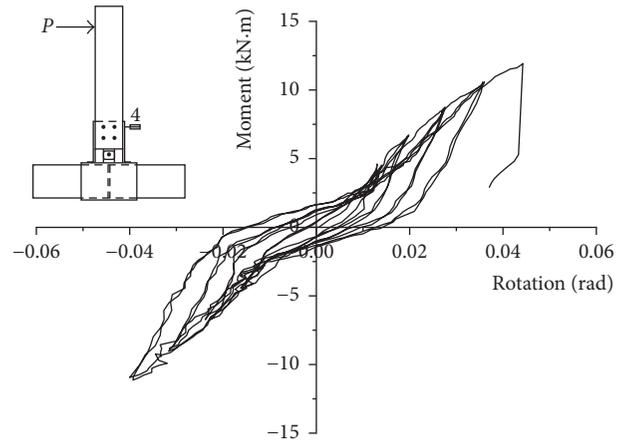
FIGURE 13: Moment-rotation hysteretic curve of the specimen CJ3.
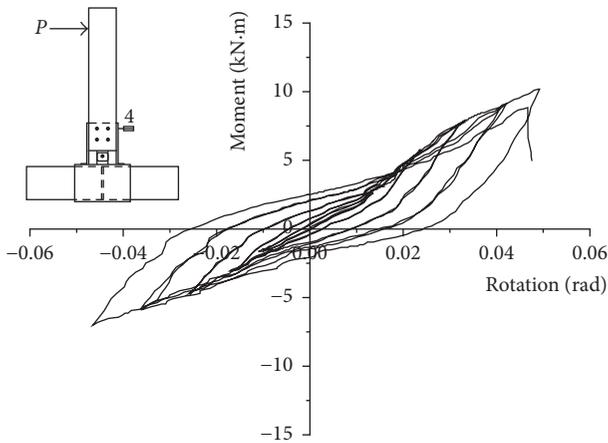
FIGURE 12: Moment-rotation hysteretic curve of the specimen CJ2.
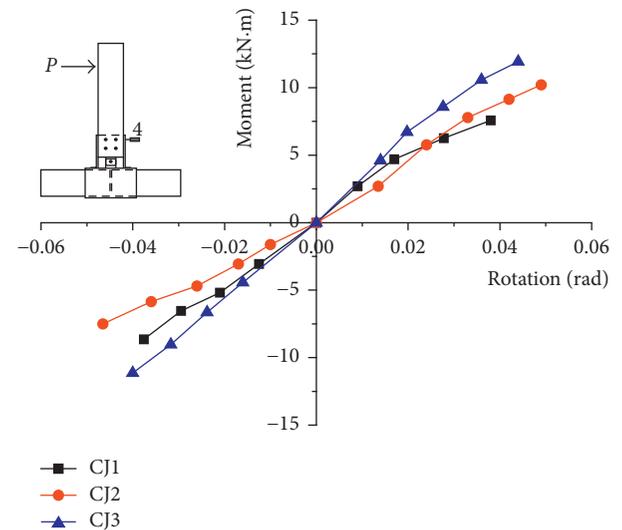
FIGURE 14: Envelope curve of the specimen under cyclic loading.

each specimen. This indicates that the thickness of the hollow steel column has an influence on the strength of connection.

It is also observed that the envelope curve under compressive load is different from the envelope curve under tensile load. This is due to the stiffness degradation of the steel plate.

4.5. Energy Dissipation. The energy dissipation of the connection is the enclosed area under cyclic loading, as shown in Figure 15, and the displacement in Figure 15 is the maximum beam tip displacement. It is an important index for evaluating seismic performance of the joint.

According to literature [25], the energy dissipation capacity coefficient E can be expressed in the following equation:

$$E = \frac{S_{ABD} + S_{CBD}}{S_{OAE} + S_{OCF}}, \tag{3}$$

Coefficient E for the three specimens CJ1, CJ2, and CJ3 is 1.70, 1.77, and 1.67, respectively. It can be seen that the specimen CJ2 has the biggest coefficient E, and the specimen

FIGURE 15: Enclosed area under cyclic loading.

FIGURE 16: Hysteresis model of connection.

TABLE 5: Model parameters of the specimens.

Specimen	Stiffness (kN·m/rad)			
	K_{ini}	K_2	K_3	K_4
CJ1	333	166	498	170
CJ2	221	205	309	116
CJ3	354	263	501	137

bending deformation of the column plate were not happening. When the unloading reaches zero, the loading in the opposite direction starts.

When the load starts to load in the opposite direction, the shear deformation of the beam and deflection of the hollow steel column recover first along with the close of the gap between the shear connection plate and the bolt, followed by the load increase of the joint. Therefore, the hysteretic curve of connection has slight pinching, and the stiffness of the slope is called as slippage stiffness K_4. Based on the tested results, the average stiffness values K_{ini}, K_2, K_3, and K_4 of each specimen are given in Table 5, in which K_2, K_3, and K_4 are the slopes of regression lines.

5. Conclusions

In this study, the mechanical performance of a new type connector in timber frame building was investigated. Three full-scale specimens with different hollow steel column thicknesses were subjected to cyclic loading up to failure, and the primary conclusions can be summarized as follows.

For the three specimens, failures were due to the compression buckling of the beam flange, and yielding in the beam flange was not observed. In addition, deformation perpendicular to the hollow steel column was observed in the specimen CJ2; however, no obvious deformation was noted in the specimens CJ1 and CJ3. Buckling of the beam flange governs the moment resistance and rotation capacity of connection.

It is also noticed that the hysteresis loops for the three specimens appear full, with slight pinching in every specimen. The energy dissipation coefficient E for the three specimens CJ1, CJ2, and CJ3 is 1.70, 1.77, and 1.67, respectively, which indicates that the three specimens have good energy dissipation. The hollow steel column thickness has significant influence on the energy dissipation of the connection. Although the thinner hollow steel column has better energy dissipation, it has less connection stiffness.

The maximum rotations of the specimens CJ1, CJ2, and CJ3 under cyclic loading are 0.0375, 0.049, and 0.044, respectively. The thinner the hollow steel column, the larger the rotation of the connection.

Under the cyclic loading, the connection undergoes substantial losses in stiffness.

According to the envelope curve and moment-rotation curve, a hysteresis model for this type of connection under cyclic loading is presented. Employing a thick hollow steel column will have bigger first secant stiffness K_{ini} under cyclic loading.

CJ3, which has the thickest hollow steel column, has the lowest coefficient E.

4.6. Hysteresis Model of Connections. Based on the moment-rotation curves showed in Figures 11–13, the simplified hysteresis model of the joint under cyclic loading is showed in Figure 16. Point A is the summit point of the first step cycle, and from point 0 to point A, the loading stiffness is expressed with secant stiffness K_{ini}. After passing point A, loading stiffness K_2 becomes smaller. This is due to the shear deformation of the beam and bending deformation of the hollow steel column. K_3 is the unloaded stiffness from point B, which is obviously larger than the loading stiffness K_2. At the start of unloading, only beam flanges act in tension and compression, and shear deformation of the beam and

Conflicts of Interest

The authors declare that they have no conflicts of interest.

Acknowledgments

References

[1] D. P. Fang, S. Iwasaki, M. H. Yu, Q. P. Shen, Y. Miyamoto, and H. Hikosaka, "Ancient Chinese timber architecture. I: experimental study," *Journal of Structural Engineering*, vol. 127, no. 11, pp. 1348–1357, 2001.

[2] W. S. King, J. Y. Richard Yen, and Y. N. Alex Yen, "Joint characteristics of traditional Chinese wooden frames," *Engineering Structures*, vol. 18, no. 8, pp. 635–644, 1996.

[3] Q. Chun, Z. Yue, and J. W. Pan, "Experimental study on seismic characteristics of typical mortise-tenon joints of Chinese southern traditional timber frame buildings," *Science China Technological Sciences*, vol. 54, no. 9, pp. 2404–2411, 2011.

[4] W. S. Chang, J. Shanks, A. Kitamori, and Kohei Komatsu, "The structural behavior of timber joints subjected to bi-axial bending," *Earthquake Engineering & Structural Dynamics*, vol. 38, no. 6, pp. 739–757, 2009.

[5] J. M. Seo, I. K. Choi, and J. R. Lee, "Static and cyclic behavior of wooden frames with tenon joints under lateral load," *Journal of Structural Engineering*, vol. 125, no. 3, pp. 344–349, 1999.

[6] W. M. Bulleit, L. Bogue Sandberg, M. W. Drewek, and T. L. O'Bryant, "Behavior and modeling of wood-pegged timber frames," *Journal of Structural Engineering*, vol. 125, no. 1, pp. 3–9, 1999.

[7] J. P. Hong, J. David Barrett, and F. Lam, "Three-dimensional finite element analysis of the Japanese traditional post-and-beam connection," *Journal of Wood Science*, vol. 57, no. 2, pp. 119–125, 2011.

[8] F. Lam, M. Schulte-Wrede, C. C. Yao et al., "Moment resistance of bolted timber connections with perpendicular to grain reinforcements," in *Proceedings of the 10th World Conference on Timber Engineering (WCTE)*, Miyazaki, Japan, June 2008.

[9] F. Lam, M. Gehloff, and M. Closen, "Moment-resisting bolted timber connections," *Proceedings of the Institution of Civil Engineers-Structures and Buildings*, vol. 163, no. 4, pp. 267–274, 2010.

[10] M. Q. Wang, X. B. Song, X. L. Gu, Y. Zhang, and L. Luo, "Rotational behavior of bolted beam-to-column connections with locally cross-laminated glulam," *Journal of Structural Engineering*, vol. 141, no. 4, pp. 1–7, 2015.

[11] M. Fragiacomo and M. Batchelar, "Timber frame moment joints with glued-in steel rods. I: design," *Journal of Structural Engineering*, vol. 138, no. 6, pp. 789–801, 2012.

[12] M. Fragiacomo and M. Batchelar, "Timber frame moment joints with glued-in steel rods. II: experimental investigation of long-term performance," *Journal of Structural Engineering*, vol. 138, no. 6, pp. 802–811, 2012.

[13] G. Tlustochowicz, E. Serrano, and R. Steiger, "State-of-the-art review on timber connections with glued-in steel rods," *Materials and Structures*, vol. 44, no. 5, pp. 997–1020, 2011.

[14] M. Vašek and R. Vyhnálek, "Timber semi rigid frame with glued-in-rods joints," in *Proceedings of the 9th World Conference on Timber Engineering (WCTE)*, August 2006.

[15] M. Vašek, "Semi rigid timber frame and space structure connections by glued-in rods," in *Proceedings of the 10th World Conference on Timber Engineering (WCTE)*, Miyazaki, Japan, June 2008.

[16] A. Bouchaïr, P. Racher, and J. F. Bocquet, "Analysis of dowelled timber to timber moment-resisting joints," *Materials and Structures*, vol. 40, no. 10, pp. 1127–1141, 2007.

[17] T. Tsuchimoto, N. Ando, T. Arima et al., "Effect of clearance on the mechanical properties of timber joint," in *Proceeding of Pacific timber engineering conference*, vol. 2, pp. 204–210pp. 204–210, Rotorua, New Zealand, March 1999.

[18] D. S. Huang, A. P. Zhou, Q. S. Zhang et al., "Quasi-static experimental research on energy dissipating joints for assembled timber frame structures," *Journal of Building Structures*, vol. 32, no. 7, pp. 87–92, 2011, in Chinese.

[19] D. S. Huang, A. P. Zhou, and Y. L. Bian, "Experimental and analytical study on the nonlinear bending of parallel strand bamboo beams," *Construction and Building Materials*, vol. 44, pp. 191–196, 2013.

[20] D. S. Huang, Y. L. Bian, A. P. Zhou, and B. Sheng, "Experimental study on stress-strain relationships and failure mechanisms of parallel strand bamboo made from phyllostachys," *Construction and Building Materials*, vol. 77, pp. 130–138, 2015.

[21] D. S. Huang, Y. L. Bian, D. M. Huang, A. Zhou, and B. Sheng, "An ultimate-state-based-model for inelastic analysis of intermediate slenderness PSB columns under eccentrically compressive load," *Construction and Building Materials*, vol. 94, pp. 306–314, 2015.

[22] GB/T 700-2006, "Carbon structural steels" (in Chinese)," 2007.

[23] European Standard EN 10002-1, *Metallic Materials–Tensile Testing–Part 1: Method of Testing at Ambient Temperature*, CEN, Brussels, Belgium, 2001.

[24] The American Society for Testing and Materials, ASTM D143–09, *Standard Test Methods for Small Clear Specimens of Timber*, ASTM, West Conshohocken, PA, USA, 2009.

[25] JGJ/T 101-2015, *Specification for Seismic Test of Building*, China Construction Industry Press, Beijing, 2015, in Chinese.

Research Article

Seismic Behavior of Rammed Earth Walls with Precast Concrete Tie Columns

Xinlei Yang [ID][1,2] **and Hailiang Wang**[1,2]

[1]*School of Civil Engineering, Tianjin Chengjian University, No. 26, Jinjing Road, Xiqing District, Tianjin 300384, China*
[2]*Tianjin Key Laboratory of Civil Buildings Protection and Reinforcement, No. 26, Jinjing Road, Xiqing District, Tianjin 300384, China*

Correspondence should be addressed to Xinlei Yang; yxl@tcu.edu.cn

Rammed earth (RE) constructions are widespread in underdeveloped rural areas in developing countries. However, these RE constructions are often susceptible to earthquake damage due to their poor seismic performance. Precast concrete tie columns and ring beam (tie bars) were proposed to improve the seismic behavior of RE constructions. Four RE walls, including a traditional RE wall and three RE walls with precast concrete tie columns and ring beam (tie bars), were tested under reversed cyclic loading, and the seismic behavior of these tested specimens was evaluated in terms of failure pattern, energy dissipation, displacement ductility, and stiffness degradation. The results showed that a significant increase of the load-bearing and deformation capacity could be achieved with the application of precast concrete tie columns in combination with RE. The load-bearing capacity and deformation capacity of traditional RE wall were increased by an average of 113% and 417%, respectively. These test results could provide reference to the design and construction of the environmental-friendly structures in rural areas.

1. Introduction

Rammed earth (RE) dwellings are widespread in underdeveloped rural areas of western China, which has several advantages over other buildings, including low cost, easy availability, thermal comfort, and low intervention with surroundings. However, RE constructions have drawbacks of sensitivity to water, propensity to shear failure, and lacking systemic engineering design concerning earthquake. They are susceptible to earthquake damage owing to low compressive strength, shear strength, and durability [1–5].

Many efforts have been undertaken to enhance the mechanical properties of rammed earth. Niroumand et al. [6] investigated the influence of nanotechnology on material characteristics of rammed earth, and the results showed that nanoclay could increase the level of compressive strength in rammed earth walls and be used as a cohesive material in the soil mixture. Venkatarama Reddy and Prasanna Kumar [7] studied the relationship among soil density, moisture

content, and compressive strength and found that the compressive strength of rammed earth was very sensitive to its dry density and moisture content. Cheah et al. [8] conducted an experimental study of the shear strength of a stabilized RE material reinforced with sisal and flax fibres. The results showed that a shear failure of the triplet test appeared along the weak interface between layers, but specimens failed along diagonal shear plane at the triaxial test. Bouhicha et al. [9] conducted a study to investigate the influence of fibre length and fibre fraction on compressive strength, flexural strength, and shear strength of rammed earth. The results proved that adding straw could decrease shrinkage damage, reduce the curing time, and improve the mechanical property. Bui et al. [10] analyzed the role of the moisture content on the mechanical characteristics and illuminated the importance of suction to RE specimens. There are limited numbers of studies on the improvement of the performance of rammed earth buildings using various reinforcement technologies. Bu et al. [11] studied the effect of

the split-level construction or pin keys on shear strength of rammed earth walls and found that the two methods were effective in improving the shear strength of construction with respect to the traditional method.

Generally, many experimental investigations have been conducted to enhance the mechanical properties of rammed earth by improvements in material characterization (chemical, physical, mechanical, and durability) and possible additions (lime, cement, straws, and fibres). However, there are limited investigations addressing the issues of the attempt to enhance seismic performance of rammed earth buildings by means of structural strengthening solutions. In this paper, precast concrete tie columns and precast concrete tie beam (tie bar) were proposed to improve the seismic behavior of RE constructions, and the effectiveness of these structural strengthening solutions is validated by conducting cyclic loading tests. The test results could provide data to support the RE construction practices.

2. Materials and Methods

2.1. Materials. In this study, the used soil was taken from Gongyi County in Henan Province, China, which is located in the East Loess Plateau. The properties of selected soil are outlined in Table 1. Generally, compaction characteristics of rammed earth are evaluated by two important parameters, that is, optimum moisture content (OMC) and maximum dry density (MDD). By the standard Proctor tests, OMC is 16.5% and MDD is 1710 kg/m^3.

In view of the availability, economy, and ease of construction, cement was selected as a stabilizer. Ordinary Portland cement of 42.5 grade was used in the experimental investigations. In the experimental investigations, 10% cement by dry mass of soil was used for production of test specimens. In the test specimens, the diameter of corrosion resistant zinc-coated wire used as tie bars is 2.6 mm. Table 2 summarizes the properties of the steel bars. During the construction of each wall, $150 \times 150 \times 150$ mm cubes were prepared to test compressive strength of cement-stabilized rammed earth (CSRE). The average compressive strength was in the range of 4.5~8.4 MPa.

2.2. Specimen Design and Construction. This research conducted experimental investigations on four 1/3-scale $1600 \times 1200 \times 200$ mm $(L \times H \times W)$ RE walls under lateral cyclic loading; considering the requirement of loading equipment, the height is 1400 mm actually. The dimensions and reinforcement details of the tested specimens are shown in Figure 1.

Specimen Q-1 was designed as a traditional CSRE wall without tie columns and tie beam (tie bar) and used as a control specimen, as shown in Figure 1(a). Specimen K-1 was designed as a frame, which consisted of a precast concrete tie beam and two concrete tie columns, as shown in Figure 1(b). The other three specimens were CSRE walls with the precast concrete tie columns, and those tie columns had the same dimensions and reinforcement details. Structural characteristics of each tested specimen are briefly summarized in Table 3.

TABLE 1: Summary of soil properties.

Property	Parameters	Value
Grain size distribution	Gravel fraction	28%
	Sand fraction	44%
	Silt fraction	13%
	Clay fraction	15%
Atterberg limit	Liquid limit	27.8%
	Plastic limit	17.7%
	Plastic index	10.1%
Proctor test	Optimum moisture content	16.5%
	Maximum dry density (kg/m^3)	1710

TABLE 2: Mechanical properties of reinforcing bars.

Bar type	Yield strength (MPa)	Ultimate tensile strength (MPa)	Elastic modulus (GPa)	Ultimate elongation (%)
Φ6	356	418	202	22.4
Φ2.6	352	435	202	15.4
Φ2	321	403	186	14.2

Specimen Q-2 was designed as a reinforced CSRE wall with a precast concrete tie beam and two concrete tie columns, as shown in Figure 1(c). Specimen Q-5 is similar to Specimen Q-2; however, one wire tie is used instead of the precast concrete tie beam, as shown in Figure 1(d). Specimen Q-7 was designed as a reinforced CSRE wall with two precast concrete tie columns and three wire ties starting at 400 mm from the top of the foundation beam that were spaced at 400 mm along the wall height, as shown in Figure 1(e). In order to prevent slippage between the CSRE wall and the steel ground beam, two rows of bolts were installed on the surface of footing and performed well as expected.

Using precast concrete tie columns and tie beam could avoid negative effects of moisture on strength of CSRE. The precast concrete tie columns and tie beam had the dimensions of 80 mm × 80 mm × 1400 mm and 80 mm × 80 mm × 1440 mm, respectively, and were constructed using C30 concrete. The longitudinal reinforcement used in the precast concrete column was four Φ6 plain bars, and the transverse reinforcement was Φ2 galvanized iron wire. The longitudinal reinforcement of precast concrete tie beam was four Φ6 plain bars, and the transverse reinforcement was Φ2 galvanized iron wire. The dimensions and reinforcement details are shown in Figure 2.

The soil was prepared to their optimum moisture content determined by the compaction test and compacted inside aluminum alloy I-beam molds to form walls. The test wall is composed of several layers of earth and constructed on a steel ground beam. The earth was poured into molds in layers approximately 350 mm thick and then compacted with a pneumatic compactor rammer. The thickness of each layer after compaction maintained roughly at 200 mm. In order to guarantee the cohesiveness between layers, compacting in corners and spraying water at each layer surface were accomplished manually.
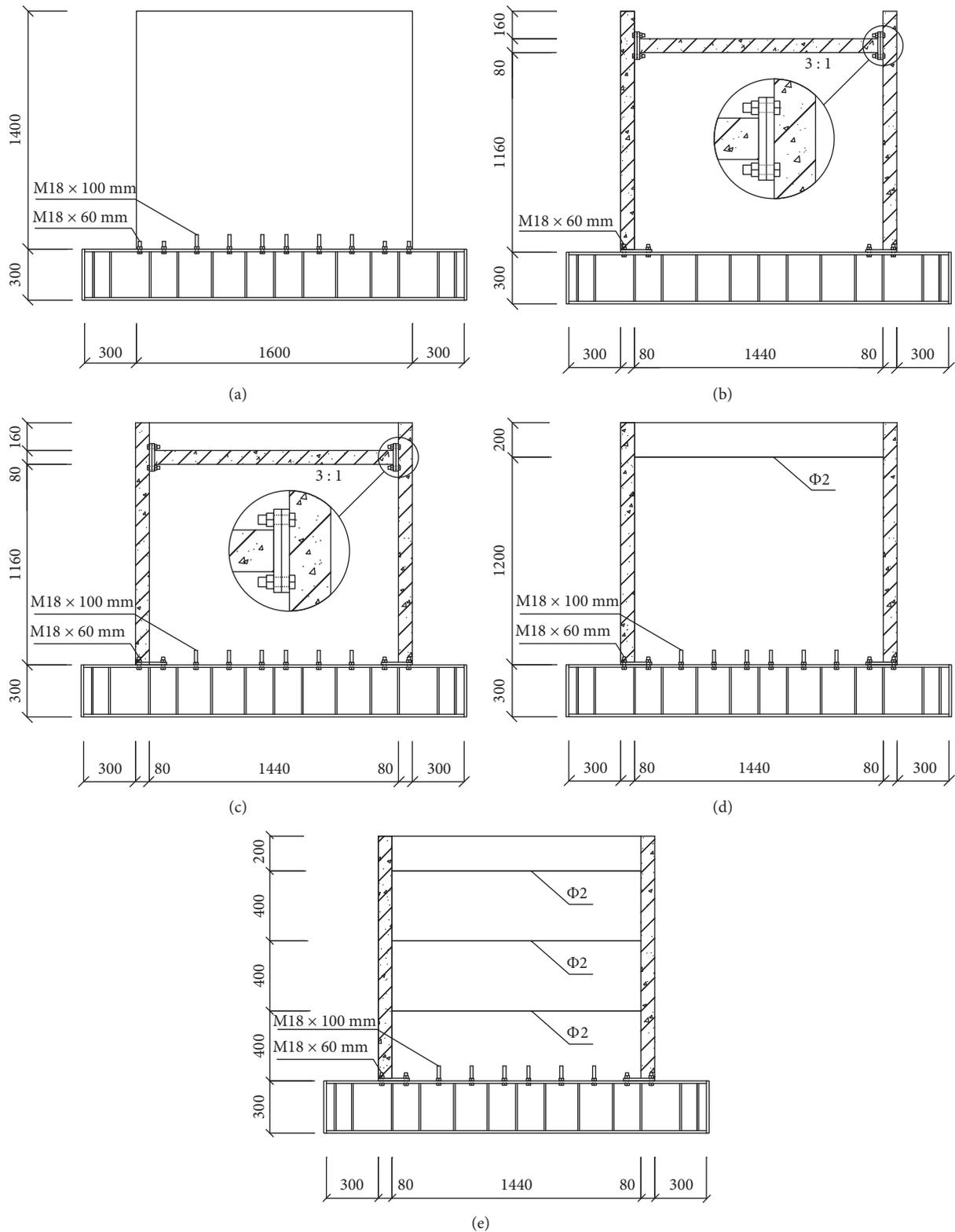
FIGURE 1: Dimensions and details of test specimens (unit: mm). (a) Q-1. (b) K-1. (c) Q-2. (d) Q-5. (e) Q-7.

2.3. *Test Setup and Instrumentation.* A servohydraulic actuator with 150 kN maximum load and a ±250 mm displacement range was used to apply a quasistatic lateral loading to 1200 mm height in two opposite directions. A hydraulic jack was used to carry out a constant axial load to the top of the wall to simulate gravity actions. Specimen K-1 was only subjected to horizontal reversed cyclic loading without the vertical load. The loading devices and

TABLE 3: Summary of structural characteristics of the tested specimens.

Specimen	Structural characteristics	Remarks
Q-1	Without tie columns	Control specimen
K-1	Precast concrete tie columns + precast concrete tie beam	
Q-2	Precast concrete tie columns + precast concrete tie beam + CSRE	
Q-5	Precast concrete tie columns + one wire tie + CSRE	
Q-7	Precast concrete tie columns + three wire ties + CSRE	

(a)   (b)
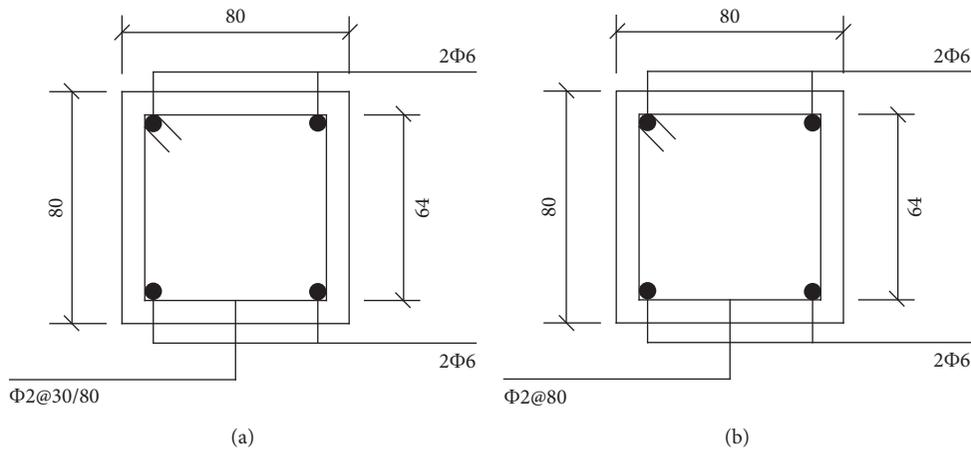
FIGURE 2: Details of the precast concrete tie column (a) and tie beam (b).

the site of test setup are shown in Figures 3 and 4, respectively.

For each test wall, a total of five displacement sensors were used to record the displacement developed at different loading stages, as shown in Figure 5. Displacement of the ground beam relative to strong floor was measured by number D_0. Displacement of the ground beam relative to wall was measured by number D_3. Lateral displacement of wall was measured by numbers D_1 and D_2, which were installed at loading position centerline. The diagonal strain of the wall is recorded by numbers D_4 and D_5, which were positioned in the diagonal direction.

2.4. Test Procedure and Loading Characteristics. A constant axial load of 26.43 kN simulated to gravity actions was applied to the wall and was maintained constant throughout each test. The applied axial load at the top of the walls includes the dead loads (self-weights of the roof and wall) and the live load (0.5 kN/m^2), which was defined by the similitude law. It represents a normal stress of 0.08 MPa, as in current rammed earth walls in a one storey house in China.

After application of the axial load to the top of the steel beam, low-rate lateral cyclic loading of increasing amplitude-simulated lateral earthquake loading was applied to a height of 1200 mm. The test walls were loaded in a displacement- (drift-) controlled mode at a constant rate of 0.2 mm/s, and two fully reversed cycles were applied at each drift. The selected drift was intended to cause displacements that investigated in-elastic deformations of the wall corresponding to earthquake action.
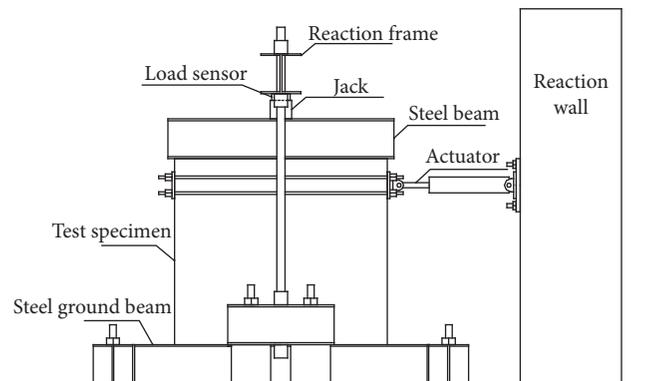
FIGURE 3: The schematic drawing of loading devices.

Each test was initiated at interval steps of 0.1% drift ratios until 0.8%. In the range of 0.8%~2% drift ratios, the specimen was cycled at interval steps of 0.2%. In the range of 2%~4% drift ratios, the specimen was cycled at interval steps of 0.4%. When the drift ratios reached 4%, interval steps of 0.8% drift ratios were imposed to the specimens until failure or instability. The lateral cyclic loading protocol is shown in Figure 6.

3. Failure Process and Modes

The final failure modes of tested specimens observed are shown in Figure 7.

Specimen Q-1: the damage was initiated at a drift ratio of approximately 0.2%, at which time the first horizontal crack appeared at a distance of 230 mm from the bottom of the wall. The horizontal crack propagated in

FIGURE 4: The picture of the test setup.

LVDT
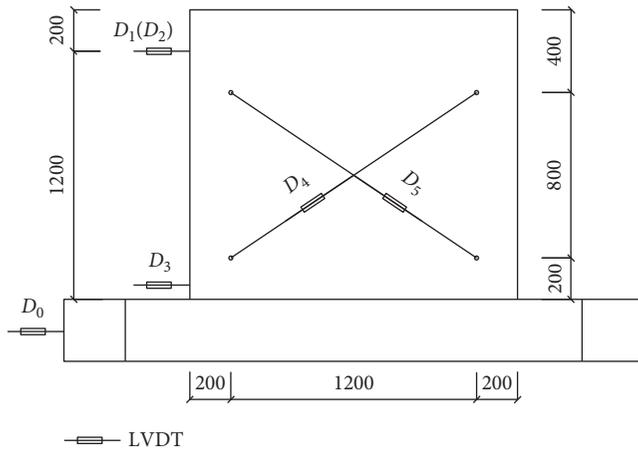
FIGURE 5: Measurement layout of instrumentation.

FIGURE 6: Loading history.

size and evolved into a horizontal penetrating crack at 0.3% drift ratio. As the drift increased, the wall was separated into two portions by this horizontal penetrating crack, and the relative slippage was observed at a drift ration of 0.8%. The cracking patterns of Specimen Q-1 are shown in Figure 7(a).

Specimen Q-2: a horizontal shrinkage crack forming at 200 mm below the loading position evolved into a horizontal penetrating crack at a drift of approximately 0.2%. When increasing displacement in both the positive and negative directions, the horizontal cracks propagated to both sides of the columns and local shear failure was observed on columns at a drift of approximately 2.4%. The ultimate failure mode refers to Figure 7(b).

Specimen Q-5: a horizontal shrinkage crack at the central region of the wall evolved into a penetrating crack at a drift ratio of 0.1%, and horizontal cracks occurred on both sides of tie columns at a drift ratio of 0.8%. The test was stopped at 6.4% drift ratio, and at the end of the test, the bearing capacity was not reduced except for the presence of out-of-plane displacements of the wall. The ultimate failure of the wall refers to Figure 7(c).

Specimen Q-7: in the middle section of the wall, a horizontal shrinkage crack penetrated into wall core at a drift of 0.2% and the crack width increased remarkably as the drift increased. Flexural cracks emerged on both sides of precast concrete tie columns at a drift ratio of

0.6%. Specimen Q-7 was loaded at increasing drift until 9.6%, at which time the test was terminated because of out-of-plane displacements of the wall. The ultimate failure mode refers to Figure 7(d).

Specimen K-1: the flexural cracks of Specimen K-1 were observed on both ends of columns at a drift ratio of 0.4% and propagated gradually along the height with the drift increasing. The concrete in the joint region spalled and crushed off at a drift ratio of 9.6%. Additionally, the column longitudinal reinforcement exposed progressed. The ultimate failure mode refers to Figure 7(e).

It could be seen from Figure 7 that the failure modes of these wall specimens were dominated by a shear failure mechanism. The horizontal penetrating cracks were mainly formed along a layer interface, illustrating that the layer interface is the weak regions in rammed earth walls. For Specimen Q-2, the earth under the precast concrete tie beam was not compacted to be very dense due to space constraints and formed a weak region, which causes the local failure appearing on both sides of precast concrete tie columns ahead of expected theoretical design attributed to uneven distributed load. The performance of Specimen Q-5 is similar to that of Specimen Q-7, in terms of crack development and reduction process of bearing capacity, respectively. With increasing drift amplitudes, the confinement effect exerted by precast concrete tie columns and wire ties gradually played a role and the load-bearing capacity of tested specimens increased slowly. Although the load had dropped to 85% below the peak value, the increase of strength at late stage of loading can be regarded as capacity reservation.

4. Results and Discussion

4.1. Overall Response. The hysteresis curves are the most important characteristic for assessing the seismic performance of tested walls under cyclic loading in terms of the energy dissipation capacity, the ductility performance, strength deterioration, and stiffness degradation of the wall. The hysteresis

(a)

(b)

(c)

(d)

(e)
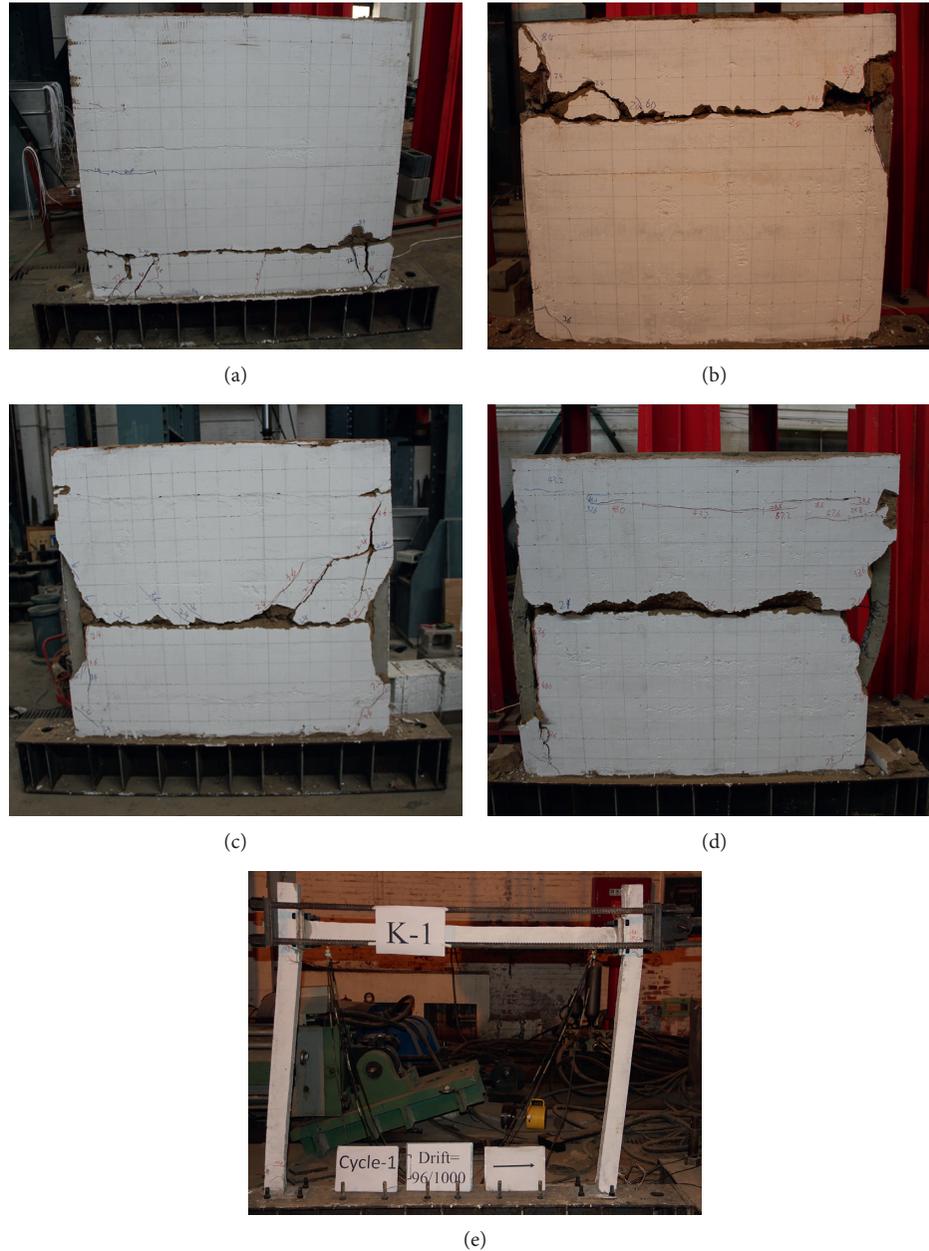
FIGURE 7: Failure mode of tested specimens. (a) Specimen Q-1. (b) Specimen Q-2. (c) Specimen Q-5. (d) Specimen Q-7. (e) Specimen K-1.

loops (load versus story drift) of four test specimens are presented in Figure 8.

It could be seen that Specimen Q-1, as a control specimen, exhibited poor hysteretic properties with a remarkable strength drop after peak load, with this unfavorable performance attributed to lack of precast concrete tie columns in the wall. Other three wall specimens with precast concrete tie columns exhibited a stable lateral load versus drift hysteretic response, especially Specimens Q-5 and Q-7, showing that the seismic performance of rammed earth walls can considerably be improved through the use of precast concrete tie columns and wire ties.

The hysteresis loops of specimen Q-2, Q-5, and Q-7 presented a fusiform shape during initial loading. With increasing cracks, and after spalling and crushing of earth,

the curve shape gradually changed into reverse S, which illustrated that cracks progressed adequately so that impossible to recover and residual deformations appeared in the later stage.

The ability of a structure to survive an earthquake depends to a large extent on its ability to dissipate the input energy. The good energy dissipation capacity indicates the capacity of the structure to perform satisfactorily in the inelastic range. The amount of cumulative energy dissipated is plotted versus the roof drift in Figure 9. The energy dissipation capacity of Specimen K-1 is significantly inferior to other three specimens at the same drift, which illustrates that the rammed earth plays a major role in energy dissipation capacity. After comparison of Specimen Q-1 and other three walls, it could be found that the cowork between
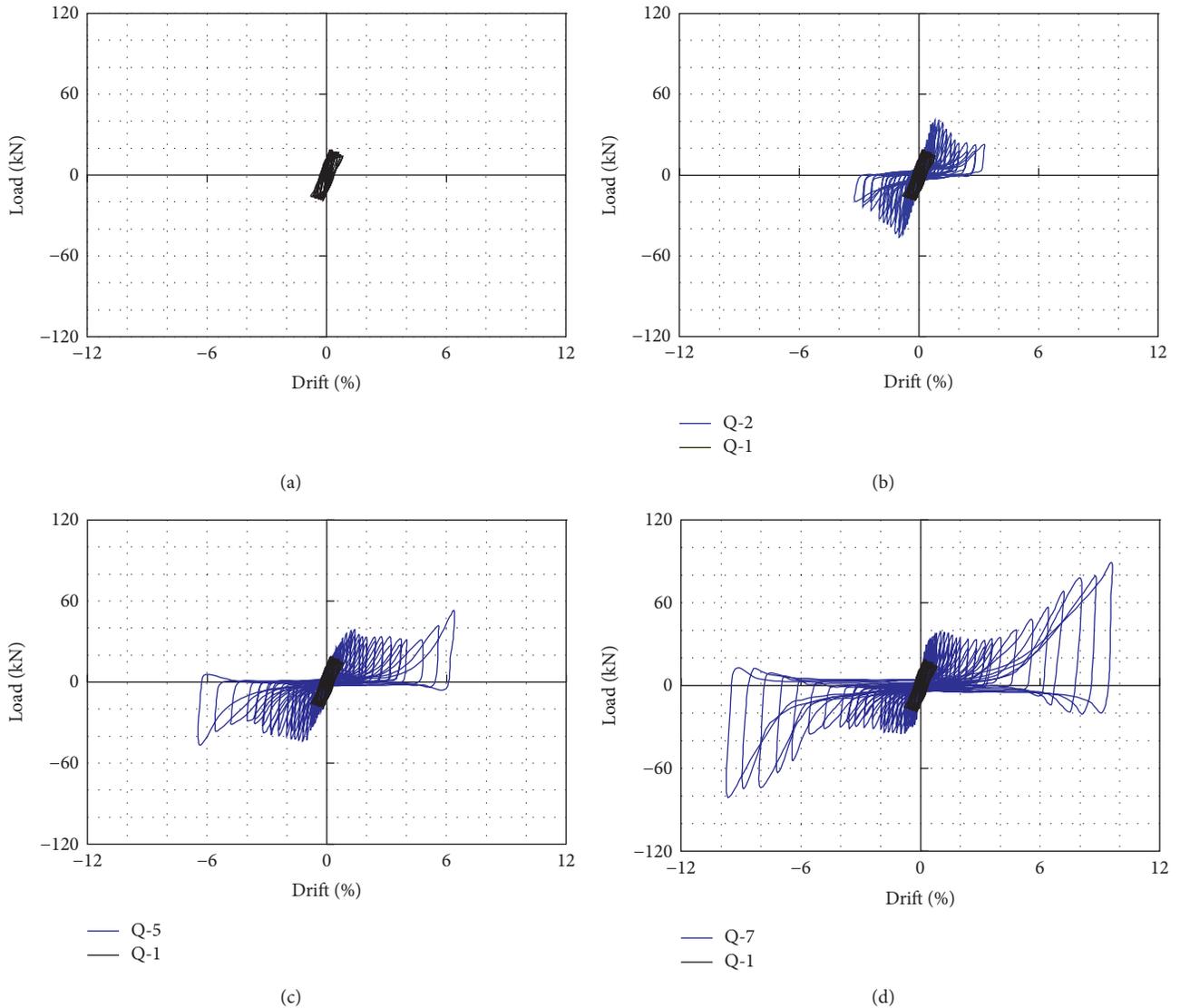
FIGURE 8: Hysteresis curves of specimens. The hysteretic response of (a) Q-1; (b) Q-1 and Q-2; (c) Q-1 and Q-5; (d) Q-1 and Q-7.
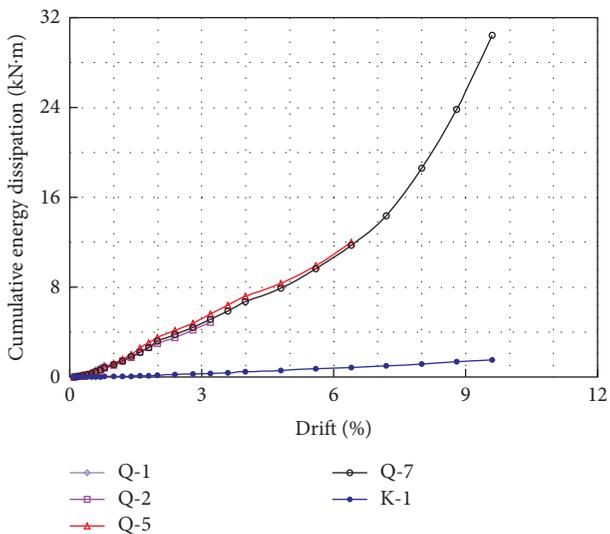
FIGURE 9: Comparison of cumulative energy dissipation of specimens.

tie columns and walls was effective on significantly improving the capacity of the energy dissipation. The energy dissipation capacity of each rammed earth wall specimen was similar at the same drift, which indicated that the energy was mainly dissipated by rammed earth.

4.2. Skeleton Curves. The comparison of skeleton curves of the RE walls is shown in Figure 10. The skeleton curve of Specimen Q-1 shows a peak load at a drift ratio of 0.2% and rapid degradation in strength properties with increasing displacement, which indicates that Specimen Q-1 did not perform as well as other three walls in terms of bearing capacity and deformability capacity. The strength of specimens Q-2, Q-5, and Q-7 reached peak load almost simultaneously at a drift ratio of 1.2%. Specimen Q-2 did not perform as well as Specimens Q-5 and Q-7, showing that wire ties are more effective than tie beam on enhancing deformation capacity. Finally, it could be concluded that the
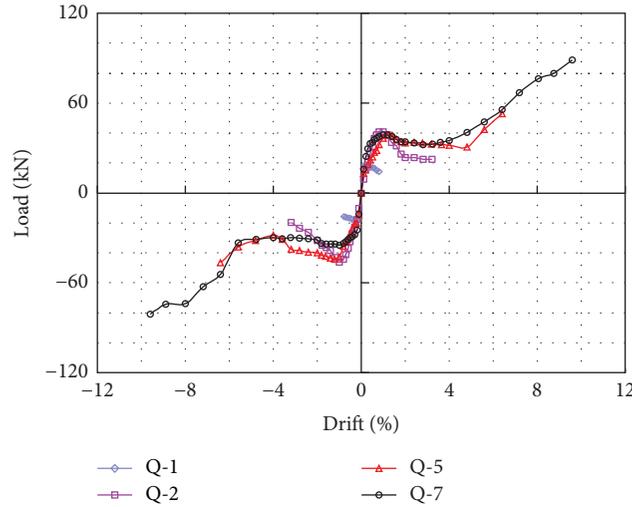
FIGURE 10: Comparison of skeleton curves of specimens.

TABLE 4: Global displacement ductility values of test specimens.

Parameter		P_y (kN)	Δ_y (mm)	P_{max} (kN)	Δ_{max} (mm)	P_u (kN)	Δ_u (mm)	$\mu = \Delta_u/\Delta_y$	Mean value of μ
Q-1	POS	18.78	1.39	18.78	2.40	15.96	7.62	5.48	5.74
	NEG	−16.65	−1.35	−19.04	−2.40	−16.18	−8.09	5.99	
Q-2	POS	26.14	4.77	40.73	9.60	34.62	16.24	3.40	3.27
	NEG	−29.09	−5.21	−46.25	−12.00	−39.31	−16.35	3.14	
Q-5	POS	25.84	5.58	38.40	16.80	32.64	38.83	6.96	6.82
	NEG	26.29	−5.76	−44.35	−14.40	−37.70	−38.47	6.68	
Q-7	POS	30.99	4.17	38.87	12.00	33.04	29.81	7.15	7.93
	NEG	−28.58	−4.30	−35.07	−12.00	−29.81	−37.43	8.70	

Note. POS: positive direction; NOG: negative direction. P_y: the yield load; Δ_y: the displacement corresponding to the yield load; P_{max}: the peak load; Δ_{max}: the displacement corresponding to the peak load; Δ_u: determined as corresponding to a 15% drop of the peak load; P_u: the load corresponding to Δ_u.

proposed precast concrete tie columns are effective on dramatically improving the performance of the seismic and deformability.

4.3. Ductility Capacity and Bearing Capacity.
The ductility capacity is identified as an important parameter for earthquake-resistant constructions, which could be calculated as the ratio of ultimate displacement to the yield displacement. Using the ultimate displacement and calculated yield, the ductility capacity value is determined as follows:

$$\mu = \frac{\Delta_u}{\Delta_y}, \tag{1}$$

where Δ_u is determined as corresponding to a 15% drop of the peak load and Δ_y is the displacement corresponding to the yield load.

The peak load, the ultimate displacement, the yield load, the yield displacement, and ductility value of the test walls are presented in Table 4. Although the ductility value of Specimen Q-2 was slightly lower than that of Specimen Q-1, the deformation capacity of Specimen Q-2 was significantly higher than that of Specimen Q-1. The ductility value of Specimens Q-5 and Q-7 is 18.79% and 38.1% higher than that of Specimen Q-1, respectively, which shows that the application
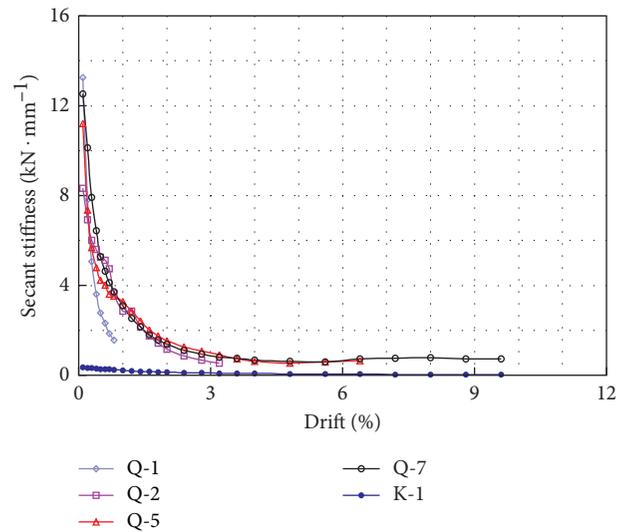
FIGURE 11: Stiffness degeneration curves.

of precast concrete tie columns and precast concrete tie beam (wire ties) could significantly improve the deformation capacity of the test walls. The ductility value of Specimens Q-7 is 16.28% higher than that of Specimen Q-5, attributed to the increase in the number of wire ties.

(a)

(b)

(c)
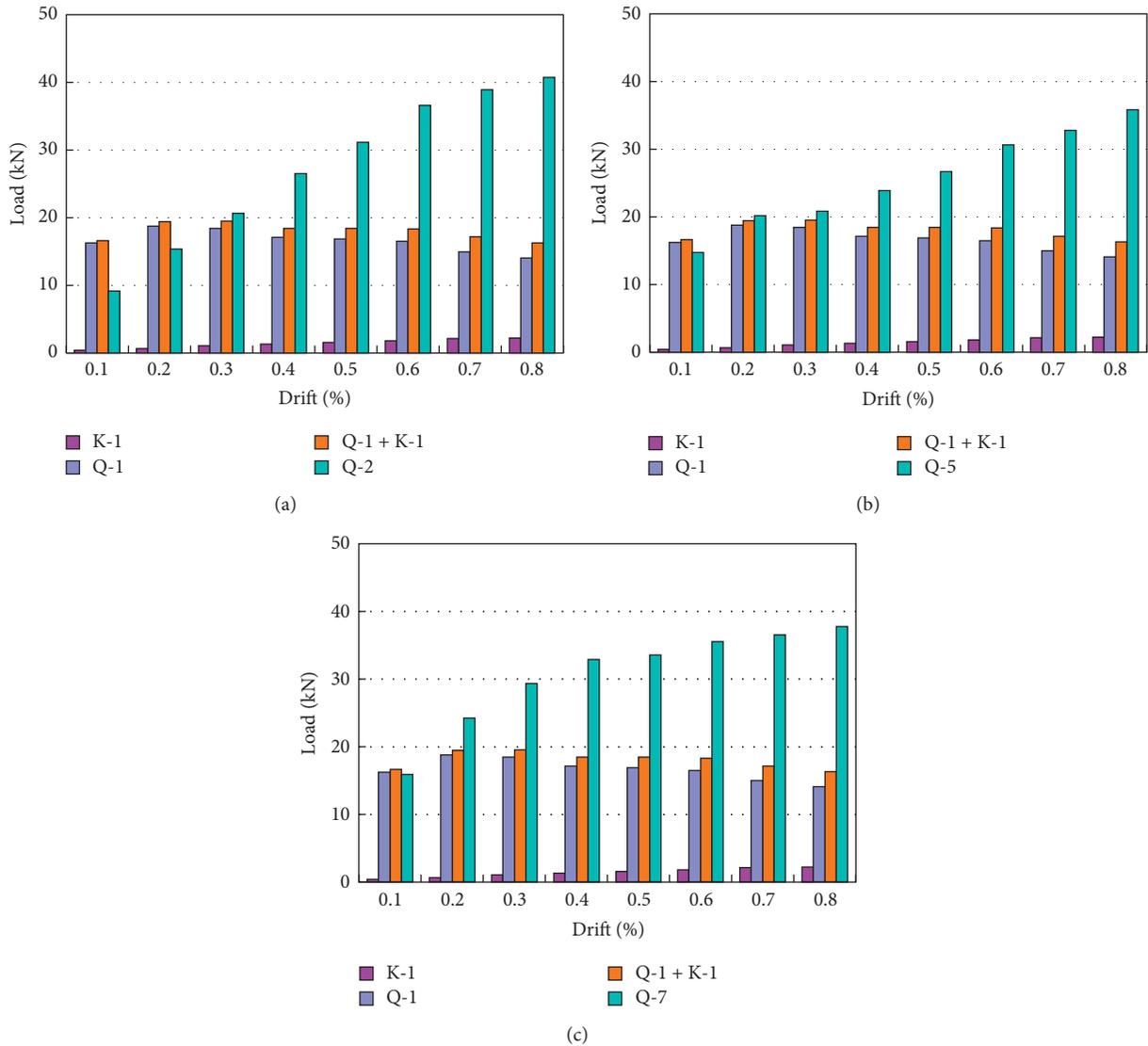
FIGURE 12: Comparison of strength of specimens at specific drifts. Comparison of strength between (a) Q-2 and Q-1; (b) Q-5 and Q-1; (c) Q-7 and Q-1.

The result clearly shows that the yield load and the yield displacement of Specimens Q-2, Q-5, and Q-7 are significantly higher than control Specimen Q-1. Compared with control Specimen Q-1, the ultimate bearing capacity of other three specimens was increased by 95%~130%, which were confined by precast concrete tie columns and precast concrete tie beam (wire ties). The maximum bearing capacity of Specimen Q-2 is the largest among four wall specimens, and the maximum bearing capacity of Specimen Q-5 was similar to that of Specimen Q-7, showing that effect of the precast concrete tie beam is better than that of tie bars in terms of maximum bearing capacity.

4.4. Stiffness Degeneration. Stiffness degradation is one of the most important criteria for evaluating the performance of test walls, when subjected to simulated lateral earthquake loading in successive low-rate reversed cycles. The stiffness at different cycles was determined using (2). This calculation

only involves the first reversal cycle. The comparison of stiffness degradation for all specimens is shown in Figure 11.

$$K_i = \frac{\left|+P_i\right| + \left|-P_i\right|}{\left|+\Delta_i\right| + \left|-\Delta_i\right|}. \tag{2}$$

The initial stiffness of the confined walls (Q-2, Q-5, and Q-7) is close to that of the control specimen, Q-1, which is attributed to low lateral stiffness of the frame (K-1). The secant stiffness of Specimen Q-1 is only approximately 40% of the other three walls at a drift ratio of 0.8%. The walls confined by precast concrete tie columns had a lower rate of stiffness degradation compared to Specimen Q-1, attributed to the restriction from precast concrete tie columns and precast concrete tie beam (wire ties).

4.5. The Influence of Tie Column and Tie Beam (Wire Ties). Figure 12 shows a comparison of bearing capacity of

five specimens at different drifts. "Q-1 + K-1" denotes the summation of the bearing capacity of Specimens K-1 and Q-1 at the specific drift. Because the test of specimen Q-1 was terminated at a drift ratio of 0.8%, it is assumed that the subsequent bearing capacity remains constant.

Referring to Figure 12, it can be seen that there is little difference between the bearing capacity of Specimens Q-2, Q-5, and "Q-1 + K-1" when the drift is not beyond 0.3%, which shows that the action of two precast concrete tie columns and one precast concrete tie beam (wire tie) is weak. The bearing capacity of Specimen Q-7 is bigger than that of "Q-1 + K-1," and this could be due to the fact that there are three wire ties; therefore, the combined action of two precast concrete tie columns and three wire ties is stronger than that of one wire ties. On the whole, the effect of precast concrete tie columns and precast concrete tie beam (wire ties) on the bearing capacity is not obvious at the initial stage of loading. When the story drift is beyond 0.3%, the effect of precast concrete tie columns and precast concrete tie beam (wire ties) on the bearing capacity is more and more obvious as the story drift increases.

5. Conclusions

Four rammed earth walls were tested under lateral cyclic loading, and the seismic performance were discussed in terms of bearing capacity, stiffness degradation, and displacement ductility, and so on. Based on the results of this investigation, the following conclusions could be drawn:

(1) A majority of cracks were observed in the middle section of the wall attributed to the low shear strength in layers. Hence, it is necessary to consider the possibility of split-level construction and pin keys to improve the shear strength.

(2) The proposed construction measures are effective on significantly improving the performance of bearing capacity and deformability.

(3) The effect of precast concrete tie columns and precast concrete tie beam (wire ties) on the bearing capacity is not obvious at the initial stage of loading; however, when the story drift is beyond 0.3%, the effect is significant.

(4) In general, the application of wire ties instead of a tie beam is practical and effective, and the number of wire ties has an effect on the seismic performance of the RE walls.

Conflicts of Interest

The authors declare that there are no conflicts of interest regarding the publication of this paper.

Acknowledgments

References

[1] R. Kumar, S. Sachdeva, and S. C. Kaushik, "Dynamic earth-contact building: a sustainable low-energy technology," *Building and Environment*, vol. 42, no. 6, pp. 2450–2460, 2007.

[2] M. I. Gomes, M. Lopes, and J. D. Brito, "Seismic resistance of earth construction in Portugal," *Engineering Structures*, vol. 33, no. 3, pp. 932–941, 2011.

[3] H. Binici, O. Aksogan, and T. Shah, "Investigation of fiber reinforced mud brick as a building material," *Construction and Building Materials*, vol. 19, no. 4, pp. 313–318, 2005.

[4] A. P. da Silva Milani and L. C. Labaki, "Physical, mechanical, and thermal performance of cement-stabilized rammed earth–rice husk ash walls," *Journal of Materials in Civil Engineering*, vol. 24, no. 6, pp. 775–782, 2012.

[5] B. V. Venkatarama Reddy and P. Prasanna Kumar, "Structural behavior of story-high cement-stabilized rammed-earth walls under compression," *Journal of Materials in Civil Engineering*, vol. 23, no. 3, pp. 240–247, 2011.

[6] H. Niroumand, M. F. M. Zain, and M. Jamil, "The role of nanotechnology in rammed earth walls and earth buildings," *Procedia—Social and Behavioral Sciences*, vol. 89, pp. 243–247, 2013.

[7] B. V. Venkatarama Reddy and P. Prasanna Kumar, "Cement stabilised rammed earth. Part B: compressive strength and stress-strain characteristics," *Materials and Structures*, vol. 44, no. 3, pp. 695–707, 2011.

[8] J. S. J. Cheah, P. Walker, A. Heath, and T. K. K. B. Morgan, "Evaluating shear test methods for stabilised rammed earth," *Proceedings of the Institution of Civil Engineers-Construction Materials*, vol. 165, no. 6, pp. 325–334, 2012.

[9] M. Bouhicha, F. Aouissi, and S. Kenai, "Performance of composite soil reinforced with barley straw," *Cement and Concrete Composites*, vol. 27, no. 5, pp. 617–621, 2005.

[10] Q.-B. Bui, J.-C. Morel, S. Hans, and P. Walker, "Effect of moisture content on the mechanical characteristics of rammed earth," *Construction and Building Materials*, vol. 54, no. 15, pp. 163–169, 2014.

[11] Y.-H. Bu, Y.-H. Wang, G. Han, and L. Li, "Experimental study on seismic behavior of raw-soil structure with rammed earth walls by different construction methods," *Journal of Chang'an University*, vol. 31, no. 6, pp. 72–76, 2011.

Research Article

Fatigue Performance of SFPSC under Hot-Wet Environments and Cyclic Bending Loads

Shanshan Luo [ID],[1] **Peiyan Huang** [ID],[1,2] **Xinyan Guo** [ID],[1] and **Xiaohong Zheng** [ID][1]

[1]*School of Civil Engineering and Transportation, South China University of Technology, Guangzhou 510640, China*
[2]*State Key Laboratory of Subtropical Building Science, South China University of Technology, Guangzhou 510640, China*

Correspondence should be addressed to Peiyan Huang; pyhuang@scut.edu.cn

A new structural material named "steel fiber polymer structural concrete (SFPSC)" with features of both high strength and high toughness was developed by this research group and applied to the bridge superstructures in the hot-wet environments. In order to investigate the fatigue performance and durability of SFPSC under hot-wet environments, the environment and fatigue load uncoupling method and the coupling action of environment and fatigue load were used or developed. Three-point bending fatigue experiments with uncoupling action of environments and cyclic loads were carried out for SFPSC specimens which were pretreated under hot-wet environments, and the experiments with the coupling action of environments and cyclic loads for SFPSC specimens were carried out under hot-wet environments. Then, the effects of hot-wet environments and the experimental methods on the fatigue mechanism of SFPSC material were discussed, and the environmental fatigue equations of SFPSC material under coupling and uncoupling action of hot-wet environments and cyclic bending loads were established. The research results show that the fatigue limits of SFPSC under the coupling action of the environments and cyclic loads were lower about 15%. The proposed fatigue equations could be used to estimate the fatigue lives and fatigue limits of SFPSC material.

1. Introduction

The durability of bridge structures in service has been a frontier research topic in civil engineering field. As a significant part of the durability issues, the study on environmental fatigue performance of structural materials often has decisive significance for assuring the safety and durability of the bridge structures. With the increase of the span of concrete bridge, the common high-strength concrete materials could no longer satisfy the comprehensive requirements of load-bearing capacity, anticracking, antideformation, and durability [1–3], and there is an urgent need to develop a new material with features of high strength and high ductility.

Steel fiber reinforced concrete (SFRC) was a compound with high strength and high ductility developed in the 20th century. After modifications and developments in many decades, SFRC had been gradually applied in the various kinds of building structures [4–6]. In the transportation field, SFRC was used mostly for constructions such as the road pavements, bridge deck pavements, and airport runway pavements. However, in many cases, it had been discovered during the observations of damaged sections of the SFRC specimens that the steel fibers in the damaged sections were broken by being "pulled out" and very few by being "broken." This was due to insufficient cohesive force between the matrixes of the steel fibers and concrete and thus resulted in the low stress levels of the steel fibers during the damage of the specimens, and their tensile properties had not been fully realized. In order to further increase the bonding strength of the steel fiber and concrete and give full play to the good mechanical properties of the steel fibers, Luo et al. [7] of this

research group added polymer latex into SFRC and developed the "steel fiber reinforced polymer concrete (SFRPC)." The experimental results showed that the new material had more superior antitensile, antibending, antifatigue, and antiimpact properties [8–10]. SFRPC belongs to medium to low strength modified concrete. Although it had been successfully applied in the construction of highway road pavements and bridge deck pavements [11], due to its insufficient strength, it was still unable to be used for main load-bearing members such as the bridge superstructures. Therefore, this research group conducted secondary development on SFRPC and developed a new high-strength concrete composite material named "steel fiber polymer structural concrete (SFPSC)." After the experiments of systematic mechanical properties and the optimum designs of the structures [12–15], SFPSC was successfully applied in the main girders (box girders) of three large-span concrete continuous rigid frame bridges on two highways in Guangdong Province, China [16, 17].

Regardless of SFRC, SFRPC, or SFPSC, there had been scarce reports about the research results of the environmental fatigue performance/durability of the concrete composite materials containing steel fibers. With regards to the bridge structures servicing in subtropical areas such as Guangdong Province, China, it is necessary to investigate its antifatigue performance/durability under hot-wet environments. Therefore, considering the actual weather conditions in the subtropical areas, the experimental studies on fatigue performance of SFPSC applied in bridges under different temperatures were carried out by this research group [14, 15], and a thermal fatigue equation for SFPSC was proposed. However, the effect of the humidity was not taken into the consideration.

In addition, for the bridge superstructures servicing in a hot-wet environment, the environment and vehicle loads are interacted, and thus their working conditions are different from the traditional environment and load uncoupling experiments. The differences in the environmental fatigue performance/durability of materials and components under uncoupling and coupling action are a scientific problem that needs to be proved but has not been proved. Therefore, in this paper, the superstructures of SFPSC bridges servicing in subtropical areas were taken as the research objects, and the environmental fatigue experimental researches and theoretical analyses were carried out based on the hot-wet environments and cyclic loads coupling and uncoupling (traditional) experimental methods, and the environmental fatigue performance/durability of SFPSC under different hot-wet conditions was discussed.

2. Fatigue Experiments under Hot-Wet Environments

In order to study the environmental fatigue performance/durability of SFPSC material under coupling and uncoupling action of hot-wet environments and cyclic loads and to prove the mechanism of the effect brought by hot-wet environments on the fatigue performance of SFPSC, in this research, three types of fatigue experiments were designed:
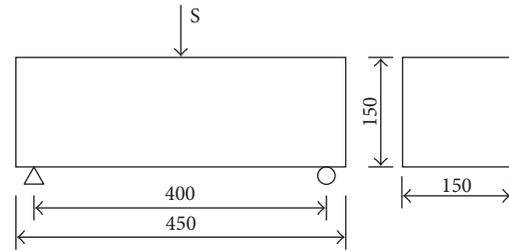
FIGURE 1: Three-point bending SFPSC beam for fatigue test (unit: mm).

(1) Fatigue experiments under room temperature and atmospheric environment. (2) Fatigue experiments under uncoupling action of hot-wet environments and cyclic loads. This is the traditional method for environmental fatigue tests. SFPSC specimens were pretreated in the hot-wet environments, and then the specimens were transferred to the test machine to carry out the fatigue experiments under room temperature and atmospheric environment. (3) Fatigue experiments under coupling action of hot-wet environments and cyclic loads. The experiments were carried out by the special testing device, and the specimens were treated by the hot-wet environments while the cyclic loads were applied.

2.1. Experimental Materials and Specimens. The specimens used for fatigue experiments were all the same and were three-point bending beams as shown in Figure 1. The specimen materials were based on the design requirements of a long-span bridge girder (box girder) of a highway in Guangdong Province and were designed for 2 types of materials: C55 concrete and SFPSC. The size of a specimen was length 450 mm × width 150 mm × height 150 mm, and the span length was $L = 400$ mm. There were total of 66 specimens produced, including five C55 concrete specimens and 61 SFPSC specimens. The usages of all specimens were as follows: five C55 concrete and five SFPSC specimens were used to test the static mechanical properties of the two types of materials. The remaining 56 SFPSC specimens were used in fatigue experiments, including 10 specimens used for the room temperature and atmospheric environmental tests (controlling experiments), 20 specimens used for the experiments under uncoupling action of hot-wet environments and cyclic loads, and 26 specimens used for the experiments under coupling action of hot-wet environments and cyclic loads.

Based on the design requirements of the superstructures (box girders) of the above bridges, the compressive strength of SFPSC should be slightly higher than that of C55 concrete. Therefore, the C55 concrete used in the experiments was designed with the standard mix ratio. The designs of the mix ratios of SFPSC should be based on the strength requirements of the structures (close to the static mechanical properties of C55 concrete); then, consider the quantity of the steel fiber to be added, the water/cement ratio, sand rate, water consumption of unit volumes, the amount of gel materials, and so on. Considerations should also be given to

TABLE 1: Static mechanical properties of SFPSC and C55 concrete.

Materials	Steel fiber (v%)	Polymer latex (wt.%)	Static mechanical properties		
			Compressive strength (MPa)	Flexural strength (MPa)	Ultimate bearing capacity (P_u/kN)
C55	0	0	69.0	5.36	36.0
SFPSC	0.580	1.30	70.1	8.68	40.4

the construction of the composite materials, such as liquidity (slump) and economy. Finally, the mix ratio of SFPSC was confirmed to be based on the standard mixture ratio, which was determined as "w(cement) : w(sand) : w(gravel) : w (water) : w(water reducer) = 1 : 1.493 : 2.432 : 0.321 : 0.012," and steel fiber of concrete volume rate of 0.58 v% and polymer latex of cement weight of 1.3 wt.% were mixed.

The details of experimental materials used were as follows: the cement was Huizhou Ta brand P.II42.5R cement; the sand was Dongjiang River natural washed-out sand, with a modulus of fineness of 2.68; the stone was 5~25 mm granite gravels; the steel fiber was the end-hook RS06073/35-800 indentation steel fiber manufactured by Shanghai Zhenjiang Fiber Co., Ltd., with the specification of $0.3 \times 1 \times 30$ mm, the length/diameter ratio of 48, and the tensile strength of 800 MPa; for the polymer latex, the VINNAPAS RE5010N cement modified special styrene butadiene latex produced by German Wacker Co., Ltd., which was kind of vinyl acetate/ethylene copolymerized emulsion powder that can be redispersed when it comes into contact with water; and the water reducer was JB-ZSC polycarboxylate concrete admixtures.

The experimental results (average) of 28 d static mechanical properties of SFPSC and C55 concrete which were designed using the above mix ratios are shown in Table 1.

2.2. Environmental Fatigue Experimental Methods.

There were three types of fatigue experiments with different environment. Fatigue experiments for group A specimens (controlling experiments) were carried out under room temperature and the atmospheric environment. In this type of the experiments, the experimental environment was recorded by measuring the temperature and humidity in the lab room during the experimental period and taking the average value (23°C and 78% RH). The methods of environmental treatment and the required devices were different for the fatigue experiments with uncoupling and coupling of hot-wet environments and cyclic loads. The two environmental treatment methods and the loading methods of all fatigue experiments were described as follows.

2.2.1. Environmental Pretreatment for Uncoupling Fatigue Experiments.

For the environmental fatigue experiments, the determination of the hot-wet environments were based on the actually measured working temperature and humidity of servicing bridges in Guangdong region, China, and its higher value (severe environment) was taken. Therefore, the experimental environments were divided into 3 groups

B~D for the fatigue experiments under uncoupling action of the hot-wet environments and the cyclic loads. Among them, the experimental temperature and humidity for 7 specimens in group B was (50°C and 80% RH), for 6 specimens in group C was (50°C and 90% RH), and for 7 specimens in group D was (50°C and 95% RH).

Regarding the specimens of groups B~D, the environment pretreatment methods were conducted with reference to the relevant stipulations of Chinese national technical standard GB/T 2573-2008 "Test method for aging properties of glass fiber reinforced plastics" [18]. Firstly, the specimens were placed in temperature and humidity test chamber (Type Number Q8-901) and pretreated with constant temperature and humidity for 6 days (144 hours), and then the specimens were removed from the environmental box to be air-cooled for 2 days to ensure the dryness of the specimens. Finally, the fatigue experiments were carried out under room temperature and atmospheric environment.

2.2.2. Hot-Wet Environments for Coupling Fatigue Experiments.

Regarding the fatigue experiments of coupling action of hot-wet environments and cyclic loads, the hot-wet environments used were the same with the above uncoupling fatigue experiments and were also divided into three groups. Among them, the temperature and humidity for 9 specimens in group E were 50°C and 80% RH, for 12 specimens in group F were 50°C and 95% RH, and for 5 specimens in group G were 35°C and 95% RH.

Regarding specimens in group E~G, the environmental treatments were completed by using the intelligent environment simulation and the controlling system, which was designed with the MTS810 material testing system by this research group (Figure 2) [19]. In order to ensure that the internal and external hot-wet conditions of the specimens were consistent at the beginning of loading action, the specimens of group E, F, and G were placed in the working box of the environment simulation and the controlling system in advance. Before the loading began, the environment simulation and controlling system was turned on for 4 hours to conduct pretreatment in hot-wet environment to reduce the influence of fatigue life by the difference of internal and external temperature and humidity of SFPSC specimen.

2.2.3. Fatigue Loading Method

(1) Loading way: the loading ways were the same for all fatigue experiments. Three-point bending loading

FIGURE 2: Intelligent environment simulation and controlling system.

way, stress controlling method, and sinusoid wave were applied; the stress ratio was $R = 0.1$. However, the loading frequencies were different in various experimental methods. Among them, the loading frequency for room temperature and atmospheric condition and for the uncoupling action of hot-wet environments and cyclic loads was fixed at 10 Hz. For the fatigue experiments with coupling action of hot-wet environments and cyclic loads, the loading frequency was reduced to 2 Hz for better coupling action of the environments and loads.

Based on the design specifications of the common concrete structures [19], if the number of loading cycles N reached 2×10^6 times, and the specimen remained unfailed, the fatigue experiment would be stopped. In other words, if the specimen still remained unfailed after 2×10^6 times of loading cycles, then it would be assumed that the specimen could endure infinite times of cyclic loads, and thus the fatigue life would be assumed to be infinite.

(2) Loading (stress) level: in order to obtain the complete fatigue curve ($S\sim N$ curve), the loading (stress) levels S_R of group A specimens were divided into three grades ($S_R = P_{max}/P_u = 0.70, 0.75,$ and 0.80). Among them, P_{max} was the maximum cyclic load, and P_u was the ultimate bearing capacity of SFPSC specimens (Table 2).

For the specimens of uncoupling action of environments and loads, the loading (stress) level S_R was set to 3 levels. Among them, group B was $S_R = 0.65, 0.70,$ and 0.75, group C was $S_R = 0.60, 0.65,$ and 0.75, and group D was $S_R = 0.60, 0.64,$ and 0.68.

For the specimens of coupling action of environments and loads, the loading (stress) level S_R was set to 4 levels. Among them, group E was $S_R = 0.6, 0.65, 0.70,$ and 0.75, group F was $S_R = 0.60, 0.67, 0.72,$ and 0.77, and group G was $S_R = 0.60, 0.70, 0.72,$ and 0.75.

The experimental conditions of group A~D specimens are shown in Table 2, and the experimental conditions of group E~G group specimens are shown in Table 3.

2.2.4. Data Acquisition and Recording. In the fatigue experiments, environmental data such as temperature and humidity were collected and recorded by the intelligent environment simulation and controlling system and are shown in Figure 2. The maximum and minimum loads, the deflections of the specimens (displacements), loading cycle number N, and other experimental data were automatically collected and recorded by the MTS810 testing system, and 8 sets of data were recorded for each loading cycle. The strain data of concrete were automatically measured and recorded by the Wavebook 516E dynamic strain device with 4 strain gages attached in the middle and bottom of the center and the lower edges of the sides of the specimen, and the sampling frequency was 100 Hz.

3. Fatigue Performance under Hot-Wet Environments

3.1. Experimental S~N Curves

3.1.1. Experimental S~N Curves under Uncoupling Action. According to the experimental conditions and the experimental methods described in Section 2, the fatigue experiments were carried out under the uncoupling action of hot-wet environments and cyclic loads for SFPSC specimens of group B~D. The controlling experiments were also carried out for group A specimens under room temperature and atmospheric environment. The experimental results of group A~D specimens are shown in Table 2. Based on the fatigue test data, the fatigue experimental curves ($S_R\sim N$ curves) represented by the loading level (stress level) S_R were obtained, as shown in Figure 3.

By using the least square method, the experimental data of the specimens of each group were fitted, respectively, and the equations of $S\sim N$ curves could be determined from the logarithmic coordinates:

$$S_R = A_i + B_i \lg(N) \quad (i = 1, 2, 3, 4), \tag{1}$$

where $S_R = P_{max}/P_u$; i indicates the group number of the specimens, and $i = 1\sim4$, respectively, represents group A~D;

TABLE 2: Experimental conditions and results of group A~D specimens.

Specimen number	Temperature, T (°C)	Relative humidity, H (%RH)	Stress level, $S_R = P_{\max}/P_u$	Loading frequency, f (Hz)	Fatigue lives, N_f/cycles
A1					>2000000
A2			0.70		>2000000
A3					825899
A4					293301
A5	23	78	0.75	10	328359
A6					349997
A7					>2000000
A8					24099
A9			0.80		35677
A10					36071
B1			0.65		>2000000
B2					1800031
B3					63470
B4	50	80	0.70	10	207900
B5					157413
B6			0.75		92486
B7					50936
C1			0.60		>2000000
C2					1784833
C3	50	90	0.65	10	166591
C4					186596
C5			0.75		7940
C6					1960
D1			0.60		>2000000
D2					>2000000
D3			0.64		22236
D4	50	95		10	62746
D5					21355
D6			0.68		3647
D7					15173

and A_i and B_i were constant coefficients, and their values are shown in Table 4.

As shown in Figure 3, the fatigue performance of SFPSC was affected significantly by the pretreatment under hot-wet environments. In contrast to the specimens under room temperature and atmospheric environment (group A), the fatigue lives of all SFPSC specimens (group B~D) which were pretreated with hot-wet environments have been remarkably decreased. Furthermore, the more severe the hot-wet environment (the higher the temperature and humidity), the less the fatigue life was shown, that is, under the same stress level, the shorter the fatigue lives of the specimens. However, for the specimens of group C (50°C and 90% RH) and group D (50°C and 95% RH), the differences of the experimental S_R~N curves were small. The reason could be that in hot-wet environments, the fatigue performance of SFPSC specimens was mainly influenced by high temperature (50°C), and the relative humidity above 90% RH could cause the saturation of the moisture absorption ability of SFPSC specimens.

3.1.2. Experimental S~N Curves under Coupling Action. According to the experimental conditions and experimental methods described in Section 2, the fatigue experiments were carried out under coupling action of hot-wet environment and cyclic loads for group E~G SFPSC specimens, and the results are shown in Table 3. Based on the fatigue test data of each group, the fatigue experimental curves (S_R~N curves) represented by the loading level (stress level) S_R were obtained, as shown in Figure 4. For the convenience of comparison, the experimental results of SFPSC specimens under room temperature and atmospheric environment (group A) were also shown in the same figure.

Using (1) and paying attention to $i = 1, 2, 3$, and using the least square method, the experimental data of the specimens of each group E~G were fitted respectively. The coefficients A_i and B_i of each S_R~N equation could be determined, and their values are shown in Table 5.

With regard to the fatigue performance of SFPSC material under coupling action of hot-wet environments

TABLE 3: Experimental conditions and results of group E~G specimens.

Specimen number	Temperature, T (°C)	Relative humidity, H (%RH)	Stress level, $S_R = P_{max}/P_u$	Loading frequency, f (Hz)	Fatigue lives, N_f/cycles
E1					1678342
E2			0.60	2	1048011
E3					410854
E4					470951
E5	50	80	0.65	2	338499
E6					336204
E7			0.70	2	249136
E8			0.75	2	3082
E9					1733
F1			0.60	2	>2000000
F2					>2000000
F3					3106
F4			0.67	2	13237
F5					18525
F6	50	95			50766
F7					4266
F8			0.72	2	15037
F9					16241
F10					223
F11			0.77	2	906
F12					151
G1			0.60		>2000000
G2			0.70		>2000000
G3	35	95	0.72	2	39535
G4					27171
G5			0.75		1549
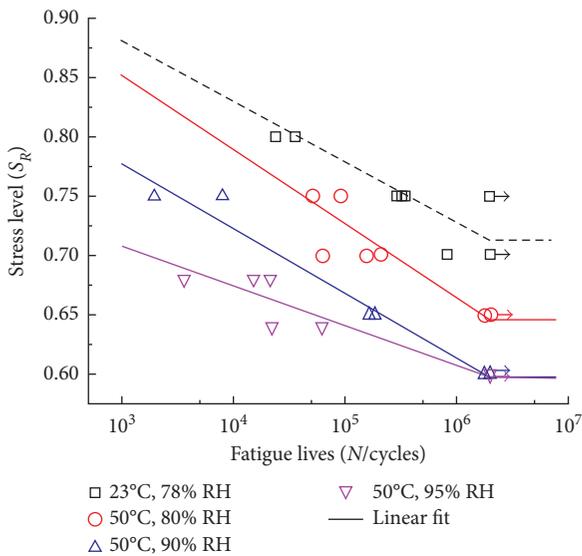
FIGURE 3: Experimental S_R~N curves under uncoupling of hot-wet environments and cyclic loads.

TABLE 4: Coefficients A_i and B_i for group A~D specimens.

Coefficients	i (group)			
	1 (group A)	2 (group B)	3 (group C)	4 (group D)
A_i	1.03	1.04	0.940	0.808
B_i	−0.0510	−0.0621	−0.0544	−0.0336

action also had shorter fatigue lives than those under room temperature and atmospheric environment (group A). Moreover, the higher the temperature and humidity, the shorter the fatigue life of SFPSC under the same stress level. In the same high humidity environment (95% RH), the fatigue life of SFPSC decreased significantly as the temperature increased. In the same high temperature (50°C) environment, the higher the humidity was, the shorter the fatigue life of SFPSC observed. However, with the increase of environmental treatment time, the decrease of fatigue lives of specimens became gradual. When the fatigue life of specimen approached to its fatigue limit, humidity had less influence on fatigue performance of SFPSC.

It is shown in Figure 4 that the influence of temperature on fatigue lives of SFPSC specimens was dominant, and the influence of humidity was secondary.

and cyclic loads, as shown in Figure 4, the experimental results were similar to that under the uncoupling action, and the specimens of each groups under the coupling
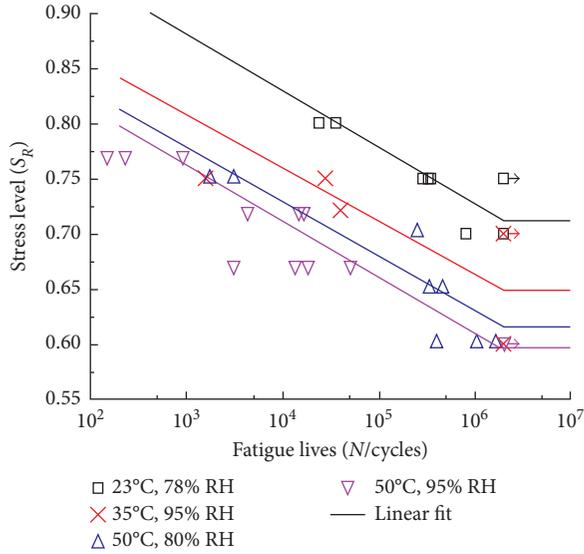
Figure 4: Experimental S_R~N curves under coupling of hot-wet environments and cyclic loads.

Table 5: Coefficients A_i and B_i for group E~G specimens.

Coefficients	i (group)		
	1 (group E)	2 (group F)	3 (group G)
A_i	0.953	0.926	0.914
B_i	−0.0482	−0.0492	−0.0508

3.2. Analysis of Failure Mechanism of SFPSC in Hot-Wet Environments. As shown in the previous sections regarding S_R~N curves, fatigue experiment results of SFPSC specimens under both the coupling/uncoupling action of hot-wet environments and cyclic loads showed that the environmental fatigue lives of the specimens were shorter than those in room temperature and atmospheric environment. Furthermore, the more severe the environments were and the higher the temperature and humidity were, the shorter the fatigue life of SFPSC was, under the same stress level. The fatigue failure mechanism of SFPSC in hot-wet environments could be analyzed as follows:

(1) The influences of the temperature and humidity on the interfaces between steel fibers and concrete matrixes. When the hot-wet environment was severe, especially when there was a big difference between the environmental humidity and the internal humidity of the concrete, the transmission of water from the surfaces to internal through the concrete pores would be intensified. Consequently, a higher surface tensile force would be generated on the liquid surfaces of the internal pores of the concrete, and such surface tensile force would intensify the crack growth within the concrete and lead to decrease of the cohesive force of the interfaces between the steel fibers and the concrete matrixes.

(2) The influences of humidity on structural compactness of SFPSC. Figure 5(a) shows that there are a lot

of needle-like crystals of calcium vanadium stone and flocculation of C-S-H gel in the hydration products of the concrete without polymer latex, which have many pores with very little connections. The combination of the hydration products was relatively loose with some large hole in the combination. Some crossed microcrack can be observed on the surface of the slurry. After mixing of the polymer latex, as shown in Figure 5(b), the gaps or the cavities of the cement hydration products would be filled up or joined by the membranous substances formed by the polymer latex, which made the hydration products in the concrete more compact, caused reduction of the microcracks, and improved the cracking resistance of the material [20]. In addition, the concrete would show the characteristics of dry shrinkage and wet expansion; the higher the strength of the concrete, the more obvious such phenomenon is. Therefore, during the pretreatment process in the hot-wet environment, when the humidity was high, the gaps and cavities in the concrete, which was originally filled by the latex membrane substance, would expand due to wet expansion, resulting in the decrease of the structural compactness, and the fatigue performance became poor. Moreover, the concrete strength used in this research was higher (C55), and such phenomenon was more obvious.

(3) The influences of temperature on the mechanical properties of polymer latex. The reactions on the mechanical properties of the polymer to temperature were rather sensitive. It was showed by existing research [14] that polymer latex would be softened as the temperature increased, and when the temperature reached to a certain value, the supporting capacities of the polymer would be lost, and thus caused greater influences on the mechanical properties of the polymer concrete.

3.3. Influence of Experimental Methods on Fatigue Performance. To study the influence of environmental fatigue test methods on the fatigue performance of SFPSC material, the fatigue experimental data of group B and E (50°C and 80% RH), as well as group C and F (50°C and 95% RH) in Tables 2 and 3 were taken and are shown in Figures 6(a) and 6(b), respectively. Figure 6(a) shows that under lower relatively humidity (80% RH), compared to the experimental method of uncoupling action of environment and loads, the fatigue lives of SFPSC would be lower for the experimental data under coupling action of the hot-wet environment and the cyclic loads, as long as they were under the same loading level regardless of high or low loading level. The whole S_R~N curve under coupling action would be below the former.

Under the same temperature (50°C), when the relative humidity was higher (95% RH), the influence rules of environmental fatigue experimental method of SFPSC to fatigue life would be changed. In such hot-wet environment,

(a)   (b)
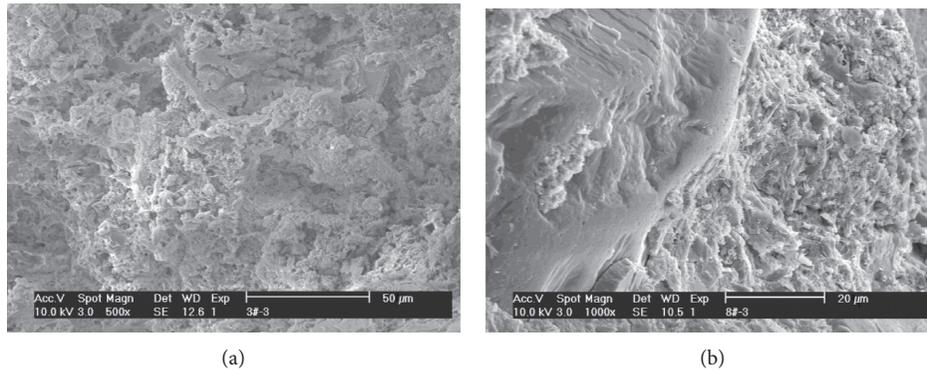
FIGURE 5: Effect of the polymer latex on the hydraulic products (SEM photos). (a) Specimens without polymer latex. (b) Specimens with polymer latex.

(a)   (b)
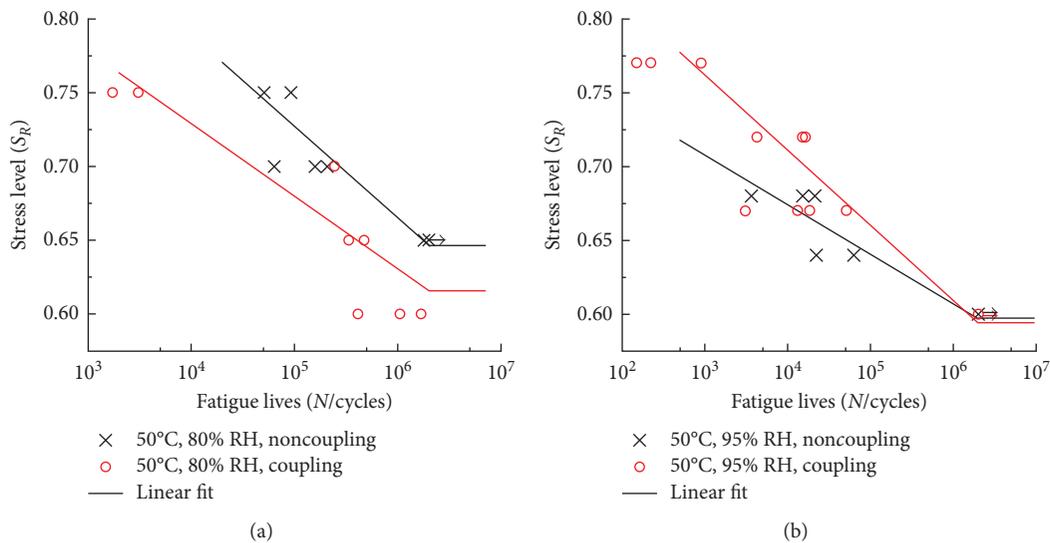
FIGURE 6: Influence of the experimental method on $S_R \sim N$ curves. (a) 50°C and 80% RH. (b) 50°C and 95% RH.

when the loading level was high, the fatigue lives under the uncoupling action were lower. When the loading level was low and especially close to the fatigue limit of the material, the fatigue lives of SFPSC under coupling action were lower.

For the analysis of the experimental results shown in Figure 6, the effect mechanism of environmental fatigue test methods on the fatigue performance of SFPSC could be considered as follows:

(i) The temperature and humidity set in these environmental fatigue experiments were higher than that in room temperature and atmospheric environment as shown in Tables 2 and 3. For the case of uncoupling action of hot-wet environments and loads, the specimens were pretreated in the environmental box and placed in room temperature and atmospheric environment to dry. Then, the fatigue experiments were carried out. During air cooling and drying, the moisture originally absorbed by concrete material of the specimens in the hot-wet

environments (environmental box) gradually vaporized, causing the gaps produced under hot-wet environments to reduce or vanish as the temperature and humidity decreased. The fatigue performance would be partially recovered.

(ii) Previous studies [20] showed that, under the conditions of coupling action of hot-wet environments and loads, the deformation of the specimens caused acceleration of moisture and heat transmission rate into the interior of concrete material and led to a decrease in fatigue performance.

Based on the analysis of (i) and (ii), under common hot-wet environments, the experimental condition was more severe under coupling action compared to uncoupling action, and it would lead to a decrease in fatigue lives, as shown in Figure 6(a).

(iii) For high temperature and high humidity environment (50°C and 95% RH), when the traditional

experimental method with uncoupling action of environment and loads was used, as described in (i), the fatigue performance of the specimens would be partially recovered if the specimens were placed in room temperature and atmospheric environment to be dried after the hot-wet pretreatment. The comparison to fatigue performance of the specimens under coupling action of environment and loads could be divided into the following two parts:

Firstly, when the experimental period was short (high loading level and low fatigue lives), high temperature and high humidity would not be able to have sufficient time to cause erosion of the specimens. Therefore, the fatigue lives of specimens were longer under coupling action during this interval.

Secondly, when the experimental time was long enough (low loading level especially close to the fatigue limit and long fatigue lives of the specimens), high temperature and high humidity would have sufficient time to cause erosion of the specimens. Due to the reason described in (ii), the fatigue lives of SFPSC specimens would be shorter than the specimens under uncoupling action of hot-wet environment and loads during this interval.

4. Environmental Fatigue Equations of SFPSC

4.1. Environmental Fatigue Equations. In the components of SFPSC, polymer latex has a consolidation action on the concrete gel and a bonding action on steel fiber. The adhesion and fixation of the steel fiber and the concrete gel were caused by the adhesion and mechanical friction of their contact interface. When SFPSC was cracked due to external loading, the steel fibers dispersed in the damaged section would be pulled out by the two ends of the concrete. However, this adhesion force would form resistance to the cracking and significantly disperse the tensile stress that was originally concentrated. Meanwhile, it would also continuously absorb the fracture energy and cause a dramatic improvement of the anticracking property of SFPSC. When the polymer latex and steel fiber in SFPSC came into contact, the surface of steel fiber would adhere to the hydrophilic base of the surfactant. As the cement hydration effect increased, water was consumed and a large amount of heat was released, and a chemical adhesion of the surface of hydrophilic base and steel fibers could be caused. Furthermore, as the temperature increased and water decreased, the adhesion effect would also increase.

When studying the effect mechanism of serving environmental temperature to the fatigue performance of SFPSC material, this research group [14, 15] considered the influence of temperature would be mainly presented in (1) thermal stress caused by different thermal expansion coefficient of each phase in the composites, (2) influence of temperature on polymer latex performance, (3) the influence of the change in polymer latex properties on the mechanical properties of the interface between steel fiber and the base matrix, and so on.

For the influence of serving environmental humidity to the mechanical properties of SFPSC, this research suggested

that (1) the high humidity environment would weaken the adhesion action of polymer latex and steel fibers and reduce the strength; (2) in high humidity environments, moisture absorption stress would be generated in the concrete, and the destruction would be accelerated, and (3) high humidity could accelerate the speed of corrosion reaction for steel fibers, leading to a decrease of its mechanical properties.

For SFPSC materials serving in the hot-wet environment, the effects of temperature and humidity on fatigue performance mentioned above should be taken into consideration. Therefore, when establishing the environmental fatigue equation of SFPSC in this paper, the previous studies by this research group on the thermal fatigue equation [21] and hot-wet fatigue equation [20] for reinforced concrete (RC) beams strengthened with carbon fiber reinforced polymer (CFRP) were used as references. It suggested that for experimental methods of both coupling and uncoupling action of hot-wet environments and cyclic loads, fatigue life $f(N)$ of SFPSC in hot-wet environments under bending loads could be presented by the following formula:

$$f(N) = \frac{[S_R + C_1 + C_2 f(T, H)]}{[C_3 + C_4 f(T, H)]}, \tag{2}$$

where S_R was the loading level (also known as the stress level, $S_R = P_{max}/P_u$) and $f(T, H)$ was the hot-wet function.

Based on the analysis of the influence mechanism of temperature and humidity on the fatigue performance of SFPSC materials and the mathematical description of the hot-wet function generated by this research group, the expression of $f(T, H)$ in this paper was taken as follows:

$$f(T, H) = C_5 e^{C_7 T} + C_6 e^{C_8 H}. \tag{3}$$

In (2) and (3), $C_1 \sim C_8$ were constant coefficients, determined by experiments.

For (2), the fatigue life function $f(N)$ could be described in single logarithmic coordinates, considering the fatigue curves (S~N curves) of the material. The expression of $f(N)$ was as follows:

$$f(N) = \lg N. \tag{4}$$

The fatigue equation of SFPSC under hot-wet environments, which was also called the hot-wet fatigue equation, was generated by ((2)~(4)).

By using these equations, the bending fatigue lives and fatigue limits of the SFPSC specimens under coupling and uncoupling action of the hot-wet environments and loads could be conveniently and accurately estimated.

4.2. Environmental Fatigue Equation under Uncoupling Action. Using the experimental data of group B~D specimens shown in Table 2 and the least squares method, the data were fitted in ((2)~(4)), and the coefficients $C_1 \sim C_8$ could be determined. Then, the expression for fatigue lives of SFPSC materials under uncoupling action of the hot-wet environments and three-point bending cyclic loads presented by loading level S_R was determined. The environmental fatigue equation of SFPSC was as follows:

(a)   (b)
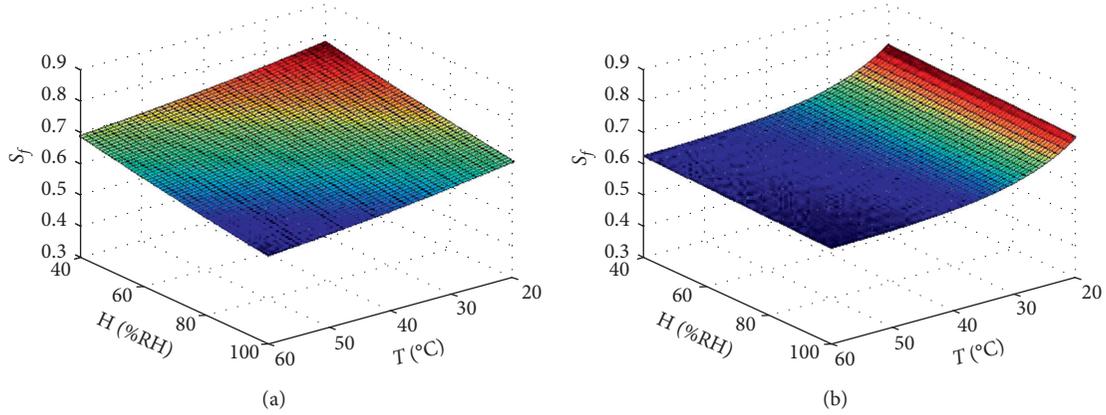
FIGURE 7: The influence of hot-wet environments on the relative fatigue limit S_f. (a) S_f under the uncoupling action. (b) S_f under the coupling action.

$$S_R = 0.343 + 0.238e^{-0.0174T} + 0.851e^{-0.619H}$$
$$- \left(0.0137 - 0.00219e^{-0.0174T} + 0.0657e^{-0.619H}\right)\lg(N), \tag{5}$$

where the unit of temperature T is presented in (°C) and humidity H is presented in (% RH).

By using (5), the fatigue lives of the SFPSC materials under uncoupling action of hot-wet environments and cyclic bending loads and the traditional environmental fatigue experimental method could be conveniently and accurately estimated.

4.3. Environmental Fatigue Equation under Coupling Action.

Similar to the analysis method shown in Section 4.2, the experimental data of group A, E, F, and G specimens and the least square method were used to fit in ((2)~(4)), and the coefficients of C_1~C_8 could be determined. Then, the expression for fatigue lives of SFPSC materials under coupling action of hot-wet environments and cyclic bending loads presented by loading level S_R was determined. The environmental fatigue equation of SFPSC was as follows:

$$S_R = 0.543 + 1.12e^{-0.0998T} + 0.412e^{-0.114H}$$
$$- \left(0.0294 + 0.0101e^{-0.0998T} + 0.0221e^{-0.114H}\right)\lg(N). \tag{6}$$

By using (6), the fatigue lives of the SFPSC materials under coupling action of hot-wet environments and cyclic bending loads could be conveniently and accurately estimated.

4.4. Fatigue Limits of SFPSC under Hot-Wet Environments.

For general concrete structures, the corresponding loading value of $N = 2 \times 10^6$ cycles could be defined as the fatigue limit (depending on the specifications, it can also be defined as $N = 4 \times 10^6$ cycles and 1×10^7 cycles). $N = 2 \times 10^6$ cycles was substituted into (5) and (6), and the relations of fatigue limits S_f of the bending SFPSC material under coupling and uncoupling action of the environments and cyclic loads

presented by S_R to the temperature T and humidity H could be obtained and the expressions were

$$S_f = 0.257 + 0.252e^{-0.0174T}$$
$$+ 0.437e^{-0.619H} \text{ (uncoupling action)}, \tag{7}$$

$$S_f = 0.358 + 1.06e^{-0.0998T} + 0.273e^{-0.114H} \text{ (coupling action)}. \tag{8}$$

Using (7) and (8), the change rules of the fatigue limits S_f of SFPSC material under different hot-wet environments and cyclic bending loads could be obtained and are shown in Figure 7. As shown in Figure 7, when the environmental temperature was increased, the relative fatigue limit S_f decreased; when the environment humidity was increased, the relative fatigue limit S_f would also be decreased. In addition, comparing Figures 7(a) and 7(b), it showed that regardless of coupling or uncoupling action of environments and loads, the rules of changes in relative fatigue limit S_f of SFPSC materials estimated by the environmental fatigue equations due to the shift in temperature T and humidity H remained congruity. However, in general, the relative fatigue limit of SFPSC material under coupling action of environments and loads was lower than that under uncoupling action. In addition, in contrast to room temperature and atmospheric environment, under the high temperature and high humidity (50°C and 95% RH) environment, the fatigue limit S_f of SFPSC would be reduced by about 15%. Therefore, the effects of the hot-wet environments on fatigue lives of SFPSC were very significant. Meanwhile, this also showed that, for the antifatigue/durability designs of the bridge structures using SFPSC material, the adverse effects of the hot-wet environments must be considered.

In order to verify the effectiveness and feasibility of (5) and (6), the experimental conditions of the hot-wet environments shown in Tables 2 and 3 were substituted into (7) and (8) separately, and the environmental fatigue limits of SFPSC under bending loads were obtained respectively, as shown in Table 6. According to Table 6, the actual experimental estimation of relative fatigue limits S_f of SFPSC

TABLE 6: Relative fatigue limits of SFPSC S_f in the hot-wet environments.

Testing method	Temperature, T (°C)	Relative humidity, H (%RH)	Relative fatigue limit S_f		Relative error (%)
			Calculated values by (7) or (8)	Experimental estimation by (1)	
Coupling action of environments and loads	23	78	0.715	0.709	0.846
	50	80	0.614	0.616	0.325
	50	95	0.611	0.594	2.86
	35	95	0.635	0.649	2.16
Uncoupling action of environments and loads	23	78	0.696	0.709	1.83
	50	80	0.629	0.649	3.08
	50	90	0.613	0.597	2.68
	50	95	0.605	0.596	1.51

obtained from two types of experimental methods well matched with the calculated values, and the average relative errors were presented as 2.28% (uncoupling action) and 1.55% (coupling action), respectively. This explained that using (5) and (6) to estimate the hot-wet environmental fatigue lives and fatigue limits of SFPSC material under coupling and uncoupling action of hot-wet environments and bending loads was effective and feasible in this research.

5. Conclusions

The experimental studies for environmental fatigue/durability of "steel fiber polymer structural concrete (SFPSC)" were conducted using the conventional uncoupling and coupling methods of hot-wet environments and cyclic bending loads. The experiments were carried out under three different hot-wet conditions (50°C and 80% RH, 50°C and 90% RH, and 50°C and 95% RH) for uncoupling action and three different hot-wet conditions (50°C and 80% RH, 50°C and 95% RH, and 35°C and 95% RH) for coupling action. The experimental results were discussed in comparison with the results obtained under room temperature and atmospheric environment (23°C and 78% RH), and conclusions were obtained as follows:

(1) The effects of hot-wet environments on the bending fatigue performance/durability of SFPSC were obvious. Within the range of testing conditions in this paper, when the environmental temperatures were the same, fatigue lives and fatigue limits of SFPSC material would decrease along with the increase of the humidity; when the humidity remained unchanged, the fatigue lives and fatigue limits would decrease along with the increase of the temperature. In comparison to the room temperature and atmospheric environment, the fatigue limit S_f would be reduced by about 15% under high temperature and high humidity (50°C and 95% RH) environment.

(2) Compared with the experimental results of traditional uncoupling environmental fatigue experiments, the fatigue lives and especially the fatigue limits of SFPSC were reduced under coupling action of hot-wet environments and cyclic loads. Therefore, in order to study the environmental

fatigue performance of the structures in service and under coupling action such as main load-bearing structures of bridges, it would be necessary to conduct the experiments under a condition close to the actual service environment, and testing method of coupling action should be used.

(3) Environmental fatigue life equations of SFPSC under the uncoupling/coupling action of hot-wet environments and cyclic bending loads (i.e., the hot-wet fatigue equations) were proposed based on the data of environmental fatigue experiments and in combination with the classical theories of fatigue strength. By using the fatigue equations, the fatigue lives and fatigue limits of the SFPSC materials in service under hot-wet environments could be conveniently and accurately estimated.

(4) This research results showed that the adverse effects of the hot-wet environments must be considered for designing of antifatigue/durability of the bridge structures of SFPSC in the subtropical areas in order to avoid safety hazards.

It is necessary to point out that the environmental fatigue equations proposed in this paper should be verified on a greater environmental scale, and more experimental data should be collected to verify its accuracy of calculation and applicability.

Conflicts of Interest

The authors declare that they have no conflicts of interest.

Acknowledgments

References

[1] F.-W. Wang and X.-F. Shi, "The research about how to control long-term deflection of large span prestressed concrete girder bridges," *Road*, vol. 8, pp. 72–76, 2006.

[2] H. S. Chiu, J. C. Chern, and K. C. Chang, "Long-term deflection control in cantilever prestressed concrete bridges I:

control method," *Journal of Engineering Mechanics*, vol. 122, no. 6, pp. 489–494, 1996.

[3] I. N. Robertson, "Prediction of vertical deflections for a long-span prestressed concrete bridge structure," *Engineering Structures*, vol. 27, no. 12, pp. 1820–1827, 2005.

[4] O. C. Choi and C. Lee, "Flexural performance of ring-type steel fiber-reinforced concrete," *Cement and Concrete Research*, vol. 33, no. 6, pp. 841–849, 2003.

[5] L. Daniel and A. Loukili, "Behavior of high-strength fiber-reinforced concrete beams under cyclic loading," *ACI Structural Journal*, vol. 99, no. 3, pp. 248–256, 2002.

[6] N. Banthia and M. Sappakittipakorn, "Toughness enhancement in steel fiber reinforced concrete through fiber hybridization," *Cement and Concrete Research*, vol. 37, no. 9, pp. 1366–1372, 2007.

[7] L.-F. Luo, M. Zhong, P.-Y. Huang et al., "Steel fibers reinforced polymers concrete and the method of it's mix ratio," China Patent for Invention ZL200410026780, 2006.

[8] L.-F. Luo, J.-C. Zhou, and P.-Y. Huang, "Reinforced mechanism with the polymer latex added in the steel fiber reinforced concrete," *Acta Materiae Compositae Sinica*, vol. 19, no. 3, pp. 46–50, 2002.

[9] L.-F. Luo, "Impact behavior of steel fiber reinforced polymer modified concrete," *China Journal of Highway and Transportation*, vol. 19, no. 5, pp. 71–76, 2006.

[10] Y.-P. Liu, L.-Q. Tang, and X.-Q. Huang, "Fatigue damage behavior of steel fiber reinforced polymer modified concrete," *Journal of South China University of Technology*, vol. 35, no. 2, pp. 18–22, 2007.

[11] L.-F. Luo, M. Zhong, and C.-Z. Huang, *Construction Technology of SFRPC Bridge Deck Pavement*, Press of South China University of Technology, Guangzhou, China, 2004.

[12] S.-C. Zheng, *Study on the Mechanical Property of Steel Fiber Polymer High Strength Structural Concrete*, South China University of Technology, Guangzhou, China, 2010.

[13] S.-C. Zheng, P.-Y. Huang, and X.-Y. Guo, "Experimental study on fatigue performance of steel fiber polymer high strength concrete," *Journal of Experimental Mechanics*, vol. 26, no. 1, pp. 1–7, 2011.

[14] S.-C. Zheng, P.-Y. Huang, X.-Y. Guo et al., "Temperature fatigue performance of steel fiber polymer high strength concrete," *Journal of South China University of Technology*, vol. 39, no. 9, pp. 88–92, 2011.

[15] H. Hu, *Temperature Fatigue Performance of Steel Fiber Polymer High Strength Concrete*, South China University of Technology, Guangzhou, China, 2011.

[16] Z.-S. Chen, *Experimental Study on Environmental Fatigue Behavior of Steel Fiber Polymer Structural Concrete*, South China University of Technology, Guangzhou, China, 2014.

[17] Z.-G. Chen, *Study on Key Mechanical Properties of Steel Fiber Polymer Structural Concrete*, South China University of Technology, Guangzhou, China, 2016.

[18] China National Technology Standard GB/T 2573-2008, *Test Method for Aging Properties of Glass Fiber Reinforced Plastics*, China National Technology Standard, 2008, in Chinese.

[19] P.-Y. Huang, H. Zhou, H.-Y. Wang, and X.-Y. Guo, "Fatigue lives of RC beams strengthened with CFRP at different temperatures under cyclic bending loads," *Fatigue and Fracture of Engineering Materials and Structures*, vol. 34, no. 9, pp. 708–716, 2011.

[20] G. Qin, P. Huang, H. Zhou, X. Guo, and X. Zheng, "Fatigue and durability behavior of RC beams strengthened with CFRP under hot-wet environment," *Construction and Building Materials*, vol. 111, pp. 735–742, 2016.

[21] P.-Y. Huang, S.-C. Zheng, W. Guo, and J. Deng, "Effect of admixtures on mechanical properties of steel fibre reinforced polymer high-strength concrete," in *Proceedings of SPIE, (ICEM 2008)*, vol. 7375, pp. 7375 6L-1–7375 6L-6, Nanjing, China, August 2008.

Research Article

Experimental Analysis of Pretensioned CLT-Glulam T-Section Beams

J. Estévez-Cimadevila [ID]**, F. Suárez-Riestra** [ID]**, D. Otero-Chans** [ID]**, and E. Martín-Gutiérrez** [ID]

Department of Construction and Architectural, Civil and Aeronautical Structures, University of A Coruña,
Campus de A Zapateira, 15071 A Coruña, Spain

Correspondence should be addressed to J. Estévez-Cimadevila; javier@udc.es

The bending behavior of T-section beams composed of a glulam web and an upper cross-laminated timber flange was studied. The influence of two fundamental factors on the bending strength and stiffness was considered: the wood species used for the webs and pretensioning with unbonded tendons. Sixteen specimens with a 9 m span were tested until failure: eight of them were nontensioned (4 *Picea abies* webs and 4 *Quercus robur* webs) and the other eight were pretensioned using threaded bars with 20 mm diameter anchored in plates fixed at the ends of the specimens (4 *Picea abies* webs and 4 *Quercus robur* webs). Pretensioning with unbonded tendons showed a clear improvement in the load capacity of the specimens with *Picea abies* webs, while the difference was not significant for the specimens with *Quercus robur* webs. Considering deflection, pretensioning gave the advantage of an initial precamber but also generated slight variations in the stiffness as a result of increasing the portion of the section that was in compression. The variation in the stiffness depended on the relation between the compressive and tensile moduli of elasticity parallel to the grain, and its influence on the deflection was analyzed using a finite element method.

1. Introduction

Pretensioning techniques are widely used for beams and slabs in concrete structures due to their ability to efficiently compensate for the reduced tensile strength of concrete through precompression. The improvement in strength achieved by pretensioning enables the use of thinner sections and provides an efficient solution for controlling material splitting and avoiding excessive deflections. For materials that have a tensile strength similar to or higher than their compressive strength, such as timber or steel, pretensioning offers significantly reduced advantages. Moreover, timber has problems with its long-term behavior; its inherent creep deflection can reduce the pretensioning effects over time, decreasing its capabilities. Therefore, the pretensioning technique is rarely used for timber.

Defect-free timber has a higher tensile strength than compressive strength. However, the inherent defects (cracks, knots, grain deviations, etc.) that are present in structural timber reduce its tensile strength. Furthermore,

typical bending failure is reached instantaneously after a brittle fracture is caused by tension in the fibers. This phenomenon has motivated research on different reinforcement solutions to improve the bending behavior of timber.

The reinforcement systems that have been used can be divided in two basic typologies: passive and active reinforcements. Passive reinforcement is made of metallic elements [1–3] or fiber-reinforced polymers (FRPs) [3–13] that are glued to the timber with structural adhesives. Active reinforcement can be made with unbonded tendons or with bonded tendons that are glued to the timber with adhesives. Active reinforcement has been used to both reinforce frame connections [14, 15] and improve the behavior of beams [16–25].

Some authors [20, 24] have studied the loss of prestressing force for LVL and glulam beams prestressed using unbonded tendons. They found a reduction in prestress from 1.4% to 10% for beams loaded parallel to the grain exposed to controlled and uncontrolled environmental conditions. They

Bending strength	$f_{m,k}$	33 MPa
Tensile strength parallel to the grain	$f_{t,0,k}$	23 MPa
Tensile strength perpendicular to the grain	$f_{t,90,k}$	0.6 MPa
Compressive strength parallel to the grain	$f_{c,0,k}$	45 MPa
Compressive strength perpendicular to the grain	$f_{c,90,k}$	8 MPa
Shear strength	$f_{v,k}$	4 MPa
Modulus of elasticity parallel to the grain	$E_{0,mean}$	14,400 MPa
Modulus of elasticity parallel to the grain	$E_{0,05}$	12,000 MPa
Modulus of elasticity perpendicular to the grain	$E_{90,mean}$	800 MPa
Modulus of elasticity perpendicular to the grain	$E_{90,05}$	660 MPa
Shear modulus	G_{mean}	850 MPa
Shear modulus	$G_{0,05}$	700 MPa
Characteristic density	ρ_k	690 kg/m^3

Table 2

Bending strength	$f_{m,k}$	24 MPa
Tensile strength parallel to the grain	$f_{t,0,k}$	14 MPa
Compressive strength parallel to the grain	$f_{c,0,k}$	22 MPa
Shear strength parallel to the grain of the boards	$f_{v,k}$	2.5 MPa
Modulus of elasticity parallel to the grain of the boards	$E_{0,mean}$	12,500 MPa
Shear modulus parallel to the grain of the boards	G_{mean}	460 MPa
Characteristic density	ρ_k	420 kg/m^3

concluded that controlling the relative humidity would reduce the losses. The use of bonded reinforcements could contribute to reduce the creep deformations in wood members [5].

This paper focuses on using active reinforcement with unbonded tendons. Therefore, an important reference is the experimental study conducted by McConnell et al. [26], regarding straight beams of laminated timber with a rectangular cross section. Their study analyzed the behavior of three types of reinforcements: beams with passive reinforcement of a 12 mm diameter steel bar, posttensioned beams with an unbonded 12 mm diameter steel tendon, and posttensioned beams with a bonded 12 mm diameter steel tendon. They concluded that posttensioning with unbonded tendons increased the bending strength by 17.6% and the stiffness by 8.1%. The small effect of pretensioning on the bending stiffness coincides with the results previously obtained by Bohannan [16].

This paper analyzes the bending behavior of T-section beams formed of glulam webs and upper cross-laminated timber (CLT) flanges. This analysis aims to determine the influence of using different wood species with different mechanical properties for the webs and the effect of pretensioning with unbonded tendons on the strength and bending stiffness of beams. The inherent loss of effectiveness of prestressing in a long-term process is assumed, but it is not considered as a determinant for the purpose of this analysis, as it is carried out in conditions of instantaneous loading.

2. Materials and Methods

2.1. Materials.
The characteristics of the materials used in the experimental study were as follows:

(i) Glulam webs made of *Picea abies*, with a strength class of GL28 h [27].

(ii) Glulam webs made of *Quercus robur* sheets LS13 [28]. The physical and mechanical properties provided by the manufacturer are in Table 1.

(iii) The CLT flanges, CLT90S L3S [29], were 90 mm thick and were composed of three sheets of 30 mm *Picea*

abies C24 [30]. The physical and mechanical properties provided by the manufacturer are in Table 2.

(iv) The connection between the webs and the flanges of the T-sections was made with $410 \times 80 \times 4$ mm perforated plates in S235 hot-dip galvanized finish steel. The circular drills of the plates had a diameter of 10 mm spaced at 5 mm. The plates were glued to the wooden specimens with a 2-component polyurethane adhesive.

(v) The pretensioning of the specimens was conducted using threaded bars of Y1100H [31] steel with a 20 mm diameter, an elastic limit of $f_{pk} = 900$ N/mm^2, and a tensile strength of $f_{pmax,k} = 1100$ N/mm^2.

2.2. Test Specimens

2.2.1. Preliminary Tests.
Two series of nondestructive tests were conducted. The aim of the first test series was to determine the global bending modulus of elasticity ($E_{m,g}$) of the timber used. The following specimens were tested:

(i) 4 *Picea abies* glulam webs with a cross section of 160×210 mm

(ii) 4 *Quercus robur* glulam webs with a cross section of 160×210 mm

(iii) 4 CLT planks with a cross section of 600×90 mm

Four-point bending tests were conducted with a span of 9 m between the supports. The tested specimens were used later to form the T-sections without pretensioning, as described in Section 2.2.2.

The purpose of the second preliminary test series was to determine the compressive elastic modulus of the webs parallel to the grain ($E_{c,0}$). The following specimens, which were obtained from the samples previously tested for bending, were tested under centered compression:

(i) 4 *Picea abies* glulam specimens of $55 \times 55 \times 330$ mm

(ii) 4 *Quercus robur* glulam specimens of $55 \times 5 \times 330$ mm

2.2.2. Tests of the T-Section Specimens.
The following characteristics of the T-sections were tested.

(1) T-Sections without Pretensioning. Eight specimens were formed using a glulam web (4 *Picea abies* specimens and 4 *Quercus robur* specimens) and upper CLT flanges (Figure 1(a)). The total length of the specimen was 9160 mm, and

the distance between the supports was $L = 9$ m. The geometric characteristics of the T-section were as follows (Figure 1(b)): $b_1 = 600$ mm, $b_2 = 160$ mm, $h_1 = 90$ mm, $h_2 = 210$ mm, and $H = 300$ mm.

The total depth (H) was established by considering the slenderness of the specimen ($L/30$). A thickness of $h_1 = 90$ mm was adopted for the CLT since this is the minimum commercial configuration for 3 plates. The width of the webs (b_2) was determined by considering the restriction of the longitudinal channel in which the tendon was placed. Finally, the width of the CLT (b_1) was selected to efficiently use the most common commercial dimensions of CLT. The adopted configuration of the T-section enables extending the results to π-shaped sections, a highly efficient typology for constructing structural floors.

The perforated plates of the connection between the web and the flanges (Figure 2) were placed as shown in Figure 3(a) for the *Picea abies* webs and as shown in Figure 3(b) for the *Quercus robur* webs.

To determine the number and distribution of the connection plates, the load capacity of the T-sections with different configurations (the pretensioned and nontensioned specimens and *Picea abies* and *Quercus robur* webs) was estimated. The load capacity was calculated considering a homogenized section obtained from the material characteristics described in Section 2 and assuming a bending failure mode.

A finite element method (FEM) analysis was performed with the obtained load values to assess the required lengths and positions of the connection plates. The adopted distribution proved to be efficient because none of the tested specimens failed at the connection between the web and flange.

(2) Pretensioned T-Sections. Eight beams were formed with a glulam web (4 *Picea abies* webs and 4 *Quercus robur* webs) and upper CLT flanges with the same characteristics as described for the nonpretensioned beams. The web cross section had a bottom groove or a cable channel of 35×85 mm, which was located 30 mm away from the bottom edge, where the tensioning tendon was placed (Figure 1(b)). The vertical dimension of the groove was oversized to accommodate two tendons, which was utilized in another test series using the same specimens. To make the groove, each web was manufactured with two 80 mm wide specimens and the groove was machined before being glued to form the final 160 mm wide web. The distribution of the perforated plates that connected the web and upper flange is shown in Figure 3(b) (*Picea abies*) and Figure 3(c) (*Quercus robur*).

Table 3 shows the geometric characteristics of all the tested specimens.

2.2.3. Test Setup. The preliminary tests conducted to determine the global bending elastic modulus (Figure 4) and the compression elastic modulus (Figure 5) considered the general criteria of regulation [32] using a frame with a 600 kN

(a)
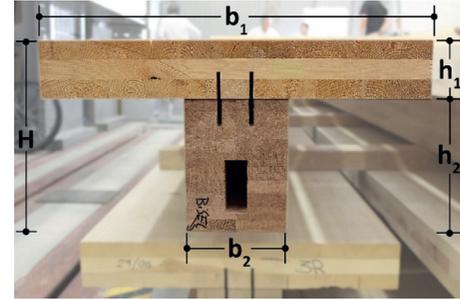
(b)

Figure 1: Picture of a solid transversal section without pretensioning (a) and a piece with a groove prepared to place the pretensioning tendon (b).

Figure 2: Discontinuous flange-to-web joint made with glued-perforated steel plates.

load cell. The bending tests were conducted using a 9 m span between the supports, and point loads were applied at one-third and two-thirds of the span; the midpoint displacement was measured using an extensometer with 100 mm of standard measurement stroke (Figure 4). The bending elastic modulus parallel to the grain ($E_{0,\text{mean}}$) was calculated using the following equation:

$$E_{0,\text{mean}} = \frac{3 \cdot a \cdot L^2 - 4 \cdot a^3}{2 \cdot b \cdot h^3 \cdot \left(\left(2 \cdot (w_2 - w_1)/(F_2 - F_1) \right) - \left(6 \cdot a/5 \cdot G_{\text{mean}} \cdot b \cdot h \right) \right)},$$

(1)

(a)

(b)

(c)
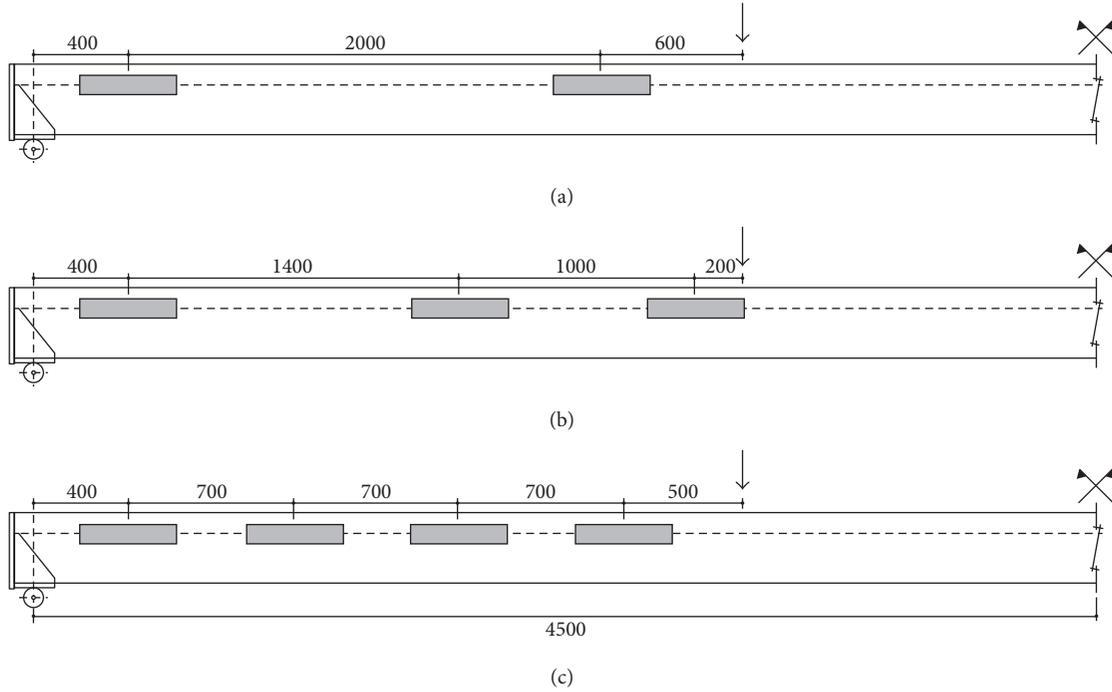
Figure 3: Dispositions of perforated steel plates adopted according to the type of piece. Nonpretensioned pieces: (a) *Picea abies* glulam webs and (b) *Quercus robur* glulam webs. Pretensioned pieces: (b) *Picea abies* glulam webs and (c) *Quercus robur* glulam webs.

Table 3: Geometric characteristics of the tested specimens.

| Type | Wood | Specimen number | Specimen geometry | | | | | | Test | Tensioning tendon Φ (mm) |
			L (mm)	H (mm)	h_1 (mm)	h_2 (mm)	b_1 (mm)	b_2 (mm)		
B/PIC-1 to 4	*Picea abies*	4	9000	—	—	210	—	160	Bending	—
B/OAK-1 to 4	*Quercus robur*	4	9000	—	—	210	—	160	Bending	—
B/CLT-1 to 4	CLT	4	9000	—	90	—	600	—	Bending	—
C/PIC-1 to 4	*Picea abies*	4	330	55	—	—	—	55	Compression	—
C/OAK-1 to 4	*Quercus robur*	4	330	55	—	—	—	55	Compression	—
F1/PIC-1 to 4	T-section with *Picea abies* web	4	9000	300	90	210	600	160	Bending	—
F1/OAK-1 to 4	T-section with *Quercus robur* web	4	9000	300	90	210	600	160	Bending	—
F2/PIC-1 to 4	T-section with *Picea abies* web	4	9000	300	90	210	600	160	Bending	20
F2/OAK-1 to 4	T-section with *Quercus robur* web	4	9000	300	90	210	600	160	Bending	20

where a is the distance between a loading point and the nearest support, L is the span of the structural element, b and h are the dimensions of the cross section of the beam, $F_2 - F_1$ is the load increase in the straight part of the load-deflection curve, and $\omega_2 - \omega_1$ is the deflection increase corresponding to load $F_2 - F_1$.

The compression elastic modulus parallel to the grain ($E_{c,0}$) was calculated using the following equation:

$$E_{c,0} = \frac{L_1 \cdot (F_2 - F_1)}{A \cdot (w_2 - w_1)}, \quad (2)$$

where L_1 is the length, 4 times the smallest dimension of the specimen; $F_2 - F_1$ is the load increase in the straight part of the load-deflection curve; A is the cross-sectional area of timber; and $\omega_2 - \omega_1$ is the deflection increase corresponding to load $F_2 - F_1$.

FIGURE 4: Bending test to determine the global bending MOE.

FIGURE 6: Test of a pretensioned T-section with *Picea abies* webs.

FIGURE 5: Test to determine the compression MOE parallel to the grain.

The T-section was tensioned using a hydraulic jack until a precamber of 18 mm ($L/500$) was obtained. The tension force applied to reach the precamber was different for each specimen due to their different stiffnesses. The tendon was locked against the plates using a domed anchor nut [33]. The tendon was placed in the groove of the web 105 mm from the tendon axis to the bottom edge of the specimen (Figure 6).

3. Results

Table 4 shows the results that were obtained from the previous tests to determine the modulus of elasticity parallel to the grain for bending and compression. The average value of the global bending modulus of the CLT specimens from the experiments was 6% lower than the one declared by the manufacturer. Compared to the theoretical values listed in Section 2, the specimens with *Picea abies* and *Quercus robur* webs exhibited much more significant decreases in the modulus of elasticity (13.7% for *Picea abies* and 17.3% for *Quercus robur*).

Table 5 shows the tensioning force applied to each specimen to reach the initial precamber (the maximum force at failure in the bar) and the failure load.

Table 6 presents the midpoint displacement of each T-section beam for two point loads of 14 kN; each load was applied at one-third of the span length. In terms of deflection, these point loads were equivalent to a uniformly distributed load of 7 kN/m^2, which is a common value for public buildings ($G_k = 2$ kN/m^2 and $Q_k = 5$ kN/m^2). The displacements listed in Table 6 do not include the deflection caused by the self-weight of the specimen because the extensometers were installed after the specimen was supported and the load had been applied. In the case of the pretensioned specimens (F2/PIC and F2/OAK), the displacement was measured after pretensioning, so such displacements were measured after some deflection had occurred; therefore, the self-weight was already considered. Thus, to determine the midpoint displacement, the 18 mm of initial precamber was subtracted from the corresponding value in Table 6.

Figures 7 and 8 show the load-displacement results that correspond to the bending tests of pretensioned and nontensioned T-sections with *Picea abies* (Figure 7) and *Quercus robur* webs (Figure 8). The minimum and maximum values obtained from the action of the two 14 kN loads applied to one-third and two-thirds of the span length are provided. For an approximate displacement of 15 mm, the load-deflection curves corresponding to the pretensioned beams show a clear change in slope caused by the increase of the effective stiffness when the wood comes into contact with the steel bar. This contact occurs when the deformation generated by the beam's self-weight and the loads applied during the test offset the 18 mm precamber produced by the initial pretensioning force.

The failure of all T-sections, both nontensioned and pretensioned, occurred instantaneously as a result of the tension in the glulam web. In the nontensioned specimens, the predominant failure mode was typical glulam bending failure (Figure 9). In the F1/PIC-3 specimen, the failure was accelerated due to the presence of significant knots in the bottom sheet of the glulam web (Figure 10). As a result, the failure load of this specimen was the lowest of all the tested specimens (Table 5). Finger-joint failure occurred in the F1/OAK-3 specimen (Figure 11), and significant variation was not observed in the failure loads of the other tested

TABLE 4: Modulus of elasticity parallel to the grain.

Type	Value for each specimen (MPa)				Standard deviation	Average value $E_{c,0, \text{ test}}$ (MPa)	Average value $E_{0,\text{mean,test}}$ (MPa)	Average value $E_{0,\text{mean}}$ (MPa)	$\frac{E_{0,\text{mean,test}}}{E_{0,\text{mean}}}$
	1	2	3	4					
			Experimental test series					Theoretical value	
B/PIC	10,880	11,450	10,510	10,658	413	—	10,875	12,600	0.86
B/OAK	11,641	11,884	12,222	11,894	238	—	11,910	14,400	0.83
B/CLT	10,913	11,091	12,833	12,157	908	—	11,748	12,500	0.94
C/PIC	10,208	11,365	11,115	8616	1244	10,326	—	—	—
C/OAK	11,676	10,767	13,375	13,248	1264	12,267	—	—	—

TABLE 5: Force in the tensioning bar and ultimate load.

Type	Initial prestressing force						Total failure load					
	Maximum force in the bar (kN)						Sum of the two specific loads applied (kN)					
	Specimen				Standard deviation	Average value	Specimen				Standard deviation	Average value
	1	2	3	4			1	2	3	4		
F1/PIC	—	—	—	—	—	—	55.25	64.15	49.48	61.97	6.67	57.71
F2/PIC	109.20	117.03	113.16	117.89	3.99	114.32	58.15	59.49	95.66	74.18	17.44	71.87
	154.17	163.79	176.55	172.57	9.95	166.77						
F1/OAK	—	—	—	—	—	—	69.89	87.54	80.36	88.28	8.54	81.52
F2/OAK	115.54	94.06	113.29	116.00	10.51	109.72	73.78	68.92	90.74	84.15	9.88	79.40
	171.81	147.61	225.99	175.49	32.92	180.23						

TABLE 6: Displacement at the midpoint of the span for two specific loads of 14 kN applied at one-third and two-thirds of the span.

Type	Value for each specimen (mm)				Standard deviation	Average value (mm)
	1	2	3	4		
F1/PIC	59.14	56.94	60.14	56.50	1.74	58.18
F2/PIC	64.86	68.63	62.01	64.14	2.76	64.91
F1/OAK	53.29	54.70	57.27	52.89	1.98	54.54
F2/OAK	65.09	63.65	62.09	61.78	1.53	63.15
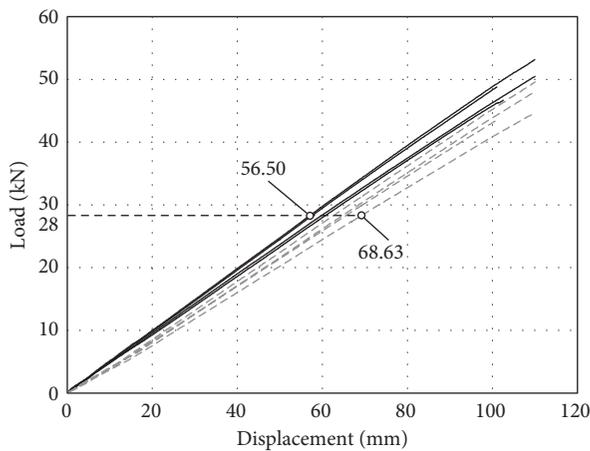
FIGURE 7: Load-displacement curves of T-sections with *Picea abies* webs: pretensioned (dashed lines) and nonpretensioned (solid lines).

specimens. In all the pretensioned specimens, with both *Picea abies* and *Quercus robur* webs, typical glulam bending failure was observed (Figure 12).

4. Discussion

4.1. Influence of the Type of Wood Used to Laminate the Web without Pretensioning. Using *Quercus robur* laminated timber webs instead of *Picea abies* webs in a nontensioned beam clearly improves the strength. The average failure load was 81.52 kN for *Quercus robur* and 57.71 kN for *Picea abies*, showing an increase of 41.2%. Moreover, the lowest failure load obtained with the *Quercus robur* webs (F1/OAK-1, 69.89 kN) was 8% higher than the highest value obtained for the *Picea abies* webs (F1/PIC-2, 64.15 kN). Since failure of both the *Picea abies* and *Quercus robur* webs occurred because of tension in the glulam web, the larger strength of the T-section with the *Quercus robur* webs was clearly directly related to the enhanced mechanical properties of the hardwood species. This conclusion can be clearly verified by examining the maximum theoretical stress on the bottom fiber (σ_{bottom}) in Table 7, which was analytically obtained using (3) and assuming a pretensioning force (N_{prest}) of zero:

$$\sigma_{\text{bottom}} = -\frac{N_{\text{prest}}}{A} + \frac{\left(M - N_{\text{prest}} \cdot e_{\text{prest}}\right) \cdot y}{I}, \quad (3)$$
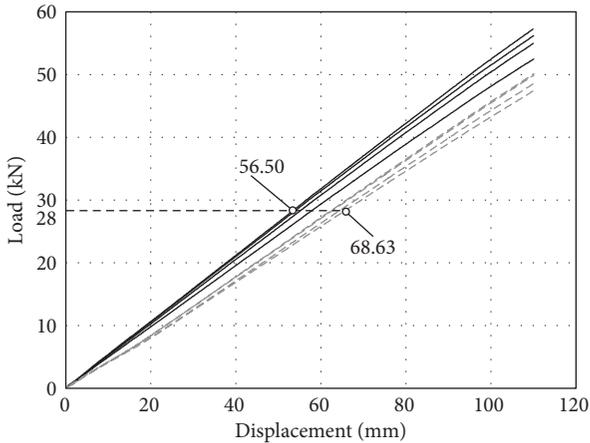
Figure 8: Load-displacement curves of T-sections with *Quercus robur* webs: pretensioned (dashed lines) and nonpretensioned (solid lines).

Figure 9: Typical bending failure in nonpretensioned T-sections corresponding to specimen F1/PIC-1.

Figure 10: Failure due to knots in the specimen F1/PIC-3.

Figure 11: Failure close to a finger joint in the specimen F1/OAK-3.

where A is the cross-sectional area of timber, M is the applied moment, e_{prest} is the eccentricity of the pretensioning tendon with respect to the center of mass of the cross section, y is the

Figure 12: Bending failure in a pretensioned T-section corresponding to specimen F2/OAK-3.

distance to the neutral axis, and I is the moment of inertia of the homogenized section.

The average global modulus of elasticity obtained from the tests on *Quercus robur* webs (11,910 N/mm^2) was 9.5% higher than that obtained from the tests on *Picea abies* webs (10,875 N/mm^2). Using the *Quercus robur* webs instead of Picea abies webs theoretically increased the bending stiffness (EI) of the homogenized T-section, including the upper CLT board, by 5.6%. The homogenized section was calculated using the average global modulus of elasticity obtained in the tests. The theoretical increase in the bending stiffness (5.6%) was similar than the reduction in the average midpoint displacement of the tested specimens (58.18 mm for the *Picea abies* webs and 54.54 mm for the *Quercus robur* webs). This low increase in the bending stiffness was easily achieved by slightly increasing the depth of the *Picea abies* webs. In the analytical case, the increase in the stiffness provided by using the *Quercus robur* webs could be achieved by increasing the depth of the *Picea abies* webs from 210 mm to 215.7 mm (a 2.7% increase in the depth).

In conclusion, the use of laminated hardwood in the webs of a T-section provides a clear increase only in strength. However, in building structures, the dimensions of simply supported specimens with a medium or long span (the appropriate spans for the type of section analyzed) are not usually determined by strength limitations but by deformation limitations. As a result, the increase in stiffness gained from using glulam hardwood can hardly compensate for the increased cost.

4.2. Influence of Pretensioning on the Bending Strength. Simply supported specimens were pretensioned with unbonded tendons to improve their strength; by applying an eccentric tensioning force, the positive bending generated from exterior loads was reduced. The magnitude of the tensioning force must be limited to ensure that the resultant precamber does not surpass the standard values of service limit states. This limitation in the negative bending magnitude that is induced by pretensioning, together with the additional compressive stresses inherent to tensioning, eliminates the relevance of the increased strength.

Table 5 shows the failure loads of all tested specimens. The specimens with *Picea abies* webs reached an average failure load of 71.87 kN in the pretensioned specimens and 57.71 kN in the nontensioned specimens. However, this increase of

TABLE 7: Maximum tensile stress estimated for the failure load.

| Type | Value for each specimen (MPa) | | | | Standard deviation | Average value (MPa) |
	1	2	3	4		
F1/PIC	25.75	29.90	23.06	28.88	3.11	26.90
F2/PIC	21.54	21.32	45.67	35.41	11.80	30.98
F1/OAK	33.06	41.41	38.01	41.76	4.04	38.56
F2/OAK	28.67	33.43	44.01	40.81	6.96	36.73

24.5% must be considered in the context of three issues. First, the small number of tested specimens prevents the results from being conclusive. Second, the low value of the failure load (49.48 kN) of test specimen F1/PIC-3 occurred due to the presence of knots on the bottom side accelerating the failure (Figure 10). Finally, the high value of the failure load (95.66 kN) reached by test specimen F2/PIC-3 resulted in a standard deviation for the pretensioned specimens (17.44) that was significantly higher than that of the nontensioned specimens (6.67). The tensioning force applied to the four tested specimens is shown in Table 5. The negative bending moment produced by tensioning was calculated using the global modulus of elasticity of each specimen and the eccentricity of the tendons in relation to the center of gravity of the homogenized sections: 12.83, 13.42, 15.93, and 15.15 kN·m for specimens F2/PIC-1 to 4, respectively. As shown, the largest negative moments (specimens 3 and 4) corresponded to the specimens that reached a higher failure load. However, expressing the negative moment values as a percentage of the isostatic moment produced by the failure load gives the following results: 33.10%, 33.84%, 24.97%, and 30.64% for specimens F2/PIC-1 to 4, respectively. The lowest percentage of the counterbalance moment was produced using specimen F2/PIC-3, which reached the highest failure load, and very significant differences were observed regarding the other specimens.

As a result, since the pretensioning and moment generated by the eccentric pretensioning load were very similar for the 4 specimens, the excellent strength behavior of such specimens could have been a direct consequence of the inherent variations in the mechanical properties of timber. This variation is also reflected in the theoretical tension at the moment of failure (Table 7).

In the specimens with *Quercus robur* webs, pretensioning did not increase the average failure load; these values were even lower than those of the nontensioned specimens (79.40 kN and 81.52 kN, resp.). Table 7 compares the results in terms of the average theoretical stress at the moment of failure. The tensioning force applied to the four *Quercus robur* test specimens and the maximum force reached by the tendon are shown in Table 5. The negative bending moments produced by the eccentric tendon at the moment of failure were 13.88, 11.89, 19.16, and 14.71 kN·m for specimens F2/OAK-1 to 4, respectively. The highest value of the counterbalance moment was once again observed in the specimen that reached the highest ultimate load value. This result was also observed when the moments were expressed as a percentage of the isostatic moment at the

ultimate load: 28.21%, 25.89%, 31.68%, and 26.23%, respectively. The obtained results reveal that the differences in the ultimate loads of the pretensioned and nontensioned specimens with *Quercus robur* webs were more closely related to the specific material properties than to the influence of pretensioning.

As a result, although it was not possible to reach definite conclusions, the test results indicate that the benefits of pretensioning on the bending strength of the specimens were not especially relevant. This observation was attributed to the fact that the maximum precamber that could be initially applied with eccentric tensioning was limited by meeting the deflection standards. An efficient way to avoid this limitation in the pretensioning force is to apply a variable tensioning force that generates a counterbalance effect relative to the applied forces. With this goal in mind, the authors developed the SsS© (Self-stressing System) [34, 35].

4.3. Influence of Pretensioning on the Bending Stiffness.
Increasing the bending strength of a specimen is not usually the fundamental objective of pretensioning because the dimensions of simply supported specimens are not typically determined by the ultimate limit states but by the service limit states.

The first positive effect provided by pretensioning is to impart a precamber to a specimen. In this way, the deflections caused by permanent actions are offset, helping to meet the service restrictions imposed by appearance considerations. Nevertheless, a precamber can be easily imparted in laminated timber during its manufacturing process. Therefore, pretensioning is not necessary if offsetting the deflections caused by permanent loads is the only goal. The other two in-service deflection conditions that must be satisfied are to ensure the integrity of the construction elements and user comfort. The essential parameter for fulfilling both requirements is the bending stiffness of the element; this aspect is especially relevant for high live loads.

The stiffness of the pretensioned specimens, with both *Picea abies* and *Quercus robur* webs, was clearly inferior to that of the nontensioned specimens, as shown in Figures 7 and 8. Table 5 shows the midpoint displacement values for a total load of 28 kN (2 loads of 14 kN applied at one-third and two-thirds of the span length, which are equivalent in deflection to a uniform distributed load of 7 kN/m^2). The average displacement value for the specimens with *Picea abies* webs was 64.91 for the pretensioned specimens and 58.18 mm for the nontensioned specimens, representing an 11.6% increase in deflection. In the case of *Quercus robur*, the average

displacement was 63.15 mm for the pretensioned specimens and 54.54 for the nontensioned specimens; thus, pretensioning increased the deflection by 15.8%. Thus, compared to the equivalent nontensioned specimens, the pretensioned specimens with unbonded tendons presented an effective loss in the stiffness, which was attributed to several factors.

The first factor that could have influenced the obtained deflection results is the use of different plate configurations for the flange-web joint of the two species. The distribution of these connection plates was determined to prevent failure at the joint, which would distort the intended analysis. According to the previous joint design, such failure did not occur; therefore, possible slip or failure was not a determining factor in comparing the results. Finally, the pretensioned specimens experienced a higher deflection than the nontensioned specimens, despite the pretensioned specimens having more connection plates in the flange-web joint.

The second factor that could explain the obtained deflection results is the lower moment of inertia in the pretensioned section because of the groove for the tendon. The groove, as mentioned previously, was vertically oversized to allow for other tensioning configurations. In the specimens with the *Picea abies* webs, the decrease in the bending stiffness (EI) of the homogenized section was 7.6%. The precamber of the nontensioned specimens measured from the tests was 58.18 mm, so the decrease in the stiffness caused by the groove could theoretically improve that value to a maximum of 62.60 mm. However, the total displacement obtained in the pretensioned specimen was 64.91 mm, representing an additional increase of 3.7%.

In the specimens with the *Quercus robur* webs, the decrease in the bending stiffness of the homogenized section, calculated with a modulus of elasticity of 11,910 MPa, was 7.4%. However, that loss did not correspond to the clear higher displacements that were measured in the tests, indicating a greater decrease in stiffness. Preliminary tests to determine the modulus of elasticity were conducted using the same webs that were used to make the nontensioned T-section specimens. The average modulus of elasticity was 11,910 MPa in the *Quercus robur* web and 10,875 MPa in the *Picea abies* web. Surprisingly, the pretensioning force needed to obtain a precamber of 18 mm was lower in the specimens with the *Quercus robur* webs (109.72 kN) than in the specimens with the *Picea abies* webs (114.32 kN). This result can be explained by considering that the timber of the webs in the pretensioned specimen had a lower modulus of elasticity. Given that we know the moment of inertia, tensioning force, and precamber for each of the F2/OAK specimens, we obtained an average modulus of elasticity of 10,090 MPa. As a result, a 16.49% decrease in stiffness was generated by the groove combined with the reduction in the modulus of elasticity E_m (from 11,910 to 10,090 MPa). This decrease in the stiffness increased the average precamber value from 54.54 mm, obtained for the solid specimen, to 63.53 mm in the specimen with the groove. This value is slightly higher than that obtained from the tests (63.15 mm, as shown in Table 8).

Finally, the third factor that explains the obtained displacement results was attributed to the differences between the modulus of the compressive modulus of elasticity ($E_{c,0}$) and the tensile modulus of elasticity ($E_{t,0}$) parallel to the grain. The pretensioning of the section increased the compressive stresses and consequently increased the compression area of the section. These are, the normal bending stresses that originated from the eccentric pretensioning and external force, combined with the normal compressive stresses due to pretensioning, led to a displacement in the neutral fiber that increased the compression area. Depending on the relative values of the tensile modulus of elasticity and the compressive modulus of elasticity, the increase in the compression section led to a slight decrease (if $E_{c,0} < E_{t,0}$) or increase (if $E_{c,0} > E_{t,0}$) in the stiffness.

To verify the proposed theory, an FEM analysis for solid specimens (types F1/PIC and F1/OAK) and specimens with grooves (types F2/PIC and F2/OAK) was conducted, considering both nontensioned and pretensioned specimens.

Three-dimensional models of hexahedral finite elements with 8 nodes containing 24 degrees of freedom (DOFs) were generated. The contact between the elements accounted for the possibility of dynamic behavior from flexible and/or rigid components, with kinematic restrictions on relative movement (displacement and rotation) between the nodes that formed the connection.

Two cases were assumed for the material properties. In the first case, the global modulus of elasticity was considered. In the second case, a bimodulus material was used to define not only the different elastic moduli for both compression and tension but also the different stress-strain curves for compression and tension.

The global bending modulus of elasticity ($E_{0,mean,test}$) and compression modulus of elasticity parallel to the grain ($E_{c,0,test}$) were determined in previous tests (Table 4). Using (4) [36], which is well known for determining the virtual modulus of elasticity (E_m) in softwood, we estimated the tensile modulus of elasticity parallel to the grain ($E_{t,0}$), using the global modulus obtained from the tests ($E_{0,mean,test}$) as the virtual modulus (E_m):

$$E_m = \frac{4 \cdot E_{t,0} \cdot E_{c,0}}{\left(\sqrt{E_{t,0}} + \sqrt{E_{c,0}}\right)^2}. \tag{4}$$

Table 8 shows the average displacement values obtained from the experimental tests and those obtained from the numerical analysis. For the pretensioned specimens, the precamber generated by the pretensioning plus the midpoint displacement is noted in parentheses in this table.

The numerical analysis conducted using the virtual modulus of elasticity (E_m) and the bimodulus ($E_{c,0}$ and $E_{t,0}$) led to interesting conclusions. In the case of the nontensioned specimens, for both the solid section and the section with a groove in the web, the analysis results using the bimodulus showed a high correlation with the results obtained using the virtual modulus of elasticity. This correlation was very similar for the specimens with *Picea abies* webs and was slightly lower for the specimens with *Quercus robur* webs; hence, we recommend checking (4) when using it for hardwood. In contrast, in the case of the pretensioned specimens, the results obtained using the bimodulus were

TABLE 8: Displacement at the midpoint of the span for two point loads of 14 kN applied at one-third and two-thirds of the span.

Type	Pretensioning force (kN)	Displacement experimental test (mm)	Modulus of elasticity (MPa)			Displacement FEM (mm)	
			E_m	$E_{c,0}$	$E_{t,0}$	With global modulus of elasticity E_m	With bimodulus $E_{c,0}$ and $E_{t,0}$
F1/PIC	—	58.18	10,875	10,326	11,470	58.98	58.95
F2/PIC	—	—	10,875	10,326	11,470	63.56	63.51
	114.32	64.91 (18.00 + 46.91)	10,875	10,326	11,470	63.48 (17.27 + 46.21)	65.64 (18.26 + 47.38)
F1/OAK	—	54.54	11,910	12,267	11,570	55.25	54.81
F2/OAK	—	—	10,090	10,390	9800	66.47	65.25
	109.72	63.15 (18.00 + 45.15)	10,090	10,390	9800	64.77 (17.22 + 47.55)	63.67 (17.38 + 46.29)
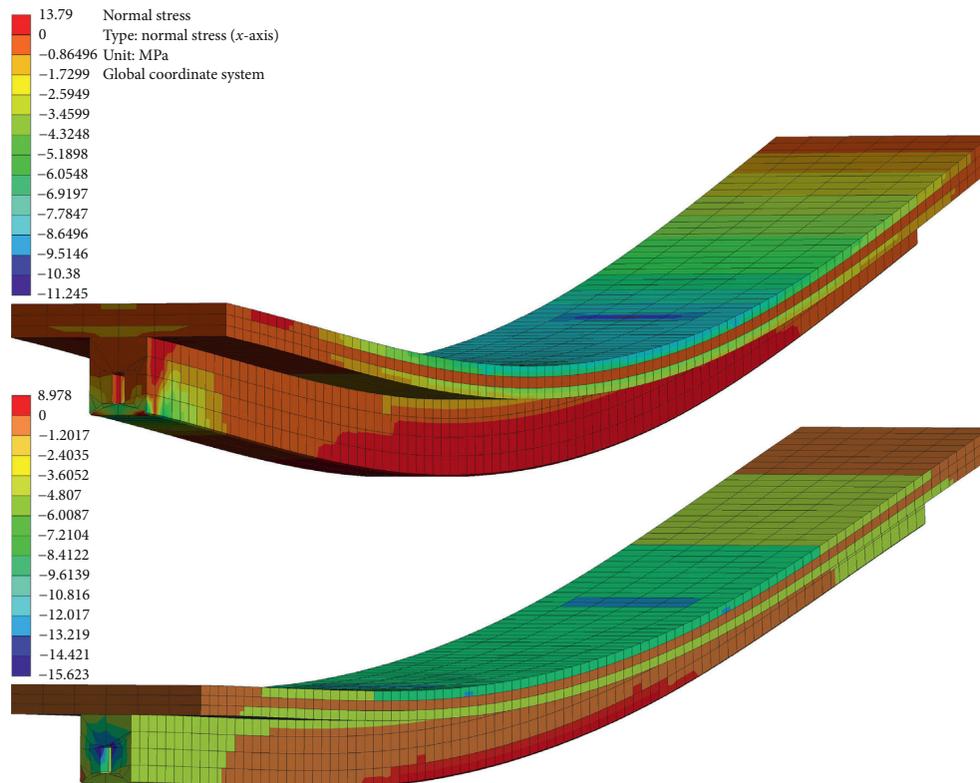
FIGURE 13: Finite element model. Visualization of the increase of the compressed zone in pieces of T-section with *Picea abies* webs: pretensioned (bottom) and nonpretensioned (top).

clearly closer to the experimental results than were the results from the analysis using the virtual modulus. The displacement of the pretensioned specimen with *Picea abies* webs obtained from the numerical model (65.64 mm) was 11.3% higher than that of the nontensioned solid specimen (58.95 mm). In the experimental tests, this increase was 11.6% (64.91 mm for the pretensioned specimen and 58.18 mm for the nontensioned specimen). In the specimens with *Quercus robur* webs, the displacement in the numerical model increased by 16.2%, which was practically the same as the increase obtained from the tests (15.8%). These results confirm that the variations in the stiffness experienced by the specimens under tension were a consequence of the significant increase in the compression area of the section (Figure 13). To help

visualize the pretensioning phenomenon, the areas with tensile stress, regardless of the magnitude, are shown in red in Figure 13.

The results presented here significantly differ from those obtained by McConnell et al. [26]. In our experimental tests, the pretensioned *Picea abies* specimens showed an 11.6% higher deflection than the nontensioned specimens. This 11.6% increase was reduced to 3.7% after disregarding the loss of inertia due to the groove where the tendon was placed. Conversely, in the tests conducted by McConnell et al. [26], the pretensioning reduced the deflection by 8.1%. This disagreement was attributed to the interactions of several factors. First, the tendon was placed much closer to the edge of the specimen (22.5 mm instead of 105 mm). Second, the

sizes of the tested specimens were different (sections of 45×145 mm with a 3 m span facing the T-sections with a 300 mm depth and 9 m span). Third, there were possible differences in the relation between the compressive and tensile moduli of elasticity parallel to the grain of the timber used in the tests. The above-mentioned circumstances could generate a greater rotational restraint at the edges of the specimens to reduce the deflection. Moreover, the benefit of pretensioning indicated by McConnell's experiments was also small.

5. Conclusions

Using *Quercus robur* instead of the usual *Picea abies* for laminating the webs of T-section specimens led to a 41.2% increase in the bending resistance and a 5.6% increase in stiffness. Given that the dimensions of simply supported specimens with a medium or long span are normally determined by deflection limitations, *Quercus robur* is generally not used due to its high cost and small benefit. The 5.6% increase in stiffness obtained in the tests could be achieved by increasing the depth of the *Picea abies* web by only 2.7%.

Pretensioning the T-sections increased the bending strength by 24.5% for the specimens with *Picea abies* webs. The average failure load of the T-sections with *Quercus robur* webs was lower in pretensioned specimens than that in the nontensioned specimens, even though the difference was only 2.6%.

The bending stiffness is a fundamental property for dimensioning simply supported specimens, and pretensioning slightly varied the stiffness of the section because of the increased compression area. We proved that such stiffness variations depend on the relation between the compressive and tensile moduli of elasticity parallel to the grain. In the analyzed cases, we found a 3.7% decrease in the stiffness of the specimens with *Picea abies* webs and a very slight increase in the specimens with *Quercus robur* webs (discounting the reduction due to the groove).

Due to the number of tested specimens and the use of different configurations for the flange-web joints with glued-perforated steel plates, we advise conducting another experimental test series to confirm the obtained conclusions.

Conflicts of Interest

The authors declare that there are no conflicts of interest.

Acknowledgments

References

[1] A. Borri and M. Corradi, "Strengthening of timber beams with high strength steel cords," *Composites: Part B*, vol. 42, no. 6, pp. 1480–1491, 2011.

[2] J. Soriano, B. P. Pellis, and N. T. Mascia, "Mechanical performance of glued-laminated timber beams symmetrically reinforced with steel bars," *Composite Structures*, vol. 150, pp. 200–207, 2016.

[3] H. Yang, W. Liu, W. Lu, S. Zhu, and Q. Geng, "Flexural behavior of FRP and steel reinforced glulam beams: experimental and theoretical evaluation," *Construction and Building Materials*, vol. 106, pp. 550–563, 2016.

[4] N. Plevris and T. C. Triantafillou, "FRP-Reinforced wood as structural material," *Journal of Materials in Civil Engineering*, vol. 4, no. 3, pp. 300–317, 1992.

[5] N. Plevris and T. C. Triantafillou, "Creep behavior of FRP-reinforced wood members," *Journal of Structural Engineering*, vol. 121, no. 2, pp. 174–186, 1995.

[6] T. C. Triantafillou, "Shear reinforcement of wood using FRP materials," *Journal of Materials in Civil Engineering*, vol. 9, no. 2, pp. 65–69, 1997.

[7] A. Yusof and A. L. Saleh, "Flexural strengthening of timber beams using glass fibre reinforced polymer," *Electronic Journal of Structural Engineering*, vol. 10, pp. 45–56, 2010.

[8] G. M. Raftery and A. M. Harte, "Low-grade glued laminated timber reinforced with FRP plate," *Composites Part B*, vol. 42, no. 4, pp. 724–735, 2011.

[9] G. M. Raftery and A. M. Harte, "Nonlinear numerical modelling of FRP reinforced glued laminated," *Composites Part B*, vol. 52, pp. 40–50, 2013.

[10] P. De La Rosa García, A. C. Escamilla, and M. N. González García, "Bending reinforcement of timber beams with composite carbon fiber and basalt fiber materials," *Composites Part B*, vol. 55, pp. 528–536, 2013.

[11] A. D'Ambrisi, F. Focacci, and R. Luciano, "Experimental investigation on flexural behavior of timber beams repaired with CFRP plates," *Composite Structures*, vol. 108, pp. 720–728, 2013.

[12] P. De La Rosa García, A. C. Escamilla, and M. N. González García, "Analysis of the flexural stiffness of timber beams reinforced with carbon and basalt composite materials," *Composites Part B*, vol. 86, pp. 152–159, 2016.

[13] I. Glisovic, B. Stevanovic, and M. Todorovic, "Flexural reinforcement of glulam beams with CGRP plates," *Materials and Structures*, vol. 49, no. 7, pp. 2841–2855, 2016.

[14] T. Smith, F. C. Ponzo, A. Cesare et al., "Post-tensioned glulam beam-column joints with advanced damping systems: testing and numerical analysis," *Journal of Earthquake Engineering*, vol. 18, no. 1, pp. 147–167, 2014.

[15] F. Wanninger and A. Frangi, "Experimental and analytical analysis of a post-tensioned timber connection under gravity loads," *Engineering Structures*, vol. 70, pp. 117–129, 2014.

[16] B. Bohannan, "Prestressed wood laminated beams," *Forest Products Journal*, vol. 12, no. 12, pp. 596–602, 1962.

[17] T. C. Triantafillou and N. Deskovic, "Prestressed FRP sheets as external reinforcement of wood members," *Journal of Structural Engineering*, vol. 118, no. 5, pp. 1270–1284, 1992.

[18] C. W. Dolan, T. L. Galloway, and A. Tsunemori, "Prestressed glued laminated timber beam—Pilot study," *Journal of Composites for Construction*, vol. 1, no. 1, pp. 10–16, 1997.

[19] A. Buchanan, A. Palermo, D. Carradine, and S. Pampanin, "Post-tensioned timber frame buildings," *Structural Engineer*, vol. 89, no. 17, pp. 24–30, 2011.

[20] M. Davies and M. Fragiacomo, "Long-term behavior of prestressed LVL members. I: experimental tests," *Journal of Structural Engineering*, vol. 137, no. 12, pp. 1553–1561, 2011.

[21] V. De Luca and C. Marano, "Prestressed glulam timbers reinforced with steel bars," *Construction and Building Materials*, vol. 30, pp. 206–217, 2012.

[22] J. Negrâo, "Prestressing systems for timber beams," in *Proceedings of World Conference on Timber Engineering WCTE-12*, vol. 1, pp. 252–261, Auckland, New Zealand, July 2012.

[23] W. Van Beerschoten, A. Palermo, D. Carradine, and S. Pampanin, "Design procedure for long-span post-tensioned timber frames under gravity loading," in *Proceedings of World Conference on Timber Engineering WCTE-12*, vol. 1, pp. 354–361, Auckland, New Zealand, July 2012.

[24] F. Wanninger, A. Frangi, and M. Fragiacomo, "Long-term behavior of posttensioned timber connections," *Journal of Structural Engineering*, vol. 141, no. 6, article 04014155, 13 pages, 2015.

[25] T. Smith, F. Sarti, G. Granello et al., "Long-term dynamic characteristics of Pres-Lam structures," in *Proceedings of World Conference on Timber Engineering WCTE 2016*, Vienna, Austria, August 2016.

[26] E. McConnell, D. McPolin, and S. Taylor, "Post-tensioning of glulam timber with steel tendons," *Construction and Building Materials*, vol. 73, pp. 426–433, 2014.

[27] EN 14080, *Timber Structures. Glued Laminated Timber and Glued Solid Timber, Requirements*, European Committee for Standardization (CEN), Brussels, Belgium, 2013.

[28] ETA 13/0642, *VIGAM-Glued Laminated Timber of Oak*, European Technical Assesment, Brussels, Belgium, 2013.

[29] ETA 14/0349, *CLT-Cross Laminated Timber*, European Technical Assesment, Brussels, Belgium, 2014.

[30] EN 338, *Structural Timber. Strength Classes*, European Committee for Standardization (CEN), Brussels, Belgium, 2009.

[31] prEN 10138–4, *Prestressing Steels—Part 4: Bars*, European Committee for Standardization (CEN), Brussels, Belgium, 2000.

[32] EN 408, 2010+A1, *Timber Structures. Structural Timber and Glued Laminated Timber. Determination of Some Physical and Mechanical Properties*, European Committee for Standardization (CEN), Brussels, Belgium, 2012.

[33] ETA 05/0123, *Dywidag-System International GmbH*, European Technical Assesment, Brussels, Belgium, 2013.

[34] J. Estévez-Cimadevila, D. Otero-Chans, E. Martín-Gutiérrez, and F. Suárez-Riestra, "Self-tensioning system for long-span wooden structural floors," *Construction and Building Materials*, vol. 102, pp. 852–860, 2016.

[35] D. Otero-Chans, J. Estévez-Cimadevila, E. Martín-Gutiérrez, and J. Pérez-Valcárcel, "Application of a new system of self-tensioning to the design of large-span wood floor framings," *Journal of Structural Engineering*, vol. 142, no. 6, p. 04016012, 2016.

[36] V. Baño, R. Argüelles-Bustillo, R. Regueira, and M. Guaita, "Determination of the stress-strain curve in specimens of Scots pine for numerical simulation of defect free beams," *Materiales de Construcción*, vol. 62, no. 306, pp. 269–284, 2012.

Research Article

Strength Characteristics and Slope Stability of Expansive Soil from Pingdingshan, China

Ju-yun Zhai [1] and Xiang-yong Cai[2]

[1]*Henan University of Urban Construction, Pingdingshan, Henan, China*
[2]*Pingdingshan Government Water Saving Management Office, Pingdingshan, Henan, China*

Correspondence should be addressed to Ju-yun Zhai; 331626242@qq.com

By analyzing the characteristics of expansive soil from Pingdingshan, China, the shear strength parameters at different water contents, dry densities, and dry-wet cycles of expansive soil are obtained. It is found that, at higher soil-water content, the internal friction angle is 0° and the shallow layer of expansive soil slope will collapse and destroy; this has nothing to do with the height of the slope and the size of the slope. The parameters of soil influenced by atmosphere are the ones which have gone through dry-wet cycles, and the parameters of soil without atmospheric influence are the same as those of natural soil. In the analysis of slope stability, the shear strength parameters of soil can be determined by using the finite element method, and the stability coefficient of the expansive soil slope can be calculated.

1. Introduction

Disasters, such as deformation and destruction, occur to natural slopes, roads, mounds, foundation pits, and artificial slopes of underground engineering excavation, resulting in great economic losses [1]. Especially, a series of disasters, such as crack, landslide, and slump, are more apt to occur to expansive soil because of the water sensitivity [2–4]. The strength of expansive soil slope shallow layers is greatly affected by climatic conditions [5–7]. The study on the strength and slope stability of expansive soil is of great significance to control and prevent the natural disasters [8–10].

Much work has been done on the expansive soils. Experimental study on drying and wetting cycles of undisturbed expansive soil in Nanning area has been done in [11]. Tang and Shi studied the deformation on drying and wetting cycles of the pukou area in nanjing [12]. Wei and Wang studied the expansion and shrinkage deformation mechanism of solidified expansive soil [13]. Zhai et al. studied the permeability and intensity characteristics of expansive soil from Pingdingshan [14]. There are few reports on the stability of the Pingdingshan expansive soil slope under the influence of the atmosphere.

This paper simulates the effects of the atmosphere. Based on the analysis of the different water contents, dry densities and strength characteristics of the expansive soil in Pingdingshan, the stability of the Pingdingshan expansive soil slope under the influence of the atmosphere is studied. It could provide a reference for engineering design.

2. Brief Introduction to Expansive Soil from Pingdingshan

The expansive soil from Pingdingshan is meanly montmorillonite. The humidity coefficient is 0.7–0.8, the depth of atmospheric influence is generally <4 m, and the sharp depth of the atmospheric influence is 1.5~1.8 m. Parameters of natural soil samples that have been tested are as follows: natural water content of 20%~26%, natural density of 1.8~2.0 g/cm^3, dry density of 1.5~1.7 g/cm^3, pore ratio of 0.69~0.81, compression index of 0.08~0.15, cohesive force of 35~85 kPa, internal friction angle of 9~27°, and free expansion rate of 51–71.

TABLE 1: Pingdingshan expansive soil chemical composition and content.

Constituent	Content (%)
SiO_2	53.26
CaO	11.02
Al_2O_3	3.46
MgO	0.416
P_2O_5	0.166
Fe_2O_3	20.37
CuO	1.275
K_2O	0.840
TiO_2	0.216
SO_3	0.131
MnO	0.0979
ZnO	0.0575
SrO	0.005
Tb_4O_7	0.002
Compton	0.866
Na_2O	0.059
PbO	0.0403
ZrO_2	0.004
Rayleigh	74.5
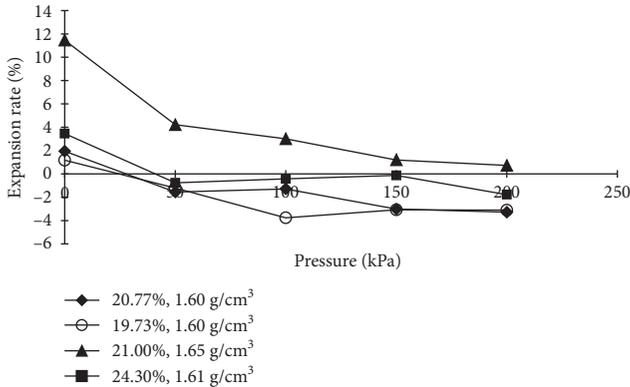
FIGURE 1: Dependence of the expansion on the vertical pressure.

3. The Characteristics of the Expansive Soil from Pingdingshan

3.1. The Selection of Expansive Soil Samples.
The disturbed soil samples of expansive soil taken for experiment are at the intersection of the construction road and the Dongfeng road in Pingdingshan city. Through the indoor soil test, the plastic limit of the expansive soil is 22.85%, the 17 mm liquid limit is 45.72%, and the free expansion rate is 55%. The chemical composition and content of expansive soil are shown in Table 1.

3.2. Deformation Parameters of Expansive Soil.
To the representative expansion soil which was air-dried, grounded, and sieved by a 2 mm sieve was added appropriate amount of water, stirred evenly, and was finally made into remolding
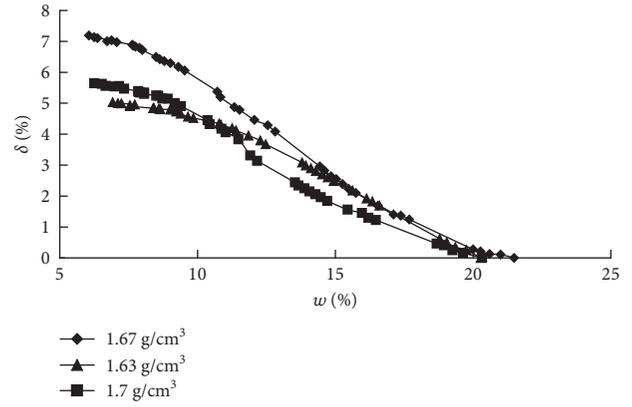
FIGURE 2: Dependence of the shrinkage on the water content A.
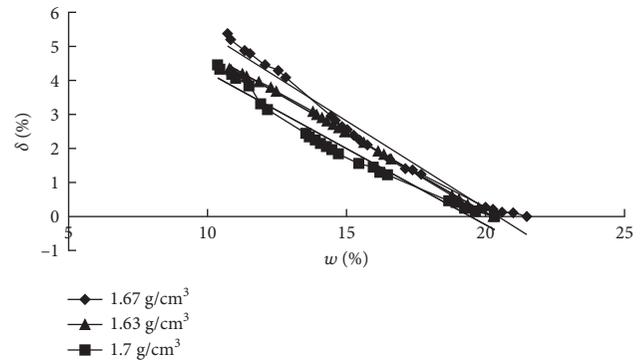
FIGURE 3: Dependence of the shrinkage on the water content B.

soil samples of different water contents and dry densities. After compaction, the diameter of the samples is 61.8 mm and the height is 20 mm. Furthermore, by studying the expansion-shrinkage deformation, the deformation parameters were obtained. The relation curves of the expansion rate with vertical pressure are shown in Figure 1.

The relation curves of the shrinkage rate with water content were obtained by shrinkage test at three different dry densities of expansive soils, as shown in Figure 2.

The straight line of Figure 2 is fitted with a straight-line equation, as shown in Figure 3.

The following can be found:

The dry density: 1.67 g/cm^3; the water content: 21%; the fitting equation: $y = -0.5144x + 10.522$; and $R^2 = 0.977$.

The dry density: 1.63 g/cm^3; the water content: 21%; the fitting equation: $y = -0.4692x + 9.4898$; and $R^2 = 0.999$.

The dry density: 1.70 g/cm^3; the water content: 20%; the fitting equation: $y = -0.4474x + 8.7071$; and $R^2 = 0.9688$.

3.3. Strength Characteristics of Expansive Soils.
The representative expansive soil that was sieved by a 2 mm sieve was made into a sample of dry soil with the dry density of 1.5 g/cm^3 and 1.6 g/cm^3 and water content of 30%, 31%, and 33%. The shear strength curve could be obtained through direct shear test at room temperature as shown in Figure 4.
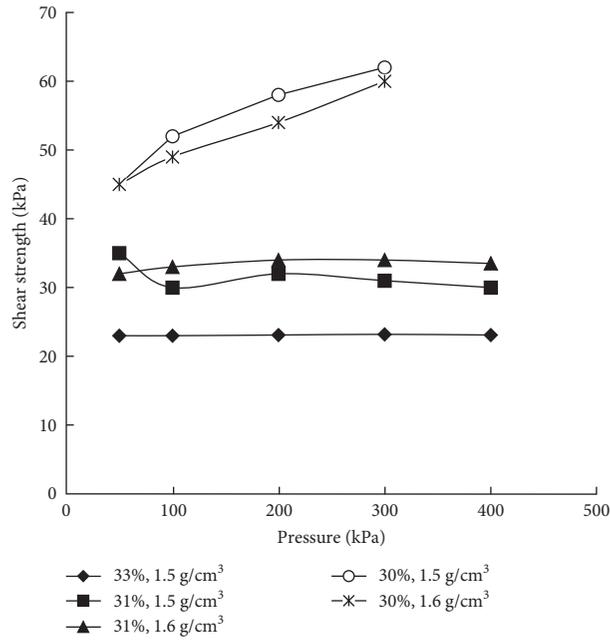
FIGURE 4: Shear strength-pressure curves at 33%, 31%, and 30% water contents.
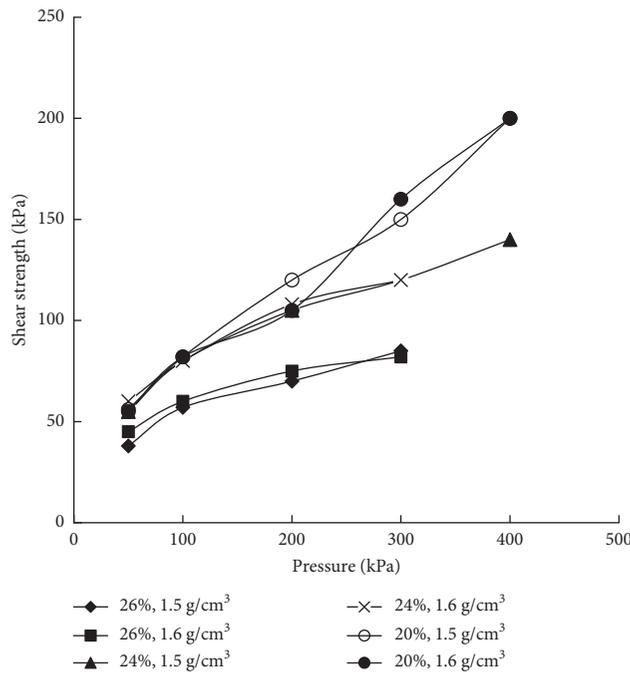
FIGURE 5: Shear strength-pressure curves at 26%, 24%, and 20% water contents.

The shear strength of the expansive soil under a high water contentunder the same pressure decreases significantly with the increase of water content (Figure 4). And the internal friction angle decreases to 0, when the water content increases over a certain degree. Meanwhile, the value of cohesion decreases significantly with the increase in water content. The collapse of slope is unconcerned about slope height and slope foot size, on a heavy rainfall condition.

Therefore, the effective measure of slope protection is to handle slope waterproofing and drainage well.

The shearing testing of the expansive soil of water content of 26%, 24%, 20%, dry density of 1.5 g/m^3, 1.6 g/m^3 is carried out. The curve is shown in Figure 5.

The internal friction angle of the expansive soil decreases with the increase of water content, under a low water content. And the shear strength changed with the density of

TABLE 2: Shear strength parameters of expansive soil at the dry density of 1.5 g/cm³.

Water content (%)	Angle of internal friction (°)	Cohesive force (kPa)
19.11	25.0	44.0
20.00	21.7	46.0
21.12	18.0	58.0
24.00	13.0	61.2
25.00	10.0	50.0
26.00	9.5	43.2
30.00	4.0	45.1
31.00	0.0	33.51
33.00	0.0	24.16

TABLE 3: Shear strength parameters of expansive soil at the dry density of 1.6 g/cm³.

Water content (%)	Angle of internal friction (°)	Cohesive force (kPa)
19.11	28.0	36.0
20.00	23.4	37.0
21.12	16.1	68.0
24.00	12.2	67.2
25.00	8.1	58.0
26.00	6.4	55.7
30.00	3.6	43.2
31.00	0.0	34.2
33.00	0.0	24.2

soil obscurely, when the water content of soil is the same, as shown in Figure 5.

The equation of soil shear strength is

$$\tau_f = \tan \varphi \cdot \sigma + C, \tag{1}$$

where τ_f is the shear strength (kPa), φ is the angle of internal friction (°), and C is the cohesive force (kPa).

Comparing the shear strength curve fitting equation of multiple water content, the shear strength characteristics of the expansive soil at the dry density of 1.5 g/cm³ are shown in Table 2.

The shear strength characteristics of the expansive soil at the dry density of 1.6 g/cm³ are shown in Table 3:

3.4. The Characteristics of Expansive Soil during Drying and Wetting Cycles. Samples of Pingdingshan expansive soil were remolded, and the attenuation law of shear strength after drying and wetting cycles was studied in the test. The shear strength sharply reduced in the first 2~4 cycles and then tended to be stable. The stable strength parameters should be taken during the construction of the project.

Take the expansive soil sample with initial water content of 24% as an example. The soil sample passes through 1, 2, 3, 4, and 5 times dry-wet cycles. The water content ranges from
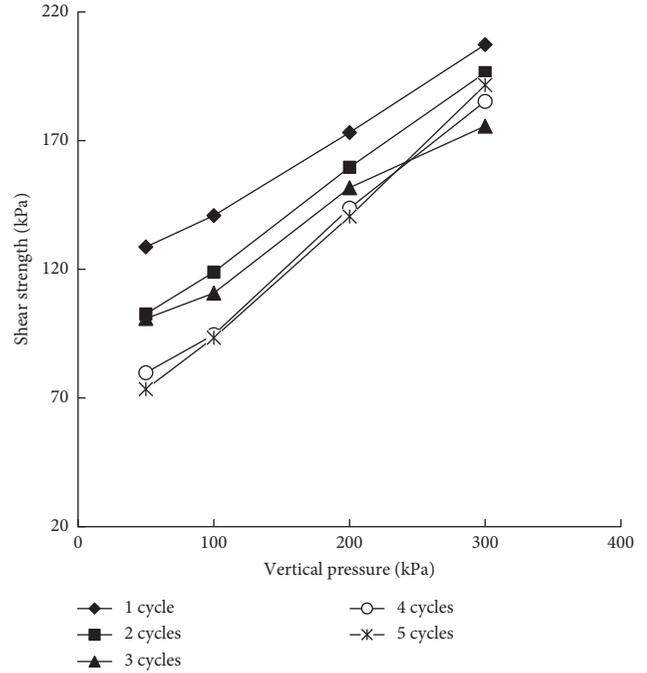
FIGURE 6: Dependence of shear strength under dry-wet cycles on the vertical pressure.

TABLE 4: The parameters of stable shear strength when the control water content is 25%.

Water content variation range (%)	Angle of internal friction (°)	Cohesive force (kPa)
32.0~13.3	9.2	20.6
32.0~17.6	7.5	44.8
32.0~25.0	8.3	35.9
29.6~15.0	7.5	40.0
29.6~16.8	9.7	38.4
29.6~18.5	10.3	44.3
27.4~16.0	10.1	39.9
27.4~17.3	11.5	45.3
27.4~18.2	13.3	40.5

24.0% to 16.6%. And then, samples of the same water content was made, which is called the control of water content. The characteristic curve of the shear strength of 20% is shown in Figure 6.

In the same way, by testing the expansive soil shear strength of other water contents under dry-wet cycles, the shear strength of the control water contents 20% and 25% is obtained. With the linear fitting of expansive soil stable strength, the strength parameters are obtained, as shown in Tables 4 and 5.

4. Calculation of Slope Stability of Expansive Soil

4.1. The Selection of the Computational Model. The stability calculation of the expansive soil slope is based on the

TABLE 5: The parameters of stable shear strength when the control water content is 20%.

Water content variation range (%)	Angle of internal friction (°)	Cohesive force (kPa)
28.0~16.1	22.5	49.6
28.0~16.9	23.7	55.1
28.0~18.7	36.5	72.8
26.0~13.6	25.5	19.9
26.0~15.8	26.0	53.376
26.0~17.6	24.0	54.2
24.0~11.8	25.3	45.4
24.0~15.1	26.5	58.0
24.0~16.6	22.5	57.0

TABLE 6: The calculation coordinates of each node with the vertical projection of 6 m.

Node label	0	−1	−2	1	2	3	4	5	6	7
X coordinate	0	6	16	−6	9	8	20	15	25	−8
Y coordinate	0	6	6	−5	−6	2	−6	3	5	0
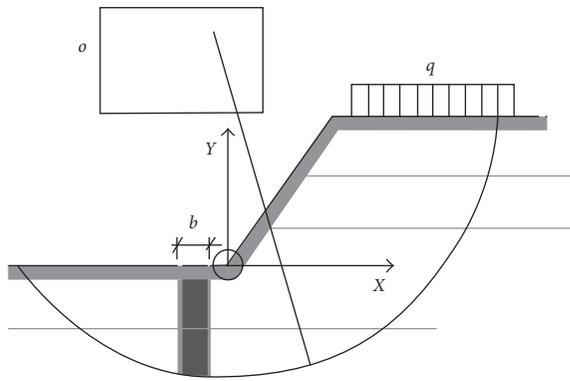
FIGURE 7: The position of the most unfavorable center.

TABLE 7: The slope safety factor and the most unfavorable center position with the horizontal projection of 10 m.

Serial number	Slope height (m)	Slope angle (°)	The most unfavorable center (m)	Radius (m)	Safety factor
1	8	38.7	(4.267, 10.133)	15.82	1.79
2	10	45.0	(1.000, 18.000)	18.03	1.52
3	11	47.7	(0.000, 18.700)	18.70	1.37
4	12	50.2	(0.000, 19.200)	19.20	1.25
5	15	56.3	(−3.000, 22.000)	22.20	1.01

TABLE 8: The safety factor and radius at the slope height of 6 m.

Serial number	Horizontal projection (m)	Slope angle (°)	The most unfavorable center (m)	Radius (m)	Safety factor
1	6	45.0	(2.400, 9.600)	9.89	2.08
2	5	50.2	(1.200, 10.800)	10.87	1.96
3	4	56.3	(1.200, 10.800)	10.87	1.95
4	3	63.4	(0.000, 9.600)	9.60	1.73
5	2	71.6	(−2.400, 10.800)	11.10	1.58
6	1	80.5	(−3.300, 9.600)	10.15	1.43
7	0	90.0	(−3.000, 0.000)	8.75	1.35

FIGURE 8: Segmentation position of the slope soil unit.

Swedish method. The safety factor could be calculated, and the position of the most unfavorable center could be searched by Lizheng software, as shown in Figure 7. In the figure, $b = 1$ m is the width of the earth bar and $q = 30$ kPa is the overload size.

Shear strength parameters of slope soil are different at different positions. The slope is divided into multiple units, as shown in Figure 8.

In the shallow layer of the soil, the shear strength parameters within 2 m from the soil surface are the same as those after dry-wet cycles. The shear strength parameters deeper than 2 m are the same as those of the initial soil.

4.2. Calculation of Slope Safety Factor. The horizontal projection of the expansive soil slope is 10 m and the vertical projection is 6 m. The coordinates of each node calculation unit are shown in Table 6.

Soil slopes are divided into multiple areas by the nodes. The density of the soil is 20 kN/m³. The water content of each area is determined by the indoor tests. The shear strength parameters of shallow soil are the stable parameters, which after the dry-wet cycles are $C = 40$ kPa and $\varphi = 11°$. The parameters of inner area are the same as natural soil strength parameters: $C = 40$ kPa and $\varphi = 17°$.

With the horizontal projection of 10 m, the slope safety factor and the most unfavorable center position at different slope heights are calculated by the Lizheng software, as shown in Table 7.

TABLE 9: The safety factor and radius at the slope height of 8 m.

Serial number	Horizontal projection (m)	Slope angle (°)	The most unfavorable center (m)	Radius (m)	Safety factor
1	9	41.6	(3.200, 12.800)	13.19	1.82
2	8	45.0	(2.133, 12.800)	12.98	1.74
3	7	48.8	(1.067, 12.800)	12.84	1.65
4	6	53.1	(0.000, 14.400)	14.40	1.57
5	5	58.0	(0.000, 12.800)	12.80	1. 50
6	4	63.4	(−2.800, 14.400)	14.67	1.41
7	3	69.4	(−2.600, 12.800)	13.06	1.33
8	2	76.0	(−7.200, 16.000)	17.54	1.22
9	1	82.9	(−7.700, 14.400)	16.33	1.13
10	0	90.0	(−6.000, 11.200)	12.54	1.07

TABLE 10: The safety factor and radius at the slope height of 9 m.

Serial number	Horizontal projection (m)	Slope angle (°)	The most unfavorable center (m)	Radius (m)	Safety factor
1	10	43.0	(2.057, 16.200)	16.33	1.70
2	9	45.0	(1.030, 16.200)	16.23	1.62
3	8	48.4	(0.000, 16.200)	16.20	1.54
4	7	52.1	(0.000, 16.200)	16.20	1.47
5	6	56.3	(0.000, 14.400)	14.40	1.41
6	5	61.0	(−2.000, 16.200)	16.32	1.34
7	4	66.0	(−4.200, 16.200)	16.74	1.27
8	3	71.6	(−6.500, 18.000)	19.14	1.19
9	2	77.5	(−8.400, 18.000)	19.86	1.11
10	1	83.7	(−9.900, 18.00)	20.54	1.03
11	0	90.0	(−9.000, 14.400)	16.81	0.97

TABLE 11: The safety factor and radius at the slope height of 10 m.

Serial number	Horizontal projection (m)	Slope angle (°)	The most unfavorable center (m)	Radius (m)	Safety factor
1	10	45.0	(1.000, 18.000)	18.03	1.52
2	8	51.3	(0.000, 17.000)	17.00	1.38
3	7	55.0	(0.000, 16.000)	16.00	1.32
4	6	59.0	(−2.130, 17.000)	17.13	1.27
5	5	63.4	(−3.000, 17.000)	17.26	2.21
6	4	68.2	(−5.600, 8.000)	18.82	1.15
7	3	73.3	(−6.500, 17.000)	18.20	1.08
8	2	78.7	(−10.800, 20.000)	22.73	1.02
9	1	84.3	(−13.200, 20.000)	23.96	0.94
10	0	90.0	(−11.000, 17.000)	20.10	0.90

Similarly, the safety factor and the radius at the slope heights of 6 m, 8 m, 9 m, and 10 m are calculated, as shown in Tables 8–11.

4.3. Analysis of Safety Factor of Expansive Soil at Different Slope Heights. The safety factor at different slope heights of 6 m, 8 m, 9 m, and 10 m, with the abscissa of level projection and the ordinate of safety factor, is shown in Figure 9.

5. Conclusion

In this paper, the physical and mechanical characteristics of expansive soils from Pingdingshan are analyzed, which provide a reliable basis for engineering design and they can be used in the calculation of slope stability. The finite element method is used to calculate the different positions of the soil slope layers and select the corresponding strength parameters.
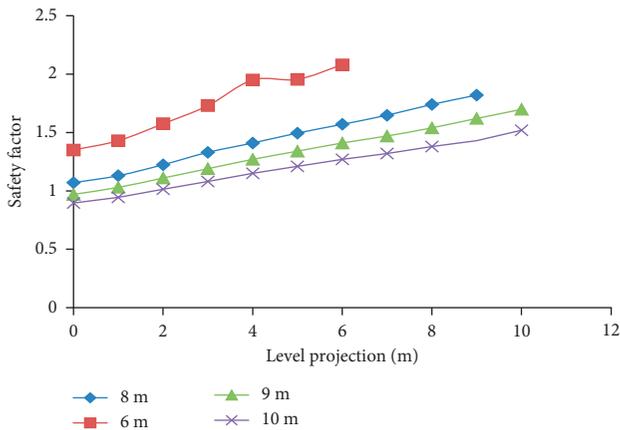
FIGURE 9: Change in slope safety factor with slope level projection.

Conflicts of Interest

No potential conflicts of interest were reported by the authors.

Acknowledgments

References

[1] D. Zhou, Y.-G. Sun, G.-Y. Le et al., "Model test of the influence of environmental factors on temperature field in expansive soil slope," *Journal of Guangxi University*, vol. 36, no. 4, pp. 653–658, 2011.

[2] L.-T. Zhan, "Study on soil-water interaction in unsaturated expansive soil slops," *Journal of Zhejiang University*, vol. 40, no. 3, pp. 496-497, 2006.

[3] T.-H. Liu, *Expansive Soil Problem of Construction*, China Architecture & Building Press, Beijing, China, 1997.

[4] Y. Xie, Z.-H. Chen, and G. Li, "Research of thermal effects on shear strength and deformation characteristics of unsaturated bentonite soils," *Chinese Journal of Geotechnical Engineering*, vol. 27, no. 9, pp. 1082–1085, 2005.

[5] B. D. De and J. F. Thimus, "The influence of temperature on mechanical characteristics of boom clay: the results of an initial laboratory programme," *Engineering Geology*, vol. 41, pp. 17–126, 1996.

[6] Y.-X. Gao, Z. Feng, and J.-L. Zheng, "Temperature properties of sheer strength for unsaturated soil," *Journal of Changsha Communications University*, vol. 18, no. 4, pp. 68–71, 2002.

[7] J.-H. Wu, J.-P. Yuan, L.-J. He, and T.-H. Lu, "Study on distribution and change laws of soil water content due to evaporation," *Journal of Disaster Prevention and Mitigation Engineering*, vol. 3, no. 3, pp. 290–294, 2013.

[8] Y. Zheng, W. Ma, and H. Bing, "Impact of freezing and thawing cycles on the structures of soil and a quantitative approach," *Journal of Glaciology and Geocryology*, vol. 37, no. 1, pp. 132–137, 2015.

[9] S. A. B. Mrabent, A. Hachichi, H. Souli, S. Taibi, and J.-M. Fleureau, "Effect of lime on some physical parameters of a natural expansive clay from Algeria," *European Journal of Environmental and Civil Engineering*, vol. 21, no. 1, pp. 108–125, 2017.

[10] A. Boukelia, H. Eslami, S. Rosin-Paumier, and F. Masrouri, "Effect of temperature and initial state on variation of thermal parameters of fine compacted soils," *European Journal of Environmental and Civil Engineering*, pp. 1–14, 2017.

[11] H.-B. Lv, Z.-T. Zeng, Y.-L. Zhao, and H. Lu, "Experimental studies of strength of expansive soil in drying and wetting cycles," *Rock and Soil Mechanics*, vol. 30, no. 12, pp. 3797–3802, 2009.

[12] C.-S. Tang and B. Shi, "Swelling and shrinkage behaviour of expansive soil during wetting-drying cycles," *Chinese Journal of Geotechnical Engineering*, vol. 33, no. 9, pp. 1376–1383, 2011.

[13] X. Wei and G. Wang, "Modeling swell-shrink behavior of compacted expansive clays subjected to cyclic drying and wetting," *Chinese Journal of Geotechnical Engineering*, vol. 36, no. 8, pp. 1423–1431, 2014.

[14] J.-Y. Zhai, X. Hao, G.-X. Wei et al., "Strength characteristics of expansive soil during drying and wetting cycles," *Electronic Journal of Geotechnical Engineering*, vol. 22, no. 12, pp. 4579–4588, 2017.

Research Article

Assessment of Real-Time Compaction Quality Test Indexes for Rockfill Material Based on Roller Vibratory Acceleration Analysis

Tianbo Hua [iD],[1,2] **Xingguo Yang** [iD],[1,2] **Qiang Yao** [iD],[1,2] **and Hongtao Li** [iD][1,2]

[1]*State Key Laboratory of Hydraulics and Mountain River Engineering, Sichuan University, Chengdu, Sichuan 610065, China*
[2]*College of Water Resource and Hydropower, Sichuan University, Chengdu, Sichuan 610065, China*

Correspondence should be addressed to Hongtao Li; htl@scu.edu.cn

Compaction quality is directly related to the structure and seepage stability of a rockfill dam. To timely and accurately test the compaction quality of the rockfill material, four real-time test indexes were chosen to characterize the soil compaction degree based on the analysis of roller vibratory acceleration, including acceleration peak value (a_p), acceleration root mean square value (a_{rms}), crest factor value (CF), and compaction meter value (CMV). To determine which of these indexes is the most appropriate, a two-part field compaction experiment was conducted using a vibratory roller in different filling zones of the dam body. Data on rolling parameters, real-time test indexes, and compaction quality indexes were collected to perform statistical regression analyses. Combined with the spectrum analysis of the acceleration signal, it was found that the CF index best characterizes the compaction degree of the rockfill material among the four indexes. Furthermore, the quantitative relations between the real-time index and compaction quality index were established to determine the control criterion of CF, which can instruct the site work of compaction quality control in the rockfill rolling process.

1. Introduction

The layered filling compaction of dam materials is an important process in the construction of a rockfill dam. An effective compaction quality control is the key to ensure the safe and stable operation of the dam. Nowadays, the compaction quality control in rockfill dam projects mainly depends on the manual control of rolling parameters and random spot tests after construction, which is normally called the "dual control method" [1]. With the expansion of the filling scale, this traditional compaction quality control method has been unable to meet the requirements of modern mechanized construction. Therefore, it has been quite necessary to develop a fast, real-time, and accurate compaction quality test method with continuous, automatic, and high precision characteristics.

To provide a quality-inspection process that is more reliable and timely, previous studies in the field of transportation engineering focused on correlating compaction quality to soil properties and construction-operating parameters that can be obtained easily and quickly from the

field. Geodynamik and Dynapac of Sweden characterized compaction quality by compaction meter value (CMV), which is the ratio between the amplitude of the first harmonic and that of the fundamental frequency [2, 3]. Previous studies verified that CMV is closely related to the fundamental reaction and physical properties of the compacted soil [4–7]. According to Forssblad [8–11], CMV has been noted to range from 40 to 70 for gravel, from 25 to 40 for sand, and from 20 to 30 for silt.

The compaction control value (CCV) adopted by Sakai company is similar to CMV, which is also determined from the measured acceleration data but based on more harmonic frequency components, including 0.5, 1, 1.5, 2, 2.5, and 3 fundamental frequency and harmonic components [12, 13]. Caterpillar used machine drive power (MDP) to determine the compaction characteristics in road work [14, 15], which originated from the study of vehicle-terrain interaction [16]. Researchers found that MDP is highly correlated with compaction density and elastic modulus of the soil [17–19].

Bomag from Germany used a software algorithm which derived from a mechanical model to calculate the dynamic

modulus E_{vib} of the material to describe the compacted condition of soil [20]. Mooney and Rinehart [21] and Rinehart and Mooney [22] proposed that the total harmonic distortion (THD) is a highly sensitivity index to evaluate the soil compaction state. The larger the THD, the stiffer the soil will be. Ammann calculated the soil stiffness, K_B, as a measure of compaction quality [23] and verified the strong correlation between K_B and soil rigidity [24, 25]. China Southwest Jiaotong University used vibratory compaction value (VCV), a dynamic subgrade structural reaction index, to evaluate the soil compaction quality and achieved good results in a roadbed continuous compaction quality test [26].

However, the abovementioned researches are mainly carried out on the subgrade filling material. In fact, there are great differences between the rockfill in earth-rock dams and the subgrade filler in road engineering in terms of the soil particle size and shape. At present, the maximum particle size of the rockfill in hydropower projects has reached 1 m, and many particles are solid block stones with sharp and jagged edges. In contrast, the maximum particle size of the subgrade filler is generally less than often 150 mm, and the main contents are spherical particles with few edges [13]. This makes the compaction characteristics of the two materials quite different. Therefore, further study is needed to know whether the index that applied well on subgrade filler can also achieve excellent test results on the rockfill material of earth-rock dams.

The objective of this study is to obtain an index that can characterize the compaction degree of the rockfill material timely and accurately. The rockfill material tested in the experiment belongs to cohesionless coarse-grained soil; therefore, the compaction degree in the study actually refers to the physical indicator of relative density. The following section first analyzes the relationship between the roller vibratory acceleration and the soil compaction degree. Then, combined with the abovementioned study, four real-time test indexes derived from acceleration signal were chosen to characterize the rockfill compaction degree. To analyze and judge the detection effect of each index on the rockfill material, comparison experiments were conducted in different filling zones of the dam body with different rolling parameters. Statistical regression analysis of test data and spectrum analysis of acceleration signal were then performed to get the final conclusions.

2. Methodology

This section first introduces the terrain-vehicle dynamical model in the existing literature and analyzes the relationship between roller vibratory acceleration and the compacted condition of soil. Next, the four real-time test indexes utilized in the experimental test are introduced, with their calculating methods and physical significances elaborated. Finally, the testing method and equipment are presented.

2.1. Vibration Model. According to the study of terrain-vehicle systems [16] and the research on the vibratory roller from Yoo and Selig [27–29], it can be known that the acceleration of the vibratory roller is closely related to the
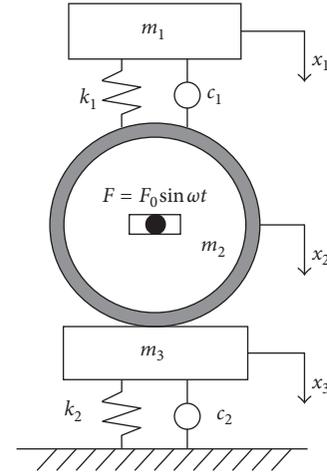
FIGURE 1: Terrain-vehicle dynamical model. m_1: frame mass, m_2: roller mass, m_3: soil mass, k_1: roller-frame stiffness, c_1: roller-frame damping, k_2: soil stiffness, c_2: soil damping, x_1: vertical displacement of frame, x_2: vertical displacement of roller, x_3: vertical displacement of soil, F: excitation force, $\ddot{x}$: acceleration.

compaction condition of the pressed material. The terrain-vehicle vibration model [29] can be described as in Figure 1.

To facilitate the calculation and analysis, the model is simplified by not taking the horizontal displacement and jump vibration of the vibratory roller into account. In such case, m_2 and m_3 always remain in contact, that is, $x_2 = x_3$. The force equations between the layers are expressed as

$$m_1 \ddot{x}_1 + c_1 (\dot{x}_1 - \dot{x}_2) + k_1 (x_1 - x_2) = 0,$$
$$(m_2 + m_3)\ddot{x}_2 + (c_1 + c_2)\dot{x}_2 + (k_1 + k_2)x_2 \qquad (1)$$
$$- c_1 \dot{x}_1 - k_1 x_1 = F_0 \sin \omega t.$$

The equations can be expressed into matrix form as

$$\begin{bmatrix} m_1 & 0 \\ 0 & m_2 + m_3 \end{bmatrix} \begin{bmatrix} \ddot{x}_1 \\ \ddot{x}_2 \end{bmatrix} + \begin{bmatrix} c_1 & -c_2 \\ -c_1 & c_1 + c_2 \end{bmatrix} \begin{bmatrix} \dot{x}_1 \\ \dot{x}_2 \end{bmatrix}$$
$$+ \begin{bmatrix} k_1 & -k_2 \\ -k_1 & k_1 + k_2 \end{bmatrix} \begin{bmatrix} x_1 \\ x_2 \end{bmatrix} = \begin{bmatrix} 0 \\ F_0 \sin \omega t \end{bmatrix}. \qquad (2)$$

By analytic calculation, we can obtain

$$|\ddot{x}_2| = \omega^2 |x_2| = \omega^2 F_0 \left(\frac{A_1^2 + B_1^2}{C^2 + D^2} \right)^{1/2} = f(k_2, c_2), \qquad (3)$$

where $A_1 = k_1 - m_1\omega^2$, $B_1 = c_1\omega$, $C = (m_2 + m_3)m_1\omega^4 - (m_2 + m_3)k_1\omega^2 - m_1k_2\omega^2 - c_1c_2\omega^2 + k_1k_2 - m_1k_1\omega^2$, and $D = k_2c_1\omega + k_1c_2\omega - (m_2 + m_3)c_1\omega^3 - m_1c_2\omega^3 - m_1c_1\omega^3$.

It can be seen from (3) that the vertical vibratory acceleration of the roller ($\ddot{x}_2$) is related only to the stiffness k_2 and damping c_2 of the pressed soil. With the stiffness and damping of the soil directly reflecting the compactness of the soil, the roller vibratory acceleration (hereinafter referred to as a) and the soil compaction degree are closely related. However, due to the complexity of (3), the relationship between k_2, c_2, and a cannot be expressed with a definite function formula. The purpose of the experiment

is to gain a dataset of roller vibratory acceleration and soil compactness, then finding out the definite relationship between them.

2.2. Real-Time Test Indexes.
The study of Zhong et al. [30, 31] and Liu et al. [32, 33] indicates that describing the soil compactness by directly using vibratory acceleration index a causes much uncertainty and volatility. Therefore, the following four derived indexes are selected by analyzing the roller acceleration signal.

2.2.1. Acceleration Peak Value (a_p).
This index describes the amplitude variation of roller acceleration signal and is calculated as

$$a_p = \max\{|a_i|\} \quad (i = 1, 2, \ldots, n), \tag{4}$$

where a_i is a random acceleration measurement and n is the number of collected samples within a certain period.

2.2.2. Acceleration Root Mean Square Value (a_{rms}).
This index reflects the effective vibratory acceleration in the rolling process, which is calculated as

$$a_{rms} = \sqrt{\frac{1}{n} \sum_{i=1}^{n} a_i^2} = \sqrt{\frac{a_1^2 + a_2^2 + \cdots + a_n^2}{n}}. \tag{5}$$

2.2.3. Crest Factor Value (CF).
This index is a common evaluation index in alternating current, which is used to describe the ability of the AC power to output peak load current [34]. The CF value of a standard sinusoidal wave is 1.414. When the wave is distorted, the CF changes significantly. It is used by the authors to describe the waveform variation law of the roller vibratory acceleration signal and is defined as

$$CF = \frac{a_p}{a_{rms}}. \tag{6}$$

The formula shows that CF is a dimensionless acceleration index that integrates the variation trend of a_p and a_{rms}. The physical meaning of the index in this experiment is to describe the ability of the roller to output peak acceleration, namely, the ability of the soil to produce the greatest reaction force to the roller.

2.2.4. Compaction Meter Value (CMV).
The index shows the ratio between the amplitude of the first harmonic and that of the fundamental frequency, which is obtained by the tuning analysis of the acceleration signal. The definition of CMV is expressed as

$$CMV = C \cdot \frac{A_1}{A_0}, \tag{7}$$

where C is the amplification coefficient and usually sets as 300, A_1 refers to the amplitude of the first harmonic of vibratory acceleration, and A_0 refers to the amplitude of the fundamental frequency of vibratory acceleration.

2.3. Testing Method.
The experiment adopts the DHDAS dynamic signal acquisition system of Donghua (Figure 2), which mainly includes the acceleration sensor, the vibration data acquisition instrument, and the monitoring and analysis software for clients. The main physical quantity tested in the experiment is the vertical vibratory acceleration of the roller and its main vibration frequency. The roller used is the 32 t single-drum vibratory roller of Jointark mechanical YZ series (Figure 3). The sensors were installed vertically on the inner frame of the roller, and the data were collected simultaneously with the dual channel.

The a_p index is directly read by DHDAS software, and a_{rms} index is calculated by (5) with the tested acceleration data in a certain period. The CF is worked out by (6) with the measured a_p and a_{rms}. CMV is calculated by (7) with the amplitude of the first harmonic and that of the fundamental frequency in the spectrum of acceleration signal, which is obtained through fast Fourier transformation (FFT) analysis.

3. Experimental Testing

3.1. Testing Site and Materials.
The experiment was carried out at the construction site of Chang-he Dam hydropower station, which located in Dadu River, China. The Chang-he Dam is a 240-meter-high core rockfill dam, and the structural design of it is shown in Figure 4. The experimental material includes the main rockfill, secondary rockfill, and filter material. Figure 5 shows the field experiment on the main rockfill, and the grain size distribution of the material is shown in Figure 6(a). The main compaction parameters of the test material are shown in Table 1.

In Table 1, the parameter "rolling times" means the compaction pass of the vibratory roller on each strip. The index relative density is defined as

$$D_r = \frac{e_{max} - e}{e_{max} - e_{min}} = \frac{(\rho_d - \rho_{d\,min})\rho_{d\,max}}{(\rho_{d\,max} - \rho_{d\,min})\rho_d}, \tag{8}$$

where e_{max} is the maximum void ratio, e_{min} is the minimum void ratio, e is the compacted void ratio, $\rho_{d\,max}$ refers to the maximum dry density, $\rho_{d\,min}$ refers to the minimum dry density, and ρ_d refers to the compacted dry density.

The index ρ_d is calculated by measuring the volume and dry weight of the soil sample collected from the field. The index $\rho_{d\,max}$ and $\rho_{d\,min}$ need to be measured in the laboratory individually. As the maximum particle size that can be tested by the device in the lab is 60 mm, the maximum grain size of the rockfill in the project has reached 800 mm. The oversize particles were replaced by the soil whose particle size is smaller than 60 mm and larger than 5 mm with equal mass, and at the ratio calculated by (9), which is called the equivalent weight replacement method [35]. The grading curve of the main rockfill after replacement is shown in Figure 6(b).

$$P_i = \frac{P_{oi}}{P_5 - P_{d\,max}} P_5, \tag{9}$$

(a)   (b)

FIGURE 2: DHDAS dynamic signal acquisition and analysis system. (a) Data acquisition instrument. (b) Data analysis system.

(a)   (b)

FIGURE 3: The vibratory roller and setting of sensors. (a) Vibratory roller. (b) Setting of sensors.
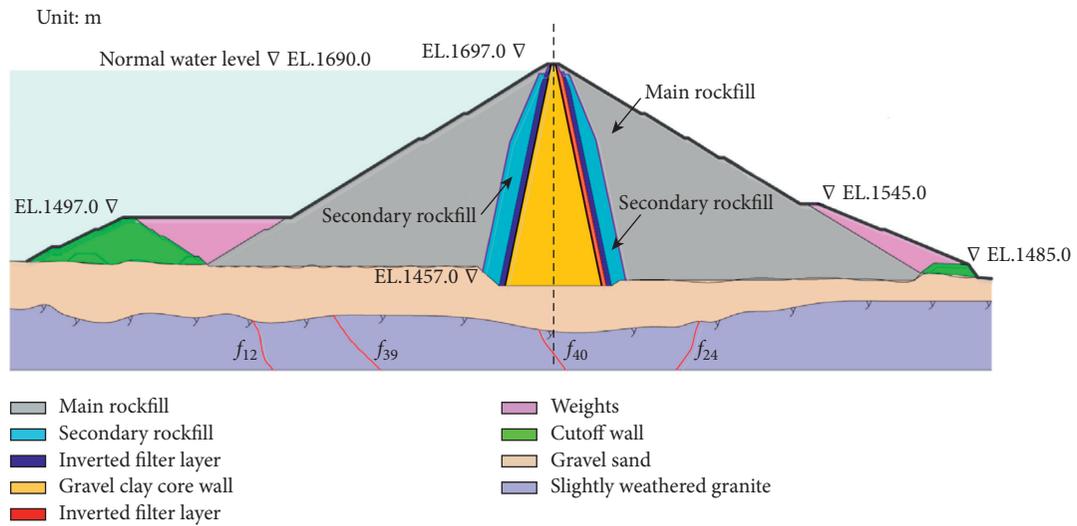
FIGURE 4: Structural diagram of Chang-he Dam.

where P_i refers to the weight percentage of some particle size group in the soil after replacement, P_{oi} refers to the weight percentage of some particle size group in the original soil, P_5 refers to the weight percentage of the soil whose particle size is larger than 5 mm, and $P_{d\max}$ refers to the weight percentage of the oversize particles in the original soil.

After the replacement work to the soil sample, $\rho_{d\min}$ and $P_{d\max}$ can be calculated out with the volume and weight of the dried soil in the sample cylinder under the state of fluffy and the state after 8 min vibration on the platform vibrator respectively, which is called the loose filling test method and the platform vibrator experiment method [35], respectively.

(a)

(b)

FIGURE 5: Field experiment on the main rockfill. (a) Main rockfill. (b) Field experiment.

(a)

(b)
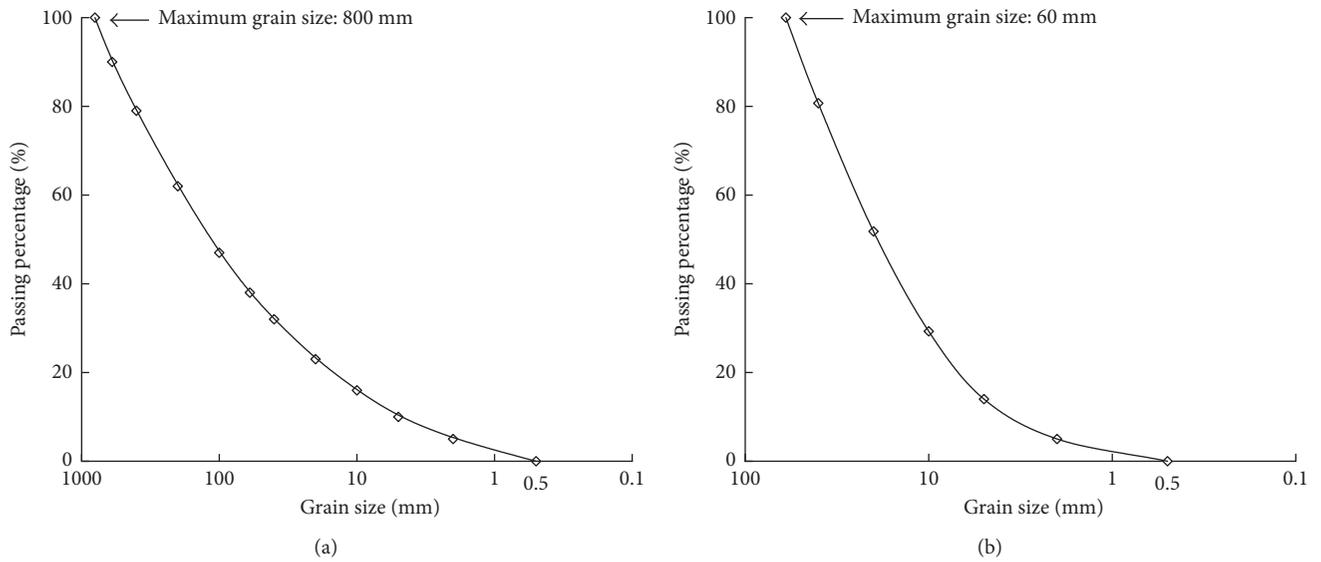
FIGURE 6: Grain size distribution of the main rockfill. (a) The original. (b) After replacement.

TABLE 1: Compaction parameters of the test material.

Testing material	Standard rolling parameters			Requirements of compaction quality indexes		
	Rolling times	Layer thickness (cm)	Driving speed (km/h)	Relative density	Dry density (g/cm^3)	Porosity
Main rockfill	Static roll (2), vibratory roll (8)	100	2.7 ± 0.2	—	≥ 2.22	$\leq 21\%$
Secondary rockfill	Static roll (2), vibratory roll (8)	50	2.7 ± 0.2	≥ 0.90	≥ 2.33	$\leq 20\%$
Filter material	Static roll (2), vibratory roll (8)	30	2.7 ± 0.2	≥ 0.85	≥ 2.08	—

3.2. Testing Program. To evaluate the test effects of indexes a_p, a_{rms}, CF, and CMV on rockfill and other dam materials comprehensively, a two-part field experiment was performed. Part 1 was used to evaluate the relationship between the four real-time test indexes and the rolling parameters. Part 2 was targeted at studying the correlation between real-time test indexes and compaction quality indexes. The results of experimental testing will provide a dataset for the subsequent modeling analysis in Section 4.

3.2.1. Experiment Part 1. Experiment part 1 was carried out with the rolling parameters of rolling times, running speed, and compaction thickness changed. Since the roller keeps in a vibration state of low frequency and high amplitude in the rolling process, the parameter of roller excitation force remains unchanged in the experiment.

For the cohesionless soil of the rockfill in the study, a high compacted dry density can be achieved under the condition of completely dry or fully saturated in the Proctor
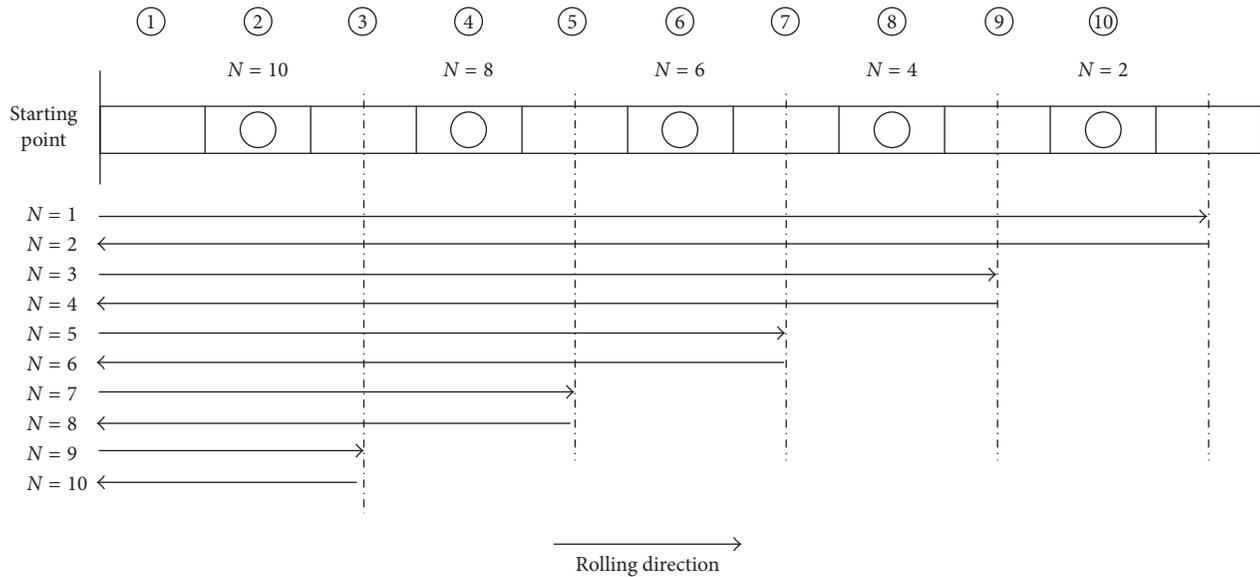
FIGURE 7: Rolling route of the vibratory roller (N: rolling times).

compaction test. However, due to the high hydraulic conductivity of the rockfill material, it is very hard for the material to keep high water content in the field compaction. And it is easy to raise dust if the dam material is completely dry, which is adverse to the construction environmental protection. Based on the comprehensive consideration of field compaction effect and construction cost and conditions, the water content of the rockfill material was kept at 1%–2% (weight ratio) in the field. The control method is to calculate and add water to the dam material automatically by using the intelligent water adding system developed by Sinohydro Bureau 5 Co., Ltd. before paving and supplement water to the paved soil with the sprinkling truck to maintain the water content before compaction.

Combined with the analysis above, the specific test plan can be made as follows by not taking the parameters of excitation force and water content into account.

(1) Change in rolling times: one rolling strip was selected in the filling zone of each test material with a length of 60 m and width of 2.2 m (width of the roller), respectively. As the dam material in the rolling strip cannot be completely even in the paving process, the data measured in different regions of the same strip change greatly. Therefore, the test strips are divided into small test areas with the grid of 5 m long and 2.2 m wide (Figure 5(b)), and the data on each small test area are analyzed separately. The standard vibratory rolling times of the test material is eight times (Table 1). In order to increase the sample volume and observe the variation trend of acceleration signal when the compaction pass exceeds standard, the number of vibratory rolling times is set at ten times.

(2) Change in running speed and compaction thickness: three adjacent strips were selected in the main and secondary rockfill zones, respectively, to analyze the change of each index brought by different running

speeds, where the vibratory roller proceeded with low speed ($v = 1.8$ km/h), medium speed ($v = 2.2$ km/h), and high speed ($v = 2.6$ km/h). The same goes to the number of test strips in the experiment of change in compaction thickness. The thickness of the test strip on main rockfill was set to be 80 cm, 100 cm, and 120 cm, respectively, and that of the secondary rockfill to be 30 cm, 60 cm, and 90 cm, respectively.

3.2.2. Experiment Part 2. To conduct the correlation test of real-time test index and compaction quality index, experiment part 2 selected four adjacent strips with a length of 50 m and width of 2.2 m in the main and secondary rockfill zones, respectively. Each test strip was divided into ten small test areas with the grid of 5 m long and 2.2 m wide and numbered ①–⑩, as shown in Figure 7. The area with odd number is the buffer area in the rolling process, and we take the test data on the even-numbered area for analysis. When the required rolling process (Figure 7) for each strip is finished, the digging test method is used to obtain the conventional compaction quality indexes in the even-numbered areas.

4. Results and Discussion

This section focuses on analyzing the correlations among rolling parameters, real-time test indexes, and compaction quality indexes according to the dataset from the two-part experiment described above. In the analysis of data correlation, the linear model and hyperbolic model are compared in a bid to determine the correlation degree of the data and establish a more appropriate correlation formula. In addition, the spectrum analysis and discussion is conducted to make an in-depth analysis on the frequency distribution regularity of acceleration signal and compare the test effects of the four indexes on different test materials.
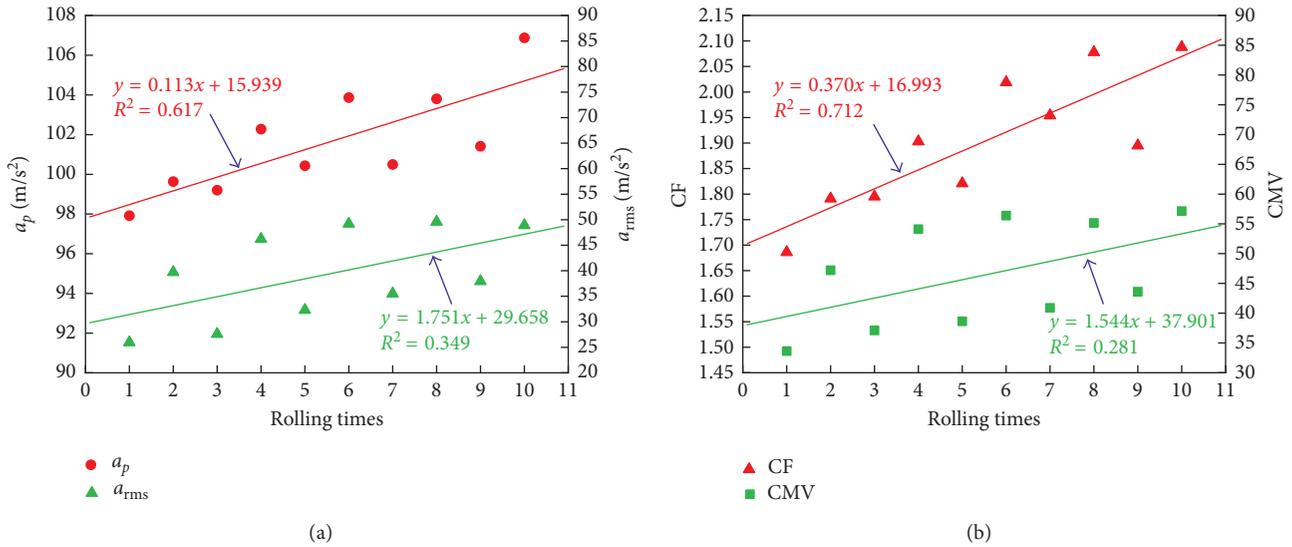
FIGURE 8: Linear relationships between real-time test indexes and rolling times. (a) a_p, a_{rms}. (b) CF, CMV.

4.1. Result Analysis of Experiment Part 1

4.1.1. Correlations between Rolling Times and the Four Indexes.
A total of 360 groups of valid data were obtained in the experiment of change in rolling times. The scatter diagram of the indexes measured on each small test area was plotted with the Origin software so as to analyze the correlation between the real-time test indexes and rolling times.

The linear model is commonly used for the correlation analysis in the study field [30–33], and the function expression of which is

$$y = a + bx, \tag{10}$$

where a and b are the regression coefficients.

Firstly, the linear model was used in the regression analysis, and the result of a certain area on the main rockfill is shown in Figure 8.

From the scatter diagram, the following two characteristics are identified:

(1) The variable y increases with the rise of x, but its growth rate gradually slows down.

(2) When variable x increases further, y gradually comes to a constant, which indicates that the curve may have a horizontal asymptote.

Thus, it can be assumed that the trend line of the scatter plot is a hyperbolic curve and the function formula of which can be expressed as

$$y = \frac{x}{ax + b}, \tag{11}$$

where a and b are the regression coefficients.

Then, the hyperbolic model was used to analyze the scatter plot described above, and the result is shown in Figure 9.

The determination coefficients (R^2) of the regression models on the small test areas of each strip are evaluated

using the trimmed mean to reduce the effect of an accidental error. The results are shown in Table 2. From this table, it can be seen that there are some correlations between all the four test indexes and rolling times on each tested dam material. Specifically, the linear correlation between CF and rolling times is the strongest, with all the determination coefficients (R^2) being over 0.7.

When considering the practical application of a test index, both its correlation degree and stability of the data in different test areas need to be taken into account. Therefore, the standard deviation coefficients (V_σ) of the 120 groups of data measured on each testing material were calculated to analyze the discrete degree of the dataset. It can be seen from the results (Table 3) that with the increase of the particle size in the filter material, the secondary rockfill and main rockfill, the V_σ of each test index also gradually increase, while the V_σ of a_p, a_{rms}, and CF stay at a low level, indicating that the data stability of a_p, a_{rms}, and CF is better.

4.1.2. Correlations between Running Speed, Compaction Thickness, and the Four Indexes.
In the experiment of change in running speed and compaction thickness, 24 sets of valid data were obtained on the main and secondary rockfill, respectively. The changes of real-time indexes brought by the two parameters on secondary rockfill are shown in Figures 10 and 11, respectively.

It can be inferred from Figures 11 and 12 that the a_p and CF show a significant downward trend with the increase of running speed and compaction thickness, respectively, and the two indexes increase regularly with the growth of rolling times. Though a_{rms} and CMV rise along with the number of rolling times in Figure 11(b), they do not show the tendency in Figure 12(b). And there is no obvious regularity in the tendencies of a_{rms} and CMV when the roller running speed and soil compaction thickness change. The results of the test on the main rockfill are the same as
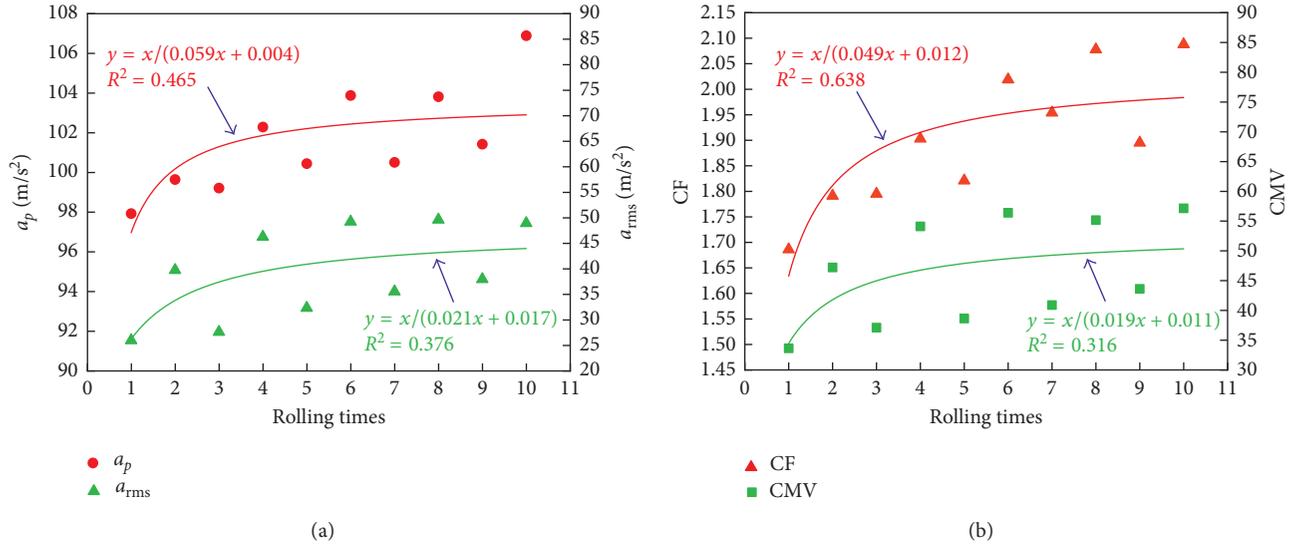
FIGURE 9: Hyperbolic relationships between real-time test indexes and rolling times. (a) a_p, a_{rms}. (b) CF, CMV.

TABLE 2: Determination coefficients (R^2) for regression analysis between real-time test indexes and rolling times.

Testing material	a_p		a_{rms}		CF		CMV	
	Linear model	Hyperbolic model	Linear model	Hyperbolic model	Linear model	Hyperbolic model	Linear model	Hyperbolic model
Main rockfill	0.601	0.628	0.584	0.486	0.731	0.679	0.496	0.498
Secondary rockfill	0.663	0.687	0.595	0.523	0.784	0.721	0.535	0.579
Filter material	0.672	0.704	0.630	0.572	0.796	0.752	0.670	0.604

TABLE 3: Standard deviation coefficients (V_σ) of real-time test indexes (%).

Testing material	a_p	a_{rms}	CF	CMV
Main rockfill	5.61	4.35	2.44	14.27
Secondary rockfill	2.90	2.88	1.27	13.28
Filter material	2.15	1.59	1.03	10.03

those on the secondary rockfill, which will not be repeated hereby.

For energy-related analysis, when the roller running speed and soil compaction thickness increase, the energy absorbed by the soil in unit and volume will decrease, respectively. With the same rolling times, the soil compaction degree is reduced. The same goes to the reaction force of the soil to the vibratory roller, which results in a decrease of the roller vibratory acceleration. Therefore, all the four derived indexes should show a declining trend, and only the tendency of a_p and CF among them are consistent with the theoretical situation.

4.2. Result Analysis of Experiment Part 2. Experiment part 2 obtained twenty groups of real-time test index and compaction quality index data on the main and secondary rockfill, respectively. For the main and secondary rockfill in the project, the main compaction quality control indexes

are porosity (P) and relative density (D_r), respectively [36]. The correlation analysis of real-time test indexes and the two compaction quality indexes is conducted in this section.

The linear regression model and hyperbolic regression model were utilized to analyze the scatter diagram plotted by the Origin software. The results of linear regression analysis on the main rockfill are shown in Figure 12, and the results on the secondary rockfill are shown in Figure 13. The determination coefficients (R^2) of the regression models are shown in Table 4.

As can be seen from Table 4, in the correlation analysis of the four test indexes and porosity, the hyperbolic model of CF and the index shows the highest R^2 of 0.823. As for relative density, the linear model of CF and the index registers the highest R^2 of 0.820. This means that the correlation between CF and the compaction quality indexes is the strongest among the four test indexes, and the regression functions can be expressed as

$$CF = \frac{P}{0.802P - 6.430}, \quad (12)$$

$$CF = 0.284D_r + 1.725. \quad (13)$$

The compaction quality control criteria on the main and secondary rockfill are $P \leq 21\%$ and $D_r \geq 0.90$, respectively. The criterion of $CF \geq 2.017$ can be got by taking $P \leq 21\%$ into (12), and $CF \geq 1.981$ can be obtained by plugging $D_r \geq 0.90$
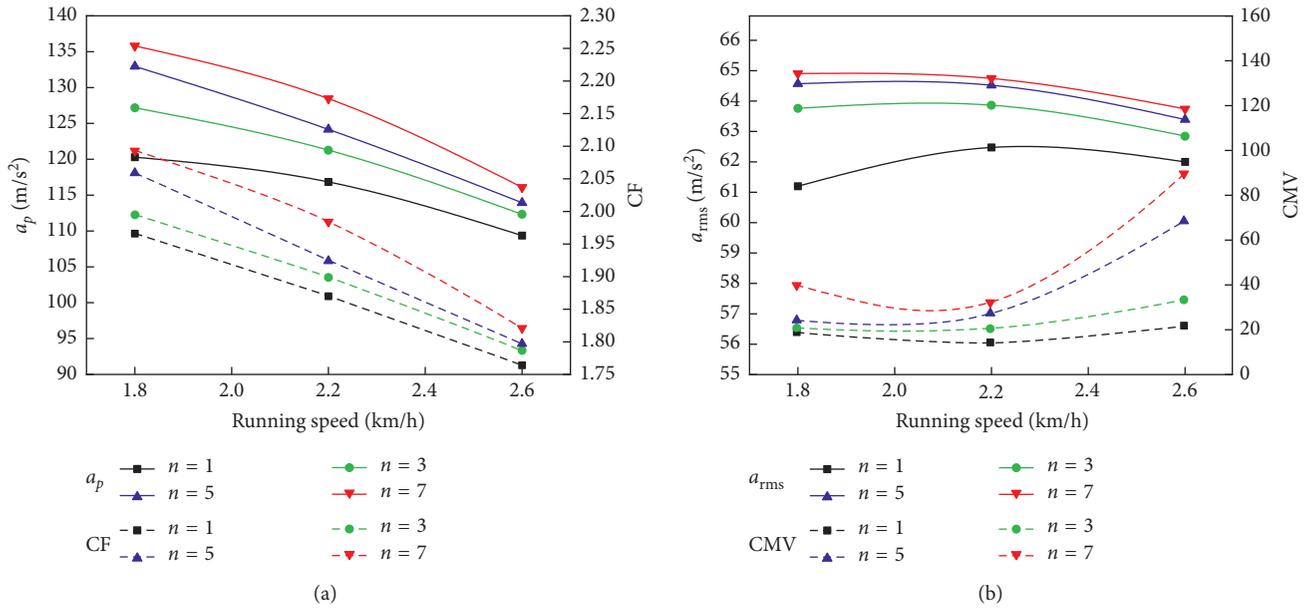
FIGURE 10: Tendency of real-time indexes with the change of running speed. (a) a_p, CF. (b) a_{rms}, CMV.
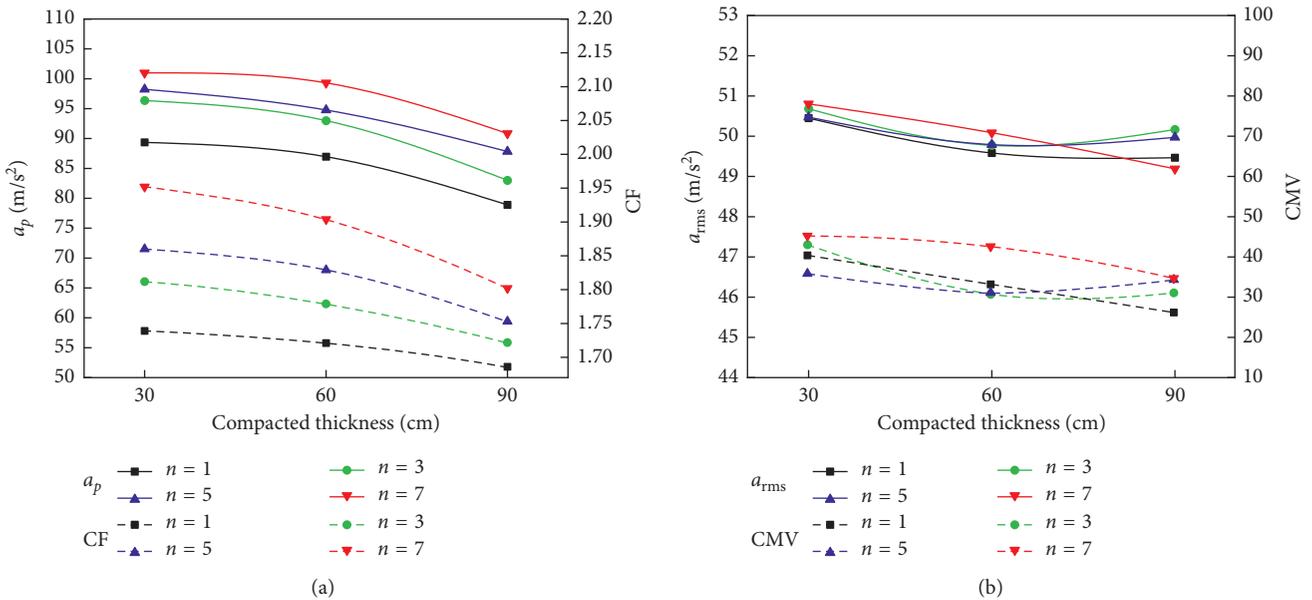
FIGURE 11: Tendency of real-time indexes with the change of compaction thickness. (a) a_p, CF. (b) a_{rms}, CMV.

into (13). It is thus tentatively believed that the compacted soil achieves the required compaction quality when the CF values reach 2.017 and 1.981 on the main and secondary rockfills, respectively. The more precise control criteria of CF values need to be determined based on the quantitative relations among the soil compaction degree, the reaction force of the soil (characterized by the acceleration indexes discussed in the paper), and the strength and stiffness of the rockfill material, which will be studied in the future work.

4.3. Spectrum Analysis and Discussion.

In order to analyze the application scope of the four indexes, this section conducted a spectrum analysis of the acceleration signal and had a further discussion about the test effects of the four indexes on different test materials. Figures 14–16 show the comparison of the acceleration signal and indexes in the eighth compaction pass of the main rockfill and filter material. The 3D spectra in Figure 15 are obtained through the fast Fourier transformation (FFT) analysis of the

(a)

(b)
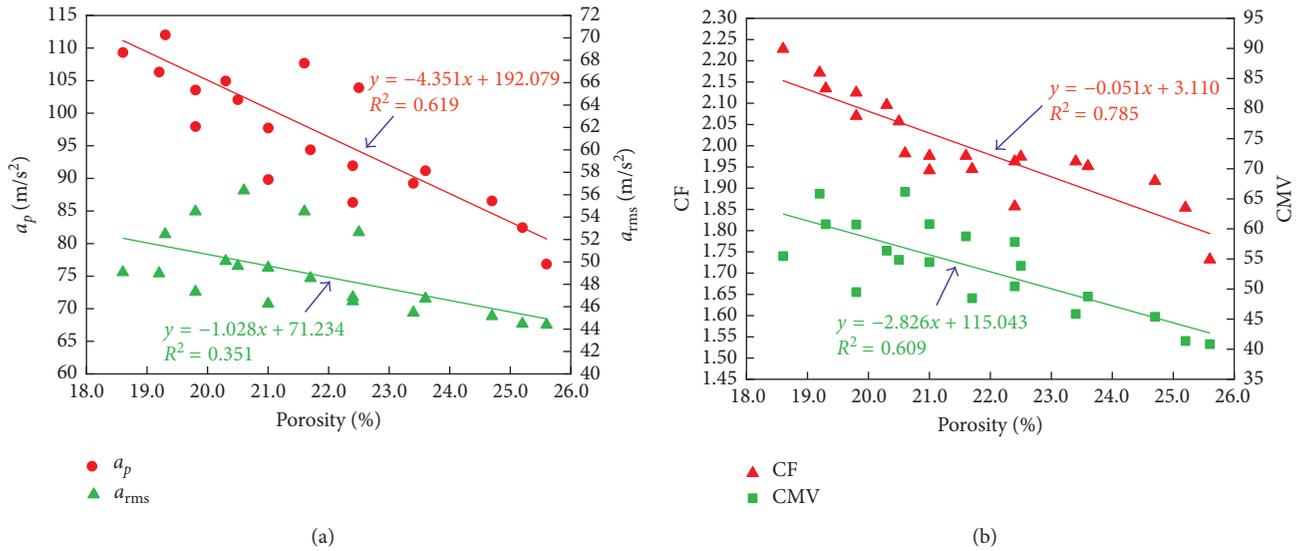
FIGURE 12: Linear relationships between porosity and real-time indexes on the main rockfill. (a) a_p, a_{rms}. (b) CF, CMV.

(a)

(b)
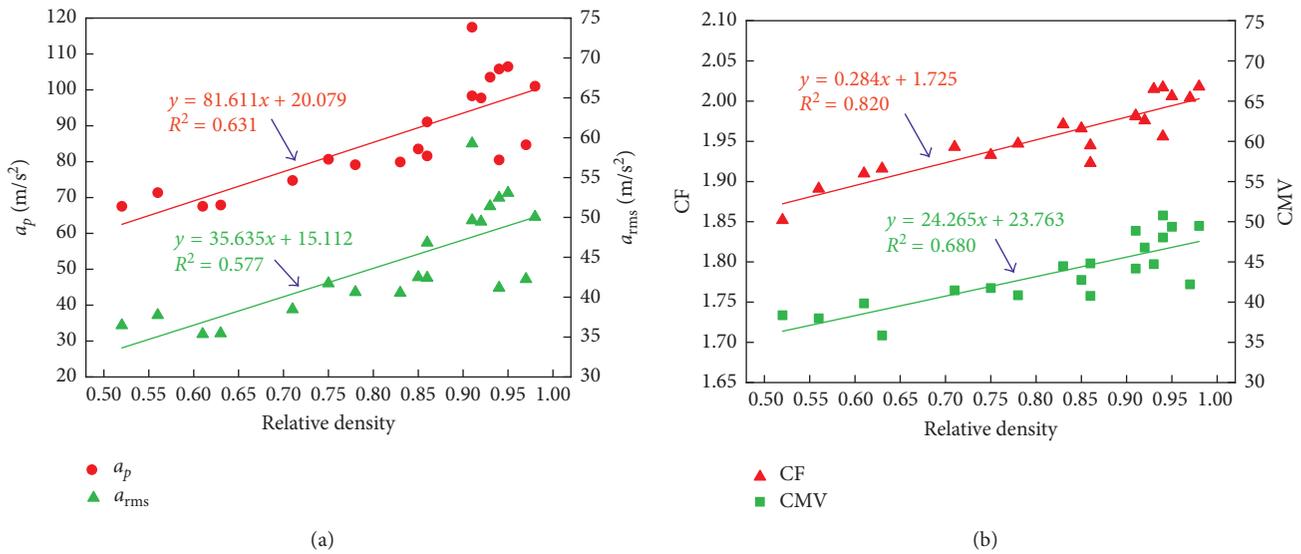
FIGURE 13: Linear relationships between relative density and real-time indexes on the secondary rockfill. (a) a_p, a_{rms}. (b) CF, CMV.

TABLE 4: Determination coefficients (R^2) for regression analysis between real-time test indexes and compaction quality indexes.

Compaction quality index	a_p		a_{rms}		CF		CMV	
	Linear model	Hyperbolic model	Linear model	Hyperbolic model	Linear model	Hyperbolic model	Linear model	Hyperbolic model
Porosity	0.619	0.580	0.351	0.308	0.785	0.823	0.609	0.528
Relative density	0.631	0.622	0.577	0.564	0.820	0.804	0.680	0.650

acceleration signal. The CF value in Figure 16 is magnified tenfold to display its tendency clearly.

As can be seen from Figure 14, the acceleration waveform is regularly distorted when the filter material get compacted, while the acceleration wave changes chaotically on the main rockfill. The spectra of Figure 15 show that the frequencies of the acceleration signal on the filter material are regularly distributed with stable fundamental frequency, first and second harmonic components, and few higher frequency components in the rolling process. While the spectrum on the main rockfill shows that the frequency distribution of the acceleration signal is irregular and disorderly with unsystematic frequency components.
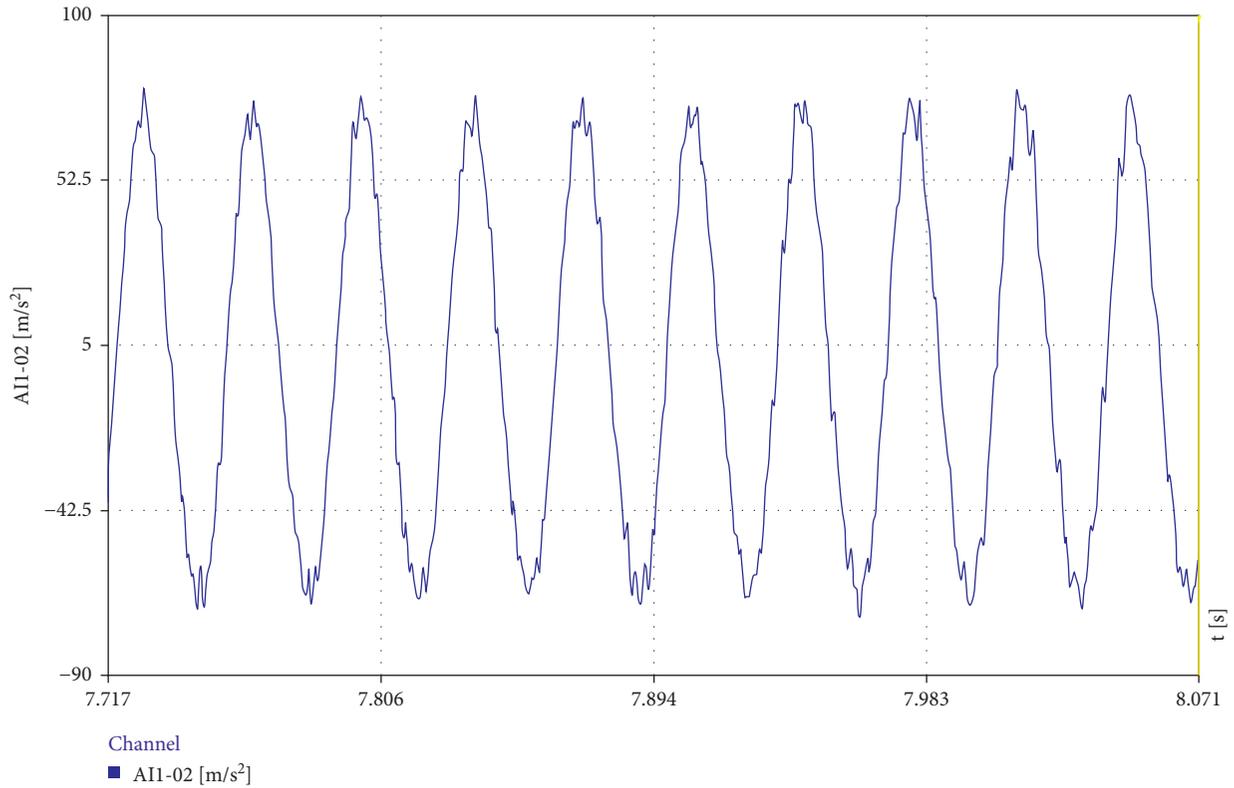
(a)
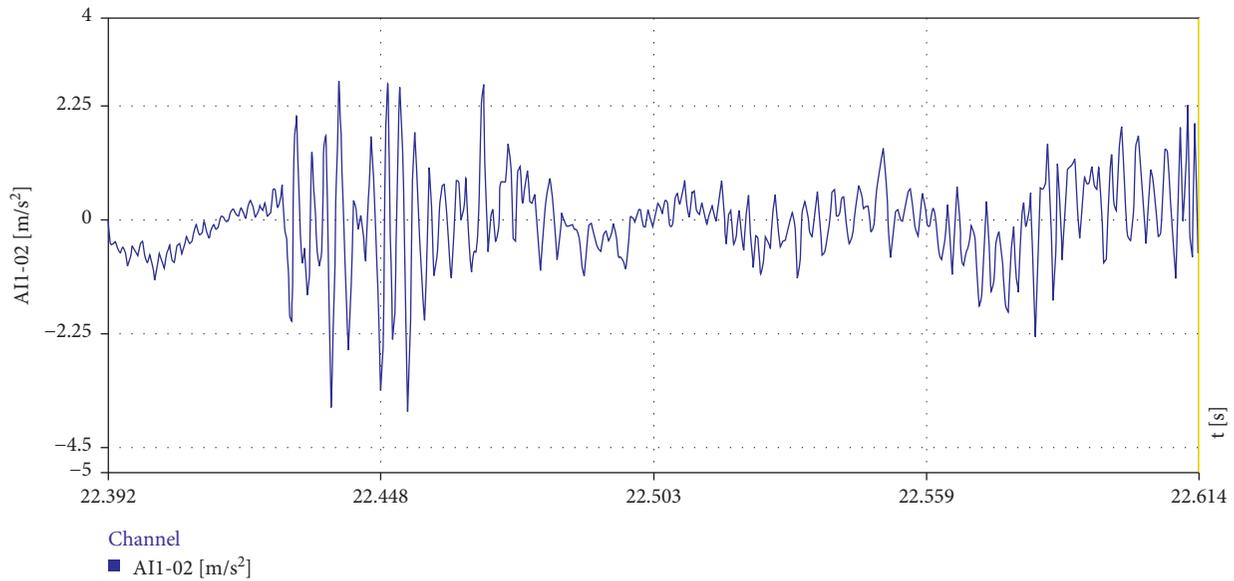
(b)

FIGURE 14: Time-history curve of acceleration signal. (a) Filter material. (b) Main rockfill.

Analysis of the reasons shows that since the main contents of the filter material are spherical particles with few edges, the contact between the soil particles and roller is relatively even, and there is not much difference among the reaction forces of the soil to the roller in unit areas. With the rolling moving on, the soil becomes more compacted and the reaction force to the roller increases, which causes a regular increase in the amplitude of the harmonic components and a regular wave distortion of the acceleration signal. Therefore, CMV and other acceleration indexes have a regular change in the rolling process, and all the four indexes can well reflect the compaction degree of the fine-grained soil.

However, in the case of the rockfill material which contains many sharp-edged stones, the contact between the
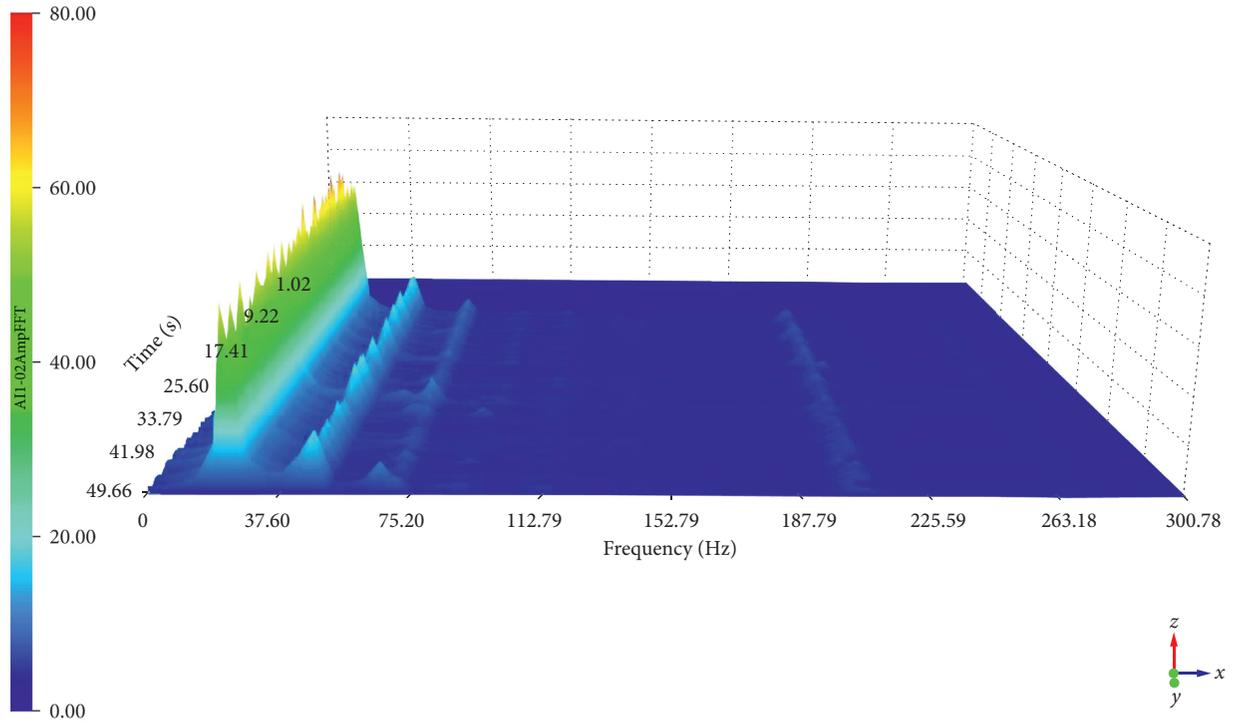
(a)
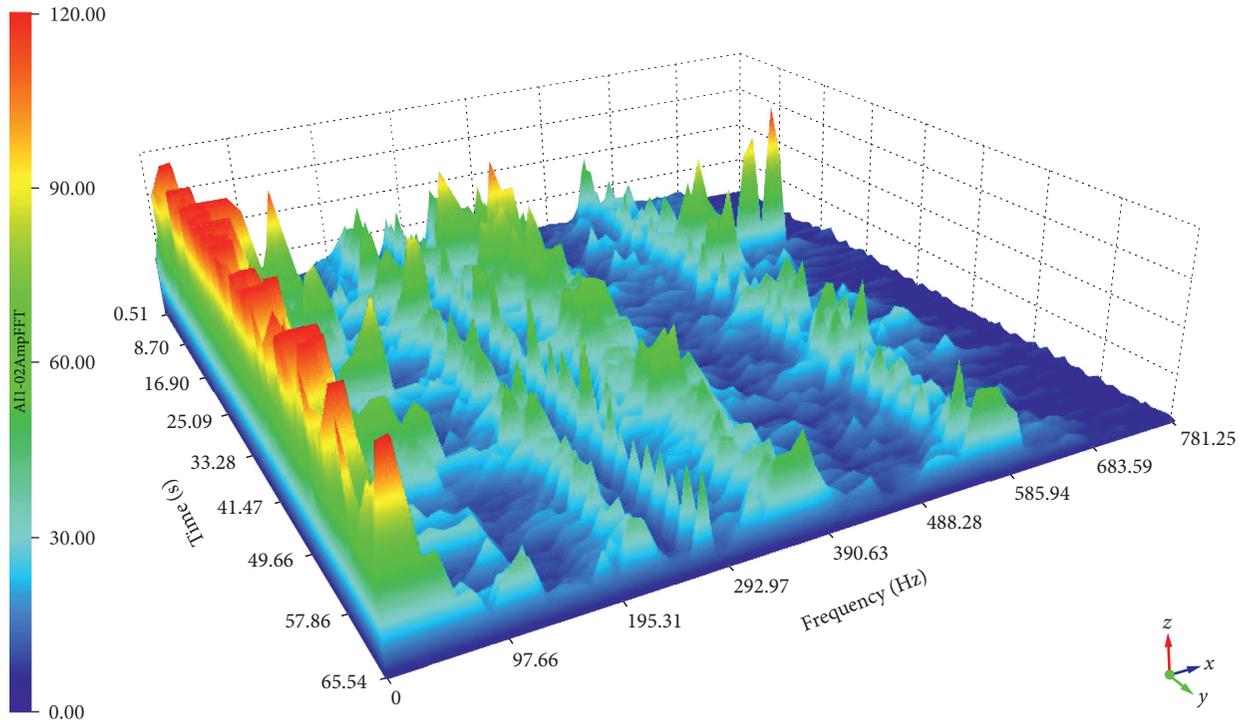
(b)

FIGURE 15: Three-dimensional spectra of acceleration signal. (a) Filter material. (b) Main rockfill.

soil particles and the roller is uneven, resulting in significant differences among the reaction forces of the soil to the roller in unit areas. The energy in the reaction force of the soil is unevenly transmitted to the roller, which leads to an irregular frequency distribution and a clutter waveform of the acceleration signal on the rockfill material. Due to the unstable change of the amplitude of fundamental frequency and first harmonic component in the rolling process, CMV
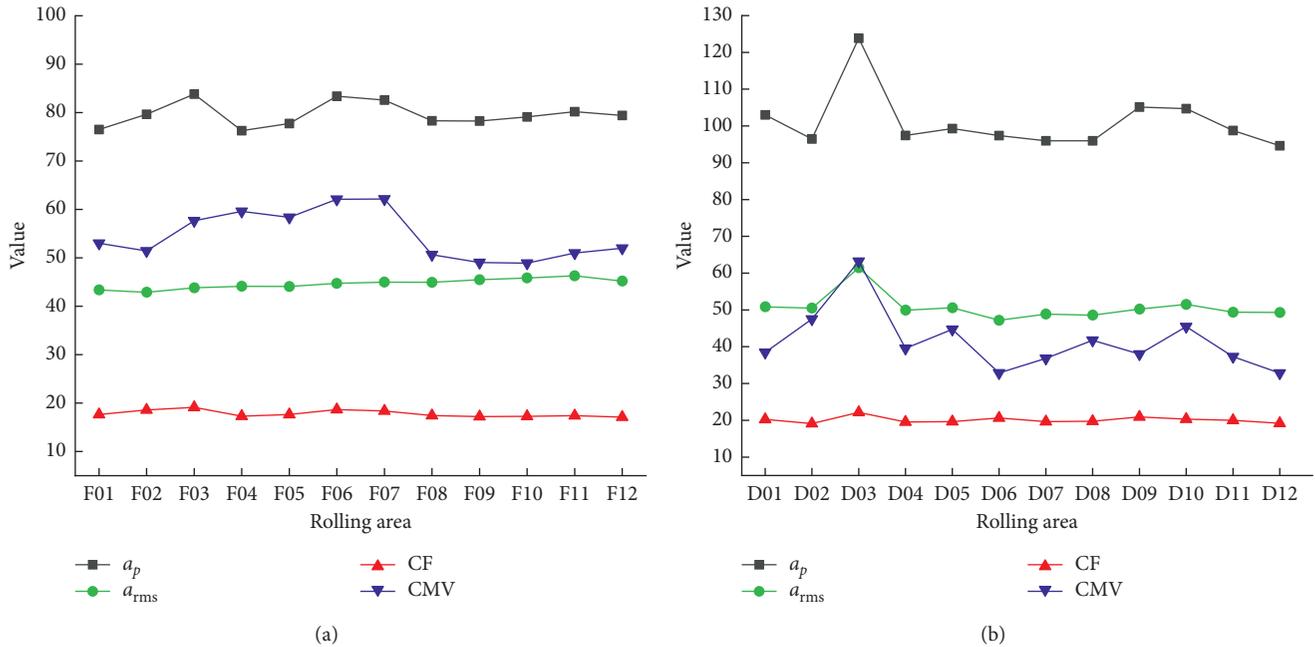
FIGURE 16: Tendency of acceleration indexes in the eighth compaction pass. (a) Filter material. (b) Main rockfill.

is disadvantaged in characterizing the compaction degree of the rockfill.

Judging from the physical meaning, the a_p and a_{rms} can only reflect part of the characteristics of the acceleration signal, while the CF combines the variation trend of them and describes the ability of the soil to produce the greatest reaction force to the roller. Therefore, the effect of the unevenness of the dam material on CF is relatively small compared to a_p and a_{rms}, which is consistent with the test result that the V_σ of CF is smaller than that of a_p and a_{rms} on all test materials (Table 3). The result can be proved by Figure 16 that the CF value changes stably while other indexes have greater volatility in the rolling process of the same dam material.

Combined with the analyses above, it can be known that the CF index best characterizes the compaction degree of the rockfill material among the four indexes. In the future, the authors will further establish a more detailed vibration model from the theoretical perspective, derive the formula, and clearly distinguish the applicability of CF index and other three acceleration indexes on the rockfill material.

5. Conclusions

In this study, the authors utilized four derived acceleration indexes to characterize the soil compaction degree, including a_p, a_{rms}, CF, and CMV. A two-part field compaction test was performed to analyze and judge the test effects of the four indexes on the rockfill and other dam materials. After the data correlation analysis and signal spectrum analysis, the following conclusions can be drawn:

(1) The data of a_p, a_{rms}, and CF are stable with low V_σ of them, and only the tendencies of a_p and CF with the change of roller running speed and compacted soil thickness are consistent with the theoretical situation. Besides, the linear correlation between CF and rolling times is the strongest, with the trimmed mean of R^2 being over 0.7 on all test materials. Thus, the correlation between CF and the rolling parameters is the strongest among the four indexes.

(2) The correlation between CF and the two compaction quality indexes is the strongest among the four indexes, with the highest R^2 of 0.823 and 0.820 in the regression analysis, respectively. The tentative control criteria of CF ≥ 2.017 on the main rockfill and CF ≥ 1.981 on the secondary rockfill are given by establishing the quantitative relations between CF and compaction quality indexes, which can instruct the field compaction quality control in the rolling process.

(3) The signal spectrum analysis shows that the frequencies of the acceleration signal on filter material are regularly distributed, and all the four indexes can well reflect the compaction degree of the fine-grained soil. The frequency distribution of the acceleration signal on main rockfill is irregular, and CMV is disadvantaged in characterizing the compaction degree of the rockfill. The effect of the unevenness of the dam material on CF is relatively small compared to a_p and a_{rms}. Combined with the results of statistical regression analyses, it can be concluded that the CF index best characterizes the compaction

degree of the rockfill material among the four indexes.

Conflicts of Interest

The authors declare that they have no conflicts of interest.

Acknowledgments

References

[1] Trade Standard of P. R. China, "Specifications for rolled earth-rockfill dam construction," Tech. Rep. DL/T 5129–2013, National Energy Administration of P. R. China, Beijing, China, 2013.

[2] H. Thurner and A. Sandstrom, "A new device for instant compaction control," in *Proceedings of the International Conference on Compaction*, vol. 2, pp. 611–614, Paris, France, 1980.

[3] A. Sandstrom and J. C. Pettersson, "Intelligent systems for QA/QC in soil compaction," in *Proceedings of the 83rd Annual Transportation Research Board Meeting, Transportation Research Board*, pp. 1–17, Washington, DC, USA, 2004.

[4] D. Adam, "Continuous compaction control (CCC) with vibratory rollers," in *Proceedings of the 1st Australia-Newzealand Conference on Environmental Geotechnics–GeoEnvironment*, pp. 245–250, Melbourne, VIC, Australia, 1997.

[5] H. Brandl and D. Adam, "Sophisticated continuous compaction control of soils and granular materials," in *Proceedings of the 14th International Conference on Soil Mechanics and Foundation Engineering*, pp. 1–6, Hamburg, Germany, 1997.

[6] D. J. White, "Report of the workshop on intelligent compaction for soils and HMA," in *Proceedings of the Workshop on Intelligent Compaction for Soils and HMA*, pp. 1–129, Des Moines, IA, USA, April 2008.

[7] G. Chang, Q. W. Xu, J. Rutledge et al., *Accelerated Implementation of Intelligent Compaction Technology for Embankment Subgrade Soils, Aggregate Base, and Asphalt Pavement Materials*, Federal Highway Administration, Washington, DC, USA, 2011.

[8] L. Forssblad, "Compaction meter on vibrating rollers for improved compaction control," in *Proceedings of the International Conference on Compaction*, vol. 2, pp. 541–546, Paris, France, 1980.

[9] L. Forssblad, *Vibratory Soil and Rock FillCompaction*, Swedish National Road and Transport Research Institute (VTI), Dynapac Maskin, Karlskrona, Sweden, 1981.

[10] L. Forssblad, "Roller-Mounted compaction meters," in *Proceedings of the 10th International Road Federation*, pp. 1–8, RJ, Brazil, 1984.

[11] L. Forssblad, "Soil compaction and compaction control," in *Proceedings of the 3rd International Geotechnical Seminar*, pp. 1–8, Singapore, 1985.

[12] H. Fujii, "Comparison of various control methods in situ," in *Proceedings of the 1st Asian-Pacific Conference of International Society Terrain-Vehicle Systems*, pp. 10–18, Beijing, China, 1986.

[13] X. L. Guo and D. Wen, *Field Compaction of Coarse Aggregates*, China Water & Power Press, Beijing, China, (Chinese), 1999.

[14] G. Komandi, "An evaluation of the concept of rolling resistance," *Journal of Terramechanics*, vol. 36, no. 3, pp. 159–166, 1999.

[15] D. J. White, T. D. Rupnow, and H. Ceylan, "Influence of subgrade/subbase non-uniformity on PCC pavement performance," in *Proceedings of the Geotechnical Engineering for Transportation Projects (GeoTrans2004)*, pp. 1058–1065, ASCE, Los Angeles, CA, USA, July 2004.

[16] M. G. Bekker, *Introduction to Terrain-Vehicle Systems*, University of Michigan Press, Ann Arbor, MI, USA, 1969.

[17] M. J. Thompson and D. J. White, "Field calibration and spatial analysis of compaction-monitoring technology measurements," *Transportation Research Record: Journal of the Transportation Research Board*, vol. 2004, pp. 69–79, 2007.

[18] M. J. Thompson and D. J. White, "Estimating compaction of cohesive soils from machine drive power," *Journal of Geotechnical and Geoenvironmental Engineering*, vol. 134, no. 12, pp. 1771–1777, 2008.

[19] D. J. White and M. J. Thompson, "Relationships between in situ and roller-integrated compaction measurements for granular soils," *Journal of Geotechnical and Geoenvironmental Engineering*, vol. 134, no. 12, pp. 1763–1770, 2008.

[20] W. Krober, R. Floss, and W. Wallrath, "Dynamic soil stiffness as quality criterion for soil compaction," *Geotechnics for Roads, Rail Tracks and Earth Structures*, pp. 189–199, Balkema, Rotterdam, Netherlands, 2001.

[21] M. A. Mooney and R. V. Rinehart, "Field monitoring of roller vibration during compaction of subgrade soil," *Journal of Geotechnical and Geoenvironmental Engineering*, vol. 133, no. 3, pp. 257–265, 2007.

[22] R. V. Rinehart and M. A. Mooney, "Instrumentation of a roller compactor to monitor vibration behavior during earthwork compaction," *Automation in Construction*, vol. 17, no. 2, pp. 144–150, 2008.

[23] R. Anderegg and K. Kaufmann, "Intelligent compaction with vibratory rollers: feedback control systems in automatic compaction and compaction control," *Transportation Research Record: Journal of the Transportation Research Board*, vol. 1868, pp. 124–134, 2004.

[24] R. Anderegg, D. A. von Felten, and K. Kaufmann, "Compaction monitoring using intelligent soil compactors," in *Proceedings of the Geotechnical Engineering in the Information Technology Age (GeoCongress2006)*, pp. 41–46, ASCE, Atlanta, GA, USA, April 2006.

[25] K. Kaufmann and R. Anderegg, "3D-construction applications III: GPS-based compaction technology," in *Proceedings of the 1st International Conference on Machine Control & Guidance*, pp. 1–10, Zurich, Switzerland, 2008.

[26] G. H. Xu and Y. Cai, "Dynamics monitor in the process of road structure forming," in *Proceedings of the 15th International Road Federation (IRF) World Meeting*, Thailand, 2005.

[27] T. S. Yoo, *A Theory for Vibratory Compaction of Soil*, pp. 44–52, State University of New York at Buffalo, New York, NY, USA, 1975.

[28] E. T. Selig and T. S. Yoo, "Fundamentals of vibratory roller behavior," in *Proceedings of the 9th International Conference*

on Soil Mechanics and Foundation Engineering, pp. 375–380, Tokyo, Japan, 1977.

[29] T. S. Yoo and E. T. Selig, "Dynamics of vibratory-roller compaction," *Journal of the Geotechnical Engineering Division*, vol. 105, no. 10, pp. 1211–1231, 1979.

[30] D. H. Zhong, B. Cui, D. H. Liu, and D. Tong, "Theoretical research on construction quality real-time monitoring and system integration of core rock-fill dam," *Science in China Series E: Technological Sciences*, vol. 52, no. 11, pp. 3406–3412, 2009.

[31] D. H. Zhong, D. H. Liu, and B. Cui, "Real-time compaction quality monitoring of high core rockfill dam," *Science China Technological Sciences*, vol. 54, no. 7, pp. 1906–1913, 2011.

[32] D. Liu, J. Sun, D. Zhong, and L. Song, "Compaction quality control of earth–rock dam construction using real-time field operation data," *Journal of Construction Engineering and Management*, vol. 138, no. 9, pp. 1085–1094, 2012.

[33] D. Liu, Z. Li, and Z. Lian, "Compaction quality assessment of earth–rock dam materials using roller-integrated compaction monitoring technology," *Automation in Construction*, vol. 44, pp. 234–246, 2014.

[34] R. B. W. Heng and M. J. M. Nor, "Statistical analysis of sound and vibration signals for monitoring rolling element bearing condition," *Applied Acoustics*, vol. 53, no. 1-3, pp. 211–226, 1998.

[35] Trade Standard of P. R. China, "Specification of soil test," Tech. Rep. SL237–1999, Ministry of Water Resources of P. R. China, Beijing, China, 1999.

[36] Trade Standard of P. R. China, "Specification on rockfill dam built with gravel and soil core wall in hydroelectric and hydraulic engineering," Tech. Rep. DL/T 5269–2012, National Energy Administration of P. R. China, Beijing, China, 2012.

Research Article

Polymer-Cement Mortar with Quarry Waste as Sand Replacement

D. N. Gómez-Balbuena,[1,2] T. López-Lara ⬡,[3] J. B. Hernandez-Zaragoza ⬡,[3] R. G. Ortiz-Mena,[2] M. G. Navarro-Rojero,[1] J. Horta-Rangel ⬡,[3] R. Salgado-Delgado,[4] V. M. Castano ⬡,[5] and E. Rojas-Gonzalez[3]

[1]CIATEQ A.C., Av. Del Retablo No. 150, Col. Constituyentes Fovissste, 76150 Santiago de Querétaro, QRO, Mexico
[2]Instituto Tecnológico Superior de Huichapan, Domicilio conocido sn Col. El Saucillo, 42411 Huichapan, HGO, Mexico
[3]División de Estudios de Posgrado, Facultad de Ingeniería, Universidad Autónoma de Querétaro, Cerro de las Campanas S/N, Col. Niños Héroes, 76010 Santiago de Querétaro, QRO, Mexico
[4]División de Estudios de Posgrado e Investigación, Instituto Tecnológico de Zacatepec, Calzada Tecnológico No. 27, Col. Centro, 62780 Zacatepec, MOR, Mexico
[5]Centro de Física Aplicada y Tecnología Avanzada, Universidad Nacional Autónoma de México, Boulevard Juriquilla 3001, 76230 Santiago de Querétaro, QRO, Mexico

Correspondence should be addressed to T. López-Lara; lolte@uaq.mx

The activities of carved Quarry extraction generate problems of landscape pollution such is the case of solid waste discharged into open land dumps in central Mexico. This article presents the technological application of this solid waste in a new polymeric material with properties similar to those of a traditional mortar. It is concluded that the polymeric material uses low amounts of cement with respect to the traditional mortar, and it is elaborated with the recycled quarry as they are presented in its granulometry. The polymer used favored a low water/cement ratio (0.3) which did not allow to decrease resistance due to the fine nature of the materials (residues and cement) in addition to maintaining the workability of the material. The quarry residue was classified as silt with low plasticity and was characterized by X-ray diffraction and Fluorescence to identify 76% of SiO_2, which is why it was used as a stone aggregate even though the fines content was approximately 93%. The maximum compression resistance obtained at 28 days were 8 Mpa with the polymer/solid ratios of 0.10, water/solids of 0.30, and quarry/solids of 0.67. Linear equations were analyzed for more representative values with R squared adjustment.

1. Introduction

The extraction activities of quarries (volcanic tuffs of the Riolitica type), as shown in Figure 1, generate a huge amount of solid waste that pollutes the environment and generate a lot of dust in the environment. The economic-mining activity in the region of Huichapan, Hidalgo, Mexico, represented by material banks for different industries ranks second in importance in the nonmetallic mining district of Hidalgo State. Companies extract carved rock that is marketed in the national and international market. The final products are tile for floors and facades, columns, blocks, and handcrafted pieces [1]. The volume of quarry mining production in the state of Hidalgo, Mexico, in the last 5 years averages 58×106 kg with an annual value over $ 214,000 USD [2]. It is estimated that about 40% of the production volume is wasted [3], which represents an annual volume of 23.2×103 kg of waste. The current waste management strategy consists of unloading them in landfills in the open, regardless of the potential use that these by-products may present to other industries. Such waste is classified into two types: solid waste resulting from quarry sites or processing units and sludge originated in the processes of cutting and detailed by the water used to cool and lubricate the machines

FIGURE 1: Accumulation of sludge (own source).

FIGURE 2: Quarry sieve analysis (own source).

used in said processes. These sludges accumulate gradually, reducing productive space within the company, or are thrown on the sides of the roads, accumulated in unused lands, which over time be leached or dragged, and obstruct the flow of aquifers or drainages. The large quantities already accumulated of the waste demand a prompt solution, which can be sustainable and economically beneficial for the quarry industry: as indicated by Galetakis and Soultana [4], the key to the successful use of quarry dust is its adequate characterization and the development of a simple and economically viable process to convert this waste material into marketable products.

The production and dumping of solid waste has exacerbated carbon emissions and increased pollution in metropolitan cities around the world. Waste management remains a global challenge for both developed and developing countries [5]. A significant number of researchers have studied the use of quarry waste in construction offering viable solutions to this problem. The predominant proposed applications are concrete production (42%), self-compacting concrete production (26%), and block production (18%) [4]. Almeida et al. [3] produced high-performance concrete using recycled stone mud and substituted 5% sand with quarry dust improving strength and durability values in all mixtures containing less than 20% dust. Balamurugan and Perumal [6] used quarry dust in the Tamil Nadu region, India as sand replacement material for concrete production, with a maximum increase in compressive strength (19.18%), tensile strength (21.43%), and resistance to bending (17.8%) with 50% replacement of sand by quarry dust. Sureshchandra et al. [7] replaced sand with quarry dust for the production of hollow concrete blocks. The blocks with replacement of 50% of sand by quarry dust had better performance than those with complete replacement of sand. Arunachalam et al. [8] used quarry powder as a light aggregate and aluminum powder as an air entraining agent for the production of lightweight concrete obtaining resistance of 3–7 MPa for mixtures with quarry dust. Adajar et al. [9] investigated the structural performance of concrete with quarry waste as a substitute for fine aggregates in a concrete mix. They formulated a model to predict the compressive strength of the mixtures made. Lohani et al. [10] replaced partially sand in concrete production. The dust content up to 30% increases the compressive strength of concrete. If the dust content exceeds 30%, the resistance
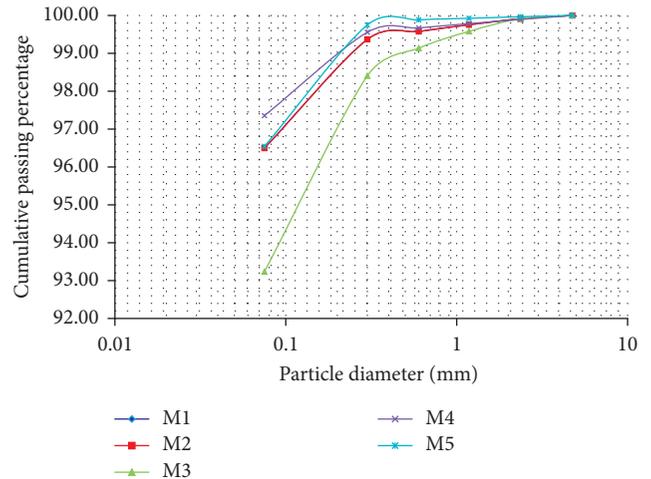
gradually decreases. Safiuddin et al. [11] concluded that the addition of fine quarry waste can be used as a good substitute for sand in the production of concrete. Galetakis et al. [12] developed a laboratory method for the production of recycled quarry construction elements. Venkatakrishnaiah and Rajkumar [13] reinforced concrete with plastic waste fibers replacing natural sand with quarry dust from the Tamil Nadu region, India. The maximum resistance and best workability were with 30% of sand replacement.

Cement mortar and concrete have disadvantages such as delayed hardening, low tensile strength, shrinkage by drying, and low chemical resistance. To reduce these disadvantages, the use of polymers to modify the properties of mortar and cement has been dominant materials in the construction industry since the 1980s, which are now popularly used in advanced countries [14, 15]. Polymer-modified cement mortars are used in civil infrastructures, bridges, insulation for walls, self-leveling mortars, and concrete for fracture repair due to their excellent resistance, environmental protection and workability [2]. There is a wide variety of commercial latex polymers mostly based on elastomeric and thermoplastic polymers that form continuous films of polymer when dehydrated [16, 17]. The latex polymers include butylbenzene latex, neoprene emulsion, polyvinyl chloride-vinylidene chloride emulsion, styrene-acrylic emulsion, styrene-butadiene carboxy latex, polyacrylate latex, and so on [18]. The dust contents that are normally handled are less than 30% in order not to affect the workability and compressive strength [19].

Polymers such as latex, redispersible polymer powders, water-soluble polymers, liquid resins, and monomers are used for the modification of mortar or cement. Latex is the most widely used additive [20]. In general, latex-type polymers are copolymer systems consisting of two or more monomers, and their total solid content corresponds to 40% or 50% of their weight [21]. The hydration of the cement precedes the process of forming thin films of polymer which leads to the monolithic comatrix phase in which the organic polymer matrix and the cement gel matrix are

FIGURE 3: Sample of recycled Quarry (own source).

FIGURE 4: X-ray diffraction spectrum of the Quarry waste used (own source).

homogenized [22, 23]. Usually, a polymer/cement ratio from 5% to 15% and a water/cement ratio from 30% to 50% of the latex modified concrete depend on the workability [24].

The growth of the construction industry has led to overexploitation of natural resources such as gravel and river sand by production of concrete. So, the global trend is to use alternative materials (recycled materials) in the construction industry to make rational and sustainable use of natural materials and therefore reduce costs of construction [9].

2. Materials and Methods

2.1. Materials. The following materials were used:

  (a) Cement CPC 30R (Ordinary Portland Cement) which complies with the characteristics established in the Mexican standard NMX-C-414-ONNCCE.

  (b) Quarry waste (rhyolitic volcanic tuff) extracted from the solid waste of stone of "Jaramillo" quarries in Maney town, Huichapan Hidalgo, Mexico. It was used Quarry as a shorthand notation of Quarry waste or Quarry residue on the text.

  (c) The polymer used was a synthetic latex emulsion and acrylic resins that had the specified requirements in the ASTM-1059-99 Type I Standard.

  (d) Water used for the mixing and curing of the material with a pH value of 7 (determined by a test strip).

2.2. Methods. The methods used for the experimentation were the following:

  (a) Geotechnical characterization of the waste. The field identification [25] of the material was done as well as the grain-size distribution [26], plasticity properties [27], and soil classification [28].

  (b) Physical-chemical characterization of the waste. The mineralogical characterization for the determination of primary mineral species (deposit mineral associations) was done by X-ray diffraction (XRD) with Bruker D8-Advance equipment using Göebel mirror (nonflat samples), high-temperature chamber (up to 900°C), X-ray generator KRISTALLOFLEX K 760-80F (power: 3000 W, voltage: 20–60 kV, and current: 5–80 mA), and a Seifert model JSO-DEBYEFLEX 2002 fitted with a copper cathode and a nickel filter.

  (c) Analysis and comparison of grain-size distributions [26] of different types of sands as well as their mineralogical composition determined by X-ray diffraction and fluorescence.
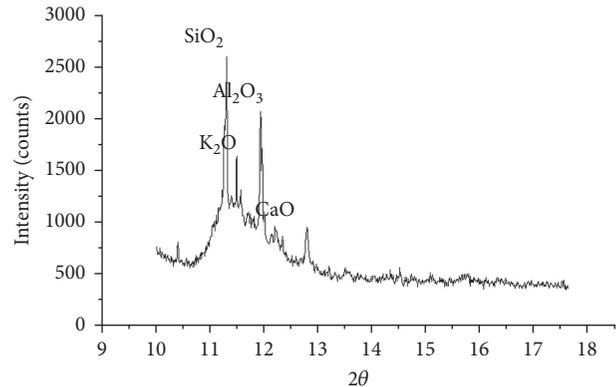
  (d) Compression test according to [29]. The compression strength of the mixtures was determined according the ASTM C39/C39M-2016b Standard Test Method for Compressive Strength of cylindrical concrete specimens at 3, 7, 14, and 28 days. For the compression test [29], a hydraulic press of 20 tons was used, with pressure sensor WIKA model A10, from 0 to 200 bar and analog output from 0 to 10 Vdc, Fluke Brand Model 115 multimeter.

3. Results and Discussion

3.1. Geotechnical Characterization of the Waste. According to the field identification, grain-size distribution analysis [26], determination of the plasticity limits (liquid and plastic) [27], and classification of soils [28], the following results were obtained:

From the field identification, the recycled quarry residues were materials with low tenacity and slow dilatation and had very low resistance in the dry state. No odor was perceived. The material color was brown to white in light tones. From the classification of soils, the material was a rock powder with little content of slightly plastic inorganic clay located below the "A" line in the plasticity chart. Figure 2 shows the grain-size distribution analysis curves of five waste samples [26]; the data showed that more than 90% of the material passed the 200 mesh. The liquid limit was 24.98%, and plastic limit was 21.25%. Plastic index was 4% on average. So, the classification of soil [28] was ML (inorganic low-compressibility lime, material whose particles have certain cohesion between them in the presence of water). Based on [24], the waste Quarry has the following important engineering properties when the material is compacted and saturated: permeability from semipermeable to impermeable, acceptable shear strength, medium compressibility, and acceptable workability as a construction material. Figure 3 shows the waste Quarry used.

3.2. Geological and Physical-Chemical Characterization of the Quarry Waste. The geological analysis of the waste [30]

TABLE 1: % of chemical composition of recycled Quarry.

Chemical composition of Quarry	SiO$_2$	Al$_2$O$_3$	K$_2$O	CaO	Na$_2$O	TiO$_2$	SO$_3$	MgO	Cl	P$_2$O$_3$
Normalized means	75.958	10.796	8.5099	2.4279	0.9631	0.4791	0.323	0.1486	0.1144	0.0567

TABLE 2: % of chemical composition of recycled Quarry.

Chemical composition of Quarry	BaO	ZrO$_2$	Rb$_2$O	ZnO	SrO	Y$_2$O$_3$	CeO$_2$	Ga$_2$O$_3$	Nb$_2$O$_3$
Normalized means	0.0541	0.0536	0.0307	0.0256	0.0209	0.0172	0.0169	0.0023	0.0021

indicated that the geology of the Huichapan caldera corresponds to an upper ignimbrite with columnar fracture and partially welded. Ignimbrite contains lithic fragments of andesite, quartz, and feldspar in a vitreous matrix (lightly crushed vitreous fragments).

The qualitative analysis by means of X-ray diffraction of Quarry dust is observed in Figure 4. The major component in the Quarry waste was silicon dioxide.

Tables 1 and 2 show the results of the X-ray fluorescence analysis of the recycled Quarry (results expressed as a percentage of the compounds present in the waste). Tables 1 and 2 show the following: (1) Silicon dioxide is the major component and is present in 76%. According to [31], the silicates are the most important component of the hydrated cement and the cause of their resistance. Silicon dioxide compound presents a significant difference between the Quarry waste and the cement, since the latter requires only 25% of content. Based on [32], this excess of silicon dioxide will favor the reduction of the porosity of the mixture to improve the interface of the Portland cement paste adhered to the aggregate. Therefore, the strength and compactness of the final product are increased. (2) CaO is the compound that provides the greatest resistance to cement [31]: in this study, the Quarry waste has much lower amounts than cement, 2.4% and 67%, respectively. It would be expected that mixtures containing high percentages of Quarry waste present low resistances. (3) Alkaline compounds (such as Na$_2$O) cause disintegration of concrete and affect the rate of increase of cement strength [31]. Na$_2$O compound (0.96%) in the Quarry waste is within of the allowable range of 0.2 to 1.3% of the cement. (4) Magnesium oxide (MgO) [31] is a substance that often accompanies calcium oxide. MgO is not combined during the cooking process of Portland cement and therefore it does not form hydraulic components but remains as free MgO. MgO is similar to lime. So water hydrates and increases the volume of MgO. A high percentage of MgO implies the risk of expansion [33]. Expansion by MgO is more dangerous because it appears very slowly over the years. For this reason, the cement standard stipulates a maximum limit of 5% for the MgO content. In this study, the MgO content was favorable with only 0.15%. The gray-green color of Portland cement is due to MgO [31].

3.3. Analysis and Comparison of Grain-Size Distributions and Mineralogical Composition of Sands.
Figure 5 shows a comparative analysis of the chemical compositions obtained by X-ray diffraction of the Quarry, river sands of Boye-HUI-53
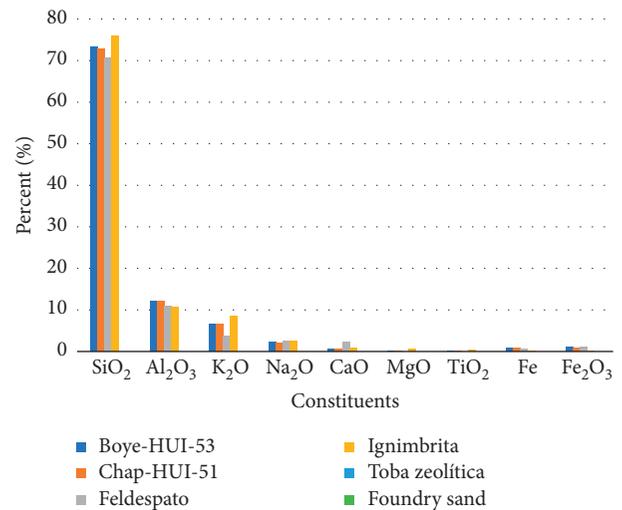
FIGURE 5: Chemical composition for different sands and ignimbrita (own source).
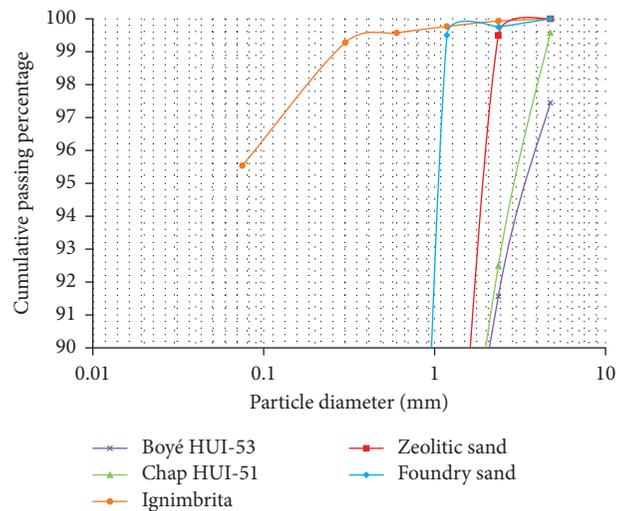
FIGURE 6: Sieve analysis for different sands [24, 29] (own source).

and Chap-HUI-51 [2], feldspathic sand, zeolitic tuff sand, and silica sand foundry. The river sands are from regions near the place where the ignimbrite (Quarry waste) was extracted. Feldspathic sand is used in the ceramics industry [34] and zeolitic tuff sand is used for lining mortar [35]. High-quality silica sand foundry is a by-product generated by the ferrous and nonferrous metal foundry [36]. The

TABLE 3: Quantities in grams for the different concrete mixtures (own source).

MIX	Cement (g)	Quarry (g)	Water (g)	Polymer (g)	Quarry/solids	Water/solids	Polymer/solids
M1				30	0.67	0.30	0.10
M2			90	45	0.67	0.30	0.15
M3				60	0.67	0.30	0.20
M4		200		30	0.67	0.40	0.10
M5			120	45	0.67	0.40	0.15
M6	100			60	0.67	0.40	0.20
M7				40	0.75	0.30	0.10
M8			120	60	0.75	0.30	0.15
M9		300		80	0.75	0.30	0.20
M10				40	0.75	0.40	0.10
M11			160	60	0.75	0.40	0.15
M12				80	0.75	0.40	0.20
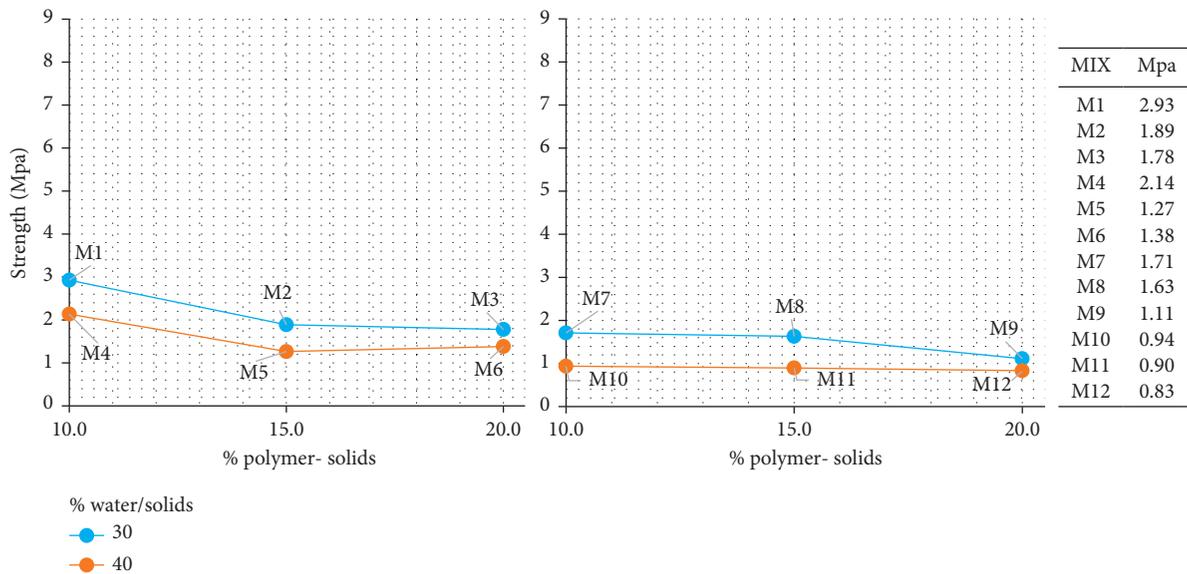
FIGURE 7: Compression resistance at 3 days (own source).

results showed that the mineralogical compositions of all the sands and quarries are very similar.

A comparative grain-size analysis distribution [26] corresponding to zeolitic sand [35], foundry sand [36], ignimbrite rhyolitic, and 2 types of sands for construction in the regions of Chapantongo and Boyé in Hidalgo México was reported in Figure 6.

From the comparison of the sands (Figure 6), it was observed that the sands of Chapantongo and Boyé had similar grain-size distributions with average grain size of 2.36 mm passing both 80% content by mesh number 16. Chapantongo sand was slightly thinner since 39% of the material analyzed passed the 50 mesh (grain size of 0.3 mm) compared to 26% of the Boyé sand that passed the same mesh. The zeolitic sand and foundry sand had a finer granulometry whose aggregates in both cases passed in 60% the 30 mesh (0.60 mm). The ignimbrite curve showed a very

smooth slope which indicates that their grain size differs significantly from the other sands. More than 95% of the ignimbrite passed the 200 mesh (0.075 mm).

Based on the comparative analysis of the physico-chemical characterization of the Quarry waste and various sands, it was observed that it could be viable to replace the sand by a fine aggregate by the similarity of chemical composition. From the grain-size distributions curves, it was observed that the sands had more uniform dimensions (sandy aggregates with very few fines). On the other hand, the ignimbrite was a fine soil, and therefore the mechanical behavior can be less favorable. However, derived from the similarity in chemical composition and granulometry between the Quarry and various sands studied, the feasibility of replacing 100% of sand as a fine aggregate by the ignimbrite can be used in the production of mortars and concretes. Based on [37], this substitution

MIX	Mpa
M1	7.04
M2	4.54
M3	3.33
M4	2.67
M5	1.93
M6	2.04
M7	4.15
M8	2.36
M9	1.56
M10	1.87
M11	1.54
M12	0.94
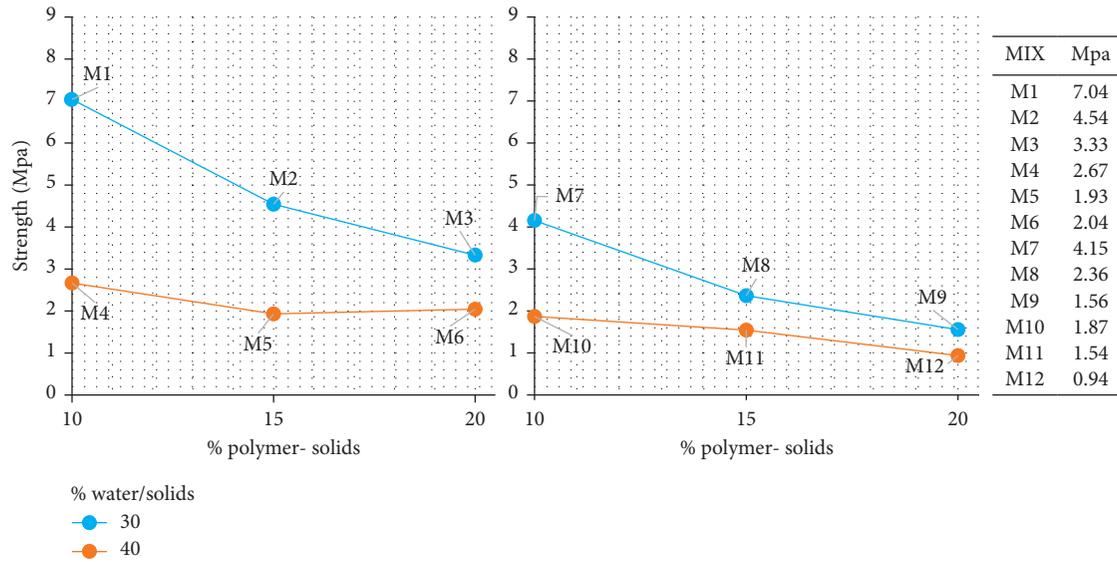
FIGURE 8: Compression resistance at 7 days (own source).

MIX	Mpa
M1	6.89
M2	5.91
M3	4.93
M4	5.98
M5	4.28
M6	4.09
M7	6.01
M8	4.98
M9	4.17
M10	2.66
M11	2.51
M12	2.89
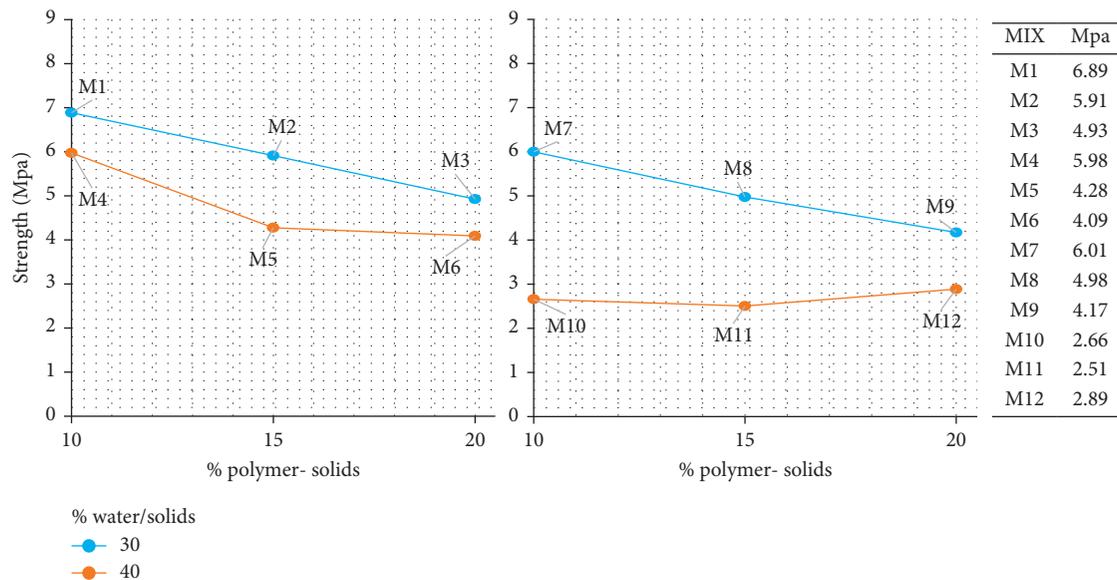
FIGURE 9: Compression resistance at 14 days (own source).

generates in the products increased tenacity and impact resistance and reduced shrinkage by drying and cracking in its hardened state.

3.4. Compression Test Analysis.

Compressive strength testing was undertaken at 3, 7, 14, and 28 days of age upon 0.051 m diameter and 0.102 m length cylindrical specimens, maintaining a length to diameter ratio of 2, according to [38]. 12 mixtures were elaborated of different proportions based on the following premises: (1) use the largest amount of quarry dust; (2) use the least amount of water without affecting aspects such as the

workability of the sample and without using additives such as superplasticizers; and (3) use the least amount of polymer. Table 3 shows the 12 proportions for the different samples considered for the present study. The samples were numbered according to the MIX column, being M1 the sample number one and so on. The columns cement, quarry, water, and polymer show the quantities used in grams for each mixture. The amount of 100 g of cement was constant in all the mixtures, adding double amount of the Quarry (200 g) for the mixtures M1 to M6 and the triple amount of Quarry (300 g) for the mixtures M7 to M12. In the Quarry/solids column, the high content of ignimbrite residue is highlighted with respect to the quantity of
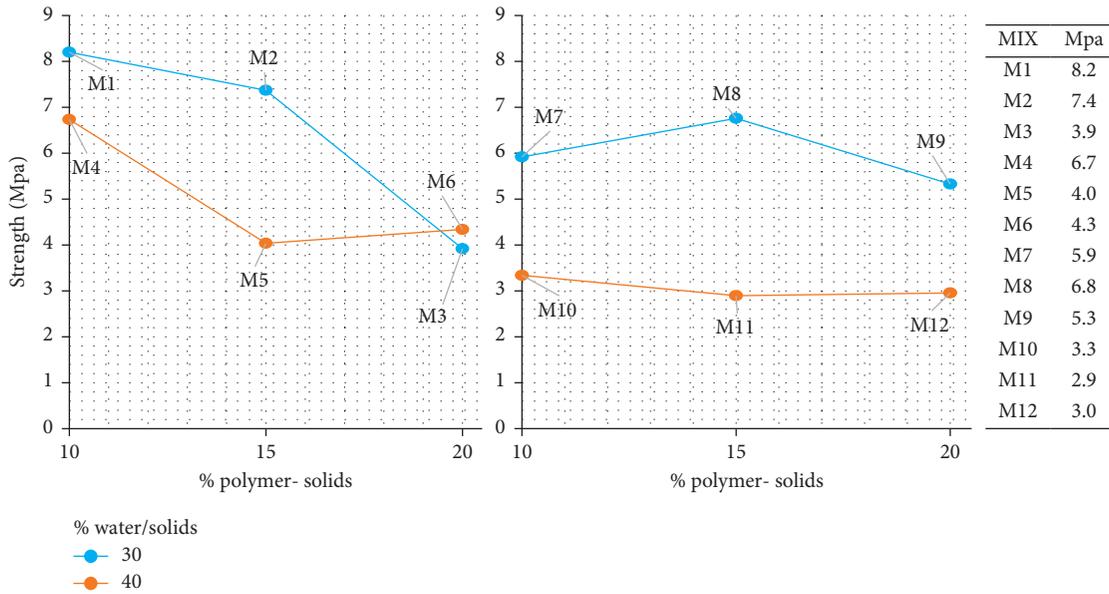
FIGURE 10: Compression resistance at 28 days (own source).
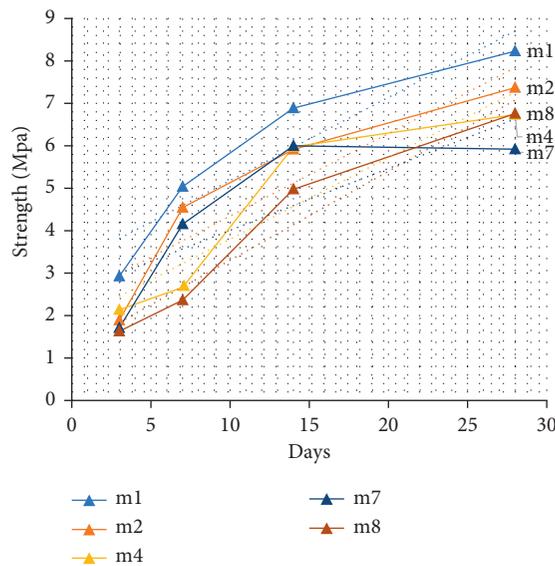
FIGURE 11: Most representative values and trend lines (own source).

solids handling values of 0.67 and 0.75 (ratios calculated by (2)). The amounts of 90, 120, and 160 g of water used in the mixtures correspond to ratios of 0.3 and 0.4 of water with respect to the amount of solids (indicated in the water/solids column and calculated by (3)). The polymer was mixed in ratios of 0.10, 0.15, and 0.20 with respect to the amount of solids (indicated in the column polymer/solids and calculated by (4)). The above-mentioned solids are indicated as the sum of cement and Quarry in (1).

$$\text{Solids} = \text{grams quarry} + \text{grams cement}, \tag{1}$$

$$\frac{\text{Quarry ratio}}{\text{Solids ratio}} = \frac{(\text{quarry grams})}{(\text{quarry grams} + \text{cement grams})}, \tag{2}$$

$$\text{Water ratio solids} = \frac{(\text{grams of water})}{(\text{grams of quarry} + \text{grams of cement})}, \tag{3}$$

$$\frac{\text{Polymer ratio}}{\text{Solids ratio}} = \frac{(\text{polymer grams})}{(\text{grams of quarry} + \text{grams cement})}. \tag{4}$$

TABLE 4: Linear equations and R-square value for most representative mixtures (own source).

Linear equations	R square value
$y1 = 0.1957x + 3.2262;$	$R^2 = 0.8707$
$y2 = 0.1943x + 2.4037;$	$R^2 = 0.8368$
$y4 = 0.1923x + 1.8775;$	$R^2 = 0.8339$
$y7 = 0.1458x + 2.5507;$	$R^2 = 0.6328$
$y8 = 0.2096x + 1.2071;$	$R^2 = 0.9445$

For compression tests according to [29] at 3, 7, 14, and 28 days, the reported results are the average of three compression tests of each of the 12 mixtures performed. The load was applied axially and continuously until failure of the specimen recording the maximum load applied and the type of fracture according to [29]. At three days, the highest resistance of 3 MPa occurred in the M1 mixture with quarry/solids ratio of 0.67, water/solids of 0.30, and polymer/solids of 0.10. The results are shown in Figure 7.

Figure 8 shows results obtained at 7 days highlighting M1 and M7 with respect to the resistance measured at 3 days with increases of 130% and 142% reaching 7 and 4 Mpa, respectively. The results at 14 days are observed in Figure 9 highlighting M4 that increased the resistance obtained to 7 days from 2.6 Mpa up to 6 MPa in 14 days with a water/solids ratio of 0.4. Another significant resistance increase occurred in M7 that reached 4 Mpa with low water/solids ratios of 0.3 and polymer/solids of 0.1 but significant Quarry/solids ratio of 0.75.

Figure 10 shows that M1 reached the highest resistance at 28 days in the order of 8 Mpa and M2 shows resistance close to M1 with a polymer/solids ratio of 0.15. M8 also stands out with resistance close to 7 MPa and the highest Quarry/solids ratio of 0.75.

Figure 11 shows the increase in resistance as the age of the specimens increases, being in all cases M1 the best behavior reaching a resistance of 8 MPa at the age of 28 days. A rapid increase in resistance is noted between the ages of 7 and 14 days. After 14 days, there is a gradual and slow increase of resistance until 28 days. Trend lines were annexed to Figure 11. The corresponding linear equations and the value of R square of trend lines are shown in Table 4. The value of R square shows that the values are attached to a straight line of trend with a deviation margin of less than 20% in most cases.

Compressive load [29] was applied at 14 days of age. Figure 12 includes only the samples of highest recorded load (M1, M3, M7, M8, and M11). The aforementioned specimens show cone-type fracture patterns, that is, cone well defined only at one end and vertical fractures through the cylindrical column (also called type two fractures). This fracture pattern is common and representative of cementing material. Only in M9, vertical fractures were formed across the ends, without well-defined cone formation or fracture type three. Figure 13 shows fractures at the age of 28 days of the specimens M1, M3, M5, M7, and M8, observing in all the cases conical fractures type two.

4. Conclusions

The waste derived from the Quarry stone was classified as inorganic low compressibility lime according the plasticity properties and grain-size distribution.
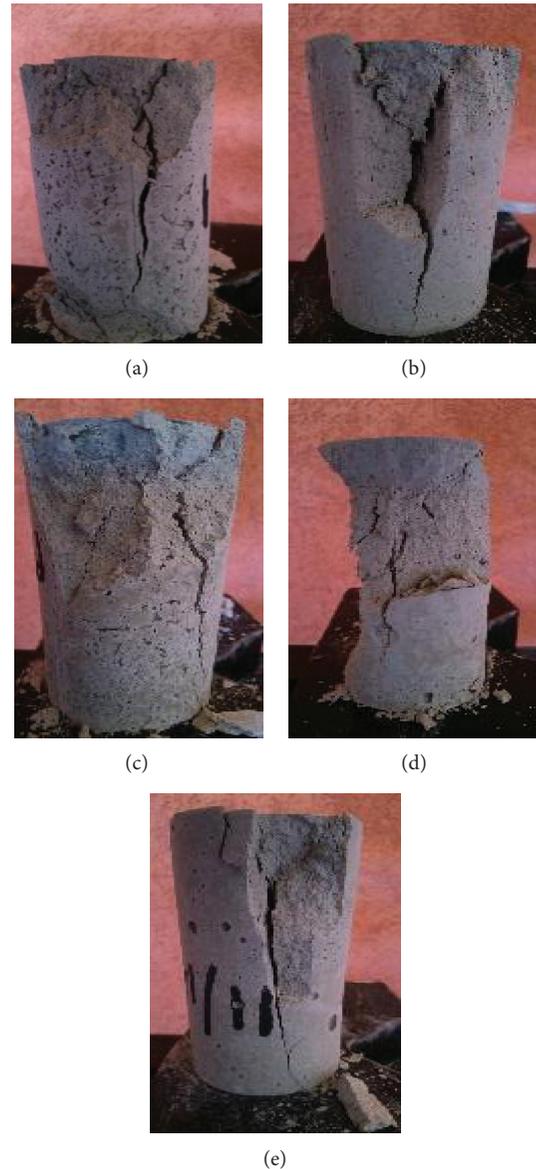
FIGURE 12: Types of fractures in samples at 14 days. Mixtures (a) M1, (b) M3, (c) M7, (d) M8, and (e) M11 with higher performance, respectively, from the left side (own source).

The geological analysis of the ignimbrite (Quarry stone) indicated that it contains lithic fragments of andesite, quartz, and feldspar in a vitreous matrix (lightly crushed vitreous fragments).

Based on the comparative analysis of the physicochemical characterization of the Quarry waste and various sands, it was observed that it could be viable to replace the sand by a fine aggregate by the similarity of chemical composition. The major component in the waste is silicon dioxide (76%), and so it was considered pertinent to replace the content of sands that generally constitutes a mortar.

It is concluded that the polymeric material uses low amounts of cement with respect to the traditional mortar, and it is elaborated with the recycled quarry as they are presented in its granulometry, which saves the process of size selection.
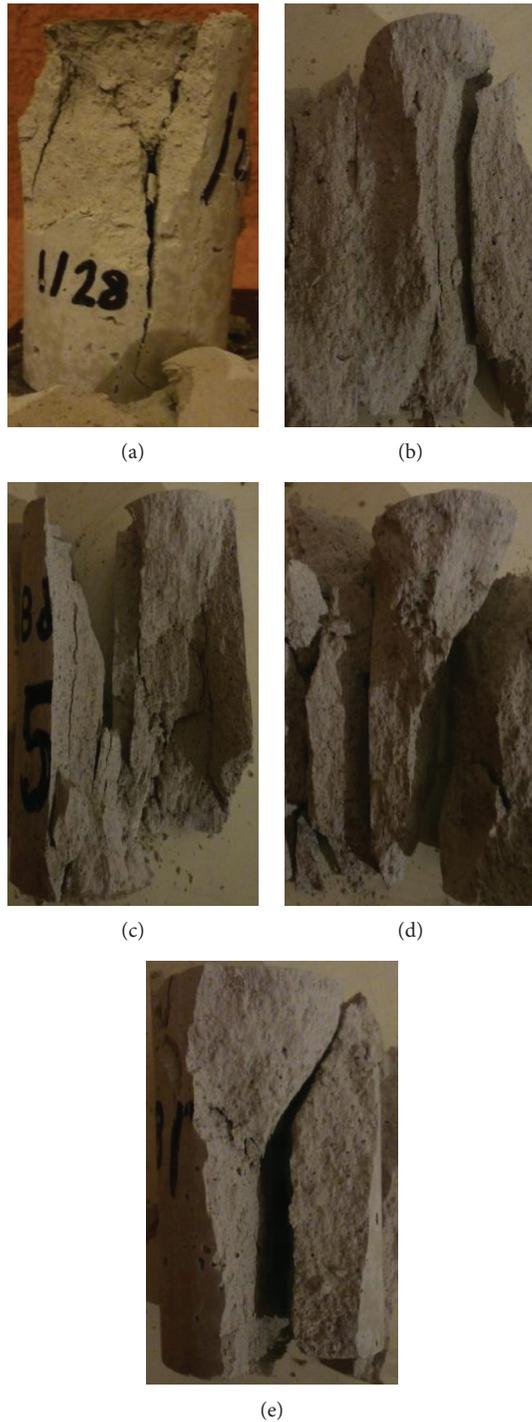
Figure 13: Types of fractures in 28-day samples. Mixtures (a) M1, (b) M3, (c) M5, (d) M7, and (e) M8 with higher performance, respectively, from the left side (own source).

According to the greater resistance obtained in the compression tests to specimens with age of 28 days, it is concluded that it is possible to replace the use of sand as fine aggregate by Quarry dust without significant reduction of the compressive strength of mortars.

The utilization of ignimbrite residues (Quarry waste) in the manufacture of mortars presents the best resistance to compression at 28 days of age with a resistance of 8 MPa with the following optimum proportions: polymer/solids of 0.1, water/solids of 0.3, and Quarry/solids of 0.67. Quantities greater than 0.15 of the polymer/solids ratio significantly decrease compressive strength [20]. Likewise, the compressive strength was considerably affected when quarry/solids ratios greater than 0.67 were used.

The polymer used in the mortar allowed a low water/solids ratio (0.3) and acceptable workability.

This strategy of reusing of ignimbrite waste has the advantage of using a large amount of these residues with respect to the amount of cement without using additional processes in the waste. The Quarry waste was used as it was collected directly from the deposits. This effective and sustainable solution is considered for the solid waste management of the Quarry industry and presents an alternative of raw material for the production of mortars.

Conflicts of Interest

The authors declare that they have no conflicts of interest.

References

[1] Servicio Geológico Mexicano, "gob.mx," August 2017, http://mapserver.sgm.gob.mx/Cartas_Online/geologia/1653_F14-C78_GM.pdf.

[2] Servicio Geológico Mexicano, "SGM," August 2017, http://www.sgm.gob.mx/pdfs/HIDALGO.pdf.

[3] N. Almeida, F. Branco, J. de Brito, and J. R. Santos, "High-performance concrete with recycled stone slurry," *Cement and Concrete Research*, vol. 37, no. 2, pp. 210–220, 2006.

[4] M. Galetakis and A. Soultana, "A review on the utilisation of quarry and ornamental stone industry fine by-products in the construction sector," *Construction and Building Materials*, vol. 105, pp. 769–781, 2015.

[5] A. K. Choudhary, J. N. Jha, K. S. Gill, and S. K. Shukla, "Utilization of fly ash and waste recycled product reinforced with plastic wastes as construction materials in flexible pavement," in *Proceedings of the Geo Congress 2014*, pp. 3890–3902, Atlanta, GA, USA, February 2014.

[6] G. Balamurugan and P. Perumal, "Behaviour of concrete on the use of quarry dust to replace sand–an experimental study," *Engineering Science and Technology*, vol. 3, no. 6, pp. 776–781, 2013.

[7] H. S. Sureshchandra, G. Sarangapani, and B. G. Naresh Kumar, "Experimental investigation on the effect of replacement of sand by quarry dust in hollow concrete block for different mix proportions," *International Journal of Environmental Science and Development*, vol. 5, no. 1, pp. 15–19, 2014.

[8] N. Arunachalam, V. Mahesh, P. Dileepkumar, and V. Sounder, "Development of innovative building blocks," *Journal of Mechanical and Civil Engineering*, vol. 1, no. 1, pp. 1–7, 2014.

[9] M. A. Q. Adajar, E. de Guzman, R. Ho, C. Palma Jr. III, and D. Sindico, "Utilization of aggregate quarry waste in construction industry," *International Journal of GEOMATE*, vol. 12, no. 31, pp. 16–22, 2017.

[10] T. K. Lohani, M. Padhi, K. P. Dash, and S. Jena, "Optimum utilization of Quarry dust as partial replacement of sand in concrete," *International Journal of Applied Sciences and Engineering Research*, vol. 1, no. 2, pp. 391–404, 2012.

[11] M. Safiuddin, S. Raman, and M. Zain, "Utilization of quarry waste fine aggregate in concrete mixtures," *Journal of Applied Sciences Research*, vol. 3, no. 3, pp. 202–208, 2003.

[12] M. Galetakis, G. Alevizos, and K. Leventakis, "Evaluation of fine limestone quarry by-products, for the production of building elements," *Construction and Building Materials*, vol. 26, no. 1, pp. 122–130, 2012.

[13] R. Venkatakrishnaiah and P. Rajkumar, "Effect of quarry dust on waste plastic fiber reinforced concrete – an experimental study," *Research in Civil and Environmental Engineering*, vol. 1, no. 4, pp. 234–238, 2013.

[14] Y. Ohama, "Recent progress in concrete-polymer composites," *Advanced Cement Based Materials*, vol. 5, no. 2, pp. 31–40, 1997.

[15] L. Czarnecki, "Concrete-polymer composites: trends shaping the future," *Journal of the Society of Materials Engineering for Resources of Japan*, vol. 15, no. 1, pp. 1–5, 2007.

[16] M. Frigione, "Concrete with polymers," *Eco-Efficient Concrete*, pp. 386–436, Woodhead Publishing limited, Cambridge, UK, 2003.

[17] Y. Ohama, "Polymer based admixtures," *Cement and Concrete Composites*, vol. 20, no. 2-3, pp. 189–212, 1998.

[18] W. Meng, "Basic mechanical properties research of SAE latex-modified mortar," *Advanced Materials Research*, vol. 1088, pp. 621–625, 2015.

[19] S. R. Bothra and Y. M. Ghugal, "Polymer-modified concrete: review," *International Journal of Research in Engineering and Technology*, vol. 4, no. 4, pp. 845–848, 2015.

[20] Y. Ohama, *Handbook of Polymer-Modified Concrete and Mortars*, William Andrew Inc., Norwich, NY, USA, 1995.

[21] Y. Ohama, "Principle of latex modification and some typical properties of latex modified mortars and concretes," *ACI Materials Journal*, vol. 84, no. 6, pp. 511–518, 1987.

[22] H. B. Wagner, "Polymer-modified hydraulic cements," *Industrial and Engineering Chemistry, Product Research and Development*, vol. 4, no. 3, pp. 191–196, 1965.

[23] L. K. Aggarwal, P. C. Thapliyal, and S. R. Karade, "Properties of polymer–modified mortars using epoxy and acrylic emulsions," *Construction and Building Materials*, vol. 21, no. 2, pp. 379–383, 2007.

[24] T. Fukuchi and Y. Ohama, "Process technology and properties of 2500 kg/cm2 strenght polymer impregnated concrete," in *Proceedings of the Second International Congress on Polymers in Concrete*, D. W. Fowler and D. R. Paul, Eds., Polymers in Concrete, Austin, TX, USA, 45–56, 1978.

[25] P. M. Cabrera Castro and E. Beira Fontaine, "Geotechnical characterization of the experimental field at the civil engineering from the University of Oriente," *Ingeniería*, vol. 11, no. 2, pp. 57–66, 2007.

[26] ASTM, ASTM D422-63, *Standard Test Method for Particle-Size Analysis of Soils*, ASTM International, West Conshohocken, PA, USA, 2007.

[27] ASTM, ASTM Standard D 4318-10, *Standard Test Methods for Liquid Limit, Plastic Limit, and Plasticity Index of Soils*, Annual Book of ASTM Standards, West Conshohocken, PA, USA, 2010.

[28] ASTM Standard D 2487-93, *Standard Test Method for Classification of Soils for Engineering Purposes*, Annual Book of ASTM Standards, West Conshohocken, PA, USA, 1993.

[29] ASTM International, "Standard test method for compressive strength of cylindrical concrete specimens," March 2017, http://www.astm.org.

[30] M. Milán, C. Yañez, L. Navarro, S. P. Verma, and G. Carrasco Nuñez, "Geología y qeoquímica de elementos mayores de la Caldera de Huichapan, Hidalgo, México," *Geofísica Internacional*, vol. 32, no. 2, pp. 261–276, 1993.

[31] A. Neville and J. J. Brooks, *Tecnología del Concreto*, Trillas, Mexico City, México, 2010.

[32] S. Valdés Constantino, "La Adición de Humo de Sílice para Concretos de Alta Resistencia," 2015.

[33] E. F. Irassar, V. L. Bonavetti, and G. Menéndez, "Cementos con material calcáreo: formación de thaumasita por ataque de sulfatos," *Revista de la Construcción*, vol. 9, no. 1, 2010.

[34] D. Laverde, J. Pedraza, S. Ospina et al., "El beneficio de arenas feldespáticas: una solución para la industria cerámica colombiana," *Dyna*, vol. 71, no. 143, pp. 45–54, 2004.

[35] G. del Carmen Tiburcio Munive, M. Sandez Aguilar, S. Aguayo Salinas, and D. BUrgos Flores, "Morteros para revestimiento de muros, utilizando arena zeolítica," *Épsilon*, vol. 1, no. 10, pp. 57–65, 2008.

[36] B. Bhardwaj and P. Kumar, "Waste foundry sand in concrete: a review," *Construction and Building Materials*, vol. 156, pp. 661–674, 2017.

[37] PINACAL, *Planes de Competitividad Innovación y Entorno*, Unión Europea, Valladolid, Spain, 2007.

[38] ASTM, ASTM C31/C31M-17, *Standard Practice for Making and Curing Concrete Test Specimens in the Field*, ASTM International, West Conshohocken, PA, USA, 2017.

Research Article

Effects of Nano-CaCO₃/Limestone Composite Particles on the Hydration Products and Pore Structure of Cementitious Materials

Huashan Yang [ID] and Yujun Che [ID]

¹School of Materials and Architecture Engineering, Guizhou Normal University, Guiyang 550025, China

Correspondence should be addressed to Huashan Yang; 13368600935@163.com

The agglomeration of nano-CaCO₃ (NC) is the largest bottleneck in applications in cementitious materials. If nano-CaCO₃ modifies the surface of micron-scale limestone powder (LS), then it will form nano-CaCO₃/limestone composite particles (NC/LS). It is known that micron-scale limestone is easily dispersed, and the "dispersion" of NC is governed by that of LS. Therefore, the dispersion of nano-CaCO₃ can be improved by the NC/LS in cementitious materials. In this work, the preparation of NC/LS was carried out in a three-necked flask using the $Ca(OH)_2$-H_2O-CO_2 reaction system. The morphology of NC/LS was observed by a field emission scanning electron microscope (FE-SEM). The effects of NC/LS on the hydration products and pore structure of cementitious materials are proposed. 5% NC/LS was added into cement paste and mortar, and the mechanical properties of the specimens were measured at a certain age. Differential scanning calorimetry (DSC), thermal gravimetric analysis (TG), and backscattered electron imaging (BSE) were conducted on the specimens to investigate the hydration products and pore structure. The properties of specimens with NC/LS were compared to that of control specimens (without NC/LS). The results revealed that NC/LS reduced the porosity and improved the mechanical properties of the cementitious materials.

1. Introduction

The development and increasing applications of green high-performance concrete (GHPC) have led to higher requirements for concrete additions, resulting in a variety of mineral additions, such as fly ash (FA), and ground granulated blast-furnace slag (GGBFS) [1–3]. The most successful of these mineral additions, FA, has seen its cost steadily increasing and its availability decreasing. One of the major drawbacks of concrete containing high volumes of FA is known to have negative impact on the early age properties [4]. It significantly slows setting and early-age compressive strength gain. An alternative solution is to use limestone powder (LS).

Considerable research has been carried out in recent years on the use of LS in Portland cement concrete [5–10]. Studies have revealed that limestone powders exhibit a filling effect on concrete [5]. Meanwhile, these powders can react with the aluminium phase in cement paste to create calcium carboaluminate hydrates [11–13] and accelerate C_3S hydration

[14, 15]. In this way, LS can improve the mechanical properties of cement, thus widely applied through various industries. It has been reported that the surface structure is an important property of LS [16]. However, there have been only few published studies concerning the effects of surface structure of LS on the fluidity and strength of Portland cement concrete [17].

In recent years, nano-CaCO₃ has been introduced in concrete [18], and some studies have suggested a potential benefit of physical properties of nano-CaCO₃ on the development of cementitious system [19–24]. However, it is believed that the most important challenge in the nano-composite research is to disperse properly the nanomaterials into the matrix [25, 26]. Due to the high surface energy of nanoparticles, nano-CaCO₃ is easy to agglomerate to form secondary particles, which will reduce the properties of cementitious materials. It is believed that nanomicron composite particle is a solution for this question [16]. If nano-CaCO₃ grows on the surface of LS, then the nano-CaCO₃/limestone composite particles (NC/LS) are prepared.
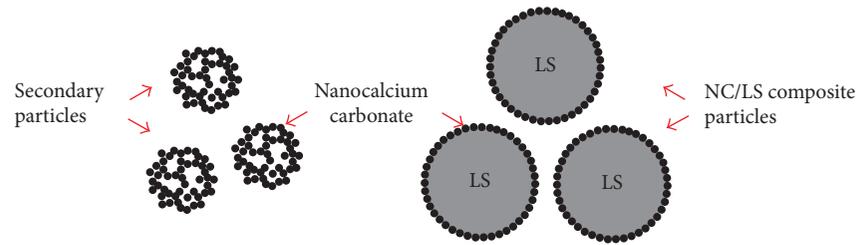
FIGURE 1: Secondary particles and nanomicron composite particles.

As it can be seen from Figure 1, this approach can readily achieve surface modification of LS. NC on the surfaces of LS means that NC is a part of LS. Thus, the "dispersion" of NC is governed by that of LS in cementitious materials. Compared to the nanoparticles, micron-scale LS is easy to obtain better dispersity due to lower surface energy. Therefore, the dispersity of nano-CaCO₃ will significantly be improved by NC/LS in cementitious materials. Furthermore, due to the sophisticated surface structures of nanomicron composite particles, it can have a significant effect on the hydration and microstructure of cementitious materials. Camiletti et al. [20] found that nano-$CaCO_3$ accelerates the setting and hardening process of ultra-high-performance concrete through providing nucleation sites, increasing contact points, and increasing the effective water-to-cement ratio. Yang et al. [16] also believes that nano-$CaCO_3$ particles on the surface of LS can act as heterogeneous nuclei for cement paste, making the size of calcium hydroxide crystals smaller, leading to a denser microstructure. Nevertheless, the effects of NC/LS on the hydration products and pore structure of cement pastes have received little attention.

This article explores the effects of NC/LS on the mechanical properties of cement paste and mortar. Differential scanning calorimetry, thermal gravimetric analysis, and backscattered electron imaging were employed to investigate the effects of NC/LS on the hydration products of cementitious materials. Cementitious materials are considered as porous composite materials that consist essentially of a binding medium within which are embedded particles or fragments of aggregate [27]. The complex pore structure of cementitious materials has great significance on their strength, permeability, and durability. The pore structure of cementitious materials was also investigated by BSE images analysis.

2. Materials and Methods

2.1. Materials. The materials involved in this study included nano-$CaCO_3$/limestone composite particles, limestone powder, calcium hydroxide, carbon dioxide, ordinary Portland cement type P.O. 42.5, and ISO standard sand. Carbon dioxide gas with a purity of 99.9% was purchased from standard commercial sources. Calcium hydroxide, P.O. 42.5 ordinary Portland cement, and ISO standard sand are also commercial products.

Nano-$CaCO_3$/limestone composite particles were prepared by heterogeneous nucleation. Via changing the reaction parameters such as mixing rate, the morphology of micron-scale limestone particles after coating has been
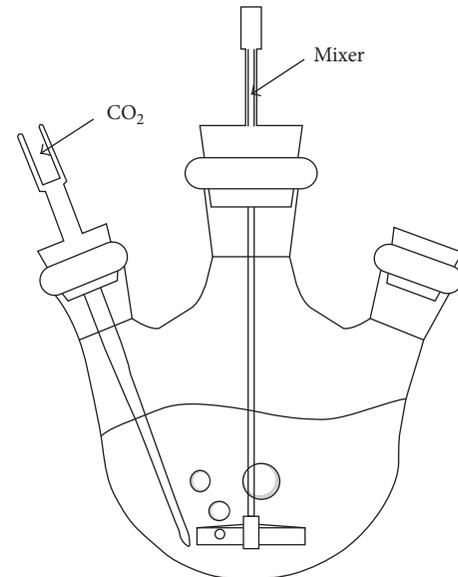
FIGURE 2: $Ca(OH)_2$-H_2O-CO_2 reaction system.

altered. The preparation of NC/LS was carried out in a three-necked flask using the $Ca(OH)_2$-H_2O-CO_2 reaction system (Figure 2). The mixtures comprising limestone powder and saturated solution of calcium hydroxide were stirred at 2400 rpm in a three-necked flask for 10 minutes. Then, carbon dioxide gas was blown into the three-necked flask with the same stirring. The pH value of the reaction solution was inspected using a pH meter. When the pH value reached 6, the reaction was completed, and then the carbon dioxide flow was stopped. The NC/LS was obtained after the slurry was washed by deionized water, filtered, and dried at 120°C in drying oven for at least 24 h. It is reported that some nanoparticles are associated with a high level of toxicity. As shown in Figure 2, the nano-$CaCO_3$/limestone composite particles were prepared by heterogeneous nucleation in a three-necked flask using the $Ca(OH)_2$-H_2O-CO_2 reaction system. Nanosized calcium carbonate particles are attached to the surface of micron-scale limestone particles. Also, acute and subchronic toxicity tests were performed to establish the safety of these products after oral administration [28]. Results showed that nano-$CaCO_3$ did not produce any obvious symptoms of toxicity, even at the highest dose administered. Thus, as a raw material of concrete, nano-$CaCO_3$ is safety.

The particle size distribution (PSD) of the LS are presented in Figure 3, which was determined by laser diffraction
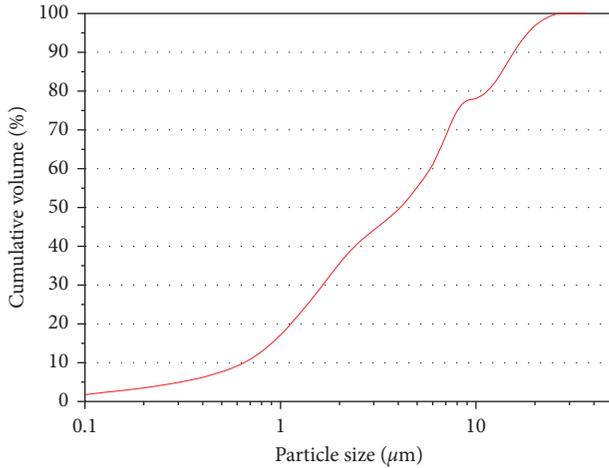
FIGURE 3: PSD of limestone powder.

FIGURE 4: XRD pattern of limestone powder.

TABLE 1: Chemical composition of cement and limestone (%).

Oxide	Portland cement	Limestone
SiO_2	21.06	4.38
Al_2O_3	6.13	1.56
Fe_2O_3	2.61	0.76
CaO	61.18	48.00
MgO	1.66	0.49
K_2O	1.06	0.14
Na_2O	0.21	0.03
SO_3	3.18	—
Loss	2.12	44.17
Others	0.80	0.13

using a laser granulometry (JL-1155, China) for grain size between 0.1 μm and 155 μm. LS has a mean particle size $D_{50} = 5\,\mu$m. The chemical composition of Portland cement and LS as given in Table 1 was determined by X-ray fluorescence (XRF). Phase identification of LS was performed at room temperature using X-ray diffraction (XRD, Bruker AXS D8-Focus, Germany) with Cu-Kα radiation in the range 2θ-scale from 5° to 65°. X-ray diffraction studies confirmed that the main phase of the LS is calcite (Figure 4).

2.2. Methods. To study the effects of NC/LS on the strength development of cement pastes and mortar, paste mixes were prepared by adopting a water-to-binder ratio of 0.4, and mortar mixes were prepared by adopting a binder-to-sand ratio of 1 : 3 and water-to-binder ratio of 0.5. Table 2 summarizes the proportions of cement paste and mortar. Specimens C-0 and M-0 are the control specimens of C-NC/LS and M-NC/LS, respectively. After 24 h, the specimens were demoulded and were immersed in water at 20°C until testing. The mechanical properties of these specimens were tested after 3 and 28 days. The test results of cement pastes are the average of three compression test. The test results of cement mortar are the average of three flexural specimens and six compression test. The amount of calcium

silicate hydrates and calcium hydroxide present in specimens after 3 days was determined by thermogravimetric analysis (PerkinElmer Instrument, USA) from 100°C to 1000°C in a nitrogen atmosphere. Samples for DSC-TG analysis were obtained from 3-day-old specimens. Before grinding, specimens were kept in absolute ethyl alcohol up to test to stop the hydration process.

It is believed that pore structure has a direct effect on properties like strength, permeability, and durability of cementitious materials. Mercury intrusion porosimetry (MIP) is a widely used method to characterize the pore structure of cementitious materials. However, the technique has several limitations [29, 30], among which are the ink bottle effect and a cylindrical pore geometry assumption that lead to inaccurate pore size distribution curves [31]. Also, Lange et al. [32] compared MIP and image analysis. Results showed that the two methods generate PSD curves of similar shape, and the image-based PSD has the advantage of being able to better describe the large porosity in the microstructure. Therefore, researchers are interested in image analysis for a more complete picture of pore structure. According to the working principles of backscattered electron imaging in scanning electron microscope, the backscattered electrons refer to the incident electrons that are reflected by atoms of the solid sample and the contrast of images are related to the atomic number distribution of sample surface atoms. Areas with high average atomic numbers generate strong signals, resulting in a bright contrast in BSE images. Therefore, the relative atomic number of different areas can be determined based on BSE images contrasts [33].

The partially reacted cement grains, cement hydrates, and pores in concrete are particularly variable, but average features can be measured, which help to understand the microstructure of cementitious materials. A JSM-IT300 scanning electron microscope was used to observe the microstructure of the specimens based on backscattered electron imaging. A small fractured sample was soaked in acetone to stop hydration and dried at 80°C for 2 h. Then, the sample was coated with 20 nm of gold to make it conductive. A magnification of 500x was used for all images. At 500x, the

TABLE 2: Proportions of cement paste and mortar.

Constitute	C-0	C-NC/LS	M-0	M-NC/LS
Cement paste				
Water-to-binder ratio	0.4	0.4	—	—
NC/LS (%)	0	5.0	—	—
Cement mortar				
Water-to-binder ratio	—	—	0.5	0.5
NC/LS (%)	—	—	0	5.0
Binder-to-sand ratio	—	—	1 : 3	1 : 3

(a)

(b)
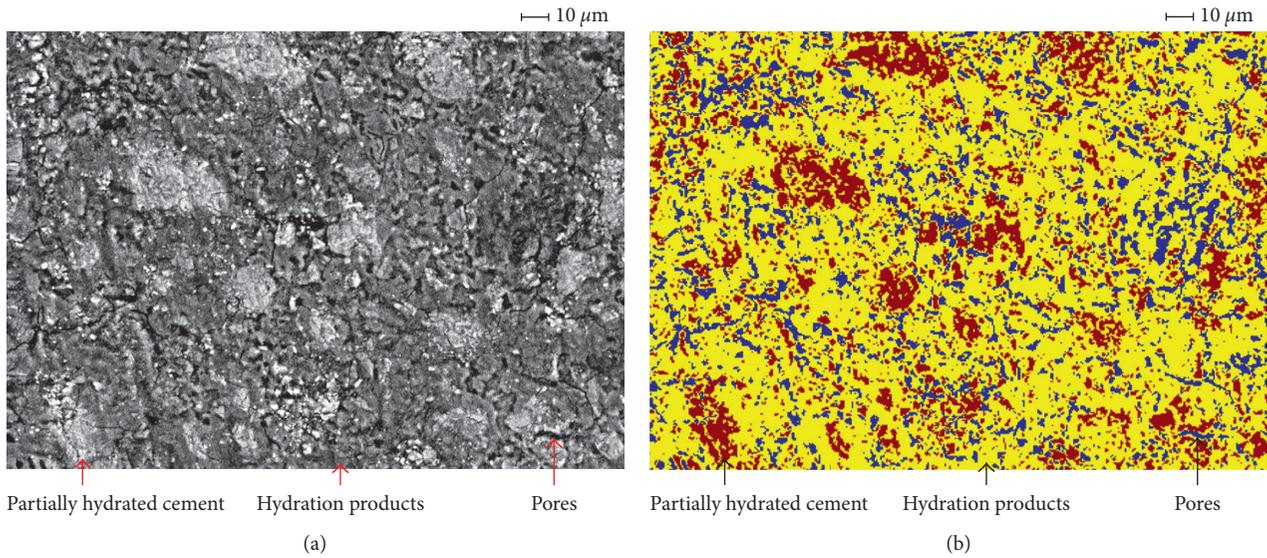
FIGURE 5: Cluster analysis of partially hydrated cement, hydration products, and pores. (a) A typical BSE image of C-0. (b) Results of cluster analysis.

resolution of the 1024×768 digital image (width of a single pixel) is $0.222\,\mu$m. Figure 5(a) shows a typical BSE image of specimen C-0. As can be seen, brighter areas correspond to partially reacted cement grains; less bright areas correspond to cement hydrates; and least bright areas correspond to pores. Cluster analysis was conducted on pretreated BSE images to separate partially reacted cement grains, cement hydrates, and pores, as shown in Figure 5(b). The effects of NC/LS on the pore structure and hydration products of cement specimens can be further investigated by calculating the respective areas of partially reacted cement grains, cement hydrates, and pores, as well as pore size distribution. Ten backscattered electron (BSE) images of random locations on the polished surface of each specimen were captured as image files in the image analysis computer.

3. Results and Discussion

3.1. Surface Structure of NC/LS. The micron-scale particles of LS and surface structure of NC/LS are shown in Figure 6(a) and (b), respectively. It is seen that LS is composed of micron-scale particles, which are characterized by smooth cleavage plane and sharp edges. However, the NC/LS, a composite of limestone powder and nanosized calcium

carbonate, has very different particle morphology from that of raw limestone particles. As shown in Figure 6(b), nanosized calcium carbonate particles are attached to the surface of micron-scale limestone particles, resulting in a sophisticated surface structure of composite particles. The sharp-pointed edges of the micron-particles are not observed. Tanaka and Koishi [34] and Felekoglu [17] proposed that properties of cementitious materials are not solely related to the particle size distribution, also particle microshape and surface characteristics are important. Thus, the microshape and surface structure of particles have an important effect on the hydration and microstructure of cementitious materials. Furthermore, the most significant issue for nanoparticles is that of effective dispersion [35]. Nano-$CaCO_3$ on the surface of the micron-scale limestone particles will also significantly improve the dispersion of nano-$CaCO_3$ in cementitious materials.

3.2. Strength Development. Figure 7 shows the compressive strength of cement pastes and the flexural and compressive strength of cement mortar after 3 and 28 days. Cement pastes with NC/LS performed better in terms of compressive strength for all ages, probably due to the formation of calcium aluminate monocarbonate and the accelerating

(a)

(b)
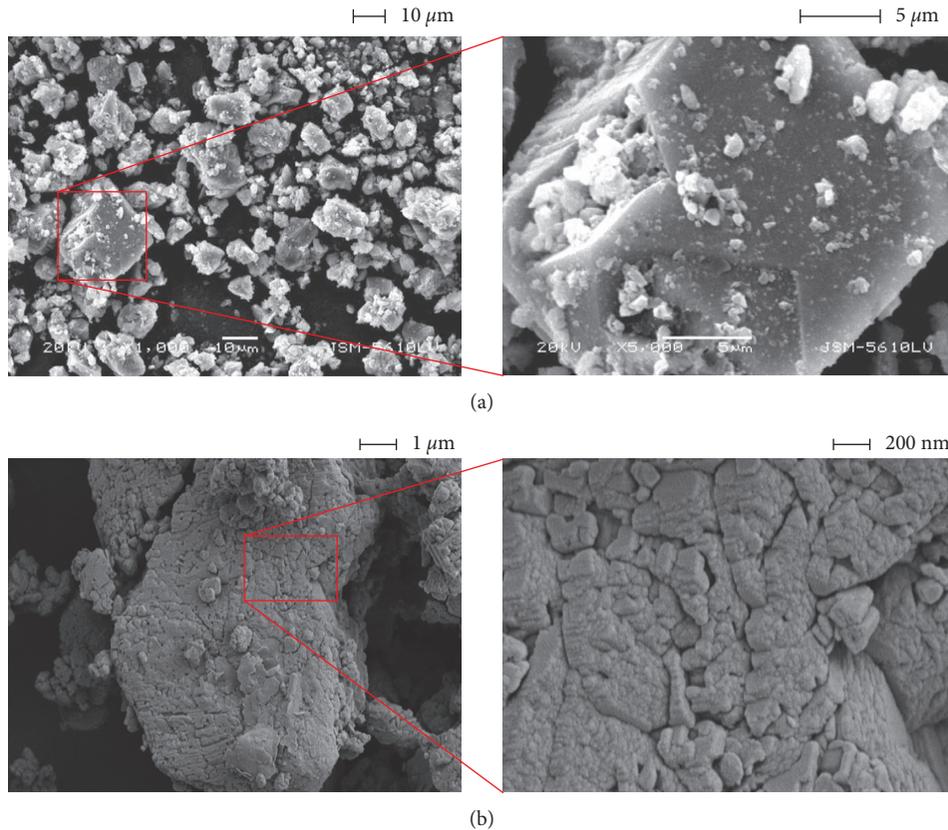
FIGURE 6: (a) Micron-scale particles of limestone powder. (b) Surface structure of NC/LS composite particles.

effect on cement hydration in the presence of calcium carbonate [11, 12, 14]. Similarly, the flexural and compressive strength of specimen M-NC/LS was higher than that of specimen M-0. These results suggest that NC/LS improved the mechanical properties of cement paste and mortar. On the other hand, the compressive strength of specimen C-NC/LS after 3 and 28 days was, respectively, 6.3% and 1.9% higher than that of specimen C-0. The compressive strength of M-NC/LS after 3 and 28 days was, respectively, 14.5% and 7.2% higher than that of M-0. These results indicate that NC/LS improves the cement paste and mortar mechanical properties significantly during the early stages.

As discussed that characteristics of NC/LS are quite different from that of LS and the surface of NC/LS is more favorable for the precipitation and further growth of calcium silicate hydrate gels. Therefore, the improved strength of specimens C-NC/LS and M-NC/LS can be attributed to the complex surface structure of NC/LS, which influenced the size and morphology of hydration products of the cement [16]. Furthermore, XRD results [16] have shown that the complex surface structure of NC/LS can disturb the nucleation and growth of calcium hydroxide, resulting in the reduction of particle size and crystal orientation degree. Furthermore, the nucleation of calcium silicate hydrate is accelerated by the presence of nano-CaCO$_3$ particles [21] because nano-CaCO$_3$ is finer than LS particles. Camiletti, Soliman, and Nehdi also believe that micro-CaCO$_3$ acted mainly as an inert filler, while nano-CaCO$_3$ accelerated the

cement hydration process through nucleation, and also acted as an effective filling material [36]. Also, it is reported that the presence of nano-CaCO$_3$ may cause acceleration of early strength development [26], compensates the dilution effect of the binding material, and thus offsets the negative effects of fly ash on early-age properties to facilitate the development of a more environmentally fly ash concrete. Hence, through the use of NC/LS, more environmentally friendly cementitious materials can be produced by reducing its cement factor, while achieving enhanced engineering properties.

3.3. Thermal Gravimetric Analysis. Figure 8 shows the DSC-TG curves of specimen C-NC/LS and C-0 after 3 days. It shows the normalized mass loss in percent (current mass divided by initial mass) versus temperature. It can be seen that the two specimens are gradually losing mass with the increasing temperature. The tendency of each curve in varying with the increasing temperature is almost the same. Mass loss between 105°C and 420°C represents the loss of combined water due to calcium silicate hydrate, aluminate hydrate, and ferroaluminate hydrate, between 420°C and 540°C, it corresponds to the dehydration of calcium hydroxide, and decarbonation of well-crystalline calcium carbonate occurs at temperature between 540°C and 750°C. In Figure 8, three main rapid losses in weight exist in the vicinities of 200°C, 500°C, and 750°C for the two specimens.

FIGURE 7: Strength of cement paste and mortar with NC/LS.

TABLE 3: Porosity and contents of partially reacted cement grain and hydration products calculated based on BSE results.

Specimen	C-0	C-NC/LS
Partially reacted cement grain (%)	18.6	24.2
Hydration products (%)	63.5	58.5
Porosity (%)	17.9	17.3

FIGURE 9: Pore size distributions of specimens.

Figure 7, cement pastes and mortar containing NC/LS exhibited higher strength than that of control specimen at 3 days. The investigation of the phenomenon will be the subject of further research by BSE analysis.

3.4. BSE Image Analysis. Based on BSE images, the contents of partially reacted cement grains and hydration products of different specimens and their respective porosities were calculated and are shown in Table 3. After 3 days, specimen C-NC/LS had higher contents of partially reacted cement grains than that in specimen C-0, and specimen C-NC/LS had lower hydration products content than did specimen C-0. However, the porosity of specimen C-NC/LS was lower than that of specimen C-0. In other words, C-NC/LS had higher structure compactness than that of specimen C-0.

It can be observed from Figure 9 that the larger pores of pastes containing NC/LS are decreased, while the smaller pores are increased. The use of NC/LS leads to a more compact paste with a reduction of larger pores, indicating that the presence of NC/LS is advantageous in pores modification. It is noted that the sophisticated surface structure of NC/LS has a significant influence in decreasing the larger pores of cement pastes and further influences its macroscopic properties [16].

As indicated by both BSE images and DSC-TG results, specimen C-NC/LS had lower contents of calcium silicate hydrate and calcium hydroxide than that in specimen C-0. However, specimen C-NC/LS had higher compressive strength than that of specimen C-0, and specimen M-NC/LS had higher flexural and compressive strength than that of

Specimen	C-0	C-NC/LS
Nonevaperable water/%	6.56	6.31
Calcium hydroxide/%	15.46	14.27

FIGURE 8: DSC-TG curves of specimens.

$\triangle W1$ corresponded to the dehydration of calcium silicate hydrates, $\triangle W2$ corresponded to the dehydration of calcium hydroxide, and $\triangle W3$ corresponded to calcium carbonate decomposition. The $\triangle W3$ of specimen C-NC/LS was higher than that of specimen C-0. This can be attributed to calcium carbonate decomposition in NC/LS. The $\triangle W1$ and $\triangle W2$ of specimen C-NC/LS is slightly lower than that of specimen C-0. This may be due to the part of Portland cement in specimen C-NC/LS which was substituted by NC/LS. On the other hand, the smaller weight loss of calcium hydroxide in specimen C-NC/LS compared to specimen C-0 indicates that the calcium hydroxide absorbs carbon dioxide to form more calcium carbonate probably. However, as shown in

specimen M-0. According to further investigations of the porosity and pore structure of specimens obtained, the improved strength of specimens C-NC/LS and M-NC/LS can be attributed to their lower porosity and better pore structure. Hence, the microstructure of cementitious materials with NC/LS depends not only on the distribution of particles but also the morphology and surface structure of the particle. Rashad' research shows that the enhancement in strength of hardened paste is related to the refinement of calcium hydroxide grains, which occurred during the hydration of cement [37]. Thus, the growth of calcium hydroxide grains in cementitious materials may be affected by NC/LS, either.

4. Conclusions

Based on the results obtained in this study, the following conclusions can be drawn:

(1) Nano-$CaCO_3$/limestone composite particles were successfully prepared using the $Ca(OH)_2$-H_2O-CO_2 reaction system. The surface structure and morphology of micron-scale limestone particles have been altered. Nano-$CaCO_3$ scattered evenly on the surface of the micron-scale limestone particles. It is an effective method to solve the dispersion problem of nano-$CaCO_3$ particles in concrete.

(2) Adding nano-$CaCO_3$/limestone composite particles resulted in reduced porosity and enhanced pore structure for hardened cementitious materials. The microstructure of hardened cementitious materials was optimized by nano-$CaCO_3$/limestone composite particles. Therefore, the mechanical properties of cement paste and mortar were improved.

Conflicts of Interest

The authors declare that there are no conflicts of interest regarding the publication of this paper.

Acknowledgments

References

[1] P. C. Aitcin, "Cements of yesterday and today: concrete of tomorrow," *Cement and Concrete Research*, vol. 30, no. 9, pp. 1349–1359, 2000.

[2] E. Gartner, "Industrially interesting approaches to "low-CO_2" cements," *Cement and Concrete Research*, vol. 34, no. 9, pp. 1489–1498, 2004.

[3] P. K. Mehta and R. W. Burrows, "Building durable structures in the 21st century," *Concrete International*, vol. 23, no. 3, pp. 57–63, 2001.

[4] S. Kawashima, J. W. T. Seo, D. Corr, M. C. Hersam, and S. P. Shah, "Dispersion of $CaCO_3$ nanoparticles by sonication and surfactant treatment for application in fly ash-cement systems," *Materials and Structures*, vol. 47, no. 6, pp. 1011–1023, 2014.

[5] V. Bonavetti, H. Donza, G. Menendez, O. Cabrera, and E. F. Irassar, "Limestone filler cement in low w/c concrete: a rational use of energy," *Cement and Concrete Research*, vol. 33, no. 6, pp. 865–871, 2003.

[6] A. A. Elgalhud, R. K. Dhir, and G. Ghataora, "Limestone addition effects on concrete porosity," *Cement and Concrete Composites*, vol. 72, pp. 222–234, 2016.

[7] M. Heikal, H. El-Didamony, and M. S. Morsy, "Limestone-filled pozzolanic cement," *Cement and Concrete Research*, vol. 30, no. 11, pp. 1827–1834, 2000.

[8] S. Palm, T. Proske, M. Rezvani, S. Hainer, C. Muller, and C. A. Graubner, "Cements with a high limestone content-mechanical properties, durability and ecological characteristics of the concrete," *Construction and Building Materials*, vol. 119, pp. 308–318, 2016.

[9] S. Tsivilis, E. Chaniotakis, G. Kakali, and G. Batis, "An analysis of the properties of Portland limestone cements and concrete," *Cement and Concrete Composites*, vol. 24, no. 3-4, pp. 371–378, 2002.

[10] N. Voglis, G. Kakali, E. Chaniotakis, and S. Tsivilis, "Portland-limestone cements. Their properties and hydration compared to those of other composite cements," *Cement and Concrete Composites*, vol. 27, no. 2, pp. 191–196, 2005.

[11] V. L. Bonavetti, V. F. Rahhal, and E. F. Irasser, "Studies on the carboaluminate formation in limestone filler-blended cements," *Cement and Concrete Research*, vol. 31, no. 6, pp. 853–859, 2001.

[12] G. Kakali, S. Tsivilis, E. Aggeli, and M. Bati, "Hydration products of C_3A, C_3S and Portland cement in the presence of $CaCO_3$," *Cement and Concrete Research*, vol. 30, no. 7, pp. 1073–1077, 2000.

[13] B. Lothenbach, G. Le Saout, E. Gallucci, and K. Scrivener, "Influence of limestone on the hydration of Portland cements," *Cement and Concrete Research*, vol. 38, no. 6, pp. 848–860, 2008.

[14] J. Pera, S. Husson, and B. Guilhot, "Influence of finely ground limestone on cement hydration," *Cement and Concrete Composites*, vol. 21, no. 2, pp. 99–105, 1999.

[15] V. Rahhal and R. Talero, "Early hydration of Portland cement with crystalline mineral additions," *Cement and Concrete Research*, vol. 35, no. 7, pp. 1285–1291, 2005.

[16] H. Yang, Y. Che, and M. Zhang, "Effect of nano-$CaCO_3$/limestone powder composite on the early age cement hydration products," *Key Engineering Materials*, vol. 703, pp. 354–359, 2016.

[17] B. Felekoglu, "Effects of PSD and surface morphology of micro-aggregates on admixture requirement and mechanical performance of micro-concrete," *Cement and Concrete Composites*, vol. 29, no. 6, pp. 481–489, 2007.

[18] F. U. A. Shaikh and S. W. M. Supit, "Mechanical and durability properties of high volume fly ash (HVFA) concrete containing calcium carbonate ($CaCO_3$) nanoparticles," *Construction and Building Materials*, vol. 70, pp. 309–321, 2014.

[19] F. U. A. Shaikh and S. W. M. Supit, "Chloride induced corrosion durability of high volume fly ash concretes containing nano particles," *Construction and Building Materials*, vol. 99, pp. 208–225, 2015.

[20] J. Camiletti, A. M. Soliman, and M. L. Nehdi, "Effect of nano-calcium carbonate on early-age properties of ultra-high-performance concrete," *Magazine of Concrete Research*, vol. 65, no. 5, pp. 297–307, 2013.

[21] T. Sato and J. J. Beaudoin, "Effect of nano-CaCO$_3$ on hydration of cement containing supplementary cementitious materials," *Advances in Cement Research*, vol. 23, no. 1, pp. 33–43, 2011.

[22] S. Kawashima, P. K. Hou, D. J. Corr, and S. P. Shah, "Modification of cement-based materials with nanoparticles," *Cement and Concrete Composites*, vol. 36, pp. 8–15, 2013.

[23] J. M. Makar, G. W. Chan, J. J. Beaudoin, F. Torres, and K. Trischuk, "Effect of n-CaCO$_3$ and metakaolin on hydrated Portland cement," *Advances in Cement Research*, vol. 24, no. 4, pp. 211–219, 2012.

[24] G. C. Long, Y. Shi, K. L. Ma, and Y. J. Xie, "Reactive powder concrete reinforced by nanoparticles," *Advances in Cement Research*, vol. 28, no. 2, pp. 99–109, 2016.

[25] A. H. Korayem, N. Tourani, M. Zakertabrizi, A. M. Sabziparvar, and W. H. Duan, "A review of dispersion of nanoparticles in cementitious matrices: nanoparticle geometry perspective," *Construction and Building Materials*, vol. 153, pp. 346–357, 2017.

[26] T. Meng, Y. Yu, and Z. Wang, "Effect of nano-CaCO$_3$ slurry on the mechanical properties and micro-structure of concrete with and without fly ash," *Composites Part B: Engineering*, vol. 117, pp. 124–129, 2017.

[27] S. W. Tang, X. H. Cai, Z. He et al., "The review of pore structure evaluation in cementitious materials by electrical methods," *Construction and Building Materials*, vol. 117, pp. 273–284, 2016.

[28] S. Huang, J. C. Chen, C. W. Hsu, and W. H. Chang, "Effects of nano calcium carbonate and nano calcium citrate on toxicity in ICR mice and on bone mineral density in an ovariectomized mice model," *Nanotechnology*, vol. 20, no. 37, pp. 1–7, 2009.

[29] S. Diamond, "Mercury porosimetry: an inappropriate method for the measurement of pore size distributions in cement-based materials," *Cement and Concrete Research*, vol. 30, no. 10, pp. 1517–1525, 2000.

[30] K. Tanaka and K. Kurumisawa, "Development of technique for observing pores in hardened cement paste," *Cement and Concrete Research*, vol. 32, no. 9, pp. 1435–1441, 2002.

[31] K. L. Willis, A. B. Abell, and D. A. Lange, "Image-based characterization of cement pore structure using wood's metal intrusion," *Cement and Concrete Research*, vol. 28, no. 12, pp. 1695–1705, 1998.

[32] D. A. Lange, H. M. Jennings, and S. P. Shah, "Image-analysis techniques for characterization of pore structure of cement-based materials," *Cement and Concrete Research*, vol. 24, no. 5, pp. 841–853, 1994.

[33] K. L. Scrivener, "Backscattered electron imaging of cementitious microstructures: understanding and quantification," *Cement and Concrete Composites*, vol. 26, no. 8, pp. 935–945, 2004.

[34] I. Tanaka and M. Koishi, "Fundamental properties of powder, paste and mortar of surface modified cement and process of the surface modification," *Construction and Building Materials*, vol. 13, no. 5, pp. 285–292, 1999.

[35] F. Pacheco-Torgal, S. Miraldo, Y. Ding, and J. A. Labrincha, "Targeting HPC with the help of nanoparticles: an overview," *Construction and Building Materials*, vol. 38, pp. 365–370, 2013.

[36] J. Camiletti, A. M. Soliman, and M. L. Nehdi, "Effects of nano- and micro-limestone addition on early-age properties of ultra-high-performance concrete," *Materials and Structures*, vol. 46, no. 6, pp. 881–898, 2013.

[37] A. M. Rashad, "Effects of ZnO$_2$, ZrO$_2$, Cu$_2$O$_3$, CuO, CaCO$_3$, SF, FA, cement and geothermal silica waste nanoparticles on properties of cementitious materials–a short guide for civil engineer," *Construction and Building Materials*, vol. 48, pp. 1120–1133, 2013.

Research Article

Investigation of Rheological Properties of Blended Cement Pastes Using Rotational Viscometer and Dynamic Shear Rheometer

Yoo Jae Kim ⬤,[1] Bum-Yean Cho,[2] Soon-Jae Lee ⬤,[1] Jiong Hu,[3] and James W. Wilde[1]

[1]Department of Engineering Technology, Texas State University, 601 University Drive, San Marcos, TX 78666, USA
[2]Department of Architectural Engineering, University of Seoul, 163 Seoulsiripdae-ro, Dongdaemun-gu, Seoul 02504, Republic of Korea
[3]Department of Civil Engineering, University of Nebraska-Lincoln, 1400 R Street, Lincoln, NE 68588, USA

Correspondence should be addressed to Yoo Jae Kim; yk10@txstate.edu

To successfully process concrete, it is necessary to predict and control its flow behavior. However, the workability of concrete is not completely measured or specified by current standard tests. Furthermore, it is only with a clear picture of cement hydration and setting that full prediction and control of concrete performance can be generalized. In order to investigate the rheological properties of blended cement pastes, a rotational viscometer (RV) was used to determine the flow characteristics of ordinary and blended pastes to provide assurance that it can be pumped and handled. Additionally, a dynamic shear rheometer (DSR) was used to characterize both the viscous and elastic components of pastes. Ordinary Portland cement paste and blended pastes (slag, fly ash, and silica fume) were investigated in this study. The stress and strain of the blended specimens were measured by the DSR, which characterizes both viscous and elastic behaviors by measuring the complex shear modulus (the ratio of total shear stress to total shear strain) and phase angle (an indicator of the relative amounts of recoverable and nonrecoverable deformation) of materials. Cement pastes generally exhibit different rheological behaviors with respect to age, mineral admixture type, and cement replacement level.

1. Introduction

The concrete industry defines workability as "the ease and homogeneity for which the concrete or mortar can be placed, consolidated, and finished" [1]. Concrete workability should ideally be characterized by its rheological properties, thus establishing a materials science basis. Cement paste plays a major role in controlling rheological properties, making it necessary to simulate the workability of concrete before it is transported and handled. However, there are no standard tests for fresh concrete that relate directly to plastic viscosity [2, 3]. Because of this, the workability of concrete is not completely measured or specified by current standard tests [4].

The flow behavior of cement paste is important because it controls the flow ability and process ability of concrete. Because the viscosity of cement paste rises with increasing concentration of solid particles, several empirical relationships between viscosity, cement concentration, and fineness have been proposed [5].

It is important to determine the setting time when testing paste specimens. As setting is significant in the development of rigidity in an initially fluid material, it is a part of rheology and the study of flow [6]. Plastic viscosity depends mainly on the volume of solid particles and how densely they are packed. The microstructure most commonly responsible for high yield stress is the three-dimensional network that often forms due to flocculation. The yield stress reflects the extent of this flocculation and the strength of the attractive interparticle forces responsible for the flocculation [7].

Hydration reactions tend to influence the viscosity results of ordinary and blended pastes because hydration generally increases both yield stress and plastic viscosity. Hydration mostly increases plastic viscosity only insofar as it increases the volume fraction of solid material [8]. Yield stress is particularly sensitive to hydration reactions, and since early hydration products cause cement particles to bond more strongly together (or increase the number of

interparticle bonds), hydration is expected to increase the yield stress [9].

In order to measure the viscosity of the blended pastes in this study, the rotational viscometer was used to determine the flow characteristics of ordinary and blended pastes and to assure that it could be pumped and handled. While a viscometer is designed to test the asphalt binder viscosity, it was used in this study to compare the viscous property of the different blended pastes at a temperature of 25°C since the temperature effects the rheological properties of the cement paste [10]. The stress and strain of the blended specimens were measured with a dynamic shear rheometer (DSR), which characterizes both viscous and elastic behavior by measuring the complex shear modulus (the ratio of total shear stress to total shear strain) and phase angle (an indicator of the relative amounts of recoverable and nonrecoverable deformation) of materials.

2. Experimental Program

2.1. Materials and Equipment. Three supplementary cementing materials (SCMs) and one Portland cement source were used in this research project. The fly ash was a class C ash from Boral Material Technologies, and the ground granulated blast furnace slag was furnished by Holcim. The silica fume was densified microsilica from Grace Construction Products, and the Type I Portland cement was furnished by LaFarge Building Materials.

Cement pastes were mixed and tested using the following equipment: (1) a Cole-Parmer servodyne mixer with a high shear mixing blade to mix the paste samples, (2) paste samples were tested for rotational viscosity with a Brookfield model DV-II+ viscometer, and (3) dynamic shear rheometry testing was performed with a Bohlin Instruments rheometer.

2.2. Sample Preparation. Paste samples were prepared by first batching the appropriate amounts of Portland cement and mineral admixture. For all testing, the weight of cementitious material used was 80 grams. Both fly ash and slag were added at dosage rates of 20%, 30%, and 40%, while silica fume was added at lower dosage rates of 5%, 10%, and 15%. DSR testing was performed with a w/c ratio of 0.40, while rotational viscosity testing was performed at w/c ratios of 0.40 and 0.50. Before the addition of water to the blend, the cementitious material was first mixed by hand to provide uniformity.

Upon the addition of water, the paste was mixed by hand for approximately 15 seconds to remove excess air and allow for the mixing water to reach the bottom of the container. The paste was then immediately mixed using the servodyne mixer with a high shear mixing blade for 1 minute at a speed of 300 RPM. This allowed for complete mixing without any visible clumps in the paste. After mixing, DSR or viscosity testing was performed on the paste samples.

2.3. Rotational Viscometer. The rotational viscometer is normally used to measure the flow characteristics of asphalt binders. For this project, however, the viscometer was used to measure the flow characteristics of cement pastes. The viscometer operates by rotating a spindle inside the

TABLE 1: Specific gravities for cementitious materials.

Material	Specific gravities
Portland cement	3.15
Silica fume	2.20
Slag	2.90
Fly ash	2.40

specimen test tube and measuring the torque required to rotate the spindle at a given speed, normally 20 RPM. Based on the torque, the viscometer determines the viscosity of the specimen in units of centipoises (cP).

There are two components for the rotational viscosity apparatus: a temperature control system and a viscosity measuring system. The temperature control system consists of a thermocontainer and temperature controller. The specimen is placed in an aluminum test tube, which is then placed into the thermocontainer. For asphalt binder testing, the test temperature is maintained at either 135°C or 165°C. Since such high temperatures would be very detrimental to cement paste, the temperature was set to 25°C for testing paste specimens. The viscosity measuring system consists of a motor, spindle, control keys, and digital readout. As the spindle spins inside the specimen, a torsional spring is wound as the torque required to rotate the spindle increases.

The spindle's shape is best described as a "plumb bob." Different-sized spindles are available, depending on the specimen that is being tested. For this work, a size 27 spindle was utilized, which is typical for modified asphalt binders. When using this size spindle for testing asphalt binders, a sample size of 8.5 grams was used. Since an asphalt binder was not used, certain assumptions had to be made to ensure that the appropriate volume of paste was placed in the test tube. Since the specific gravity of asphalt binder is roughly 1.030, a sample size of 8.5 grams of asphalt binder would yield a volume of 8.25 cm^3. When performing calculations to determine the weight of cement paste to add to the test tube to obtain a volume of 8.25 cm^3, specific gravities of the materials used were assumed, as was an air void content of zero percent. Table 1 illustrates the specific gravities used for the calculations.

Sample calculations are shown below for determining the weight of cement paste to test for rotational viscosity.

$$
\begin{aligned}
\text{For 20\% fly ash, } & \text{w/c} = 0.50, \text{ and SG of water} \\
& = 1.00, \text{ combined SG} : [(0.5)(1.00) \\
& \quad + (0.20)(2.40) + (0.80)(3.15)]/1.5 \\
& = 2.333, \text{ weight} = \text{SG}^*\text{volume} \\
& = 2.333^*8.25\text{cm}^3 = 19.2 \text{ grams.}
\end{aligned}
\tag{1}
$$

$$
\begin{aligned}
\text{For 30\% slag, } & \text{w/c} = 0.50, \text{ and SG of water} \\
& = 1.00, \text{ combined SG} : [(0.5)(1.00) \\
& \quad + (0.30)(2.90) + (0.70)(3.15)]/1.5 \\
& = 2.383, \text{ weight} = \text{SG}^*\text{volume} \\
& = 2.383^*8.25\text{cm}^3 = 19.7 \text{ grams.}
\end{aligned}
\tag{2}
$$
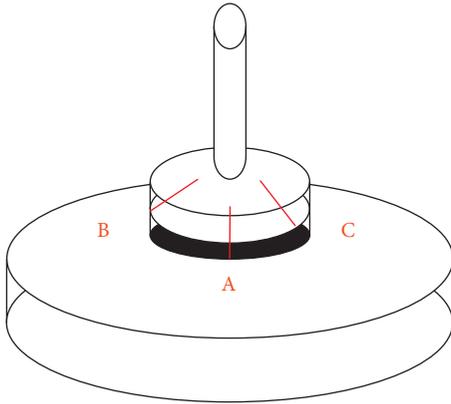
FIGURE 1: Dynamic shear rheometer operation.

FIGURE 2: G^* sin(delta) with time after mixing (0.4 w/c ratio).

The paste specimens were added to the test tube upon completion of mixing. It should be noted that it was difficult to obtain the exact amount of paste in the test tube due to the thickness of the paste. Once the specimen was loaded into the test tube, it was placed into the thermocontainer. The spindle was then lowered into the test tube, and the test began. Viscosity testing for asphalt binders requires only three measurements (one measurement every minute for three minutes). For the cement paste samples, testing was performed for 30 minutes with the viscometer recording the data every minute.

2.4. Dynamic Shear Rheometer. The dynamic shear rheometer (DSR) is used to characterize both the viscous and elastic components of asphalt binders. The DSR is able to do this by applying shear stress to the sample. Shear stress is applied by placing a fixed plate below the sample and an oscillating plate above the sample. The DSR was programmed to operate at a frequency of 10 radians per second or approximately 1.59 Hz (cycles per second). During each cycle, the centerline of the top plate passed from point A to point B (Figure 1). From point B, the top plate rotated to point C after passing point A. The cycle was completed when the top plate returned to point A from point C [11].

For an asphalt binder sample, a silicone mold is used to form a disc-shaped specimen. The use of this mold is impractical for a cement paste sample because the paste would have to set before it could be removed and maintain the proper shape. As a result, the paste samples were placed directly onto the fixed plate and shaped with a spatula. Paste samples were tested using a 2000 micron gap spacing between the two plates. The gap spacing was originally set to 2050 microns, and the samples were "trimmed." After trimming, the gap spacing was set to 2000 microns. Tests with the DSR are normally conducted at the high-temperature grade of an asphalt binder, but for this testing, the temperature was maintained at 25°C.

The results of DSR testing are the complex shear modulus (G^*) and phase angle (δ). The shear modulus is a measure of the materials resistance to deformation when tested under repeated shear stress. This shear modulus has both a viscous and elastic component, and the relative amounts of each are determined by the phase angle. A sample with a phase angle of 90° would be characterized as a completely viscous material. Likewise, a sample with a phase angle of 0° would be classified as a completely elastic material. For asphalt binders, temperature and aging conditions are the two main properties that change the shear modulus and phase angle. For cement pastes, time is the main factor that can change the results. As a cement paste begins to harden, its behavior should change from more viscous to more elastic.
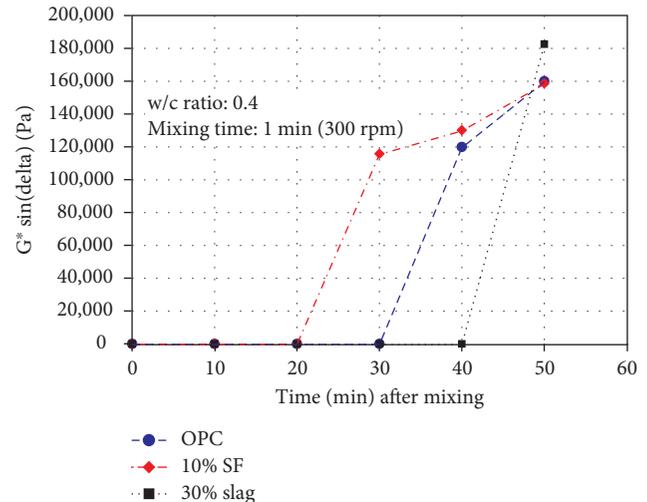
During this research, paste samples were originally left between the two plates of the DSR, with testing occurring at various time intervals. This method of testing, while adequate for asphalt binder samples, did not work well for paste samples. The prolonged time between the two plates caused the paste to dry out. This probably occurred due to either the thickness of the paste sample (2000 microns) or from the constant pressure applied to the sample by the plates or a combination of both. It was determined that the best method for testing the paste over time was to test an individual sample only once. For the different time periods investigated, a new sample was obtained from the mixing container, as the paste remained fluid for a much longer time in the mixing container. Upon testing paste samples made with a w/c ratio of 0.40, there was a noticeable discoloration on the bottom plate of the DSR.

3. Results and Discussion

3.1. Dynamic Shear Rheometer. As expected, differences in DSR data were observed for the various mineral admixtures. Figure 2 illustrates the viscous modulus at the midvalues of the mineral admixture content. The efficiency of the admixture types in terms of early hydration occurred in the following sequence: 10% SF (the cement paste with 10% silica fume) > OPC (the cement paste with no admixture) > 30% slag (the cement paste with 30% slag). The DSR results confirmed what was expected in that the silica fume blended paste reacted more quickly
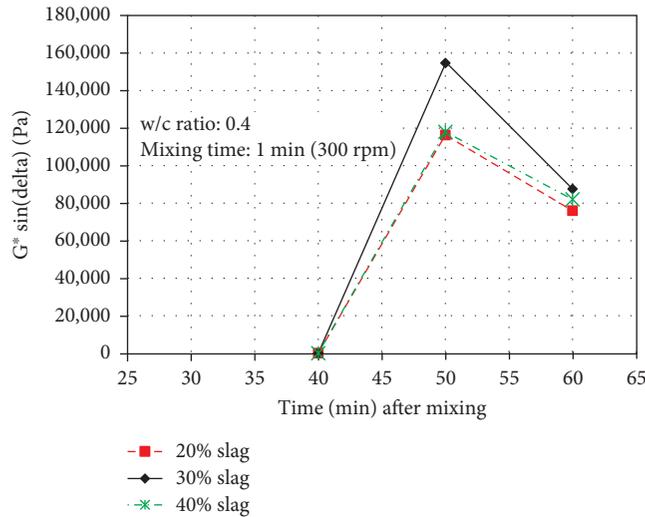
FIGURE 3: G^* sin(delta) with slag content (0.4 w/c ratio).
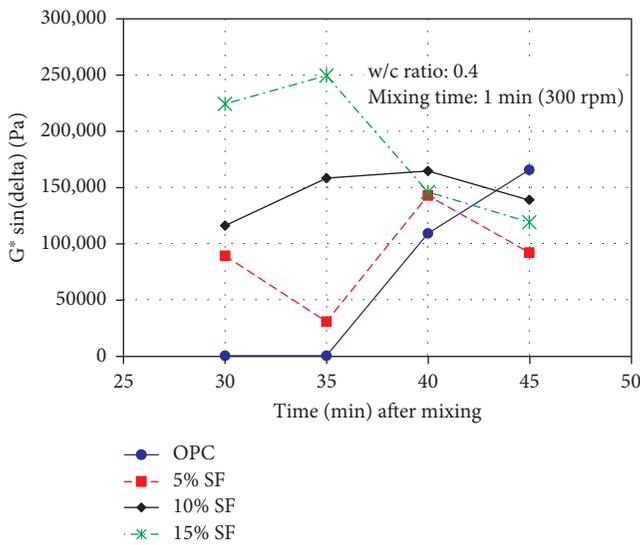
FIGURE 4: G^* sin(delta) with silica fume content (0.4 w/c ratio).
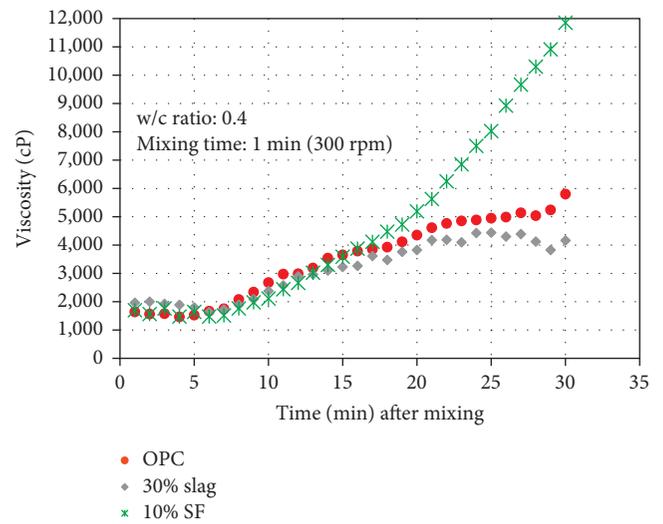
FIGURE 5: Viscosity with time after mixing (0.4 w/c ratio).

than the control, which reacted faster than the slag blended paste.

Fly ash data for the DSR are not shown due to variations in the testing technique. The cement pastes containing fly ash were tested in a slightly different manner than the other types of cement paste. Once this difference was noticed, it was determined that the cement pastes should not be tested in the DSR due to discoloration of the base plate. For the fly ash samples, as with the silica fume and slag, it was difficult to find a trend with varying fly ash replacement levels.

It is assumed that the effects of admixtures are linearly dependent on the admixture content. Even if this is not true in all cases, it is expected that there is a significant relationship with admixture content. DSR test results with 3 different slag contents are shown in Figure 3. Using the DSR, it was difficult to find any trend when varying the

slag content. It was expected that the viscous modulus would decrease with increased levels of slag due to the latent hydraulic nature and high fineness of slag. Possible reasons for these variations are that the DSR is originally designed to measure the rheological properties of asphalt binders at intermediate and high temperatures. In this study, however, the rheological properties of cement pastes were measured at 25°C.

3.1.1. Tester Technique. After considerable trial and error, the application of the DSR with cement pastes was found to be possible. However, there was no fixed method to follow, and several experimental errors could be a reason for the irregular trends.

DSR test results with 3 different silica fume contents are shown in Figure 4. Similar to slag, no trend was found in the cement paste with different silica fume contents. For the
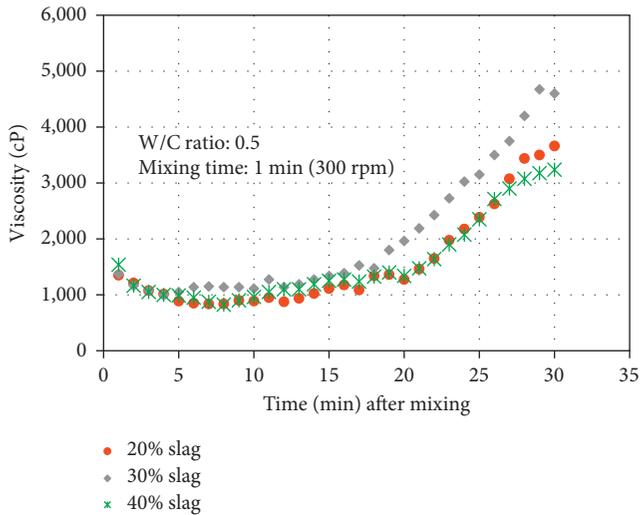
FIGURE 6: Viscosity with slag content (0.5 w/c ratio).

FIGURE 7: Viscosity with silica fume content (0.4 w/c ratio).

silica fume, it was expected that increased amounts of silica fume would increase the viscous modulus.

3.2. Rotational Viscometer.

3.2. Rotational Viscometer. Variations in hydration reactions between the different cement pastes can be seen in Figure 5. The graph shows viscosity results at midvalues of mineral admixture content at a 0.40 w/c ratio. The results based on reaction time were in the following sequence: 30% slag (the cement paste with 30% slag) > OPC (the cement paste with no admixture) > 10% SF (the cement paste with 10% silica fume). The paste with silica fume began to react more quickly than the control paste, which, in turn, began to react faster than the latently hydraulic slag paste. The results of the rotational viscometer test show approximately the same trend as those of the DSR test.

When looking at each individual mineral admixture employed at various replacement levels in the preliminary tests, it was found that no trend with admixture content was shown at a 0.4 w/c ratio. This was true for all mineral admixtures except for silica fume. At a 0.40 w/c ratio, the viscosity of silica fume paste increased from 5% to 10%. However, the viscosity dropped from 10% to 15%. These results confirmed that as the silica fume content increases to a certain level, the plastic viscosity also increases. For the remaining mineral admixtures, a 0.5 w/c ratio was used for all viscosity tests for the different replacement levels.

The rotational viscometer test results with 3 different slag contents are shown in Figure 6. Using the rotational viscometer, it was difficult to find a trend with slag content. After discussion, the following reasons were suggested.

3.2.1. Rotational Viscometer Equipment. It is originally designed to measure the rheological properties of the asphalt binder at high temperatures (135°C and 165°C). In this study, the rheological properties of cement paste were measured at 25°C.
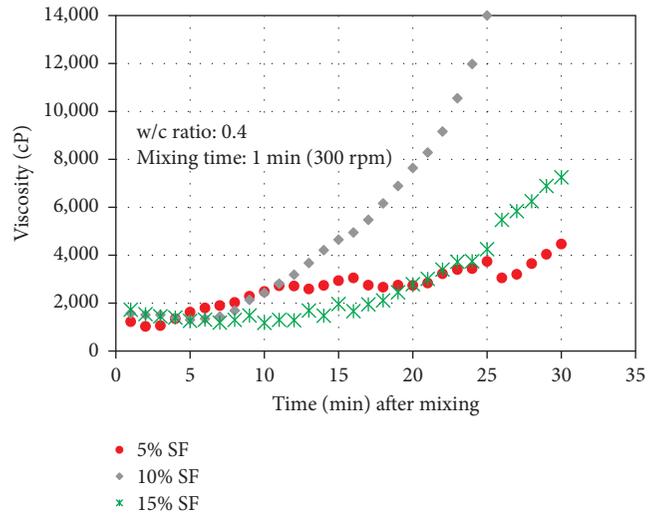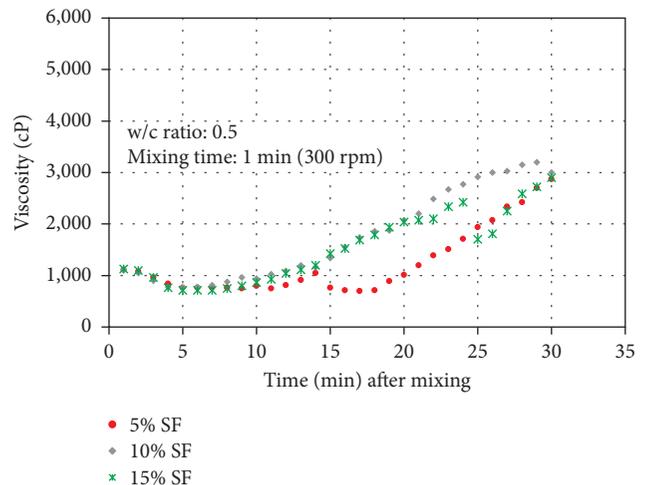
FIGURE 8: Viscosity with silica fume content (0.5 w/c ratio).

3.2.2. Cement Paste Sample. In each test, roughly 20 g of cement paste was used. The calculated amount of cement paste in each test was different because of the difference of specific gravity between slag and cement. At 25°C, the cement paste was not fluid because the asphalt binder was at 135°C. It was very difficult to obtain the exact amount of paste in the test tubes needed for the appropriate volume.

Rotational viscometer test results with 3 different silica fume contents are shown in Figures 7 and 8. For both w/c ratios, the viscosity increased from 5% to 10% but decreased when taken up to 15%.

Rotational viscometer test results with 3 different fly ash contents are shown in Figure 9. As the fly ash content increased, the viscosity decreased. Fly ash lowered the water demand in concrete. With increasing amounts of fly ash and the same w/c ratio, the higher fly ash replacement levels should have lower viscosities. With more fly ash, there were also fewer cement hydration products.
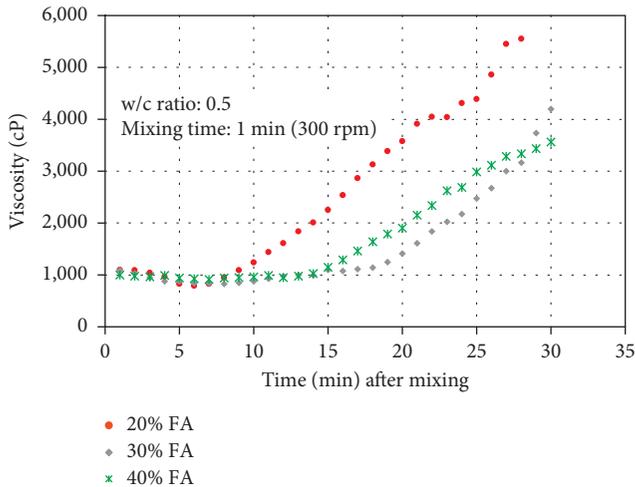
Figure 9: Viscosity with fly ash content (0.5 w/c ratio).

4. Conclusions

Cement pastes exhibit different rheological behaviors with respect to age, mineral admixture type, and cement replacement levels. Results from testing indicated that the rotational viscometer can be used to study the flow characteristics of cement pastes with or without mineral admixtures.

(1) The data for silica fume and fly ash at a w/c ratio of 0.50 demonstrated the expected trends. For silica fume, the viscosity increased from 5% to 10% and then increased from 10% to 15%. This corresponds to the effects observed in previous research, in which high amounts of silica fume lowered the plastic viscosity.

(2) For fly ash, the viscosity decreased as the amount of cement replacement increased. As the fly ash content increased, the amount of free water also increased due to the lowered water demand of fly ash. Additionally, fewer hydration products formed with lower amounts of cement in the relatively short time periods investigated.

(3) The viscosity data for slag, however, did not follow the expected trends. It was expected that an increase in the slag content would lower the viscosity of the paste due to the latent hydraulic nature of slag. With increased amounts of cement replacement, there should be lowered amounts of hydration products. In addition, high amounts of slag should lower the water demand of the paste, thus artificially increasing the w/c ratio.

The data for the dynamic shear rheometer are imprecise at best. The expected results from DSR testing were not obtained for any of the mineral admixtures.

Conflicts of Interest

The authors declare that there are no conflicts of interest regarding the publication of this paper.

References

[1] American Concrete Institute, *ACI Manual of Concrete Practice*, American Concrete Institute, Farmington Hills, MI, USA, 2017.

[2] W. Chen and H. Huang, "Effect of fly ash on rheological properties of cement paste," *Journal of Wuhan University of Technology*, vol. 32, no. 17, pp. 186–192, 2010.

[3] J. E. Wallevik, "Rheological properties of cement paste: thixotropic behavior and structural breakdown," *Cement and Concrete Research*, vol. 39, no. 1, pp. 14–29, 2009.

[4] C. F. Ferraris and N. S. Martys, "Relating fresh concrete viscosity measurements from different rheometers," *Journal of Research of the National Institute of Standards and Technology*, vol. 108, no. 3, pp. 229–234, 2003.

[5] L. Struble and G.-K. Sun, "Viscosity of Portland cement paste as a function of concentration," *Advanced Cement Based Materials*, vol. 2, no. 2, pp. 62–69, 1995.

[6] K. Kovler and N. Roussel, "Properties of fresh and hardened concrete," *Cement and Concrete Research*, vol. 41, no. 7, pp. 775–792, 2011.

[7] L. Struble and R. Szecsy, "Rheology of Fresh Concrete," *Materials for the New Millennium: Proceedings of the Fourth Materials Engineering Conference*, K. P. Chong, ed., pp. 1121–1128, American Society of Civil Engineers, Washington, DC, USA, 1996.

[8] M. Bellotto, "Cement paste prior to setting: a rheological approach," *Cement and Concrete Research*, vol. 52, pp. 162–168, 2013.

[9] P. Banfill, "The rheology of fresh cement and concrete–a review," in *Proceedings of the 11th International Cement Chemistry Congress*, Watt University, Durban, South Africa, May 2003.

[10] J. E. Wallevik, "Thixotropic investigation on cement paste: experimental and numerical approach," *Journal of Non-Newtonian Fluid Mechanics*, vol. 132, no. 1–3, pp. 86–99, 2005.

[11] The Asphalt Institute, *Superpave Series No. 1-Performance Graded Asphalt: Binder Specification and Testing*, The Asphalt Institute, Lexington, KY, USA, 2003.

Research Article

Investigation of the Effects of Marble Material Properties on the Surface Quality

Sümeyra Cevheroğlu Çıra [ID],[1] **Ahmet Dağ,**[2] **and Askeri Karakuş** [ID][1]

[1]*Mining Engineering Department, Faculty of Engineering, Dicle University, Diyarbakır, Turkey*
[2]*Mining Engineering Department, Faculty of Engineering, Çukurova University, Adana, Turkey*

Correspondence should be addressed to Sümeyra Cevheroğlu Çıra; sumeyra@dicle.edu.tr

This study aims to investigate the effects of material properties of marble on surface roughness and glossiness. For this purpose, four types of limestones were investigated. Physicomechanical properties of samples were determined through laboratory measurements. Mineralogical and petrographical characterizations were made using thin-section analysis. X-ray fluorescence (XRF) semiquantitative method was used for chemical analysis. Six different grinding-polishing tests for each marble unit were done under fixed operational conditions using the same abrasive series. Relationship between the material properties and the surface quality was investigated. Although the polishing-grinding tests were conducted under the same operational conditions, different levels of roughness and glossiness were observed on different samples. Data obtained from the study proved that the main cause of this difference is textural and chemical composition variations of the marble specimen. Moreover, statistical evaluations showed that porosity, uniaxial compressive strength, and indirect tensile strength have strong effects on the surface roughness and glossiness of the marble specimen. The presence of an inverse relationship between the glossiness and roughness levels was determined as the result of this study as well.

1. Introduction

Marble is an extremely popular ornamental stone for architectural and sculptural purposes. It also has a high potential of taking a polish. Grinding and polishing processes are generally used as the finishing process to obtain polished surfaces which are widely preferred in the global market for decorative purposes due to the pleasing appearance they present [1]. The parameters affecting the efficiency of grinding and polishing processes have been widely investigated in previous studies; however, it is still not understood exactly how the parameters affect the final polish [2]. The effects of material properties on surface quality were investigated by Erdoğan [3], and factors such as porosity, distinct crystal boundaries, cleavages, fillings in the microfractures, and obliqueness between the crystal orientation and the cutting plane were found to be adversely affecting the surface quality. Görgülü and Ceylanoğlu [4]

investigated the effects of diamond and SiC abrasives on the surface quality and discovered that surface roughness and glossiness of the stone samples they examined were independent of the abrasive type used. For that reason, the importance of choosing the appropriate series of abrasives and adjusting operational conditions specifically for the stone properties to achieve the desired surface quality was emphasized. The microstructure detection of a glossy granite surface at each separate stage ranging from sawing to grinding was studied by Huang et al. [5]. They concluded that the highest glossiness surface of the workpiece was also the lowest roughness surface which was shaped by diamond grinding in the ductile mode. Ersoy and Kose [6] investigated the relationship between polishing ease and mechanical properties of marble. Their research showed that the strength to wear by friction affects the brightness in marbles, and there is an inverse relationship between the brightness and the abrasion index.

Yavuz et al. [7] examined the effects of belt speed on surface quality by performing polishing tests at various constant rotational speed values and pressure levels of the polishing head. According to the data obtained, optimum polishing quality conditions were met at the belt speed value of 1.3 m/min. Karaca [2] studied the relationship between mechanical properties and the surface roughness of true marble samples and found that there are significant correlations between uniaxial compressive strength, tensile strength, and the surface roughness of the marble specimens. It has not been clearly demonstrated whether the value of the Böhme abrasion loss correlates with the polished marble surface roughness. Gürcan et al. [8] emphasized that different microroughness levels and gloss values were observed due to the different textures and chemical compositions of marble samples studied. Ersoy et al. [9] investigated the effect of abrasive head rotation on the surface quality and revealed that smoother and brighter surfaces are obtained by increasing the abrasive head's rotational speed.

The main objective of this study is to determine the effects of physicomechanical and mineralogical-petrographical properties and chemical contents of limestones on their final glossiness and roughness values. To that end, physicomechanical properties such as unit weight (UW), porosity (P), uniaxial compressive strength (UCS), flexural strength (FS), indirect tensile strength (ITS), Böhme abrasion resistance (BAR), and Schmidt hardness (SH) were determined first. Mineralogical-petrographical characterizations of the samples were done using thin-section analysis, and chemical content of samples was determined by the application of XRF semiquantitative method. Then, polishing tests were conducted, and surface roughness and glossiness of marble strips were measured. Finally, interpreting the obtained data, the effect of material properties on surface quality of marble specimen was determined.

2. Materials and Experimental Procedure

2.1. Determining Material Properties. To determine the physicomechanical properties of the selected marble samples, workpieces were prepared and UW, P, UCS, SH, and ITS tests were conducted according to ISRM [10] standards, whereas FS and BAR tests were conducted according to TS 699 [11]. Thin sections of marble samples were analyzed for mineralogical-petrographical characterizations.

2.2. Polishing Tests. Polishing tests were carried out by using a laboratory-scaled polishing machine designed to be similar to an industrial-scaled machine, equipped with a conveyor belt of 60 cm width and four polishing heads of 35 cm diameter (Figure 1). An abrasive series consisting of 60, 80, 120, 180, 220, 280, 320, 380, 600, and 800, 5 Extra, and a felt pad (Pulitore) were used. The workpieces were obtained from a marble processing plant and were calibrated with diamond abrasives in dimensions of 500 mm long, 300 mm wide, and 20 mm thick. Ten points were marked on the edges of the strips to ensure that the roughness and glossiness measurements were taken from the same points for all

Figure 1: Laboratory-scaled polishing machine.

samples. Operational polishing machine variables such as belt speed and rotational speed of the polishing head were fixed at 1.48 m/min and 499.5 rpm, respectively. Pressure of the polishing head was kept at 1.25 bar for 60–800 numbered abrasives and reduced to 1 bar for 5 Extra and Pulitore cases. 60 numbered five abrasives were mounted on a grinding head, and six separate polishing tests were conducted for each marble unit by using only one polishing head. After the polishing stage, a compressor was used to blow off the dust and the water drops remaining on the surface of the strips.

2.3. Surface Quality Measurements. To determine the surface quality of the strips, roughness and glossiness measurements were taken. Taylor Hobson Surtronic 3+ portable surface roughness tester and Konica Minolta Multigloss 268 glossmeter are shown in Figure 2, respectively. The roughness values were measured in terms of the most commonly used parameter "R_a," and the glossiness values were evaluated for a 60° angle and a 9×15 mm area. Arithmetic mean of ten measurements was calculated, and surface profiles of the strips were determined after all six polishing tests were carried out. The same procedure was repeated for the rest of the abrasive series, and the final surface quality of the strips was assessed after Pulitore was used for each marble unit.

3. Results and Discussion

The results of the laboratory measurements and the chemical content of the workpieces are presented in Tables 1 and 2, respectively [1]. Mineralogical and petrographical characterizations of marble samples are given in Table 3 [1].

The average roughness and glossiness values obtained from the six polishing tests versus abrasive numbers for each marble unit are given in Figure 3. It is seen from Figure 3 that roughness values follow an exponentially decreasing trend towards the end of the abrasive series, while it is exponentially increasing for glossiness values for the majority of the surface finish operations as expected [2, 4, 5, 7, 8]. It is clear that small abrasive numbers 60, 80, and 120 with coarse abrasive grains have a more prominent effect on the decrease

(a)

(b)
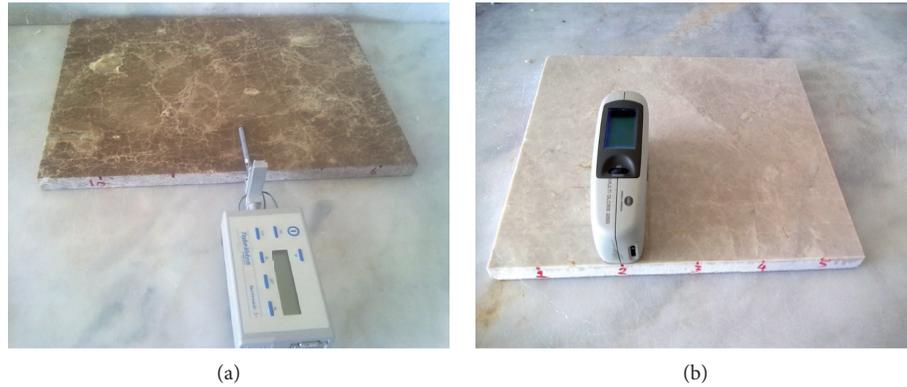
FIGURE 2: Measurement of (a) surface roughness and (b) glossiness.

TABLE 1: Results of physicomechanical tests.

Marble unit	UW (kN/m³)	P (%)	UCS (MPa)	FS (MPa)	ITS (MPa)	BAR (cm³/50 cm²)	SH
Adara	25.7	0.39	77.9	15.01	7.53	15.76	39.2
Emperador	25.8	1.85	61.69	13.44	7.23	18.79	41.2
Crema nera	26.59	0.34	83.99	12.9	8.6	15.41	43.6
Sand wave	27.08	1.46	72.05	8.96	7.35	7.95	40

Unit weight (UW), porosity (P), uniaxial compressive strength (UCS), flexural strength (FS), indirect tensile strength (ITS), Böhme abrasion resistance (BAR), and Schmidt hardness (SH).

TABLE 2: Results of XRF semiquantitative analysis.

Content (%)	Marble unit			
	Adara	Emperador	Crema nera	Sand wave
CaO	55.16	47.06	55.09	55.03
MgO	0.67	14.7	1.13	0.53
Al_2O_3	0.38	—	0.16	0.3
MnO	0.035	0.022	0.02	—
CuO	0.026	0.032	0.026	—
Fe_2O_3	0.21	0.14	0.105	0.33
Cr_2O_3	0.058	0.04	0.025	0.036
SO_3	0.117	—	0.066	0.084
Lu_2O_3	0.02	0.055	0.04	0.04
V_2O_5	—	0.058	—	0.008
SrO	—	0.17	—	—
MoO_3	—	0.63	—	—
Yb_2O_3	—	0.01	—	—
La_2O_3	—	—	0.06	—
TiO_2	—	—	—	0.03
Eu_2O_3	—	—	—	0.06
Tu_2O_3	—	—	—	0.32
Loss on ignition	43.3	37.0	43.3	43.2

in surface roughness, and finer-grained abrasives (360, 600, and 800) cause a significant increase in surface glossiness values but the most pronounced effect is due to 5 Extra and Pulitore. It can also be seen from Figure 3 that there is an inverse relationship between final surface roughness and glossiness. Therefore, a distribution plot was drawn in order to show the relationship between roughness and glossiness values and calculate the correlation coefficient (Figure 4, $r = -0.96$) [1].

Analysis of the final roughness and glossiness values showed that glossiness of each marble unit was more than 87% except Emperador. Although the polishing tests were

TABLE 3: Mineralogical and petrographical characterizations of the marble samples.

Sample Name	Petrographic description	Thin section
Adara	Yellowish gray-colored, massive, and fine-grained "micritic limestone." The main component is micritic carbonate minerals; however, large carbonate crystals (calcite) are also present. In some sections, calcite minerals are observed to be dense and in contact with each other. Binding between minerals is not observed. Numerous thin veins intersecting each other give a segmented appearance to the marble and can be observed in macroscopic scale. Veins are filled with carbonate crystals (calcite)	
Emperador	Pale yellowish brown, massive, and fine-grained "calcitic dolomite." It consists of crystalline carbonate minerals (dolomite and a small amount of calcite). Marble gains rotational movement because of its position between nonparallel strike-slip faults. It shows a tectonite structure with both small and large particles, and these particles are bound to each other with calcite cement. Heterogeneously distributed, irregular, carbonate-filled veined structure is observed throughout the grains	
Crema nera	A very pale orange-colored, massive, and fine-crystallized "micritic limestone." It consists of micritic carbonate minerals. Slightly larger grains of carbonate (calcite) were observed to be bound by the cryptocrystalline mud binding	
Sand wave	Yellowish gray, massive, and fine-grained "biomicritic limestone." The main component is micritic carbonate minerals. The interiors of these small grains are filled with micritic carbonate minerals. Also, fine-grained carbonate oolite and fossil shells were observed in some places. There is ferrous water in its structural stilolit gaps, and this hematite-stained water causes redness in these parts	
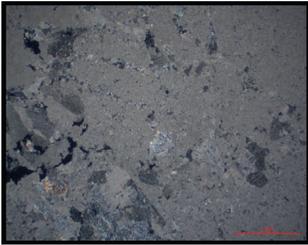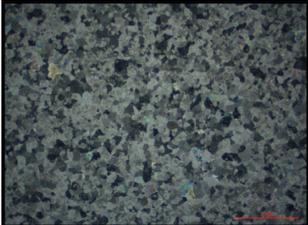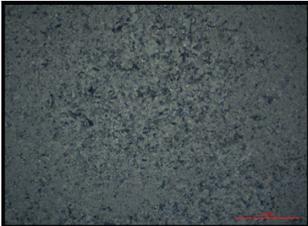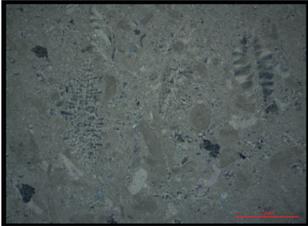
conducted under the same operational conditions, the glossiness of Emperador turned out to be 80% which is lower than the other samples. In order to clarify the reason behind this difference, parameters affecting the surface glossiness were investigated. In a previous study conducted by Erdoğan [3], it was stated that geologic discontinuities such as cleavage, porosity, crystal boundary, fillings of the microfractures, and also the types of mineral constituting the rock have a negative effect on the surface glossiness [3]. In terms of physical properties, the Emperador unit was found to be more porous (Table 1) than the other marble units. The micro- and macropores in the structure of the Emperador absorb incoming beams and diminish the surface glossiness values. By taking mineralogical and petrographical characterizations into account, we can say that discontinuities such as filled fractures and the intersecting veins reflect the incoming beams in different directions. When analyzed in terms of the chemical content, the higher rate of MgO and the lower rate of CaO in the structure of the Emperador (Table 2) compared to the other marble units are significant. It was stated in previous studies that the increase in MgO ratio in the marble

structure has a negative effect on surface roughness and glossiness [8, 12], which supports our findings.

To examine the effects of each physicomechanical property on surface roughness and glossiness values, correlation and regression analyses were conducted. A linear correlation ($r \geq 0.95$) was observed between porosity and the surface quality. With increasing porosity, roughness also increased while glossiness decreased (Figures 5(a) and 5(b)). There is an inverse relationship between UCS and roughness as well as ITS and roughness (Figures 5(c) and 5(e)), whereas the relationship between UCS (or ITS) and glossiness is directly proportional (Figures 5(d) and 5(f)). The correlation coefficients between the UW, BAR, FS, and SH test results and polishing test results were lower than 48%, and thus, these values were not high enough to suggest the existence of a relationship between them.

4. Conclusion

In this study, polishing tests were applied on four types of limestones under fixed operational conditions. Glossiness and roughness values were measured after each polishing

(a)

(b)

(c)

(d)
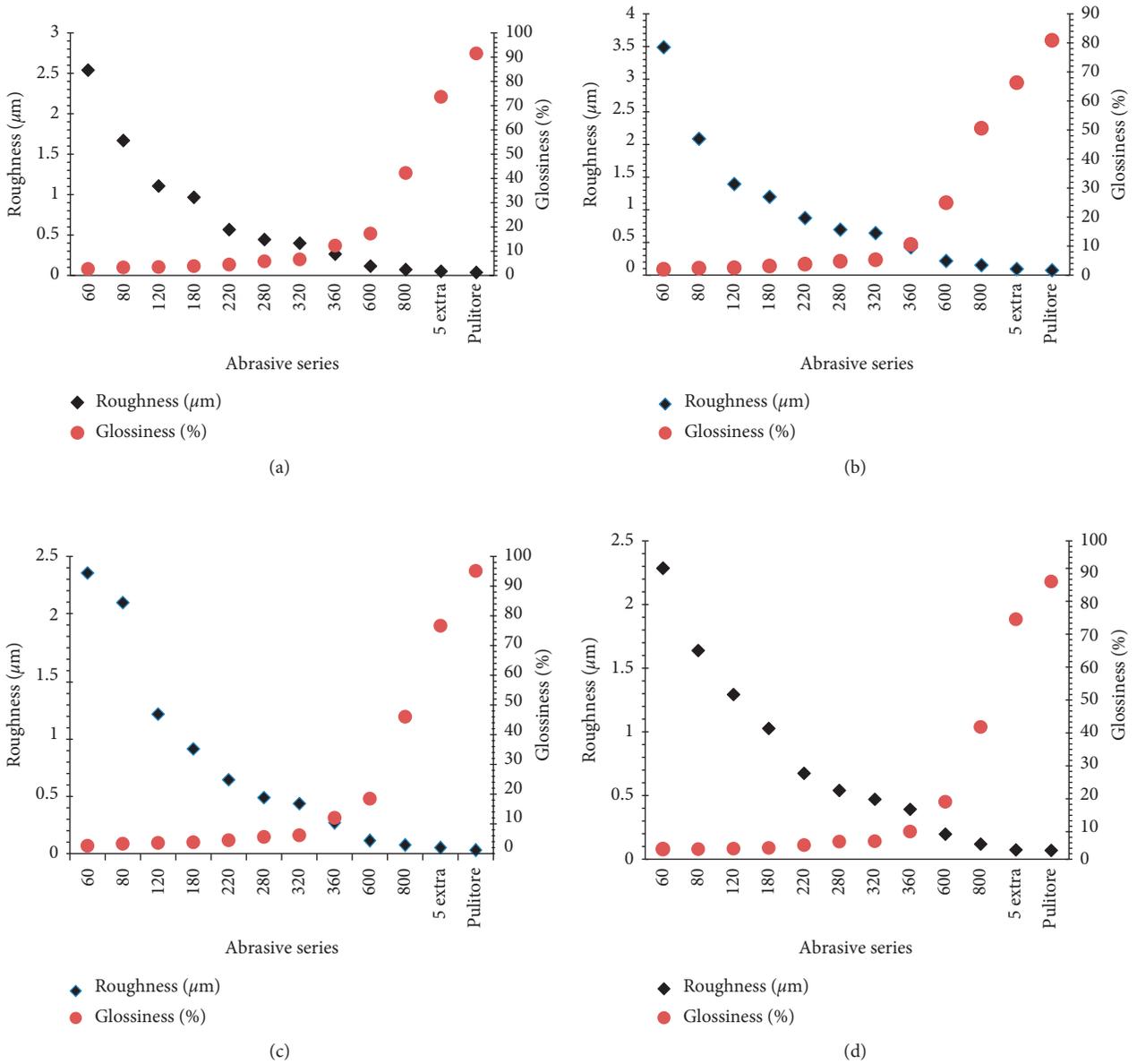
Figure 3: Surface roughness and glossiness values versus abrasive number for (a) Adara, (b) Emperador, (c) Crema nera, and (d) Sand wave.

$$y = -0.000x^2 + 0.018x - 0.606$$
$$R^2 = 0.916$$
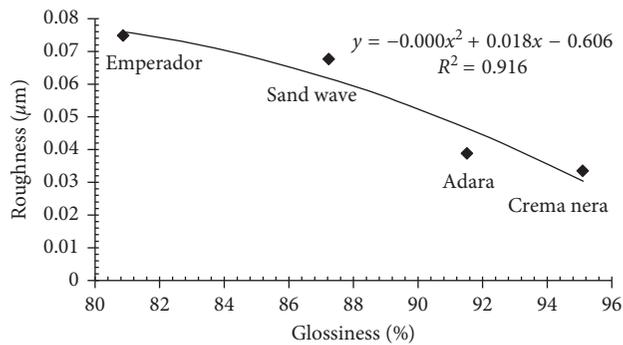
Figure 4: Roughness versus glossiness.

(a)

(b)

(c)

(d)

(e)

(f)
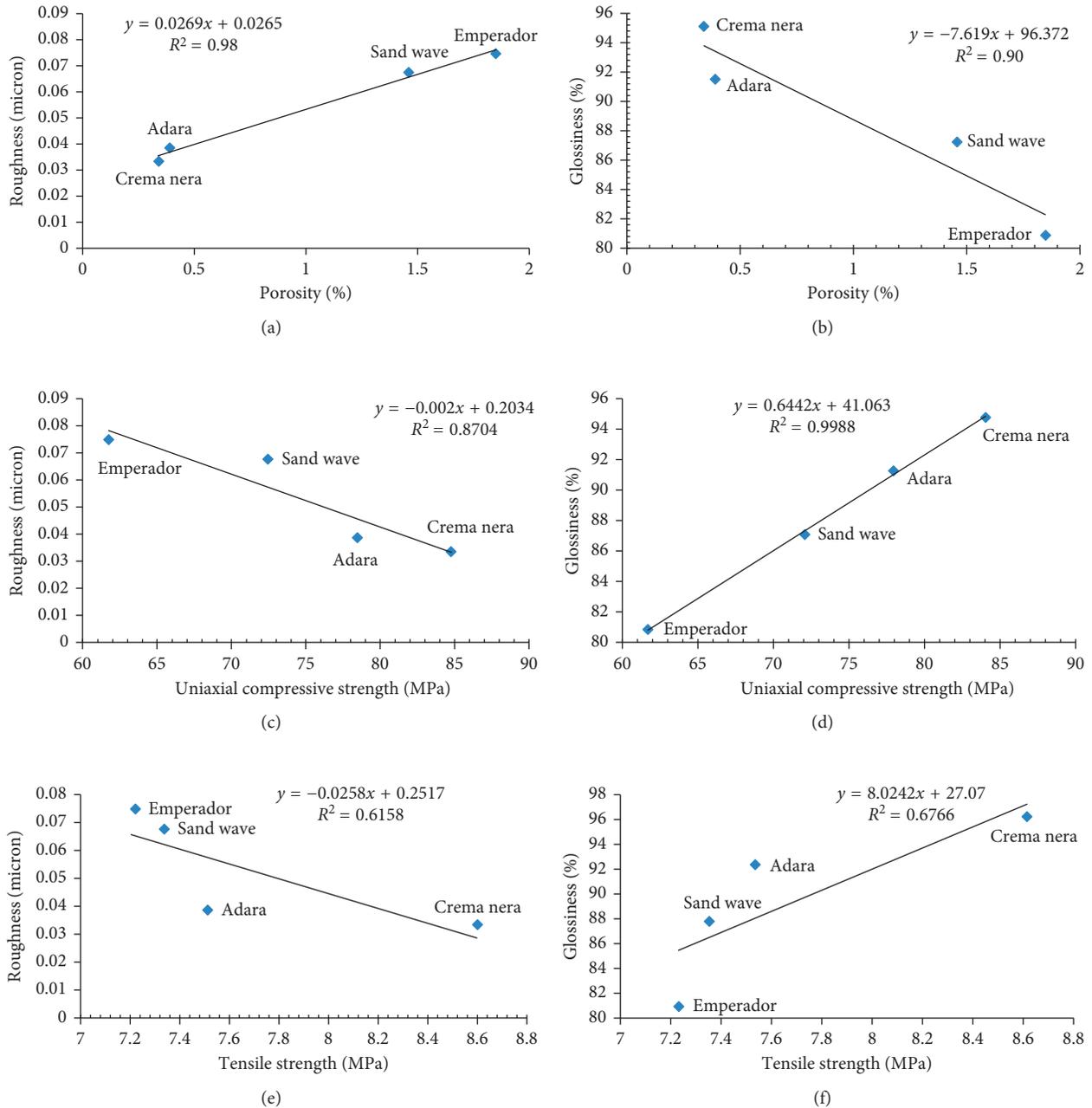
FIGURE 5: Physicomechanical properties versus roughness and glossiness. (a) Porosity versus roughness. (b) Porosity versus glossiness. (c) Uniaxial compressive strenght versus roughness. (d) Uniaxial compressive strenght versus glossiness. (e) Tensile strenght versus roughness. (f) Tensile strenght versus glossiness.

stage for all specimens. Considering the polishing test results, it is clear that 60, 80, and 120 numbered abrasives with coarse grains have a more prominent effect on the decrease of the surface roughness levels while glossiness values did not show a remarkable increase up to 320 numbered abrasive, and also finer-grained abrasives have the dominant effect on the increase of the glossiness values. It was seen that there is a good correlation ($r = 0.96$) between final surface glossiness and roughness values, and glossiness increases with decreasing roughness.

Although all the marble samples were of limestone and the polishing tests were applied under the same operating conditions, final surface glossiness of the Emperador unit was lower than the other units. The reason for that is the fact that the micro- and macropores in the structure of Emperador absorb the beams rather than reflecting them, and discontinuities such as filled fractures and intersecting veins reflect the incoming beams in different directions. Also, a high amount of MgO in marble samples has a negative effect on the surface quality. Based on laboratory

measurements, linear relationships were found between P, UCS, and ITS and the surface quality.

Conflicts of Interest

The authors declare that they have no conflicts of interest.

References

[1] S. Cevheroğlu Çıra, *The Investigation of the Effects of Operational Variables of Polishing Machine and Material Properties of Marble on Surface Quality and Optimization*, Ph.D. thesis, Çukurova University, Adana, Turkey, 2014.

[2] Z. Karaca, "Relationship between the mechanical properties and the surface roughness of marble," *International Journal of Materials Research*, vol. 103, no. 5, pp. 633–637, 2012.

[3] M. Erdoğan, "Measurement of polished rock surface brightness by image analysis method," *Engineering Geology*, vol. 57, no. 1-2, pp. 65–72, 2000.

[4] K. Görgülü and A. Ceylanoğlu, "Evaluation of continuous grinding tests on some marble and limestone units with silicon carbide and diamond type abrasives," *Journal of Materials Processing Technology*, vol. 204, no. 1–3, pp. 264–268, 2008.

[5] H. Huang, Y. Li, J. Y. Shen, H. M. Zhu, and X. P. Xu, "Microstructure detection of a glossy granite surface machined by the grinding process," *Journal of Materials Processing Technology*, vol. 129, no. 1–3, pp. 403–407, 2002.

[6] M. Ersoy and H. Kose, "The relationship between easiness to polishing and mechanical properties of marbles," in *Proceedings of the National Marble Symposium*, pp. 337–349, Afyon, Turkey, June 2001, http://www.maden.org.tr/resimler/ekler/e4243f5511fd6efek.pdf.

[7] H. Yavuz, T. Özkahraman, and S. Demirdağ, "Polishing experiments on surface quality of building stone tiles," *Construction and Building Materials*, vol. 25, no. 4, pp. 1707–1711, 2011.

[8] S. Gürcan, R. M. Goktan, and A. Yıldız, "Effect of mineralogical and microstructural properties on surface roughness and gloss of some ornamental marbles subjected to polishing process," *X-Ray Spectrometry*, vol. 43, no. 2, pp. 70–78, 2014.

[9] M. Ersoy, L. Yeşilkaya, M. Y. Çelik, and Y. Geçer, "Investigation of the belt conveyor speed effect to the surface quality in marble polishing process," *Journal of Polytechnic*, vol. 17, no. 4, pp. 153–160, 2014.

[10] International Society for Rock Mechanics, "Rock characterization, testing and monitoring," in *ISRM Suggested Methods*, E. T. Brown, Ed., ISRM, Oxford, UK, 1981.

[11] Türk Standartları Enstitüsü, *TS 699: Tabii Yapı Taşları–Muayene ve Deney Metotları*, Ankara, Turkey, 1987.

[12] Z. Karaca, "Effect of Head Pressure and Abrasive Series on Surface Roughness of Marbles," in *Proceedings of the 22nd International Conference on Surface Modification Technologies*, vol. 22–24, pp. 289–296, Trollhattan, Sweden, September 2008.

Research Article

Finite Element Analysis and Lightweight Optimization Design on Main Frame Structure of Large Electrostatic Precipitator

Xuewen Wang ⓘ, Bo Li ⓘ, and Zhaojian Yang ⓘ

*Shanxi Key Laboratory of Fully Mechanized Coal Mining Equipment, College of Mechanical Engineering,
Taiyuan University of Technology, Taiyuan 030024, China*

Correspondence should be addressed to Xuewen Wang; wxuew@163.com

The geometric modeling and finite element modeling of the whole structure of an electrostatic precipitator and its main components consisting of top beam, column, bottom beam, and bracket were finished. The strength calculation was completed. As a result, the design of the whole structure of the electrostatic precipitator and the main components were reasonable, the structure was in a balance state, its working condition was safe and reliable, its stress variation was even, and the stress distribution was regular. The maximum von Mises stress of the whole structure is 20.14 MPa. The safety factor was large, resulting in a waste of material. An optimization mathematical model is established. Using the ANSYS first-order method, the dimension parameters of the main frame structure of the electrostatic precipitator were optimized. After optimization, more reasonable structural design parameters were obtained. The model weight is 72,344.11 kg, the optimal weight is 49,239.35 kg, and the revised weight is 53,645.68 kg. Compared with the model weight, the optimal weight decreased by 23,104.76 kg and the objective function decreased by 31.94%, while the revised weight decreased by 18,698.43 kg and the objective function decreased by 25.84%.

1. Introduction

The control of industrial pollution emissions and the treatment of industrial flue gas pollution are the most important measures of environmental protection. With the advantages of high dusting efficiency, convenience management, low fault rate, and strong adaptability, the electrostatic precipitator (ESP) is widely applied for industrial flue gas treatment in nonferrous metals, metallurgy, construction materials, coal, petrochemicals, and electricity [1–6].

The large electrostatic precipitator is usually composed of dust-precipitator shell (main frame structure), inlet and outlet smoke box, ash storage system, anode and cathode system, rapping device and power supply part, stair platform, and insulation shell part.

The main frame structure is usually composed of top box beam and roof slab, column and side wall, bottom beam, and bracket, which are used for bearing and sealing of electrostatic precipitator, also used as the space for installation and positioning of other parts. The top beam,

column, bottom beam, and bracket constitute spatial mechanical rigid frame. The planar frames are sealed, linked, fixed, and installed by longitudinal components such as roof slab, side wall, and bottom beam, forming a closed self-balance system, protection system, and spatial load-carrying system. All kinds of load on the electrostatic precipitator, the insulation, and protection of dedusting system are born by the system. With the advantages of small deformation, easy control, good stability, and seismic performance, the structure can bear large load and effectively protect the other internal systems [7, 8].

The relevant study on an electrostatic precipitator is mainly focused on the dusting principle or filtration characterics [9, 10], the collection efficiency or dusting method [11–13], the collected dust or the particulate matter [14, 15], the analysis of the operating [16, 17], and the electrode system or recovery system [18–20] but ignored the study of its bearing structure [21, 22]. The main frame structure is often designed and transformed by companies with analogy method and empirical design instead of precise and scientific calculation. What's worse, the main structure is designed

only from the aspect of security, ignoring the accounting and evaluation of the cost and other aspects. As a result, the material is wasted enormously, and the products are short of market competitiveness from the aspects of shape and cost, which seriously affects the economic benefits of companies.

In this study, the finite element strength analysis [23, 24] and lightweight optimization design of the main structure of the large electrostatic precipitator were carried out using advanced design technologies such as finite element method, optimization design, and virtual prototype. The purpose is to obtain more scientific structure and more reasonable design parameters. What's more, the design and manufacturing costs could be reduced to improve the market competitiveness of products.

2. Geometric Model of the Main Structure

The schematic sketch of the main structure of a certain type of electrostatic precipitator is shown in Figure 1. The main structure of this type of electrostatic precipitator consisted of three parts: top beam, column, bottom beam, and bracket.

2.1. Top Beam. The top beam of a certain type of electrostatic precipitator consisted of a wide girder and two narrow girders. With the box structure, the girder was made up of slabs and few I-beam steel cross brackets. Between the steel slab and the steel slab, the steel slab and the bracket were the welding relations.

The dimensions of the wide girder were 6814 mm in length, 1640 mm in width, and 1500 mm in height. The dimensions of the narrow girder were 6814 mm in length, 1040 mm in width, and 1500 mm in height. Geometric models are shown in Figures 2 and 3.

2.2. Column and Side Wall. The column with complex structure bears greater load. Every column was a combined member bar, which was made by linking channel steels and angle steels with steel slabs. The height of the column was 8.370 m (Figure 4).

The wide wall was made by welding from steel slabs with the thickness of 5 mm. The channel steels, angle steels, and crescent costal boards were welded on the steel slab.

The column system was made by linking six columns with side walls, consisting of two wide columns and four narrow columns. The column system (Figure 5) was a large steel structural assembly, made by linking three column supports (Figure 6) together. The dimensions of the whole mode were 10.860 m in length, 6.590 m in width, and 8.370 m in height.

2.3. Bottom Beam and Bracket. The bottom beam had a frame structure made up of one front mudsill, one back mudsill, one middle mudsill, and two side mudsills. The length of the bottom beam was 10.865 m, the width was 6.614 m, the height was 1.16 m, and the weight was 6.812 t. The main body of front and back mudsills was made by welding channel steel and steel slab together, with channel
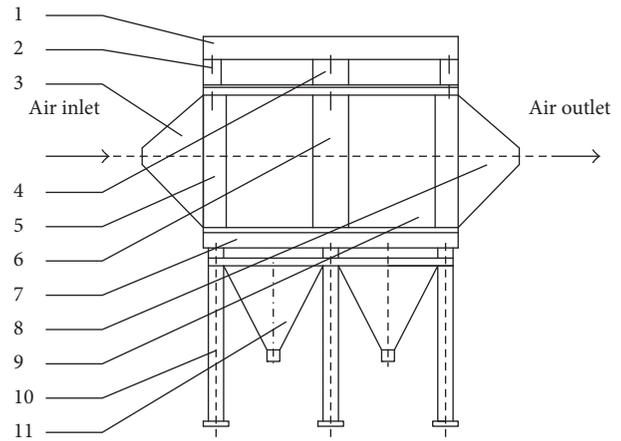
Figure 1: The schematic sketch of main structure of electrostatic precipitator. (1) Top lifting cradle, (2) narrow girder, (3) inlet smoke box, (4) wide girder, (5) narrow column, (6) wide column, (7) bottom beam, (8) outlet smoke box, (9) side wall, (10) bottom bracket, (11) ash bucket.
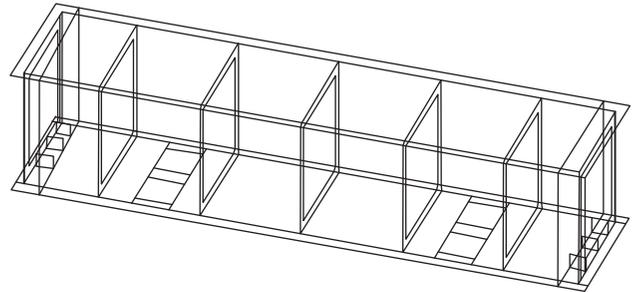
Figure 2: The model of the wide girder.
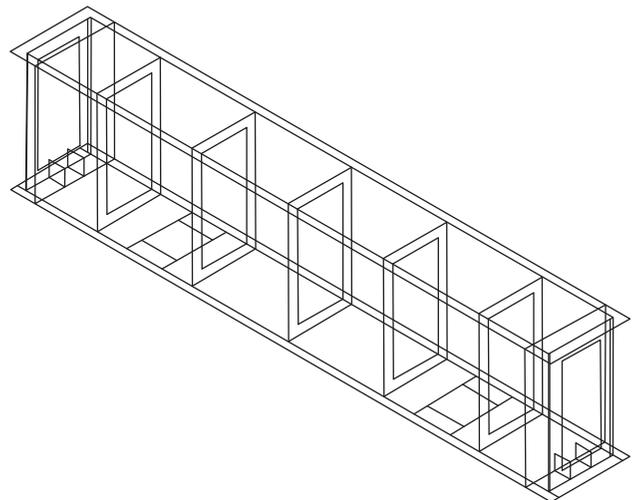
Figure 3: The model of the narrow girder.

steel reinforcing plate in the middle and angle steel support frame in upside.

The front and back mudsills were linked with the bottom edge of inlet and outlet smoke box of the electrostatic precipitator. The main body of the side mudsill was also
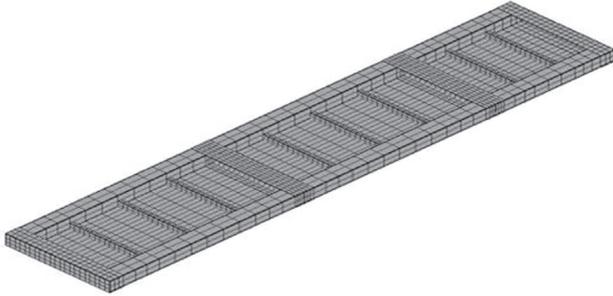
FIGURE 4: The model of the single column.
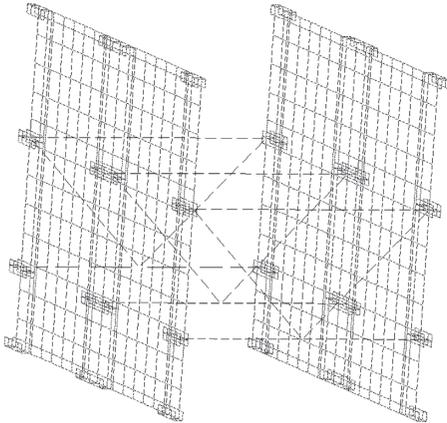
FIGURE 5: The whole model of the column component.

FIGURE 6: The model of column support.

FIGURE 7: The model of the bottom beam.
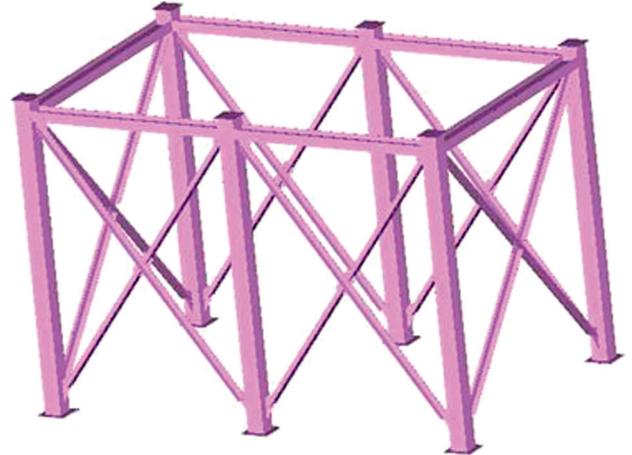
FIGURE 8: The model of the bracket.

made as a box structure by welding channel steel and steel plate together, in the middle of which was a channel steel reinforcing plate. Taking hot rolled h-shaped steel as prototype design, the middle mudsill was welded in the middle of two side mudsills, forming a framed steel structure with high stiffness and strength (Figure 7).

The mode of the bracket is shown in Figure 8. The bracket was made by linking six pillars as the main body, I

steel as cross linking components, and two-L abreast angle steel frame as support. The pillar was made by welding from slabs. The total length of the bracket was 11.050 m, the total width was 7.040 m, the total height was 7.520 m, and the weight was 13.899 t. The bracket with this structure has enough stiffness, strength, and good stability.

The bottom beam was at the top of the bracket. The solid model after assembly is shown in Figure 9.

2.4. Whole Structure. The whole solid model of the main structure of a certain type of electrostatic precipitator is shown in Figure 10, and the dimensions were 14 m long, 8.5 m wide, and 22 m high. The space structure of the electrostatic precipitator was reproduced virtually and realistically by a virtual model. The geometry of structural appearance and spatial assembly relation could also be reflected.

3. Finite Element Modeling

3.1. Element Type. The structure of the large electrostatic precipitator was complex, and its geometric model has block structure, plate structure, cylindrical structure, and tubular structure. Thus, many element couplings were used for building the realistic finite element model of the electrostatic precipitator. The ANSYS built-in elements used in the analysis of this study were as follows.

(1) Element SHELL63 [25, 26]: the electrostatic precipitator had many slab structures such as cover

FIGURE 9: The assembly model of the bottom beam and bracket.

plate, web plate, filling-up plate, and diaphragm plate of top beam parts and connecting plate, side wall plate, and storage ash strickle plate outside column. The sizes of those slab structures in length and width direction were much larger than that in thickness direction. For the relative thickness of those slab structures was small, the analysis was mainly aimed at the static strength, while the transverse shear deformation was not very important. The simulation was carried out by using element SHELLl63.

(2) Element BEAM188 [27, 28]: the beam element was used for analyzing the structures standing lateral or transverse load, such as the column of electrostatic precipitator and the main load-carrying components of the supporting column. The ratio of length to cross-sectional area was larger, which was the characteristic of those structures. The BEAM188 element was used for simulating the rod and beam components of the main structure.

(3) Element SOLID45 [29–31]: some components of the main structure of the electrostatic precipitator were three-dimensional solid block structure, such as bottom beam and support body part. The element SOLID45 was selected for simulating those structures.

3.2. Finite Element Model. According to the geometric complexity of different parts of main structure of electrostatic precipitator, structured and unstructured grids were used synthetically in the finite element model [32–35].

In the process of the grid, to effectively balance the calculation accuracy and the calculation scale, the following principles were considered: appropriate number of grids, reasonable mesh density, appropriate element order, high mesh quality, correctly handled grid interface and the boundary point, ensured displacement compatibility, the overall layout of the grid, and reasonable numbered node and unit.

The finite element analysis models of some parts of the main structure of the electrostatic precipitator are shown in Figures 11–13. The finite element analysis of the main structure of the electrostatic precipitator is shown in Figure 14.

4. Finite Element Analysis

The main structure material of the electrostatic precipitator was Q235 steel, and the material properties are shown in Table 1.

4.1. Top Beam. The top beam mainly consisted of a wide girder and two narrow girders.

According to the loading characteristics and the actual working conditions of the load-carrying girder of a certain type of electrostatic precipitator, the load acted on the girder could be transformed into 4 types: static load, live load, snow load, and temperature load. The live load consisted of the people load, ash load and so on, which was external load acting on the girders. The snow load was carried by the snow. Because the girders were working in a certain temperature environment, the temperature load needed to be applied in the calculation.

The static load which girders bear mainly consisted of deadweight, roof slab, anode system, cathode system, top crane, grooved plate system, and transformer. Load values of the girder are shown in Table 2.

According to the actual connection between the girders and other structures of the electrostatic precipitator, the translation and rotational freedom in the X and Y direction at one end of girders was restrained, and then the translation and rotational freedom in the Z direction were released. The rotational freedom in the X direction and the translation and the rotational freedom in the Z direction at other end of girders were released.

Results for stress values are shown in Tables 3–5, and the negative represented direction. The stress values of three girders were less than the yield limit of the material, and the girders were in safe working condition.

The von Mises stress nephogram of girders is shown in Figures 15–17. From Figures 15–17, for the upper cover plate was more complex and bearing more load, a greater stress area was concentrated in some parts of the upper cover plate. There were lesser stress values in lower cover plate, web plate, and filling-up plate.

In conclusion, the stress values of the three girders were within failure stress. The stress variation was smooth, and the stress distribution was regular. So the structure design was reasonable. In addition to the upper cover plate, the safety factor of other structures such as web plate, filling-up plate, lower cover plate, inner reinforcing plate, and diaphragm plate was large. The stress values of those structures were much less than the yield limit of the material, which resulted in the material waste. So the lightweight optimization design was feasible.

4.2. Column. The column system was made by linking six columns with side walls. The column was the key bearing
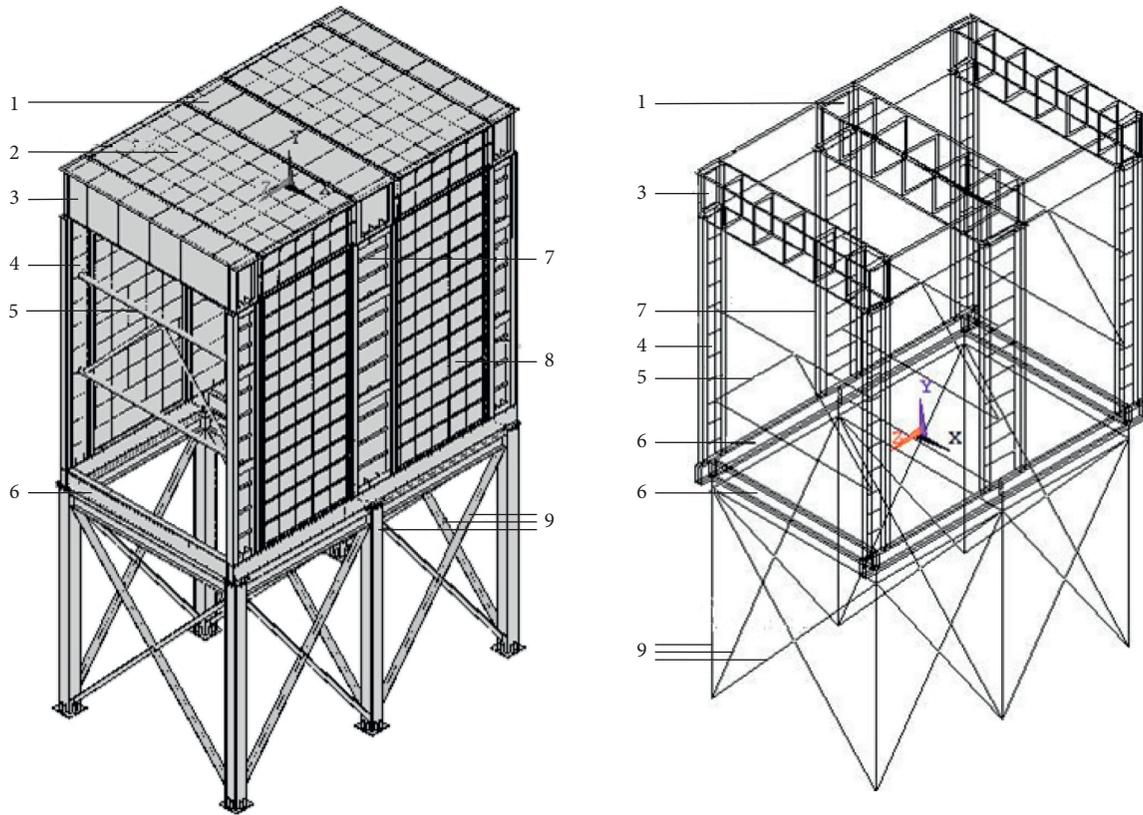
FIGURE 10: The solid model of main structure of the larger electrostatic precipitator. (1) Wide girder, (2) roof slab, (3) narrow girder, (4) narrow column, (5) column support, (6) bottom beam, (7) wide column, (8) side wall slab, (9) bracket.
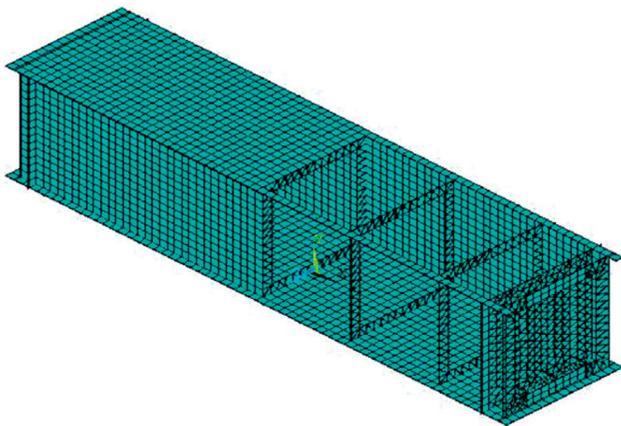
FIGURE 11: The finite element model of girder.
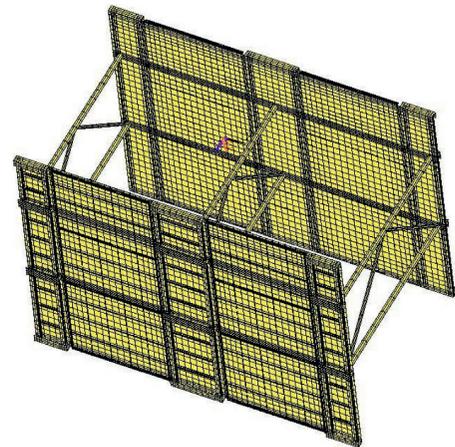
FIGURE 12: The finite element model of column, column support, and side wall.

component of electrostatic precipitator, which bore various loads of electrostatic precipitator, including static load, live load, snow load, and temperature load.

The static load which column system bears mainly consisted of the deadweight and the weight of girder, roof slab, anode system, cathode system, top crane, inlet and outlet smoke box, grooved plate system, and insulation layer. Load values of the column are shown in Table 6.

According to the actual connection between the column system and other structures of the electrostatic precipitator, all DOF of the column and the leftmost node outside the

bottom surface of the side wall was restrained. The translation and rotational freedom in Y and Z direction of the rest nodes outside were restrained, while the translation and rotational freedom in X direction were released. The translation and rotational freedom in X and Z direction of the leftmost node inside were restrained, and the translation and rotational freedom in Z direction of the rest nodes inside were restrained. The translation and rotational freedom in X and Y direction of the column and the leftmost node outside the top surface of side wall were restrained, and the
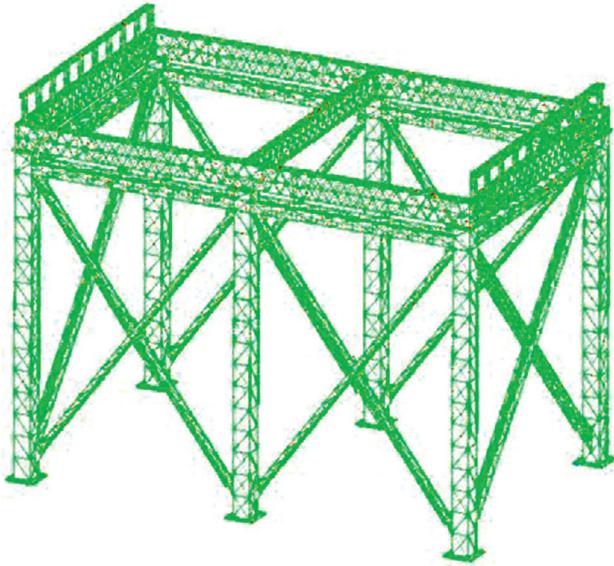
FIGURE 13: The finite element model of the bottom beam and bracket.

translation and rotational freedom in Y direction of the rest nodes inside were restrained.

Results for stress values of column system are shown in Table 7. The maximum stress was less than the failure stress σ_s, and the column system was in safe working condition.

The von Mises stress nephogram of column system is shown in Figure 18. From the figure, the stress value of the total column system was small, and the largest stress value (147 MPa) was in the joint between the column and side wall.

In conclusion, the column system was in the state of balance, and the working condition was safe and reliable. From the von Mises stress nephogram, the stress of the column system changed flatly and was distributed evenly, so the structure design was reasonable. But the safety factor was large, which resulted in the material waste. So the lightweight optimization design was feasible.

4.3. Bottom Beam and Bracket. The bottom beam and bracket were under the electrostatic precipitator, as the key bearing components. The bottom beam and bracket bore various loads of electrostatic precipitator, including the deadweight of total electrostatic precipitator, the weight of ash on the polar plates and in the ash bucket, roof live load, negative pressure, wind load, snow load, and temperature load. According to the loading characteristics and the actual working conditions of bottom beam and bracket of electrostatic precipitator, the load which bottom beam and bracket bear could be transformed into 4 types: static load, live load, snow load, and temperature load.

The static load which the bottom beam and bracket bore mainly consisted of their deadweight and the weight of girder, roof slab, anode system, cathode system, top crane, column, side wall, and ash bucket. Load values of the bottom beam and bracket are shown in Table 8.
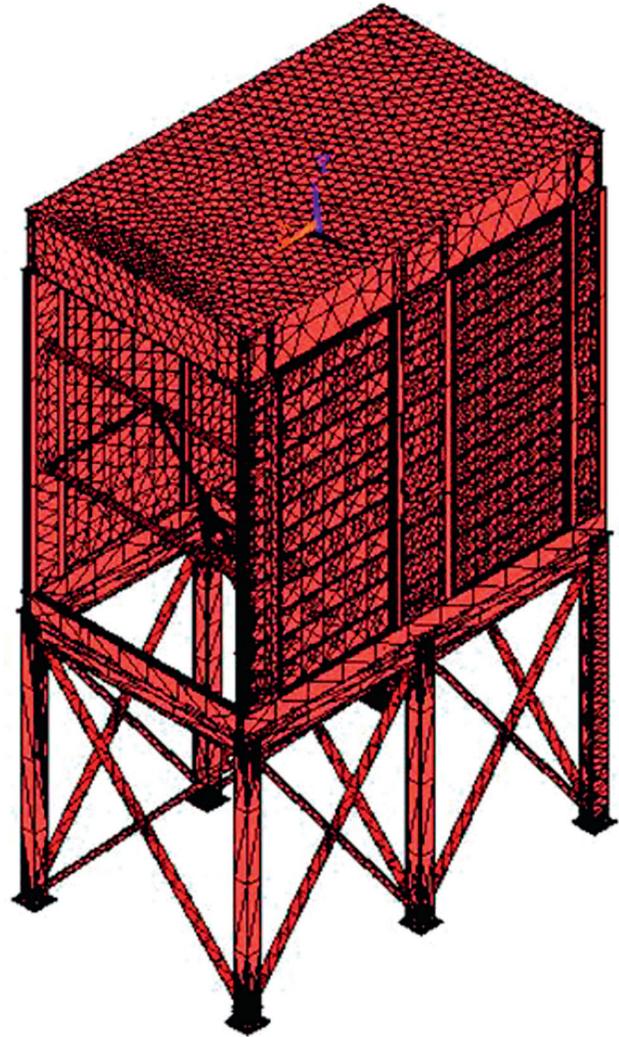
FIGURE 14: The finite element whole model of the overall main structure of the electrostatic precipitator.

TABLE 1: The main structure material properties of the electrostatic precipitator.

Young modulus	Material density	Thermal expansion coefficient	Poisson's ratio	Yield limit
2.1×1011 Pa	$7850\,\text{kg/m}^3$	1.22×10^{-5}	0.3	185–235 MPa

TABLE 2: The load information of girders.

	Static load	Snow load	Live load	Temperature load
Wide girder	235638 N	2682 N	43064 N	200°C
Narrow girder 1	108482 N	1601.25 N	25620 N	200°C
Narrow girder 2	150370 N	1601.25 N	25620 N	200°C

TABLE 3: The maximum principal stress and maximum von Mises stress of the wide girder (Pa).

σ_1	σ_2	σ_3	von Mises
$0.14329E + 09$	$0.10723E + 09$	$-0.17110E + 09$	$0.15219E + 09$

TABLE 4: The maximum principal stress and maximum von Mises stress of the narrow girder in air inlet side (Pa).

σ_1	σ_2	σ_3	von Mises
$0.37945E+08$	$-0.27370E+08$	$-0.53613E+08$	$0.47672E+08$

TABLE 5: The maximum principal stress and maximum von Mises stress of the narrow girder in air outlet side (Pa).

σ_1	σ_2	σ_3	von Mises
$0.46308E+08$	$-0.26552E+08$	$-0.56078E+08$	$0.49689E+08$

63399 $0.604E+08$ $0.121E+09$ $0.181E+09$ $0.241E+09$
   $0.302E+08$ $0.906E+08$ $0.151E+09$ $0.211E+09$
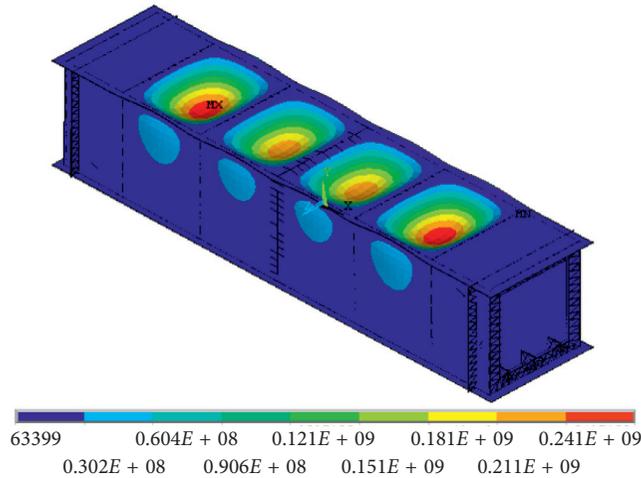
FIGURE 15: The von Mises stress nephogram of the wide girder (Pa).

23975 $0.111E+08$ $0.221E+08$ $0.331E+08$ $0.442E+08$
   $0.554E+07$ $0.166E+08$ $0.276E+08$ $0.387E+08$
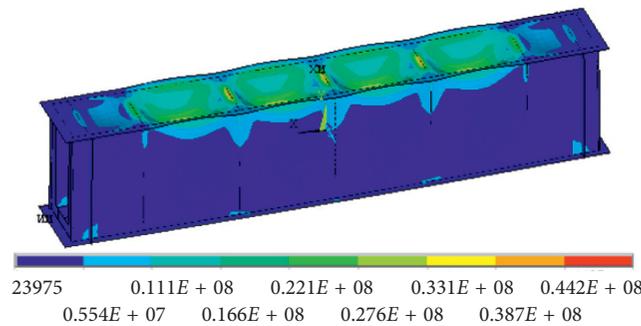
FIGURE 16: The von Mises stress nephogram of the narrow girder in air inlet side (Pa).

17455 $0.106E+08$ $0.212E+08$ $0.318E+08$ $0.424E+08$
   $0.532E+07$ $0.159E+08$ $0.265E+08$ $0.371E+08$
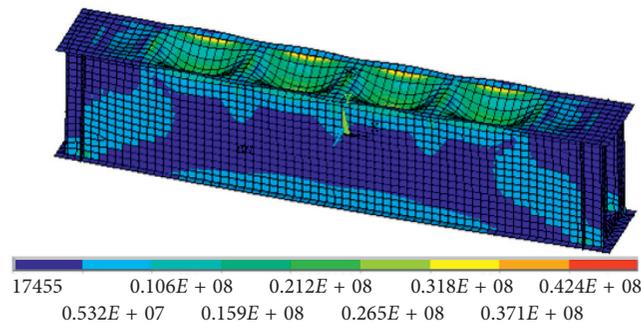
FIGURE 17: The von Mises stress nephogram of the narrow girder in air outlet side (Pa).

TABLE 6: The load information of column.

	Static load	Snow load and live load	Temperature load
Wide girder	242452 N	208250 N	200°C
Narrow girder 1	192717 N	208250 N	200°C
Narrow girder 2	227820 N	208250 N	200°C

TABLE 7: The maximum principal stress and maximum von Mises stress of column system (Pa).

σ_1	σ_2	σ_3	von Mises
$0.60356E+08$	$-0.49690E+08$	$-0.77296E+08$	$0.67757E+08$

2152 $0.327E+08$ $0.654E+08$ $0.981E+08$ $0.131E+09$
   $0.164E+08$ $0.491E+08$ $0.818E+08$ $0.114E+09$ $0.147E+09$
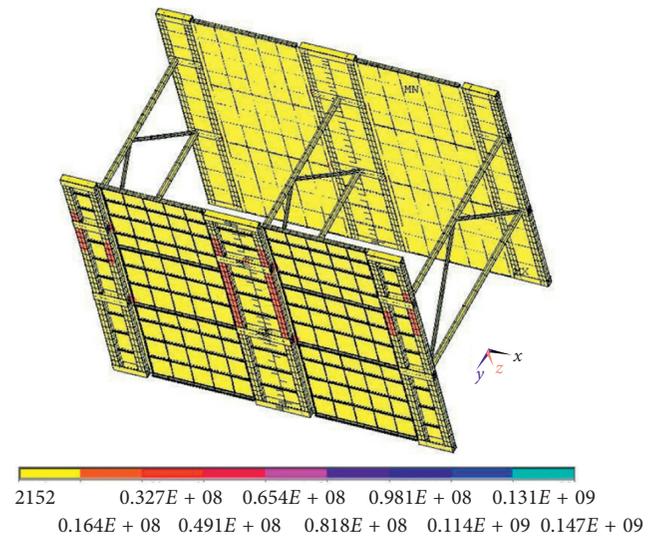
FIGURE 18: The von Mises stress nephogram of the column system (Pa).

According to actual installation requirements of the bottom beam and bracket, the all DOF of the bottom surface of six supports of the bracket was restrained.

Results for stress values of the bottom beam and bracket structure are shown in Table 9. The stress of the bottom beam and bracket was even and mostly less than 10 MPa (Figure 19). The bottom beam and bracket were in the safe working condition, so the structure was reasonable. A large stress area was concentrated inside the joint between the column and bottom beam, which was in accord with the structural characteristics of the bracket.

In conclusion, the stress of the bottom beam and bracket was less than the failure stress. From the stress nephogram, the stress and deformation of the assembly were even and change regularly. The stress and main deformation area were concentrated in the middle mudsill, the front and back mudsill, and the joint between the bracket and bottom beam. So the structure design was reasonable. The structural safety was high and the design was conservative, so the lightweight optimization design was feasible.

4.4. Global Analysis. According to the industry habits, the load of main structure of the electrostatic precipitator was

TABLE 8: The load information of the bottom beam and bracket.

Static load	Snow load	Live load	Ash load	Ash bucket load	Temperature load
472683 N	18466 N	295456 N	179144 N	688977 N	200°C

TABLE 9: The maximum principal stress and maximum von Mises stress of the bottom beam and bracket component (Pa).

σ_1	σ_2	σ_3	von Mises
$0.7403E+05$	$0.2891E+05$	$-0.7324E+05$	$0.6814E+05$

TABLE 10: The maximum combined stress (MPa).

Stress intensity σ_I	von Mises σ_v
22.18	20.14

TABLE 11: The maximum normal stress and shear stress results (MPa).

σ_x	σ_y	σ_z	τ_{xy}	τ_{yz}	τ_{xz}
-8.70	-21.46	-11.00	4.03	-4.91	-4.96

TABLE 12: The maximum principal stress results (MPa).

σ_1	σ_2	σ_3
8.78	-9.89	-21.58
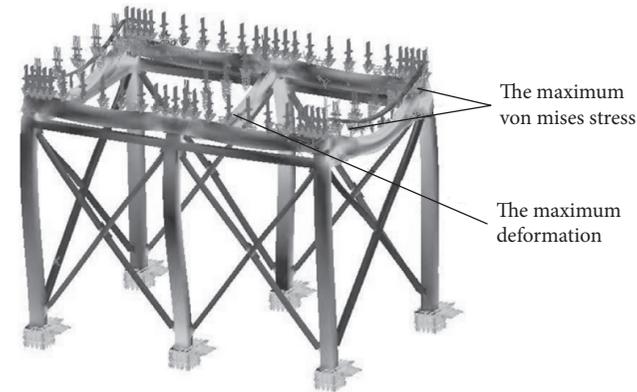
FIGURE 19: The von Mises stress nephogram of the bottom beam and bracket component (Pa).

divided into three types: static load, live load, and temperature load. After assembly of all components, the freedom in the X, Y, and Z direction of the six stand bars of the bracket was restrained. The column components were braced against the mudsills upside bracket, and only the narrow column bottom in the foremost front of the picture was fixed (i.e., the freedom in the X, Y, and Z direction was restrained). The bottom of the other 5 columns was supported by the ball, so that the upper part of the bottom beam can freely stretch in the horizontal direction, reducing additional stress.

From the results in Tables 10–12, the material strength had adequate reserves. The maximum von Mises stress is 20.14 MPa. From the stress nephogram in Figure 20, the stress in the web plate of three girders, roof slab, and side wall slab was small, while the stress in the column, column support, and bracket was larger relatively. Because the structure of the bottom beam was strong, its overall stress was small and changed evenly. The stress in rest parts changed evenly, and the maximum stress was at the joint between the column in the side of positive Z direction and column supports.

In conclusion, the main structure of this type of electrostatic precipitator had adequate reserves. The stress of the total structure was uniform and even, so the structure design was reasonable. However, the safety factor was large, so the lightweight optimization design was feasible.

5. Lightweight Optimization Design

5.1. Defining Design Variables. Taking the sizes of the beam, column, bracket plate, and various types of steel sections

357.282	0.567E + 07	0.113E + 08

0.113E + 08	0.170E + 08	0.227E + 08

FIGURE 20: The von Mises stress nephogram of the main structure of the electrostatic precipitator (MPa).

as the object, 26 design variables (Table 13) were selected to form the design variable vector $X = (x_1, x_2,..., x_{26})^T$. Among them, there were 6 variables in the top beam part, 12 in column and side wall part, and 8 in bottom beam and bracket part.

TABLE 13: The optimization results.

Design variable		Optimal value (m)	Revised value (m)	Comments
Top beam (Figures 2 and 3)	DL_SGB	$0.300E - 2$	$0.450E - 2$	DL_SGB, DL_XGB, DL_FUB, DL_DUB, DL_GEB1, DL_GEB2, LZ_GB5, LZ_GB12, LZ_H_T, Z_M_T1, Z_M_T2, Z_LZ_T. Due to the limit of width and length, hot rolled heavy steel plate (GB/T709-1998) was selected [36] and those sizes of 0.004 m were all optimized to 0.0045 m; LZ_CAO was originally 20# channel steel size. Due to the structural relationship, this channel steel can only choose 20 or 20a channel steel. Therefore, the size of 0.0040045 m was optimized to 20a cannel steel size of 0.007 m (GB/T 707-1988) [37]; LZ_H_W was the structure size of the connection between the column and column support. Due to the structural relationship, the size of 0.19 m was optimized to 0.2 m; LZ_J1W, LZ_J1H, LZ_J1D were originally 10/6.3 scalene angle steel $100 \times 63 \times 6$. According to optimization, those sizes were revised to 5/3.2 scalene angle $50 \times 32 \times 4$ (GB/T 9787-1988) [38]; LZ_ZHI_O, LZ_ZHI_I, LZ_LA_O, and LZ_LA_I were the geometric sizes of the column support of contacting column, and the column support was the hollow steel pipe. Taking into account the choice of materials, those sizes were revised to 0.086 m, 0.082 m, 0.053 m, and 0.049 m; Z_T_W, Z_T_H, Z_T_T1, and Z_T_T2 were the sizes of the original structure which was composed of two 14# equal-leg angle steel. According to the optimization, the structure was revised to 9# equal-leg angle steel composite structure (GB/T 9787-1988) [38], those sizes were revised, respectively, to 0.180 m, 0.09 m, 0.006 m, and 0.012 m.
	DL_XGB	$0.300E - 2$	$0.450E - 2$	
	DL_FUB	$0.400E - 2$	$0.450E - 2$	
	DL_DUB	$0.400E - 2$	$0.450E - 2$	
	DL_GEB1	$0.400E - 2$	$0.450E - 2$	
	DL_GEB2	$0.400E - 2$	$0.450E - 2$	
Column and side wall (Figures 4–6)	LZ_GB5	$0.300E - 2$	$0.450E - 2$	
	LZ_GB12	$0.400E - 2$	$0.450E - 2$	
	LZ_CAO	$0.400E - 2$	$0.700E - 2$	
	LZ_H_W	0.190	0.200	
	LZ_H_T	$0.400E - 2$	$0.450E - 2$	
	LZ_J1W	$0.310E - 1$	$0.320E - 1$	
	LZ_J1H	$0.450E - 1$	$0.500E - 1$	
	LZ_J1D	$0.300E - 2$	$0.400E - 2$	
	LZ_ZHI_O	$0.830E - 1$	$0.860E - 1$	
	LZ_ZHI_I	$0.820E - 1$	$0.820E - 1$	
	LZ_LA_O	$0.500E - 1$	$0.530E - 1$	
	LZ_LA_I	$0.490E - 1$	$0.490E - 1$	
Bottom beam and bracket (Figures 7–9)	Z_M_T1	$0.400E - 2$	$0.450E - 2$	
	Z_M_T2	$0.400E - 2$	$0.450E - 2$	
	Z_T_W	0.145	0.180	
	Z_T_H	$0.850E - 1$	$0.900E - 1$	
	Z_T_T1	$0.400E - 2$	$0.600E - 2$	
	Z_T_T2	$0.913E - 2$	$0.120E - 1$	
	Z_LZ_T	$0.400E - 2$	$0.450E - 2$	
	Z_LZ_H	0.240	0.280	
WT (kg)		49,239.35	53,645.68	

Model weight: 72,344.11 kg; optimal weight: 49,239.35 kg (compared with the model weight, the optimal weight decreased by 23,104.76 kg and the objective function decreased by 31.94%); revised weight: 53,645.68 kg (compared with the model weight, the revised weight decreased by 18,698.43 kg and the objective function decreased by 25.84%).

The design variables of DL_SGB, DL_XGB, DL_FUB, DL_DUB, DL_GEB1, and DL_GEB2 belong to the top beam (Figures 2 and 3).

The design variables of LZ_GB5, LZ_GB12, LZ_CAO, LZ_H_W, LZ_H_T, LZ_J1W, LZ_J1H, LZ_J1D, LZ_ZHI_O, LZ_ZHI_I, LZ_LA_O, and LZ_LA_I belong to the column and side wall (Figures 4–6).

The design variables of Z_M_T1, Z_M_T2, Z_T_W, Z_T_H, Z_T_T1, Z_T_T2, Z_LZ_T, and Z_LZ_H belong to the bottom beam and bracket (Figures 7–9).

5.2. Defining State Variables.
The state variable was the maximum von Mises stress SMAX. SMAX only defined the upper limit. The material of main structure was Q235 steel, and the yield limit (failure stress) of the material was 185~235 MPa. According to numerous experiment and engineering practice results, the plastic material safety co-efficient in static load conditions was 1.2–1.5. Therefore, according to $(\sigma) = \sigma_s/n_s$, the material allowable stress (σ) take a conservative value $185 \div 1.5 \approx 120$ MPa, that was SMAX = $(\sigma) = 120$ MPa.

5.3. Defining Objective Function.
The total weight WT was set as the objective function to be minimized, which was a function of the design variables.

The objective function did not need a given range, but it needed to be given a convergence tolerance. The convergence tolerance of WT was set to 10 kg.

5.4. Result Analysis.
In the optimization calculation, a total of 25 iteration cycles were designed, forming 25 design sequences. Those sequences were all feasible designs, and the structural weight was optimized in the twenty-third design sequence.

Figure 21 is the objective function curve. From the figure, the weight of the structure decreased steadily and finally tended to the best design, achieving the lightest structure.

Figure 22 is the state variable curve. From the figure, with the decline of the objective function, the state variables increased gradually but did not exceed the allowable stress 120 MPa. It could be seen that all design sequences were of feasible design, and the maximum stress value tended to be stable in the last few iterations and finally achieved the optimal design.

After finishing arranging the result data, from Table 13, it could be seen that the effect of lightweight optimization design was obvious. The total structure weight of the simplified model was 72,344.11 kg. After optimization, compared with the simplified model, the total structure weight

(×10**1)
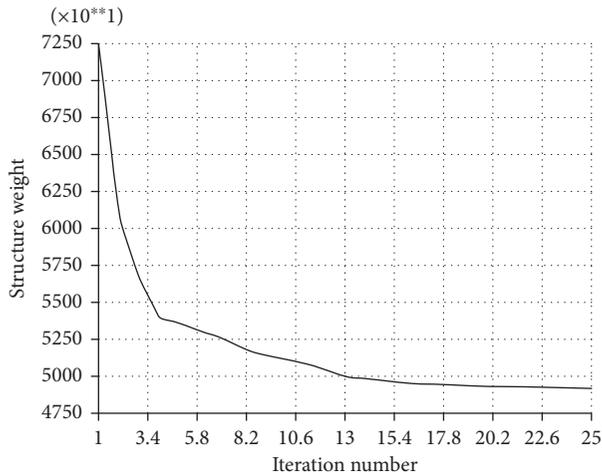
Figure 21: The objective function curve.

(×10**5)
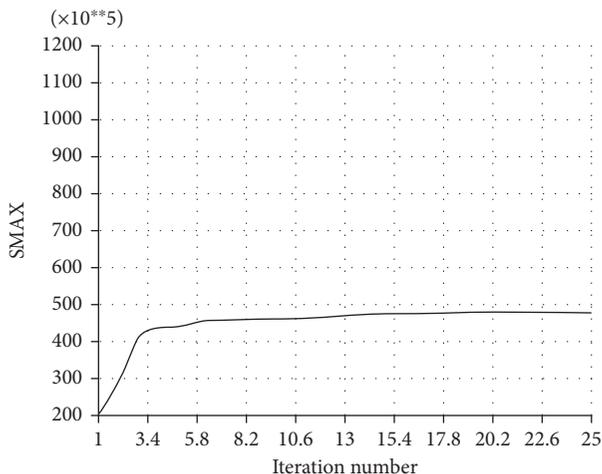
Figure 22: The state variable curve.

was reduced by 31.94% and the total weight decreased by about 25.84% after rounding off the parameter values.

6. Conclusion

(1) The geometric modeling and finite element modeling of the whole structure of the electrostatic precipitator and main components consisting of top beam, column, bottom beam, and bracket were finished in this study. Based on detailed discussion of load transfer information and boundary simulation, the strength calculation was completed. As a result, the design of the whole structure of electrostatic precipitator and the main components were reasonable. In the work, the structure was in a balanced state, and the working condition was safe and reliable. The stress was flat. The stress variation was even, and the stress distribution was regular. However, the safety factor was large, resulting in a waste of material, and the lightweight optimization design was feasible.

(2) On the basis of finite element analysis and CAE optimization analysis method, the dimension parameters of the main whole structure model of electrostatic precipitator were optimized. After optimization, more reasonable structural design parameters were obtained. The model weight is 72,344.11 kg, the optimal weight is 49,239.35 kg, and the revised weight is 53,645.68 kg. Compared with the model weight, the optimal weight decreased by 23,104.76 kg and the objective function decreased by 31.94%, while the revised weight decreased by 18,698.43 kg and the objective function decreased by 25.84%.

Conflicts of Interest

The authors declare that they have no financial and personal relationships with other people or organizations that can inappropriately influence their work, and there is no professional or other personal interest of any nature or kind in any product, service, and/or company that could be construed as influencing the position presented in the manuscript.

Acknowledgments

References

[1] J. Huang, H. Wang, Y. Shi et al., "Performance of a pilot-scale wet electrostatic precipitator for the control of sulfuric acid mist," *Environmental Science and Pollution Research*, vol. 23, no. 19, pp. 19219–19228, 2016.

[2] H. Bin, Z. Lin, Y. Yang, L. Fei, L. Cai, and Y. Linjun, "PM2.5 and SO_3 collaborative removal in electrostatic precipitator," *Powder Technology*, vol. 318, pp. 484–490, 2017.

[3] Y.-C. Ahn, S.-D. Kim, S.-H. Lee et al., "Physical, chemical and electrical analysis of dust generated from cement plants for dust removal with an electrostatic precipitator," *Korean Journal of Chemical Engineering*, vol. 21, no. 1, pp. 182–186, 2004.

[4] A. Berhardt, F. Lezsovits, and B. Groß, "Integrated electrostatic precipitator for small-scaled biomass boilers," *Chemical Engineering & Technology*, vol. 40, no. 2, pp. 278–288, 2017.

[5] J. I. Levy, L. Biton, P. K. Hopke, K. M. Zhang, and L. Rector, "A cost-benefit analysis of a pellet boiler with electrostatic precipitator versus conventional biomass technology: a case study of an institutional boiler in Syracuse, New York," *Environmental Research*, vol. 156, pp. 312–319, 2017.

[6] F. Kherbouche, Y. Benmimoun, A. Tilmatine, A. Zouaghi, and N. Zouzou, "Study of a new electrostatic precipitator with asymmetrical wire-to-cylinder configuration for cement particles collection," *Journal of Electrostatics*, vol. 83, pp. 7–15, 2016.

[7] S. Qiao, X. Han, K. Zhou, and W. Li, "Conceptual configuration and seismic performance of high-rise steel braced

frame," *Steel and Composite Structures*, vol. 23, no. 2, pp. 173–186, 2017.

[8] G. Toutant, Y. B. Minouei, A. Imanpour, S. Koboevic, and R. Tremblay, "Stability of steel columns in steel concentrically braced frames subjected to seismic loading," in *Proceedings of Structures Congress 2017: Buildings and Special Structures*, pp. 143–154, Denver, CO, USA, April 2017.

[9] C. Huang, X. Ma, M. Wang, Y. Sun, C. Zhang, and H. Tong, "Property of the PVC dust collecting plate used in wet membrane electrostatic precipitator," *IEEE Transactions on Plasma Science*, vol. 42, no. 11, pp. 3520–3528, 2014.

[10] Z. Feng, Z. Long, and T. Yu, "Filtration characteristics of fibrous filter following an electrostatic precipitator," *Journal of Electrostatics*, vol. 83, pp. 52–62, 2016.

[11] Z. He, E. T. Mohan Dass, and G. Karthik, "Design of electrostatic precipitator to remove suspended micro particulate matter from gas turbine inlet airflow: part I. Experimental study," *Journal of Aerosol Science*, vol. 108, pp. 14–28, 2017.

[12] T.-C. Hsiao, H.-C. Chuang, C.-W. Chen, T.-J. Cheng, and Y. C. C. Chien, "Development and collection efficiency of an electrostatic precipitator for in-vitro toxicity studies of nano- and submicron-sized aerosols," *Journal of the Taiwan Institute of Chemical Engineers*, vol. 72, pp. 1–9, 2017.

[13] Z. Qi, J. Li, D. Wu, X. Wie, X. Li, and C. Liu, "Particulate matter emission characteristics and removal efficiencies of a low-low temperature electrostatic precipitator," *Energy & Fuels*, vol. 31, no. 2, pp. 1741–1746, 2017.

[14] J. Li, X. Li, C. Zhou et al., "Correlation between polycyclic aromatic hydrocarbon concentration and particulate matter during the removal process of a low-low temperature electrostatic precipitator," *Energy & Fuels*, vol. 31, no. 7, pp. 7256–7262, 2017.

[15] C. Lanzerstorfer and D. Steiner, "Characterization of sintering dust collected in the various fields of the electrostatic precipitator," *Environmental Technology*, vol. 37, no. 12, pp. 1559–1567, 2016.

[16] C. Lu, C. Yi, R. Yi, and S. Liu, "Analysis of the operating parameters of a vortex electrostatic precipitator," *Plasma Science & Technology*, vol. 19, no. 2, p. 025504, 2017.

[17] S. Arif, D. J. Branken, R. C. Everson, H. W. J. P. Neomagus, L. A. le Grange, and A. Arif, "CFD modeling of particle charging and collection in electrostatic precipitators," *Journal of Electrostatics*, vol. 84, pp. 10–22, 2016.

[18] S. Zou, Y. Liao, S. Xiong, N. Huang, Y. Geng, and S. Yang, "H_2S-Modified Fe-Ti spinel: a recyclable magnetic sorbent for recovering gaseous elemental mercury from flue gas as a co-benefit of wet electrostatic precipitators," *Environmental Science & Technology*, vol. 51, no. 6, pp. 3426–3434, 2017.

[19] T. H. Jun, M. J. Kim, S. Kim, Y. H. Jung, H.-R. Moon, and K.-S. Kim, "Evaluation of activated carbon-coated electrode in electrostatic precipitator and its regeneration for volatile organic compounds removal," *Water Air and Soil Pollution*, vol. 228, no. 3, p. 110, 2017.

[20] M. Ali, K. Alam, Y. T. A. Al-Majali, and M. Kennedy, "Novel hybrid composite discharge electrode for electrostatic precipitator," *Journal of the Air & Waste Management Association*, vol. 67, no. 9, pp. 1036–1045, 2017.

[21] J. Ji and X. Ding, "Stiffener layout optimization of inlet structure for electrostatic precipitator by improved adaptive growth method," *Advances in Mechanical Engineering*, vol. 6, p. 979604, 2014.

[22] R. S. Adhav, A. Samad, and F. Kenyery, "Optimal designs of an ESP to handle upto 10% GVF," *International Journal of Oil Gas and Coal Technology*, vol. 13, no. 4, pp. 338–358, 2016.

[23] H. Shinde, A. Sangle, S. Shendkar et al., "Optimization of vibration of collecting plates of electrostatic precipitator through FEA," in *Lecture Notes in Mechanical Engineering*, pp. 455–460, Springer, Berlin, Germany, 2016.

[24] N. Hamou, A. Massinissa, A. Hakim, and Z. Youcef, "Finite element method investigation of electrostatic precipitator performance," *International Journal of Numerical Modelling: Electronic Networks, Devices and Fields*, vol. 28, no. 2, pp. 138–154, 2015.

[25] M. Aydin Komur and M. Sonmez, "Elastic buckling of perforated plates subjected to linearly varying in-plane loading," *Structural Engineering and Mechanics*, vol. 28, no. 3, pp. 353–356, 2008.

[26] D. Coutu, V. Brailovski, and P. Terriault, "Promising benefits of an active-extrados morphing laminar wing," *Journal of Aircraft*, vol. 46, no. 2, pp. 730–731, 2009.

[27] Z. Xiao-Shun, Z. Ding-Guo, and C. Si-Jia, "Several dynamic models of a large deformation flexible beam based on the absolute nodal coordinate formulation," *Acta Physica Sinica*, vol. 65, no. 9, p. 094501, 2016.

[28] Y.-L. Guo, P. Zhou, M.-Z. Wang, Y.-L. Pi, M. A. Bradford, and J.-Z. Tong, "Experimental and numerical studies of hysteretic response of triple-truss-confined buckling-restrained braces," *Engineering Structures*, vol. 148, pp. 157–174, 2017.

[29] G. Vasudevan and S. Kothandaraman, "RC beams retrofitted using external bars with additional anchorages-a finite element study," *Computers and Concrete*, vol. 16, no. 3, pp. 415–428, 2015.

[30] G. Vasudevan and S. Kothandaraman, "Finite element analysis of bearing capacity of RC beams retrofitted with external bars," *Strength of Materials*, vol. 46, no. 6, pp. 831–842, 2014.

[31] P. Yang, J. Gong, H. Yang, and X. Tang, "Fatigue analysis on thermal characteristics for PBGA by using finite element method," *Journal of Thermal Stresses*, vol. 37, no. 9, pp. 1052–1065, 2014.

[32] H. Chen, Z. Lu, and T. Guo, "A hybrid dynamic mesh generation method for multi-block structured grid," *Advances in Applied Mathematics and Mechanics*, vol. 9, no. 4, pp. 887–903, 2017.

[33] D. Jarema, H. J. Bungartz, T. Goerler, F. Jenko, T. Neckel, and D. Told, "Block-structured grids in full velocity space for Eulerian gyrokinetic simulations," *Computer Physics Communications*, vol. 215, pp. 49–62, 2017.

[34] S. Krishnan, E. S. G. Shaqfeh, and G. Iaccarino, "Fully resolved viscoelastic particulate simulations using unstructured grids," *Journal of Computational Physics*, vol. 338, pp. 313–338, 2017.

[35] G. Hu, "A numerical study of 2D detonation waves with adaptive finite volume methods on unstructured grids," *Journal of Computational Physics*, vol. 331, pp. 297–311, 2017.

[36] Chinese National Standard-GB/T 709-1988, *Dimension, Shape, Weight and Tolerances for Hot-Rolled Plates and Sheets*, 1988.

[37] Chinese National Standard-GB/T 707-1988, *Dimension, Shape, Weight and Tolerances for Hot-Rolled Channel Angle Steel*, 1988.

[38] Chinese National Standard-GB/T 9787-1988, *Dimension, Shape, Weight and Tolerances for Hot-Rolled Equal-Leg Angle Steel*, 1988.